LIPID-PROTEIN MESOPHASES AND CELL ORGANELLE ULTRASTRUCTURE IN HEALTH AND DISEASE

EDITED BY: Yuru Deng, Angelina Angelova, George Attard and
Shamim Hossain
PUBLISHED IN: Frontiers in Cell and Developmental Biology and
Frontiers in Physiology

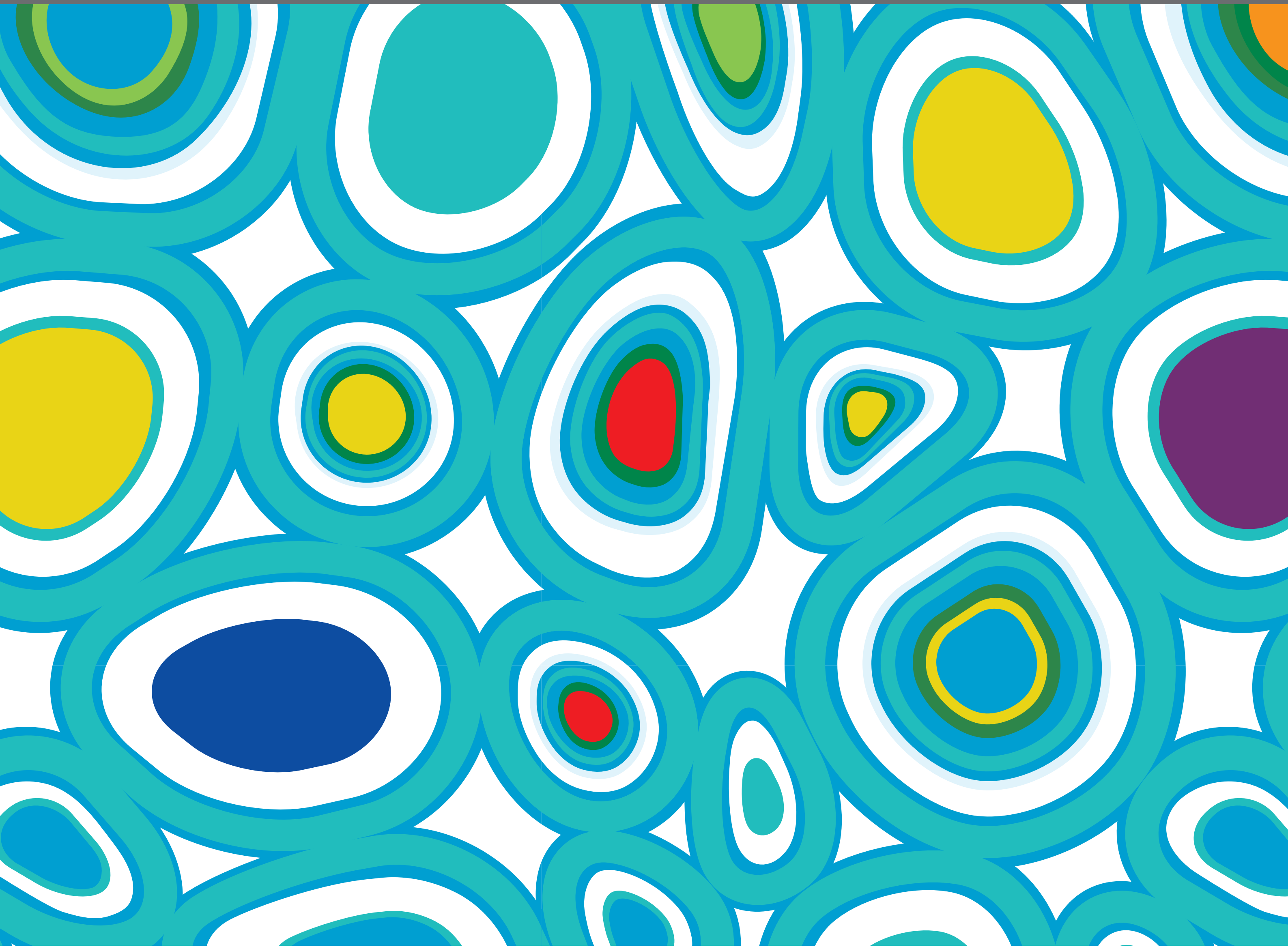

frontiers Research Topics

ISSN 1664-8714
ISBN 978-2-88971-713-2
DOI 10.3389/978-2-88971-713-2

About Frontiers

Frontiers is more than just an open-access publisher of scholarly articles: it is a pioneering approach to the world of academia, radically improving the way scholarly research is managed. The grand vision of Frontiers is a world where all people have an equal opportunity to seek, share and generate knowledge. Frontiers provides immediate and permanent online open access to all its publications, but this alone is not enough to realize our grand goals.

Frontiers Journal Series

The Frontiers Journal Series is a multi-tier and interdisciplinary set of open-access, online journals, promising a paradigm shift from the current review, selection and dissemination processes in academic publishing. All Frontiers journals are driven by researchers for researchers; therefore, they constitute a service to the scholarly community. At the same time, the Frontiers Journal Series operates on a revolutionary invention, the tiered publishing system, initially addressing specific communities of scholars, and gradually climbing up to broader public understanding, thus serving the interests of the lay society, too.

Dedication to Quality

Each Frontiers article is a landmark of the highest quality, thanks to genuinely collaborative interactions between authors and review editors, who include some of the world's best academicians. Research must be certified by peers before entering a stream of knowledge that may eventually reach the public - and shape society; therefore, Frontiers only applies the most rigorous and unbiased reviews.
Frontiers revolutionizes research publishing by freely delivering the most outstanding research, evaluated with no bias from both the academic and social point of view. By applying the most advanced information technologies, Frontiers is catapulting scholarly publishing into a new generation.

What are Frontiers Research Topics?

Frontiers Research Topics are very popular trademarks of the Frontiers Journals Series: they are collections of at least ten articles, all centered on a particular subject. With their unique mix of varied contributions from Original Research to Review Articles, Frontiers Research Topics unify the most influential researchers, the latest key findings and historical advances in a hot research area! Find out more on how to host your own Frontiers Research Topic or contribute to one as an author by contacting the Frontiers Editorial Office: frontiersin.org/about/contact

LIPID-PROTEIN MESOPHASES AND CELL ORGANELLE ULTRASTRUCTURE IN HEALTH AND DISEASE

Topic Editors:
Yuru Deng, University of Chinese Academy of Sciences, China
Angelina Angelova, UMR8612 Institut Galien Paris Sud (IGPS), France
George Attard, University of Southampton, United Kingdom
Shamim Hossain, Kyushu University, Japan

Citation: Deng, Y., Angelova, A., Attard, G., Hossain, S., eds. (2021). Lipid-Protein Mesophases and Cell Organelle Ultrastructure in Health and Disease. Lausanne: Frontiers Media SA. doi: 10.3389/978-2-88971-713-2

Table of Contents

frontiers
in Cell and Developmental Biology

ORIGINAL RESEARCH
published: 28 May 2020
doi: 10.3389/fcell.2020.00404

Construction of *Escherichia coli* Whole-Cell Biosensors for Statin Efficacy and Production Test

Huanjie Li[1,2,3†], Qingda Wang[2], Rui Zhao[2], Yunshan Wang[1,3], Luying Xun[2,4] and Huaiwei Liu[2*†]

[1] School of Medicine, Cheeloo College of Medicine, Shandong University, Jinan, China, [2] State Key Laboratory of Microbial Technology, Shandong University, Qingdao, China, [3] Medical Research and Laboratory Diagnostic Center, Jinan Central Hospital, Cheeloo College of Medicine, Shandong University, Jinan, China, [4] School of Molecular Biosciences, Washington State University, Pullman, WA, United States

Statins are widely used cholesterol-lowering drugs. Their potential application in anti-cancer treatment is also under investigation. The individual variance in statin response has been observed, which may be caused by the variation in human HMG-CoA reductase (hHMGR)—the inhibition target of statin drugs. Herein, we reported the design and construction of two *Escherichia coli* whole-cell biosensors. The first one is statin-efficacy testing sensor, which is composed of two separate modules: a hybrid mevalonate (MVA) pathway and a HMG-CoA sensing system. A truncated hHMGR was used as the key enzyme of the MVA pathway and a promiscuous transcription factor (TF) BsFapR was used as the HMG-CoA sensor. When hHMGR was inhibited by statins, HMG-CoA accumulated intracellularly and was sensed by BsFapR, which subsequently turned on its cognate promoter. This biosensor has the potential to be used as a "precision medicine" tool—selecting potent statin drugs for individual patients. The second one is a statin-production testing sensor, which is based on another promiscuous TF AraCM that can sense statins. This biosensor can be used in optimization of statin-producing strains. The prototypes of these two biosensors were successfully constructed and their further optimization is highly expected.

Keywords: synthetic biology, biosensor, statin, precision medicine, HMGR

OPEN ACCESS

Edited by:
Angelina Angelova,
UMR 8612 Institut Galien Paris Sud (IGPS), France

Reviewed by:
Maria Antonietta Vanoni,
University of Milan, Italy
Francesca Aiello,
University of Calabria, Italy

****Correspondence:***
Huaiwei Liu
liuhuaiwei@sdu.edu.cn

†ORCID:
Huanjie Li
orcid.org/0000-0002-4997-0927
Huaiwei Liu
orcid.org/0000-0002-0483-5318

Specialty section:
This article was submitted to Cellular Biochemistry, a section of the journal Frontiers in Cell and Developmental Biology

Received: *31 March 2020*
Accepted: *04 May 2020*
Published: *28 May 2020*

Citation:
Li H, Wang Q, Zhao R, Wang Y, Xun L and Liu H (2020) Construction of Escherichia coli Whole-Cell Biosensors for Statin Efficacy and Production Test. Front. Cell Dev. Biol. 8:404. doi: 10.3389/fcell.2020.00404

INTRODUCTION

Statins are a class of cholesterol-lowering drugs that are widely used in clinical practice (Rizzo et al., 2012; Garattini and Padula, 2017; Hennekens et al., 2017). They are competitive inhibitors of the HMG-CoA reductase (HMGR) that catalyzes the conversion of HMG-CoA to mevalonate (Endo, 1992; Istvan, 2003). HMGR is the rate-controlling enzyme of the mevalonate (MVA) pathway in human cell and is the target of statin inhibitors that regulate cholesterol concentration in human blood (Tabernero et al., 1999; Vögeli et al., 2019); hence, once HMGR is inhibited by statins, the cholesterol synthesis is impeded (**Figure 1A**). In addition to the usage as cholesterol-lowering medicines, recent studies also proposed the potential application of statins as anti-cancer drugs (Iannelli et al., 2018). Statins are able to affect cancer cell through mevalonate-dependent mechanisms (Mullen et al., 2016), and modulate specific signal transduction pathways to influence several cellular processes, such as angiogenesis, metastasis, apoptosis, and cell proliferation (Sopková et al., 2017). Despite the generally good treatment effect of statins, notable individual variation in response has been reported (Armitage, 2007; Wysockakapcinska et al., 2009; Sopková et al., 2017). This could be caused by the HMGR variance in different individuals. Human HMGR (hHMGR) has 1677 single nucleotide variants (NCBI), and diverse statin drugs are in the market as well; therefore, it is beneficial to construct a biosensor for pre-testing the inhibition effect of different statin drugs upon an individual hHMGR clinical treatment.

Natural statins are produced from polyketide biosynthetic pathways (PKS) of various microorganisms. For instance, lovastatin is produced by *Aspergillus terreus,* and mevastatin by *Penicillium citrinum* (Manzoni and Rollini, 2002). Tremendous efforts have been made to increase the production and yield of these strains, but their potentials have not been fully developed, mainly due to the complexity of PKS pathways and related enzymes (Campbell and Vederas, 2010). Although the biosynthesis of these compounds is not yet completely understood, rational metabolic engineering approaches targeting on construction of more efficient heterologous cell factories are on the way (Vajdić et al., 2014). For further optimization of either native or non-native statin-producing strains, development of biosensors that can quickly detect the statin production will be helpful. Until now, no such biosensor has been reported yet.

Signal-responsive transcription factors (TFs) play a major role in biosensor design (Mahr and Frunzke, 2016). The DNA binding activities of this type of TFs are affected by effectors, such as small molecules, ions, temperature, pH, or light, which subsequently lead to switch-like change of their cognate promoters (ON/OFF). These TFs can be directly applied in biosensor design (Siedler et al., 2014), or can be modified to construct non-natural biosensors (Bitzur et al., 2013; Morsut et al., 2016; Khatun et al., 2018). Herein, we reported the development of two prototypes of TF-based whole-cell biosensors. One is for statin-efficacy testing and another is for statin-production testing. For the statin-efficacy testing sensor, we used a HMG-CoA sensing TF to monitor the activity of HMGR. For the statin-production testing sensor, we employed a mutant TF that can directly sense the presence of statin. Both sensors were constructed in the *Escherichia coli* platform.

RESULTS AND DISCUSSION

Design and Computational Modeling of the Statin-Efficacy Testing Sensor

Computational modeling has become a useful tool in developing synthetic gene networks with designed functions (Gould et al., 2014; Berset et al., 2017). Herein, we used it to guide the design and construction of the statin-efficacy testing sensor. The whole design consists of two separate modules: the hHMGR-based MVA pathway module and the MVA pathway monitoring module (**Figures 1A,B**). Statins inhibit the activity of hHMGR in the first module, which causes the accumulation of HMG-CoA. This process can be modeled with an IC_{50} equation (**Figure 1C**). A linear equation is used to model the relationship between hHMGR activity and HMG-CoA concentration (**Figure 1D**). In the second module, TF sensing the accumulation of HMG-CoA and turning on the expression of a reporter, GFP (**Figure 1E**). This process is modeled by a Hill equation (**Figure 1F**). Computational modeling indicates that the hHMGR activity, HMG-CoA accumulation, and GFP expression all show responses to statin in a dose-dependent mode (**Supplementary Figure S1**), suggesting they all can be indicators of statin efficacy.

A global equation was obtained by combining the three equations (**Figure 1F**). This equation indicated the K_a value, which represents the HMG-CoA concentration inducing half turn-on of the GFP promoter, is critical for the whole design. K_a value is mainly determined by the binding affinity of HMG-CoA sensing TF. If a TF with a too high K_a is used, GFP expression cannot be turned ON even when intracellular HMG-CoA accumulates to the maximum concentration caused the completely inhibition of hHMGR by statin. In this case, GFP expression will be constantly OFF no matter statin is present or not. If a TF with a too low K_a is used, GFP expression will be turned ON at low concentrations of HMG-CoA. In this case, a low concentration/efficacy of statin can lead to maximum GFP expression. Therefore, HMG-CoA-sensing TF is the key element that determines the performance of the statin biosensor.

Expression of a Truncated hHMGR in *E. coli*

The hHMGR (GenBank: XP_011541659.1) is a transmembrane protein that contains two main domains: a conserved N-terminal sterol-sensing domain anchored in the membrane of the endoplasmic reticulum, and a C-terminal catalytic domain in the cytosol, which is also the target domain of statins (Roitelman et al., 1992). We synthesized a codon optimized ORF encoding the C-terminal domain (residues 493-908) of hHMGR. This truncated hHMGR (thHMGR) gene was ligated to pET30a plasmid and transformed into *E. coli* BL21 (DE3). The N-terminal His-tag was used for purification. SDS-PAGE analysis indicated the expressed thHMGR was soluble in *E. coli* cytoplasm (**Supplementary Figure S2A**). After purification, we assayed the activity of thHMGR. The thHMGR catalyzes the reduction of HMG-CoA to mevalonic acid using NADPH as the coenzyme. We observed the NADPH consumption evidenced by the decrease of absorbance at 340 nm, indicating that the thHMGR expressed by *E. coli* retained the catalytic activity (**Supplementary Figure S2B**). To check the sensitivity of thHMGR to statin drugs, we added different concentrations of statins to the reaction system. The activity of thHMGR was significantly inhibited by both pure simvastatin (*ps*) and statin medicine (*cm*). The IC_{50} values were calculated to be 31.19 and 22.20 μg/mL, respectively (**Figures 2A,B**). The IC_{50} value of *ps*

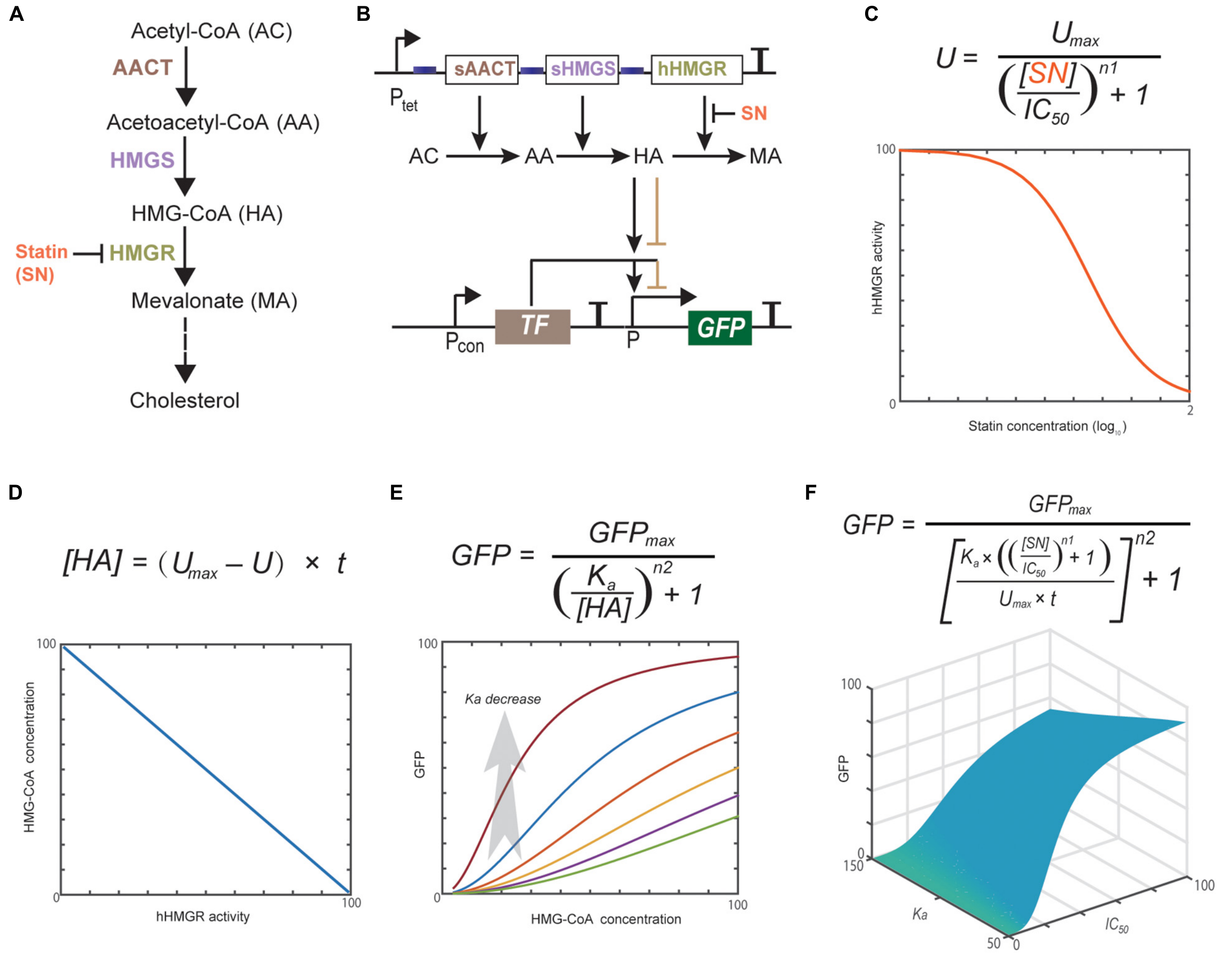

FIGURE 1 | Statins block cholesterol synthesis through inhibiting hHMGR **(A)**. Schematic representation of the whole design of statin-efficacy testing sensor **(B)** and computational modeling of the dynamics of each component **(C–F)**. Modeling parameters are provided in **Supplementary Material**. Computational modeling indicates that the hHMGR activity, HMG-CoA accumulation, and GFP expression all show responses to statin in a dose-dependent mode.

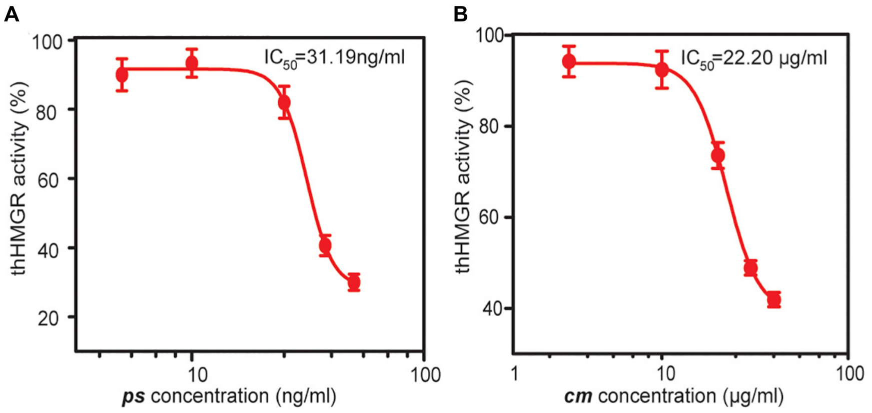

FIGURE 2 | The inhibition effects of statin drugs on thHMGR. A pure simvastatin (*ps*) **(A)** and a commercial statin medicine (*cm*) **(B)** were used to treat purified thHMGR. The activity of untreated thHMGR was defined as 100%. The IC_{50} values of simvastatin and statin medicine were calculated to be 31.19 and 22.20 μg/mL, respectively.

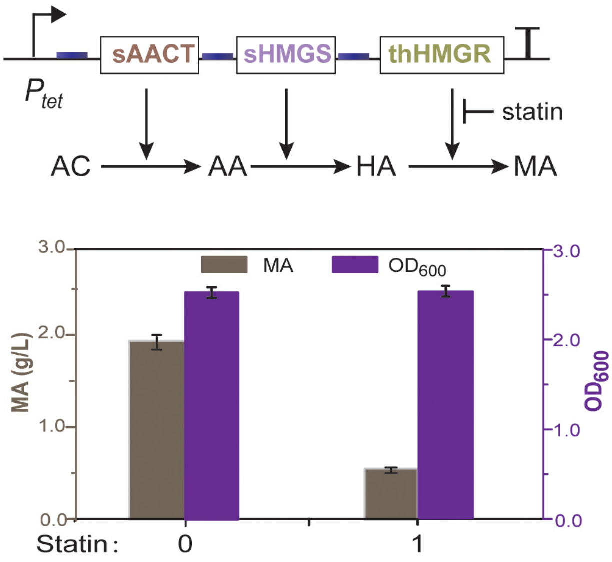

FIGURE 3 | Mevalonate production of the thHMGR-based MVA pathway. *E. coli* BL21 harboring the MVA pathway was used. Pure simvastatin (50 ng/mL) was added into the LB medium and 1.9 g/L of mevalonic acid was produced.

was three orders of magnitude lower than that of *cm*, which should be owing to *ps* is a relatively pure compound (simvastatin content ≥97%), while *cm* is clinical used drug containing much less simvastatin.

Construction of the MVA Pathway With thHMGR

To check whether *E. coli* has unspecific HMGR activity that may disturb further analysis, we first constructed an operon encoding acetyl-CoA thiolase (AACT) and HMG-CoA synthase (HMGS). These two enzymes are obtained from *Saccharomyces cerevisiae*, which can convert acetyl-CoA to HMG-CoA (**Figure 1B**). This operon was driven by an aTc (anhydrotetracycline) inducible promoter P_{tet} (P_{tet}-AACT-HMGS) and expressed in *E. coli* BL21. HPLC analysis showed that no mevalonic acid was produced after aTc induction, indicating no unspecific HMGR activity is present in *E. coli*. We then co-expressed thHMGR with AACT and HMGS as one operon, using the same promoter P_{tet} (P_{tet}-AACT-HMGS-thHMGR). HPLC analysis showed that when aTc was added, 1.9 g/L of mevalonic acid was produced (**Figure 3**). These results indicated the thHMGR-dependent MVA pathway was successfully constructed in *E. coli*. To test the inhibition effects of statin drugs at whole cell background, we added *ps* (50 ng/mL) simultaneously with aTc. The production of mevalonic acid was decreased to 0.6 g/L, indicating statin can penetrate *E. coli* cell and inhibit the intracellular thHMGR enzyme.

Construction of TF-Based Biosensor for Detecting HMG-CoA

No HMG-CoA specific TF has been reported so far. We turned to the TFs that can sense analogs of HMG-CoA. Three types of fatty acyl-CoA binding TF have been identified (Albanesi et al., 2013). FadR that binds long-chain fatty acyl-CoAs, DesT that binds unsaturated acyl-CoAs, and FapR that binds malonyl-CoA. Among them, FapR attracted our attention due to its ligand malonyl-CoA is structurally the most similar to HMG-CoA (**Figure 4A**). The FapR-ligand binding mechanism has been elucidated at structural level (Albanesi et al., 2013). Briefly, the ligand binding domain of FapR forms a "hot-dog" fold (**Figure 4B**). The malonyl moiety is involved in the binding whereas the CoA moiety locates outsides of the binding cavity. The binding of malonyl-CoA leads to series of conformational changes of FapR and finally makes it release from its DNA binding site. Hence, FapR is a derepression TF and malonyl-CoA is its native inducer.

To predict the possibility of FapR-HMG-CoA binding, we performed protein-ligand binding simulations using the AutoDock software. The *Bacillus subtilis* FapR (BsFapR, PDB: 2F3X) was used as the docking protein. The BsFapR-malonyl-CoA binding simulation gave a result very similar to the experimental confirmed conformation (**Figure 4C**), suggesting the algorithm and parameters used for BsFapR simulation was reliable. The BsFapR-HMG-CoA binding simulation produced a result having similar binding energy but higher affinity to that of BsFapR-malonyl-CoA (**Figure 4D** and **Supplementary Table S1**). These results suggested HMG-CoA can be a candidate ligand of BsFapR.

Both *in vitro* and *in vivo* experiments were performed to test the actual interaction between BsFapR and HMG-CoA. For *in vitro* experiments, BsFapR was expressed in *E. coli* BL21 (DE3) and purified using the N-terminal His-tag. A reporter DNA fragment was constructed, which contains an artificial promoter composed of P_{trc} core sequence (−10 and −35) and two FapR binding sites (*fapO*). After this promoter is the mKate reporter gene (**Figure 5A**). The purified BsFapR and constructed reporter DNA fragment were mixed in the *in vitro* transcription-translation system. If HMG-CoA can actually work as a ligand of FapR, it will induce the release of FapR from the fapO site, transcription of mKate mRNA and subsequent translation will be detected from the *in vitro* system. Results showed that high amount of mKate was synthesized when no BsFapR was present, whereas much lower amount was synthesized when BsFapR was added into the *in vitro* system. When HMG-CoA was added simultaneously with BsFapR, the amount of synthesized mKate significantly increased. As a control, when malonyl-CoA was added simultaneously with BsFapR, the amount of synthesized mKate was higher than that of HMG-CoA addition (**Figure 5B**).

For the *in vivo* experiments, a plasmid was constructed containing the reporter DNA. When the reporter plasmid was transformed into *E. coli* BL21, no obvious mKate expression was detected. However, when it was co-transformed with P_{tet}-AACT-HMGS, the HMG-CoA producing plasmid, high expression of mKate was observed. The expression could be further increased when aTc was added (**Figure 5C**). Both *in vitro* and *in vivo* results indicated that in consistent with AutoDock simulation, HMG-CoA indeed, although not as

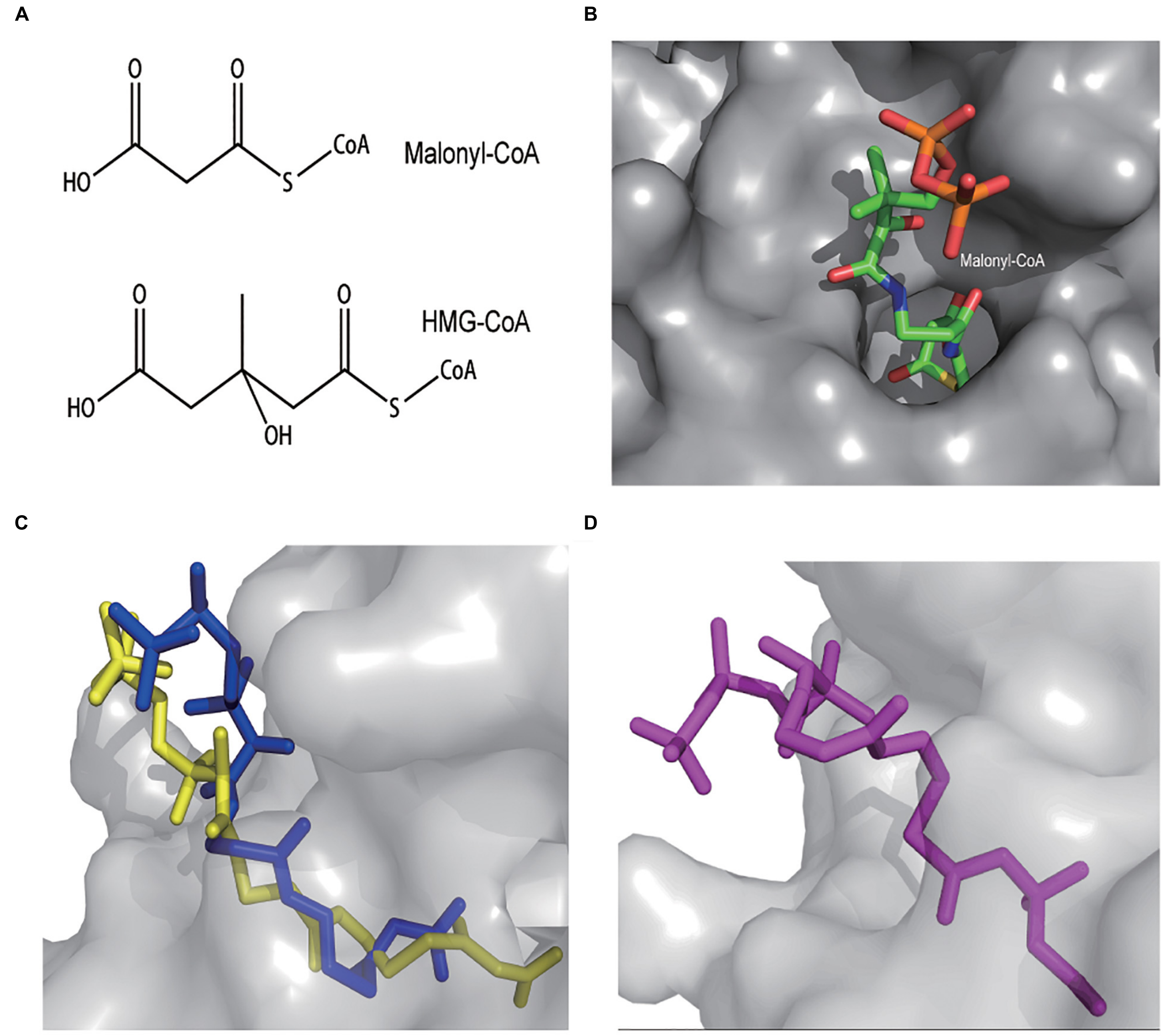

FIGURE 4 | Both malonyl-CoA and HMG-CoA have a carboxyl group and a carbonyl group **(A)**. The FapR dimer forms a "hot-dog" pocket where malonyl-CoA locates in (top view). The malonyl moiety is deeper inside whereas the CoA moiety is mostly outside **(B)**. AutoDocK simulation of BsFapR-malonyl-CoA interaction (side view). Dark blue represents the actual binding conformation determined by crystallography and light yellow represents the simulated binding conformation **(C)**. AutoDocK simulation of BsFapR-HMG-CoA interaction **(D)**.

efficient as malynol-CoA, can react with BsFapR and induce the derepression process.

Construction of the Statin-Efficacy Testing Sensor

The reporter and the P_{tet}-AACT-HMGS-thHMGR plasmids were co-transformed into BL21 to make the final whole-cell biosensor. Pure simvastatin (*ps*) was firstly tested on the obtained biosensor. Without presence of *ps*, mKate expression was low, indicating thHMGR was active. When *ps* was added (20, 50, 100, 200, 500 ng/mL), mKate expression was turned on, indicating thHMGR was inhibited by *ps*. The IC_{50} value of *ps* was calculated to be 16.36 ng/mL using the mKate fluorescence intensity as the indicator (**Figure 6A**). The commercial medicine (*cm*) were also tested (5, 10, 20, 50, 100 μg/mL) on this biosensor and its IC_{50} was calculated to be 6.04 μg/mL (**Figure 6B**). The IC_{50} values calculated from mKate intensity were about half to one third of the data calculated from the enzyme inhibition experiments (**Figure 2**). This should be caused by the relative lower sensitivity BsFapR (K_a) to HMG-CoA. Other statins with high-purity (≥97%), including lovastatin, mevastatin, pravastatin, fluvastatin were also tested by this sensor and their IC_{50} values were calculated (**Figures 6C–F**). We also performed toxicity testing experiments with these statins. None of them showed inhibition effect on growth of *E. coli* BL21 (**Supplementary Figure S3**), indicating statins only target for thHMGR in the strain.

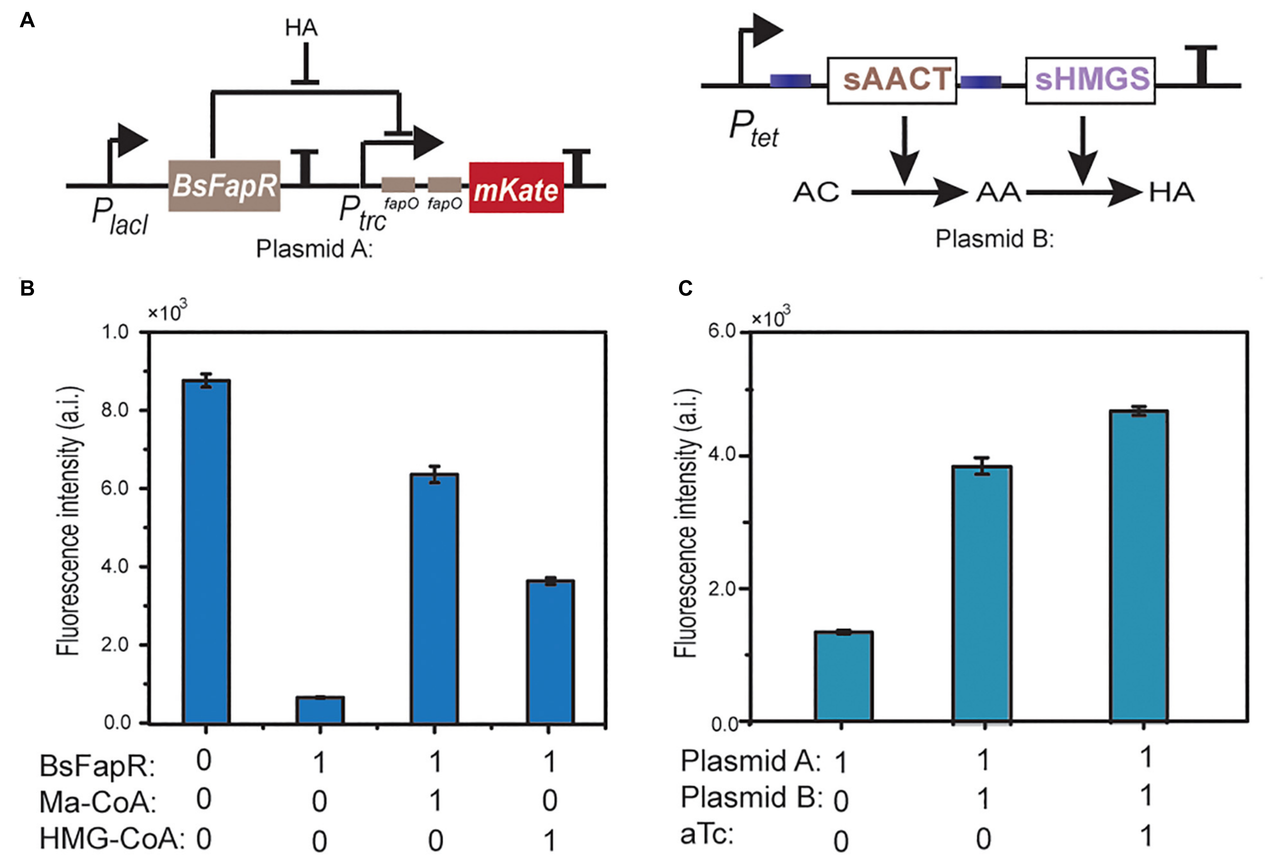

FIGURE 5 | Schematic representation of the HMG-CoA (HA) sensing module and the HMG-CoA producing module **(A)**. *In vitro* transcription-translation test of the derepression effect of HMG-CoA. A DNA fragment containing P_{trc}-(*fapO*)$_2$-mKate was used as the template. Ma-CoA represents malonyl-CoA. The number 0 represents no addition and 1 represents addition **(B)**. *In vivo* test of the derepression effect of HMG-CoA. *E. coli* BL21 containing plasmid A or both A and B plasmids were used. aTc is the inducer of P_{tet} **(C)**.

It needs to emphasize that the biosensor reported herein is the first version. Although it successfully indicates the statin efficacy difference, there is still much room for its improvement. First, the MVA pathway module needs to be further optimized. The range of mevalonate production is between 0.6 g/L (with excess statin) to 1.9 g/L (without statin), HMG-CoA production should be also in a narrow range, which limits the sensitivity of the biosensor. Using more efficient AACT and/or HMGS enzymes to enhance the metabolic flux to MVA pathway, or balance their activities should further amplify the HMG-CoA production range, hence improve the sensitivity of the sensor. Second, the binding affinity of BsFapR to HMG-CoA is critical for the statin sensor. Using protein engineering methods to construct FapR mutant with higher HMG-CoA affinity should significantly increase the sensitivity of biosensor.

Construction of the Statin-Production Testing Sensor

Compared with the statin-efficacy testing sensor, the design principle and construction of statin-production testing sensor is relatively simpler. Statins are extracellular products of some microorganisms; hence, a co-cultured strain containing a statin-sensing TF and a reporter gene can be used as a whole-cell biosensor. No such TF has been reported so far. Istvan and Deisenhofer (2001) reported that statins interact with HMGR through the carboxyl and hydroxyl groups on their tails, and the binding pocket of HMGR locates at an open zone of surface. This finding gave us a clue that the TF having a similar pocket and statin tail-like ligand may have the potential to bind statins. AraCM is a mutant of AraC (the arabinose sensing TF) that can sense mevalonic acid, whose structure is very similar to that of statin tails (**Figure 7A**). The crystal structure of AraCM is not available. We modeled its 3D structure by using SWISS-MODEL. AraC (PDB: 1XJA) at 2.4 Å resolution was used as the template (61% sequence similarity). The global QMEAN score is 0.65 for this model, implying the predicted models are valid. The AraCM-mevalonic acid binding simulation was performed using the AutoDock software. The simulation results showed that mevalonic acid binding site locates at a pocket of AraCM surface (**Figure 7B**).

Based on this finding, we constructed a statin-sensing plasmid, which contains AraCM, its cognate promoter P_{bad}, and the GFP reporting gene (**Figure 7C**). The plasmid was transformed into *E. coli* BL21. Pure compounds of simvastatin, lovastatin,

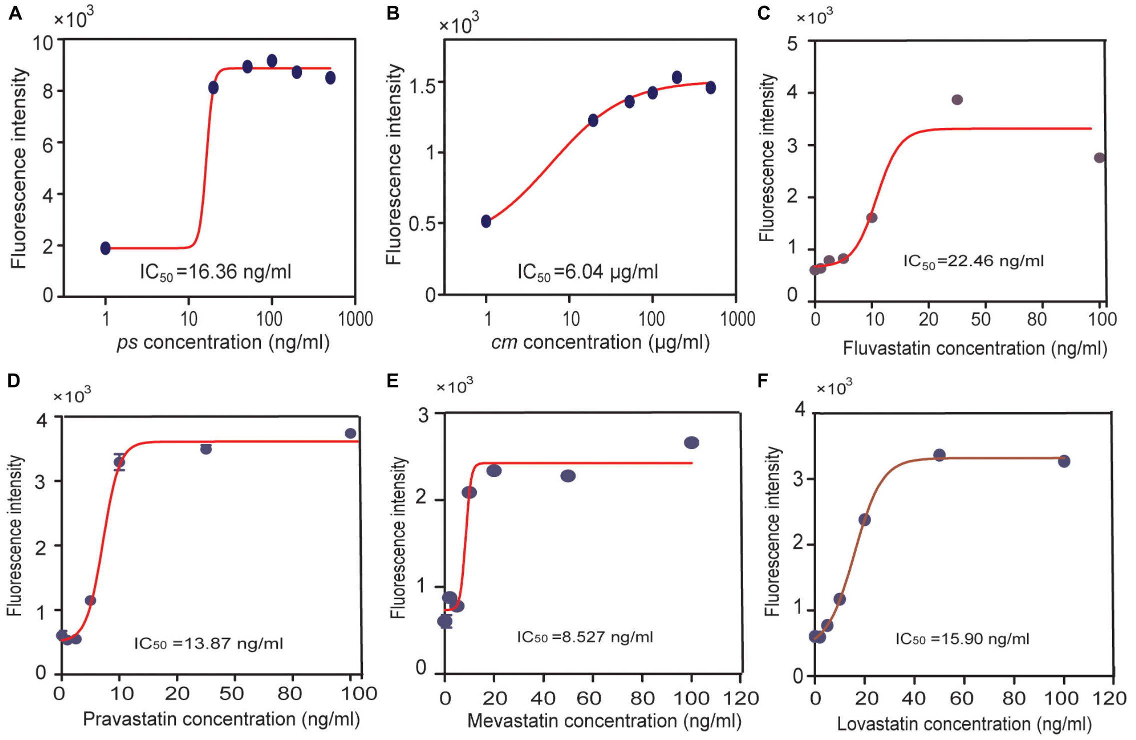

FIGURE 6 | Using the statin-efficacy testing sensor in drug test. *E. coli* BL21 harboring both the reporter and the P_{tet}-AACT-HMGS-thHMGR plasmids were used. A pure simvastatin (*ps*), **(A)** a commercial simvastatin containing drug (*cm*), **(B)** and other statins were tested including fluvastatin **(C)**, pravastatin **(D)**, mevastatin **(E)**, lovastatin **(F)**. IC_{50} values of different statins were all tested by this sensor and calculated.

fluvastatin, pravastatin, and mevastatin were used to treat the plasmid containing *E. coli*. All statins induced more or less expression of GFP, and dose-response relationships were also observed (**Figure 7D**). These results indicated that AraCM indeed can sense statins and the statin-sensing biosensor was successfully constructed. The AraCM-based sensor can be introduced into statin-producing strains directly, or the *E. coli* containing AraCM-based sensor can be co-cultured with statin-producing strains for screening more efficient statin-producing cell factories. It is noteworthy that the increase of GFP expression caused by statins were less than twofold, indicating the sensitivity of AraCM to statins is limited. To construct more sensitive biosensors, further screening more statin-sensitive TFs or modifying AraCM with protein engineering methods is required.

CONCLUSION

In conclusion, we successfully developed two prototypes of statin biosensors. The first one has the potential to be used as a tool for "precision medicine." Among the 1677 single NCBI of hHMGR, 176 are missense variants and 11 are frame-shift variants, which alters the amino acid sequence of hHMGR. Statins are one of the most commonly used medications to lower cholesterol (Ahmed et al., 2020), which have been known to cause various side effects such as muscle pain, muscle weakness, rhabdomyolysis, especially high-dosage statins (Bitzur et al., 2013; Ahmed et al., 2020; Won et al., 2020). By replacing the thHMGR gene with the individual's variant in the statin-efficacy testing sensor, we can test which statin drug has the best inhibition effect on his/her HMGR activity, and what is the best dosage. Based on this test, we can provide personal tailored therapy plan, and hence it is possible to control the usage of statins and avoid side effect of the drugs, such targeting a drug(s) to an individual patient or a subclass of patients is a strategy of precision medicine. The second biosensor can be used for screening of statin-producing strains. The AraCM based reporter also can be transferred into statin-producing strains, which may work as a useful tool for strain optimization or metabolic engineering modification.

There are still some weaknesses in application of sensors, such as the human-derived proteins being expressed in *E. coli* requiring future optimization, as well as solubility problems of statins during the experiment. These issues may be the limiting aspects of sensor applications. Further optimization of these two biosensors with more rounds of "design-construction-test-learn" cycles is expected.

MATERIALS AND METHODS

Strains and Growth Conditions

Escherichia coli DH5α was used as the plasmid construction host, *E. coli* BL21 (DE3) was used as the protein expression

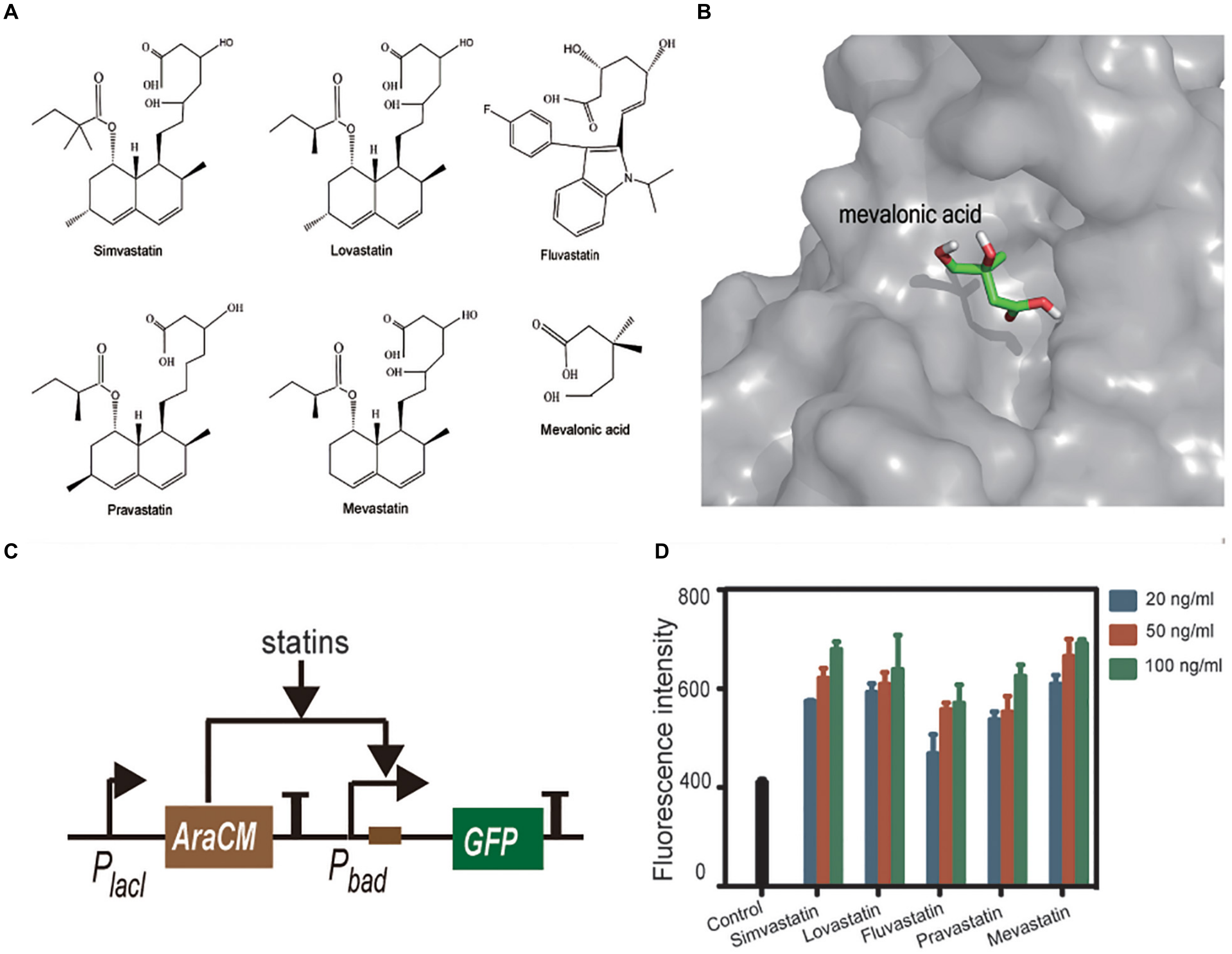

FIGURE 7 | Statins **1** and mevalonic acid **2** in linear form **(A)**. AutoDockK simulation of AraCM-mevalonic acid interaction **(B)**. Schematic presentation of the statin sensing circuit **(C)**. Statins were tested in *E. coli* BL21 containing the statin-sensing plasmid. Control is the strain without statin treatment. All statins induced more or less expression of GFP, and dose-response relationships were also observed **(D)**.

host and the biosensor construction platform. Luria-Bertani (LB) medium (1% NaCl, 0.5% yeast extract, and 1% tryptone) was used for *E. coli* cultivation. When needed, antibiotics were added at required concentration. Simvastatin (*ps*) was purchased from Sigma-Aldrich, commercial simvastatin containing drug (*cm*) was purchased from a local pharmacy, lovastatin, mevastatin, pravastatin, and fluvastatin were purchased from MedChem Express.

Plasmid Construction and DNA Manipulation

Plasmids used in this study are listed in **Table 1** and primers are listed in **Supplementary Table S2**. Plasmid construction was performed using the In-Fusion method (Invitrogen). The ORF of thHMGR sequence was synthesized by the BGI Company and its codon was adapted to fit the *E. coli* translation system. The ORF of BsFapR was cloned from *B. subtilis* and the ORF of AraC was cloned from *E. coli* DH5α. Site-specific mutations were performed on AraC to make AraCM using a previously reported method (Roitelman et al., 1992).

Protein Expression and Purification

The protein ORFs were cloned into vector pET30a at the *Bam*HI and *Xho*I sites with an N-terminal His-tag. The recombinant plasmids were transformed into *E. coli* BL21 (DE3). The recombinant *E. coli* was grown in LB at 30°C with shaking until $OD_{600\ nm}$ reached about 0.6. When isopropyl-β-D-thiogalactopyranoside (IPTG) was added, the final concentration was 0.2 mM, and the cells were further cultivated at 16°C for 20 h. Cells were harvested via centrifugation, washed twice with ice-cold lysis buffer (50 mM NaH_2PO_4, 300 mM NaCl, and 20 mM imidazole, pH 8.0), and broken through the high pressure crusher SPCH-18 (STANSTED). Cells were removed via centrifugation and the supernatant was loaded onto the nickel-nitrilotriacetic acid (Ni-NTA) agarose resin (Invitrogen). The resin was washed with 5 column volumes (CV) of resuspension buffer, and added the His-tagged protein

TABLE 1 | Strains and plasmids used in this study.

Plasmids/strains	Genetic characteristics	Source
Plasmids		
P_{Trc}-His2A	P_{Trc} promotor plasmid, Amp^R	Lab collection
pkd46	P_{BAD} promotor carrying *araC* gene, Amp^R	Lab collection
pET30a	enzymes expression plasmid, Kan^R	Lab collection
pBAD33MevT	P_{BAD} promotor carrying *araC* gene, Cm^R	addgene#17814
pLeiss-3a-mkate	pLeiss plasmid with *rfp* report gene, Amp^R	Lab collection
pTDFOR-sfGFP	pTD plasmid with *gfp* report gene, Amp^R	Lab collection
P_{Trc}-bFapR	p_{Trc} plasmid with *bfapR* regulator, Amp^R	Lab collection
pET-HMGR	pET carrying HMGR protein	This study
pET-bFapR	pET carrying bFapR protein	This study
P_{Trc}-fapo-mkate-T7-bFapR	P_{Trc} carrying *fapo* site, T7 promotor, *fapR*, *mkate* genes	This study
P_{Trc}-fapo-mkate-lacI-bFapR	P_{Trc} carrying *fapo* site, *lacI* promotor, *fapR*, *mkate* genes	This study
P_{Trc}-(fapo)$_2$-mkate-lacI-bFapR	P_{Trc} carrying two *fapo* sites, *lacI* promotor, *fapR*, *mkate* genes	This study
P_{Trc}-His2A-araCM	P_{Trc} carrying *araC* mutant gene	This study
P_{Trc}-His2A-araC-Mev-pBad-GFP	P_{Trc} carrying *araC* mutant gene, pBad promotor, and *gfp* genes	This study
P_{Trc}-His2A-T7-araC-Mev-pBad-GFP	P_{Trc} carrying araC mutant gene, T7 promotor, pBad promotor, and GFP	This study
P_{Tet}-AACT-HMGS	P_{Tet} plasmid carrying AACT and HMGS gene	This study
P_{Tet}-AACT-HMGS-thHMGR	P_{Tet} plasmid carrying AACT, HMGS and HMGR gene	This study
***E. coli* strains**		
BL21(DE3)	Host strain for enzymes expression	Lab collection
BL21-P_{Trc}-bFapR-mkate	BL21 (DE3) with P_{Trc}-fapo-mkate-lacI-bFapR	This study
BL21-P_{Tet}-HMGR-P_{Trc}-bFapR-mkate	BL21 (DE3) with P_{Trc}-fapo-mkate-lacI-bFapR and pTet-AACT-HMGS-HMGR	This study
BL21-P_{Trc}-T7-araC-P_{Bad}-GFP	BL21 (DE3) with P_{Trc}-His2A-T7-araC-Mev-pBad-GFP	This study
BL21-P_{Tet}-HMGR-P_{Trc}-T8-araC-pBad-GFP	BL21 (DE3) with P_{Trc}-His2A-T7-araC-Mev-pBad-GFP and P_{Tet}-AACT-HMGS	This study
BL21-P_{Tet}-AACT-P_{Trc}-bFapR-mkate	BL21 (DE3) with P_{Trc}-fapo-mkate-lacI-bFapR and P_{Tet}-AACT-HMGS-HMGR	This study
BL21-P_{Tet}-AACT-P_{Trc}-T8-araC-pBad-GFP	BL21 (DE3) with P_{Trc}-His2A-T7-araC-Mev-pBad-GFP and P_{Tet}-AACT-HMGS	This study
BL21-pET-HMGR	BL21 (DE3) with pET-HMGR	This study
BL21-pET-bFapR	BL21 (DE3) with pET-bFapR	This study

with an elution buffer (50 mM NaH_2PO_4, 300 mM NaCl, and 250 mM imidazole, pH 8.0). The eluted fractions with the c were loaded onto a PD-10 desalting column (GE Healthcare) for buffer exchange (25 mM Hepes, 300 mM NaCl, and 10% glycerol, pH 8.0). Dithiothreitol (1 mM) was added into the resuspension buffer. Purity of the proteins was analyzed by SDS-PAGE.

HMG-CoA Reductase Activity Assay

The activity of thHMGR was assayed using the HMGR-CoA Reductase Assay Kit (Sigma CS1090). Experiments were performed by following the manufacturer's protocol. Briefly, the reaction was conducted in a 96-well UV plate and monitored with a microplate reader (Synergy H1). Purified thHMGR, HMG-CoA, and the coenzyme NADPH were mixed in the reaction buffer. The total volume of the reaction mixture was 100 μL. After a 10 s blending, the 340 nm absorbance of the mixture was continuously monitored for 10 min. The HMGR activity was normalized to the protein concentration. For statin inhibition efficacy assay, different amount of statin drugs were added into the reaction mixture. The thHMGR activity data were plotted against the statin concentration data, and the IC_{50} was calculated by fitting the curve into an IC_{50} equation embedded in Graphpad.

HPLC Analysis

For mevalonate production analysis, 50 μl overnight cultures of *E. coli* BL21/P_{tet}-AACT-HMGS and *E. coli* BL21/P_{tet} -AACT-HMGS-thHMGR were individually inoculated into 5 mL fresh LB medium and cultivated at 30°C with 200 rpm shaking. After 2 h, 50 ng/mL of anhydrotetracycline (aTc, Clontech) was added and the cultivation continued for 3 h. After removing the cells by centrifugation, the cultivation supernatant was treated with 0.5 mM of sulfuric acid and then subjected to HPLC analysis. Shimadzu HPLC equipped with a Bio-Rad HPX-87H column (Bio-Rad) and a RID-10A refractive index detector were used. The HPX-87H column was kept at 55°C. Sulfuric acid solution (0.5 mM) was used as mobile phase and the flow rate was set to 0.4 mL/min; mevalonic acid lithium (purity $\geq$97%) was used as the external standard for quantificational analysis.

In vitro Transcription-Translation Assay

The *in vitro* protein synthesis kit PURExpress®, RNA polymerase, and RNAase inhibitor were purchased from New England Biolabs. Purified BsFapR and the DNA fragment containing P_{Trc}-$(fapO)_2$-mKate were used. The experiment was carried out according to the manufacturer's instructions with slight adjustments. Briefly, The reaction system contained 5 μL solution A, 3.5 μL solution B, 10 units RNase inhibitor (NEB), 100 ng DNA template (0.2 pmol), and 0.8 μL *E. coli* RNA polymerase. When required, 0.2 μL FapR (0.6 pmol) and 0.8 μL Malonyl-CoA (30 pmol) or HMG-CoA (60 pmol) was added. The total volume of the mixture was 12.5 μL. The reaction mixture was incubated at 37°C for 3 h, followed by cooling to 4°C.

To check the synthesized mKate, the reaction mixture was diluted, then subjected to fluorescence analysis. The microplate reader (Synergy H1) was used and the excitation and emission wavelengths were set to 588 and 633 nm, respectively.

In silico Analysis

Computational modeling was performed using MATLAB (v2014b). The BsFapR-ligands and AraCM-mevalonic acid interactions were performed using AutoDock (v4.2.6) (Albanesi et al., 2013). The BsFapR structural data was from Protein Database Bank (PDB: 2F3X). Its docking center was assigned with $x = 4$, $y = -28$, and $z = 60$. Search space was assigned with $x = 30$ Å, $y = 60$ Å, and $z = 50$ Å, and exhaustiveness was assigned with 10. The 3D structure of AraCM was generated by SWISS-MODEL[1]. AraC (PDB: 1XJA) at 2.4 Å resolution was used as the template (61% sequence similarity). The generated model was analyzed using PyMOL-1.5.0.3. Its docking center was assigned with $x = 122.1$, $y = 28.9$, and $z = 0.722$. Search space was assigned with $x = 44$ Å, $y = 44$ Å, and $z = 32$ Å, and exhaustiveness was assigned with 10. Grid maps were automatically computed.

Using Whole-Cell Biosensors in Drug Tests

Escherichia coli whole-cell biosensors were grown and tested in LB medium. Overnight cultured bacteria (100 μL) was inoculated into 10 mL fresh LB in 50 mL corning tubes and cultivated at 37°C for 3 h with 200 rpm shaking. Then statin drugs and inducer (aTc, 0.1 μg/mL) were added simultaneously into the culture. The cultivation was continued for another 2 h, then 1mL of *E. coli* cells were collected by centrifugation and washed twice with 0.9% NaCl solution. The obtained cells were re-suspended in 200 μL of 0.9% NaCl solution and subjected to fluorescence analysis. The microplate reader (Synergy H1) was used and for mKate analysis, the excitation and emission wavelengths were set to 588 and 633 nm, respectively; for GFP analysis, the excitation and emission wavelengths were set to 485 and 528 nm, respectively. Cell density ($OD_{600\ nm}$) was also analyzed by the microplate reader and the fluorescence intensity was normalized to per unit $OD_{600\ nm}$ of cells.

DATA AVAILABILITY STATEMENT

The raw data supporting the conclusions of this article will be made available by the authors, without undue reservation, to any qualified researcher.

AUTHOR CONTRIBUTIONS

LX and HWL conceived and designed the study. HJL and QW performed the experiments. RZ performed the computational work. HWL drafted the manuscript. All authors have given approval to the final version of the manuscript.

FUNDING

The work was financially supported by grants from the National Natural Science Foundation of China (31770093), Shandong Medical and Health Science and Technology Development Project (2017WS013), and the State Key Laboratory of Microbial Technology at Shandong University.

SUPPLEMENTARY MATERIAL

The Supplementary Material for this article can be found online at: https://www.frontiersin.org/articles/10.3389/fcell.2020.00404/full#supplementary-material

---

[1] http://swissmodel.expasy.org/

REFERENCES

Ahmed, S., Capric, V., Khan, M., and Koneru, P. (2020). A rapidly progressive case of statin-induced necrotizing autoimmune myopathy. *Cureus* 12:e7021. doi: 10.7759/cureus.7021

Albanesi, D., Reh, G., Guerin, M. E., Schaeffer, F., Debarbouille, M., Buschiazzo, A., et al. (2013). Structural basis for feed-forward transcriptional regulation of membrane lipid homeostasis in *Staphylococcus aureus*. *PLoS Pathog.* 9:108. doi: 10.1371/journal.ppat.1003108

Armitage, J. (2007). The safety of statins in clinical practice. *Lancet* 370, 1781–1790. doi: 10.1016/S0140-6736(07)60716-8

Berset, Y., Merulla, D., Joublin, A., and Hatzimanikatis, V., (2017). Mechanistic modeling of genetic circuits for ArsR arsenic regulation. *ACS Synthet. Biol.* 6:364. doi: 10.1021/acssynbio.6b00364

Bitzur, R., Cohen, H., Kamari, Y., and Harats, D. (2013). Intolerance to statins: mechanisms and management. *Diabetes Care* 36, S325–S330. doi: 10.2337/dcS13-2038

Campbell, C. D., and Vederas, J. C. (2010). Biosynthesis of lovastatin and related metabolites formed by fungal iterative PKS enzymes. *Biopolymers* 93, 755–763. doi: 10.1002/bip.21428

Endo, A. (1992). The discovery and development of HMG-CoA reductase inhibitors. *J. Lipid Res.* 33, 1569–1582. doi: 10.1016/j.atherosclerosissup.2004.08.026

Garattini, L., and Padula, A. (2017). Cholesterol-lowering drugs: science and marketing. *J. R. Soc. Med.* 110, 57–64. doi: 10.1177/0141076816681951

Gould, N., Hendy, O., and Papamichail, D. (2014). Computational tools and algorithms for designing customized synthetic genes. *Front. Bioeng. Biotechnol.* 2:41. doi: 10.3389/fbioe.2014.00041

Hennekens, C. H., Teng, B., and Pfeffer, M. A. (2017). Statins and diabetes: current perspectives and implications for clinicians. *Am. J. Med.* 130, 504–506. doi: 10.1016/j.amjmed.2016.12.022

Iannelli, F., Lombardi, R., Milone, M. R., Pucci, B., De Rienzo, S., Budillon, A., et al. (2018). Targeting mevalonate pathway in cancer treatment: repurposing of statins. *Recent Pat Anticancer Drug Discov.* 13, 184–200. doi: 10.2174/1574892812666171129141211

Istvan, E. (2003). Statin inhibition of HMG-CoA reductase: a 3-dimensional view. *Atheroscler. Suppl.* 4, 3–8. doi: 10.1016/s1567-5688(03)00003-5

Istvan, E. S., and Deisenhofer, J. (2001). Structural mechanism for statin inhibition of HMG-CoA reductase. *Science* 292, 1160–1164. doi: 10.1126/science.1059344

Khatun, M. A., Hoque, M. A., Zhang, Y., Lu, T., Cui, L., Zhou, N. Y., et al. (2018). Bacterial consortium-based sensing system for detecting organophosphorus pesticides. *Anal. Chem.* 90, 10577–10584. doi: 10.1021/acs.analchem.8b02709

Mahr, R., and Frunzke, J. (2016). Transcription factor-based biosensors in biotechnology: current state and future prospects. *Appl. Microbiol. Biotechnol.* 100, 79–90. doi: 10.1007/s00253-015-7090-3

Manzoni, M., and Rollini, M. (2002). Biosynthesis and biotechnological production of statins by filamentous fungi and application of these cholesterol-lowering drugs. *Appl. Microbiol. Biotechnol.* 58, 555–564. doi: 10.1007/s00253-002-0932-9

Morsut, L., Roybal, K., Xin, X., Gordley, R., Coyle, S., Thomson, M., et al. (2016). Engineering customized cell sensing and response behaviors using synthetic notch receptors. *Cell* 164, 780–791. doi: 10.1016/j.cell.2016.01.012

Mullen, P. J., Yu, R., Longo, J., Archer, M. C., and Penn, L. Z. (2016). The interplay between cell signalling and the mevalonate pathway in cancer. *Nat. Rev. Cancer* 16, 718–731. doi: 10.1016/j.cell.2016.01.012

Rizzo, M., Montalto, G., and Banach, M. (2012). The effects of statins on blood pressure: current knowledge and future perspectives. *Archiv. Med. Sci.* 8, 1–3. doi: 10.1016/j.cell.2016.01.012

Roitelman, J., Olender, E. H., Barnun, S. Jr., Dunn, W., and Simoni, R. D. (1992). Immunological evidence for eight spans in the membrane domain of 3-hydroxy-3-methylglutaryl coenzyme A reductase: implications for enzyme degradation in the endoplasmic reticulum. *J. Cell Biol.* 117, 959–973. doi: 10.1083/jcb.117.5.959

Siedler, S., Schendzielorz, G., Binder, S., Eggeling, L., Bringer, S., and Bott, M. (2014). SoxR as a single-cell biosensor for NADPH-consuming enzymes in *Escherichia coli*. *ACS Synthet. Biol.* 3, 41–47. doi: 10.1021/sb400110j

Sopková, J., Vidomanová, E., Strnádel, J., Škovierová, H., and Halašová, E. (2017). The role of statins as therapeutic agents in cancer. *Gen. Physiol. Biophys.* 36, 501–511. doi: 10.4149/gpb_2017045

Tabernero, L., Bochar, D. A., Rodwell, V. W., and Stauffacher, C. V. (1999). Substrate-induced closure of the flap domain in the ternary complex structures provides insights into the mechanism of catalysis by 3-hydroxy-3-methylglutaryl-CoA reductase. *Proc. Natl. Acad. Sci. U.S.A.* 96, 7167–7171. doi: 10.1073/pnas.96.13.7167

Vajdić, T., Ošlaj, M., Kopitar, G., and Mrak, P. (2014). Engineered, highly productive biosynthesis of artificial, lactonized statin side-chain building blocks: the hidden potential of *Escherichia coli* unleashed. *Metab. Eng.* 24, 160–172. doi: 10.1016/j.ymben.2014.05.012

Vögeli, B., Shima, S., Erb, T. J., and Wagner, T. (2019). Crystal structure of archaeal HMG-CoA reductase: insights into structural changes of the C-terminal helix of the class-I enzyme. *FEBS Lett.* 593, 543–553. doi: 10.1002/1873-3468.13331

Won, K. J., Goh, Y. J., and Hwang, S. H. (2020). Lysophosphatidic acid inhibits simvastatin-induced myocytoxicity by activating LPA receptor/PKC pathway. *Molecules* 25:529. doi: 10.3390/molecules25071529

Wysockakapcinska, M., Lutyknadolska, J., Kiliszek, M., Plochocka, D., Maciag, M., Leszczynska, A., et al. (2009). Functional expression of human HMG-CoA reductase in *Saccharomyces cerevisiae*: a system to analyse normal and mutated versions of the enzyme in the context of statin treatment. *J. Appl. Microbiol.* 106, 895–902. doi: 10.1111/j.1365-2672.2008.04060.x

Conflict of Interest: The authors declare that the research was conducted in the absence of any commercial or financial relationships that could be construed as a potential conflict of interest.

frontiers
in Cell and Developmental Biology

ORIGINAL RESEARCH
published: 11 August 2020
doi: 10.3389/fcell.2020.00768

Dynamic Blood Concentrations of $A\beta_{1-40}$ and $A\beta_{1-42}$ in Alzheimer's Disease

Yuan-Han Yang[1,2,3,4,5], Ling-Chun Huang[1,2], Sun-Wung Hsieh[1,6] and Li-Ju Huang[1,3]*

[1] Department of Neurology, Kaohsiung Medical University Hospital, Kaohsiung Medical University, Kaohsiung, Taiwan, [2] Department of Neurology, Kaohsiung Municipal Ta-Tung Hospital, Kaohsiung Medical University Hospital, Kaohsiung, Taiwan, [3] Center of Teaching and Research, Kaohsiung Municipal Hsiao-Kang Hospital, Kaohsiung Medical University, Kaohsiung, Taiwan, [4] Department of and Master's Program in Neurology, Faculty of Medicine, Kaohsiung Medical University, Kaohsiung, Taiwan, [5] Neuroscience Research Center, Kaohsiung Medical University, Kaohsiung, Taiwan, [6] Department of Neurology, Kaohsiung Municipal Hsiao-Kang Hospital, Kaohsiung Medical University, Kaohsiung, Taiwan

Amyloid-beta (Aβ) is produced by the cleavage of amyloid precursor proteins in the cell membrane by β-secretase and γ-secretase into a monomeric form with peptides of different lengths such as $A\beta_{1-40}$ or $A\beta_{1-42}$, which is then transformed into oligomeric and fibril forms and is considered to be one of the hallmarks of Alzheimer's disease (AD). The plasma concentrations of $A\beta_{1-40}$ and $A\beta_{1-42}$ are unstable after blood samples have been obtained. In order to examine the dynamic changes of plasma $A\beta_{1-42}$ and $A\beta_{1-40}$ in blood samples, we used fresh blood samples in ethylenediaminetetraacetic acid tubes from 32 clinically diagnosed AD patients. Each sample was subdivided into eight sub-samples, and levels of $A\beta_{1-40}$ and $A\beta_{1-42}$ were measured at 0 (baseline), 0.5, 1, 2, 3, 5, 8, and 24 h, respectively. All samples were incubated at 37°C before being measuring. The results showed that compared to baseline, 87.5 and 62.5% of the patients had higher plasma levels of $A\beta_{1-42}$ and $A\beta_{1-40}$ at 24 h, respectively. The patients with an increased amyloid level did not have a significantly different apolipoprotein E4 allele (APOE4) gene status for either $A\beta_{1-40}$ ($p = 0.422$) or $A\beta_{1-42}$ ($p = 1.000$). However, for plasma $A\beta_{1-42}$, the APOE4 carriers had a significantly lower level than the non-carriers at baseline [31.2 ± 6.5 (mean ± SD) ng/ml vs. 50.4 ± 47.7 ng/ml, $p = 0.031$] and 0.5 h (37.5 ± 7.6 ng/ml vs. 51.9 ± 30.8 ng/ml, $p = 0.043$). There were no significant differences between the APOE4 carriers and non-carriers in plasma $A\beta_{1-42}$ concentration at 1, 2, 3, 5, 8, and 24 h ($p = 0.112$, $p = 0.086$, $p = 0.112$, $p = 0.263$, $p = 0.170$ and $p = 0.621$, respectively). The $A\beta_{1-40}$ level was related to disease severity as assessed using the clinical dementia rating (CDR) scale. Patients with advanced stages of dementia (CDR = 1 and CDR = 2) had a significantly higher $A\beta_{1-40}$ level compared to those with very mild stage dementia (CDR = 0.5) at all time points ($p < 0.05$) except for 24 h ($p = 0.059$). Our findings illustrate the effects of APOE4 status on dynamic changes in plasma $A\beta_{1-40}$ and $A\beta_{1-42}$ levels, and significant associations between $A\beta_{1-40}$ level and disease severity. Further studies are needed to investigate the exact mechanisms of how APOE4 affects the dynamic changes in plasma $A\beta_{1-40}$ and $A\beta_{1-42}$, and the association between $A\beta_{1-40}$ and advanced dementia.

Keywords: amyloid-beta-protein, Alzheimer's disease, APOE, CDR, dementia

Edited by:
Md. Shamim Hossain,
Kyushu University, Japan

Reviewed by:
Sandra Donnini,
University of Siena, Italy
Sangjune Kim,
School of Medicine, Johns Hopkins University, United States

****Correspondence:***
Yuan-Han Yang
endlessyhy@gmail.com

Specialty section:
This article was submitted to Cellular Biochemistry, a section of the journal Frontiers in Cell and Developmental Biology

***Received:** 07 April 2020*
***Accepted:** 21 July 2020*
***Published:** 11 August 2020*

Citation:
Yang Y-H, Huang L-C, Hsieh S-W and Huang L-J (2020) Dynamic Blood Concentrations of $A\beta_{1-40}$ and $A\beta_{1-42}$ in Alzheimer's Disease. Front. Cell Dev. Biol. 8:768. doi: 10.3389/fcell.2020.00768

INTRODUCTION

As people age, the aging process, cardiovascular disease (Prince, 2015; Yang et al., 2018) and other factors (Winblad et al., 2016; Yang et al., 2019) may increase the risk of Alzheimer's disease (AD). It has been estimated that 46.8 million people worldwide were living with dementia in 2015, and this number is expected to reach 74.7 million by 2030 and 131.5 million by 2050 (Hebert et al., 2004; Prince, 2015). AD is the most common form of dementia worldwide (Hebert et al., 2004; Prince, 2015; Yang et al., 2019). The neuropathological hallmarks of AD are formations of senile plaques composed of amyloid-beta (Aβ) peptides and neurofibrillary tangles consisting of abnormal deposition of tau protein in the brain (Karn et al., 2007; Tapiola et al., 2009). Aβ is produced by the cleavage of amyloid precursor proteins into a monomeric form with peptides of different lengths by β-secretase and γ-secretase, which is then transformed into oligomeric and fibril forms, and eventually into amyloid plaques (Haass and Selkoe, 2007; Tapiola et al., 2009) in brain tissue. $A\beta_{1-42}$ and $A\beta_{1-40}$ in cerebrospinal fluid (CSF) are regarded to be biomarkers in the diagnosis of AD (Strozyk et al., 2003; Tapiola et al., 2009), although consensus with regards to the standard procedures for detecting $A\beta_{1-42}$ and $A\beta_{1-40}$ concentrations in CSF is currently lacking. Moreover, given the invasiveness of obtaining CSF for examinations and inter-laboratory variability in the detection of $A\beta_{1-42}$ and $A\beta_{1-40}$ concentrations (Mattsson et al., 2010, 2012, 2013), CSF examinations for $A\beta_{1-40}$ and $A\beta_{1-42}$ level are not always practical.

To overcome this problem, many researchers have focused on identifying blood-based biomarkers for AD, however the results have been inconsistent (van Oijen et al., 2006). van Oijen et al. (2006) reported that a higher $A\beta_{1-40}$ concentration but not $A\beta_{1-42}$ or $A\beta_{1-40}/A\beta_{1-42}$ ratio was associated with a higher risk of AD. In addition, several studies have reported that a higher plasma $A\beta_{1-42}$ level was mildly associated with AD, but that this association was not found in subsequent longitudinal examinations of $A\beta_{1-40}$, $A\beta_{1-42}$ level, or its ratio (Lopez et al., 2008; Mayeux and Schupf, 2011). These discrepant results may be due to several causes. First, it is not currently known whether plasma $A\beta_{1-40}$ or $A\beta_{1-42}$ peptides in AD patients originate from the brain, peripheral tissues or both sources (Kuo et al., 1999). Second, variations in laboratory protocols for handling samples of $A\beta_{1-40}$ and $A\beta_{1-42}$, and the physicochemical properties of $A\beta_{1-40}$ and $A\beta_{1-42}$ peptides. However, supporting evidence for these hypotheses is currently lacking (Mattsson et al., 2011; Rissman et al., 2012).

Enzyme-linked immunosorbent assay (ELISA) has been reported to be a standardized method for the quantification of $A\beta_{1-40}$ and $A\beta_{1-42}$ in clinical studies as biomarkers of AD (Mattsson et al., 2012). In a comparison study of different immunoassay platforms, the Alzheimer's Association quality-control program (Mattsson et al., 2013) reported 20–30% within- and between-laboratory variability in the quantification of $A\beta_{1-42}$ and $A\beta_{1-40}$. A consensus with regards to the protocol for the ELISA quantification of $A\beta_{1-42}$ and $A\beta_{1-40}$ is still lacking.

Confounding factors for ELISA measurements include automatic plate washing, the use of polypropylene plates for pre-incubation, and the duration of sample thawing at room temperature. ELISA usually uses samples that are thawed at room temperature before being measured, which does not accurately reflect the condition in human blood, at around 37°C. In addition, the duration of sample thawing at room temperature may be associated with changes in the concentration of amyloid peptides because the process of amyloid aggregation from monomers to oligomers or fibrils is continuous, and some peptides would degrade over time.

The aim of this study was to understand the actual status of $A\beta_{1-40}$ and $A\beta_{1-42}$ in human blood and the possible changes in $A\beta_{1-40}$ and $A\beta_{1-42}$ during the measuring process in relation to other factors such as apo-lipoprotein E gene (APOE) status (Kang et al., 2015) and disease severity. We examined the concentrations of plasma $A\beta_{1-40}$ and $A\beta_{1-42}$ at different time points and assessed their associations with APOE genetic status and disease severity in fresh blood samples obtained from AD patients.

MATERIALS AND METHODS

Patients

All patients diagnosed with AD were recruited from the Department of Neurology, Kaohsiung Municipal Ta-Tung Hospital, an area hospital in southern Taiwan. The diagnosis of AD was based on the NINCDS-ADRDA criteria (McKhann et al., 2011), and involved a series of comprehensive neuropsychological tests, including the Mini-Mental State Examination (MMSE) derived from the Cognitive Abilities Screening Instrument (CASI) (Lin et al., 2002), CASI, and Clinical Dementia Rating (CDR) scale (Morris, 1991). Patients with other conditions possibly contributing to the diagnosis of AD were excluded.

Evaluations

All procedures were approved by the Kaohsiung Medical University Hospital Institutional Review Board, and written informed consent was obtained from all participants or their legal representatives. For each recruited AD patient, a series of neuropsychological assessments, including the MMSE, CASI, and CDR, were administered every 12 months to trace the clinical outcomes. The MMSE, CASI, and CDR were conducted by a senior neuropsychologist and an experienced physician based on information from a knowledgeable collateral source (usually a spouse or adult child).

Apolipoprotein E (APOE) Genotyping

For every AD patient, restriction enzyme isotyping of the APOE allele was performed following a modification of the protocol developed by Pyrosequencing[1]. In brief, 10 ng of DNA was amplified in a 20 μL reaction volume in which dGTP was replaced by a mixture of 25% dGTP and 75% dITP to facilitate analysis of the GC-rich fragment. A 276-bp fragment was generated using the forward primer AGA CGC GGG CAC GGC TGT and reverse biotin-labeled primer CTC GCG

---

[1] http://www.pyrosequencing.com

GAT GGC GCT GAG. Single-strand DNA was prepared using streptavidin coated beads, and APOE gene variants at codons 112 and 158 were sequenced using the following primers and dispensation order: SNP112 GAC ATG GAG GAC GTG and SNP158 CCG ATG ACC TGC AGA and dispensation order GCTGAG CTAGCGT. Individuals with one or two copies of the APOE4 allele were considered to be APOE4 positive [APOE4(+)], and otherwise APOE4 negative [APOE4(−)].

Plasma Sample for ELISA

Venous blood was drawn by venipuncture in the morning after an overnight fast. Plasma samples were collected in ethylenediaminetetraacetic acid (EDTA) vacutainers, which were immediately centrifuged for 10 min at 3000 rpm. After centrifugation, each sample was divided into eight sub-samples and incubated at 37°C. $A\beta_{1-42}$ and $A\beta_{1-40}$ levels were measured in the eight sub-samples at different time points, including baseline (0 h), immediately after obtaining the blood sample (0.5 h), and then at 1, 2, 3, 5, 8, and 24 h, respectively. All samples were incubated at 37°C before being measured. An increase in $A\beta_{1-42}$ or $A\beta_{1-40}$ level was defined according to the difference in concentration between baseline and 24 h. If the 24-h concentration was higher/lower than the baseline level, the patient was defined as having an increase/decrease in $A\beta_{1-42}$ or $A\beta_{1-40}$. Quantification of $A\beta_{1-42}$ and $A\beta_{1-40}$ in plasma was performed using a specific ELISA kit (Human Amyloid β(1–40) Assay Kit – IBL, code number 27713; and Human Amyloid β(1–42) Assay Kit – IBL, code number 27711). All assays were performed according to the manufacturer's protocol. All reagents were prepared at room temperature (20–25°C) approximately 30 min before use.

Statistical Analysis

Data analysis was performed using SPSS statistical software (Standard version 11.5.0; SPSS Inc., Chicago, IL, United States). All statistical tests were two-tailed, and $p > 0.05$ was taken to indicate significance. Age, education, CASI, MMSE, $A\beta_{1-42}$, and

TABLE 1 | Demographic characteristics of the recruited patients.

***N* = 32**	
Age, years (mean ± SD)	77.7 ± 7.3
Education, years (mean ± SD)	8.9 ± 5.0
Female (n, %)	17, 53.1%
APOE4(+)* (n, %)	9, 28.1%
CDR stage	
0.5	11, 34.4%
1	17, 53.1%
2	4, 12.5%
CASI	55.3 ± 22.7
MMSE	16.5 ± 6.3
Increased amyloid β_{1-40} ^ (n, %)	20, 62.5%
Increased amyloid β_{1-42} ^ (n, %)	28, 87.5%

*CDR, Clinical Dementia Rating; CASI, Cognitive Ability Screening Instrument; MMSE, Mini-mental Status Examination. *At least having an allele of apolipoprotein E4 gene. Defined as 24 h level – baseline level ≥ 0.*

TABLE 2 | Plasma concentration of amyloid β_{1-40} ($A\beta_{1-40}$) by time in the patients with Alzheimer's disease.

	Total sample *N* = 32	***p*-value**	**APOE4(+)$^{\$}$ *n* = 9**	**APOE4(−)$^{\#}$ *n* = 23**	***p*-value**	**CDR = 0.5 *n* = 11**	**CDR > 0.5 *n* = 21**	***p*-value**
$A\beta_{1-40}$, pg/ml (mean ± SD)		$p = 0.001$						
Time (h)								
0	314.1 ± 178.9		286.4 ± 196.4	325.0 ± 175.0	0.564	201.3 ± 152.7	369.5 ± 168.5	0.010
0.5	318.5 ± 178.1		302.1 ± 183.8	324.8 ± 179.6	0.681	199.1 ± 143.1	381.0 ± 164.2	0.004
1	330.1 ± 184.2		326.2 ± 191.6	332.6 ± 185.5	0.869	219.8 ± 166.4	389.0 ± 168.5	0.011
2	361.7 ± 184.8		355.0 ± 184.9	364.3 ± 190.9	0.902	250.0 ± 159.3	420.1 ± 172.6	0.011
3	373.4 ± 189.3		359.3 ± 184.9	379.0 ± 194.8	0.837	254.8 ± 165.2	435.6 ± 173.5	0.008
5	384.5 ± 187.2		383.7 ± 199.8	384.9 ± 186.7	0.773	272.5 ± 175.6	443.2 ± 168.4	0.012
8			381.5 ± 193.9	389.5 ± 194.6	1.000	283.9 ± 171.2	441.3 ± 181.9	0.024
24	320.3 ± 157.9		268.6 ± 112.1	340.6 ± 170.4	0.386	247.8 ± 169.4	358.4 ± 141.0	0.059
Increased* (n/N, %)	20/32, 62.5%		7/9, 77.8%	13/23, 56.5%	0.422	9/11, 81.8%	11/21, 52.4%	0.104

*CDR, Clinical Dementia Rating. *Defined as 24 h level – baseline level ≥ 0. $^{\$}$At least having an allele of apolipoprotein E4 gene. $^{\#}$No allele of the apolipoprotein E4 gene.*

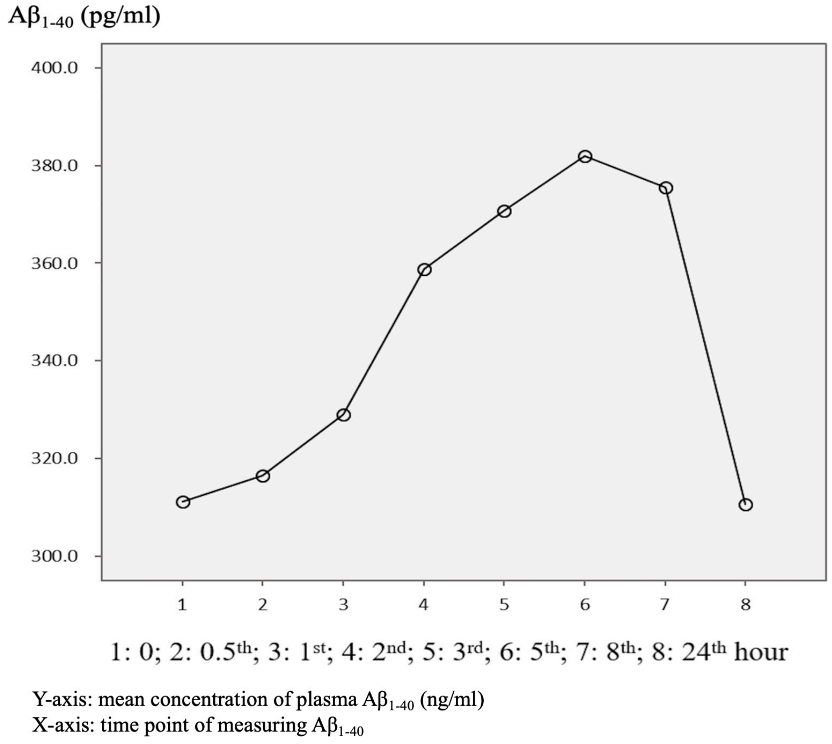

FIGURE 1 | Overview of mean plasma beta-amyloid$_{1-40}$ (Aβ_{1-40}) concentration in AD patients (*N* = 32) in relation to time.

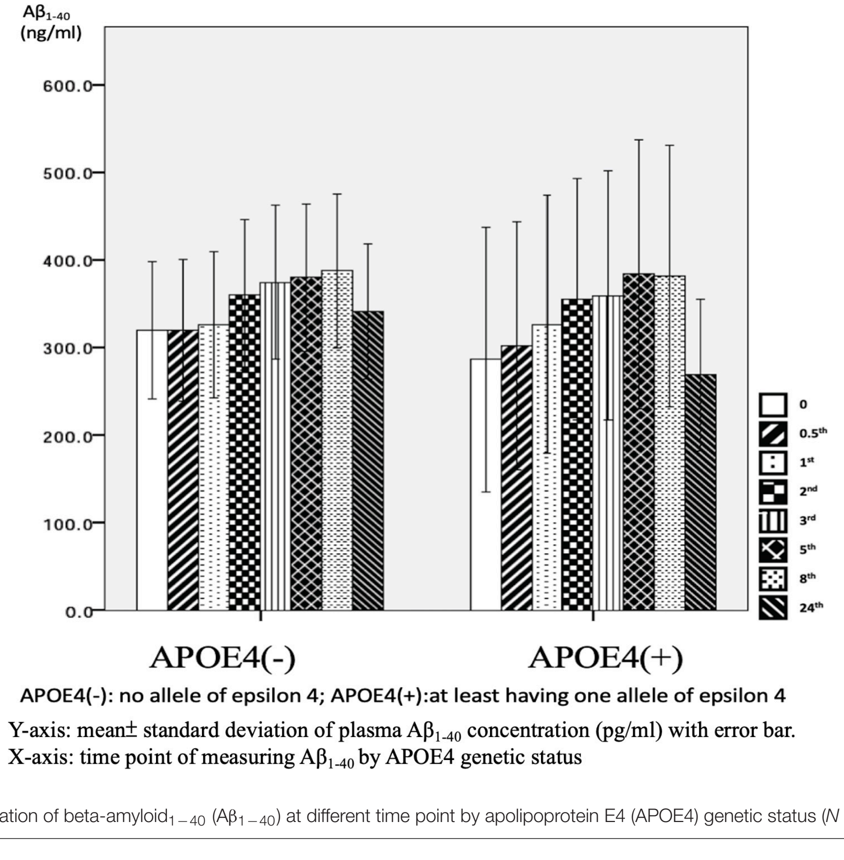

FIGURE 2 | Plasma concentration of beta-amyloid$_{1-40}$ (Aβ_{1-40}) at different time point by apolipoprotein E4 (APOE4) genetic status (*N* = 32).

$A\beta_{1-40}$ were treated as continuous variables, and sex, APOE4 status, CDR, increase in $A\beta_{1-40}$ and increase in $A\beta_{1-42}$ were treated as categorical variables.

Independent *t*-tests for the two independent groups [APOE4(+) and APOE4(−) groups] were used to assess differences in plasma concentrations of $A\beta_{1-42}$ and $A\beta_{1-40}$. Repeated measures ANOVA was used to examine differences in $A\beta_{1-42}$ and $A\beta_{1-40}$ across all eight sub-samples.

RESULTS

In total, 32 AD patients were recruited into the study. The mean (±SD) age of the patients was 77.7 ± 7.3 years, and 28.1% were APOE4(+) (**Table 1**). Each patient had eight samples in which plasma $A\beta_{1-42}$ and $A\beta_{1-40}$ levels were measured at different time points. Compared to the baseline level, 87.5 and 62.5% of the patients had an increase in plasma $A\beta_{1-42}$ and $A\beta_{1-40}$ levels at 24 h, respectively (**Table 1**). Other clinical and demographic characteristics are shown in **Table 1**.

The mean baseline level of plasma $A\beta_{1-40}$ was 314.1 ± 178.9 pg/ml, compared to 320.3 ± 157.9 pg/ml at 24 h. Overall, 62.5% of the patients had an increase in the level of plasma $A\beta_{1-40}$ at 24 h (**Table 2** and **Figure 1**). There was no significant difference in the ratio of AD patients having an increase in $A\beta_{1-40}$ level between the APOE4(+) and APOE4(−) groups ($p = 0.422$).

There were significant differences in $A\beta_{1-40}$ level at all time points, and the concentration for any one was significantly different to the others ($p = 0.001$). However, there were no significant differences in $A\beta_{1-40}$ level at any time point between the APOE4(+) and APOE4(−) groups ($p = 0.386$–1.000) (**Table 2** and **Figure 2**). In addition, there were significant differences in $A\beta_{1-40}$ level according to disease severity at all time points ($p = 0.008$–0.024) except for 24 h ($p = 0.059$) (**Table 2**). The patients with very mild stage dementia (CDR = 0.5) had a lower $A\beta_{1-40}$ level compared to those with an advanced stage of dementia (CDR > 0.5) (**Table 2** and **Figure 3**).

The mean baseline plasma $A\beta_{1-42}$ level was 45.0 ± 41.3 pg/ml, compared to 63.6 ± 59.4 pg/ml at 24 h. Compared to the baseline level, 87.5% of the patients had an increase in the level at 24 h (**Table 3** and **Figure 4**). There was no significant difference in the ratio of AD patient having an increase in $A\beta_{1-40}$ level between the APOE4(+) and APOE4(−) groups ($p = 1.000$).

There were significant differences in $A\beta_{1-42}$ level at all time points, and the concentration for any one was significantly different to the others ($p = 0.042$). There were significant differences between the APOE4(+) and APOE4(−) groups in $A\beta_{1-42}$ level at baseline (31.2 ± 6.5 pg/ml vs. 50.4 ± 47.7

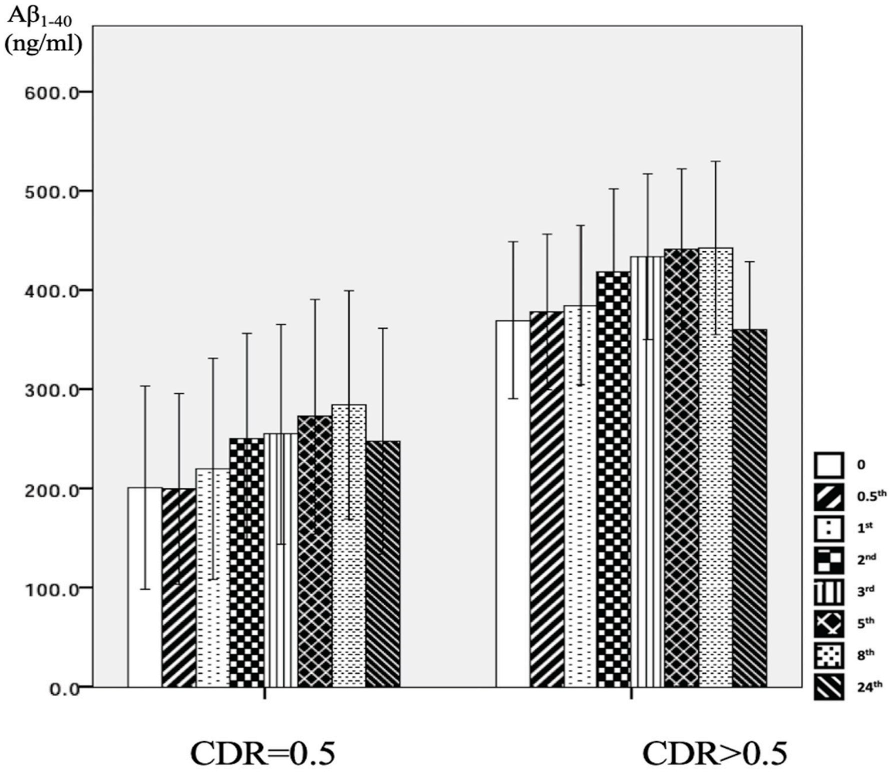

CDR: clinical dementia rating
Y-axis: mean± standard deviation of plasma $A\beta_{1-40}$ concentration (pg/ml) with error bar
X-axis: time point of measuring $A\beta_{1-40}$ by disease severity

FIGURE 3 | Plasma concentration of beta-amyloid$_{1-40}$ ($A\beta_{1-40}$) at different time point by disease severity ($N = 32$).

TABLE 3 | Plasma concentration of amyloid β_{1-42} ($A\beta_{1-42}$) by time in the patients with Alzheimer's disease.

	Total samples *N* = 32	***p*-value**	**APOE4(+)$^{\$}$ *N* = 9**	**APOE4(−)$^{\#}$ *N* = 23**	***p*-value**	**CDR = 0.5**	**CDR > 0.5**	***p*-value**
$A\beta_{1-42}$ pg/ml (mean ± SD)		$p = 0.042$						
Time (h)								
0	45.0 ± 41.3		31.2 ± 6.5	50.4 ± 47.7	0.031	40.9 ± 28.5	47.2 ± 47.1	0.691
0.5	47.8 ± 27.1		37.5 ± 7.6	51.9 ± 30.8	0.043	44.9 ± 16.8	49.4 ± 31.4	0.663
1	48.6 ± 28.9		39.6 ± 8.2	52.1 ± 33.3	0.112	46.0 ± 13.7	49.9 ± 34.6	0.721
2	51.6 ± 26.7		42.6 ± 9.5	55.1 ± 30.5	0.086	48.7 ± 12.7	53.1 ± 31.9	0.671
3	53.0 ± 22.6		45.1 ± 9.1	56.1 ± 25.5	0.112	50.8 ± 11.4	54.2 ± 26.8	0.699
5	52.9 ± 18.2		46.9 ± 9.5	55.3 ± 20.4	0.263	52.2 ± 11.2	53.3 ± 21.3	0.867
8	55.1 ± 19.0		48.4 ± 10.3	57.8 ± 21.1	0.170	52.9 ± 9.2	56.3 ± 22.7	0.632
24	63.6 ± 59.4		60.8 ± 42.4	64.7 ± 65.7	0.621	52.6 ± 9.5	69.4 ± 72.9	0.455
Increased* (n/N, %)	(28/32, 87.5%)		8/9, 88.9%	20/23, 87.0%	1.000	9/11, 81.8%	19/21, 90.5%	0.427

*CDR, Clinical Dementia Rating. *Defined as 24 h level − baseline level ≥ 0. $^{\$}$At least having an allele of apolipoprotein E4 gene. $^{\#}$No allele of the apolipoprotein E4 gene.*

pg/ml, $p = 0.031$) and 0.5 h (37.5 ± 7.6 pg/ml vs. 51.9 ± 30.8 pg/ml, $p = 0.043$). Apart from these two time points, there were no significant differences in the other time points between the APOE4(+) and APOE4(−) groups ($p = 0.086$–0.621) (**Table 3** and **Figure 5**). There were also no significant differences in $A\beta_{1-42}$ level at any time point by disease severity ($p = 0.427$–0.867) (**Table 3** and **Figure 6**). We also analyzed the associations between the $A\beta_{1-40}/A\beta_{1-42}$ ratio and APOE4 genotypes and disease severity at all time points, and the results were similar to those for $A\beta_{1-40}$ and $A\beta_{1-42}$ alone. $A\beta_{1-40}/A\beta_{1-42}$ ratio was not significantly associated with APOE4(+) status or disease severity at any of the eight time points (all $p > 0.05$).

We further compared the standard deviation of $A\beta_{1-42}$ level between the APOE4(+) and APOE4(−) patients, and found that the APOE4(+) patients had smaller standard deviations at each time point (**Table 3**).

DISCUSSION

In this study, we investigated dynamic changes in plasma $A\beta_{1-40}$ and $A\beta_{1-42}$ concentrations from fresh blood samples at eight time points. The results showed that not every sample had a consistent increase in $A\beta_{1-40}$ and $A\beta_{1-42}$ level after 24 h ($A\beta_{1-40}$: 62.5% and $A\beta_{1-42}$: 87.5%). The effects of APOE4 genetic status on plasma $A\beta_{1-42}$ level were observed only in sample measured within 30 min. Moreover, APOE4 genetic status did not affect plasma $A\beta_{1-40}$ level at any time point. However, $A\beta_{1-40}$ level was significantly higher in the patients with advanced stage dementia (CDR = 1 and CDR = 2) compared to those with mild stage dementia (CDR = 0.5).

Effect of APOE4 Gene Status on Plasma $A\beta_{1-40}$ and $A\beta_{1-42}$ Levels

We used fresh plasma, and found significant differences in plasma $A\beta_{1-42}$ at baseline ($p = 0.031$) and 0.5 h ($p = 0.043$) by APOE4 genetic status. However, no significant effects were noted at any other time points (**Table 3**), and no significant effects were observed in $A\beta_{1-40}$ level at any time point. These findings are to some extent different to another study which examined plasma amyloid peptides in 19 non-demented participants immediately and after storage at room temperature for 24 and 48 h, respectively (Bibl et al., 2012). In their study, the authors reported that sample storage led to a significant loss of measurable amyloid peptide levels, and that this was most pronounced during the first 24 h of storage regardless of whether the distinct Aβ peptide species was $A\beta_{1-42}$ or $A\beta_{1-40}$ (Bibl et al., 2012). The differences between our study and Bibl's study are that their samples came from non-demented participants, and they did not analyze changes in $A\beta_{1-42}$ or $A\beta_{1-40}$ between baseline and 24 h or control for APOE genetic status in their participants.

The effects of APOE4 genetic status on plasma $A\beta_{1-42}$ level but not $A\beta_{1-40}$ level in our samples indicates the possibility that there is an increase in the aggregation process of $A\beta_{1-42}$ from the monomer to fibril form in APOE4 carriers. Similar findings have also been reported in a previous study, in which apo-lipoprotein E4 protein, mediated by the APOE4 gene, was

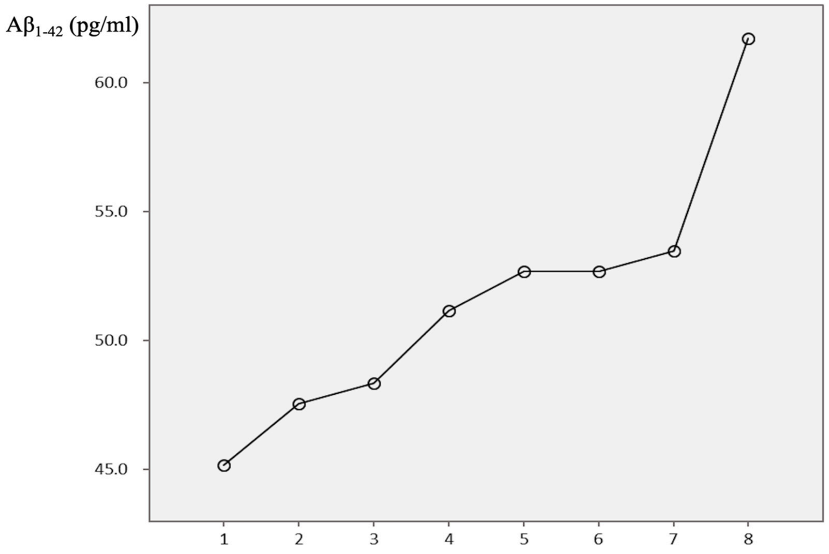

1: 0; 2: 0.5th; 3: 1st; 4: 2nd; 5: 3rd; 6: 5th; 7: 8th; 8: 24th hour

Y-axis: mean concentration of plasma $A\beta_{1-42}$ (ng/ml)
X-axis: time point of measuring $A\beta_{1-42}$

FIGURE 4 | Overview of mean plasma beta-amyloid$_{1-40}$ ($A\beta_{1-40}$) concentration in AD patients (N = 32) in relation to time.

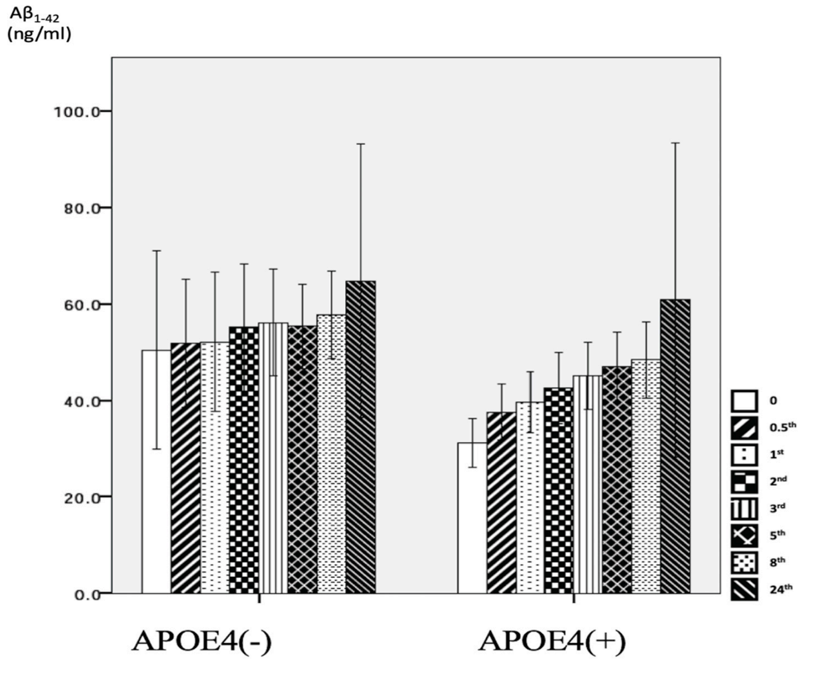

APOE4(-): no allele of epsilon 4; APOE4(+):at least having one allele of epsilon 4

Y-axis: mean± standard deviation of plasma $A\beta_{1-42}$ concentration (pg/ml) with error bar
X-axis: time point of measuring $A\beta_{1-42}$ by APOE4 genetic status

FIGURE 5 | Plasma concentration of beta-amyloid$_{1-42}$ ($A\beta_{1-42}$) at time point by apolipoprotein E4 (APOE4) genetic status (N = 32).

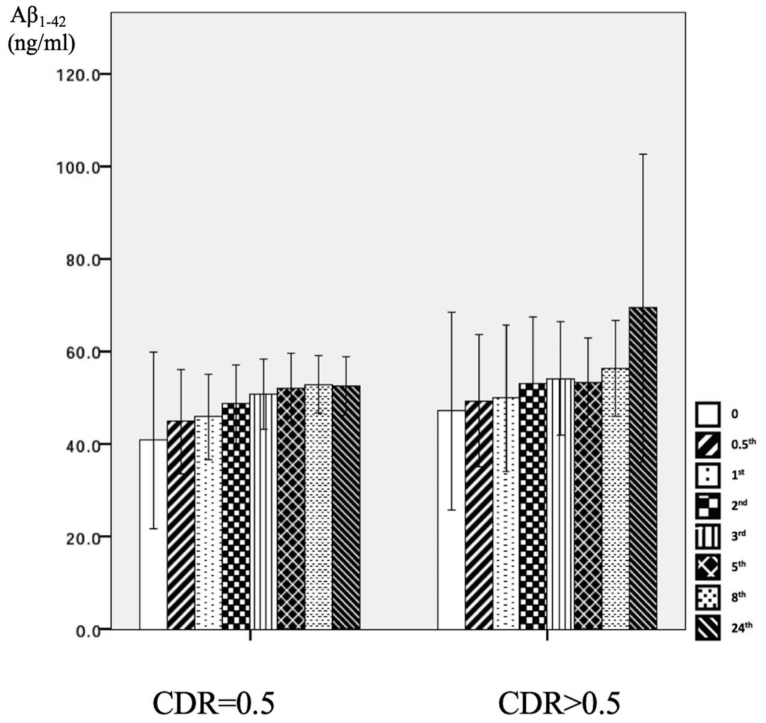

CDR: clinical dementia rating
Y-axis: mean± standard deviation of plasma $A\beta_{1-42}$ concentration (pg/ml) with error bar
X-axis: time point of measuring $A\beta_{1-42}$ by disease severity

FIGURE 6 | Plasma concentration of beta-amyloid$_{1-42}$ ($A\beta_{1-42}$) at different time point by disease severity (*N* = 32).

shown to induce the aggregation of $A\beta_{1-42}$ more specifically and rapidly than that of $A\beta_{1-40}$ (Kang et al., 2015). The authors used a simple method to assess APOE4-mediated Aβ aggregation in physiological conditions using single gold nanoparticles based on localized surface plasmon resonance, which could be directly observed with a dark-field microscope or even by the naked eye, although some evidence of the biophysical properties of the interaction between apo-lipoprotein E4 protein and $A\beta_{1-42}$ was unclear (Kang et al., 2015).

$A\beta_{1-40}$ and $A\beta_{1-42}$ Levels in Relation to the Severity of AD

As mentioned, our results indicated that minor effects of APOE4 on plasma $A\beta_{1-42}$ level and no significant effect on $A\beta_{1-40}$ level. This is consistent with a previous longitudinal study which examined $A\beta_{1-40}$ and $A\beta_{1-42}$ levels in clinical trials (Donohue et al., 2015). In that study, there were no significant differences in $A\beta_{1-40}$ and $A\beta_{1-42}$ levels between AD patients who were and were not APOE4 carriers. However, there were significant differences in patients with mild cognitive impairment who had minor symptoms that were not sufficiently severe to be classified as AD (Donohue et al., 2015). The exact and detailed mechanisms by which APOE4 genetic status affects $A\beta_{1-40}$ and $A\beta_{1-42}$ levels should be clarified in other studies. However, the effects of APOE4 genetic status on our 0 and 0.5-h samples could more directly reflect the real situation of $A\beta_{1-42}$ and $A\beta_{1-40}$ in human blood because of the limited time from obtaining the venous samples.

In our samples, the patients with an advanced stage of dementia (CDR = 1 and CDR = 2) had increased $A\beta_{1-40}$ levels compared to those with a very mild stage of dementia (CDR = 0.5). These findings could be, in part, attributed to the increased vascular contributions in advanced dementia (Yang et al., 2018), as the $A\beta_{1-40}$ level has been reported to be higher in vascular amyloid deposition compared to $A\beta_{1-42}$ (Iwatsubo et al., 1994; Gravina et al., 1995).

Sample Storage

In this study, 87.5% of the AD patients had a higher mean $A\beta_{1-42}$ level after 24 h (**Figure 4**), whereas only 62.5% of the AD patients had a higher mean $A\beta_{1-40}$ level after 24 h (**Figure 1**). This finding is different to previous studies that reported a significant loss of measurable $A\beta_{1-42}$ and $A\beta_{1-40}$ peptide levels in their stored samples (Donohue et al., 2015; Kang et al., 2015). Donohue et al. (2015) examined the plasma concentrations of $A\beta_{1-42}$ or $A\beta_{1-40}$ after a longer storage time ranging from 0 to 1.8 years, and found that they declined significantly over time (−14.42 pg/ml $A\beta_{1-40}$ per storage year, $p < 0.001$; −1.893 pg/ml $A\beta_{1-42}$ per storage year,

$p = 0.003$). In addition, Kang et al. (2015) reported that the loss of $A\beta_{1-40}$ and $A\beta_{1-42}$ was most pronounced during the first 24 h, in which the level of $A\beta_{1-40}$ decreased from 267 ± 46 pg/ml at baseline to 190 ± 41 pg/ml at 24 h, and the level of $A\beta_{1-42}$ decreased from 29 ± 4 pg/ml at baseline to 2 ± 4 pg/ml at 24 h. In order to avoid these declines or loss of $A\beta_{1-40}$ and $A\beta_{1-42}$, the authors recommended completing the measurements within 24 h after collecting the sample (Donohue et al., 2015). Compared to these studies, we provide more precise information with eight time points for both $A\beta_{1-42}$ and $A\beta_{1-40}$ levels within 24 h, and found that the changes in plasma $A\beta_{1-42}$ and $A\beta_{1-40}$ were dynamic and individualized.

Measurement of Beta-Amyloid

The increase in mean plasma $A\beta_{1-42}$ level at each time point in our AD patients may be due to several reasons. First, the $A\beta_{1-42}$ aggregation process is continuous, from monomer, oligomer, protofibril, and eventually to fibril forms (Sinha and Lieberburg, 1999; Selkoe and Hardy, 2016). Compared to healthy subjects, the plasma of AD patients has been hypothesized to have a tendency to foster $A\beta_{1-42}$ aggregation (Haass and Selkoe, 2007; Youn et al., 2019). Consistent with this hypothesis, the detected $A\beta_{1-42}$ plasma levels increased from baseline to 24 h in this study. Second, the commercial kit that used to detect $A\beta_{1-42}$ may not have only examined the monomer form of $A\beta_{1-42}$, as the antibody in the kit may also have recognized the specific area of amyloid peptide, and amyloid peptide would continue the aggregation process to the formation of the fibril form. Third, $A\beta_{1-42}$ may bind to carrier proteins such as apo-lipoprotein E and apo-lipoprotein J present in plasma (Matsubara et al., 1995; Zlokovic, 1996) that would possibly make the measurements difficult and result in a higher level. It is also possible that the commercial kit captured and detected oligomers in the sample. This would have resulted in an increase in the detected $A\beta_{1-42}$ level at 24 h.

Strengths and Limitations

This study has several strengths. First, we examined eight time points from 0 to 24 h and reported detailed changes in $A\beta_{1-42}$ and $A\beta_{1-40}$, and we also examined the effects of APOE4 genetic status and disease severity on plasma levels of $A\beta_{1-42}$ and $A\beta_{1-40}$. Second, we incubated all of the samples at 37°C before measurement to mimic the temperature of human blood in order to reduce possible confounding effects and approximate the actual level of $A\beta_{1-42}$ and $A\beta_{1-40}$. However, we do not know how beneficial this study design was, and the detailed effects and mechanisms of such design could be examined in another study. Third, we used the same protocol, commercial kits, and technician for all the examinations to avoid variabilities. There are also several limitations to this study. We reported changes in plasma $A\beta_{1-42}$ and $A\beta_{1-40}$ across all time points, however we did not examine the exact mechanisms, especially with regards to the possible effects of APOE genetic status, disease severity, or the possible bidirectional conversion between monomers and fibrils or oligomers. As there is currently no consensus on how best to evaluate dynamic changes in plasma $A\beta_{1-42}$ and $A\beta_{1-40}$, we chose the eight time points arbitrarily. These time points could be revised in future studies. In addition, our sample size was small, and further studies with a larger sample size comprehensively controlling for other confounding factors are warranted.

DATA AVAILABILITY STATEMENT

The raw data supporting the conclusions of this article will be made available by the authors, without undue reservation, to any qualified researcher.

ETHICS STATEMENT

The studies involving human participants were reviewed and approved by the Kaohsiung Medical University Hospital IRB. The patients/participants provided their written informed consent to participate in this study.

AUTHOR CONTRIBUTIONS

Y-HY designed the study and wrote the manuscript. L-CH and S-WH recruited patients and collected samples. L-JH performed the ELISA analyses. All authors contributed to the article and approved the submitted version.

FUNDING

This study was supported by the Neuroscience Research Center, Kaohsiung Medical University (Grant No: KMU-TC108B01; KMTTH-DK109007).

REFERENCES

Bibl, M., Welge, V., Esselmann, H., and Wiltfang, J. (2012). Stability of amyloid-β peptides in plasma and serum. *Electrophoresis* 33, 445–450. doi: 10.1002/elps.201100455

Donohue, M. C., Moghadam, S. H., Roe, A. D., Sun, C.-K., Edland, S. D., Thomas, R. G., et al. (2015). Longitudinal plasma amyloid beta in Alzheimer's disease clinical trials. *Alzheimers Dement.* 11, 1069–1079.

Gravina, S. A., Ho, L., Eckman, C. B., Long, K. E., Otvos, L., Younkin, L. H., et al. (1995). Amyloid β Protein (Aβ) in Alzheimeri's disease brain biochemical and immunocytochemical analysis with antibodies specific for forms ending at Aβ40 or Aβ42 (43). *J. Biol. Chem.* 270, 7013–7016.

Haass, C., and Selkoe, D. J. (2007). Soluble protein oligomers in neurodegeneration: lessons from the Alzheimer's amyloid β-peptide. *Nat. Rev. Mol. Cell Biol.* 8, 101–112. doi: 10.1038/nrm2101

Hebert, L., Scherr, P., Bienias, J., Bennett, D., and Evans, D. (2004). State-specific projections through 2025 of Alzheimer disease prevalence. *Neurology* 62:1645. doi: 10.1212/01.wnl.0000123018.01306.10

Iwatsubo, T., Odaka, A., Suzuki, N., Mizusawa, H., Nukina, N., and Ihara, Y. (1994). Visualization of Aβ42 (43) and Aβ40 in senile plaques with end-specific Aβ monoclonals: evidence that an initially deposited species is Aβ42 (43). *Neuron* 13, 45–53. doi: 10.1016/0896-6273(94)90458-8

Kang, M. K., Lee, J., Nguyen, A. H., and Sim, S. J. (2015). Label-free detection of ApoE4-mediated β-amyloid aggregation on single nanoparticle uncovering

Alzheimer's disease. *Biosens. Bioelectron.* 72, 197–204. doi: 10.1016/j.bios.2015.05.017

Karn, S., Wei, Z., MacTavish, D., Kabogo, D., Song, M.-S., and Jhamandas, J. H. (2007). *Amyloid β-Peptide and Central Cholinergic Neurons: Involvement in Normal Brain Function and Alzheimer's Disease Pathology. Abeta Peptide and Alzheimer's Disease*. Cham: Springer, 159–178.

Kuo, Y.-M., Emmerling, M. R., Lampert, H. C., Hempelman, S. R., Kokjohn, T. A., Woods, A. S., et al. (1999). High levels of circulating Aβ42 are sequestered by plasma proteins in Alzheimer's disease. *Biochem. Biophys. Res. Commun.* 257, 787–791. doi: 10.1006/bbrc.1999.0552

Lin, K.-N., Wang, P.-N., Liu, C.-Y., Chen, W.-T., Lee, Y.-C., and Liu, H.-C. (2002). Cutoff scores of the cognitive abilities screening instrument, Chinese version in screening of dementia. *Dement. Geriatr. Cogn. Disord.* 14, 176–182. doi: 10.1159/000066024

Lopez, O., Kuller, L., Mehta, P., Becker, J., Gach, H., Sweet, R., et al. (2008). Plasma amyloid levels and the risk of AD in normal subjects in the Cardiovascular Health Study. *Neurology* 70, 1664–1671. doi: 10.1212/01.wnl.0000306696.82017.66

Matsubara, E., Frangione, B., and Ghiso, J. (1995). Characterization of apolipoprotein J-Alzheimer's Aβ interaction. *J. Biol. Chem.* 270, 7563–7567.

Mattsson, N., Andreasson, U., Persson, S., Arai, H., Batish, S. D., Bernardini, S., et al. (2011). The Alzheimer's Association external quality control program for cerebrospinal fluid biomarkers. *Alzheimers Dement.* 7, 386.e6–395.e6.

Mattsson, N., Andreasson, U., Persson, S., Carrillo, M. C., Collins, S., Chalbot, S., et al. (2013). CSF biomarker variability in the Alzheimer's Association quality control program. *Alzheimers Dement.* 9, 251–261.

Mattsson, N., Blennow, K., and Zetterberg, H. (2010). Inter-laboratory variation in cerebrospinal fluid biomarkers for Alzheimer's disease: united we stand, divided we fall. *Clin. Chem. Lab. Med.* 48, 603–607.

Mattsson, N., Zegers, I., Andreasson, U., Bjerke, M., Blankenstein, M. A., Bowser, R., et al. (2012). Reference measurement procedures for Alzheimer's disease cerebrospinal fluid biomarkers: definitions and approaches with focus on amyloid β42. *Biomark. Med.* 6, 409–417. doi: 10.2217/bmm.12.39

Mayeux, R., and Schupf, N. (2011). Blood-based biomarkers for Alzheimer's disease: plasma Aβ40 and Aβ42, and genetic variants. *Neurobiol. Aging* 32, S10–S19.

McKhann, G. M., Knopman, D. S., Chertkow, H., Hyman, B. T., Jack, C. R. Jr., Kawas, C. H., et al. (2011). The diagnosis of dementia due to Alzheimer's disease: recommendations from the National Institute on Aging-Alzheimer's Association workgroups on diagnostic guidelines for Alzheimer's disease. *Alzheimers Dement.* 7, 263–269.

Morris, J. C. (1991). The Clinical Dementia Rating (CDR): current version and. *Young* 41, 1588–1592.

Prince, M. J. (2015). *World Alzheimer Report 2015: The Global Impact of Dementia: An Analysis of Prevalence, Incidence, Cost and Trends*. London: Alzheimer's Disease International.

Rissman, R. A., Trojanowski, J. Q., Shaw, L. M., and Aisen, P. S. (2012). Longitudinal plasma amyloid beta as a biomarker of Alzheimer's disease. *J. Neural. Transm.* 119, 843–850. doi: 10.1007/s00702-012-0772-4

Selkoe, D. J., and Hardy, J. (2016). The amyloid hypothesis of Alzheimer's disease at 25 years. *EMBO Mol. Med.* 8, 595–608.

Sinha, S., and Lieberburg, I. (1999). Cellular mechanisms of β-amyloid production and secretion. *Proc. Natl. Acad. Sci. U.S.A.* 96, 11049–11053. doi: 10.1073/pnas.96.20.11049

Strozyk, D., Blennow, K., White, L., and Launer, L. (2003). CSF Aβ 42 levels correlate with amyloid-neuropathology in a population-based autopsy study. *Neurology* 60, 652–656. doi: 10.1212/01.wnl.0000046581.81650.d0

Tapiola, T., Alafuzoff, I., Herukka, S.-K., Parkkinen, L., Hartikainen, P., Soininen, H., et al. (2009). Cerebrospinal fluid β-amyloid 42 and tau proteins as biomarkers of Alzheimer-type pathologic changes in the brain. *Arch. Neurol.* 66, 382–389.

van Oijen, M., Hofman, A., Soares, H. D., Koudstaal, P. J., and Breteler, M. M. (2006). Plasma Aβ1–40 and Aβ1–42 and the risk of dementia: a prospective case-cohort study. *Lancet Neurol.* 5, 655–660. doi: 10.1016/s1474-4422(06)70501-4

Winblad, B., Amouyel, P., Andrieu, S., Ballard, C., Brayne, C., Brodaty, H., et al. (2016). Defeating Alzheimer's disease and other dementias: a priority for European science and society. *Lancet Neurol.* 15, 455–532.

Yang, Y., Fuh, J., and Mok, V. C. (2018). Vascular contribution to cognition in stroke and Alzheimer's disease. *Brain Sci. Adv.* 4, 39–48. doi: 10.26599/bsa.2018.9050001

Yang, Y.-H., Liscic, R., and Dominguez, J. (2019). Framework of treating Alzheimer's dementia. *Brain Sci. Adv.* 5, 82–93. doi: 10.1177/2096595820902580

Youn, Y. C., Kang, S., Suh, J., Park, Y. H., Kang, M. J., Pyun, J.-M., et al. (2019). Blood amyloid-β oligomerization associated with neurodegeneration of Alzheimer's disease. *Alzheimers Res. Ther.* 11:40.

Zlokovic, B. V. (1996). Cerebrovascular transport of Alzheimer's amyloidβ and apolipoproteins J and E: possible anti-amyloidogenic role of the blood-brain barrier. *Life Sci.* 59, 1483–1497. doi: 10.1016/0024-3205(96)00310-4

Conflict of Interest: The authors declare that the research was conducted in the absence of any commercial or financial relationships that could be construed as a potential conflict of interest.

frontiers
in Cell and Developmental Biology

REVIEW
published: 31 August 2020
doi: 10.3389/fcell.2020.00765

Advances in the Biosynthetic Pathways and Application Potential of Plasmalogens in Medicine

*Yulong Zhou[1,2], Ning Yu[2], Jie Zhao[3], Zhenming Xie[2], Zhaonan Yang[1,2] and Bing Tian[2]**

[1] Key Laboratory for Green Processing of Chemical Engineering of Xinjiang Bingtuan, School of Chemistry and Chemical Engineering, Shihezi University, Shihezi, China, [2] MOE Key Laboratory of Biosystem Homeostasis and Protection, College of Life Sciences, Zhejiang University, Hangzhou, China, [3] Department of Applied Biological Science, Zhejiang University, Hangzhou, China

OPEN ACCESS

Edited by:
Shamim Hossain,
Kyushu University, Japan

Reviewed by:
Genny Orso,
University of Padua, Italy
Giuseppe Calamita,
University of Bari Aldo Moro, Italy

***Correspondence:**
Bing Tian
tianbing@zju.edu.cn

Specialty section:
This article was submitted to Cellular Biochemistry, a section of the journal Frontiers in Cell and Developmental Biology

Received: *07 May 2020*
Accepted: *21 July 2020*
Published: *31 August 2020*

Citation:
Zhou Y, Yu N, Zhao J, Xie Z, Yang Z and Tian B (2020) Advances in the Biosynthetic Pathways and Application Potential of Plasmalogens in Medicine. Front. Cell Dev. Biol. 8:765. doi: 10.3389/fcell.2020.00765

Plasmalogens are a special class of polar glycerolipids containing a vinyl-ether bond and an ester bond at sn-1 and sn-2 positions of the glycerol backbone, respectively. In animals, impaired biosynthesis and regulation of plasmalogens may lead to certain neurological and metabolic diseases. Plasmalogens deficiency was proposed to be strongly associated with neurodegenerative and metabolic diseases, such as Alzheimer's disease (AD) and Parkinson's disease (PD), and appropriate supplement of plasmalogens could help to prevent and possibly provide therapy of these diseases. Plasmalogens evolved first in anaerobic bacteria with an anaerobic biosynthetic pathway. Later, an oxygen-dependent biosynthesis of plasmalogens appeared in animal cells. This review summarizes and updates current knowledge of anaerobic and aerobic pathways of plasmalogens biosynthesis, including the enzymes involved, steps and aspects of the regulation of these processes. Strategies for increasing the expression of plasmalogen synthetic genes using synthetic biology techniques under specific conditions are discussed. Deep understanding of plasmalogens biosynthesis will provide the bases for the use of plasmalogens and their precursors as potential therapeutic regimens for age-related degenerative and metabolic diseases.

Keywords: plasmalogens, biosynthesis, anaerobic, oxygen-dependent, aging disease

INTRODUCTION

Plasmalogens (1-*O*-alk-1′-enyl 2-acyl glycerol phospholipids and glycolipids), also called plasmenyl phospholipid and plasmenyl glycolipids, are a special group of polar lipids, accounting for approximately 18–20 mol% of the total phospholipids in cell membranes of almost all mammalian. They are the constituents of biomembranes, which has a diversity of functions such as cell homeostasis, signaling and neural transmission (Ferlay et al., 2015; Dean and Lodhi, 2018). Plasmalogen contains a vinyl ether (-O-CH = CH-)-linked chain at sn-1 position and an ester chain at sn-2 position of glycerol backbone (Snyder, 1999; Braverman and Moser, 2012), respectively (**Figure 1**). Plasmalogens in animal tissues usually have a polyunsaturated acyl chain at the sn-2 position. Most of the polyunsaturated fatty acids (PUFAs) at sn-2 of plasmalogens are docosahexaenoic acid (DHA; C22:6 n-3) or arachidonic acid (AA; C20:4 n-6) in animals (Nagan and Zoeller, 2001). The representative plasmalogens in mammalian tissues are plasmalogen phosphatidylethanolamine (PlsEtn) and phosphatidylcholine plasmalogen (PlsCho)

(Heymans et al., 1983), and a small portion is present as plasmenylserine (PlsSer) and phosphatidic acid plasmalogen (Deeley et al., 2009; Ivanova et al., 2010; Nagy et al., 2012). PlsEtns constitute up to 50% of ethanolamine containing glycerophospholipids in the brain (Maeba et al., 2018).

Plasmalogens evolved first in anaerobic bacteria, but they are absent in facultative and aerobic bacteria except for Myxobacteria, which were recently found to use an oxygen-dependent synthetic pathway (Lorenzen et al., 2014; Gallego-García et al., 2019). Plasmalogens are not found in fungi or plants (Goldfine, 2010). It has been proposed that plasmalogen biosynthesis requiring molecular oxygen appeared later in animal cells as respiration evolved, indicating the emergence, disappearance and recurrence of plasmalogens during evolution. This disrupted evolution of plasmalogen may be due to the sensitivity of plasmalogens to reactive oxygen species (ROS) after the concentration of oxygen increased in the early earth's history, which will cause rapid degradation at the vinyl ether bond. However, the ability of higher organisms to use plasmalogen in an advantageous manner with special features of plasmalogens as found in animals, including antioxidant capacity, intracellular signaling and preservation of transmembrane ion gradients, may account for their reappearance (Goldfine, 2010; Lorenzen et al., 2014).

Lipid metabolism abnormalities are related to the occurrence of many human diseases (Fhaner et al., 2012). Plasmalogens are highly expressed in the nervous system and play an important role in many cellular functions of neurons (Maeba et al., 2018). Defects in plasmalogen synthesis are associated with neurodegenerative and metabolic diseases, such as Zellweger syndrome, Alzheimer's disease (AD), and Parkinson's disease (PD) (Yamashita et al., 2017; Dean and Lodhi, 2018). Among them, AD is an age-related progressive neurodegenerative disease and the cause of common dementia symptoms. The number of AD patients might reach more than 74 million worldwide by 2030, while the pathogeny of AD remains unclear (World Alzheimer Report, 2015). Plasmalogens were considered to be one of the oxidation targets of AD (Wood et al., 2010). The level of plasmalogens in blood and cerebrospinal fluid of AD patients is decreased (Goodenowe et al., 2007), and serum PlsEtn was suggested to be one of the cognitive decline markers (Maeba et al., 2018). In recent years, increasing studies demonstrated that supplemental of plasmalogens can be used to treat the symptoms of AD patients. Patients with mild AD showed a significant decrease in plasma PlsEtn in the placebo group than in the treatment group with oral administration of plasmalogens, and plasmalogens may improve cognitive functions of mild AD (Fujino et al., 2017). Moreover, serum plasmalogen levels have been used to diagnose and successfully stratify AD patients (Wood et al., 2015). These illustrate the importance of comprehensive understanding of the functions and biosynthesis of plasmalogens, which might be developed as a potential medicine for AD.

This review summarized the enzymes (genes) and steps involved in the aerobic and anaerobic pathways of plasmalogens biosynthesis. The significance of recently found important genes and strategies for increasing the production and application potential of plasmalogens in medicine are discussed.

PLASMALOGENS BIOSYNTHESIS IN ANAEROBIC BACTERIA

The biosynthesis of plasmalogens differs in synthetic enzymes (genes) and substrates between anaerobic microorganisms and animals. In anaerobic bacteria, glycerol 3-phosphate has been confirmed as the precursor for plasmalogen synthesis (Hill and Lands, 1970; Prins and Van Golde, 1976), while dihydroxyacetone phosphate (DHAP) is the precursor of plasmalogens in animals. The enzymes related to phospholipid and plasmalogens synthesis identified in anaerobic bacteria up to date are listed in **Table 1**.

By measuring the kinetics of incorporation of ^{32}Pi and ^{14}C into the diacylphosphatides and plasmalogens using radioautography, the reaction steps of anaerobic pathway were investigated. In *Clostridium beijerinckii* ATCC 6015, rapid incorporation of ^{32}Pi into diacylphosphatidylethanolamine (diacyl-PtdEtn) and diacyl N-monomethyl PtdEtn, and a delayed incorporation into their corresponding plasmalogens, indicating that diacylphosphatide could be substrates for the corresponding plasmalogens (Baumann et al., 1965). A subsequent ^{14}C-labeled acetate incorporation study also demonstrated a consistent precursor-product relationship between the chains attached to the phosphatidyl and alkyl-1-alkenyl ethers (Hagen and Goldfine, 1967). Moreover, labeling of the plasmalogen forms of phosphatidylglycerol (PtdGro) and cardiolipin is also delayed relative to the labeling of all acyl forms in *C. beijerinckii* (Koga and Goldfine, 1984). When hydroxylamine was added to the medium to block the decarboxylation of phosphatidylserine (PtdSer), there was initially 95% diacyl form and a 5% plasmalogen form of PtdSer; PtdSer was rapidly decarboxylated to form PtdEtn followed by the PlsEtn after the removal of hydroxylamine (Goldfine, 2017).

A pathway of plasmalogen synthesis in anaerobic bacteria was proposed as shown in **Figure 2** (Raetz and Dowhan, 1990; Dowhan, 1997; Zhang and Rock, 2008; Goldfine, 2010, 2017). First, fatty acyl-carrier protein (ACP) and glycerol 3-phosphate serve as precursors of phosphate acid (PA) under the catalysis of PlsX and PlsY. PA with cytidine triphosphate (CTP) is converted to cytidine diphosphate diacylglycerol (CDP-DAG) using CDP-diacylglycerol synthase (CdsA). Next, two additional transformations are required to produce PtdEtn or PtdGro. For PtdEtn synthesis, CDP-DAG can be converted to phosphatidylserine (PtdSer) using PtdSer synthase (PssA), and then PtdSer is converted to PtdEtn by PtdSer decarboxylase (Psd). For the branch of PtdGro synthesis, CDP-DAG is converted to phosphatidylglycerol 3-phosphate (PGP) by PGP synthase (PgsA) and then the 3-phosphate can be removed by a PGP phosphatase (PgpA or PgpB) to generate PtdGro (Dowhan, 1997). Finally, PtdEtn and PtdGro will be transformed into PlsEtn and PlsGro, respectively, under the catalysis of unknown enzymes. Although plasmalogens have been

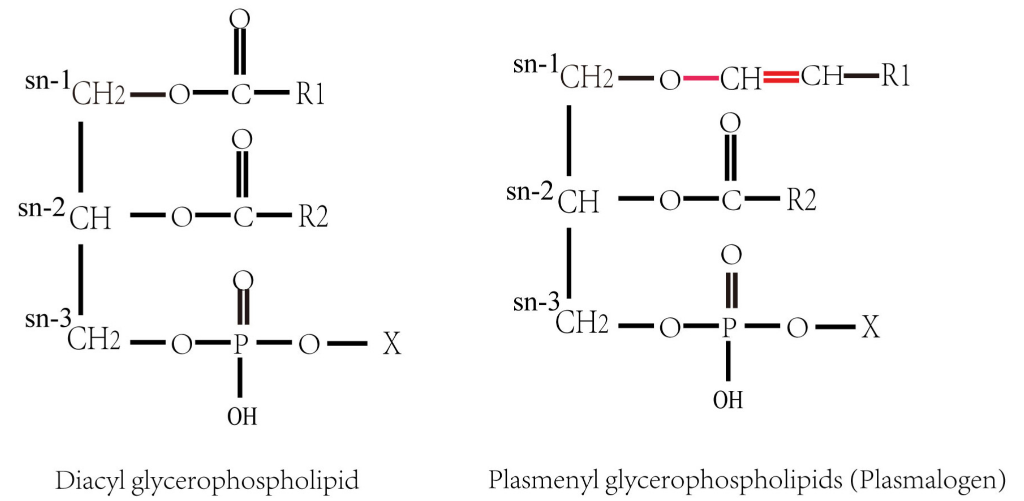

FIGURE 1 | Structures of diacyl glycerophospholipid and plasmenyl glycerophospholipids (plasmalogens). X denotes the polar head group, such as ethanolamine or choline. R1 and R2 denote the hydrocarbon chains at the sn-1 and the sn-2 positions, respectively.

TABLE 1 | Enzymes related to plasmalogens biosynthesis in anaerobic bacteria.

Enzyme name	Function descriptions
PlsX/Y	Glycerol 3-phosphate acyltransferase
CdsA	CDP-diacylglycerol synthase
PgsA	Phosphatidylglycerol phosphate synthase
PssA	Phosphatidylserine synthase
Psd	Phosphatidylserine decarboxylase
PgpA/PgpB	PGP phosphatases

CDP, cytidine diphosphate; PGP, phosphatidylglycerol phosphate.

identified in anaerobic bacteria for nearly 50 years (Wegner and Foster, 1963; Goldfine, 1964), gene(s) and mechanism corresponding to the formation of the vinyl ether bond of plasmalogens remain unclear.

THE OXYGEN-DEPENDENT PATHWAY OF PLASMALOGENS BIOSYNTHESIS

Phosphatidylethanolamine plasmalogen is the basic components of cell bilayers, accounting for about 20% of human phospholipids (Farooqui and Horrocks, 2001; Lessig and Fuchs, 2009; Braverman and Moser, 2012; Dorninger et al., 2015; Dean and Lodhi, 2018). Particularly, high concentrations of PlsEtn were found in the brain, retina, and other nervous tissues, accounting for 60% and 80% of the total ethanolamine phospholipids in gray and white matter, respectively (Saab et al., 2014). The plasmalogen-associated genes in animals have been studied as listed in **Table 2**. Among them, plasmanyl desaturase (1′-alkyl desaturase) is a predicted unstable membrane enzyme that remains to be identified for many years. In a recent report, the enzyme CarF found in an aerobic bacterium Myxobacteria

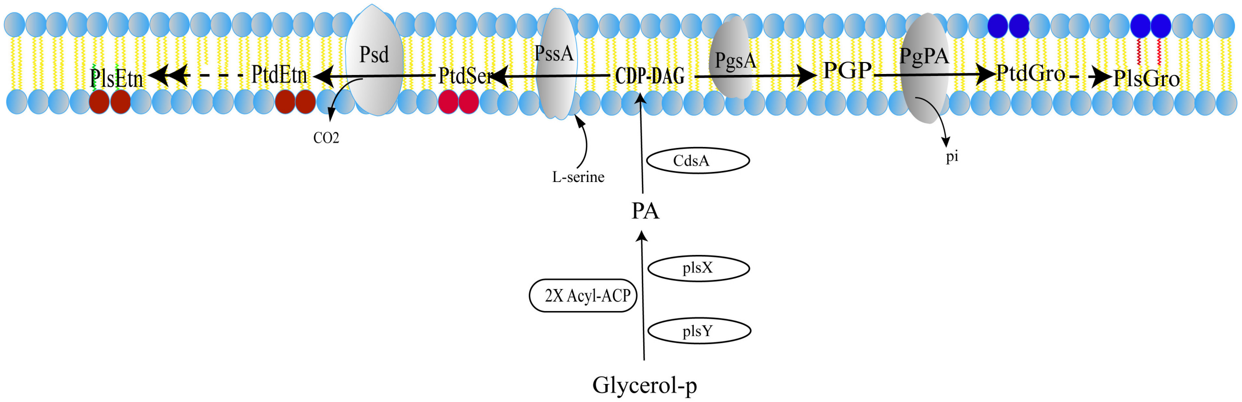

FIGURE 2 | Anaerobic pathway for plasmalogen synthesis in bacteria. PA, phosphatidic acid; CDP-DAG, CDP-diacylglycerol; PGP, phosphatidylglycerol 3-phosphate; PtdEtn, phosphatidylethanolamine; PtdSer, phosphatidylserine; PtdGro, phosphatidylglycerol; PlsGro, phosphatidylglycerol plasmalogen; PlsEtn, phosphatidylethanolamine plasmalogen. The detail of enzyme and mechanism leading from the diacyl phospholipids to plasmalogens is still unknown.

TABLE 2 | Enzymes related to plasmalogen biosynthesis in animals.

Enzyme name	Function descriptions
FAS	Fatty acid synthase
ACS	Acyl-CoA synthase
FAR-1/2	Fatty acyl-CoA reductase 1 or 2
DHAP-AT	DHAP acyltransferase
ADHAP-S	Alkyl DHAP synthase
AADHAP-R	Alkyl/acyl-DHAP-reductase
AAG3P-AT	Alkyl/acyl-glycero-3-phosphate acyltransferase
PH	Phosphohydrolase
E-PT	Ethanolamine phosphotransferase
TMEM189 homolog	plasmanylethanolamine desaturase

DHAP, dihydroxyacetone phosphate.

was confirmed to be the 1′-alkyl desaturase for the last step of plasmalogen formation (Gallego-García et al., 2019). Its homolog TMEM189 was successively identified in mice and human (Gallego-García et al., 2019; Werner et al., 2020). Knock out of the animal homolog in human cell lines resulted in the deficiency of plasmalogens, indicating that TMEM189 is needed to catalyze the final step in plasmalogen synthesis in human cells (Gallego-García et al., 2019).

Plasmalogen biosynthesis occurs in peroxisomes, an oxidative organelle found in virtually all eukaryotic cells, and terminates in the endoplasmic reticulum (ER) (Wallner and Schmitz, 2011). Based on the identified enzymes in previous publications (Wallner and Schmitz, 2011; Gallego-García et al., 2019; Werner et al., 2020), an overview of the synthetic pathway is proposed in **Figure 3**.

Plasmalogens biosynthesis in peroxisomes of animals starts with acyl-CoA and DHAP. Under the action of DHAP-acyltransferase (DHAP-AT), DHAP is converted into 1-*O*-acyl DHAP, and then the acyl chain is replaced by a long-chain fatty alcohol from Acyl-CoA synthesis pathway (McIntyre et al., 2008) or from foods. DHAP-acyltransferase is also known as glyceronephosphate *O*-acyltransferase (GNPAT) (Nagan and Zoeller, 2001),which initiates the esterification of DHAP with a long-chain acyl-CoA (Hajra, 1997). Next, alkyl DHAP synthase (ADHAP-S) catalyzes the replacement of acyl group of 1-*O*-acyl DHAP with a long-chain fatty alcohol to generate 1-*O* alkyl-DHAP (Hajra, 1995; Hayashi and Sato, 1997; Cheng and Russell, 2004; Honsho et al., 2010; Wallner and Schmitz, 2011). The fatty alcohols are synthesized by fatty acyl-CoA reductases 1 and 2 (Far1/2) (Hajra, 1995, 1997; Nagan and Zoeller, 2001; Wallner and Schmitz, 2011) or directly taken up from diet. Notably, the Far1 is regulated by negative feedback of cellular plasmalogen levels (Honsho et al., 2010). Therefore, the formation and supply of long-chain fatty alcohols are considered to be one of the rate-limiting steps of the plasmalogen biosynthetic pathway (Paul et al., 2019). The alkyl-DHAP is then transferred from the peroxisome into the ER.

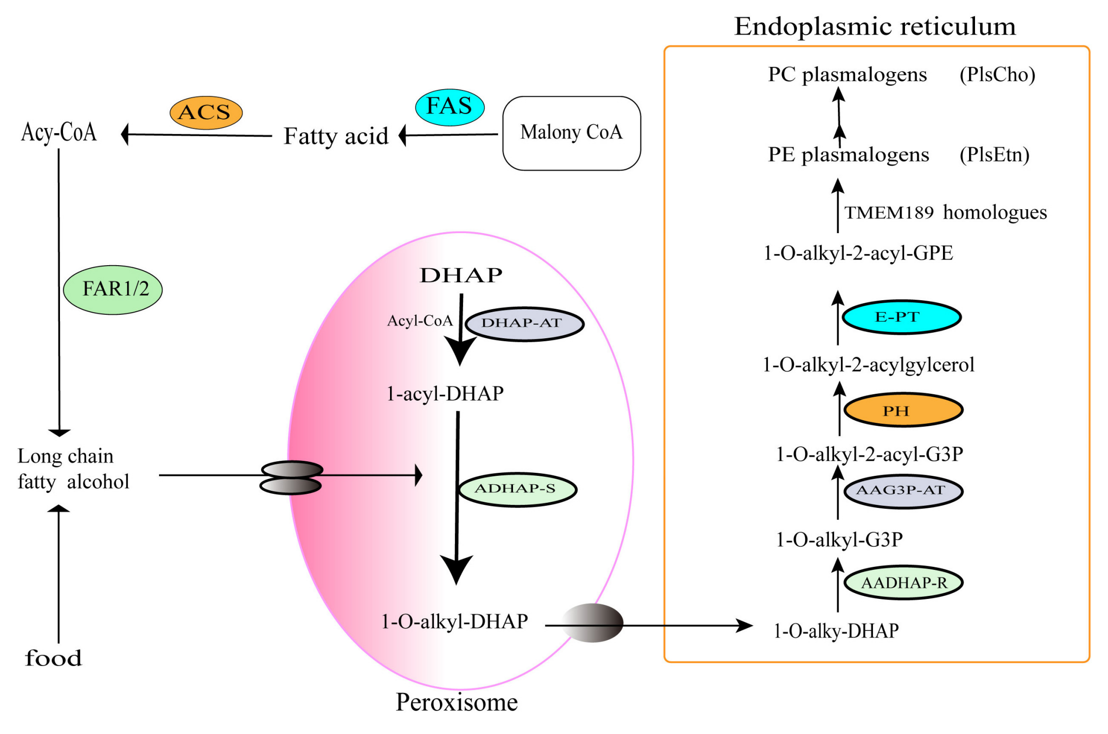

FIGURE 3 | Oxygen-dependent pathway of plasmalogens biosynthesis in animals. The enzymes involved in the indicated steps: FAS, fatty acid synthase; ACS, acyl-CoA synthase; FAR1/2, fatty acyl-CoA reductase 1 or 2; DHAP-AT, DHAP acyltransferase; ADHAP-S, alkyl-DHAP synthase; AADHAP-R, NADPH:alkyl-DHAP oxidoreductase; AAG3P-AT, acyl-CoA:1-alkyl-2-lyso-sn-glycero-3-phosphate acyltransferase; PH, 1-alkyl-2-acyl-sn-glycero-3-phosphate phosphohydrolase; E-PT, CDP-ethanolamine:1-alkyl-2-acyl-sn-glycerol ethanolamine phosphotransferase; TMEM189 homologs, plasmanylethanolamine desaturases.

In the ER, acyl/alkyl DHAP reductase (AADHAP-R) catalyzes the reduction of 1-*O*-alkyl-DHAP to form 1-*O*-alkyl-2-hydroxyl-sn-glycerol-3-phosphate (1-*O*-alkyl-G3P) (Hajra, 1997). Then, the acyl/alkyl-G3P-acyltransferase (AAG3P-AT) catalyzes acylation with an acyl-CoA at the sn-2 position of the 1-*O*-alkyl-G3P to form 1-*O*-alkyl-2-acyl-G3P. The phosphate group of -*O*-alkyl-2-acyl-G3P is removed by phosphohydrolase (PH) to form 1-*O*-alkyl-2-acylglycerol (Wallner and Schmitz, 2011). Next, ethanolamine phosphate head group is added to 1-*O*-alkyl-2-acylglycerol by the ethanolamine phosphotransferase (E-PT) to generate plasmanylethanolamine (1-*O*-alkyl-2-acyl-GPE) (Brites et al., 2004). Finally, plasmanylethanolamine is converted into 1-*O*-alk-1′-enyl 2-acyl phosphatidylethanolamine (PlsEtn) through the action of 1′-alkyl desaturase (TMEM189 homolog) in the presence of molecular oxygen and NADPH. Because there is no plasmenylcholine desaturase found in animals, choline plasmalogens (PlsCho) might be formed only following the hydrolysis of ethanolamine plasmalogens into form 1-*O* -(1Z-alkenyl)-2-acyl-sn-glycerol, which was then modified by choline phosphotransferase and CDP-choline (Lee, 1998).

PERSPECTIVES OF PLASMALOGENS BIOSYNTHESIS USING SYNTHETIC BIOLOGY METHODS AND APPLICATION POTENTIALS IN MEDICINE

Traditionally, plasmalogens are obtained using chemical synthetic method or extraction from animal tissue. However, the need for large amounts of chemicals as well as generation of potential hazardous waste during the chemical synthetic process of plasmalogens limit the applications of the chemical synthetic method. Although plasmalogens are widely found and can be prepared from marine animals or bird tissues, the amount of plasmalogens from these natural materials are very low and only account for less than 10% of the phospholipids in cell membrane of the tissues used.

Synthetic biology is a discipline that uses biological functional elements, devices and systems to carry out targeted genetic design and transformation of living organisms, to enable cells and organisms to generate specific biological functions or produce natural materials and even to synthesize "artificial life." Using the synthetic biology techniques, artificial PUFA biosynthetic gene cluster (BGC) including a polyketide synthase-like PUFA synthetase from Myxobacteria has been introduced into yeast *Yarrowia lipolytica*, and successfully produces the highest level of DHA (16.8% of total fatty acid) among PUFA-producing *Y. lipolytica* (Gemperlein et al., 2019).

With the elucidation of plasmalogen biosynthesis genes and pathway for aerobic organisms, especially the recent identification of 1′-alkyl desaturase responsible for the conversion of plasmanylphospholipid into plasmalogens (Gallego-García et al., 2019), designing and efficient expression of plasmalogen biosynthetic modules in engineering host cells such as yeast cells become possible. The production and composition of plasmalogens is controlled by synthetic genes and certain rate-limiting steps in biosynthesis such as Far1/2 and 1-alkyl-DHAP (Paul et al., 2019). It was found that supplementation with alkyl glycerol can increase plasmalogen levels in cultured cells (Marigny et al., 2002), animals (Brites et al., 2011), and humans (Das et al., 1992). The most commonly used alkyl glycerols to increase plasmalogen levels in mammalian research are chimyl (O-16:0), batyl (O-18:0), and selachyl (O-18:1) alcohols (Brites et al., 2011; Rasmiena et al., 2015; Tham et al., 2018). Therefore, expression of plasmalogen products can be regulated under specific conditions through the genetic circuit designing and integration of gene modules composed of plasmalogen-related genes and rate-limiting elements. Standard and modularized biological elements can be used to reconstruct the metabolic network in host cells to efficiently synthesize or improve plasmalogen products that meet needs. For anaerobic biosynthesis of plasmalogen, it is necessary for us to identify the key gene(s) responsible for the formation of the vinyl ether bond of plasmalogens in anaerobic bacteria before its synthetic biological study and application.

It has been known that cultured cells and animal tissues lacking plasmalogen are more sensitive to oxidative damage than their wild-type counterparts (Zoeller et al., 1988; Reiss et al., 1997). This is due to the presence of vinyl ether bonds making plasmalogens efficient antioxidants (Broniec et al., 2011). In particular, plasmalogens can protect unsaturated membrane lipids from oxidation by singlet oxygen and participate in the removal of various ROS (Maeba et al., 2002; Skaff et al., 2008). Plasmalogen is susceptible to cleavage by ROS, yielding products that may act as second messengers (Lorenzen et al., 2014). More importantly, plasmalogen deficiency correlates with various human neurological and aging diseases, such as AD and PD (Nadeau et al., 2019; Paul et al., 2019).

Alzheimer's disease is a complex neurodegenerative disease characterized by progressive memory loss and progressive loss of neuronal cells mainly observed in the hippocampus (Fujino et al., 2017; Jan et al., 2017). Although the gradual accumulation of β-amyloid fibers (Aβ plaque) and abnormal forms of tau (tau tangles) inside and outside neurons are considered the neuropathology of AD, the causes and mechanisms of AD have not been fully elucidated (Fujino et al., 2017; Jan et al., 2017). Accumulation of β-amyloid in AD leads to the increase of ROS levels in cells and reduces the activity of ADHAP-S, which might result in the decrease of plasmalogens (Grimm et al., 2011). Plasmalogen levels in human serum decrease with age and reductions in alkyl PtdCho and alkyl PtdEtn levels have been observed in patients with hypertension (Graessler et al., 2009). The content of plasmalogens in the brain of AD patients after death is very low (Wood et al., 2010; Braverman and Moser, 2012). Among them, the PlsEtn decreased by about 70%(Wood et al., 2010; Onodera et al., 2015). Hossain et al. (2013, 2016) found that PlsEtn inhibited the death of hippocampal neurons by increasing the phosphorylation of Akt and ERK kinases through activating the neuronal specific orphan G-protein coupled receptors (GPCRs). In their study, pan GPCR inhibitors significantly reduce the plasmalogens-induced ERK signaling in nerve cells, indicating that plasmalogens could activate GPCR-induced signaling, Plasmalogens-mediated phosphorylation of ERK was inhibited in five of the GPCRs' knockdown cells. Overexpression of these GPCRs enhanced the plasmalogens-mediated phosphorylation of ERK and Akt, and the GPCRs-mediated cellular signaling was reduced significantly when the endogenous plasmalogens were reduced, suggesting for the first time a possible mechanism of plasmalogens-induced cell signaling in the nervous system (Hossain et al., 2016). Direct consumption of plasmalogen or related phospholipids can be used to treat dementia. For example, DHA-PC and DHA-PS can restore the content of DHA-containing PS and PlsEtn in the brain, and significantly restore the lipid homeostasis of dementia mice (SAMP8 mice), which have a phenotype that accelerates aging (Zhao et al., 2020). Oral administration of PtdEtn rich in plasmalogens (PlsEtn) from viscera of marine animals ameliorated cognitive impairment and improved the learning ability in amyloid (Aβ)-infused rats (Yamashita et al., 2017). In recent human trials, Fujino et al. (2017) reported that oral supplementing scallop-derived purified plasmalogens (1 mg/day) for 24 weeks improved memory function of patients with mild AD. Hossain et al. (2018) reported that oral ingestion of plasmalogens can attenuate the lipopolysaccharide-induced memory loss and microglial activation in mice. These findings suggest the importance of comprehensive understanding of the functions and biosynthesis of plasmalogens, which might be developed as a potential medicine for AD. Due to the increasing need of plasmalogens, it is possible to biosynthesize plasmalogens on a large scale using synthetic biological strategy.

Parkinson's disease is a metabolic disorder and neurodegenerative disease. The pathological feature is the abnormal aggregation of SNCA/α-synuclein in the brain and the loss of dopaminergic neurons in the substantia nigra (Ho et al., 2020). The relationship between PD and plasmalogen was controversial. Although the initial study found no changes in the PlsEtn of PD patients compared with the control group (Ginsberg et al., 1995), recent studies have found that the serum concentration of PlsEtn in PD patients is reduced and low levels of plasmalogen have also been detected in frontal lobe sebaceous rafts of PD patients (Dragonas et al., 2009; Fabelo et al., 2011). Nadeau et al. (2019) reported the neuroprotective and immunomodulatory effects of plasmalogen precursors on mice with PD. They found that the supplement of DHA-containing PlsEtn precursor PPI-1011 in the intestine of mice treated with 1-methyl-4-phenyl-1,2,3,6- tetrahydropyridine (MPTP) could not only prevent MPTP-induced decrease in PlsEtn levels but also reduce macrophage infiltration in the intermuscular plexus of MPTP-treated mice (Nadeau et al., 2019). These results indicate the potential application of PlsEtn in the treatment of PD.

CONCLUSION

This review summarizes the current knowledge in the field of anaerobic and aerobic biosynthetic pathways and application potential of plasmalogens in medicine. The anaerobic biosynthesis of plasmalogens differs in synthetic genes and precursors from that of oxygen-dependent biosynthesis pathway. Two different biosynthetic pathways demonstrate the significant functions and evolution of plasmalogens in organisms. The recent identification of 1′-alkyl desaturase elucidated the aerobic plasmalogen biosynthesis pathway and opened the door to the aerobic synthesis of plasmalogens using synthetic biological strategy. Further investigation on the genes responsible for the critical step in anaerobic synthesis pathway is required for the comprehensive understanding of plasmalogens evolution and functions. Because of the relevance of plasmalogens to neurological diseases, it is increasingly important to investigate the production and application of plasmalogens as potential therapeutic strategies for treating and preventing neurodegenerative and metabolic diseases.

AUTHOR CONTRIBUTIONS

BT and YZ conceived the review and wrote the manuscript. NY, JZ, ZX, and ZY revised the literature and helped to writing the manuscript. BT supervised the overall project and edited the manuscript. All authors had the opportunity to discuss and comment on the manuscript.

FUNDING

This study was supported by grants from the National Natural Science Foundation of China (31670083 and 31870025), the National Key R&D Program of China (2019YFA0905400), and the Fundamental Research Funds for the Central Universities.

REFERENCES

Baumann, N. A., Hagen, P. O., and Goldfine, H. (1965). Phospholipids of *Clostridium butyricum*. studies on plasmalogen composition and biosynthesis. *J. Biol. Chem.* 240, 1559–1567.

Braverman, N. E., and Moser, A. B. (2012). Functions of plasmalogen lipids in health and disease. *Biochim. Biophys. Acta* 1822, 1442–1452. doi: 10.1016/j.bbadis.2012.05.008

Brites, P., Ferreira, A. S., da Silva, T. F., Sousa, V. F., Malheiro, A. R., Duran, M., et al. (2011). Alkyl-glycerol rescues plasmalogen levels and pathology of ether-phospholipid deficient mice. *PLoS One* 6:e28539. doi: 10.1371/journal.pone.0028539

Brites, P., Waterham, H. R., and Wanders, R. J. (2004). Functions and biosynthesis of plasmalogens in health and disease. *Biochim. Biophys. Acta* 1636, 219–231. doi: 10.1016/j.bbalip.2003.12.010

Broniec, A., Klosinski, R., Pawlak, A., Wrona-Krol, M., Thompson, D., and Sarna, T. (2011). Interactions of plasmalogens and their diacyl analogs with singlet oxygen in selected model systems. *Free Radic Biol. Med.* 50, 892–898. doi: 10.1016/j.freeradbiomed.2011.01.002

Cheng, J. B., and Russell, D. W. (2004). Mammalian wax biosynthesis I. Identifification of two fatty acyl-Coenzyme A reductases with different substrate specifificities and tissue distributions. *J. Biol. Chem.* 279, 37789–37797. doi: 10.1074/jbc.m406225200

Das, A. K., Holmes, R. D., Wilson, G. N., and Hajra, A. K. (1992). Dietary ether lipid incorporation into tissue plasmalogens of humans and rodents. *Lipids* 27, 401–405. doi: 10.1007/bf02536379

Dean, J. M., and Lodhi, I. J. (2018). Structural and functional roles of ether lipids. *Protein Cell* 9, 196–206. doi: 10.1007/s13238-017-0423-5

Deeley, J. M., Thomas, M. C., Truscott, R. J., Mitchell, T. W., and Blanksby, S. J. (2009). Identification of abundant alkyl ether glycerophospholipids in the human lens by tandem mass spectrometry techniques. *Anal. Chem.* 81, 1920–1930. doi: 10.1021/ac802395d

Dorninger, F., Brodde, A., Braverman, N. E., Moser, A. B., Just, W. W., Forss-Petter, S., et al. (2015). Homeostasis of phospholipids - The level of phosphatidylethanolamine tightly adapts to changes in ethanolamine plasmalogens. *Biochim. Biophys. Acta* 1851, 117–128. doi: 10.1016/j.bbalip.2014.11.005

Dowhan, W. (1997). Molecular basis for membrane phospholipid diversity: why are there so many lipids? *Annu. Rev. Biochem*. 66, 199–232. doi: 10.1146/annurev.biochem.66.1.199

Dragonas, C., Bertsch, T., Sieber, C. C., and Brosche, T. (2009). Plasmalogens as a marker of elevated systemic oxidative stress in Parkinson's disease. *Clin. Chem. Lab. Med.* 47, 894–897.

Fabelo, N., Martín, V., Santpere, G., Marín, R., Torrent, L., Ferrer, I., et al. (2011). Severe alterations in lipid composition of frontal cortex lipid rafts from Parkinson's disease and incidental Parkinson's disease. *Mol. Med.* 17, 1107–1118. doi: 10.2119/molmed.2011.00119

Farooqui, A. A., and Horrocks, L. A. (2001). Plasmalogens: workhorse lipids of membranes innormal and injured neurons and glia. *Neuroscientist* 7, 232–245. doi: 10.1177/107385840100700308

Ferlay, J., Soerjomataram, I., Dikshit, R., Eser, S., Mathers, C., Rebelo, M., et al. (2015). Cancer incidence and mortality worldwide: sources, methods and major patterns in GLOBOCAN 2012. *Int. J. Cancer* 136, E359–E386.

Fhaner, C. J., Liu, S., Ji, H., Simpson, R. J., and Reid, G. E. (2012). Comprehensive lipidome profiling of isogenic primary and metastatic colon adenocarcinoma cell lines. *Anal. Chem.* 84, 8917–8926. doi: 10.1021/ac302154g

Fujino, T., Yamada, T., Asada, T., Tsuboi, Y., Wakana, C., Mawatari, S., et al. (2017). Efficacy and blood plasmalogen changes by oral administration of plasmalogen in patients with mild Alzheimer's disease and mild cognitive impairment: a multicenter, randomized, double-blind, placebo-controlled trial. *eBio Med.* 17, 199–205. doi: 10.1016/j.ebiom.2017.02.012

Gallego-García, A., Monera-Girona, A. J., Pajares-Martínez, E., Bastida-Martínez, E., Pérez-Castaño, R., Iniesta, A. A., et al. (2019). Bacterial light response reveals an orphan desaturase for human plasmalogen synthesis. *Science* 366, 128–132. doi: 10.1126/science.aay1436

Gemperlein, K., Dietrich, D., Kohlstedt, M., Zipf, G., Bernauer, H. S., Wittmann, C., et al. (2019). Polyunsaturated fatty acid production by *Yarrowia lipolytica* employing designed myxobacterial PUFA synthases. *Nat. Commun.* 10:4055. doi: 10.1038/s41467-019-12025-8

Ginsberg, L., Rafique, S., Xuereb, J. H., Rapoport, S. I., and Gershfeld, N. L. (1995). Disease and anatomic specificity of ethanolamine plasmalogen deficiency in Alzheimer's disease brain. *Brain Res.* 698, 223–226. doi: 10.1016/0006-8993(95)00931-f

Goldfine, H. (1964). Composition of the aldehydes of *Clostridium butyricum* plasmalogens: cyclopropane aldehydes. *J. Biol. Chem.* 239, 2130–2134.

Goldfine, H. (2010). The appearance, disappearance and reappearance of plasmalogens in evolution. *Prog. Lipid Res.* 49, 493–498. doi: 10.1016/j.plipres.2010.07.003

Goldfine, H. (2017). The anaerobic biosynthesis of plasmalogens. *FEBS Lett.* 591, 2714–2719. doi: 10.1002/1873-3468.12714

Goodenowe, D. B., Cook, L. L., Liu, J., Lu, Y., Jayasinghe, D. A., Ahiahonu, P. W., et al. (2007). Peripheral ethanolamine plasmalogen deficiency: a logical causative factor in Alzheimer's disease and dementia. *J. Lipid Res.* 48, 2485–2498. doi: 10.1194/jlr.p700023-jlr200

Graessler, J., Schwudke, D., Schwarz, P. E., Herzog, R., Shevchenko, A., and Bornstein, S. R. (2009). Top-down lipidomics reveals ether lipid deficiency in blood plasma of hypertensive patients. *PLoS One* 15:e6261. doi: 10.1371/journal.pone.006261

Grimm, M. O., Kuchenbecker, J., Rothhaar, T. L., Grösgen, S., Hundsdörfer, B., Burg, V. K., et al. (2011). Plasmalogen synthesis is regulated via alkyl-dihydroxyacetonephosphate-synthase by amyloid precursor protein processing and is affected in Alzheimer's disease. *J. Neurochem.* 116, 916–925. doi: 10.1111/j.1471-4159.2010.07070.x

Hagen, P. O., and Goldfine, H. (1967). Phospholipids of *Clostridium butyricum*. 3. Further studies on the origin of the aldehyde chains of plasmalogens. *J. Biol. Chem.* 242, 5700–5708.

Hajra, A. K. (1995). Glycerolipid biosynthesis in peroxisomes (microbodies). *Prog. Lipid Res.* 34, 343–364. doi: 10.1016/0163-7827(95)00013-5

Hajra, A. K. (1997). Dihydroxyacetone phosphate acyltransferase. *Biochim. Biophys. Acta* 1348, 27–34.

Hayashi, H., and Sato, A. (1997). Fatty alcohol synthesis accompanied with chain elongation in liver peroxisomes. *Biochim. Biophys. Acta* 1346, 38–44. doi: 10.1016/s0005-2760(97)00020-9

Heymans, H. S. A., Schutgens, R. B. H., Tan, R., van den Bosch, H., and Borst, P. (1983). Severe plasmalogen defificiency in tissues of infants without peroxisomes (Zellweger syndrome). *Nature* 306, 69–70. doi: 10.1038/306069a0

Hill, E. E., and Lands, W. E. (1970). Formation of acyl and alkenyl glycerol derivatives in *Clostridium butyricum*. *Biochim. Biophys. Acta* 202, 209–211. doi: 10.1016/0005-2760(70)90239-0

Ho, P. W., Leung, C. T., Liu, H., Pang, S. Y. Y., Lam, C. S. C., Xian, J., et al. (2020). Age-dependent accumulation of oligomeric SNCA/α-synuclein from impaired degradation in mutant LRRK2 knockin mouse model of Parkinson disease: role for therapeutic activation of chaperone-mediated autophagy (CMA). *Autophagy* 16, 347–370. doi: 10.1080/15548627.2019.1603545

Honsho, M., Asaoku, S., and Fujiki, Y. (2010). Posttranslational regulation of fatty acyl-CoA reductase 1, Far1, controls ether glycerophospholipid synthesis. *J. Biol. Chem.* 285, 8537–8542. doi: 10.1074/jbc.m109.083311

Hossain, M. S., Ifuku, M., Take, S., Kawamura, J., Miake, K., and Katafuchi, T. (2013). Plasmalogens rescue neuronal cell death through an activation of AKT and ERK survival signaling. *PLoS One* 8:e83508. doi: 10.1371/journal.pone.0083508

Hossain, M. S., Mineno, K., and Katafuchi, T. (2016). Neuronal orphan G-protein coupled receptor proteins mediate plasmalogens-induced activation of ERK and Akt signaling. *PLoS One* 11:e0150846. doi: 10.1371/journal.pone.00150846

Hossain, M. S., Tajima, A., Kotoura, S., and Katafuchi, T. (2018). Oral ingestion of plasmalogens can attenuate the LPS-induced memory loss and microglial activation. *Biochem. Biophys. Res. Commun.* 496, 1033–1039. doi: 10.1016/j.bbrc.2018.01.078

Ivanova, P. T., Milne, S. B., and Brown, H. A. (2010). Identification of atypical ether-linked glycerophospholipid species in macrophages by mass spectrometry. *J. Lipid Res.* 51, 1581–1590. doi: 10.1194/jlr.d003715

Jan, A. T., Azam, M., Rahman, S., Almigeiti, A. M. S., Choi, D. H., Lee, E. J., et al. (2017). Perspective insights into disease progression, diagnostics, and therapeutic approaches in Alzheimer's disease: a judicious update. *Front. Aging Neurosci.* 9:356. doi: 10.3389/fnagi.2017.00356

Koga, Y., and Goldfine, H. (1984). Biosynthesis of phospholipids in *Clostridium butyricum*: kinetics of synthesis of plasmalogens and the glycerol acetal of ethanolamine plasmalogen. *J. Bacteriol.* 159, 597–604. doi: 10.1128/jb.159.2.597-604.1984

Lee, T. C. (1998). Biosynthesis and possible biological functions of plasmalogens. *Biochim. Biophys. Acta* 1394, 129–145. doi: 10.1016/s0005-2760(98)00107-6

Lessig, J., and Fuchs, B. (2009). Plasmalogens in biological systems: their role in oxidative processes in biological membranes, their contribution to pathological processes and aging and plasmalogen analysis. *Curr. Med. Chem.* 16, 2021–2041. doi: 10.2174/092986709788682164

Lorenzen, W., Ahrendt, T., Bozhüyük, K. A., and Bode, H. B. (2014). A multifunctional enzyme is involved in bacterial ether lipid biosynthesis. *Nat. Chem. Biol.* 10, 425–427. doi: 10.1038/nchembio.1526

Maeba, R., Araki, A., and Fujiwara, Y. (2018). Serum ethanolamine plasmalogen and urine myo-inositol as cognitive decline markers. *Adv. Clin. Chem.* 87, 69–111. doi: 10.1016/bs.acc.2018.08.001

Maeba, R., Sawada, Y., Shimasaki, H., Takahashi, I., and Uetaa, N. (2002). Ethanolamine plasmalogens protect cholesterol-rich liposomal membranes from oxidation caused by free radicals. *Chem. Phys. Lipids* 120, 145–151. doi: 10.1016/s0009-3084(02)00101-9

Marigny, K., Pedrono, F., Martin-Chouly, C. A., Youmine, H., Saiag, B., and Legrand, A. B. (2002). Modulation of endothelial permeability by 1-O-alkylglycerols. *Acta Physiol. Scand.* 176, 263–268. doi: 10.1046/j.1365-201x.2002.01037.x

McIntyre, T. M., Snyder, F., and Marathe, G. K. (2008). "Ether-linked lipids and their bioactive species," in *Biochemistry of Lipids, Lipoproteins and Membranes*, eds D. E. Vance and J. E. Vance (Amsterdam: Elsevier), 245–276. doi: 10.1016/b978-044453219-0.50011-8

Nadeau, J., Smith, T., Lamontagne-Proulx, J., Bourque, M., Al Sweidi, S., Jayasinghe, D., et al. (2019). Neuroprotection and immunomodulation in the gut of parkinsonian mice with a plasmalogen precursor. *Brain Res.* 1725:146460. doi: 10.1016/j.brainres.2019.146460

Nagan, N., and Zoeller, R. A. (2001). Plasmalogens: biosynthesis and functions. *Prog. Lipid Res.* 40, 199–229. doi: 10.1016/s0163-7827(01)00003-0

Nagy, K., Brahmbhatt, V. V., Berdeaux, O., Bretillon, L., Destaillats, F., and Acar, N. (2012). Comparative study of serine-plasmalogens in human retina and optic nerve: identification of atypical species with odd carbon chains. *J. Lipid Res.* 53, 776–783. doi: 10.1194/jlr.d022962

Onodera, T., Futai, E., Kan, E., Abe, N., Uchida, T., Kamio, Y., et al. (2015). Phosphatidylethanolamine plasmalogen enhances the inhibiting effect of phosphatidylethanolamine on γ-secretase activity. *J. Biochem.* 157, 301–309. doi: 10.1093/jb/mvu074

Paul, S., Lancaster, G. I., and Meikle, P. J. (2019). Plasmalogens: a potential therapeutic target for neurodegenerative and cardiometabolic disease. *Prog. Lipid Res.* 74, 186–195. doi: 10.1016/j.plipres.2019.04.003

Prins, R. A., and Van Golde, L. M. (1976). Entrance of glycerol into plasmalogens of somestrictly anaerobic bacteria and protozoa. *FEBS Lett.* 63, 107–111. doi: 10.1016/0014-5793(76)80204-9

Raetz, C. R., and Dowhan, W. (1990). Biosynthesis and function of phospholipids in *Escherichia coli*. *J. Biol. Chem.* 265, 1235–1238.

Rasmiena, A. A., Barlow, C. K., Stefanovic, N., Huynh, K., Tan, R., Sharma, A., et al. (2015). Plasmalogen modulation attenuates atherosclerosis in ApoE- and ApoE/GPx1-deficient mice. *Atherosclerosis* 243, 598–608. doi: 10.1016/j.atherosclerosis.2015.10.096

Reiss, D., Beyer, K., and Engelmann, B. (1997). Delayed oxidative degra dation of polyunsaturated diacyl phospholipids in the presence of plasmalogen phospholipids in vitro. *Biochem. J.* 323, 807–814. doi: 10.1042/bj3230807

Saab, S., Mazzocco, J., Creuzot-Garcher, C. P., Bron, A. M., Bretillon, L., and Acar, N. (2014). Plasmalogens in the retina: from occurrence in retinal cell membranes to potential involvement in pathophysiology of retinal diseases. *Biochimie* 107(Pt A), 58–65. doi: 10.1016/j.biochi.2014.07.023

Skaff, O., Pattison, D. I., and Davies, M. J. (2008). The vinyl ether linkages of plasmalogens are favored targets for myeloperoxidase-derived oxidants: a kinetic study. *Biochemistry* 47, 8237–8245. doi: 10.1021/bi800786q

Snyder, F. (1999). The ether lipid trail: a historical perspective. *Biochim. Biophys. Acta* 1436, 265–278.

Tham, Y. K., Huynh, K., Mellett, N. A., Henstridge, D. C., Kiriazis, H., Ooi, J. Y. Y., et al. (2018). Distinct lipidomic profiles in models of physiological and pathological cardiac remodeling, and potential therapeutic strategies. *Biochim. Biophys. Acta Mol. Cell Biol. Lipids* 1863, 219–234. doi: 10.1016/j.bbalip.2017.12.003

Wallner, S., and Schmitz, G. (2011). Plasmalogens the neglected regulatory and scavenging lipid species. *Chem. Phys. Lipids* 164, 573–589. doi: 10.1016/j.chemphyslip.2011.06.008

Wegner, G. H., and Foster, E. M. (1963). Incorporation of isobutyrate and valerate into cellular plasmalogen by *Bacteroides succinogenes*. *J. Bacteriol.* 85, 53–61. doi: 10.1128/jb.85.1.53-61.1963

Werner, E. R., Keller, M. A., Sailer, S., Lackner, K., Koch, J., Hermann, M., et al. (2020). The TMEM189 gene encodes plasmanylethanolamine desaturase which introduces the characteristic vinyl ether double bond into plasmalogens. *Proc. Natl. Acad. Sci. U.S.A.* 117, 7792–7798. doi: 10.1073/pnas.1917461117

Wood, P. L., Locke, V. A., Herling, P., Passaro, A., Vigna, G. B., Volpato, S., et al. (2015). Targeted lipidomics distinguishes patient subgroups in mild cognitive impairment (MCI) and late onset Alzheimer's disease (LOAD). *BBA Clin.* 5, 25–28. doi: 10.1016/j.bbacli.2015.11.004

Wood, P. L., Mankidy, R., Ritchie, S., Heath, D., Wood, J. A., Flax, J., et al. (2010). Circulating plasmalogen levels and Alzheimer Disease Assessment Scale-Cognitive scores in Alzheimer patients. *J. Psychiatry Neurosci.* 35, 59–62. doi: 10.1503/jpn.090059

World Alzheimer Report (2015). *The Global Impact of Dementia: An Analysis of Prevalence, Incidence, Cost and Trends*. London: Alzheimer's Disease International.

Yamashita, S., Hashimoto, M., Haque, A. M., Nakagawa, K., Kinoshita, M., Shido, Q., et al. (2017). Oral administration of ethanolamine glycerophospholipid containing a high level of plasmalogen improves memory impairment in myloid β-infused rats. *Lipids* 52, 575–585. doi: 10.1007/s11745-017-4260-3

Zhang, Y. M., and Rock, C. O. (2008). Membrane lipid homeostasis in bacteria. *Nat. Rev. Microbiol.* 6, 222–233. doi: 10.1038/nrmicro1839

Zhao, Y. C., Zhou, M. M., Zhang, L. Y., Cong, P. X., Xu, J., Xue, C. H., et al. (2020). Recovery of brain DHA-containing phosphatidylserine and ethanolamine plasmalogen after dietary DHA-enriched phosphatidylcholine and phosphatidylserine in SAMP8 mice fed with high-fat diet. *Lipids Health Dis.* 19:104.

Zoeller, R. A., Morand, O. H., and Raetz, C. R. (1988). A possible role for plasmalogens in protecting animal cells against photosensitized killing. *J. Biol. Chem.* 263, 11590–11596.

Conflict of Interest: The authors declare that the research was conducted in the absence of any commercial or financial relationships that could be construed as a potential conflict of interest.

frontiers in Cell and Developmental Biology

ORIGINAL RESEARCH
published: 08 October 2020
doi: 10.3389/fcell.2020.586628

Spatial Nano-Morphology of the Prolamellar Body in Etiolated *Arabidopsis thaliana* Plants With Disturbed Pigment and Polyprenol Composition

Michał Bykowski[1], Radosław Mazur[2], Daniel Buszewicz[3], Joanna Szach[1], Agnieszka Mostowska[1] and Łucja Kowalewska[1]*

[1] Department of Plant Anatomy and Cytology, Institute of Plant Experimental Biology and Biotechnology, Faculty of Biology, University of Warsaw, Warsaw, Poland, [2] Department of Metabolic Regulation, Institute of Biochemistry, Faculty of Biology, University of Warsaw, Warsaw, Poland, [3] Institute of Biochemistry and Biophysics, Polish Academy of Sciences, Warsaw, Poland

OPEN ACCESS

Edited by:
Yuru Deng,
University of Chinese Academy of Sciences, China

Reviewed by:
Beata Joanna Mysliwa-Kurdziel,
Jagiellonian University, Poland
John Michael Seddon,
Imperial College London, United Kingdom

***Correspondence:**
Łucja Kowalewska
lucja.kowalewska@uw.edu.pl

Specialty section:
This article was submitted to Cellular Biochemistry, a section of the journal Frontiers in Cell and Developmental Biology

Received: *23 July 2020*
Accepted: *14 September 2020*
Published: *08 October 2020*

Citation:
Bykowski M, Mazur R, Buszewicz D, Szach J, Mostowska A and Kowalewska Ł (2020) Spatial Nano-Morphology of the Prolamellar Body in Etiolated Arabidopsis thaliana Plants With Disturbed Pigment and Polyprenol Composition. Front. Cell Dev. Biol. 8:586628. doi: 10.3389/fcell.2020.586628

The prolamellar body (PLB) is a periodic bicontinuous membrane structure based on tubular tetrahedral units. PLBs are present in plant etioplasts and, upon illumination, directly transform into the lamellar thylakoid networks within chloroplasts. Efficient tubular-lamellar rearrangement and later formation of the photosynthetically active thylakoid membranes are crucial steps in the development of plant autotrophy. PLB membranes are mainly composed of galactolipids, carotenoids, and protochlorophyllide (Pchlide), the chlorophyll precursor, bound in a complex with NADPH and Pchlide oxidoreductase. Although the PLB structure has been studied for over 50 years, the direct role of particular membrane components in the formation of the PLB paracrystalline network remains elusive. Moreover, despite the numerous literature data regarding the PLB geometry, their reliable comparative analysis is complicated due to variable experimental conditions. Therefore, we performed comprehensive ultrastructural and low-temperature fluorescence analysis of wild type *Arabidopsis thaliana* (Arabidopsis) seedlings grown in different conditions typical for studies on etiolated seedlings. We established that the addition of sucrose to the growing media significantly affected the size and compactness of the PLB. The etiolation period was also an important factor influencing the PLB structural parameters and the ratio of free to complex-bound Pchlide. Thus, a reliable PLB structural and spectral analysis requires particular attention to the applied experimental conditions. We investigated the influence of the pigment and polyprenol components of the etioplast membranes on the formation of the PLB spatial structure. The PLB 3D structure in several Arabidopsis mutants (*ccr1-1*, *lut5-1*, *szl1-1npq1-2*, *aba1-6, pif1*, *cpt7*) with disturbed levels of particular pigments and polyprenols using electron tomography technique was studied. We found that the PLB nano-morphology was mainly affected in the *pif1* and *aba1-6* mutants. An increased level of Pchlide (*pif1*) resulted in the substantial shift of the structural balance between outer and inner PLB water channels and overall PLB compactness compared to wild type plants. The decrease in the relative content of β-branch xanthophylls in *aba1-6* plants was manifested by local disturbances in the paracrystalline structure of the PLB network. Therefore, proper levels of particular etioplast pigments are essential for the formation of stable and regular PLB structure.

Keywords: etioplast, prolamellar body, protochlorophyllide, cubic membranes, electron tomography, carotenoids, polyprenols

INTRODUCTION

The prolamellar body (PLB) is a unique periodic bicontinuous membrane structure of angiosperm etioplasts. It is formed mainly in young, light-deprived tissues having a photosynthetic potential when exposed to light (reviewed in Solymosi and Aronsson, 2013; Pogson et al., 2015; Kowalewska et al., 2019). Therefore, PLBs are persistent structures of plastids in cotyledons or the first true leaves of dark-germinating seedlings, but are also present in, e.g., close buds of some species (Solymosi and Böddi, 2006; Solymosi and Schoefs, 2010). Although the PLB was visualized for the first time already in the 1950s (Leyon, 1954), but still the knowledge about the structural pathway of its formation remains elusive and requires further investigation. On the other hand, the on-light transformation of the paracrystalline PLB into the lamellar structure of grana and stroma thylakoids is well known (Gunning, 1965; Forger and Bogorad, 1973; Bradbeer et al., 1974; Robertson and Laetsch, 1974; Mostowska, 1986; Rudowska et al., 2012), however, the spatial structural details of the tubular-lamellar membrane transformation during the chloroplast biogenesis was only recently shown (Kowalewska et al., 2016). Thus, the PLB is a direct precursor of one of the most complicated and important membrane systems in nature, i.e., the thylakoid network of chloroplasts hosting light-dependent reactions of the photosynthesis. Due to a specific composition and the structural configuration of an exceptionally high surface-to-volume ratio (Gunning, 2001), the PLB is considered to play various functions during the chloroplast development. For instance, PLB is a lipid reservoir for developing thylakoids, and a significant increase in *de novo* lipid synthesis was detected only when no remnants of PLB were visible (Armarego-Marriott et al., 2019). Moreover, we have shown previously that the presence of large and stable PLB correlates with a highly efficient formation of grana structures during the early stages of the chloroplast biogenesis (Kowalewska and Mostowska, 2016).

More generally, PLB, similar to cubic membranes in other configurations, separate aqueous phase into a two-channel system enabling their different molecular composition and, therefore, function. The size of the water channels, controlled by the scale of the structure, can exclude or enable the localization of certain molecules on the particular side of the membrane (Mezzenga et al., 2019). In such way, we can directly link the ultrastructural features of the PLB, length-scale in particular, with new possible biological functions of this membrane arrangement performed on the molecular level. At the 3D level the balance between channels can be expressed as a ratio of inner and outer volumes of the PLB lattice modeled region.

The PLB structure is in general based on the triply periodic minimal surface template; however, it is characterized by the asymmetry leading to a geometrical imbalance between two sides of the membrane (Mezzenga et al., 2019). The majority of PLB configurations is formed via repetition of a basic tetrahedral tubular element forming 3D hexagonal lattice with the same symmetry as the zinc sulfide crystal – wurtzite or zincblende (Gunning and Steer, 1975; Murakami et al., 1985; Lindblom and Rilfors, 1989; Lindstedt and Liljenberg, 1990; Williams et al., 1998; Selstam et al., 2007). PLB can also adapt a geometry based on different polyhedrons forming so-called "open" type arrangements (Gunning, 2001). It is worth mentioning that even PLBs having the same geometrical configuration can markedly differ in terms of length-scale and balance between different structural features like the tubule diameter or hexagon size.

The paracrystalline PLB structure is determined by its specific composition; however, the role of only several components of the internal etioplast network in the formation and maintenance of such unique cubic arrangement has been identified so far. The crucial role of polar lipids – monogalactosyldiacylglycerol (MGDG) and digalactosyldiacylglycerol (DGDG) in this process was recently shown by Fujii et al. (2017, 2018, 2019) using *dgd1* mutant and DEX-inducible amiR-*MGD1* line. It was proposed already in earlier studies, that the proper MGDG/DGDG ratio could play a role in the PLB organization (Selstam and Sandelius, 1984). Such hypotheses were mainly based on different roles of the conically shaped MGDG and the bilayer-forming DGDG in the bending of etioplast membranes (Demé et al., 2014). Etioplasts with a decreased MGDG and DGDG levels exhibit a severe decrease in the PLB size and show aberrations in its geometrical configuration (Fujii et al., 2017, 2018).

Apart from lipid components, the PLB also contains over 60 proteins from, e.g., pigment biosynthesis pathways, Calvin–Benson–Bassham components, and thylakoid photosynthesis proteins (Dehesh and Ryberg, 1985; Blomqvist et al., 2008). The most abundant protein is the light-dependent protochlorophyllide oxidoreductase (LPOR) enzyme; its key role in the formation of PLB has been previously shown using the *porA-1* mutant (Paddock et al., 2012). The accumulation of LPOR proteins can restore PLBs in the constitutive photomorphogenic (*cop1*) mutants highlighting the central role of LPOR in the maintenance of the PLB structure (Sperling et al., 1998). The LPOR protein forms a ternary complex with NADPH and protochlorophyllide (Pchlide) – chlorophyll precursor, the most abundant pigment of PLB membranes (Armstrong et al., 1995; Blomqvist et al., 2008). Plants defective in the Pchlide accumulation do not develop PLBs (Von Wettstein et al., 1995;

Franck et al., 2000), which might be directly related to lack of the Pchlide:LPOR:NADPH complex associated previously with the PLB structure formation (Böddi et al., 1989; Lebedev et al., 1995; Sperling et al., 1997; Selstam et al., 2011; Myśliwa-Kurdziel et al., 2013). It was shown that the LPOR abundance is proportional to the photoactive (bound in the ternary complex) Pchlide content, which correlates with the increased ratio of the photoactive to non-photoactive (free) Pchlide and with the PLB size (Franck et al., 2000). High photoactive/non-photoactive Pchlide ratio was also registered for seedlings germinated on a medium with sucrose (Suc) (e.g., Samol et al., 2011; Fujii et al., 2017) compared to these etiolated on a medium solution without additional carbon source (Franck et al., 2000; Huq et al., 2004; Aronsson et al., 2008). However, no correlation of such results with PLB structural parameters was given. Reliable analysis of the literature data linking the ultrastructural and spectral level of the PLB organization is particularly difficult due to various experimental setups used and lack of systematic analysis that could possibly show the influence of the nutrition media and the etiolation time on the PLB formation.

Carotenoids form another group of molecules that are highly abundant in the PLB membrane fraction. Their structural role in the PLB formation was demonstrated in the PLB-deficient *ccr2* mutant, which accumulates particular poly-*cis* carotenoids and maintains wild type levels of LPOR and Pchlide (Park et al., 2002; Cuttriss et al., 2007; Cazzonelli et al., 2020). In the *ccr2* mutant, restoration of the PLB structure is possible due to further mutations in the ζ-carotene isomerase (ZISO) pointing directly to the role of the *cis*-carotenoid component in the PLB structure development (Cazzonelli et al., 2020). However, because carotenoids are a large and diverse group of the lipophilic pigments, the role of other molecules from this group in the PLB formation cannot be excluded and remains to be studied. Finally, PLB and developed thylakoid membranes share similarities in composition, especially in terms of lipids (Selstam and Sandelius, 1984). Nonetheless, the role of many membrane components in the formation of grana and stroma thylakoid structure has been proposed, while their role in the PLB structure development still remains elusive, e.g., curvature-inducing proteins from CURT1 family or plastidial polyprenols (linear polyisoprenoids structurally similar to carotenes) (Armbruster et al., 2013; Akhtar et al., 2017).

The main goal of this study was to reveal the structural role of different pigments and polyprenols localized in the PLB membranes in the formation of their ordered bicontinuous configuration. Moreover, we checked the influence of experimental setup on the PLB formation and spectral properties of *Arabidopsis thaliana* (Arabidopsis) etioplasts. We established that changes in the experimental conditions substantially influence the etioplast development. Such observation might explain ambiguity in the previously published results regarding the PLB structure and its correlation with the Pchlide spectra pattern in the wild type and different Arabidopsis mutants. The 2D and 3D analyses of the PLB arrangement in pigment and polyprenol deficient Arabidopsis mutants pointed to a significant influence of Pchlide and β-β-xanthophylls on the PLB nano-morphology. Finally, we gave a direct experimental evidence that spatial parameters of PLB might be reliably predicted from the generated 3D theoretical models based only on measurements of the 2D TEM cross-sections.

MATERIALS AND METHODS

Growth Conditions

Seeds of *Arabidopsis thaliana* mutants *ccr1-1* (N68151, *sdg8*; Park et al., 2002), *lut5-1* (N616660, SALK_116660; Kim and DellaPenna, 2006), *szl1-1npq1-2* (N66023; Li et al., 2009), *aba1-6* (N3772; Niyogi et al., 1998), *pif1* (N66041; Huq et al., 2004), *cpt7* (N48213, SALK_022111; Akhtar et al., 2017), and ecotype Col-0 (N1092, wild type) were obtained from The European Arabidopsis Stock Center. Seedlings were grown in Petri dishes on Murashige and Skoog Basal Medium and Gamborg's vitamins supplemented with 0.8% Phytagel^{TM} (P8169, Sigma-Aldrich). For particular experiments, the nutrition medium was additionally supplemented with 1% of Suc. Etiolation (3–6 days in 23°C) was preceded with a 24 h stratification in 4°C and 4 h illumination (120 μmol photons m^{-2} s^{-1} in 23°C) to induce germination. All samples were collected in the darkness with photomorphogenetically inactive dim green light.

Transmission Electron Microscopy (TEM)

Samples for TEM were fixed for 2 h in 2.5% glutaraldehyde in 50 mM cacodylate buffer (pH 7.4), postfixed in 2% OsO_4 at 4°C overnight and dehydrated in a graded series of acetone using the following sequence: 10 min, 30% (v/v); 10 min, 40% (v/v); 10 min, 60% (v/v); 30 min, 70% (v/v); 40 min, 80% (v/v); 3 × 40 min, 100%. Dehydrated samples were infiltrated in acetone:resin mixtures (3:1; 1:1; 1:3) and finally embedded in a pure resin medium (Agar 100 Resin Kit). Blocks with samples were cut into 90 nm specimens using the Leica UCT ultramicrotome. TEM images were performed with the help of the JEM 1400 (JEOL) equipped with Morada G2 CCD camera (EMSIS GmbH) in the Laboratory of Electron Microscopy, Nencki Institute of Experimental Biology of Polish Academy of Sciences, Warsaw, Poland. The PLB ultrastructural characteristics were calculated with the help of ImageJ software (Abramoff et al., 2004). PLB cross-sectional area was measured from 2D images of whole etioplasts using manual polygon tracing of PLB cubic region visible on the micrograph (**Supplementary Figure 1A**). Periodicity parameter was calculated based on averaged values obtained from Fast Fourier Transform (FFT) of 2D cross sections of micrographs showing nearly hexagonal planar lattice (**Supplementary Figures 1B–D**). PLB tubule width was established via manual measurement of the diameter of PLB tubules visible in particular orientations of PLB cross sections (examples show in **Supplementary Figure 1E**); measurements were based on the outer limits of each tubule (**Supplementary Figure 1F**).

Electron Tomography (ET) and 3D Theoretical Models

For ET experiments, samples were fixed as described above, and 200 nm thick leaf sections were placed on 100 mesh nickel grids for further analysis. Tomograms were collected from +60° to −60° at the 1° increment around one axis using the same

JEM 1400 electron microscope equipped with the tomography supply at the voltage of 120 kV. Aligned tomogram tilts were reconstructed by 100 iterations of the SIRT algorithm in the TomoJ (ImageJ plugin) software (Messaoudii et al., 2007). PLB segmentations were done via generation of PLB membrane isosurfaces in the Imaris 8.4.2 software (Bitplane AG) (surface detail 3.5 nm, background subtraction 6.2 nm). Spatial structural parameters were calculated using the MeasurementPro package of Imaris 8.4.2. Area and inner volume of PLB isosurface were automatically generated from the obtained model, while outer volume was calculated as a volume of the space outside the isosurface placed inside the cuboid of the modeled region (**Supplementary Figures 1G–I**). Theoretical 3D models were generated using the Autodesk Fusion 360 software based on the exact structural parameters obtained from TEM cross-sections.

Low-Temperature Fluorescence (77 K)

Steady-state low-temperature (77 K) fluorescence emission spectra of Pchlide were recorded using a modified Shimadzu RF-5301PC spectrofluorometer with optical fibers guiding the excitation and emission beams (fluorescence emission detection at 0° angle). Freshly collected seedling samples ($n \approx$ 50–100 plants per single measurement) were tightly packed and placed directly between polytetrafluoroethylene and non-fluorescent glass plates of 15 mm diameter. Sample holder was submerged in liquid nitrogen and scans were taken in the range of 600–800 nm and 1 nm interval through the LP600 filter. The excitation wavelength was set at 440 nm, the excitation and emission slits were set at 10 and 5 nm, respectively. Raw spectra were subtracted using spectrum obtained for empty sample holder (both plates), smoothed and normalized to the value indicated in the particular figure captions.

Pigment Extraction and Chromatography

Pigments were extracted from cotyledons and upper parts (∼2–4 mm) of seedling hypocotyls (n ≈ 200) in 1 mL acetone:ethyl acetate 3:2 (v/v) as described in Cuttriss et al., 2007. Extracted pigments were separated using the Shimadzu Prominence HPLC System with PDA detector on Atlantis C-18 (4.6 × 250 mm, 5 μm, 100 Å) column (Waters). Elution was performed using ethyl acetate gradient in acetonitrile:water:triethylamine 9:1:0.01 (v/v) at 1 mL min^{-1} for 40 min according to the following timetable (0–2 min, 0% ethyl acetate; 2–32 min 0–66.7%, 32.2–37 min 66.7–100%). Compounds were identified, and the HPLC peak areas were integrated based on absorption spectra and retention times, according to Cuttriss et al. (2007); peak areas were integrated at 456 nm.

Polyprenol Extraction and Chromatography

The procedure of polyprenol extraction and analysis was performed as described in Akhtar et al. (2017). Briefly, 350 mg of snap-frozen etiolated seedlings were grounded in liquid nitrogen using mortar and pestle, suspended in a mixture of chloroform:methanol 1:1 (v/v), supplemented with 10 μg of internal standard (Prenol-27; Collection of Polyprenols, Institute of Biochemistry and Biophysics, Polish Academy of Sciences) and incubated for 72 h at 4°C in darkness. The extracts were filtered, evaporated under a stream of nitrogen, and hydrolyzed for 1 h at 95°C in a mixture of toluene:7.5% KOH (in water):95% ethanol 20:17:3 (v/v). Next, lipids were extracted three times with hexane, applied to a silica gel 60 column, and purified using the isocratic elution with 20% (v/v) diethyl ether in hexane. Polyprenols were analyzed by HPLC, as described previously (Skorupińska-Tudek et al., 2003). Extracts were separated by HPLC (Waters) using a ZORBAX XDB-C18 (4.6 × 75 mm, 3.5 μm) reverse-phase column (Agilent). Polyprenols were eluted with a linear gradient from 0% to 100% of methanol:isopropanol:hexane 2:1:1 (v/v) in water:methanol 1:9 (v/v) at a flow rate of 1.5 mL/min. Polyprenols were detected by absorption at 210 nm and quantified relative to the internal standard.

Statistical Analysis

For determination of the statistical significance of differences between results, one-way ANOVA with *post hoc* Tukey test at $p = 0.05$ was applied. All experiments were performed in three repetitions at least. Structural cross-sectional features were calculated for ≥ 20, while 3D spatial parameters from three modeled regions of interest per each variant.

RESULTS

In the first part of this study, we addressed the literature discrepancies regarding the correlation of PLB structure with etioplast spectral properties by testing the sampling methods, type of nutrition media, and time of etiolation. Further, after the selection of preferable experimental setup, we performed detailed 2D and 3D structural analysis of PLBs in plants with altered levels of polyprenols and different pigments, present in etiolated tissue.

Etioplast Distribution in Arabidopsis Seedlings

The ultrastructural analysis of plastids in subsequent regions of the shoot in 5-day etiolated Arabidopsis seedlings (**Figure 1**) revealed that etioplasts, characterized by the presence of paracrystalline PLB structure, were located in cotyledons and the first 2 mm of upper hypocotyl part (**Figures 1A,B**). However, etioplasts were more abundant in TEM cross-sections of cotyledons, and the regularity of the PLB located in this part of the seedling was higher compared with the upper hypocotyl part. In the middle and lower parts of the shoot, we did not observe PLB in the plastid cross-sections; only porous prothylakoids, vesicular structures, and plastoglobules were visible. This result points to the presence of proplastids in the middle and lower hypocotyl sections (**Figure 1C**). Moreover, we measured the 77 K emission spectra of Pchlide (i) in the total shoot fraction, (ii) in cotyledons and small hypocotyl parts (both including etioplasts), as well as (iii) in the middle and lower hypocotyl parts enriched with proplastids (**Figure 1D**). All analyzed spectra had two characteristic bands (∼632 and ∼653 nm). The first one corresponded to non-photoconvertible, free Pchlide species, while the second was related to the Pchlide:LPOR:NADPH complex (e.g., Ryberg and Sundqvist, 1982; Schoefs and Franck, 2003, 2008). Slight differences in the 632/653 nm peak ratios were

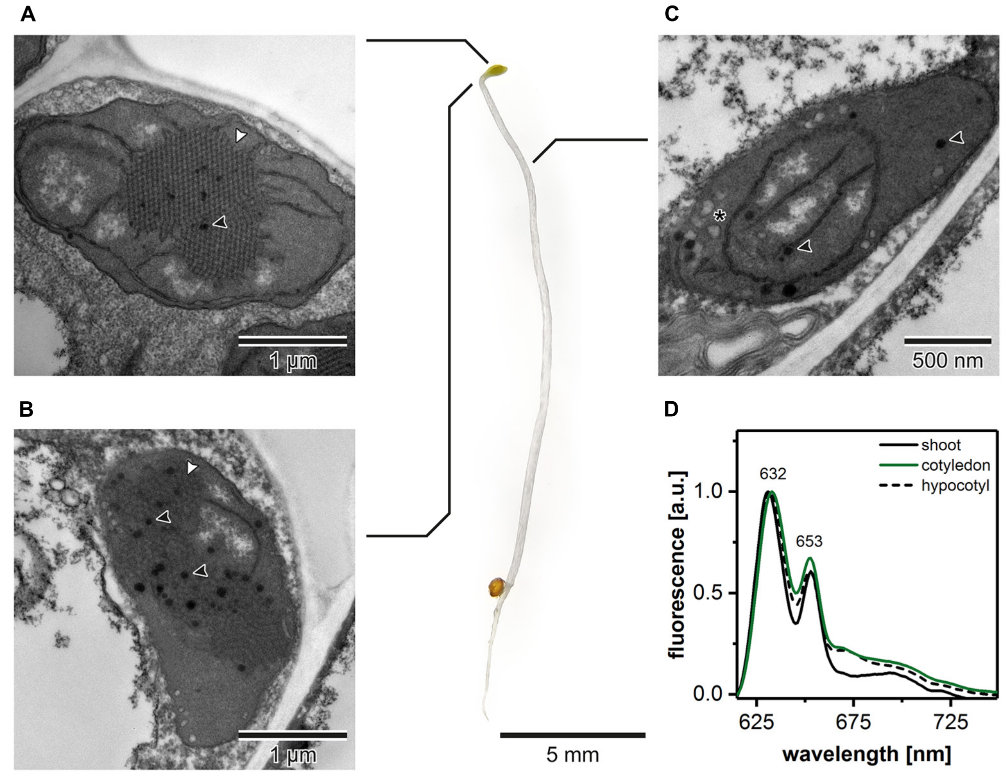

FIGURE 1 | Ultrastructure of plastids in different shoot regions of 5-day etiolated Arabidopsis (Col-0) seedling grown on Murashige and Skoog medium without sucrose supplementation; white arrowhead – prolamellar body (PLB), black arrowhead – plastoglobule, asterisk – vesicle **(A–C)**. Representative low-temperature (77 K) fluorescence emission spectra (excitation at 440 nm) of shoot (hypocotyl and cotyledons), cotyledons and upper 2 mm of hypocotyl, and hypocotyl **(D)**; all spectra were normalized to the maximal value; note that the same, representative Col-0 "cotyledon" spectra (green) is also presented in **Figures 3**, **4**, **6** – color code is preserved throughout the manuscript.

observed between samples from different seedling regions. The higher signal coming from Pchlide:LPOR:NADPH complex was registered in cotyledon samples, which correlates with the PLB presence registered in TEM data (**Figures 1A,B,D**). For all further experiments, we decided to collect seedling regions enriched with etioplasts only. Moreover, all TEM and tomography data were obtained from the central part of the cotyledon blade.

The Role of Nutrition Media in the Formation of the PLB Structure

Due to the fact that the etiolation and de-etiolation process in Arabidopsis is studied using nutrition media supplemented with 1–2% Suc or depleted in an additional carbon source, we decided to test how such variability in growing conditions could influence the PLB structure and etioplast spectral properties (**Figure 2**). We established that the Suc supplementation resulted in an increased rate of the storage lipid degradation, i.e., no lipid bodies were visible in TEM sections of cotyledon cells (**Figures 2A,D**). Moreover, the addition of Suc was correlated with a markedly larger PLB size (**Figures 2B,E,G** and **Supplementary Figure 1A**) and an increased periodicity (**Supplementary Figures 1B–D**) of the PLB lattice compared with plants etiolated on a medium without sugar supplementation (**Figures 2C,F,G**). Periodicity is a parameter describing distances (nm) between the neighboring cross-sectional unit cells of the PLB hexagonal lattice; the higher the value, the more loose the PLB structure. Changes in the PLB structure were related with the fluorescence results in which larger PLB coincided with an increased contribution of the 653 nm band in the Pchlide emission spectra (**Figures 2G,I**). Although lack of lipid bodies in the cell cytoplasm is a factor that makes TEM analyses easier, we decided to use Suc-free nutrition media to follow a more natural pattern of seedling growth. Sugar metabolism is very complex and can influence different aspects of seedling development, including lipid and protein composition. Moreover, sugars also serve as signaling molecules, which can severely affect different metabolic pathways playing a central role in plastid biogenesis (Tognetti et al., 2013; Lastdrager et al., 2014).

The Size of the PLB and Etioplast Spectral Properties During the Etiolation Process

Etiolation of Arabidopsis seedlings is a process that requires preceding stratification and exposition of seeds to light to induce the coordinated germination of seedlings (**Figure 3A**). We analyzed the PLB structure and its spatial properties in plants etiolated for 3, 4, 5, and 6 days to establish how does the etiolation time influence the etioplast development. We registered the PLB-containing etioplasts in cotyledons of all examined seedlings

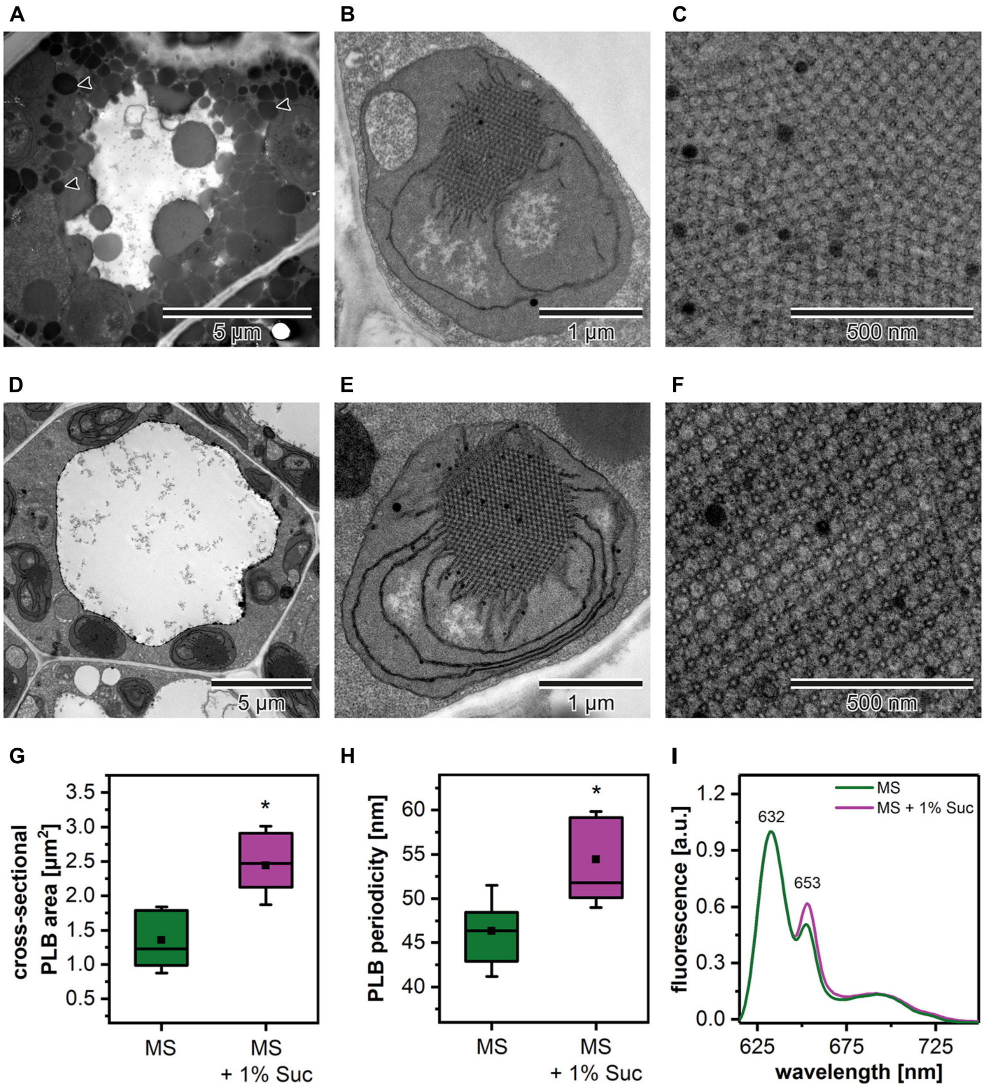

FIGURE 2 | Cotyledon ultrastructure of 5-day etiolated Arabidopsis (Col-0) seedlings grown on Murashige and Skoog (MS) medium without **(A–C)** and with sucrose (1% Suc) supplementation **(D–F)**; electron micrographs showing whole cell (black arrowhead – lipid body) **(A,D)**, etioplast ultrastructure **(B,E)**, and prolamellar body (PLB) nano-morphology **(C,F)**. Measurements of the PLB structural parameters **(G,H)**; the horizontal line and black square in each box represent the median and mean value of the distribution, respectively; the bottom and top of each box represent 25 and 75 percentile; whiskers denotes standard deviation (SD); results from MS + 1% Suc samples marked with asterisk differ significantly at $p = 0.05$ from MS samples. Representative low-temperature (77 K) fluorescence emission spectra (excitation at 440 nm) of cotyledons and upper ∼ 2 mm of hypocotyl **(I)**; all spectra were normalized to the maximal value.

(**Figures 3B–E**). The area of PLB increased gradually up to 5 days of etiolation and decreased markedly during the last day of the experiment (**Figure 3G**). The PLB periodicity slightly decreased during the etiolation; however, no significant differences between subsequent days were noted (**Figures 3F,H**). Pchlide low-temperature emission spectra obtained from 3- and 4-day etiolated seedlings showed an additional red-shifted band with a maximum at around 670 nm (**Figure 3I**). This peak was previously attributed to the aggregates of free Pchlide (Myśliwa-Kurdziel et al., 2013). Therefore, in this case, the proportion of 632/652 nm bands did not properly reflect the ratio of free and complex-bound Pchlide. In the case of seedlings etiolated for 5 and 6 days, the Pchlide spectra were similar, with a small decrease in the signal coming from the Pchlide:LPOR:NADPH in the latter (**Figure 3I**). In experiments on the Arabidopsis mutants, we decided to use samples collected during the 5th day of etiolation showing a large PLB and a typical Pchlide fluorescence pattern with a relatively high contribution of the photoactive Pchlide.

2D PLB Morphology in Plants With Disturbed Levels of Pigments and Polyprenols

To elucidate the structural role of pigment and polyprenol components in the formation of PLB structure, we selected different Arabidopsis mutants with disturbed levels of particular

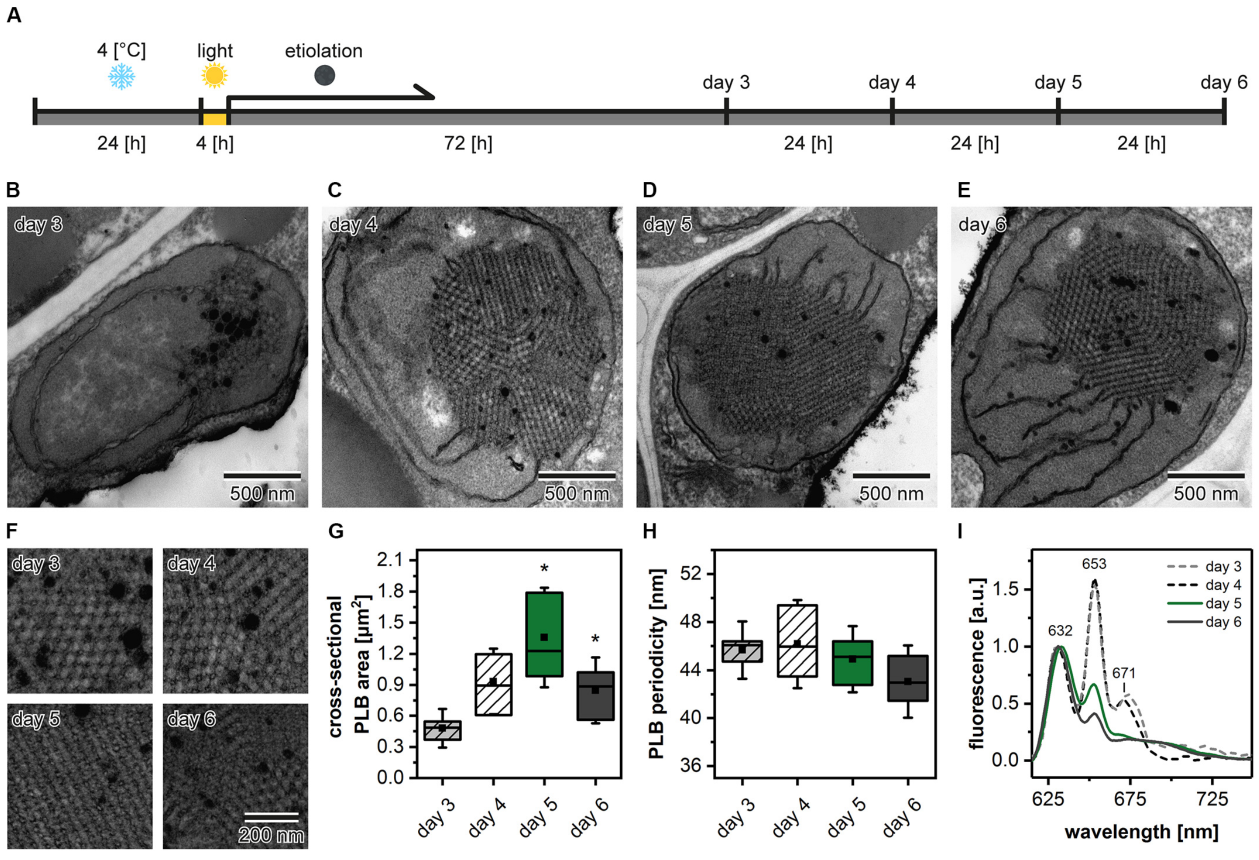

FIGURE 3 | Scheme of the applied experimental setup. After stratification in 4°C plants were grown in the optimal (22°C) temperature **(A)**. Ultrastructure of cotyledon etioplasts **(B–E)** and prolamellar bodies (PLB) **(F)** of 3- to 6-day etiolated Arabidopsis (Col-0) seedlings; all PLBs **(F)** are shown in identical magnification indicated in the lower right panel. Measurements of the PLB structural parameters **(G,H)**; description of the chart box as in **Figure 2**; results marked with asterisk on the top of the boxplot differ significantly at $p = 0.05$ from the previous day of etiolation. Fluorescence emission spectra (excitation at 440 nm) of cotyledons and the upper 2 mm of hypocotyl **(I)**; all spectra were normalized to 1 at 632 nm.

PLB membrane components (**Figure 4**). The first group of mutants was aberrant in the carotenoid composition. The *ccr1-1* mutant had a significantly decreased lutein (Lut) and violaxanthin (Vio) contribution in the total carotenoid pool. Moreover, the accumulation of pro-lycopene (p-Lyc), as well as ζ carotene (ζ-Car), was registered in the *ccr1-1* mutant only (**Figure 4A**). In the carotenoid composition of the *lut5-1* seedlings, the most significant difference compared with the Col-0 ecotype was an increase in the neoxanthin (Neo) contribution to the total carotenoid pool (**Figure 4A**). The opposite effect was observed in the *szl1-1npq1-2* plants in which a decrease in the Neo contribution was accompanied by lowered levels of Vio and a substantial increase in the Lut content compared with Col-0 plants (**Figure 4A**). We also registered Lut-overaccumulation in *aba1-6* plants in which the complete depletion of Neo and Vio was detected (**Figure 4A**). Moreover, a small amount of β-cryptoxanthin (β-Ctx) was detected in Col-0 plants, and only traces of this pigment were registered in the examined mutants. Pchlide is the most abundant precursor pigment of PLBs, and, as we mentioned above, plants depleted of this molecule do not form the PLB paracrystalline lattice. In this study, we used the Pchlide over-accumulating *pif1* mutant (Huq et al., 2004), which accumulates the non-photoconvertible form of this precursor pigment (**Figure 4B**). This enables us to reveal if increased Pchlide level can modulate the PLB morphology. To decipher the role of polyprenols in the PLB formation, we used the *cpt7* mutant deficient in plastidial polyprenols (**Figure 4C**).

In the ultrastructure of all examined mutant etioplasts, we observed well-differentiated PLB arrangements (**Figure 5**). Qualitative analysis revealed that in *aba1-6* plants, local disturbances in the paracrystalline structure of the PLB network were present (**Figure 5D**). In other mutants, we observed a uniform bicontinuous PLB structure. However, in all examined genotypes, particular PLBs were composed of several identical periodic configurations connected at different angles forming pseudo polycrystalline arrangements (**Figures 5A–F, 6A**). In the quantitative analysis, we established that the PLB periodicity is most severely affected in the *pif1* plants in which high PLB compactness was observed (**Figures 5E,G**). Moreover, due to a substantial increase in the diameter of the PLB-building tubule (**Figure 5H** and **Supplementary Figures 1E,F**), the observed PLB configuration in the *pif1* mutant was highly balanced in

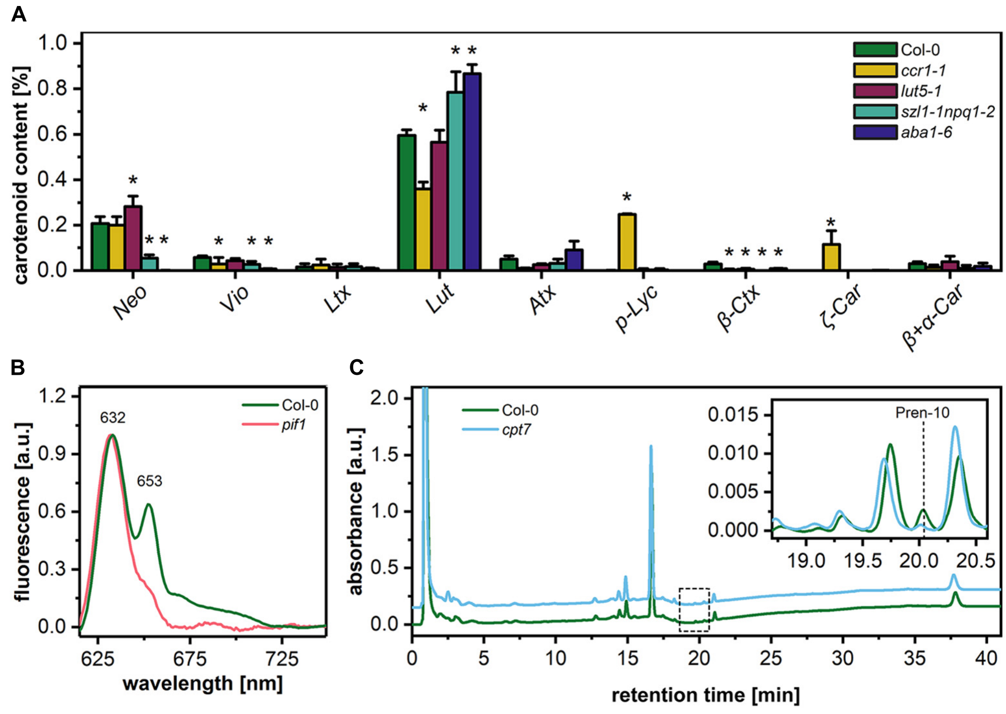

FIGURE 4 | Percentage contribution of particular carotenoids (Neo – neoxanthin, Vio – violaxanthin, Ltx – luteoxanthin, Lut – lutein, Atx – anteraxanthin, p-Lyc – pro-lycopene, Ctx – cryptoxanthin, Car – carotene) in the total carotenoid pool of 5-day etiolated seedlings of Col-0 and carotenoid deficient Arabidopsis mutants (*ccr1-1*, *lut5-1*, *szl1-1npq1-2*, *aba1-6*) **(A)**; data are mean values ± SD from at least three independent experiments; results marked with asterisk on the top of the bar differ significantly at $p = 0.05$ from Col-0. Representative low-temperature (77 K) fluorescence emission spectra (excitation at 440 nm) of cotyledons and the upper 2 mm of hypocotyl of 5-day etiolated Col-0 and *pif1* seedlings **(B)**; all spectra were normalized to the maximal value. HPLC/UV chromatograms of total polyprenol extracts obtained from 5-day etiolated seedlings of Col-0 and *cpt7* mutant **(C)**; the main polyprenol (Pren-10) peak is indicated on the representative chromatograms.

terms of outer and inner channel widths (**Figures 5G,H**, **8G,H**). Such an arrangement is typical for many nature-occurring cubic membrane structures (reviewed in Almsherqi et al., 2009); however, it has not been observed yet in the etioplast PLBs. Slightly increased PLB periodicity was detected in the *ccr1-1, aba1-6*, and *cpt7* mutants compared with Col-0 plants (**Figure 5G**). In the case of *ccr1-1 and cpt7* plants, a decreased PLB compactness was accompanied by an increase in the PLB tubule width (**Figure 5H**). We did not recognize any correlation between the PLB organization, its cross-sectional size, and the Pchlide fluorescence pattern in the analyzed plants (**Figures 5A–F**, **6B,C**).

The Spatial Arrangement of PLB in Plants With Pigment and Polyprenol Deficits

We studied the PLB organization in 3D using the ET method (**Figure 7**). Based on the reconstructed tomography stacks, we rendered isosurfaces reflecting the PLB lattice configuration visible from the angle determined by the cross-section orientation (**Figures 7A–G**). Due to the randomness of TEM/ET sample-cutting, the PLB lattices of different genotypes were analyzed from various angles (**Figures 7A–G**). Weakness of this method had, however, a limited impact on the calculated spatial PLB parameters (**Figure 7H**). It was due to the fact that every tomogram (at least 3) obtained for a particular genotype was positioned at different angles, and the visualized region typically covered polycrystalline configurations. The inner/outer volume ratio (I_v/O_v) (**Supplementary Figures 1G–I**) is a spatial parameter reflecting the balance between inner and outer PLB regions that represent the lumen and stroma compartment, respectively. The I_v/O_v ratio calculated from the 3D models was significantly increased in the *pif1* plants, reaching the value of about 0.85, which indicated an increased balance between the PLB water channels of this mutant (**Figure 7H**). On the contrary, the I_v/O_v ratio was decreased in all other examined mutants, *cpt7* in particular. The local PLB structural aberrations resulted in a higher standard deviation (SD) of the I_v/O_v parameter in *aba1-6* plants compared to other analyzed genotypes. In terms of the surface area to I_v ratio, significantly different values from Col-0 were registered in the *szl1-1npq1-2* plants only (**Figure 7H**).

The Relevance of Theoretical 3D Models in the Analysis of Spatial PLB Parameters

Based on measurements of the PLB structural parameters from the TEM cross-sections, we generated 3D theoretical models of the PLB lattice in Col-0 plants and two mutants showing the most significant aberrations in the PLB nano-morphology (*aba1-6* and *pif1*) (**Figure 8**). Similarly to data obtained from the tomography-based 3D isosurfaces, we calculated the I_v/O_v ratio for the theoretical models

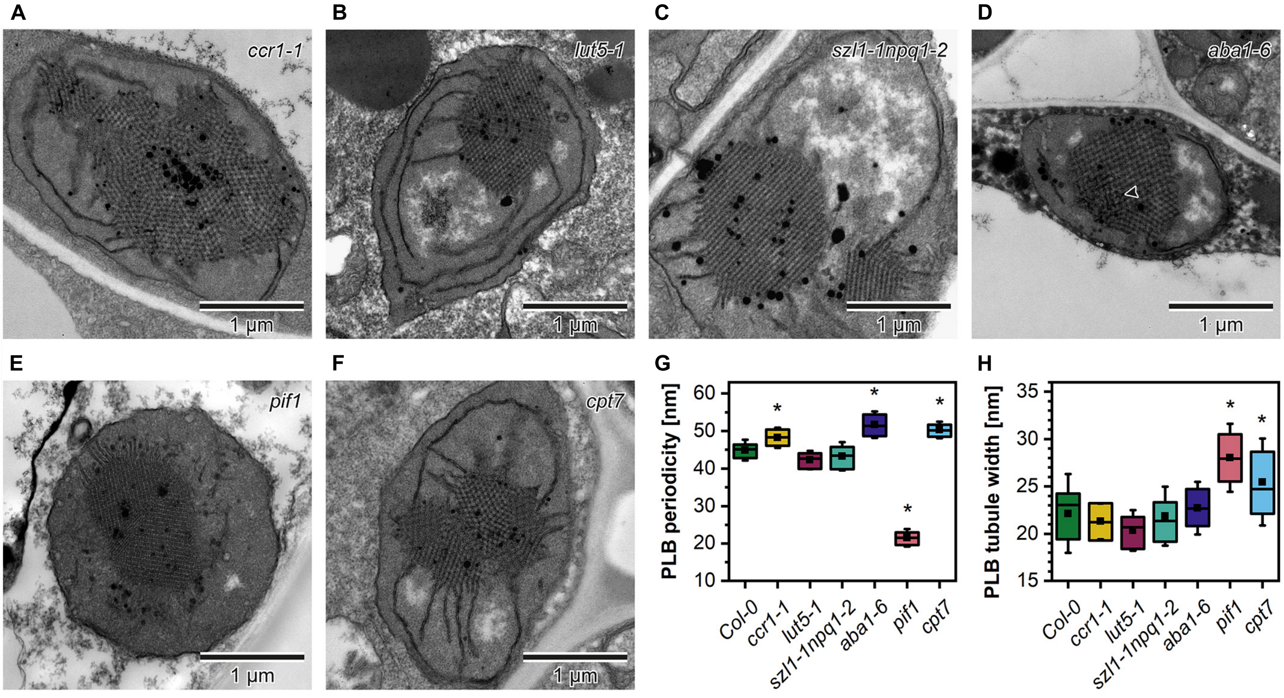

FIGURE 5 | Ultrastructure of cotyledon etioplasts of 5-day etiolated seedlings of Arabidopsis carotenoid deficient mutants (*ccr1-1*, *lut5-1*, *szl1-1npq1-2*, *aba1-6*) **(A–F)**; black arrowhead – distortion in the bicontinuous structure of the *aba1-6* prolamellar body (PLB). Measurements of the PLB structural parameters **(G,H)**; description of the chart box as in **Figure 2**; results marked with asterisk on the top of the boxplot differ significantly at $p = 0.05$ from Col-0.

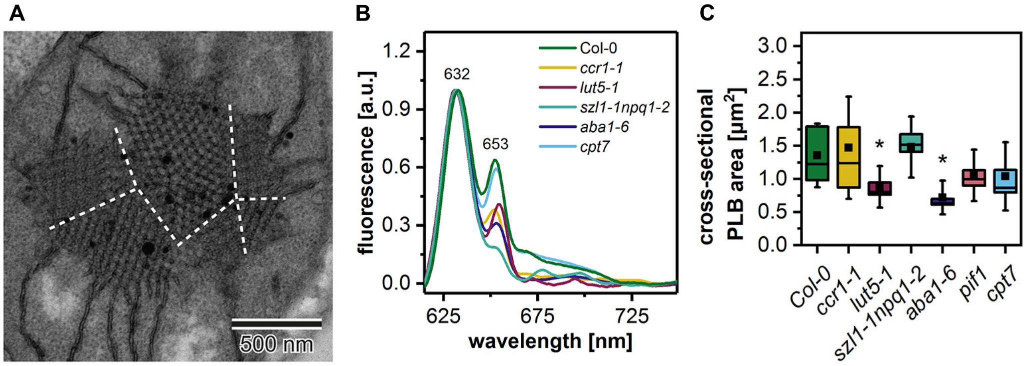

FIGURE 6 | Electron micrograph of a "polycrystalline" prolamellar body (PLB) **(A)**; dashed white lines separate PLB regions arranged at different angles; note that PLB image is an enlargement of the **Figure 5F** micrograph. Representative low-temperature (77 K) fluorescence emission spectra (excitation at 440 nm) of cotyledons and the upper 2 mm of hypocotyl of 5-day etiolated Col-0 and *ccr1-1*, *lut5-1*, *szl1-1npq1-2*, *aba1-6, cpt7* seedlings **(B)**; all spectra were normalized to the maximal value. Measurements of the PLB cross-sectional area **(C)**; description of the chart box as in **Figure 2**; results marked with asterisk on the top of the boxplot differ significantly at $p = 0.05$ from Col-0.

(**Figure 8A**). The results based on the experimental and theoretical models correlate quite accurately (less than 10% differences) (**Figure 8A**). This indicates that, in terms of spatial parameters, theoretical 3D models of highly repetitive cubic structures based on 2D TEM measurements can serve as a reasonable replacement for time and money consuming tomography experiments (**Figures 8B–H**). Such assumption was confirmed for significantly different PLB structures of three selected genotypes.

DISCUSSION

This work concerns the interplay between the structure and composition of the cubic membranes, as exemplified by the influence of carotenoid and polyprenol on the PLB nano-morphology. Therefore, in a broader context, our studies provide a better understanding of membrane folding at the molecular level. This remains one of the key topics in cell biology, still poorly understood.

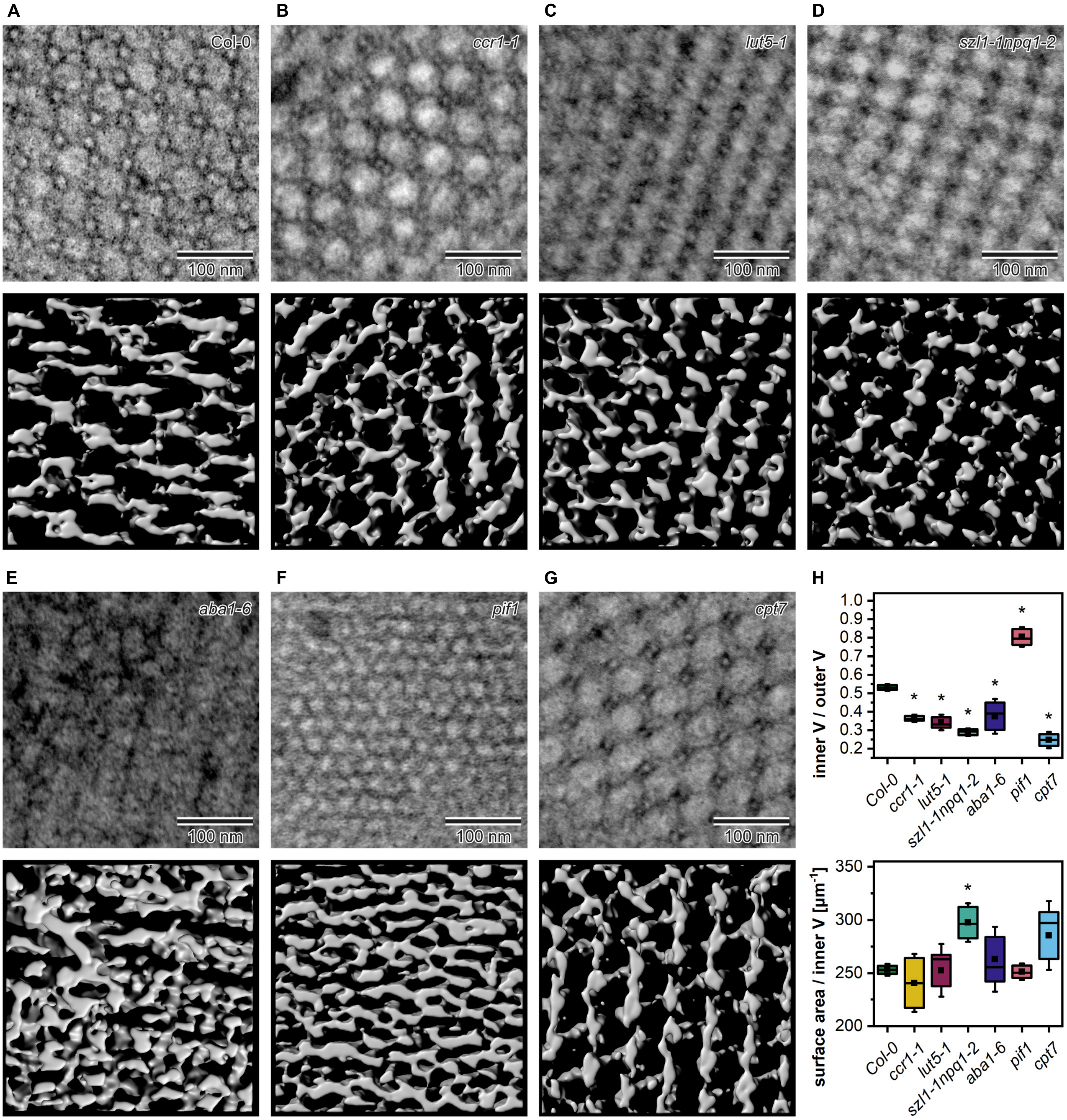

FIGURE 7 | Middle layer of the tomography stack (upper panel) and rendered 3D membrane isosurface from the same region of the prolamellar body (PLB) (lower panel) of 5-day etiolated Col-0 and mutant (*ccr1-1*, *lut5-1*, *szl1-1npq1-2*, *aba1-6, pif1*, *cpt7*) seedlings **(A–G)**. Measurements of the spatial PLB parameters **(H)**; V – volume; description of the chart box as in **Figure 2**; results marked with asterisk on the top of the boxplot differ significantly at $p = 0.05$ from Col-0.

The Importance of Experimental Setup in PLB Morphology Studies

Although the skotomorphogenesis (etiolated growth) has been a subject of many studies and the use of the etioplast model to track the chloroplast biogenesis at different levels of their organization is quite common (reviewed in Adam et al., 2011; Gabruk and Mysliwa-Kurdziel, 2015; Pogson et al., 2015; Rast et al., 2015; Mechela et al., 2019; Armarego-Marriott et al., 2020), no uniform model of plant cultivation was established. In this study, we examined whether different, typically used, conditions of Arabidopsis etiolation could impact the PLB development, and therefore, be the source of literature discrepancies.

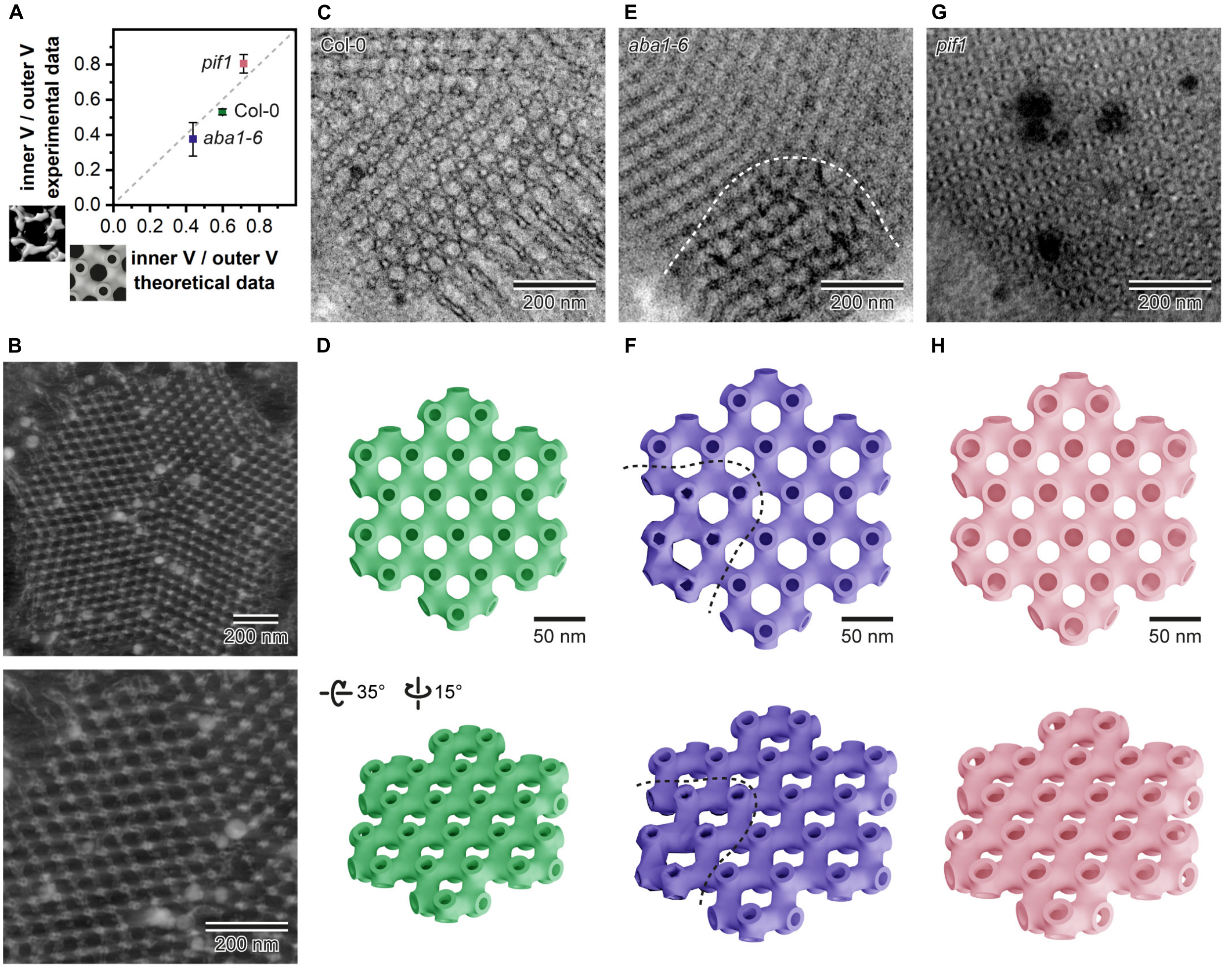

FIGURE 8 | Comparison of the inner/outer volume (V) ratio obtained from the isosurface models based on tomography data (Y axis) and data generated from the theoretical 3D models rendered according to the prolamellar body (PLB) lattice dimensions calculated from the 90 nm thick 2D TEM sections for Col-0, *aba1-6*, and *pif1* cotyledons **(A)**. Reconstructed exemplary PLB tomography volume displayed in Imaris software **(B)**; whole PLB (upper panel) and magnified lattice fragment (lower panel). Exemplary micrograph of the Col-0 PLB cut at an angle showing the hexagonal pattern of the lattice **(C)**. Theoretical model of a single layer of the Col-0 PLB network seen from two different angles (upper/lower panel) **(D)**. Exemplary micrograph of the *aba1-6* PLB showing regular bicontinuous configuration and a region exhibiting distortions in the lattice structure separated by a dashed white curved line **(E)**; note that the orientation of the *aba1-6* PLB cut is not parallel to the one in Col-0 shown in panel C. Theoretical model of a single layer of the *aba1-6* PLB network seen from two different angles (upper/lower panel); regular and aberrant region of the model is divided by a dashed curved line **(F)**. Exemplary micrograph of the *pif1* PLB cut at an angle showing a hexagonal pattern of the balanced lattice of this mutant **(G)**. Theoretical model of a single layer of the *pif1* PLB network seen from two different angles (upper/lower panel) **(H)**. Note that all theoretical models were rendered using mean values calculated form the multiple 2D PLB cross-sections of respective genotypes; membrane thickness in all theoretical models was fixed to 6 nm.

In many studies on the Arabidopsis etiolated seedlings, the Suc-supplement nutrition media is applied. Probably, it is mostly related to the fact that the addition of Suc results in an increase of the seedling size by promoting cell proliferation and in a delay of the switch to cell expansion via the glucose-6-phosphate transporter pathway (Van Dingenen et al., 2016). Due to very small size of the Arabidopsis etiolated seedlings such procedure is very useful in, e.g., biochemical experiments that require sufficiently large sample biomass. However, it should be noticed that Suc plays also a signaling role in plastid development, affecting the chloroplast structure and biogenesis in the early stages of leaf development (Van Dingenen et al., 2016). Similarly, using etiolated seedlings, we showed that the PLB nano-morphology and etioplast spectral properties are altered in plants growing on Suc-supplemented media (**Figure 2**). The observed changes in the chloroplast development are probably mainly related to the repression of the plastid and nucleus-encoded photosynthetic proteins (Krapp et al., 1993). The influence of Suc on the regulation of the biosynthesis of components localized in PLB remains to be tested. However, based on the different structural responses of etioplasts on various nutrition media (**Figure 2**), we argue for using experimental setup in which no additional carbon source is applied. Only such approach will enable reliable use of dark-grown seedlings in further de-etiolation experiments.

The structural pathways of PLB formation during the process of skotomorphogenesis have been a subject of several studies performed on bean, pea, oat, and tobacco plants (Von Wettstein, 1967; Ikeda, 1968; Weier and Brown, 1970; Klein and Schiff, 1972; Kesselmeier, 1980; Lütz, 1981; Mostowska, 1986). So far, however, no consensus on the way of the formation of the PLB cubic structure has been reached. The obtained data suggest different possible formation patterns, including fusion of vesicles or contraction of porous membranes into regularly ordered tubules. Studies on PLB formation are particularly difficult because PLB structures are found even in the early stages of etiolation (Kowalewska and Mostowska, 2016). Similarly, in this study, we showed that the developed bicontinuous regular PLB structure is detected already after 3 days of etiolation (**Figure 3**), arguing for a short timescale of the PLB formation. Such observations suggest a rapid PLB accumulation, which is performed via an organized phase transition rather than a unit-by-unit way of assembly proposed earlier as a possible general way of cubic membrane folding (Landh, 1996). However, further, highly resolved studies are required to address this topic. In subsequent days of etiolation the PLB enlarges, the network periodicity undergoes a gradual decrease, and the Pchlide fluorescence pattern changes (**Figure 3**). Therefore, particular attention should be drawn to the comparison of the structural and spectral results obtained for different dark-growth times. The same caution should be applied for seedling region subjected for further analysis (**Figure 1**) to exclude non-uniform plastid pool.

The Role of Pigments and Polyprenols in the PLB Structure Assembly

Carotenoids and chlorophylls are essential components of the thylakoid network of chloroplasts, and their complete depletion is lethal. In the thylakoid membranes, these pigments are mainly bound with the photosynthetic proteins and they together play both structural and functional roles in the establishment of the photosynthetic efficiency (Lundqvist and Franckowiak, 2003; Dall'Osto et al., 2014). However, it has been estimated that about 15% of the chloroplast thylakoid carotenoids in Arabidopsis are localized in the lipid matrix phase influencing the physical properties of the membrane (Dall'Osto et al., 2010). Since PLB membranes are deficient in such pigment-binding proteins (Blomqvist et al., 2008), probably almost all carotenoids of etioplasts are located directly in the lipid phase of PLBs and prothylakoids. Therefore, their direct influence on the PLB structure might be even more pronounced than in the lamellar arrangement of the chloroplast thylakoids. It should be stressed that at least part of the PLB carotenoid pool could be located in the plastoglobules directly interconnected with the cubic lattice. The presence of particular carotenoids was confirmed in plastoglobules of chromo- and chloroplasts; however, the pigment composition of etioplast plastoglobules has not yet been identified (Ytterberg et al., 2006; Van Wijk and Kessler, 2017).

We tested four Arabidopsis mutants (*ccr1-1*, *lut5-1*, *szl1-1npq1-2*, *aba1-6*) deficient in different carotenoid classes (**Figure 4**). These mutants were earlier studied using fully developed plants, mainly in the context of the efficiency of the photosynthetic apparatus (e.g., Niyogi et al., 1998; Park et al., 2002; Kim and DellaPenna, 2006; Li et al., 2009). However, their role in the formation of the chloroplast thylakoid network structure is still elusive. Regarding the PLB organization, we registered the most pronounced changes in *aba1-6* plants, which over-accumulated Lut and were depleted in Neo and Vio (**Figure 4**). Local disturbances in bicontinuous PLB configurations were visible in this mutant (**Figures 5**, **7**, **8**). An increase in Lut contribution was earlier attributed to a decrease in membrane fluidity (Gruszecki and Strzałka, 2005), due mostly to specific Lut structure enabling its molecules in the all-*trans* conformation to adopt two orthogonal orientations in the lipid bilayer (Sujak et al., 1999). The role of Lut- and DGDG-dependent membrane rigidification of dark-chilled cucumber etioplasts in the switch from "close" to "open" PLB structure was shown before; however, no disturbances in the bicontinuous PLB lattice configuration were registered (Skupień et al., 2017). Such results, together with the fact that no aberration in the PLB structure was detected in the *szl1-1npq1-2* plants (**Figures 5**, **7**), points to limited role of Lut over-accumulation in the maintenance of the PLB cubic configuration. We rather presume that the β-β-xanthophylls (Neo, Vio), which are depleted in *aba1-6* seedlings, could play a stabilizing role in the PLB formation. However, it is worth noting that in the *aba1-6* plants, characterized by a decreased level of the abscisic acid (Peskan-Berghöfer et al., 2015), levels of other PLB membrane components might be disturbed due to a broad regulatory role of this phytohormone (Wasilewska et al., 2008). Therefore, further studies are required to address this topic both in the context of etioplast PLBs but also of the chloroplast thylakoid membranes. Surprisingly, although the carotenoid composition is severely affected in the *ccr1-1* plants (**Figure 4**), the PLB in this mutant is fully developed and regularly arranged (**Figures 5**, **7**). It was previously established that in the *ccr2* plants, the formation of PLB is completely arrested (Park et al., 2002; Cazzonelli et al., 2020). Such fact was attributed to the accumulation of *cis*-carotenes – p-Lyc and pro-neurosporene in particular. Park et al. (2002) presented a theoretical scheme showing how the steeped structure of *cis*-carotenes could prevent formation of the membrane curvature necessary for the PLB development. Restoration of the PLB structure is possible in the *ccr2* mutant via further mutation in the ζ-carotene isomerase (ZISO), resulting in the block of *cis*-carotenes synthesis (Cazzonelli et al., 2020). The reason for the wild-type like PLB formation in the *cis*-carotenoid accumulating *ccr1-1* mutant remains unclear (**Figures 4**, **5**). We hypothesize however, that milder *ccr1-1* phenotype compared to *ccr2* plants, visible as only a partial decrease of the amount of Lut and a lower abundance of *cis*-carotenoids (pro-neurosporene and neurosporene particularly), is the most probable reason for PLB survival in the *ccr1-1* plants. Moreover, it is possible that accumulated *cis*-carotenoids do not form any type of steric hindrance for the PLB membrane bending. We can speculate that lack of PLB in the *ccr2* plants is related to other, not identified yet membrane component and its level regulated via an apo-carotenoid signaling pathway.

Pchlide is the most abundant in the diverse group of PLB pigments; its importance in the PLB formation was studied previously using plants with decreased levels of this precursor pigment. Here we used the Pchlide over-accumulating *pif1* plants to check whether increased Pchlide level can influence PLB structure. It was suggested before, that the complex-bound Pchlide is located in the PLB lattice, while free non-photoconvertible Pchlide is rather located in the prothylakoids, loosely arranged around PLB lattice (Lindsten et al., 1988). It was also proposed that an increased contribution of the photoconvertible Pchlide in the fluorescence spectra could serve as an adaptation mechanism maximizing the use of light during the Pchlide transformation and promoting efficient conversion of PLB to thylakoids (Aronsson et al., 2008). However, our studies on pigment and polyprenol deficient mutants did not reveal any pattern linking the PLB periodicity, its cross-sectional size, and the Pchlide 632/653 nm ratio (**Figures 5**, **6**). This suggests that photo and non-photoconvertible Pchlide forms could be located both in PLB and prothylakoids. We showed that even in hypocotyl regions deprived of PLB structures, the fluorescence spectra have similar ratio of 632/653 nm peaks to the seedling shoot including whole hypocotyl and PLB-rich cotyledons (**Figure 1**). Therefore, Pchlide:LPOR:NADPH complex might be located in prothylakoids, which was also confirmed earlier on isolated and fractionated internal etioplast membranes of wheat (Ryberg and Sundqvist, 1982). Based on our structural and spectral analyses, we presume that free Pchlide overaccumulated in the *pif1* plants is located directly in the PLB lattice, causing an increase in its compactness. Similar spectral pattern together with comparable PLB periodicity value were detected earlier in *cop1*/PBO-1 line characterized by *cop1* mutation (lack of PLB structure and complex-bound Pchlide) and simultaneous overexpression of PORB protein rescuing PLB cubic arrangement and partial formation of Pchlide:LPOR:NADPH complex (Sperling et al., 1998). Probably Pchlide-dependent decrease in PLB periodicity is not directly related to the Pchlide molecule shape but is rather connected with the imbalance between different groups of the PLB building blocks, a relative decrease in the polar-lipid contribution particularly. Studies on ER-originating cubic membranes in the fibroblast cell culture lines revealed that over-accumulation of particular ER-resident proteins markedly changing the protein/lipid ratio results in formation of the cubic arrangements (Snapp et al., 2003; Almsherqi et al., 2006). Such observations of even distant biological species are particularly relevant for a better understanding of cubic membrane differentiation. This is based on the assumption that the formation and stability of membrane configurations can be understood from the same basic principles because formation mechanisms are probably dictated by the charge and geometry of molecules rather than a specific amino acid sequence or lipid class.

Finally, we tested the role of plastid-located polyprenols in the PLB formation. The possible structural role of polyprenols in the chloroplast thylakoid membranes was raised before (Akhtar et al., 2017); however, no data concerning their potential role in the PLB formation were available. Due to a lower protein/lipid ratio in the etioplast membranes compared to thylakoids (Solymosi and Aronsson, 2013), it is highly probable that polar and non-polar lipid components play crucial role in the establishment of the cubic arrangement. However, diminish in plastidic polyprenols in the *cpt7* mutant had a limited influence on the PLB arrangement causing only a slight decrease in the PLB compactness (**Figures 4**, **5**). It might be related to the fact that even in etiolated seedlings of wt plants, polyprenol level is relatively low, and the abundance of only main plastidial polyprenol (Pren-10) was registered. Such result is consistent with earlier studies indicating induction of polyprenol accumulation on light and substantial increase of their content in photosynthetic tissue during leaf senescence (reviewed in Swiezewska and Danikiewicz, 2005).

Studies on the 3D PLB nano-morphology are particularly complicated due to small dimensions of the PLB lattice. Previously, a template matching technique was applied to predict the spatial arrangement of cubic membranes visible in the TEM cross-sections (Deng and Mieczkowski, 1998). However, no spatial parameters of the predicted structures nor a confirmation in the 3D experimental data were provided. Here, we obtained the actual 3D models of the PLB lattices from the ET experiments and compared the structural parameters with the ones generated from rendered spatial theoretical models based on the 2D TEM information (**Figure 8**). High level of correlation of these results gives an experimental evidence directly justifying further development of the matching technique. Progress in this method will enable prediction of the cubic spatial parameters in a faster and more efficient way than by using time and money-consuming 3D electron microscopy experiments.

CONCLUSION

This study provides a comprehensive analysis of the influence of different experimental setups typically used in etiolation/de-etiolation studies on the PLB nano-morphology. Our results point to the important role of Suc supplementation of the nutrition media and the duration of etiolation on the compactness and size of the PLB, as well as etioplast spectral properties. Therefore, particular attention should be drawn whether data obtained in different etiolation conditions are reliably comparable. In our studies using different Arabidopsis mutants with disturbed levels of the PLB pigments and polyprenols, we pointed out the important role of β-β-xanthophylls in the stabilization of the bicontinuous PLB structure, as well as the Pchlide level in the control of PLB compactness. This study broadens our understanding of the mechanisms governing cubic membrane formation, shedding light on the role of other than polar lipid and protein components in the cubic structure development. Further studies should consider how the disturbed PLB structure can influence the process of the tubular-lamellar transformation taking place during the chloroplast biogenesis. Irregular, over-compacted, or very loosely arranged PLB structure could substantially retard the chloroplast biogenesis via, e.g., trapping of molecules in hyperbended membranes or providing a limited lipid reservoir for the developing structures.

DATA AVAILABILITY STATEMENT

The raw data supporting the conclusions of this article will be made available by the authors, without undue reservation.

AUTHOR CONTRIBUTIONS

ŁK and AM provided the conception of the manuscript. MB, ŁK, RM, DB, and JS performed experiments. MB, ŁK, RM, and DB analyzed and processed data. ŁK coordinated the project. ŁK wrote the manuscript with a contribution of AM and DB. AM secured funding. All authors contributed to the article and approved the submitted version.

FUNDING

Presented work was financed by the National Science Centre (NCN), Poland, Grant No. 2014/13/B/NZ3/00413. The polyprenol analysis was financed by the National Science Centre (NCN), Poland, Grant No. 2017/26/D/NZ1/00833.

ACKNOWLEDGMENTS

Part of the experiments was conducted in the University of Warsaw Biological and Chemical Research Centre. We thank Szymon Suski for the operation of the tomography supply.

SUPPLEMENTARY MATERIAL

The Supplementary Material for this article can be found online at: https://www.frontiersin.org/articles/10.3389/fcell.2020.586628/full#supplementary-material

REFERENCES

Abramoff, M. D., Magalhaes, P. J., and Ram, S. J. (2004). Image processing with imageJ. *Biophotonics Int.* 11, 36–42.

Adam, Z., Charuvi, D., Tsabari, O., Knopf, R. R., and Reich, Z. (2011). Biogenesis of thylakoid networks in angiosperms: knowns and unknowns. *Plant Mol. Biol.* 76, 221–234. doi: 10.1007/s11103-010-9693-5

Akhtar, T. A., Surowiecki, P., Siekierska, H., Kania, M., Van Gelder, K., Rea, K. A., et al. (2017). Polyprenols are synthesized by a plastidial cis-prenyltransferase and influence photosynthetic performance. *Plant Cell* 29, 1709–1725. doi: 10.1105/tpc.16.00796

Almsherqi, Z. A., Kohlwein, S. D., and Deng, Y. (2006). Cubic membranes: a legend beyond the Flatland* of cell membrane organization. *J. Cell Biol.* 173, 839–844. doi: 10.1083/jcb.200603055

Almsherqi, Z. A., Landh, T., Kohlwein, S. D., and Deng, Y. (2009). Cubic membranes: the missing dimension of cell membrane organization. *Int. Rev. Cell Mol. Biol.* 274, 275–341. doi: 10.1016/s1937-6448(08)02006-6

Armarego-Marriott, T., Kowalewska, Ł, Burgos, A., Fischer, A., Thiele, W., Erban, A., et al. (2019). Highly resolved systems biology to dissect the etioplast-to-chloroplast transition in tobacco leaves. *Plant Physiol.* 180, 654–681. doi: 10.1104/pp.18.01432

Armarego-Marriott, T., Sandoval-Ibañez, O., and Kowalewska, Ł (2020). Beyond the darkness: recent lessons from etiolation and de-etiolation studies. *J. Exp. Bot.* 71, 1215–1225. doi: 10.1093/jxb/erz496

Armbruster, U., Labs, M., Pribil, M., Viola, S., Xu, W., Scharfenberg, M., et al. (2013). *Arabidopsis* CURVATURE THYLAKOID1 proteins modify thylakoid architecture by inducing membrane curvature. *Plant Cell* 25, 2661–2678. doi: 10.1105/tpc.113.113118

Armstrong, G. A., Runge, S., Frick, G., Sperling, U., and Apel, K. (1995). Identification of NADPH:protochlorophyllide oxidoreductases A and B: a branched pathway for light-dependent chlorophyll biosynthesis in *Arabidopsis thaliana*. *Plant Physiol.* 108, 1505–1517. doi: 10.1104/pp.108.4.1505

Aronsson, H., Schöttler, M. A., Kelly, A. A., Sundqvist, C., Dörmann, P., Karim, S., et al. (2008). Monogalactosyldiacylglycerol deficiency in *Arabidopsis* affects pigment composition in the prolamellar body and impairs thylakoid membrane energization and photoprotection in leaves. *Plant Physiol.* 148, 580–592. doi: 10.1104/pp.108.123372

Blomqvist, L. A., Ryberg, M., and Sundqvist, C. (2008). Proteomic analysis of highly purified prolamellar bodies reveals their significance in chloroplast development. *Photosynth. Res.* 96, 37–50. doi: 10.1007/s11120-007-9281-y

Böddi, B., Lindsten, A., Ryberg, M., and Sundqvist, C. (1989). On the aggregational states of protochlorophyllide and its protein complexes in wheat etioplasts. *Physiol. Plant* 76, 135–143. doi: 10.1111/j.1399-3054.1989.tb05622.x

Bradbeer, J. W., Gyldenholm, A. O., Ireland, H. M. M., Smith, J. W., Rest, J., and Edge, H. J. W. (1974). Plastid development in primary leaves of *Phaseolus vulgaris*. *New Phytol.* 73, 271–279. doi: 10.1111/j.1469-8137.1974.tb04760.x

Cazzonelli, C. I., Hou, X., Alagoz, Y., Rivers, J., Dhami, N., Lee, J., et al. (2020). A cis-carotene derived apocarotenoid regulates etioplast and chloroplast development. *Elife* 31:e45310. doi: 10.7554/eLife.45310

Cuttriss, A. J., Chubb, A. C., Alawady, A., Grimm, B., and Pogson, B. J. (2007). Regulation of lutein biosynthesis and prolamellar body formation in *Arabidopsis*. *Funct. Plant Biol.* 34, 663–672. doi: 10.1071/FP07034

Dall'Osto, L., Bassi, R., and Ruban, A. (2014). "Photoprotective mechanisms: carotenoids," in *Plastid Biology. Advances in Plant Biology*, Vol. 5, eds S. Theg, and F. A. Wollman (New York, NY: Springer), 393–435. doi: 10.1007/978-1-4939-1136-3_15

Dall'Osto, L., Cazzaniga, S., Havaux, M., and Bassi, R. (2010). Enhanced photoprotection by protein-bound vs free xanthophyll pools: a comparative analysis of chlorophyll b and xanthophyll biosynthesis mutants. *Mol. Plant* 3, 576–593. doi: 10.1093/mp/ssp117

Dehesh, K., and Ryberg, M. (1985). The NADPH-protochlorophyllide oxidoreductase is the major protein constituent of prolamellar bodies in wheat (*Triticum aestivum* L.). *Planta* 164, 396–399. doi: 10.1007/bf00402952

Demé, B., Cataye, C., Block, M. A., Maréchal, E., and Jouhet, J. (2014). Contribution of galactoglycerolipids to the 3-dimensional architecture of thylakoids. *FASEB J.* 28, 3373–3383. doi: 10.1096/fj.13-247395

Deng, Y., and Mieczkowski, M. (1998). Three-dimensional periodic cubic membrane structure in mitochondria of amoebae chaos carolinensis. *Protoplasma* 203, 16–25. doi: 10.1007/BF01280583

Forger, J., and Bogorad, J. (1973). Steps in the acquisition of photosynthetic competence by plastids of maize. *Plant Physiol.* 52, 491–497. doi: 10.1104/pp.52.5.491

Franck, F., Sperling, U., Frick, G., Pochert, B., van Cleve, B., Apel, K., et al. (2000). Regulation of etioplast pigment-protein complexes, inner membrane architecture, and protochlorophyllide a chemical heterogeneity by light-dependent NADPH:protochlorophyllide oxidoreductases A and B. *Plant Physiol.* 124, 1678–1696. doi: 10.1104/pp.124.4.1678

Fujii, S., Kaushik, M. K., Zhou, X., Korkutata, M., and Lazarus, M. (2019). Acute social defeat stress increases sleep in mice. *Front. Neurosci.* 3:322. doi: 10.3389/fnins.2019.00322

Fujii, S., Kobayashi, K., Nagata, N., Masuda, T., and Wada, H. (2017). Monogalactosyldiacylglycerol facilitates synthesis of photoactive protochlorophyllide in etioplasts. *Plant Physiol.* 174, 2183–2198. doi: 10.1104/pp.17.00304

Fujii, S., Kobayashi, K., Nagata, N., Masuda, T., and Wada, H. (2018). Digalactosyldiacylglycerol is essential for organization of the membrane structure in etioplasts. *Plant Physiol.* 177, 1487–1497. doi: 10.1104/pp.18.00227

Gabruk, M., and Mysliwa-Kurdziel, B. (2015). Light-dependent protochlorophyllide oxidoreductase: phylogeny, regulation, and catalytic properties. *Biochemistry* 54, 5255–5262. doi: 10.1021/acs.biochem.5b00704

Gruszecki, W. I., and Strzałka, K. (2005). Carotenoids as modulators of lipid membrane physical properties. *Biochim. Biophys. Acta* 1740, 108–115. doi: 10.1016/j.bbadis.2004.11.015

Gunning, B. E. (2001). Membrane geometry of "open" prolamellar bodies. *Protoplasma* 215, 4–15. doi: 10.1007/BF01280299

Gunning, B. E. S. (1965). The greening process in plastids. *Protoplasma* 60, 111–130. doi: 10.1007/bf01248133

Gunning, B. E. S., and Steer, M. W. (1975). *Ultrastructure and the Biology of Plant Cell*. London: Edward Arnold.

Huq, E., Al-Sady, B., Hudson, M., Kim, C., Apel, K., and Quail, P. H. (2004). Phytochrome-interacting factor 1 is a critical bHLH regulator of chlorophyll biosynthesis. *Science* 305, 1937–1941. doi: 10.1126/science.1099728

Ikeda, T. (1968). Analytical studies on structure of prolamellar body. *Bot. Mag.* 81, 517–527. doi: 10.15281/jplantres1887.81.517

Kesselmeier, J. (1980). Development of chloro-etioplasts containing prolamellar bodies and steroidal saponins in suspension cultures of Nicotiana tabacum. *Protoplasma* 104, 295–306. doi: 10.1007/BF01279774

Kim, J., and DellaPenna, D. (2006). Defining the primary route for lutein synthesis in plants: the role of *Arabidopsis* carotenoid β-ring hydroxylase CYP97A3. *Proc. Natl. Acad. Sci. U.S.A.* 103, 3474–3479. doi: 10.1073/pnas.0511207103

Klein, S., and Schiff, J. A. (1972). The correlated appearance of prolamellar bodies, protochlorophyll(ide) species, and the shibata shift during development of bean etioplasts in the dark. *Plant Physiol.* 49, 619–626. doi: 10.1104/pp.49.4.619

Kowalewska, Ł, Bykowski, M., and Mostowska, A. (2019). Spatial organization of thylakoid network in higher plants. *Bot. Lett.* 166, 326–343. doi: 10.1080/23818107.2019.1619195

Kowalewska, Ł, Mazur, R., Suski, S., Garstka, M., and Mostowska, A. (2016). Three-dimensional visualization of the tubular-lamellar transformation of the internal plastid membrane network during runner bean chloroplast biogenesis. *Plant Cell* 28, 875–891. doi: 10.1105/tpc.15.01053

Kowalewska, Ł, and Mostowska, A. (2016). "Biogenesis of thylakoid membranes: correlation of structure and function," in *Handbook of Photosynthesis*, 3rd Edn, ed. M. Pessarakli (Boca Raton, FL: CRC Press), 1–15. doi: 10.1201/b19498-3

Krapp, A., Hofmann, B., Schäfer, C., and Stitt, M. (1993). Regulation of the expression of *rbcS* and other photosynthetic genes by carbohydrates: a mechanism for the 'sink regulation' of photosynthesis. *Plant J.* 3, 817–828. doi: 10.1111/j.1365-313X.1993.00817.x

Landh, T. (1996). *Cubic Cell Membrane Architectures. Taking Another Look at Membrane Bound Cell Spaces*. Ph.D. thesis, Sweden, Lund University.

Lastdrager, J., Hanson, J., and Smeekens, S. (2014). Sugar signals and the control of plant growth and development. *J. Exp. Bot.* 65, 799–807. doi: 10.1093/jxb/ert474

Lebedev, N., Van Cleve, B., Armstrong, G., and Apel, K. (1995). Chlorophyll synthesis in a deetiolated (det340) mutant of arabidopsis without NADPH-protochlorophyllide (PChlide) oxidoreductase (POR) A and photoactive PChlide-F655. *Plant Cell* 7, 2081–2090. doi: 10.1105/tpc.7.12.2081

Leyon, H. (1954). The structure of chloroplasts. VI. the origin of the chloroplast laminae. *Exp. Cell Res.* 7, 609–611. doi: 10.1016/s0014-4827(54)80115-7

Li, Z., Ahn, T. K., Avenson, T. J., Ballottari, M., Cruz, J. A., Kramer, D. M., et al. (2009). Lutein accumulation in the absence of zeaxanthin restores nonphotochemical quenching in the *Arabidopsis thaliana* npq1 mutant. *Plant Cell* 21, 1798–1812. doi: 10.1105/tpc.109.066571

Lindblom, G., and Rilfors, L. (1989). Cubic phases and isotropic structures formed by membrane lipids — possible biological relevance. *Biochim. Biophys. Acta Rev. Biomembr.* 988, 221–256. doi: 10.1016/0304-4157(89)90020-8

Lindstedt, I., and Liljenberg, C. (1990). On the periodic minimal surface structure of the plant prolemallar body. *Physiol. Plant* 80, 1–4. doi: 10.1034/j.1399-3054.1990.800101.x

Lindsten, A., Ryberg, M., and Sundqvist, C. (1988). The polypeptide composition of highly purified prolamellar bodies and prothylakoids from wheat (*Triticum aestivum*) as revealed by silver staining. *Physiol. Plant* 72, 167–176. doi: 10.1111/j.1399-3054.1988.tb06639.x

Lundqvist, U., and Franckowiak, J. D. (2003). "Chapter 5 Diversity of barley mutants," in *Diversity in Barley (Hordeum Vulgare)*, Vol. 7, eds R. von Bothmer, Th van Hintum, H. Knüpffer, and K. Sato (Amsterdam: Elsevier Science B.V), 77–96. doi: 10.1016/S0168-7972(03)80007-5

Lütz, C. (1981). On the significance of prolamellar bodies in membrane development of etioplasts. *Protoplasma* 108, 99–115. doi: 10.1007/BF01276886

Mechela, A., Schwenkert, S., and Soll, J. (2019). A brief history of thylakoid biogenesis. *Open Biol.* 9:180237. doi: 10.1098/rsob.180237

Messaoudii, C., Boudier, T., Sanchez Sorzano, C. O., and Marco, S. (2007). TomoJ: tomography software for three-dimensional reconstruction in transmission electron microscopy. *BMC Bioinformatics* 8:288. doi: 10.1186/1471-2105-8-288

Mezzenga, R., Seddon, J. M., Drummond, C. J., Boyd, B. J., Schröder-Turk, G. E., and Sagalowicz, L. (2019). Nature-inspired design and application of lipidic lyotropic liquid crystals. *Adv Mater.* 31:e1900818. doi: 10.1002/adma.201900818

Mostowska, A. (1986). Changes induced on the prolamellar body of pea seedlings by white, red and blue low intensity light. *Protoplasma* 131, 166–173. doi: 10.1007/BF01285038

Murakami, S., Yamada, N., Nagano, M., and Osumi, M. (1985). Three-dimensional structure of the prolamellar body in squash etioplasts. *Protoplasma* 128, 147–156. doi: 10.1007/bf01276336

Myśliwa-Kurdziel, B., Kruk, J., and Strzałka, K. (2013). Protochlorophyllide in model systems-an approach to in vivo conditions. *Biophys. Chem.* 175-176, 28–38. doi: 10.1016/j.bpc.2013.02.002

Niyogi, K. K., Grossman, A. R., and Björkman, O. (1998). *Arabidopsis* mutants define a central role for the xanthophyll cycle in the regulation of photosynthetic energy conversion. *Plant Cell* 10, 1121–1134. doi: 10.2307/3870716

Paddock, T., Lima, D., Mason, M. E., Apel, K., and Armstrong, G. A. (2012). *Arabidopsis* light-dependent protochlorophyllide oxidoreductase A (PORA) is essential for normal plant growth and development. *Plant Mol. Biol.* 78, 447–460. doi: 10.1007/s11103-012-9873-6

Park, H., Kreunen, S. S., Cuttriss, A. J., DellaPenna, D., and Pogson, B. J. (2002). Identification of the carotenoid isomerase provides insight into carotenoid biosynthesis, prolamellar body formation, and photomorphogenesis. *Plant Cell* 14, 321–332. doi: 10.1105/tpc.010302

Peskan-Berghöfer, T., Vilches-Barro, A., Müller, T. M., Glawischnig, E., Reichelt, M., Gershenzon, J., et al. (2015). Sustained exposure to abscisic acid enhances the colonization potential of the mutualist fungus Piriformospora indica on *Arabidopsis thaliana* roots. *New Phytol.* 208, 873–886. doi: 10.1111/nph.13504

Pogson, B. J., Ganguly, D., and Albrecht-Borth, V. (2015). Insights into chloroplast biogenesis and development. *Biochim. Biophys. Acta* 1847, 1017–1024. doi: 10.1016/j.bbabio.2015.02.003

Rast, A., Heinz, S., and Nickelsen, J. (2015). Biogenesis of thylakoid membranes. *Biochim. Biophys. Acta* 1847, 821–830. doi: 10.1016/j.bbabio.2015.01.007

Robertson, D., and Laetsch, W. M. (1974). Structure and function of developing barley plastids. *Plant physiol.* 54, 148–159. doi: 10.1104/pp.54.2.148

Rudowska, L., Gieczewska, K., Mazur, R., Garstka, M., and Mostowska, A. (2012). Chloroplast biogenesis - correlation between structure and function. *Biochim. Biophys. Acta* 1817, 1380–1387. doi: 10.1016/j.bbabio.2012.03.013

Ryberg, M., and Sundqvist, C. (1982). Characterization of prolamellar bodies and prothylakoids fractionated from wheat etioplasts. *Physiol Plant* 56, 125–132. doi: 10.1111/j.1399-3054.1982.tb00313.x

Samol, I., Rossig, C., Buhr, F., Springer, A., Pollmann, S., Lahroussi, A., et al. (2011). The outer chloroplast envelope protein OEP16-1 for plastid import of NADPH:protochlorophyllide oxidoreductase A in *Arabidopsis thaliana*. *Plant Cell Physiol.* 52, 96–111. doi: 10.1093/pcp/pcq177

Schoefs, B., and Franck, F. (2003). Protochlorophyllide reduction: mechanisms and evolution. *Photochem. Photobiol.* 78, 543–557. doi: 10.1562/0031-8655(2003)0780543prmae2.0.co2

Schoefs, B., and Franck, F. (2008). The photoenzymatic cycle of NADPH: protochlorophyllide oxidoreductase in primary bean leaves (Phaseolus vulgaris) during the first days of photoperiodic growth. *Photosynth. Res.* 96, 15–26. doi: 10.1007/s11120-007-9274-x

Selstam, E., Brain, A. P., and Williams, W. P. (2011). The relationship between different spectral forms of the protochlorophyllide oxidoreductase complex and the structural organisation of prolamellar bodies isolated from Zea mays. *Photosynth. Res.* 108, 47–59. doi: 10.1007/s11120-011-9653-1

Selstam, E., and Sandelius, A. S. (1984). A comparison between prolamellar bodies and prothylakoid membranes of etioplasts of dark-grown wheat concerning lipid and polypeptide composition. *Plant Physiol.* 76, 1036–1040. doi: 10.1104/pp.76.4.1036

Selstam, E., Schelin, J., Williams, W. P., and Brain, A. P. (2007). Structural organisation of prolamellar bodies (PLB) isolated from Zea mays. parallel TEM, SAXS and absorption spectra measurements on samples subjected to freeze-thaw, reduced pH and high-salt perturbation. *Biochim. Biophys. Acta* 1768, 2235–2245. doi: 10.1016/j.bbamem.2007.05.005

Skorupińska-Tudek, K., Bieńkowski, T., Olszowska, O., Furmanowa, M., Chojnacki, T., Danikiewicz, W., et al. (2003). Divergent pattern of polyisoprenoid alcohols in the tissues of Coluria geoides: a new electrospray ionization MS approach. *Lipids* 38, 981–990. doi: 10.1007/s11745-003-1152-3

Skupień, J., Wójtowicz, J., Kowalewska, Ł, Mazur, R., Garstka, M., Gieczewska, K., et al. (2017). Dark-chilling induces substantial structural changes and modifies galactolipid and carotenoid composition during chloroplast biogenesis in cucumber (Cucumis sativus L.) cotyledons. *Plant Physiol. Biochem.* 111, 107–118. doi: 10.1016/j.plaphy.2016.11.022

Snapp, E. L., Hegde, R. S., Francolini, M., Lombardo, F., Colombo, S., Pedrazzini, E., et al. (2003). Formation of stacked ER cisternae by low affinity protein interactions. *J. Cell Biol.* 163, 257–269. doi: 10.1083/jcb.200306020

Solymosi, K., and Aronsson, H. (2013). "Etioplasts and their significance in chloroplast biogenesis," in *Plastid Development in Leaves During Growth and Senescence. Advances in Photosynthesis and Respiration (Including Bioenergy and Related Processes)*, Vol. 36, eds B. Biswal, K. Krupinska, and U. Biswal (Dordrecht: Springer), 39–71. doi: 10.1007/978-94-007-5724-0_3

Solymosi, K., and Böddi, B. (2006). Optical properties of bud scales and protochlorophyll(ide) forms in leaf primordia of closed and opened buds. *Tree Physiol.* 26, 1075–1085. doi: 10.1093/treephys/26.8.1075

Solymosi, K., and Schoefs, B. (2010). Etioplast and etio-chloroplast formation under natural conditions: the dark side of chlorophyll biosynthesis in angiosperms. *Photosynth. Res.* 105, 143–166. doi: 10.1007/s11120-010-9568-2

Sperling, U., Franck, F., van Cleve, B., Frick, G., Apel, K., and Armstrong, G. A. (1998). Etioplast differentiation in arabidopsis: both PORA and PORB restore the prolamellar body and photoactive protochlorophyllide-F655 to the cop1 photomorphogenic mutant. *Plant Cell* 10, 283–296. doi: 10.1105/tpc.10.2.283

Sperling, U., van Cleve, B., Frick, G., Apel, K., and Armstrong, G. A. (1997). Overexpression of light-dependent PORA or PORB in plants depleted of endogenous POR by far-red light enhances seedling survival in white light and protects against photooxidative damage. *Plant J.* 12, 649–658. doi: 10.1046/j.1365-313x.1997.00649.x

Sujak, A., Gabrielska, J., Grudziński, W., Borc, R., Mazurek, P., and Gruszecki, W. I. (1999). Lutein and zeaxanthin as protectors of lipid membranes against oxidative damage: the structural aspects. *Arch. Biochem. Biophys.* 371, 301–307. doi: 10.1006/abbi.1999.1437

Swiezewska, E., and Danikiewicz, W. (2005). Polyisoprenoids: structure, biosynthesis and function. *Prog. Lipid Res.* 44, 235–258. doi: 10.1016/j.plipres.2005.05.002

Tognetti, J. A., Pontis, H. G., and Martínez-Noël, G. M. (2013). Sucrose signaling in plants: a world yet to be explored. *Plant Signal. Behav.* 8:e23316. doi: 10.4161/psb.23316

Van Dingenen, J., De Milde, L., Vermeersch, M., Maleux, K., De Rycke, R., De Bruyne, M., et al. (2016). Chloroplasts are central players in sugar-induced leaf growth. *Plant Physiol.* 171, 590–605. doi: 10.1104/pp.15.01669

Van Wijk, K. J., and Kessler, F. (2017). Plastoglobuli: Plastid microcompartments with integrated functions in metabolism, plastid developmental transitions, and environmental adaptation. *Annu. Rev. Plant Biol.* 68, 253–289. doi: 10.1146/annurev-arplant-043015-111737

Von Wettstein, D. (1967). "Chloroplast structure and genetics," in *Harvesting the Sun*, eds A. San Pietro, F. A. Greer, and T. D. Army (New York, NY: Academic Press), 153–190.

Von Wettstein, D., Gough, S., and Kannangara, C. G. (1995). Chlorophyll biosynthesis. *Plant Cell* 7, 1039–1057. doi: 10.1105/tpc.7.7.1039

Wasilewska, A., Vlad, F., Sirichandra, C., Redko, Y., Jammes, F., Valon, C., et al. (2008). An update on abscisic acid signaling in plants and more. *Mol. Plant.* 1, 198–217. doi: 10.1093/mp/ssm022

Weier, T. E., and Brown, D. L. (1970). Formation of the prolamellar body in 8-day, dark-grown seedlings. *Am. J. Bot.* 57, 267–275. doi: 10.2307/2485302

Williams, W. P., Selstam, E., and Brain, T. (1998). X-ray diffraction studies of the structural organisation of prolamellar bodies isolated from Zea mays. *FEBS Lett.* 422, 252–254. doi: 10.1016/s0014-5793(98)00019-2

Ytterberg, A. J., Peltier, J. B., and van Wijk, K. J. (2006). Protein profiling of plastoglobules in chloroplasts and chromoplasts. a surprising site for differential accumulation of metabolic enzymes. *Plant Physiol.* 140, 984–997. doi: 10.1104/pp.105.076083

Conflict of Interest: The authors declare that the research was conducted in the absence of any commercial or financial relationships that could be construed as a potential conflict of interest.

frontiers
in Cell and Developmental Biology

ORIGINAL RESEARCH
published: 14 December 2020
doi: 10.3389/fcell.2020.617406

Cubic Membranes Formation in Synchronized Human Hepatocellular Carcinoma Cells Reveals a Possible Role as a Structural Antioxidant Defense System in Cell Cycle Progression

Deqin Kong[1], Rui Liu[1], Jiangzheng Liu[1], Qingbiao Zhou[1], Jiaxin Zhang[1], Wenli Li[1], Hua Bai[1,2]* and Chunxu Hai[1]*

[1] Shaanxi Provincial Key Lab of Free Radical Biology and Medicine, The Ministry of Education Key Lab of Hazard Assessment and Control in Special Operational Environment, Department of Toxicology, School of Public Health, Air Force Medical University (Fourth Military Medical University), Xi'an, China, [2] Frontiers Science Center for Flexible Electronics, Xi'an Institute of Flexible Electronics (IFE) and Xi'an Institute of Biomedical Materials & Engineering, Northwestern Polytechnical University, Xi'an, China

OPEN ACCESS

Edited by:
Yuru Deng,
University of Chinese Academy of Sciences, China

Reviewed by:
Cheng-wu Zhang,
Nanjing Tech University, China
Jingke Guo,
Zhejiang Gongshang University, China

***Correspondence:**
Hua Bai
hua_bai@126.com
Chunxu Hai
cx-hai@fmmu.edu.cn

Specialty section:
This article was submitted to Cellular Biochemistry, a section of the journal Frontiers in Cell and Developmental Biology

Received: *14 October 2020*
Accepted: *23 November 2020*
Published: *14 December 2020*

Citation:
Kong D, Liu R, Liu J, Zhou Q, Zhang J, Li W, Bai H and Hai C (2020) Cubic Membranes Formation in Synchronized Human Hepatocellular Carcinoma Cells Reveals a Possible Role as a Structural Antioxidant Defense System in Cell Cycle Progression. Front. Cell Dev. Biol. 8:617406. doi: 10.3389/fcell.2020.617406

Cubic membranes (CMs) represent unique biological membrane structures with highly curved three-dimensional periodic minimal surfaces, which have been observed in a wide range of cell types and organelles under various stress conditions (e. g., starvation, virus-infection, and oxidation). However, there are few reports on the biological roles of CMs, especially their roles in cell cycle. Hence, we established a stable cell population of human hepatocellular carcinoma cells (HepG2) of 100% S phase by thymidine treatment, and determined certain parameters in G2 phase released from S phase. Then we found a close relationship between CMs formation and cell cycle, and an increase in reactive oxygen species (ROS) and mitochondrial function. After the synchronization of HepG2 cells were induced, CMs were observed through transmission electron microscope in G2 phase but not in G1, S and M phase. Moreover, the increased ATP production, mitochondrial and intracellular ROS levels were also present in G2 phase, which demonstrated a positive correlation with CMs formation by Pearson correlation analysis. This study suggests that CMs may act as an antioxidant structure in response to mitochondria-derived ROS during G2 phase and thus participate in cell cycle progression.

Keywords: cubic membranes (CMs), cell cycle, reactive oxygen species (ROS), mitochondria, cell synchronization

INTRODUCTION

It is universally known that all organisms except viruses have biomembranes. The emergence of biomembranes, which enable cells to exist independently of environment, is a leap in biological evolution. Generally, the morphology of biomembranes is a bimolecular lamellar structure. However, there are also non-lamellar membrane structures in the cells, such as the cubic membranes (CMs), which have highly curved 3D nanoscale periodic structure with a 3-fold periodic minimum surface (Almsherqi et al., 2012; Paillusson et al., 2016; Deng et al., 2017). CMs seem to be evolutionally conserved and have been continually discovered by transmission electron microscopy in all the five kingdoms of life, namely monera, protista, fungi, plant, and animalia (Almsherqi et al., 2009; Zhan et al., 2017).

Although the precise biological role of CMs is unclear until now, research in recent decades has provided some clues. Chong et al. found that in the case of starvation, the inner membrane of mitochondria of amoeba was transformed into a cubic membrane structure to enhance mitochondrial function and maintain ATP production-a process critical for survival (Chong et al., 2018). The formation of cubic mitochondrial cristae in amoeba cells protects them against oxidative damage by enhancing the leakage of H_2O_2 and reactive oxygen species (ROS) in mitochondria and reducing the sensitivity of membrane lipids to oxidants (Deng et al., 2002). In addition, it is found that phospholipids rich in long chain polyunsaturated fatty acids in CMs can preferentially bind with superoxide anions, thus inhibiting the oxidative damage of RNA induced by ROS (Deng and Almsherqi, 2015). Another role of CMs is a "virus factory" in the host cells infected by virus. Virus infection can lead to rearrangement of cell biomembrane system and induce appearance of CMs, which is likely to provide a protective microenvironment for virus assembly and proliferation (Deng et al., 2010).

Of particular concern is the potential role of CMs in cell cycle progression. In 1965, an observational study found that a large number of CMs from mitochondria appeared during mitosis in amoebae (Daniels et al., 1965). Although the role of CMs is unknown, the study suggests the possibility that CMs may get involved in cell division. Since then, however, this phenomenon seems not to be confirmed in mammalian cells, particularly in the cells derived from humans. Hence, by employing the universally accepted cell synchronization method (Banfalvi, 2017), we tried to investigate the changes of CMs in different cell cycle phases of synchronized HepG2 cells. Our study demonstrated the appearance of CMs at G2 phase of cell cycle in mammalian cells, and by evaluating the levels of mitochondrial ROS and ATP, we conducted further research on the potential roles of CMs in cell cycle.

MATERIALS AND METHODS

Cell Culture

HepG2, human hepatocellular carcinoma cell line, was obtained from the American Type Culture Collection (ATCC) and cultured with RPMI 1640 medium (HyClone) containing 10% fetal bovine serum at 37°C in 5% CO_2 and saturated humidity. When the confluence reached 80%, the cells were digested with 0.25% trypsin (HyClone) for generation or subsequent experiments.

The Acquisition of Synchronized Cells

HepG2 cells were seeded in 6-well plates, and when the adherent rate was about 50%, the cells were treated with 1 mM thymidine (Sigma, T1895) for 48 h. The cells were washed with warm fresh medium twice and 25 μM deoxycytidine (Sigma-Aldrich) in medium was added to promote release. The cells in G2/M and G1 phases were collected at indicated time points.

The Detection of Cell Cycle Distribution

The cell cycle detection kit (KeyGEN BioTECH, KGA512) was used to detect cell cycle distribution according to the instructions. Briefly, the cells were fixed with 70% ethanol and stored at 4°C overnight. Then, the fixed cells were centrifuged at 1,000 g for 5 min. After being washed with the PBS buffer, the cell samples were incubated with 100 μL RNAase at 37°C for 30 min and then with 400 μL PI at 4°C for 30 min under a dark condition. The flow cytometry (BD Biosciences) was used to detect fluorescence signal at FL2-A channel by the CFlow Plus software. A quantitative analysis of the proportion of each phase in a cell cycle was conducted by the LT ModFit software.

The Detection of Cell Apoptosis

Cell apoptosis was detected by the AnnexinV-FITC/propidium iodide (PI) staining (Mao et al., 2019). When the treatment was completed, the cells were harvested and washed twice with PBS. After centrifugation, cells were resuspended at 2×10^5/mL and assayed by the AnnexinV-FITC/PI kit in accordance with the manufacturer's instructions. In each sample, 500 μL binding buffer, 5 μL Annexin V-FITC and 5 μL PI were added in turn and incubated at a room temperature for 15 min under a dark condition. Apoptosis was detected by flow cytometry (BD Biosciences). Annexin V-FITC and PI fluorescents were detected by FL1 and FL3 channels, respectively.

The Ultrastructural Study by Transmission Electron Microscope

HepG2 cells were seeded in T75 cell culture flask. After synchronization and release at indicated time points, the cells were collected and fixed by 2.5% glutaraldehyde. After ultrathin sections were made, the ultrastructure was observed and the number of CMs in cells was counted by transmission electron microscope (Tecnai G2, FEI).

The Determination of ROS

The intracellular ROS level was determined by DCFH-DA staining as described (Kong et al., 2019). After the cells were collected and washed with PBS, DCFH-DA dye (Sigma, D6883) with a final concentration of 10 μmol/L was used to incubate with each sample for 30 min at 37°C under a dark condition. Intracellular ROS levels were detected by flow cytometry (BD Biosciences) (EX/EM: 488 nm /530 nm). The CFlowPlus software was used to collect and process the data.

The Measurement of Mitochondrial ROS (mtROS)

A mitochondria-targeted MitoSOX probe was used to measure mtROS levels as described (Gao and Zhang, 2020). After the cells were collected and washed with PBS, each sample was added into 5 μmol/L MitoSOX (Invitrogen, M36008). After incubation for 30 min at 37°C under a dark condition, the flow cytometry

(BD Biosciences) was employed to detect fluorescence intensity at FL2A channel (EX/EM: 510 nm /580 nm).

The Detection of ATP Content

Enhanced ATP Assay Kit (Beyotime Biotechnology, S0027) was employed to detect the ATP content as described (Ding et al., 2020). After lysis of the cells on the ice, the lysate was centrifuged at 4°C for 5 min and the supernatant was taken to store at 4°C. One hundred microliter ATP-detection solution was added to the test wells for 5 min. Twenty microliter samples or standard products were added to the test wells and RLU values were detected by multifunctional microplate reader (Tecan Group Ltd.). The concentrations of ATP in the samples were calculated by the standard curve. The protein concentration was determined by BCA assay kit (Thermo Scientific) and ATP content was normalized by protein concentration.

Statistical Analysis

The values were expressed as the mean ± SD. Statistical comparison was estimated by a one-way ANOVA followed by a Dunnett-*t* test for comparing all the groups with the control group. All analyses were performed using the Statistical Package for the Social Sciences 20.0 (SPSS20.0) software. In all the cases, a two-tailed p-value lower than 0.05 was considered statistically significant.

RESULTS

The Highly Synchronized Cells Were Induced by Thymidine Treatment

The cultured cells *in vitro* were a mixture of cells in all phases. By collecting the cells at indicated times after seeding, we found that the percentage of all phases remained relatively constant and the cells in G1, S and G2/M phases accounted for about 54.87, 36.22, and 8.90%, respectively (**Figure 1A**).

In order to collect synchronized cells, we screened a series of synchronization methods and employed thymidine treatment as a reversible blocking agent to induce cell synchronization. After treatment with 1 mM thymidine for 24 and 48 h, the distribution of cell phases showed a significant change in a time-dependent manner (**Figures 1B,C**). At 24 h, the cell proportion in G1 phase decreased and the cell proportion in G2/M phase reached nearly zero. The cells in S phase markedly increased to about 70%. At 48 h, the unique peak (i.e., S peak) appeared and the percentage of cells in S phase reached 100%. As an ideal synchronization method should not cause obvious apoptosis, we thus examined cell apoptosis after treatment with thymidine for 48 h. As shown in **Figure 1D**, the percentage of live cells at 48 h was about 98%, which was roughly the same as that at 0 h. Thus, treatment with thymidine for 48 h did not induce apoptosis, suggesting that thymidine treatment was a reasonable and reliable method for cell synchronization.

The Cells in G2, M and G1 Phases Were Collected After S Phase-Blocking Cells Were Released

To collect the cells in other phases, the S phase-blocking cells were released and then DNA contents were determined at different time points (0, 2, 4, 5, 6, 7, 8, 9, 10, and 12 h). As shown in **Figures 2A,B**, the distribution of cell phases at 2 h was the same as that at 0 h. However, the phase peaks dramatically altered 2 h later. The cells in G2/M phase robustly increased to 75% at 4 h, reached nearly the maximal level (∼80%) at 6–7 h. At 8 h, the percentage of G2/M phase slightly decreased. At 9 h, the cells in G2/M phase decreased dramatically and G1 peak suddenly rose,

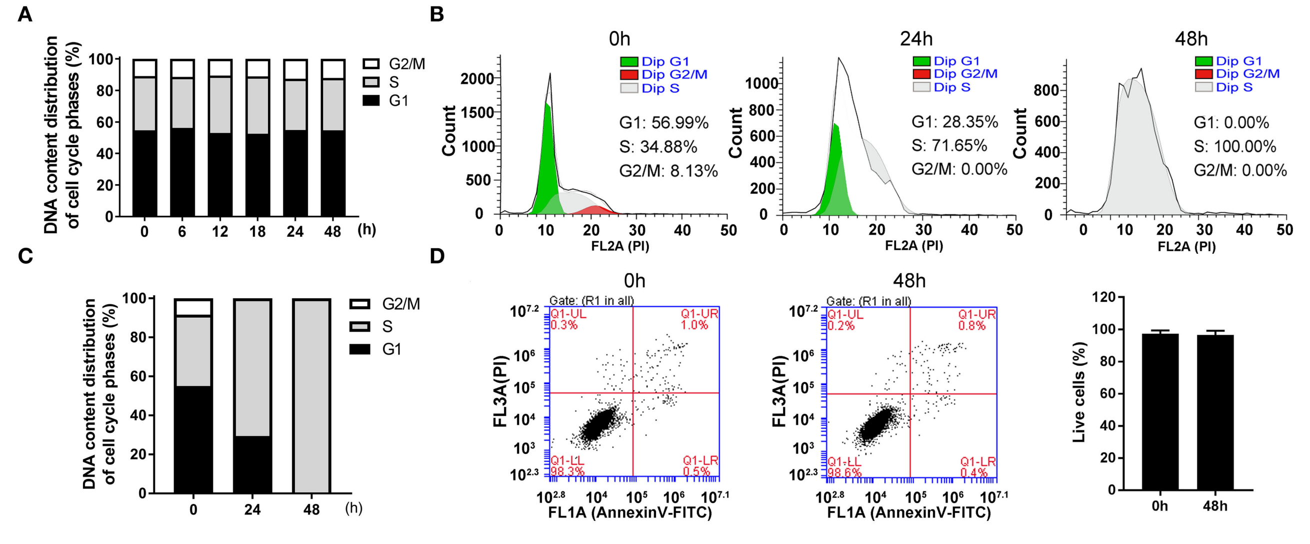

FIGURE 1 | The highly synchronized cells in S phase were induced by thymidine for 48 h. **(A)** The distributions of cell cycle at indicated time after seeding asynchronous HepG2 cells. **(B)** Flow cytometric analysis showed the changes of cell cycle distributions after treatment with 1 mM thymidine for 0, 24, and 48 h, and the percentages of cells in G1, S and G2/M phases were statistically shown in **(C)**. **(D)** After treatment with 1 mM thymidine for 48 h, AnnexinV-FITC/PI staining was employed to assess cell apoptosis, and the percentage of live cells was shown in the histogram. All data were denoted as the means ± SD; *N* = 3.

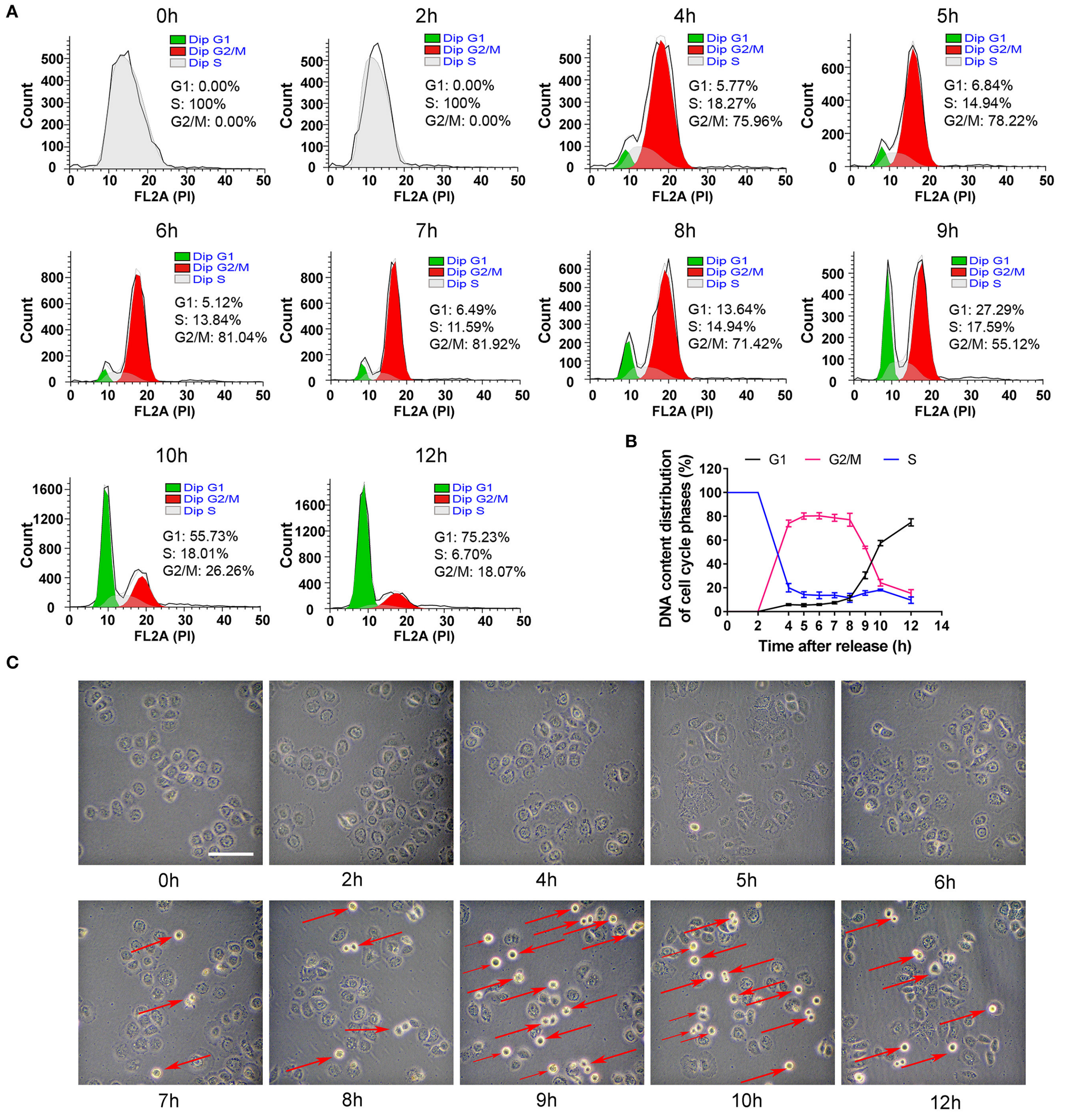

FIGURE 2 | The distribution changes of cells in G2, M and G1 phase after S phase-blocking cells were released. **(A)** The distributions of cell cycle phases were measured by flow cytometry at indicated time points after releasing from S phase, and the dynamic changes of G1, S and G2/M phases were shown in **(B)**. All of the values were denoted as the means ± SD; *N* = 3. **(C)** Representative photos showed the changes of general morphology of cells at indicated time points. The red arrow marking round cells represents those undergoing mitosis. The scale is 100 µm.

and the cells in G1 phase were about 30% in cell population. More than half of the cells were in G1 phase at 10 h and the synchronization rate of 75% was achieved at 12 h. Based on an analysis of the time-dependent changes of cell cycle, G2 phase of cell cycle was from 4 to 8 h, and M phase was taken about 2 h from 8 to 10 h, which was verified by morphology showing that the round cells (undergoing mitosis) substantially appeared at 9 h (**Figure 2C**). Additionally, cells entered G1 phase at 12 h.

CMs Formed in the Cells of G2 Phase

Based on the results presented above, we identified some more targeted time points (0, 2, 4, 5, 5.5, 6, 6.5, 7, 7.5, 8, 9, and 12 h), trying to observe CMs by transmission electron microscope. As shown in **Figure 3A**, CMs weren't observed at 0 h and 2 h. However, different sizes of CMs were observed from 4 to 8 h except 7 h (i.e., in G2 phase). At 9 and 12 h, CMs were in absence. In conclusion, CMs formed in G2 phase of cell cycle, and they were more likely to be observed in cells at 5 and 8 h, which showed a bimodal distribution (**Figure 3B**).

The Formation of CMs Was Positively Correlated With ROS Level

Because recent studies show that CMs correlate with cellular antioxidant activity, we measured the levels of intracellular ROS and mtROS. As shown in **Figures 4A,B**, intracellular ROS level showed a dynamic change with bimodal distribution and significantly increased at 5–5.5 h and 7.5–8 h. Then, we conducted a Pearson' correlation analysis to identify the relationship between CMs formation and intracellular ROS level, and found a positive correlation ($r = 0.7263$, $p < 0.05$, **Figure 4C**). Similarly, mtROS level rose at 5 and 7.5 h (**Figures 5A,B**), demonstrating a positive correlation with CMs formation (**Figure 5C**).

The Presence of CMs Had a Positive Correlation With ATP Level

Because of the relationship of CMs with mtROS and their potential association with mitochondrial function, ATP levels were detected to assess the mitochondrial function at indicated time. According to **Figure 6A**, the ATP levels significantly increased within the range from 4 to 8 h, reaching the peak levels at 5 and 8 h. Moreover, Pearson's correlation analysis showed a positive correlation between CMs formation and ATP level ($r = 0.8999$, $p < 0.001$, **Figure 6B**).

DISCUSSION

Although CMs are found in many cell types, there still lacks a comprehensive understanding of their biological role. The role of CMs in cell cycle has been of interest since the discovery of CMs in amoeba cells during mitosis in 1965. However, there seems to be no evidence for the existence of CMs in mammalian cell cycle. This study proves that CMs exist in the mammalian (more specifically in human) cell cycle and only in G2 phase, and that CMs are associated with mitochondria-derived ROS. It is thus suggested that CMs, as a structural antioxidant defense system, may play an important role in cell cycle.

Generally, proliferating cells go through four phases, G1, S, G2, and M, among which G2/M phase takes the least time (Mercadante et al., 2020). Therefore, the proportion of G2/M cells is the lowest, for example, only 8.9% in HepG2 cells (**Figure 1A**). Obviously, the observation of events in G2/M phase requires cell synchronization, a technique of driving cells into one phase by certain drugs or other methods (Banfalvi, 2017). In this study, we used thymidine treatment as a synchronization method, which is widely used in cell cycle studies (Banfalvi, 2017; Booy et al., 2017). The ideal synchronization cannot cause damage to cells, and the cells can continue to complete mitosis after the synchronization treatment was removed. The synchronization method employed in this study was suitable, as it did not cause apoptosis or abnormal cell division (**Figures 1D**, **2C**). It was due to the application of cell synchronization that in this study CMs were observed during G2 phase of the mammalian cell cycle. Compared with the CMs discovered in amoeba cells in G2 phase by Daniels et al. (1965), the CMs discovered in this study seem to have a similar structure (parallel, wavy or zig-zag configuration) and also appear in G2 phase, suggesting that CMs may be conservative in cell cycle. Compared with the method to roughly determine cell phase by cell morphological observation applied by Daniels et al. (1965), the synchronization method in this study can provide more details about CMs, such as the higher possibility of CMs to appear in the early and late G2 phase. Therefore, cell synchronization method was needed in the study of CMs in cell cycle.

It is well-known that ROS have both beneficial and deleterious effects, and "eustress" is employed to describe physiological stress (Sies, 2017; Antonioni et al., 2020; Sies and Jones, 2020). Obviously, the increase in ROS level in G2 phase of cell cycle belongs to eustress. However, the mechanism by which the high level of ROS does not cause oxidative damage remains unclear. This study found that the occurrence of CMs in G2 phase was closely related to the increased ROS, suggesting that CMs may be involved in cell cycle as an antioxidant. In fact, oxidant treatment has been reported to induce CMs formation (Sankhagowit et al., 2016). Although there is no report on the antioxidant effects of CMs in mammals, Deng et al. found that starvation-induced CMs in the amoeba *Chaos* protected RNAs and the gene expression regulatory system from oxidative damage caused by fasting, suggesting that CMs may play a protective role as an antioxidant and further promote cell survival under starvation-induced stress (Deng and Almsherqi, 2015; Deng et al., 2017; Chong et al., 2018). CMs are considered as an antioxidant defense system in organisms because of an abundance of plasmalogens with antioxidant properties in CMs (Deng and Almsherqi, 2015; Luoma et al., 2015). Plasmalogens are kinds of glycerophospholipids containing ether bonds, which are widely distributed in mammalian tissues, especially in heart, brain and muscle tissues (Paul et al., 2019). It is reported that plasmalogens can play a protective role against oxidative damage due to the special molecular composition and spatial conformation, and the supplementation of plasmalogens has a potential treatment effect on cardiometabolic and neurodegenerative diseases, such as Alzheimer's disease and Parkinson's disease (Luoma et al., 2015; Zhou et al., 2020). Hence, there is a high possibility that the appearance of CMs in G2 phase of cell cycle provides a shelter for RNAs which is critical to G2/M transition and mitosis, in case of attack by elevated ROS.

Mitochondrion is an energy factory of cells. When it produces ATP, some electrons in the electron transport chain of mitochondria inevitably leak out to produce mtROS (Figueira et al., 2013). Although the source of intracellular ROS includes but is not limited to mitochondria, peroxidase and

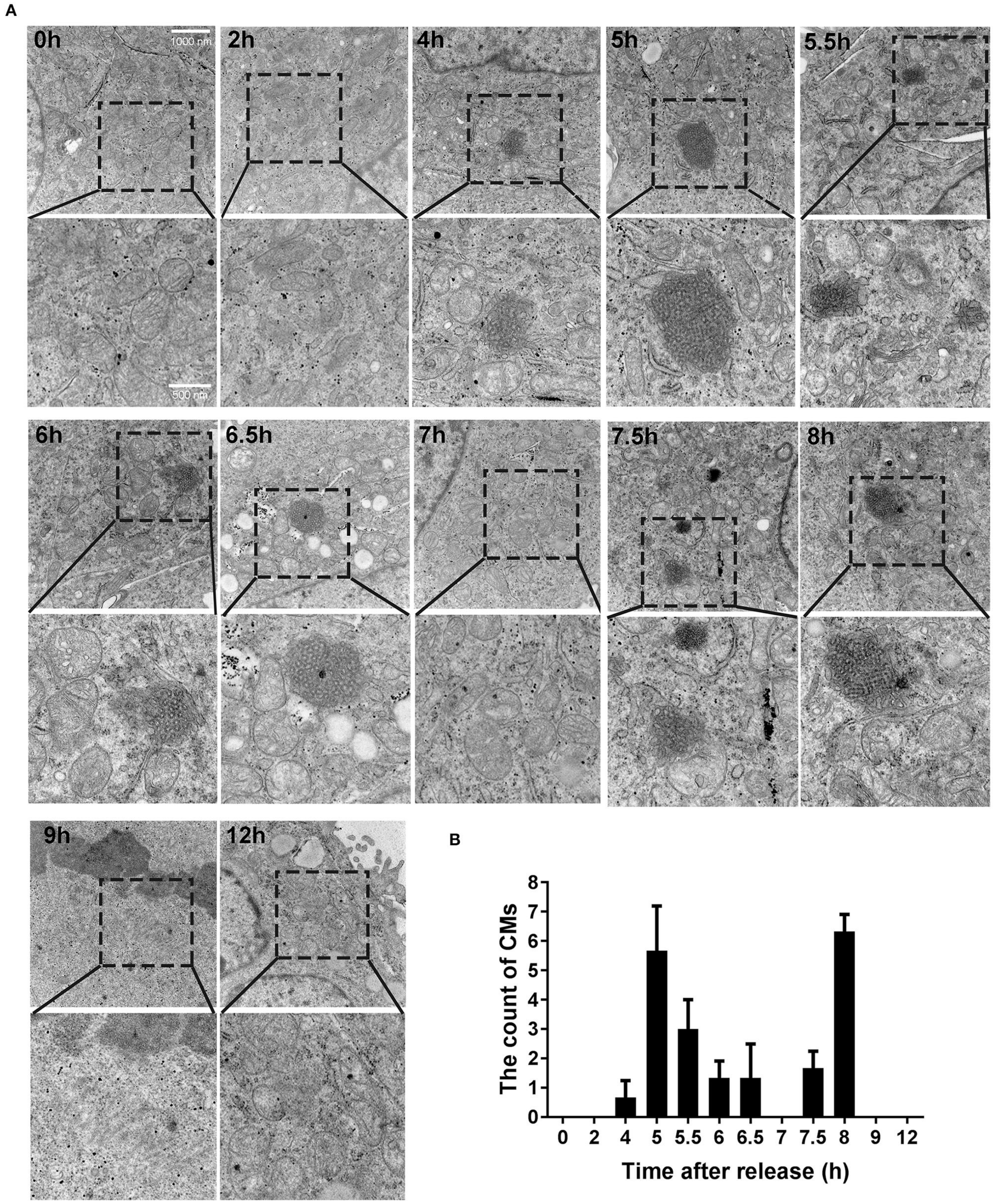

FIGURE 3 | CMs appeared in G2 phase of cell cycle. **(A)** Ultrastructural observations of cells at indicated time points after releasing from S phase. Representative images (20500X magnification) by transmission electron microscope were shown and the enlarged images in the rectangular area were placed below, respectively. **(B)** Statistics of CMs in every 100 cells at indicated time points. All values were denoted as the means ± SD; *N* = 3.

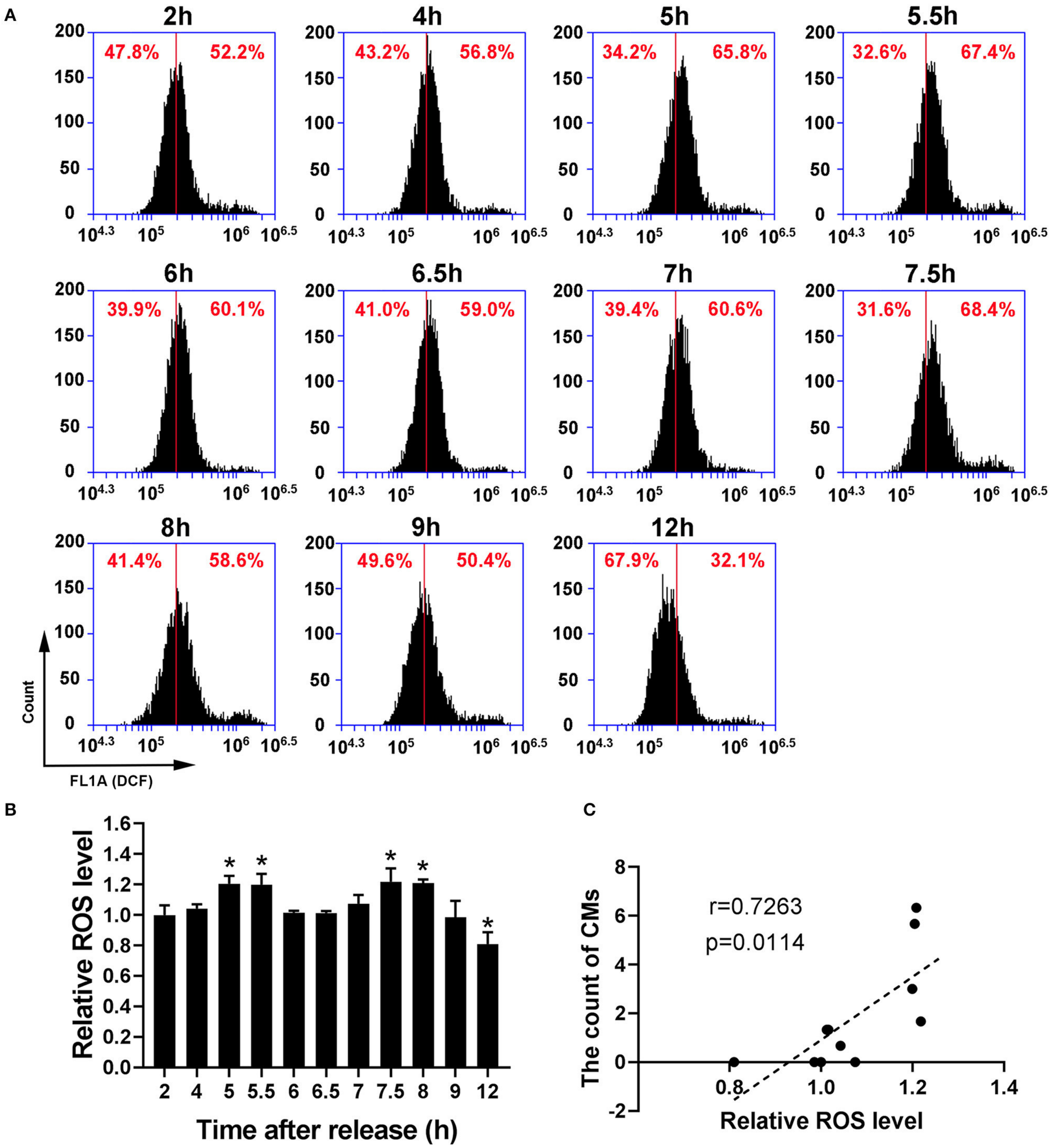

FIGURE 4 | The occurrence of CMs in G2 phase was correlated with ROS level. **(A)** Representative charts showing the change of ROS peaks after releasing from S phase which were detected by flow cytometry. The middle line was as a reference. **(B)** The histogram represented the change of ROS levels at indicated time points by analysis of fluorescence intensity. All values were denoted as the means ± SD; $N = 3$. $^*P \leq 0.05$, compared to the 2 h group. **(C)** The correlation between the average count of CMs and relative ROS level was shown by Pearson's correlation analysis.

NADPH oxidase complex under certain pathological condition, mitochondria are considered to be the most important ROS source in mammalian cells (Mailloux, 2020; Mari et al., 2020). MnSOD located in mitochondria is an important antioxidant enzyme. The methylation-dependent conformational change of MnSOD can gradually reduce its activity from G1 phase to G2/M

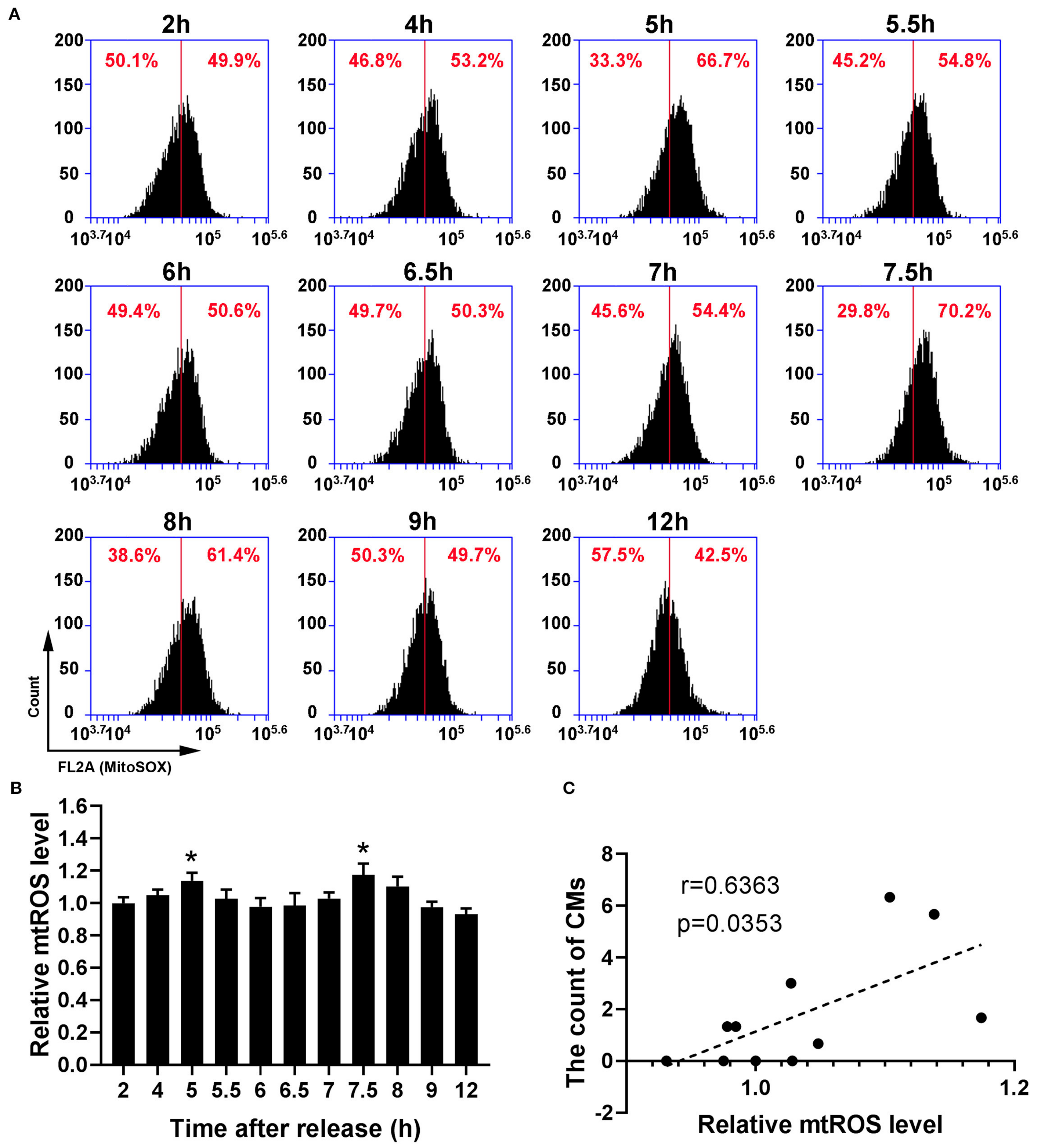

FIGURE 5 | The presence of CMs in G2 phase was correlated with mtROS level. **(A)** Representative charts showing the shift of mtROS peaks after releasing from S phase which were detected by flow cytometry, and the middle line was as a reference. **(B)** The change of mtROS levels at indicated time points was shown by analysis of fluorescence intensity. All data were expressed as the means ± SD; $N = 3$. $^*P \leq 0.05$, compared to the 2 h group. **(C)** The correlation between the average count of CMs and relative mtROS level was shown by Pearson's correlation analysis.

phase, resulting in the increase in superoxide anion content in G2/M phase, which may be an important reason for the rise of ROS in G2 phase (Sarsour et al., 2012). This study found that mtROS (by employing mitochondria-targeted probe MitoSOX) and ATP levels increased in G2 phase, showing a similar trend as ROS. Moreover, the increase in mtROS level is correlated with the

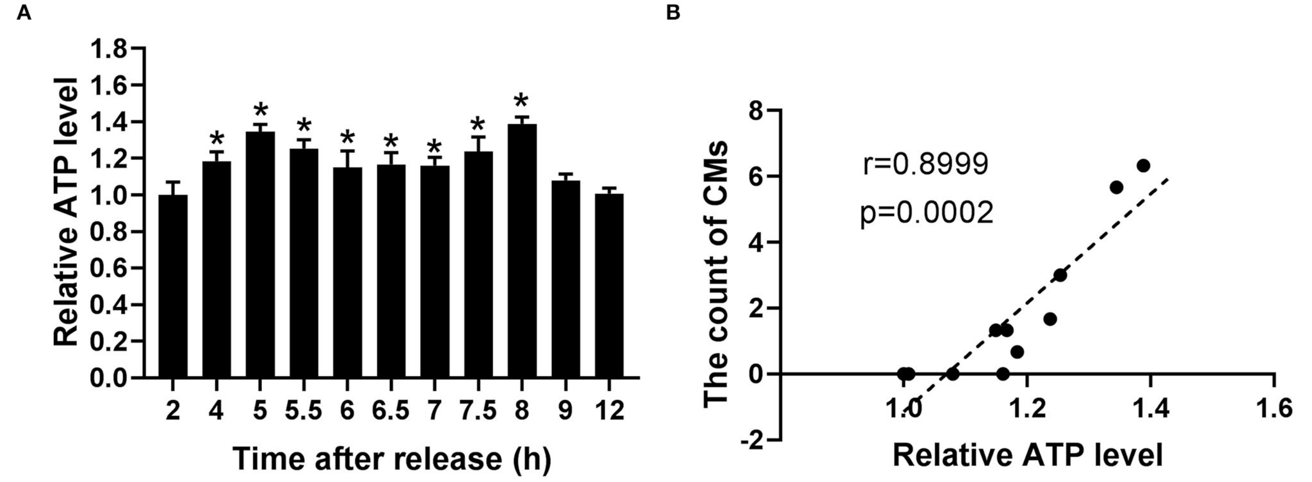

FIGURE 6 | The occurrence of CMs in G2 phase was correlated with ATP level. **(A)** Histograms represented the change of ATP level at indicated time points after release. All of the values were denoted as the means ± SD; $N = 3$. $^*P \leq 0.05$, compared to the 2 h group. **(B)** Pearson's correlation analysis showed the correlation between the average count of CMs and relative ATP level.

emergence of CMs, suggesting that the enhanced mitochondrial function (providing energy for mitosis) in G2 phase may lead to the increase in ROS level and the subsequent CMs formation. Accumulating evidence suggests that mitochondrial function has a dynamic change in cell cycle (Owusu-Ansah et al., 2008; Horbay and Bilyy, 2016; Mascanzoni et al., 2019), and ATP production is much more dependent on mitochondrial respiration in G2/M phase of cell cycle (Bao et al., 2013). This may be due to cell cycle machinery cyclin B1/Cdk1, which localized to the matrix of mitochondria and phosphorylated a cluster of mitochondrial proteins, and eventually resulted in the enhanced mitochondrial respiration and ATP generation in G2 phase (Wang et al., 2014).

Taken together, this study provides clues and methods for further research on the role of CMs in cell cycle progression. Future research is suggested to focus on the molecular regulatory mechanisms underlying the formation and depolymerization of CMs, a more detailed identification of the role of CMs in cell cycle, and their relationship with tumor. The elucidation of these issues will provide us with a more in-depth insight into the role of biomembranes.

DATA AVAILABILITY STATEMENT

The original contributions presented in the study are included in the article/supplementary material, further inquiries can be directed to the corresponding author/s.

AUTHOR CONTRIBUTIONS

HB and CH: conceptualization. DK, RL, JZ, and QZ: methodology. DK: investigation. DK and JL: writing. DK, HB, JL, and RL: funding acquisition. WL and CH: supervision. All authors contributed to the article and approved the submitted version.

FUNDING

This work was funded by the National Natural Sciences Foundation of China under Grant Numbers 81573126, 31200635, 31900892, Natural Science Basic Research Program of Shaanxi under Grant Number 2019JM-130, Military Medical Science and Technology Cultivation Project under Grant number 15QNP064, and Open Project of the Ministry of Education Key Lab of Hazard Assessment and Control in Special Operational Environment.

ACKNOWLEDGMENTS

We thank Ms. Fan Wang for her professional proofreading.

REFERENCES

Almsherqi, Z., Margadant, F., Deng, Y. (2012). A look through 'lens' cubic mitochondria. *Interface Focus* 2, 539–545. doi: 10.1098/rsfs.2011.0120

Almsherqi, Z. A., Landh, T., Kohlwein, S. D., Deng, Y. (2009). Chapter 6: cubic membranes the missing dimension of cell membrane organization. *Int. Rev. Cell Mol. Biol.* 274, 275–342. doi: 10.1016/S1937-6448(08)02006-6

Antonioni, A., Dimauro, I., Fantini, C., Barone, R., Macaluso, F., Di Felice, V., et al. (2020). alphaB-crystallin response to a pro-oxidant non-cytotoxic environment in murine cardiac cells: An "*in vitro*" and "*in vivo*" study. *Free Radic. Biol. Med.* 152, 301–312. doi: 10.1016/j.freeradbiomed.2020.03.013

Banfalvi, G. (2017). Overview of cell synchronization. *Methods Mol. Biol.* 1524, 3–27. doi: 10.1007/978-1-4939-6603-5_1

Bao, Y., Mukai, K., Hishiki, T., Kubo, A., Ohmura, M., Sugiura, Y., et al. (2013). Energy management by enhanced glycolysis in G1-phase in human colon cancer cells *in vitro* and *in vivo*. *Mol Cancer Res*. 11, 973–985. doi: 10.1158/1541-7786.MCR-12-0669-T

Booy, E. P., McRae, E. K., Koul, A., Lin, F., and McKenna, S. A. (2017). The long non-coding RNA BC200 (BCYRN1) is critical for cancer cell survival and proliferation. *Mol. Cancer* 16:109. doi: 10.1186/s12943-017-0679-7

Chong, K., Almsherqi, Z. A., Shen, H. M., and Deng, Y. (2018). Cubic membrane formation supports cell survival of amoeba Chaos under starvation-induced stress. *Protoplasma* 255, 517–25. doi: 10.1007/s00709-017-1169-x

Daniels, E. W., Breyer, E., and (1965). Differences in mitochondrial fine structure during mitosis in amoebae. *J. Protozool*. 12, 417–422. doi: 10.1111/j.1550-7408.1965.tb03235.x

Deng, Y., Almsherqi, Z. A. (2015). Evolution of cubic membranes as antioxidant defence system. *Interface Focus* 5:20150012. doi: 10.1098/rsfs.2015.0012

Deng, Y., Almsherqi, Z. A., Ng, M. M., Kohlwein, S. D. (2010). Do viruses subvert cholesterol homeostasis to induce host cubic membranes? *Trends Cell Biol*. 20, 371–379. doi: 10.1016/j.tcb.2010.04.001

Deng, Y., Kohlwein, S. D., and Mannella, C. A. (2002). Fasting induces cyanide-resistant respiration and oxidative stress in the amoeba Chaos carolinensis: implications for the cubic structural transition in mitochondrial membranes. *Protoplasma* 219, 160–167. doi: 10.1007/s007090200017

Deng, Y., Lee, E. L., Chong, K., and Almsherqi, Z. A. (2017). Evaluation of radical scavenging system in amoeba Chaos carolinense during nutrient deprivation. *Interface Focus* 7:20160113. doi: 10.1098/rsfs.2016.0113

Ding, Y., Kong, D., Zhou, T., Yang, N. D., Xin, C., Xu, J., et al. (2020). alpha-arbutin protects against parkinson's disease-associated mitochondrial dysfunction *in vitro* and *in vivo*. *Neuromolecul Med*. 22, 56–67. doi: 10.1007/s12017-019-08562-6

Figueira, T. R., Barros, M. H., Camargo, A. A., Castilho, R. F., Ferreira, J. C., Kowaltowski, A. J., et al. (2013). Mitochondria as a source of reactive oxygen and nitrogen species: from molecular mechanisms to human health. *Antioxid Redox Signal*. 18, 2029–74. doi: 10.1089/ars.2012.4729

Gao, F., Zhang, S. (2020). Loratadine alleviates advanced glycation end product-induced activation of NLRP3 inflammasome in human chondrocytes. *Drug Des. Devel Ther*. 14, 2899–2908. doi: 10.2147/DDDT.S243512

Horbay, R., and Bilyy, R. (2016). Mitochondrial dynamics during cell cycling. *Apoptosis* 21, 1327–1335. doi: 10.1007/s10495-016-1295-5

Kong, D., Ding, Y., Liu, J., Liu, R., Zhang, J., Zhou, Q., et al. (2019). Chlorogenic acid prevents paraquat-induced apoptosis via Sirt1-mediated regulation of redox and mitochondrial function. *Free Radic. Res*. 53, 680–693. doi: 10.1080/10715762.2019.1621308

Luoma, A. M., Kuo, F., Cakici, O., Crowther, M. N., Denninger, A. R., Avila, R. L., et al. (2015). Plasmalogen phospholipids protect internodal myelin from oxidative damage. *Free Radic Biol Med*. 84, 296–310. doi: 10.1016/j.freeradbiomed.2015.03.012

Mailloux, R. J. (2020). An update on mitochondrial reactive oxygen species production. *Antioxidants* 9:472. doi: 10.3390/antiox9060472

Mao, J., Tian, Y., Wang, C., Jiang, K., Li, R., Yao, Y., et al. (2019). CBX2 regulates proliferation and apoptosis via the phosphorylation of YAP in hepatocellular carcinoma. *J. Cancer* 10, 2706–2719. doi: 10.7150/jca.31845

Mari, M., de Gregorio, E., de Dios, C., Roca-Agujetas, V., Cucarull, B., Tutusaus, A., et al. (2020). Mitochondrial glutathione: recent insights and role in disease. *Antioxidants*. 9:909. doi: 10.3390/antiox9100909

Mascanzoni, F., Ayala, I., Colanzi, A. (2019). Organelle inheritance control of mitotic entry and progression: implications for tissue homeostasis and disease. *Front Cell Dev. Biol*. 7:133. doi: 10.3389/fcell.2019.00133

Mercadante, A. A., Dimri, M., and Mohiuddin, S. S. (2020). "Biochemistry, replication and transcription," in *StatPearls [Internet]*. Treasure Island, FL: StatPearls Publishing.

Owusu-Ansah, E., Yavari, A., Mandal, S., Banerjee, U. (2008). Distinct mitochondrial retrograde signals control the, G1-S cell cycle checkpoint. *Nat. Genet*. 40, 356–361. doi: 10.1038/ng.2007.50

Paillusson, F., Pennington, M. R., Kusumaatmaja, H. (2016). Phase separation on bicontinuous cubic membranes: symmetry breaking, reentrant, and domain faceting. *Phys. Rev. Lett*. 117:58101. doi: 10.1103/PhysRevLett.117.058101

Paul, S., Lancaster, G. I., Meikle, P. J. (2019). Plasmalogens: a potential therapeutic target for neurodegenerative and cardiometabolic disease. *Prog. Lipid Res*. 74, 186–195. doi: 10.1016/j.plipres.2019.04.003

Sankhagowit, S., Lee, E. Y., Wong, G. C., and Malmstadt, N. (2016). Oxidation of membrane curvature-regulating phosphatidylethanolamine lipid results in formation of bilayer and cubic structures. *Langmuir* 32, 2450–2457. doi: 10.1021/acs.langmuir.5b04332

Sarsour, E. H., Kalen, A. L., Xiao, Z., Veenstra, T. D., Chaudhuri, L., Venkataraman, S., et al. (2012). Manganese superoxide dismutase regulates a metabolic switch during the mammalian cell cycle. *Cancer Res*. 72, 3807–3816. doi: 10.1158/0008-5472.CAN-11-1063

Sies, H. (2017). Hydrogen peroxide as a central redox signaling molecule in physiological oxidative stress: oxidative eustress. *Redox Biol*. 11, 613–619. doi: 10.1016/j.redox.2016.12.035

Sies, H., and Jones, D. P. (2020). Reactive oxygen species (ROS) as pleiotropic physiological signalling agents. *Nat. Rev. Mol. Cell Biol*. 21, 363–383. doi: 10.1038/s41580-020-0230-3

Wang, Z., Fan, M., Candas, D., Zhang, T. Q., Qin, L., Eldridge, A., et al. (2014). Cyclin B1/Cdk1 coordinates mitochondrial respiration for cell-cycle G2/M progression. *Dev. Cell* 29, 217–232. doi: 10.1016/j.devcel.2014.03.012

Zhan, T., Lv, W., and Deng, Y. (2017). Multilayer gyroid cubic membrane organization in green alga Zygnema. *Protoplasma* 254, 1923–1930. doi: 10.1007/s00709-017-1083-2

Zhou, Y., Yu, N., Zhao, J., Xie, Z., Yang, Z., Tian, B. (2020). Advances in the biosynthetic pathways and application potential of plasmalogens in medicine. *Front Cell Dev Biol*. 8:765. doi: 10.3389/fcell.2020.00765

Conflict of Interest: The authors declare that the research was conducted in the absence of any commercial or financial relationships that could be construed as a potential conflict of interest.

ORIGINAL RESEARCH
published: 18 December 2020
doi: 10.3389/fphys.2020.592117

NACore Amyloid Formation in the Presence of Phospholipids

Jon Pallbo[1]*, Masayuki Imai[2], Luigi Gentile[3], Shin-ichi Takata[4], Ulf Olsson[1] and Emma Sparr[1]

[1] Division of Physical Chemistry, Department of Chemistry, Lund University, Lund, Sweden, [2] Department of Physics, Graduate School of Science, Tohoku University, Sendai, Japan, [3] Department of Chemistry, University of Bari Aldo Moro, Bari, Italy, [4] J-PARC Center, Japan Atomic Energy Agency, Tokai, Japan

Amyloids are implicated in many diseases, and disruption of lipid membrane structures is considered as one possible mechanism of pathology. In this paper we investigate interactions between an aggregating peptide and phospholipid membranes, focusing on the nanometer-scale structures of the aggregates formed, as well as on the effect on the aggregation process. As a model system, we use the small amyloid-forming peptide named NACore, which is a fragment of the central region of the protein α-synuclein that is associated with Parkinson's disease. We find that phospholipid vesicles readily associate with the amyloid fibril network in the form of highly distorted and trapped vesicles that also may wet the surface of the fibrils. This effect is most pronounced for model lipid systems containing only zwitterionic lipids. Fibrillation is found to be retarded by the presence of the vesicles. At the resolution of our measurements, which are based mainly on cryogenic transmission electron microscopy (cryo-TEM), X-ray scattering, and circular dichroism (CD) spectroscopy, we find that the resulting aggregates can be well fitted as linear combinations of peptide fibrils and phospholipid bilayers. There are no detectable effects on the cross-β packing of the peptide molecules in the fibrils, or on the thickness of the phospholipid bilayers. This suggests that while the peptide fibrils and lipid bilayers readily co-assemble on large length-scales, most of them still retain their separate structural identities on molecular length-scales. Comparison between this relatively simple model system and other amyloid systems might help distinguish aspects of amyloid-lipid interactions that are generic from aspects that are more protein specific. Finally, we briefly consider possible implications of the obtained results for *in-vivo* amyloid toxicity.

Keywords: amyloids, peptides, NACore, fibrillation, aggregation, lipids, vesicles, bilayers

Edited by:
George Attard,
University of Southampton,
United Kingdom

Reviewed by:
Richard M. Epand,
McMaster University, Canada
Jaydeep Kumar Basu,
Indian Institute of Science (IISc), India

***Correspondence:**
Jon Pallbo
jon.pallbo_arvidsson@fkem1.lu.se

Specialty section:
This article was submitted to
Membrane Physiology
and Membrane Biophysics,
a section of the journal
Frontiers in Physiology

Received: 06 August 2020
Accepted: 02 December 2020
Published: 18 December 2020

Citation:
Pallbo J, Imai M, Gentile L,
Takata S, Olsson U and Sparr E
(2020) NACore Amyloid Formation
in the Presence of Phospholipids.
Front. Physiol. 11:592117.
doi: 10.3389/fphys.2020.592117

INTRODUCTION

Aberrant protein folding and aggregation are closely related to many diseases. Amyloids are one type of aberrant protein aggregates made of stacked β-sheets that form highly ordered fibrillar structures. Amyloids are associated especially with diseases that cause neural degeneration such as Alzheimer's and Parkinson's diseases (Chiti and Dobson, 2017; Eisenberg and Sawaya, 2017). In addition to proteins, a large variety of other biomolecules exist in the biological environment. One type is lipids, such as phospholipids, which make up the basic structures of cellular membranes in the form of bilayers. Lipids constitute roughly 40% of the non-protein dry mass of mammalian cells (Alberts et al., 2008), and amyloid formation thus occurs in a lipid-rich environment. Lipids have been of interest in relation to amyloids because they have been found accumulated with the protein material in amyloid deposits in diseased tissues. Reports of lipids present in amyloid deposits can be found at least as far back as 1969 (Bonar et al., 1969). In that early study, X-ray scattering experiments suggested the presence of lipids in amyloid deposits isolated from diseased spleen tissue. Lipids have also been found together with amyloids in neural tissues, such as in the brains of people with Alzheimer's or Parkinson's disease (Gellermann et al., 2005; Kiskis et al., 2015; Kaya et al., 2017; Shahmoradian et al., 2019). Furthermore, *in vitro* studies have demonstrated co-localization and disruptive effects of amyloids on phospholipid bilayers (Janson et al., 1999; Butterfield and Lashuel, 2010; Zhang et al., 2014; Kollmer et al., 2016). It has also been shown that lipid membranes may strongly interfere with the aggregation process and affect the kinetics during amyloid formation (Gorbenko and Kinnunen, 2006; Galvagnion et al., 2015; Iyer and Claessens, 2019). For these and other reasons, the interplay between lipids and amyloid forming peptides and proteins is believed to potentially play a key role in the pathophysiology of amyloid associated diseases. This might be particularly significant in neurodegenerative disorders since the function of neural tissues is dependent on lipid structures in axons, dendrites, and synaptic vesicles.

In this report we have investigated amyloid formation by the amyloid model peptide NACore and how the formed aggregates are affected by the presence of phospholipids, from a structural perspective on nanometer length-scales. NACore is an eleven amino acid residue peptide from the so-called non-amyloid-β component (NAC) region of the Parkinson's disease associated protein α-synuclein (68-GAVVTGVTAVA-78) (Bodles et al., 2001; Rodriguez et al., 2015; Pallbo et al., 2019). This peptide has previously shown cytotoxic effects on cells *in vitro* (Bodles et al., 2001; Rodriguez et al., 2015). The short model peptide is suitable for studies of physicochemical aspects of amyloid formation and can further bring insights into the role of the amyloid-forming NACore segment in relation to the remaining segments of the full length protein. We have studied the effect of varying the lipid composition in terms of headgroup charge and acyl chain saturation. The structures of the aggregates were analyzed with cryogenic transmission electron microscopy (cryo-TEM), small and wide angle X-ray scattering (SAXS, WAXS), and small angle neutron scattering (SANS), as well as circular dichroism (CD) spectroscopy. One question we address is how intimate the interaction of lipids and amyloids are on the molecular level. In other words, to what extent there is formation of new peptide-lipid-mixed structures that are distinct from both pure peptide fibrils and pure lipid bilayers. We believe that the results obtained here, with the relatively simple model systems outlined above, give important clues about the underlying physico-chemical mechanisms of phospholipid-amyloid interactions. In the end, this might help us to better understand the role of lipids in the pathophysiology of amyloid associated diseases.

MATERIALS AND METHODS

NACore Peptide and Phospholipids

Lyophilized NACore peptide powder was purchased from Innovagen AB [GAVVTGVTAVA, 944 g/mol, trifluoroacetic acid (TFA) salt, >95% purity as specified by the supplier] and used as supplied. The concentrations specified in the report refer to the amount of lyophilized peptide powder used. Phospholipids were purchased from Avanti Polar Lipids Inc., United States in powder form and were used as supplied. The phospholipids used in the experiments were mixtures in various proportions of 1-palmitoyl-2-oleoyl-glycero-3-phosphocholine (POPC), 1-palmitoyl-2-oleoyl-sn-glycero-3-phospho-L-serine (POPS), 1,2-dimyristoyl-sn-glycero-3-phosphocholine (DMPC), and 1,2-dimyristoyl-sn-glycero-3-phospho-L-serine (DMPS).

Phospholipid Vesicle Preparation

The desired phospholipids were dissolved in a 9:1 mixture of chloroform and methanol (volume ratio) at a total lipid concentration of 10 mM. The required amount of solution was then dried into a lipid film in a glass vial under a stream of nitrogen gas, followed by further drying in vacuum overnight. A sodium phosphate solution (∼ pH 7) was then added to the film. A dispersion of small vesicles was obtained by vortexing followed by tip sonication (Sonics & Materials, Inc., United States, Vibra-Cell VCX 130). The sonication time was 10–15 min for POPC:POPS 8:2 and DMPC:DMPS 8:2, and 30 min for POPC in on-off cycles of 5–10 s, at an amplitude of 50–60%. Debris from the sonication tip was pelleted by centrifugation at 16 000 Relative Centrifugal Force (RCF) for 5 min, and the resulting supernatant was used as the final phospholipid vesicle dispersion for the experiments. For POPC:POPS 8:2 and DMPC:DMPS 8:2, the vesicle suspension appeared clear to the eye under ambient light, but for POPC alone some turbidity remained despite the longer duration of tip sonication (presumably due to lack of electrostatic repulsion between the bilayers).

Peptide Fibrillation Procedure

Lyophilized NACore peptide was dissolved at the desired concentration in 2 mM NaOH (pH 11.3). Fibrillation was induced by mixing the dissolved peptide with a sodium phosphate solution, which lowered the pH to about 7 and yielded a final sample with either 0.1 mg/ml peptide + 1 mM NaH_2PO_4 + 1 mM Na_2HPO_4 (for the cryo-TEM experiments), or 0.3 mg/ml peptide + 2 mM NaH_2PO_4 + 2 mM Na_2HPO_4 (for the X-ray scattering and CD measurements). The concentrations used differed because the different techniques required different amounts of material (and the experiments were initially carried out as parts of different data sets). When fibrillation was performed together with phospholipid, the vesicle dispersion was added together with the sodium phosphate solution as the pH was lowered. Approximately equimolar amounts of peptide and phospholipid molecules were present in the samples.

Cryogenic Transmission Electron Microscopy (cryo-TEM)

Vesicles composed of either POPC:POPS 8:2 or POPC only were prepared, and peptide fibrillation was induced by a change in pH. After 4 h of quiescent incubation at room temperature, a small part of the sample was taken out, vitrified, and observed with a JEM-2200FS (JEOL) transmission electron microscope with an accelerating voltage of 200 kV and an in-column energy filter for zero-loss imaging (Omega Filters, India), as has previously been described (Pallbo et al., 2019). Images were recorded digitally using a TVIPS TemCam-F416 digital camera.

Small and Wide Angle X-Ray Scattering (SAXS and WAXS)

The peptide alone and peptide-lipid samples were prepared as described above and then incubated quiescently over night at room temperature. The aggregated material was collected as a pellet by centrifugation for 3 h at 10 000 RCF at room temperature (resulting in a roughly 10 times increase in concentration of aggregated material, as estimated from the volume of the pellet). Part of the collected material was then placed in a glass capillary tube, and X-ray scattering was performed using a Ganesha 300XL system (SAXSLab) with a Cu ULD SL X-ray source (Xenocs) and a 2D PILATUS 300k detector (Dectris). The measurements were done in vacuum at room temperature unless stated otherwise, and a total of three detector distances were used (corresponding to different q-value ranges, from about $3{\cdot}10^{-2}$ to 25 nm^{-1}), with a total of 6 h of exposure time for each sample. Phospholipid vesicles incubated alone without the peptide were also investigated in a similar way, as well as water which was used as background. The scattering from the water was subtracted from the scattering curves of the samples before plotting. Fittings were performed in MATLAB by implementing standard form factor scattering models from SasView[1], see **Supplementary Table 1** for details. Polydispersity in the models was simulated by drawing 10^4 values of the polydisperse parameter from a lognormal probability distribution, calculating the scattering profile for each value, and averaging of all the resulting curves.

Circular Dichroism (CD) Measurements

Samples were prepared in the same way as for X-ray scattering, except that they were not concentrated by centrifugation. At different time points of the incubation, 300 μl of each sample was transferred a 1 mm path length quartz cuvette (Hellma, Germany, 110-QS), followed by measurement of the CD spectrum using a JASCO J-715 instrument at room temperature (two accumulations, scan rate of 20 nm/min, 2 s response time, and 2 nm band width, resulting in a HT voltage below 600 V at all wavelengths). The CD spectrum from the same cuvette filled with water was used as a reference and subtracted from the sample spectra before plotting.

RESULTS

We have previously reported that pH can be used to control the fibrillation of NACore (Pallbo et al., 2019). At high pH, the peptide has a net negative charge and a higher aqueous solubility than at lower pH closer to its isoelectric point (∼ pH 5.5). Fibrillation of dissolved NACore can thereby be induced by lowering the pH toward the isoelectric point. For the present experiments, we prepared the initial peptide solution at pH 11.3 (2 mM NaOH) and induced fibrillation by the addition of NaH_2PO_4 solutions to a final pH of about 7. We performed fibrillation both in the absence and presence of phospholipids. The phospholipids were either a mixture of 80 mol% POPC and 20 mol% POPS (POPC:POPS 8:2), POPC alone, or a mixture of 80 mol% DMPC and 20 mol% DMPS (DMPC:DMPS 8:2). In all samples that contained both peptide and phospholipids the amounts of peptide and lipids were approximately equimolar.

Cryo-TEM Reveals Affinity Between NACore Fibrils and Phospholipid Vesicles

Cryogenic transmission electron microscopy shows that fibrils are formed both in the absence and presence of phospholipid vesicles (**Figures 1**, **2** and **Supplementary Figures 1–3**). In the samples containing peptide and phospholipids, highly distorted vesicles can be observed interspersed among the fibrils (**Figure 1** and **Supplementary Figures 1**, **2**). In the case of POPC:POPS, many vesicles have highly distorted shapes as they are trapped in the fibril network, mainly as a consequence of the vesicle diameter being larger than the network mesh size. In the case of pure POPC, we observe lipid structures that strongly deviate from the originally sonicated vesicle dispersion. Many vesicles are much larger than in the original dispersion, presumably as a result of fusion events. Moreover, the shapes of these large vesicles deviate strongly from spheres and they appear to wet the fibril surfaces, indicative of an attractive fibril-bilayer interaction. It is also noted that substantially fewer fibrils are observed in the samples where NACore was aggregated in the presence of POPC vesicles (**Figure 1B**), compared to the sample with POPC:POPS vesicles (**Figure 1A**). While the distorted vesicles in both types of samples are associated with the fibrils, the bilayers of these distorted vesicles can still be rather clearly distinguished from the fibrils. In the samples containing POPC vesicles, some of them are multilamellar (**Figure 1B**) which is probably due to lack of electrostatic repulsion between the bilayers due to the zwitterionic nature of the glycero-3-phosphocholine (PC) head group (Scott et al., 2019). Multilamellar vesicles were observed also for POPC without NACore present (**Supplementary Figure 4**). In summary, the cryo-TEM images clearly show fibril-bilayer co-association, but they do not provide definite information about whether phospholipids are incorporated into the cross-β structure of the fibrils or if they are only adsorbed at the fibril surface.

---

[1] http://www.sasview.org/

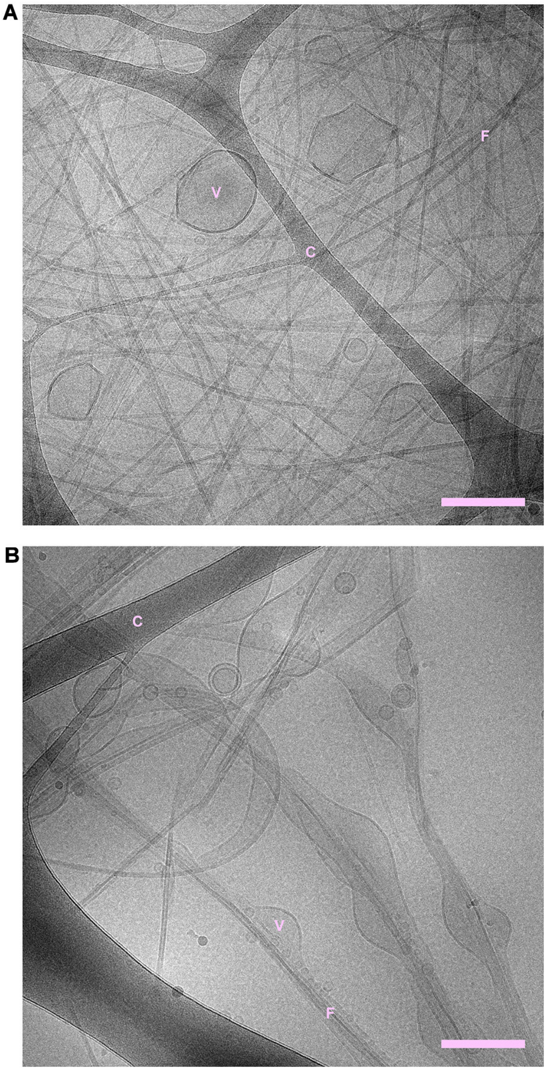

FIGURE 1 | (A) NACore fibrillated in the presence of POPC:POPS vesicles. **(B)** NACore fibrillated in the presence of POPC vesicles. In both cases, highly distorted and trapped vesicles can be observed among the fibrils. There are more bilayer structures relative to the number of visible fibrils in the case of NACore with POPC than with POPC:POPS. "C" denotes the cryo-TEM carbon grid, "F" denotes fibrils, and "V" denotes distorted vesicles. Scale bars show 200 nm.

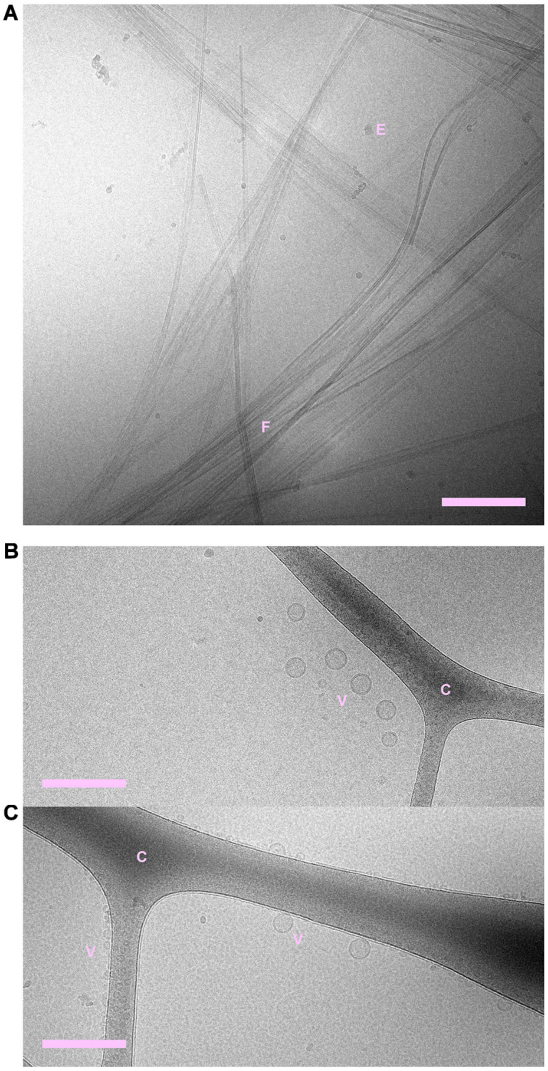

FIGURE 2 | (A) NACore fibrillated in the absence of phospholipids. **(B)** POPC:POPS vesicles in the absence of NACore. **(C)** POPC vesicles in the absence of NACore. POPC vesicles were mainly found associated with the cryo-TEM carbon grid, rather than free in the solution. "C" denotes the cryo-TEM carbon grid, "F" denotes fibrils, "V" denotes vesicles, and "E" denotes suspected ethane contamination (not part of the sample itself). Scale bars show 200 nm.

X-Ray Scattering of NACore Fibrillated in the Presence of POPC:POPS and POPC Vesicles

In order to gain further insight into the structure of the fibrils formed when NACore is incubated in the presence of phospholipid vesicles at smaller length scales, we performed small and wide angle X-ray scattering experiments (SAXS and WAXS). Below, we first describe the X-ray scattering data for samples composed either of peptide fibrils or lipid vesicles by themselves, and thereafter we analyze the aggregates formed when peptide has been left to aggregate in the presence of vesicles with different composition. **Figure 3** shows WAXS and combined SAXS/WAXS data for aggregates formed by peptide alone. Here, the scattered intensity I(q) is plotted against the scattering vector q. These X-ray scattering patterns are in close agreement with previously reported data for NACore peptide fibrils formed under similar conditions, showing a characteristic power law scattering pattern at low q-values, and several Bragg peaks at higher q-values (Pallbo et al., 2019). The two main peaks occurring at $q = 13.6\ \text{nm}^{-1}$ and $7.6\ \text{nm}^{-1}$, are associated with the β-strand separation of 0.46 nm and the β-sheet lamination distance of 0.82 nm (PDB ID: 4RIL) (Rodriguez et al., 2015). The SAXS pattern shows a power law dependence of about −2.3 at low q-values, with a cross-over to

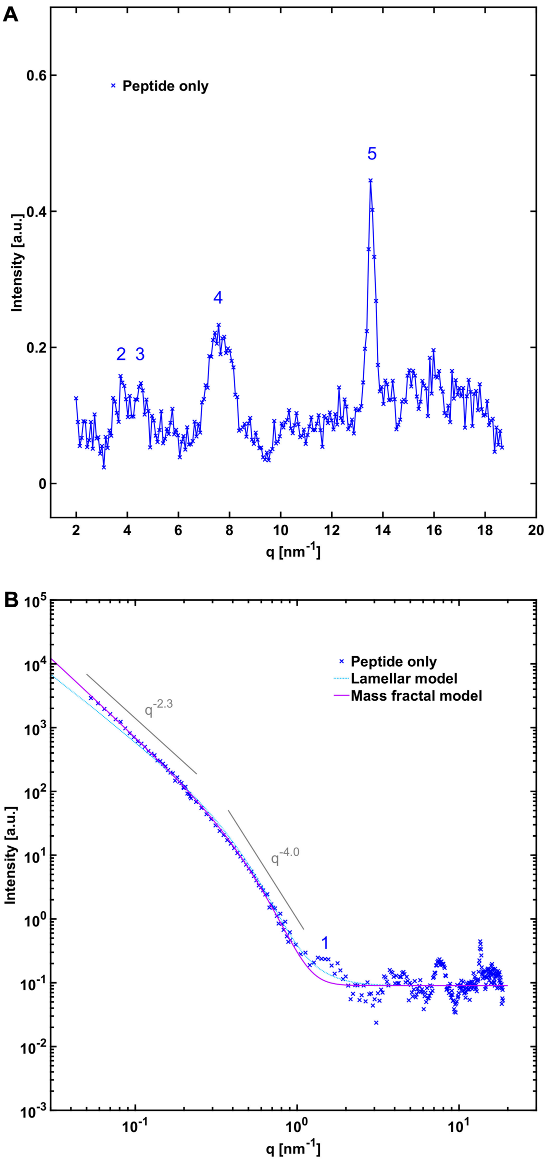

FIGURE 3 | (A) WAXS and **(B)** SAXS profile of NACore fibrillated in the absence of phospholipids. The numbers denote crystal diffraction peaks corresponding to miller indices of 1 = [2, 0, 0], 2 = [2, 0, −1], 3 = [2, 0, 1], 4 = ([2, 0, −2], [0, 0, 2], [2, 0, 2]), and 5 = ([1, 1, −1], [1, 1, 1]) in the NACore crystal structure reported by Rodriguez et al. (PDB ID: 4RIL) (Rodriguez et al., 2015; Pallbo et al., 2019; see also **Supplementary Figure 5**). In **(B)** two theoretical fits are shown. One is an infinite lamellar model with a polydisperse average layer thickness of 6.5 nm (see **Supplementary Table 1** for details). The other one is a mass fractal model with polydisperse average building block radius of 4.3 nm (see **Supplementary Table 1**).

a power law of −4 (Porod regime) occurring around a *q*-value of 0.3 nm^{-1} (**Figure 3B**). The latter being consistent with an average cross section radius of the fibrils of circa 4 nm, which in turn is consistent with the cryo-TEM images. For long thin fibrils we would expect to see $I(q) \sim q^{-1}$ at lower *q*-values (Lindner and Zemb, 2002). The fact that we see a much steeper decay, $q^{-2.3}$, indicates attractive fibril–fibril interactions resulting in an inhomogeneous distribution of fibrils forming clusters. The value 2.3 can be interpreted as a mass fractal dimension of the clusters (Solomon and Spicer, 2010).

The average X-ray scattering length densities (electron densities) of the phospholipid bilayers investigated are close to that of water (approximately $9.8 \cdot 10^{-6}$ Å^{-2} and $9.5 \cdot 10^{-6}$ Å^{-2} for the bilayers and water, respectively), which means that the vesicles scatter very little at lower *q*-values. Consequently, the size and shape of the vesicles cannot be easily determined using SAXS. However, because of the relatively strong difference in scattering length density between the phospholipid headgroups and the acyl chains ($13.5 \cdot 10^{-6}$ Å^{-2} and $8.0 \cdot 10^{-6}$ Å^{-2}), there is a significant electron density variation and hence contrast in the direction normal to the bilayer. This allows some features of the bilayers to be determined, such as the thickness and overall internal structure. We can see from the scattering pattern of POPC:POPS vesicles that it fits well with the scattering pattern of a single bilayer with a headgroup-to-headgroup distance of about 3.8 nm (**Figure 4B**), consistent with expectations from the literature (Kucerka et al., 2011; Eicher et al., 2017; Scott et al., 2019). In the case of vesicles composed of POPC only, we can fit them with the scattering of bilayers with the same headgroup-to-headgroup thickness as for POPC:POPS (**Figure 5B**).

A comparison of the X-ray scattering pattern between peptide fibrillated in the absence and presence of phospholipid vesicles provides information about how the structures are affected at nanometer length-scales. We are here interested in knowing whether the phospholipids from the vesicles are incorporated into the cross-β structure of the fibrils, or whether vesicles are just associated with the exterior fibril surfaces as, for example, adsorbed vesicles or deposited lipid bilayers. One way to obtain such information is to look at the positions of the Bragg peaks at high *q*-values, which arise from the crystal-like cross-β molecular packing of the peptide molecules within the fibrils, and how they are affected by the presence of phospholipids. To probe structural changes on slightly longer length-scales, we investigated whether the X-ray scattering pattern can be fitted as a linear combination of peptide fibrils alone and phospholipid bilayers alone, which should be the case if most of the phospholipid bilayers and fibrils exist as independent structures. If a linear combination of the individual components agrees poorly with the data, it would be an indication of new structures formed, or of substantial inter-species interactions.

From the X-ray scattering experiments we find that the positions of the two major cross-β associated Bragg peaks at 7.6 nm^{-1} and 13.6 nm^{-1} (corresponding to 0.82 nm and 0.46 nm periodicities in real space) are not markedly affected by the presence of POPC:POPS bilayers (**Figure 4A**). However, we note that the intensity of the peaks is substantially lower in the co-incubated sample, relative to peptide alone. This is consistent with a reduced amount of peptide fibrils in the presence of lipids. This will be discussed in more detail below. In the case of NACore together with vesicles composed of POPC only, the position of the peak at 13.6 nm^{-1} was unchanged, whereas the signal was too weak to resolve the peak at 7.6 nm^{-1} (**Figure 5A**). Furthermore, the X-ray scattering pattern of co-incubated peptide and POPC:POPS or POPC vesicles can be very

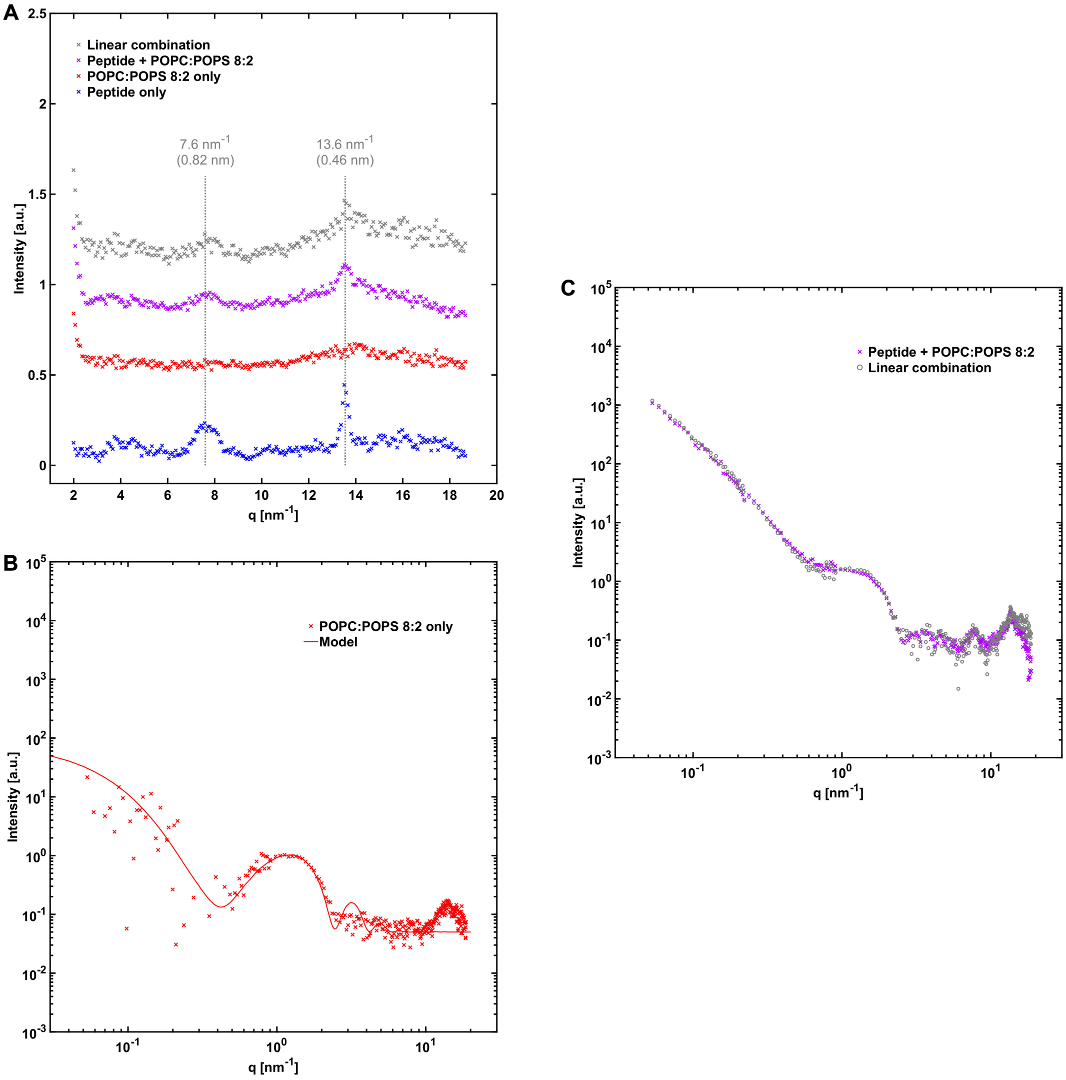

FIGURE 4 | NACore together with POPC:POPS. **(A)** WAXS profile of NACore with POPC:POPS, POPC:POPS by itself, and the peptide by itself. The position of the two main diffraction peaks are indicated with dashed lines. For comparison, the gray curve shows the expected scattering for the same linear combination as in **(C)**. **(B)** SAXS profile of 2.4 mM POPC:POPS without the peptide, together with a simple unilamellar vesicle model fit (see **Supplementary Table 1**). **(C)** SAXS profile of co-incubated NACore and POPC:POPS, together with a linear combination of scattering from peptide fibrils (**Figure 3B**) and POPC:POPS vesicles **(B)** (0.40·fibril + 1.55·vesicles).

well fitted as a linear combination of the scattering pattern of the two separate components (**Figures 4C**, **5C**). This suggests that the co-incubation with phospholipids does not considerably alter the bulk of the structure of the fibrils on nanometer length scales. It also indicates that the bulk of the POPC:POPS and POPC bilayers are not considerably altered by the presence of the NACore peptide in terms of bilayer thickness and overall internal structure. However, these X-ray scattering experiments are not very sensitive to changes in features such as the size or shape of the vesicles. We finally conclude that most of the phospholipids that were present in the initial co-incubation suspensions were co-pelleted together with the fibrils in the centrifugation step, as judged by the bilayer contribution in the linear combinations used to fit the scattering data for the samples containing both peptide and lipid. This was the case both for NACore aggregated together with POPC:POPS vesicles and POPC vesicles (**Figures 4**, **5**). The vesicles alone are not pelleted by the centrifugation step when they are small and unilamellar. This observation thus gives further support to the conclusion based on the cryo-TEM experiments that vesicles become attached to the fibrils.

Effect of Phospholipids on the Amount of Fibrils

One observation from the X-ray scattering data is that the scattering intensity at low *q*-values was substantially lower in the presence of phospholipid vesicles than for peptide fibrillated

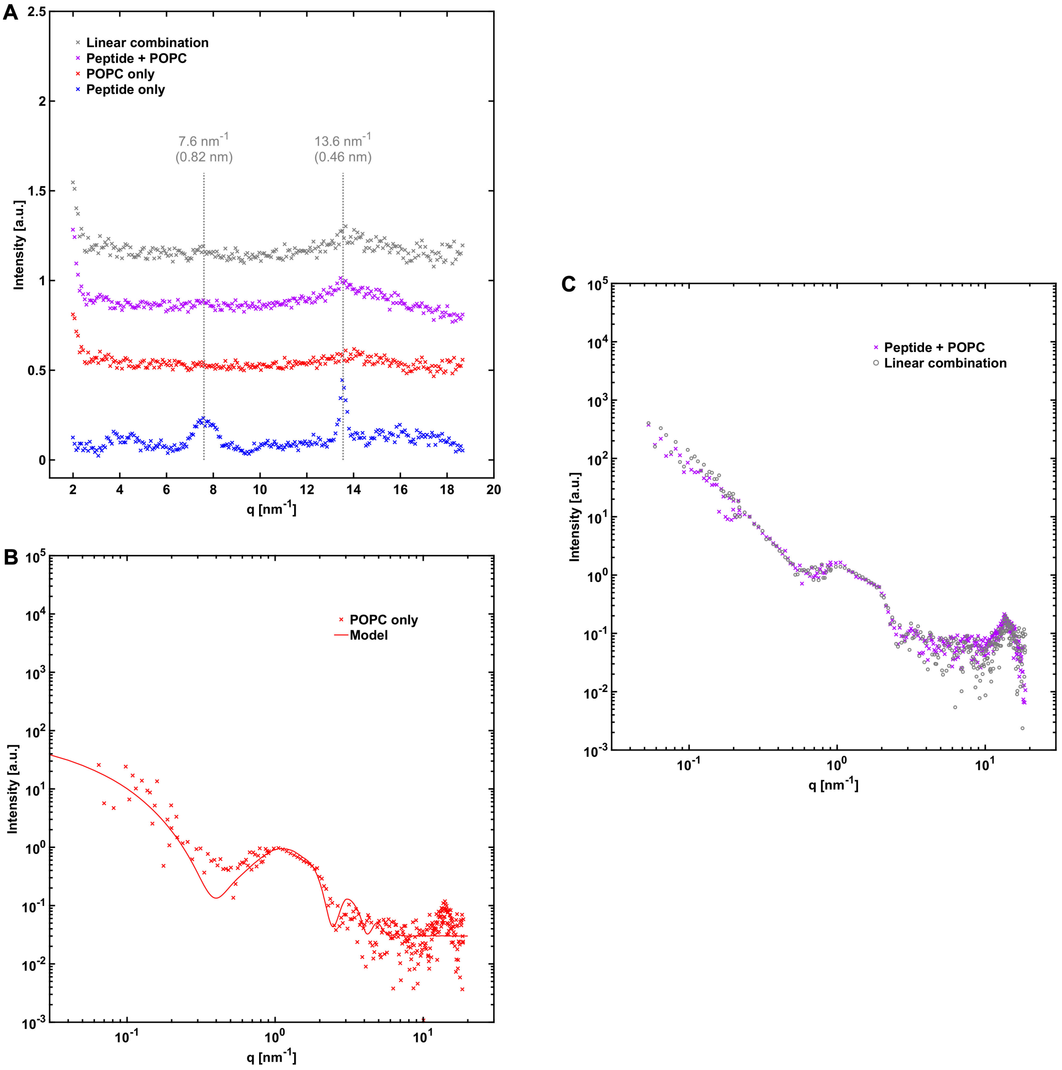

FIGURE 5 | NACore together with POPC. **(A)** WAXS profiles similar to those in **Figure 4A**, except that POPC was used instead of POPC:POPS. **(B)** 2.4 mM POPC without the peptide together with a simple vesicle model fit with 90% unilamellar and 10% bilamellar vesicles (see **Supplementary Table 1**). **(C)** SAXS profile of NACore co-incubated with POPC, together with a linear combination of scattering from peptide fibrils (**Figure 3B**) and POPC vesicles **(B)** (0.15·fibrils + 1.40·vesicles).

alone. This was especially true in the case when the peptide was fibrillated in the presence of POPC vesicles, where the intensity is almost an order of magnitude lower compared to the sample with peptide alone (15% of the intensity, **Figure 5**, compared to 40% for POPC:POPS, **Figure 4**). The difference between the case with POPC and POPC:POPS was also indicated by fewer fibrils found in the cryo-TEM images in the presence of POPC vesicles (**Figure 1**). This indicates that after 1 day of aggregation, the samples with phospholipids contain lower amounts of fibrils. To further investigate these differences, we performed CD measurement on peptide fibrillated in the presence and absence of POPC:POPS or POPC vesicles at various time points of incubation (**Figure 6**). The CD measurements give information about the secondary structure of the peptide and can be used to monitor the peptide fibrillation process (Kelly et al., 2005; Pallbo et al., 2019). Initially, the peptide has a disordered structure as judged from the CD spectra. The spectra for the initial state (t = 0) are essentially identical for all three samples (**Figure 6A**), implying that the structure of the initial unfibrillated peptide is the same in all cases, and that the phospholipids did not contribute with a CD signal of their own. After fibrillation has been induced, the CD spectra transform and reveal the presence of β-sheet-rich structures, which constitute the building blocks of the NACore amyloid fibrils (**Figure 6B**). Consistent with the X-ray scattering data, the CD measurements confirmed a rather substantial reduction of β-sheet content in the presence of both types of phospholipid vesicles, with the most prominent difference in the presence of POPC vesicles. This supports the conclusion that the differences in intensity observed in the X-ray scattering experiments were due to actual differences in amounts of fibrillated material. Another implication from the CD and X-ray measurements is that although samples were prepared with an approximately equimolar amount of total peptide and phospholipid molecules at $t = 0$, the molar fraction of fibrillated peptide relative to phospholipid was probably substantially lower than 1 at the time point of the X-ray scattering measurements (roughly 0.2–0.4 for POPC:POPS and 0.05–0.15 for POPC).

Fibrillation in the Presence of DMPC:DMPS Vesicles

For further characterization of peptide-phospholipid interactions we performed X-ray scattering, contrast variation SANS, and cryo-TEM analysis for NACore that was aggregated together with vesicles composed of DMPC:DMPS, in both hydrogenated and deuterated form. DMPC and DMPS were used instead of POPC and POPS because the latter are not readily available in fully deuterated form. The WAXS pattern for the peptide together with DMPC:DMPS gave similar results as with the other lipid compositions in that the positions of the major cross-β associated Bragg peaks were not altered by the co-incubation with the lipids (**Figure 7A**). However, the scattering profile at lower q-values revealed a difference compared to the results with POPC:POPS and POPC. A small peak was present at 1.4 nm^{-1} in the scattering profile, which could not be fitted as a linear combination of the scattering from the separate components (**Figure 7B**). Further analysis based on neutron scattering and cryo-TEM data revealed that this was due to the presence of long multilamellar helical tubes in the samples (**Supplementary Section 1**). The peak at $q = 1.4$ nm^{-1} arise from the periodic spacing of $d = 4.4$ nm in the multi-lamellar tube wall. Similar structures have been reported before for other lipids (Fuhrhop and Helfrich, 1993), and for lipids with sn-glycero-3-phospho-L-serine (PS) head groups in the presence of divalent metal ions (Ca^{2+} in particular) which are then referred to as cochelates (Papahadjopoulos et al., 1975; Nagarsekar et al., 2016). We believe this is also the structures observed in our samples with DMPC:DMPS. Ca^{2+} can leach from some types of glassware under high pH conditions, and we found small amounts of Ca^{2+} that appeared to be present along with the lyophilized peptide powder (about 16 μM, see **Supplementary Section 2**). Indeed, when the X-ray scattering experiments were repeated in the presence of 0.1 mM added ethylenediaminetetraacetic acid (EDTA), the sharp peak at 1.4 nm^{-1} was absent and the resulting scattering curve more closely resembled those obtained with POPC:POPS and POPC. However, the fit obtained from a linear combination of the components was still slightly worse than for the other lipid systems (**Figure 7C**). We note that these samples were prepared and measured at 37°C instead of room temperature, due to the relatively high hydrocarbon chain melting point of DMPC:DMPS.

DISCUSSION

Here we have studied the 11 amino acid residue peptide NACore that is a fragment from the central NAC region of the 140 amino acid residue protein α-synuclein. NACore can form amyloid fibrils by itself without the rest of the full-length α-synuclein protein (Rodriguez et al., 2015; Pallbo et al., 2019), indicating that the driving forces for amyloid formation are still present for this small peptide fragment. However, other properties will of course differ between the NACore peptide fragment and the full-length α-synuclein protein. For example, NACore does not include segments of α-synuclein that are considered crucial for some of its interaction with lipid membranes. Monomeric α-synuclein has a strong affinity for anionic phospholipid bilayers. The N-terminal region of α-synuclein (from approximately residue 1 to 100) folds into an α-helix when it adsorbs to such anionic membranes. The C-terminal region, on the other hand, remains unstructured in the membrane-bound state and extends from the membrane surface (Pfefferkorn et al., 2012). An adsorbed layer of α-synuclein on anionic lipid membranes might be crucial for triggering α-synuclein amyloid formation (Galvagnion et al., 2015; Gaspar et al., 2020). Similarities and differences between the lipid interactions of the short NACore peptide fragment studied in this report, full length α-synuclein, and other proteins might highlight which features of the interactions are likely to be generic for most amyloid forming peptides and proteins, and which might be more protein specific. We have focused on the effects of phospholipids on the cross-β packing in the fibrils, lipid-peptide co-assembly, as well as on effects of lipids on the fibrillation process. Below these aspects will be discussed separately. Finally, the potential *in-vivo* significance will be considered.

Effects on Cross-β Packing and Fibril Morphology

One finding from the present study is that although there is lipid-protein co-assembly at larger length scales, the presence of phospholipids has no detectable effect on the cross-β organization in the amyloid fibrils at the resolution of our measurements. This suggests that the peptide-peptide interaction in the crystal-like fibrils is stronger than the peptide-lipid interaction, and that is perhaps not very surprising considering the typical observation of low solubility of solutes in crystalline solids. For example, crystallization is commonly used as a way of purifying chemicals from a mixture of substances (Mullin, 2001). The observation of no effect on the position of the main cross-β associated Bragg peaks from the peptide fibrils is also consistent with the very early report of amyloid lipid co-aggregation in diseased spleen tissue that was mentioned in the introduction (Bonar et al., 1969). In wide angle X-ray scattering they observed peaks typical of the cross-β structure found in amyloids, together with additional peaks that were likely due to lipid material. Delipidation of the sample removed the extra peaks but left the cross-β-associated peaks of the amyloid material unaffected, suggesting that the internal structure of the amyloid fibrils remained the same. However, it cannot be excluded that differences could be found by more sensitive measurements than those reported here. We also note that the fibril morphology, such as cross section

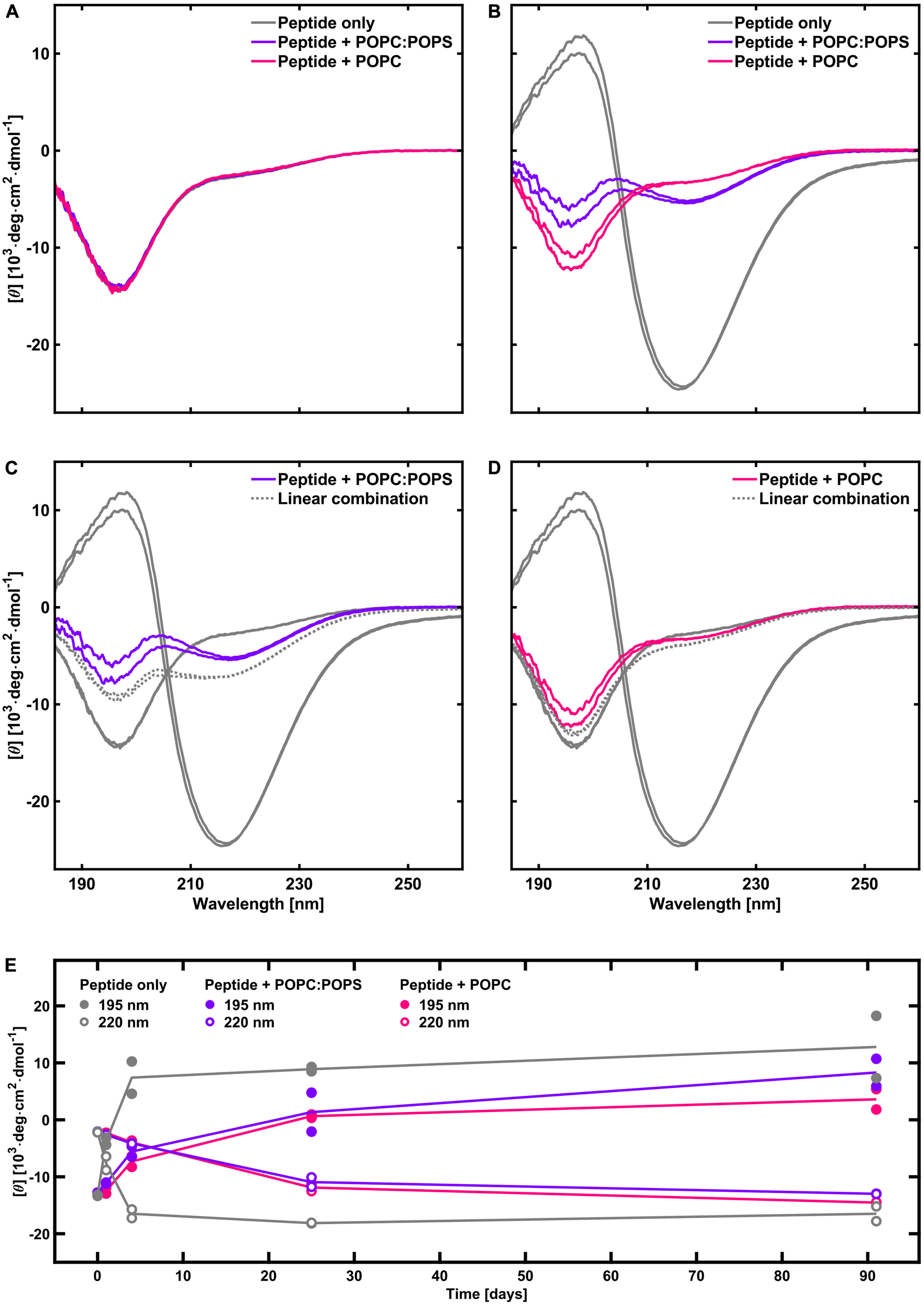

FIGURE 6 | CD spectra of peptide in the absence and presence of phospholipids, with duplicate samples for each system. **(A)** Initial time point. **(B)** After 1 day. **(C)** Estimation of the extent of fibrillation in the presence POPC:POPS (gray dotted line) relative to peptide fibrillated alone, based on a linear combination of the spectra for peptide alone at *t* = 0 and at *t* = 1 day (80% of the spectrum at *t* = 0 plus 20% of the spectrum at *t* = 1 day). **(D)** Same as **(C)** but with POPC instead of POPC:POPS. The linear combination shows 95% of the peptide alone spectrum at *t* = 0 plus 5% of the spectrum at *t* = 1 day. **(E)** Time evolution of the CD intensity at 195 and 220 nm, with and without phospholipid vesicles (based on a different peptide batch). It shows that the fibrillation continues to increase after 1 day in the presence of phospholipids. Phospholipids thus have an inhibiting effect on the rate of fibrillation.

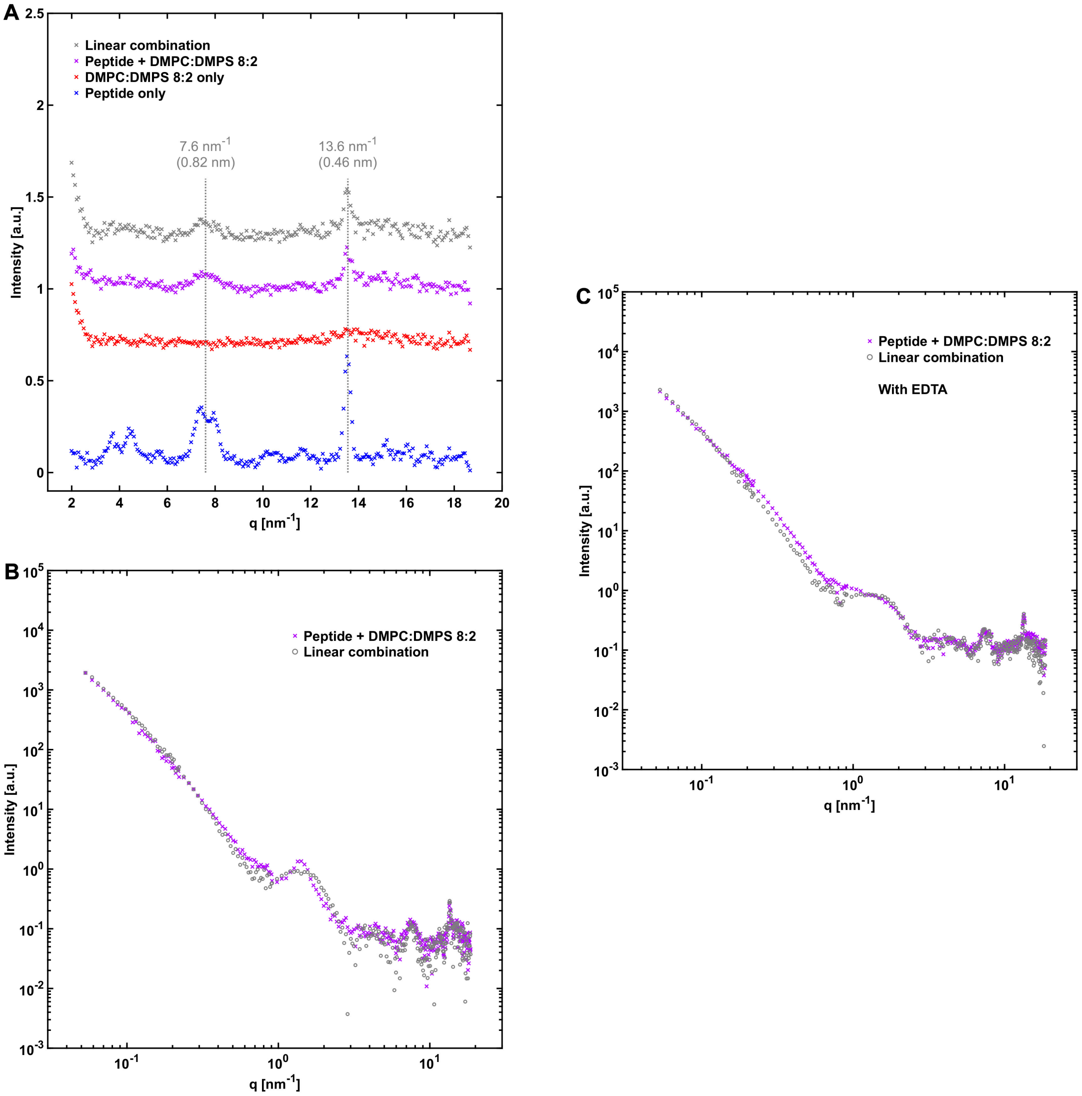

FIGURE 7 | NACore together with DMPC:DMPS. **(A)** WAXS profiles similar to those in **Figures 4A**, **5A**, but with DMPC:DMPS as the lipid system. **(B)** SAXS profile of NACore co-incubated with DMPC:DMPS, together with a linear combination of scattering from fibrils and vesicles (0.30 fibrils + 1.20·vesicles). A sharp peak at $q = 1.4$ nm^{-1} is present in the scattering profile of the co-incubated sample. **(C)** SAXS profile of NACore co-incubated with DMPC:DMPS, together with a linear combination of scattering from fibrils and vesicles (0.70·fibrils + 0.90·vesicles), with 0.1 mM added EDTA. The sharp peak at $q = 1.4$ nm^{-1} is not present. For all experiments with this lipid system incubation and measurements were done at 37°C instead of at room temperature.

dimensions, were not significantly altered when fibrillation occurred in the presence of lipid vesicles, compared with fibrillation in the absence of lipid. The SAXS pattern of mixed systems could be well described by a superposition of pure fibril and vesicle scattering. This implies that whatever the lipid-fibril interaction, final fibril morphology is not substantially affected.

Effect on Lipid Self-Assembly

The bilayer cross section form factors of POPC:POPS and pure POPC lipid systems were not affected by the presence and fibrillation of the NACore peptide (**Figures 4C**, **5C**), as data from the mixed fibril-lipid systems could be described by a superposition of the scattering patterns observed in pure lipid and peptide samples, respectively. In fact, the SAXS cross section form factor of lipid bilayers is generally sensitive to variations in bilayer thickness and area per lipid molecule (head group area density) (Pabst et al., 2000; Saveyn et al., 2009). From this we may conclude that the lipid bilayers remain essentially intact in the presence of peptide. Thus, there are no indications of significant solubilization of peptide monomers in the bilayer membranes. Similar conclusions can be drawn for the case of DMPC:DMPS.

Co-aggregation With Lipids

We can distinguish between association of lipids and peptide in the monomeric and in the fibrillar state. In the present study we found a clear affinity between peptide fibrils and phospholipid vesicles. The lipid bilayers of the vesicles seem to have high affinity for the fibril surface, leading to vesicle attachment and deformations. Similar behavior has been demonstrated with amyloid fibrils made of proteins such as β2-microglobulin (Milanesi et al., 2012) and α-synuclein when aggregated with an excess of anionic vesicles (Hellstrand et al., 2013). Complete rupture of vesicles was observed for some lipid compositions and lipid-protein ratios (Hellstrand et al., 2013; Galvagnion et al., 2019). Some studies have also identified interaction with amyloid fibril ends as being especially disruptive for phospholipid vesicles (Milanesi et al., 2012; Kollmer et al., 2016). However, due to the long nature of the fibrils in our system, meaning low occurrence of ends, we could not readily assess that mode of interaction for NACore. The observed co-existence of fibrils and surface-associated vesicles is consistent with the X-ray scattering data (**Figures 4**, **5**) since the SAXS profiles of the fibrillated samples containing both peptide and lipid could be fitted as linear combinations of fibrils and bilayers.

The fibrillation experiments were performed by dropping the pH from 11 to 7, where the hydrophobic peptide has essentially zero net charge. The aqueous solubility of the peptide is thereby drastically reduced, the solution becomes supersaturated, and the peptide precipitates out of solution. The self-assembly is driven by hydrophobic interactions. The fibrillar aggregates formed are also hydrophobic, and further aggregate into clusters as seen by the power law dependence $I(q) \sim q^{-2.3}$ at lower q-values. Thus, we may in principle expect hydrophobic attraction both between fibril and bilayer and between peptide monomer and bilayer. The different faces of the NACore amyloid fibrils are expected to have different surface properties. Based on the known crystal structure of NACore (Rodriguez et al., 2015; Pallbo et al., 2019) two faces of the fibrils have no charges and consist mostly of non-polar amino acid side chains. The other two exposed sides consist of oppositely charged N- and C-terminals of the peptide, stacked next to each other. As the fibrils have a net zero charge, hydrophobic interactions are most likely the dominating attractive interaction between the fibrils and lipid bilayers. Previous studies of co-assemblies of α-synuclein and phospholipids have demonstrated reduced molecular dynamics in the associated lipid molecules both in the headgroups and in hydrocarbon chain segments close to the headgroups (Hellstrand et al., 2013; Galvagnion et al., 2019).

Next, we consider the possibility of peptide-lipid co-assembly already in the initial stage of the process at about $t = 0$, when the peptide is still in monomer form. If a large proportion of monomeric NACore peptide is adsorbed to the phospholipid bilayers already at $t = 0$, we can tell from the CD spectra that the adsorption in such a case is not associated with any detectable conformation change. The CD spectra at short times are essentially identical in the presence and in the absence of lipid (**Figure 6A**). From a colloidal point of view, it is not surprising if the degree of association between the peptide and the lipid bilayer would increase as the peptide particles grow larger, such as when they form fibrils, because as the particles grow larger the strength of the interactions per particle increases. It is thus possible that the affinity between monomeric NACore peptide and phospholipid vesicles is rather weak, while the affinity is very strong between the fibrils and the vesicles.

Effects on the Fibrillation Process

An important finding from the CD (**Figure 6**) and X-ray scattering experiments is that the presence of phospholipids reduces the amount of fibrils formed after 1 day of incubation. This is observed both for the system containing POPC:POPS vesicles and POPC vesicles, with the strongest reduction observed for the latter system. As shown by the long time CD study (**Figure 6E**), this can be explained by a slowing down of the fibrillation kinetics rather than just a reduction of the final steady-state amounts of fibrils formed. This is because the extents of β-sheet signal have approached each other for all the samples at the longest time point relative to the earliest time points. This behavior is different from that observed with full-length α-synuclein, where fibrillation instead is accelerated by the presence of anionic vesicles for certain protein-to-lipid ratios (Galvagnion et al., 2015; Gaspar et al., 2018). One difference between these systems is that monomeric α-synuclein adsorbs to anionic membranes where it adopts a partial α-helical structure, while there are no signs of conformational changes for the NACore peptide when exposed to either zwitterionic or anionic vesicles. In quiescent conditions and pure buffer solutions, monomeric α-synuclein does not readily nucleate within time frames of several days. Lipid bilayers are thought to act as sites of primary nucleation (Galvagnion et al., 2015; Gaspar et al., 2018). In the kind of experiments with NACore performed here, the nucleation of fibrils occurs spontaneously also in the absence of phospholipid bilayers, and the rate of fibril formation is instead decreased due to some interaction with the bilayers. Assuming that extinction coefficients of the peptide UV absorption is unaffected by the presence of lipid, then we can use the CD signal to estimate the amounts of fibrils formed. For example, we can follow the time evolution of the CD signal at 220 nm, as presented in **Figure 6E**. From comparing the time evolutions in the presence of lipid with that in absence of lipid, it is revealed that the presence of lipid reduces the fibrillation rate by more than an order of magnitude. On the other hand, the amounts of fibrils that have formed at long time when steady state has been achieved, is only reduced by 10–20%, if at all.

Both lipid-fibril and lipid-monomer interactions may affect the fibrillation rate. Lipids may adsorb onto the growing fibrils, obstructing the attachment of peptide monomers to the aggregates. Such a mechanism has been observed for other systems, such as for the inhibiting effect of the polymer polyvinylpyrrolidone (PVP) on the crystal growth rate of bicalutamide (Lindfors et al., 2008). In that study, PVP was found to adsorb to the particle surfaces and thereby reduce the rate of crystal growth. PVP, however, was found not to affect the initial nucleation rate. When, in a nucleation and growth process, the growth rate is reduced without affecting the nucleation rate, this is expected to lead to smaller particles but larger in number. As these peptide fibrils in general grow to become very long, it is not possible to clearly say from the cryo-TEM images and SAXS patterns that they are significantly shorter in the presence of lipid. It is at the same time clear that we do not see evidence for a large fraction of relatively small fibrils ($<$100 nm). The fibrils observed in cryo-TEM (**Figures 1**, **2** and **Supplementary Figures 1–3**) are all very long also in the presence of lipid.

A reduced fibrillation rate may also result from peptide monomers being solubilized in, or adsorbed to lipid bilayers, thereby reducing the effective supersaturation. The peptide fibrillation can be seen as the precipitation of a solid crystalline phase. In the aqueous bulk monomer solution (m), the (monomer) peptide chemical potential can be written as $\mu_m = \mu_m^0 + k_B T \ln c_m$, where μ_m^0 is the concentration independent part and c_m is the bulk monomer concentration. $k_B T$ is the thermal energy with k_B being Boltzmann's constant and T the absolute temperature. In the solid fibril phase (f), the corresponding peptide chemical potential can be considered as constant, $\mu_f = \mu_f^0$. The equilibrium monomer concentration, S, coexisting with the fibril phase, i.e., the monomer solubility, is then given by $S = \exp\left\{\left(\mu_f^0 - \mu_m^0\right)\big/ k_B T\right\}$. Fibrils are nucleated from supersaturated solutions where $c_m > S$, and the rate of nucleation, and also aggregate growth, is usually a strong function of the degree of supersaturation, c_m/S (Kashchiev, 2000), also in the case of peptide fibrillation. The lipid bilayers can be seen as a third phase. If monomers have affinity to that phase, being adsorbed or solubilized, c_m is reduced. If the peptides would dissolve mostly within the membrane, we would expect that to involve a change in secondary structure, e.g., to α-helix, with hydrogen bonding to water being replaced by intramolecular hydrogen bonding. No sign of this is observed in the CD spectrum at short times. Nor do we see by SAXS any change in the lipid bilayer form factor in the presence of peptide. Therefore, if the peptide monomers have an affinity for the lipid bilayers, they are likely adsorbed within the headgroup region, still hydrated and with random coil conformation. In the case of adsorption, we expect the adsorbed amount, Γ, to be proportional to c_m, unless we are close to saturation (Evans and Wennerström, 1999). For reversible monomer adsorption, this mechanism may lead to a significant reduction of nucleation and growth rates, with only a minor decrease in final fibril concentration, as the adsorbed monomers still act as a reservoir due to reversibility, decreasing Γ as c_m decreases. If the adsorption is saturated initially, $\Gamma \sim c_m$ may be achieved at later times.

In the present experiments, the peptide-to-lipid molar ratio was close to one. Hence, if one peptide monomer adsorbs to every second lipid molecule, that is, to every lipid molecule of the outer monolayers of the vesicle bilayers, then c_m is initially reduced by approximately one half. Whether this mechanism may quantitatively explain the observed kinetics remains to be shown. Discriminating whether peptide monomer-lipid association is occurring requires further studies. This may be done by measuring fibrillation kinetics as a function of peptide concentration and as a function of the peptide-lipid molar ratio.

In-vivo Significance

One important part of the physiology of cells and neural tissues is vesicle transport. Even without total disruption of vesicles, hindering of vesicle transport could be a mechanism of toxicity for cells (Auluck et al., 2010). In our experiments we have seen clear evidence of vesicles being trapped in fibril networks. Similar effects of organelles and lipid structures being entangled in fibrils have been seen in other studies (Auluck et al., 2010; Shahmoradian et al., 2019). Misfolding and fibrillation of proteins results in long colloidal objects with a lot of potentially very sticky surface area. When such sticky surfaces in the cellular environment lead to capture and entanglement of vesicles and organelles it could thus potential lead to cellular toxicity.

DATA AVAILABILITY STATEMENT

The raw data supporting the conclusions of this article will be made available by the authors, without undue reservation.

AUTHOR CONTRIBUTIONS

JP, UO, and ES designed the research and wrote the manuscript with input from MI, LG, and ST. JP, LG, MI, and ST performed neutron scattering experiments. JP performed all other experiments except the cryo-TEM imaging and elemental analysis and analyzed the data with input from UO and ES. All authors approved the manuscript before submission.

FUNDING

This research was financed by the Knut and Alice Wallenberg Foundation (KAW 2014.0052 and KAW 2016.0074). This research was also supported by JSPS and STINT under the Japan-Sweden Research Cooperative Program. It also benefited from the use of the SasView application (http://www.sasview.org/), originally developed under NSF award DMR-0520547. SasView contains code developed with funding from the European Union's Horizon 2020 research and innovation program under the SINE2020 project, grant agreement No 654000.

ACKNOWLEDGMENTS

We thank Anna Carnerup for cryo-TEM imaging at the National Center for High Resolution Electron Microscopy (nCHREM) in Lund (Sweden), J-PARC for beamtime on the TAIKAN BL-15 beamline (proposal No. 2018A0112), and Sofia Mebrahtu Wisén (Inorganic Analysis Laboratory, Department of Biology, Lund University) for inorganic elemental analysis.

SUPPLEMENTARY MATERIAL

The Supplementary Material for this article can be found online at: https://www.frontiersin.org/articles/10.3389/fphys.2020.592117/full#supplementary-material

REFERENCES

Alberts, B., Johnson, A., Lewis, J., Raff, M., Roberts, K., and Walter, P. (2008). *Molecular Biology of the Cell*, 5 Edn. New York, NY: Garland Science.

Auluck, P. K., Caraveo, G., and Lindquist, S. (2010). Alpha-synuclein: membrane interactions and toxicity in Parkinson's disease. *Annu. Rev. Cell Dev. Biol.* 26, 211–233.

Bodles, A. M., Guthrie, D. J. S., Greer, B., and Irvine, G. B. (2001). Identification of the region of non-A beta component (NAC) of Alzheimer's disease amyloid responsible for its aggregation and toxicity. *J. Neurochem.* 78, 384–395. doi: 10.1046/j.1471-4159.2001.00408.x

Bonar, L., Cohen, A., and Skinner, M. (1969). Characterization of amyloid fibril as a cross-beta protein. *Proc. Soc. Exp. Biol. Med.* 131, 1373–1375.

Butterfield, S. M., and Lashuel, H. A. (2010). Amyloidogenic protein membrane interactions: mechanistic insight from model systems. *Angew. Chem. Int. Edn.* 49, 5628–5654. doi: 10.1002/anie.200906670

Chiti, F., and Dobson, C. M. (2017). Protein misfolding, amyloid formation, and human disease: a summary of progress over the last decade. *Annu. Rev. Biochem.* 86, 27–68. doi: 10.1146/annurev-biochem-061516-045115

Eicher, B., Heberle, F. A., Marquardt, D., Rechberger, G. N., Katsaras, J., and Pabst, G. (2017). Joint small-angle X-ray and neutron scattering data analysis of asymmetric lipid vesicles. *J. Appl. Crystallogr.* 50, 419–429. doi: 10.1107/S1600576717000656

Eisenberg, D. S., and Sawaya, M. R. (2017). Structural studies of amyloid proteins at the molecular level. *Annu. Rev. Biochem.* 86, 69–95. doi: 10.1146/annurev-biochem-061516-045104

Evans, D. F., and Wennerström, H. (1999). *The Colloidal Domain: Where Physics, Chemistry, Biology, and Technology Meet*, 2 Edn. Weinheim: Wiley-VCH.

Fuhrhop, J., and Helfrich, W. (1993). Fluid and solid fibers made of lipid molecular bilayers. *Chem. Rev.* 93, 1565–1582. doi: 10.1021/cr00020a008

Galvagnion, C., Buell, A. K., Meisl, G., Michaels, T. C. T., Vendruscolo, M., Knowles, T. P. J., et al. (2015). Lipid vesicles trigger alpha-synuclein aggregation by stimulating primary nucleation. *Nat. Chem. Biol.* 11, 229–234. doi: 10.1038/NCHEMBIO.1750

Galvagnion, C., Topgaard, D., Makasewicz, K., Buell, A. K., Linse, S., Sparr, E., et al. (2019). Lipid dynamics and phase transition within alpha-Synuclein amyloid fibrils. *J. Phys. Chem. Lett.* 10, 7872–7877. doi: 10.1021/acs.jpclett.9b03005

Gaspar, R., Lund, M., Sparr, E., and Linse, S. (2020). Anomalous salt dependence reveals an interplay of attractive and repulsive electrostatic interactions in alpha-synuclein fibril formation. *Q. Rev. Biophys. Discov.* 1:e2.

Gaspar, R., Pallbo, J., Weininger, U., Linse, S., and Sparr, E. (2018). Ganglioside lipids accelerate alpha-synuclein amyloid formation. *Biochim. Biophys. Acta Proteins Proteom.* 1866, 1062–1072. doi: 10.1016/j.bbapap.2018.07.004

Gellermann, G. P., Appel, T. R., Tannert, A., Radestock, A., Hortschansky, P., Schroeckh, V., et al. (2005). Raft lipids as common components of human extracellular amyloid fibrils. *Proc. Natl. Acad. Sci. U.S.A.* 102, 6297–6302. doi: 10.1073/pnas.0407035102

Gorbenko, G. P., and Kinnunen, P. K. J. (2006). The role of lipid-protein interactions in amyloid-type protein fibril formation. *Chem. Phys. Lipids* 141, 72–82. doi: 10.1016/j.chemphyslip.2006.02.006

Hellstrand, E., Nowacka, A., Topgaard, D., Linse, S., and Sparr, E. (2013). Membrane lipid co-aggregation with alpha-synuclein fibrils. *PLoS One* 8:e77235. doi: 10.1371/journal.pone.0077235

Iyer, A., and Claessens, M. M. A. E. (2019). Disruptive membrane interactions of alpha-synuclein aggregates. *Biochim. Biophys. Acta Proteins Proteom.* 1867, 468–482. doi: 10.1016/j.bbapap.2018.10.006

Janson, J., Ashley, R. H., Harrison, D., McIntyre, S., and Butler, P. C. (1999). The mechanism of islet amyloid polypeptide toxicity is membrane disruption by intermediate-sized toxic amyloid particles. *Diabetes* 48, 491–498. doi: 10.2337/diabetes.48.3.491

Kashchiev, D. (2000). *Nucleation*, 1 Edn. Oxford: Butterworth-Heinemann.

Kaya, I., Brinet, D., Michno, W., Baskurt, M., Zetterbergt, H., Blenow, K., et al. (2017). Novel trimodal MALDI imaging mass spectrometry (IMS3) at 10 mu m reveals spatial lipid and peptide correlates implicated in A beta plaque pathology in Alzheimer's disease. *ACS Chem. Neurosci.* 8, 2778–2790. doi: 10.1021/acschemneuro.7b00314

Kelly, S. M., Jess, T. J., and Price, N. C. (2005). How to study proteins by circular dichroism. *Biochim. Biophys. Acta Proteins Proteom.* 1751, 119–139. doi: 10.1016/j.bbapap.2005.06.005

Kiskis, J., Fink, H., Nyberg, L., Thyr, J., Li, J. Y., and Enejder, A. (2015). Plaque-associated lipids in Alzheimer's diseased brain tissue visualized by nonlinear microscopy. *Sci. Rep.* 5:13489. doi: 10.1038/srep13489

Kollmer, M., Meinhardt, K., Haupt, C., Liberta, F., Wulff, M., Linder, J., et al. (2016). Electron tomography reveals the fibril structure and lipid interactions in amyloid deposits. *Proc. Natl. Acad. Sci. U.S.A.* 113, 5604–5609. doi: 10.1073/pnas.1523496113

Kucerka, N., Nieh, M. P., and Katsaras, J. (2011). Fluid phase lipid areas and bilayer thicknesses of commonly used phosphatidylcholines as a function of temperature. *Biochim. Biophys. Acta Biomembr.* 1808, 2761–2771. doi: 10.1016/j.bbamem.2011.07.022

Lindfors, L., Forssen, S., Westergren, J., and Olsson, U. (2008). Nucleation and crystal growth in supersaturated solutions of a model drug. *J. Coll. Interface Sci.* 325, 404–413. doi: 10.1016/j.jcis.2008.05.034

Lindner, P., and Zemb, T. (eds) (2002). *Neutrons, X-Rays and Light: Scattering Methods Applied to Soft Condensed Matter*. Amsterdam: Elsevier.

Milanesi, L., Sheynis, T., Xue, W. F., Orlova, E. V., Hellewell, A. L., Jelinek, R., et al. (2012). Direct three-dimensional visualization of membrane disruption by amyloid fibrils. *Proc. Natl. Acad. Sci. U.S.A.* 109, 20455–20460. doi: 10.1073/pnas.1206325109

Mullin, J. W. (2001). *Crystallization*, 4 Edn. Amsterdam: Elsevier.

Nagarsekar, K., Ashtikar, M., Steiniger, F., Thamm, J., Schacher, F., and Fahr, A. (2016). Understanding cochleate formation: insights into structural development. *Soft Matter* 12, 3797–3809. doi: 10.1039/c5sm01469g

Pabst, G., Rappolt, M., and Amenitsch, H. (2000). Structural information from Multilamellart liposomes at full hydration: full 1-range fitting with high quality X-ray Data. *Phys. Rev. E* 62, 4000–4009. doi: 10.1103/physreve.62.4000

Pallbo, J., Sparr, E., and Olsson, U. (2019). Aggregation behavior of the amyloid model peptide NACore. *Q. Rev. Biophys.* 52:e4. doi: 10.1017/S0033583519000039

Papahadjopoulos, D., Vail, W., Jacobson, K., and Poste, G. (1975). Cochleate lipid cylinders: Formation by fusion of unilamellar lipid vesicles. *Biochim. Biophys. Acta* 394, 483–491. doi: 10.1016/0005-2736(75)90299-0

Pfefferkorn, C. M., Jiang, Z., and Lee, J. C. (2012). Biophysics of alpha-synuclein membrane interactions. *Biochim. Biophys. Acta Biomembr.* 1818, 162–171. doi: 10.1016/j.bbamem.2011.07.032

Rodriguez, J. A., Ivanova, M. I., Sawaya, M. R., Cascio, D., Reyes, F. E., Shi, D., et al. (2015). Structure of the toxic core of alpha-synuclein from invisible crystals. *Nature* 525, 486–490. doi: 10.1038/nature15368

Saveyn, P., Van der Meeren, P., Zackrisson, M., Narayanan, T., and Olsson, U. (2009). Subgel transition in diluted vesicular DODAB dispersions. *Soft Matter* 5, 1735–1742. doi: 10.1039/b821387a

Scott, H. L., Skinkle, A., Kelley, E. G., Waxham, M. N., Levental, I., and Heberle, F. A. (2019). On the mechanism of bilayer separation by extrusion, or why your LUVs are not really unilamellar. *Biophys. J.* 117, 1381–1386. doi: 10.1016/j.bpj.2019.09.006

Shahmoradian, S. H., Lewis, A. J., Genoud, C., Hench, J., Moors, T. E., Navarro, P. P., et al. (2019). Lewy pathology in Parkinson's disease consists of crowded organelles and lipid membranes. *Nat. Neurosci.* 22, 1099–1109. doi: 10.1038/s41593-019-0423-2

Solomon, M. J., and Spicer, P. T. (2010). Microstructural regimes of colloidal rod suspensions, gels, and glasses. *Soft Matter* 6, 1391–1400. doi: 10.1039/b918281k

Zhang, M., Zhao, J., and Zheng, J. (2014). Molecular understanding of a potential functional link between antimicrobial and amyloid peptides. *Soft Matter* 10, 7425–7451. doi: 10.1039/c4sm00907j

Conflict of Interest: The authors declare that the research was conducted in the absence of any commercial or financial relationships that could be construed as a potential conflict of interest.

frontiers
in Cell and Developmental Biology

ORIGINAL RESEARCH
published: 26 January 2021
doi: 10.3389/fcell.2020.592520

Non-linear Conductance, Rectification, and Mechanosensitive Channel Formation of Lipid Membranes

Karis Amata Zecchi and Thomas Heimburg*

Membrane Biophysics Group, Niels Bohr Institute, University of Copenhagen, Copenhagen, Denmark

There is mounting evidence that lipid bilayers display conductive properties. However, when interpreting the electrical response of biological membranes to voltage changes, they are commonly considered as inert insulators. Lipid bilayers under voltage-clamp conditions display current traces with discrete conduction-steps, which are indistinguishable from those attributed to the presence of protein channels. In current-voltage (I-V) plots they may also display outward rectification, i.e., voltage-gating. Surprisingly, this has even been observed in chemically symmetric lipid bilayers. Here, we investigate this phenomenon using a theoretical framework that models the electrostrictive effect of voltage on lipid membranes in the presence of a spontaneous polarization, which can be recognized by a voltage offset in electrical measurements. It can arise from an asymmetry of the membrane, for example from a non-zero spontaneous curvature of the membrane. This curvature can be caused by voltage via the flexoelectric effect, or by hydrostatic pressure differences across the membrane. Here, we describe I-V relations for lipid membranes formed at the tip of patch pipettes situated close to an aqueous surface. We measured at different depths relative to air/water surface, resulting in different pressure gradients across the membrane. Both linear and non-linear I-V profiles were observed. Non-linear conduction consistently takes the form of outward rectified currents. We explain the conductance properties by two mechanisms: One leak current with constant conductance without pores, and a second process that is due to voltage-gated pore opening correlating with the appearance of channel-like conduction steps. In some instances, these non-linear I-V relations display a voltage regime in which dI/dV is negative. This has also been previously observed in the presence of sodium channels. Experiments at different depths reveal channel formation that depends on pressure gradients. Therefore, we find that the channels in the lipid membrane are both voltage-gated and mechanosensitive. We also report measurements on black lipid membranes that also display rectification. In contrast to the patch experiments they are always symmetric and do not display a voltage offset.

Keywords: permeability, ion channels, rectification, lipid membrane, flexoelectricity, thermodynamics, voltage-gating, mechanosensitivity

Edited by:
Angelina Angelova,
UMR8612 Institut Galien Paris Sud (IGPS), France

Reviewed by:
Leonel Malacrida,
Universidad de la República, Uruguay
Charles David Cox,
Victor Chang Cardiac Research Institute, Australia

***Correspondence:**
Thomas Heimburg
theimbu@nbi.ku.dk

Specialty section:
This article was submitted to Cellular Biochemistry, a section of the journal Frontiers in Cell and Developmental Biology

Received: *11 August 2020*
Accepted: *10 December 2020*
Published: *26 January 2021*

Citation:
Zecchi KA and Heimburg T (2021) Non-linear Conductance, Rectification, and Mechanosensitive Channel Formation of Lipid Membranes.
Front. Cell Dev. Biol. 8:592520.
doi: 10.3389/fcell.2020.592520

1. INTRODUCTION

The permeability of biological membranes is of immense biological importance. The biological membrane separates inside and outside of cells and has to be selectively permeable to ions and substrates in order to establish well-defined chemical potential gradients of the components between inside and outside of the cells. Since this is a formidable task, it is believed that nature must control this by an appropriate "smart" mechanism, in particular by providing selective ion channels and pumps to cell membranes (Hille, 1992). The picture is that of an intelligent pump station with many switches, in which the opening and closing of individual pipes is controlled by substrates or system parameters, such as transmembrane voltage, mechanical membrane tension, or temperature. Channels that respond to these variables are called voltage-gated channels (e.g., Doyle et al., 1998; Bezanilla, 2005; Schmidt et al., 2006), mechano-sensitive channels (e.g., Martinac et al., 1990; Cruickshank et al., 1997; Corey et al., 2004; Syeda et al., 2016), or heat- and cold receptors (e.g., Voets et al., 2004, 2005). A complete field has dedicated its research to the investigation of the molecular nature of the switches. Since there are many substrates and ions, the whole machinery of the biological membrane is complex. In order to understand the working of a membrane with such a complex composition of "intelligent" components, one imagines a network of sequential (mostly binary) molecular interactions called pathways. This picture is inherently non-thermodynamic. Instead of making use of thermodynamic variables that act on a complete system with energy, entropy and distributions of states, the channels and receptors seemingly act as receptors to voltage and other intensive variables on the level of single molecules. This picture does not account for the thermodynamic nature of complex biological ensembles, which must undoubtably exist.

It comes as a profound surprise that appearance of channel-like conduction events can also be seen in pure lipid membranes in the absence of any proteins and macromolecules, i.e., in the complete absence of any single molecule that could act as a channel (e.g., Antonov et al., 1980, 2005; Kaufmann and Silman, 1983; Blicher et al., 2009; Wunderlich et al., 2009; Heimburg, 2010; Blicher and Heimburg, 2013; Mosgaard and Heimburg, 2013). These channel events are indistinguishable from those of proteins in so far as the current-traces alone do not provide any indication of whether the events originate from proteins or pure lipid membranes. Their single channel conductance, open-lifetime distributions and voltage dependence are very similar to those reported for proteins (Blicher and Heimburg, 2013). We have called the channels found in lipid membranes "lipid ion channels" (Heimburg, 2010) in order to stress these similarities. Lipid channels are thought being due to pores in the lipid membrane that open and close as a consequence of thermodynamic fluctuations. Due to the fluctuation-dissipation theorem, fluctuations become large close to melting transitions. Therefore, in this temperature regime lipid channels and lipid membrane conductance are strongly temperature sensitive (Papahadjopoulos et al., 1973; Nagle and Scott, 1978; Sabra et al., 1996; Blicher et al., 2009). We and others have shown that biological membranes display melting transition slightly below physiological temperature with heat capacity maxima in the range of 20–25°C, which in many electrophysiological experiments is the experimental temperature. The lipid membrane permeability is voltage-gated and can display rectified behavior, i.e., the conductance can be largely different at positive and negative voltage (Blicher and Heimburg, 2013; Mosgaard and Heimburg, 2013; Mosgaard et al., 2015a,b), especially when measured on patch pipettes. Since pure lipid membranes do not contain single macromolecules that could account for the formation of pores, these current fluctuations must be controlled by the thermodynamics of the membrane as a whole. This is striking because one can define a self-consistent macroscopic thermodynamic theory that describes these channels (Heimburg, 2010) without any need for macromolecules. It has even been shown that channels can be seen at the interface of patch pipettes with rubber surfaces (Sachs and Qin, 1993).

Such findings represents a serious problem for the interpretation of electrophysiological data. It is easy to demonstrate that quantized conduction events exist in lipid membranes in the absence of proteins. However, it is practically impossible to investigate channel proteins in the absence of membranes. A common approach in electrophysiology is to consider the lipid membrane as an insulator with very high resistance and attribute all discrete opening- and closing events to channel proteins. This is obviously not permissible if the membrane itself can display channels with similar appearance. Many publications have shown that the lipid membrane is not generally an insulator (e.g., Papahadjopoulos et al., 1973; Nagle and Scott, 1978; Sabra et al., 1996; Blicher et al., 2009). A complete field exists that describes the formation of nano pores in lipid membranes by voltage pulses (electroporation) (e.g., Neumann et al., 1999; Böckmann et al., 2008). This has found clinical applications in drug-delivery and the treatment of cancer (Gehl, 2003; Højholt et al., 2019). Thus, the interpretation of current traces in electrophysiological experiments rests on assumptions that are provably not generally true.

While the body of research on protein channels is huge, the permeability of pure membranes is still under-investigated. However, it seems unlikely that on one hand lipid pores represent the sole possible permeation mechanism in synthetic membranes but that on the other hand this mechanism is completely absent in cell membranes. It is interesting to ask the question whether including the thermodynamics of lipid channels into a picture for the biological membrane will help to elucidate the function of cell membranes. Most importantly, it is not known to which degree lipid pores and protein channels may share a similar mechanism or may even be the same. In Mosgaard and Heimburg (2013), we have proposed that proteins could act as catalysts for lipid pore formation, a view that is in line with the experimental finding that truncated proteins that cannot span through the membrane nevertheless can induce pores in biomembranes (Stoddart et al., 2014).

Besides the fact that lipid pores display a similar appearance as protein channels, it is not known what they look like. Glaser et al. (1988) have proposed that there exist hydrophobic and hydrophilic pores with openings on nanoscale, a view that is consistent with molecular dynamics simulations (Böckmann et al., 2008).

In this paper we study I-V profiles of synthetic lipid membrane patches using patch-clamp recordings. We use the droplet-technique, in which the membrane is formed across a patch pipette that is in contact with the aqueous surface of a buffer (Hanke et al., 1984; Gutsmann et al., 2015). In this setup, the depth of the pipette can be altered. This will influence the pressure gradients across the membrane. We study the depth dependence, analyze the theory of the I-V profiles and combine it with theoretical consideration about the equilibration processes directly after a voltage jump. We compared the patch experiments with black lipid membrane (BLM) experiments which are performed on much larger membranes. Finally, we compare our findings with potassium channels.

2. MATERIALS AND METHODS

2.1. Lipids and Chemicals

1,2-dimyristoyl-*sn*-glycero-3-phosphocholine (DMPC), 1,2-dilauroyl-*sn*-glycero-3-phosphocholine (DLPC) and cholesterol were purchased from Avanti Polar Lipids (Alabaster/AL, US), stored in a freezer and used without further purification. Lipid patches consisted of DMPC:DLPC = 10:1 (mol:mol) for the patch clamp experiments and of DMPC:DLPC:cholesterol = 77.3:7.7:15 (mol:mol:mol) for the black lipid membrane experiment. Each lipid was suspended separately in chloroform and then mixed to the desired ratio. The mixture was then dried under vacuum. In the patch experiments, the dry lipids were resuspended in Hexane:Ethanol = 4:1(mol:mol) to a final concentration of 2mM for the patch clamp experiment. The cholesterol mixture used in the BLM experiments was dissolved in decane to a final concentration of 10 mg/mL.

In the patch clamp experiment, the electrolyte solution used on both sides of the membrane consisted of 150 mM KCl, 150 mM NaCl and it was buffered with 50 mM TRIS to a final pH of 7.6. All water used in the experiments was purified with a Direct-Q Water Purification System (Merck Millipore, Germany) and had a resistivity larger than 18.1 MΩ·cm. In the BLM experiments we used 150 mM KCl, 150 mM NaCl, 2 mM HEPES, and 1 mM EDTA (both from Sigma-Aldrich, Germany), pH was adjusted to 7.4.

Pores in lipid membranes occur due to fluctuations in the membrane. According to the fluctuation theorem, the heat capacity is proportional to the fluctuations in enthalpy. Therefore, one finds more pores close to transitions. However, large fluctuations also destabilize the membrane because there are cases when large pores start to grow and rupture the membranes. Thus, when we choose a lipid mixture we always try to be at the upper edge of a melting transition such that fluctuations are present but not large enough to rupture the membrane (see **Figure 1**). The DMPC-DLPC mixture displays a transition peak close to 22°C with heat capacity events extending out to 25°C. Experiments were done at room temperature (24–24.5°C) at the surface of a beaker exposed to air. This is just below the upper end of the transition. The DMPC-DLPC mixture was not stable in BLM experiments. This might be due to the fact that the area of the BLM membrane is about 150 times larger than the patch in the pipette experiment, and rupture due to a growing pore is much more likely. Since cholesterol stabilizes membranes—probably at least partially because it broadens the transition and lowers the heat capacity—we used a different mixture in the BLM experiments. Since the BLMs are completely surrounded by water, it is much easier to control the temperature. In our experiment it was 32.4°C as measured close to the membranes. Note that the heat capacity in the BLM experiments is about an order of magnitude lower as in the patch pipette experiments.

2.2. Methods

2.2.1. Patch Clamp Experiments

Glass micropipettes were pulled from borosilicate capillaries with a vertical PC-10 puller (Narishe Group, Japan) following the two-steps procedure explained in Laub et al. (2012). They were then fire-polished using a Narishige MF-900 Microforge, which created pipette openings on the order of 10 μm.

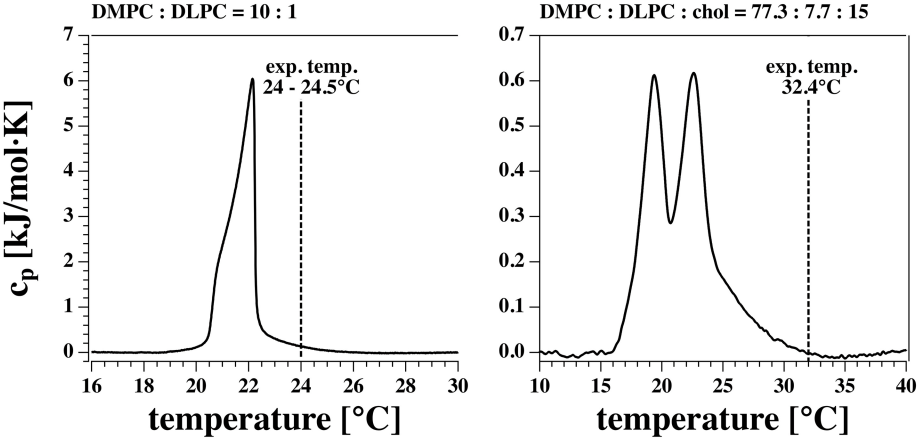

FIGURE 1 | Calorimetric profiles of the two lipid mixtures used. The vertical dashed line indicates the experimental temperature at which I-V profiles and currents were measured.

Lipid membrane patches were reconstituted on the tip of glass pipettes following the method introduced by Hanke et al. (1984) and described in detail in Laub et al. (2012) and Gutsmann et al. (2015). According to the protocol a droplet of lipid solution is placed on the outer wall of a glass micropipette filled with the electrolyte. The pipette stands vertically with its tip in contact with the liquid/air interface of a buffered electrolyte filled glass beaker. As the lipid droplet flows down to the pipette tip, it gets sealed by a spontaneously formed lipid bilayer.

Two Ag/AgCl electrodes were placed one inside the pipette and the other one in the bulk electrolyte, the latter acting as ground electrode. They were both connected to a patch clamp amplifier (Axopatch 200B, Molecular Devices, US) through a headstage to which the pipette was also secured. The amplifier was run in whole cell mode, the signal was sampled at a frequency of 10 kHz and filtered with a 2 kHz low pass Bessel filter. The headstage was allowed to move vertically with the aid of a micromanipulator (Luigs & Neumann, Germany), with which the vertical position of the tip relative to the electrolyte surface could be monitored.

An equivalent circuit of the pipette at an aqueous surface is given in **Figure 2**. It contains a voltage-dependent pore conductance g_p, a leak conductance g_L that contains contributions from the seal between membrane and pipette walls and defects in the membrane, a series resistance R_S inside of the pipette, a capacitive element $C_{pipette}$ between glass wall and buffer, and an applied voltage V. The charge on the membrane capacitor is given by $q = C_m(V + V_0)$ (see section 3.3.1), where C_m is the voltage-dependent membrane capacitance and V_0 is the offset potential cause by a (voltage dependent) polarization of the membrane (Petrov and Sachs, 2002; Mosgaard et al., 2015a). This can be written as $q = C_m^* \cdot V$, where $C_m^* = C_m(1 + V_0/V)$ is an effective capacitance that includes polarization effects. This element is shown in **Figure 2**. The arrows across conductive and capacitive elements indicate the voltage-dependence.

2.2.2. Black Lipid Membrane Experiments

A DMPC:DLPC:cholesterol = 77.3:7.7:15 (mol:mol:mol) mixture was dissolved in decane to a final concentration of 10 mg/mL. Black lipid membranes were formed on a circular aperture in a 25 μm thick Teflon film. We used commercially available horizontal bilayer slides (Ionovation GmbH, Germany) made of two microchambers (filled with ∼150 μl of the same electrolyte solution) separated by an horizontal Teflon film. The upper and lower chambers are connected only through the 120 μm aperture in the film. Once a small droplet (≈0.2 μl) of lipid solution is placed in the upper chamber close to the aperture, a bilayer is formed automatically by a microfluidic perfusion system (Ionovation Explorer, Ionovation GmbH, Germany). The membrane formation was monitored with capacitance measurements and was automatically repeated until the membrane capacitance was stable above a minimum threshold value of 40 pF. The bilayer slide was placed on the work stage of a in inverted microscope (IX70, Olympus, Japan) which allowed for optical monitoring of the bilayer formation. See Zecchi et al. (2017) for more details.

2.2.3. Differential Scanning Calorimetry

Heat capacity profiles were obtained using a VP scanning-calorimeter (MicroCal, Northampton, MA) at a scan rate of 5°/h.

2.3. Electrophysiological Experiments

All experiments are representative and qualitatively reproducible. However, membranes break easily. In patch clamp measurements, voltage-jumps were performed between 200 and −200 mV in steps of 25 mV (**Figure 3**). Each step lasts 3.1 s for 17 different voltage-clamp traces needed for one I-V profile. Thus, each series lasts about 53 s. Only few membranes are stable long enough for a complete series of voltage jumps that lead to a single I-V profiles. Even less membranes allow for recording several I-V profiles to check for reproducibility and the variation of pipette depth. The typical interval between two I-V profiles recorded on the same membrane is 1–5 min.

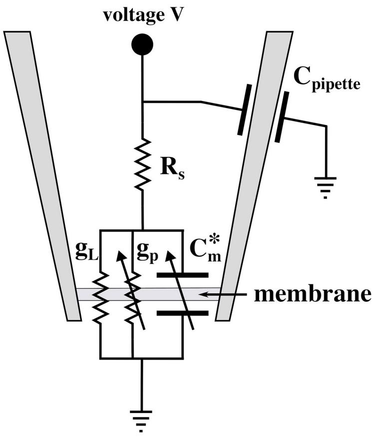

FIGURE 2 | Equivalent circuit diagram of the patch experiment. Here, C_m^* is the effective voltage-dependent capacitance of the membrane (see text), g_p is the voltage-dependent conductance of the lipid pores, g_L is the constant leak conductance, R_S is a series resistance of the pipette interior, $C_{pipette}$ is the capacitance of the pipette, and V is the externally applied voltage.

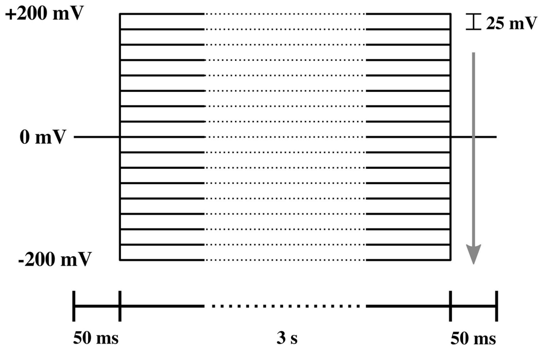

FIGURE 3 | Protocol of the voltage steps used in the I-V measurement. The lower bar indicates the duration of each part of the protocol. The arrow shows the direction of voltage steps, which ranged from 200 to −200 mV in steps of −25 mV.

The series of I-V profiles shown in **Figure 7** (top) contains five traces for one single depth of the pipette in the aqueous medium, which corresponds to 10–25 min. Since we could measure on this membrane at three different depths, the membrane was stable for a total of ∼30 min–1 h. In total, we had nine membrane patches that were stable enough to allow us obtaining complete I-V profiles. Of those, three did not show channels but only leak conductance. There were six membranes that displayed both linear and rectified I-V profiles. Two of those were stable enough to record so many I-V profiles that one could obtain several curves for several depths of the pipette. For this reason, all patch clamp data shown in this paper originate from two different membrane patches. We name them membrane 1 and membrane 2 throughout the text. Those experiments are included in this work. However, the other membranes displayed similar behavior. We also obtained several membranes in the BLM-setup. They always yield symmetric IV-profiles.

The voltage-jump protocol for the BLM measurements shown in **Figure 11** was different. Here, we changed the voltage from +10 to −10 mV, then to 20 and −20 mV, and so on (not shown).

3. RESULTS

3.1. Description of the Experiment

After a voltage jump, all the current traces measured showed an initial transient decay of about 10 ms from a current peak at $t = 50$ ms (the time of the voltage step, see **Figure 4**) to their steady state value (the current value at $t = 3$ s). The transient part of the current contains information about the charging of the pipette (and electrodes), the charging of the membrane and any relaxation phenomena in the membrane which can lead to changes in resistance, capacitance, and polarization.

The relaxation processes are well-described by a biexponential function (**Figure 4**). We decided to not include the first data point in the fit. This corresponds to the first 100 μs which is the time resolution of our experiment.

The current response of the membrane after a voltage jump was measured. As an example, we show two sets of recordings in **Figures 5A,B**. Possible voltage offsets were corrected by subtracting the mean value of the current at the holding voltage from the corresponding current trace during the step protocol.

In order to obtain steady state currents for the I-V profiles, we restricted ourselves to determine averages of the second half of the current traces corresponding to the last 1.5 s after each voltage step (open circles in **Figures 5C,D**).

3.2. General Trends

Both recordings in **Figures 5A,B** were obtained from the same membrane (membrane 1). Nevertheless, they show distinct features that are representative of all the recordings made on the two membranes used in the patch clamp measurements described in this work. These are outlined below.

Figure 5A shows the current response of the membrane when the tip of the pipette was at the air/water interface. The current traces are symmetric with respect to voltage and their relatively small value indicates a large membrane resistance. This can be quantified by inspection of the correspondent current-voltage relationship (**Figure 5C**). A linear fit to the data in **Figure 5C** gives a value for the conductance of $g_L = (372 \pm 4)$ pS, or equivalently, a membrane resistance of about $R_0 = 2.69$ GΩ. The conductance in this case is constant and independent of voltage.

A different scenario is shown in the traces plotted in **Figure 5B**, measured for the same membrane at a different depth with respect to the water surface (3 mm). Here, the current response to positive and negative voltage-jumps is clearly different, as confirmed by the asymmetric and non-linear I-V curve in **Figure 5D**. The membrane appears to be more conductive at positive voltages, showing a fairly constant conductance of about $g = 1.7$ nS (or resistance of roughly $R = 500$ MΩ), as obtained by a linear fit to the positive voltage range. Thus, it is almost five times larger than the linear I-V profile shown in **Figure 5C**. The response to negative voltages, in contrast, is slightly non-linear and less pronounced, comparable in magnitude to the linear case.

The data point at 200 mV in **Figure 5D** has not been included in the fit. In our protocol this is the first datapoint. The corresponding current trace shows a transient behavior and does not equilibrate fully in the 3 s of the test pulse. This

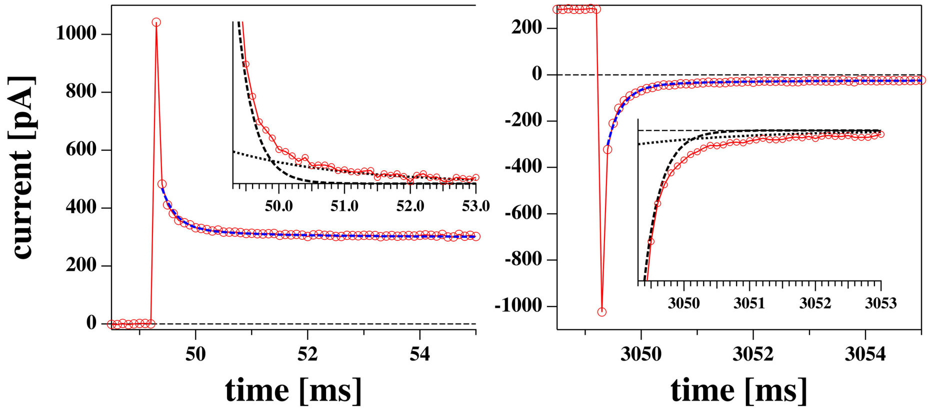

FIGURE 4 | Initial phase of a voltage jump from 0 to 0.175 V (left) and back (right) from the experiment shown in **Figures 5B,D**. The profiles are reasonably well-fitted by a biexponential function with the same two relaxation times for the jump in both directions. The two exponential functions are shown in the inserts.

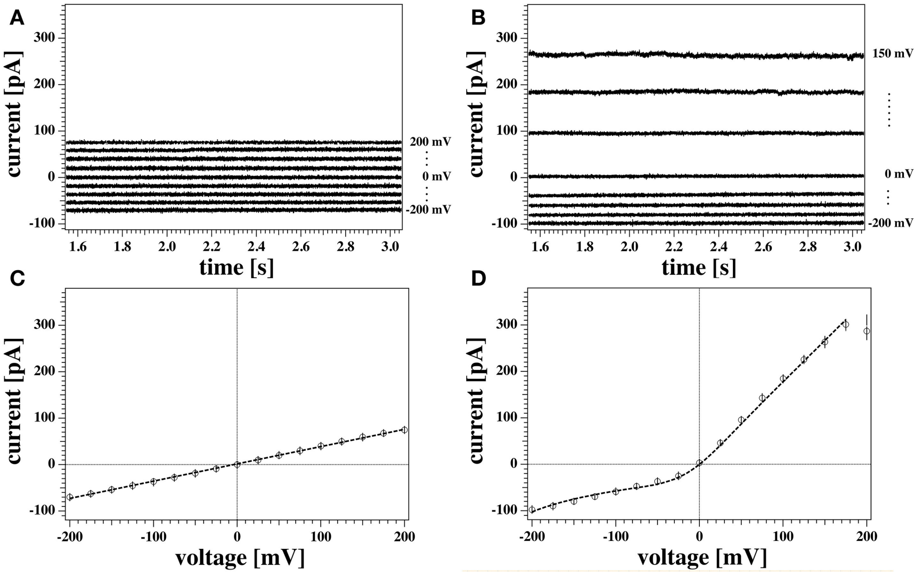

FIGURE 5 | (A,B) Detail of the last 1.5 s of two representative current responses to the voltage pulses shown in **Figure 3** recorded from the same membrane. The graph shows the response to only every other voltage step for clarity. Current traces were corrected for the initial offset at zero voltage. Currents in **(A)** were measured with the tip of the pipette at the air/water interface. Traces in **(B)** were measured with the tip of the pipette 3 mm below the water surface. **(C,D)** Current-voltage relationship for the traces in **(A,B)**, respectively. All points of all the current traces between 1.5 and 3 s were plotted and fitted. The model used for the fit were a linear relation in **(C)**, and Equation (5) in **(D)** as outlined in the Theory section. The fit gives a conductance of $g_L = 372 \pm 4$ pS for the recording in **(A,C)**, and a voltage offset of $V_0 = 209$ mV for the recording in **(B,D)**. Solid circles show the average values of the current. The measurements were performed at a temperature of $T = 297.85$ K.

transient behavior of the current starting from a low conductance value and increasing without reaching a steady state was not uncommon. It was only observed at positive high voltages, and under few instances (in case of reversed voltage protocol) at high negative voltages. In the absence of any satisfactory explanation, in this work traces showing similar behaviors were discarded from steady-state analysis. Further, we generally find that the first datapoint in each I-V profile is an outlier with respect to an otherwise systematic behavior. This might also be related to an equilibration of the membrane patch after the first voltage jump of a series.

The two sets of recordings shown in **Figures 5A,B** have been performed at different depths of the pipette tip with respect to the bath surface. Different vertical positions of the pipette relative to the surface correspond to different values of hydrostatic pressure at the bath-facing leaflet of the membrane. Since the pressure at the inner leaflet is constant, this corresponds to different pressure gradients across the membrane. A pressure difference between the two leaflets can result into a net curvature according to the Young-Laplace law. Curvature in a chemically symmetric membrane can break the otherwise symmetric charge and dipole distribution, and therefore produce a voltage offset, as outlined in Mosgaard et al. (2015a).

3.3. Theoretical Considerations

3.3.1. Current-Voltage Relations

The general tendency of a membrane to display a higher conductance at positive as compared to negative voltages is known as outward rectification. In the case of biological membranes, it's customary to ascribe electrical rectifications like the one shown here to the voltage dependent behavior of certain protein-channels spanning the membrane. However, outward rectified I-V curves like the one of **Figure 5D** have already been observed earlier in protein-free membranes (Laub et al., 2012; Blicher and Heimburg, 2013). In these publications, the rectified behavior was explained on the basis of a capacitor model like the one introduced below. It requires the formation of membrane pores and a spontaneous electrical membrane polarization as caused from an asymmetry between the two monolayers of a bilayer (Mosgaard et al., 2015b). This could, for instance, originate from membrane curvature that changes the relative lipid dipole density on the two monolayers of the membrane.

We will describe the conductance of a membrane by using a description from Mosgaard et al. (2015a).

We assume that the membrane contains pores with an open probability that display a quadratic voltage dependence (Winterhalter and Helfrich, 1987; Blicher and Heimburg, 2013). The chemical potential difference between open and closed pore, μ_0, is given by

$$\Delta\mu_0 = \Delta\mu(0) + \alpha\left[(V + V_0)^2 - V_0^2\right] \qquad (1)$$

Here, $\Delta\mu(0)$ is the free energy of a pore at a voltage of $V = 0$ V, and α is a coefficient. $\Delta\mu_0$ displays a minimum at $V = -V_0$, where V_0 is the voltage offset that originates from a polarization of the membrane. Its origin will be discussed below. Defining an equilibrium constant $K = \exp(-\Delta\mu_0/kT)$ between a closed and an open pore, we obtain for the probability of finding an open or a closed pore, P_{open} or P_{closed}, respectively:

$$P_{open} = \frac{K}{1+K} \quad \text{and} \quad P_{closed} = \frac{1}{1+K} \tag{2}$$

which sum up to one. This formalism assumes that the membrane is equilibrated. This is permissible for the following reason: In the past, we have investigated equilibration processes in membranes (Grabitz et al., 2002; Seeger et al., 2007). We generally found that the relaxation time is proportional to the heat capacity. The relaxation times in DPPC multilayers are about 30 s at the heat capacity maximum, in large unilamellar vesicles of DPPC they are about 1–2 s, in biological preparation, such as lung surfactant about 100 ms at the maximum. At the edge of transitions, the relaxation time is of the order of 1–100 ms. Since we attribute the lipid pores to fluctuations of the membrane state, the open-close kinetics of the pores is in fact identical to the relaxation time scale. In the experiments shown in **Figures 8–10**, the open lifetime of the channels is of the order of 10–100 ms. Thus, equilibration happens on a time scale much shorter than our experimental time of 3 s. We also see in **Figure 12** (section 3.3.6) that relaxation processes are on the time scale of a few milliseconds.

If we assume that conduction occurs exclusively via open pores in the membranes, the overall current through the membrane pores will be given by

$$I_p = g_{pore} N P_{open} V \equiv g_p P_{open} V\ , \tag{3}$$

where g_{pore} is the conductance of a single open pore, N is the total number of pores, and $g_p = N g_{pore}$ is the conductance of N open pores.

In the experimental section we find that there exist current traces that do not display any open pore events. This is mostly the case when the current-voltage relation is linear. It is therefore possible that there exists a voltage-independent leak current, I_L, and voltage-dependent current through pores in a membrane, I_p. If this were the case, the current-voltage relation in Equation (3) would be given by

$$I = I_L + I_p = \left(g_L + g_p P_{open}\right) V \tag{4}$$

where g_L is a constant leak-conductance of the membrane in the absence of pores. This equation assumes identical ion concentrations on both sides of the membrane (Nernst potential E_0 is zero). If the ion concentrations were different from zero, we would obtain

$$I = \left(g_L + g_p P_{open}\right)(V - E_0) \tag{5}$$

with $E_0 = (RT/zF)\ln(c_{out}/c_{in})$ for an ion with charge z and the concentrations c_{out} and c_{in} outside and inside of the pipette, respectively. Since we use the same buffer in the pipette and in the external medium, the Nernst potential in our experiments is $E_0 = 0$ V.

Figure 6 shows the non-linear rectified I-V profile from **Figure 5D** and three attempts to describe it. We expect the I-V profile to pass through zero ($E_0 = 0$) because we have the same ion concentrations on both sides of the membrane. We corrected for slight deviations in the current at zero voltage. For the fit in **Figure 6A** we assumed that there is only one single permeation process by pores and no leak-conductance (ie, $g_L = 0$ in Equation 5). The fit is reasonable but not perfect. The insert shows the calculated pore open-probability. It displays a minimum at -162 mV corresponding to a spontaneous polarization of the membrane that leads to a voltage offset of $V_0 = +162$ mV. The minimum open-probability at this voltage is about 0.27 which requires 27% of all pores being open. However, we will see below that no open pores can be detected at this voltage. For this reason we decided that this is not the most likely scenario. **Figure 6C** shows a free fit allowing for a variation of the leak conductance g_L. The straight line in this panel corresponds to the leak currents $I_L = g_L \Delta V$. In this fit, the open probability of the pores reaches a minimum at -208 mV and the minimum open probability of pores is below 1%. Since there is one more fit parameter, it is not surprising that this describes the measured I-V profile

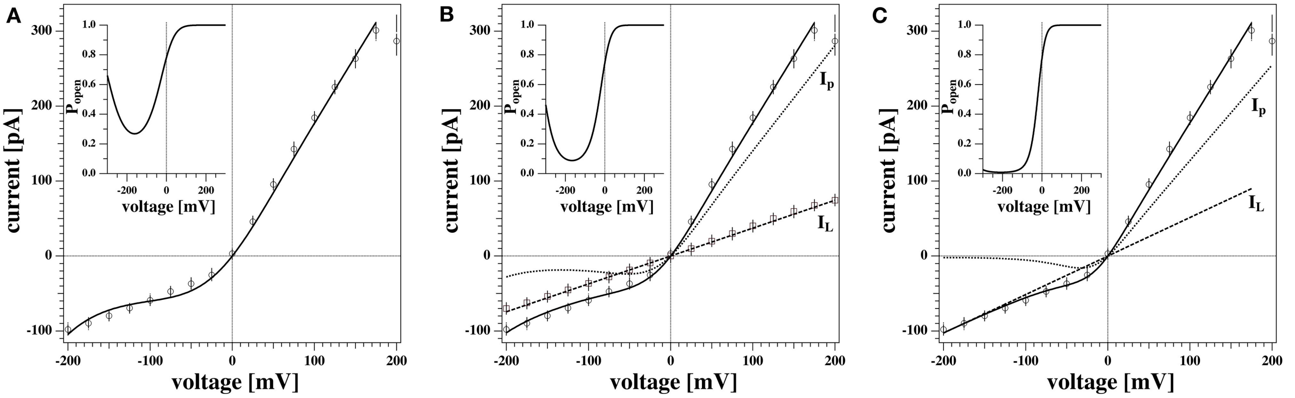

FIGURE 6 | Three different scenarios to fit the non-linear current-voltage relations. **(A)** Conductions by pores only ($g_L = 0$). **(B)** Conduction by voltage-dependent pores and a voltage-independent fixed leak current taken from the experiment in **Figure 5C**. **(C)** Same as **(B)** but the leak current was not fixed. The latter fit describes the data best. The inserts show the pore open probability for the three different scenarios. The minimum of P_{open} represents the offset voltage $-V_0$. See text for details.

better. However, what also speaks in favor of this description is that one does not expect open pores at negative voltages. Only at positive voltages, the open probability of pores is significantly different from zero. The fit in **Figure 6C** is composed of a leak current I_L and a pore current I_p, which are independently shown in the figure.

In our experiments we sometimes find linear I-V relations and sometime outward rectified profiles. It is not exactly clear why both cases occur with the same experimental settings for the same membrane. Interestingly, the linear I-V profile (**Figures 5C**, **6B**) yields a quite similar conductance g_L as leak current I_L in **Figure 6C**. This supports our assumption that the conductance of the lipid membranes is a phenomenon described by two different processes: A voltage-independent leak conductance and a voltage-gated pore formation process.

Therefore, we tentatively assumed that the two cases are only distinguished by the presence or absence of pre-pores that are ready to open but that the leak conductance of the membrane is identical in all experiments. **Figure 6B** shows a fit where the leak conductance g_L was obtained from the linear I-V profile shown in **Figure 5C**. Its value was kept constant for fitting the rectified profile. We see that this describes the I-V profile quite well.

3.3.2. Relaxation Processes

In **Figure 4** one could see that the initial current during equilibration displays more than one exponential component. Time-dependent changes of the membrane current can have two origins. The first is the charging of the membrane capacitor, of pipette walls and electrodes. The charge on a capacitor is given by

$$q = C_m V + A \cdot P_0 \qquad \left(\equiv C_m(V + V_0)\right) , \tag{6}$$

where C_m is the capacitance, A is the area of the capacitor and P_0 is its spontaneous polarization (Mosgaard et al., 2015a), which is related to the voltage offset V_0 described above. The capacitive current is therefore given by

$$I_c(t) = C_m \frac{dV}{dt} + V \frac{C_m}{dt} + \frac{d}{dt}(A \cdot P_0) \tag{7}$$

The first term on the right hand side is considered in electrophysiology, while the second and third term are neglected. Thus, in the textbooks it is assumed that the capacitance of the membrane and all membrane properties are constant after a voltage jump. This assumption requires that the membrane structure is independent of voltage, which is practically impossible for a soft molecular layer the will deform in the presence of electrostatic forces. The time constant of charging a constant capacitor in an electrolyte solution, τ_0, is typically fast because it is dominated by the low resistance of the electrolytic medium. The second term in Equation (7) represents the time-dependent change in capacitance caused by a voltage-induced structural change in the membrane, and the third term is the related voltage-induced change in the spontaneous polarization of the membrane, for instance caused by changes in lipid head-group orientation or changes in curvature. Due to electrostriction, the capacitance of membranes is voltage-dependent (Heimburg, 2012; Mosgaard et al., 2015a,b). The capacitance of a membrane is given by $C_m = \varepsilon_0 \varepsilon A/D$ where A is the membrane area and D is the membrane thickness. Electrostriction reduces the membrane thickness and increases the membrane area. Both effects lead to an increase in capacitance, ΔC_m. This effect is most pronounced close to melting transitions in membranes because here the membranes are softest. This is the situation treated in this paper (see **Figure 1**). In this paper we assume that the slow timescale of capacitance and polarization changes, τ_m, results from the relaxation processes in membranes, which are in the millisecond regime (Grabitz et al., 2002; Seeger et al., 2007).

A further time-dependent change in the membrane current may originate from voltage-induced changes in the membrane conductance, Δg, due to changes in membrane structure. It is known that membranes are more permeable in their melting transitions (Papahadjopoulos et al., 1973; Nagle and Scott, 1978; Sabra et al., 1996; Blicher et al., 2009). Therefore, a voltage-induced change in membrane structure as caused by electrostriction will also change the conductance of the membrane. In the presence of a spontaneous voltage-offset (polarization) of the membrane, this effect will be different for positive and negative voltages, i.e., it will be rectified. Since it is related to structural changes in the membrane, the time-scale of its changes will also be dictated by the relaxation time-scale in the membrane, τ_m, where we have assumed a single-exponential relaxation process (as described in Grabitz et al., 2002; Seeger et al., 2007).

For the total membrane current we obtain for a jump from voltage V_b before the jump to a voltage V_a after the jump:

$$\begin{aligned} I(t) &= \frac{C_{m,b}}{\tau_0} \Delta V e^{-\frac{t}{\tau_0}} + \left(\Delta C_m V_a + \Delta(AP_0)\right) \frac{e^{-\frac{t}{\tau_m}}}{\tau_m} \\ &\quad + \left(g_b + \Delta g \left(1 - e^{-\frac{t}{\tau_m}}\right)\right) V_a = \\ &= g_a V_a + \frac{C_{m,b}}{\tau_0} \Delta V e^{-\frac{t}{\tau_0}} \\ &\quad + \left(\frac{\Delta C_m V_a + \Delta(AP_0)}{\tau_m} - \Delta g V_a\right) e^{-\frac{t}{\tau_m}} = \\ &= g_a V_a + A_0 e^{-\frac{t}{\tau_0}} + A_m e^{-\frac{t}{\tau_m}} , \end{aligned} \tag{8}$$

where the term related to charging the capacitor is described by the timescale τ_0 and the amplitude A_0. All terms related to changes in membrane structure change with the time constant τ_m and amplitude A_m. $C_{m,b}$, $C_{m,a}$, g_b, and g_a are the steady-state capacitance and conductance before and after the voltage jump, respectively. $\Delta V = V_a - V_b$, $\Delta C_m = C_{m,a} - C_{m,b}$, $\Delta g = g_a - g_b$, and $\Delta(AP_0)$=$(AP_0)_a - (AP_0)_b$ are the differences of the respective functions in steady state before and after the voltage change. We see that the steady-state current after a jump is given by

$$I(V_a) = g_a V_a . \tag{9}$$

The time-dependent current contributions are dominated by two time-scales. One of them, τ_0, is related to charging a constant capacitor, while the second one, τ_m, is slow and dominated by the relaxation process of conductance, capacitance and polarization of the membrane.

3.3.3. Experiments at Different Pipette Depths

In order to better understand the appearance of the non-linear behavior and the origin of the voltage offset, I-V measurements were performed on the same membrane at different positions of the tip in the water bath. This is an indirect attempt of controlling the hydrostatic pressure gradient across the membrane, which increases linearly with the depth, *h*.

With the aid of a micromanipulator, the tip of the pipette was lowered from its initial position (close to the water surface) down to different depths inside the water bath. **Figure 7** shows two series of I-V curves measured for the same membrane (membrane 1) at different positions, i.e., at 1 and 3 mm below the water surface, corresponding to a pressure difference of about 98 and 294 Pa. The numbers close to each curve indicate the temporal order of the recording in each sequence. The time interval between subsequent recording was not fixed but was never more than 5 min (with an average of 1 min and a half). Fits for the I-V profiles were generated by using Equation (4) and the procedure used in **Figure 6C**. The two contributions to the conductance are displayed separately in the small panels. No qualitative differences can be observed between the recordings at 1 and 3 mm. Both positions produce consistently both linear and non-linear responses, the latter being always in the form of outward rectified I-V curves. Interestingly, during

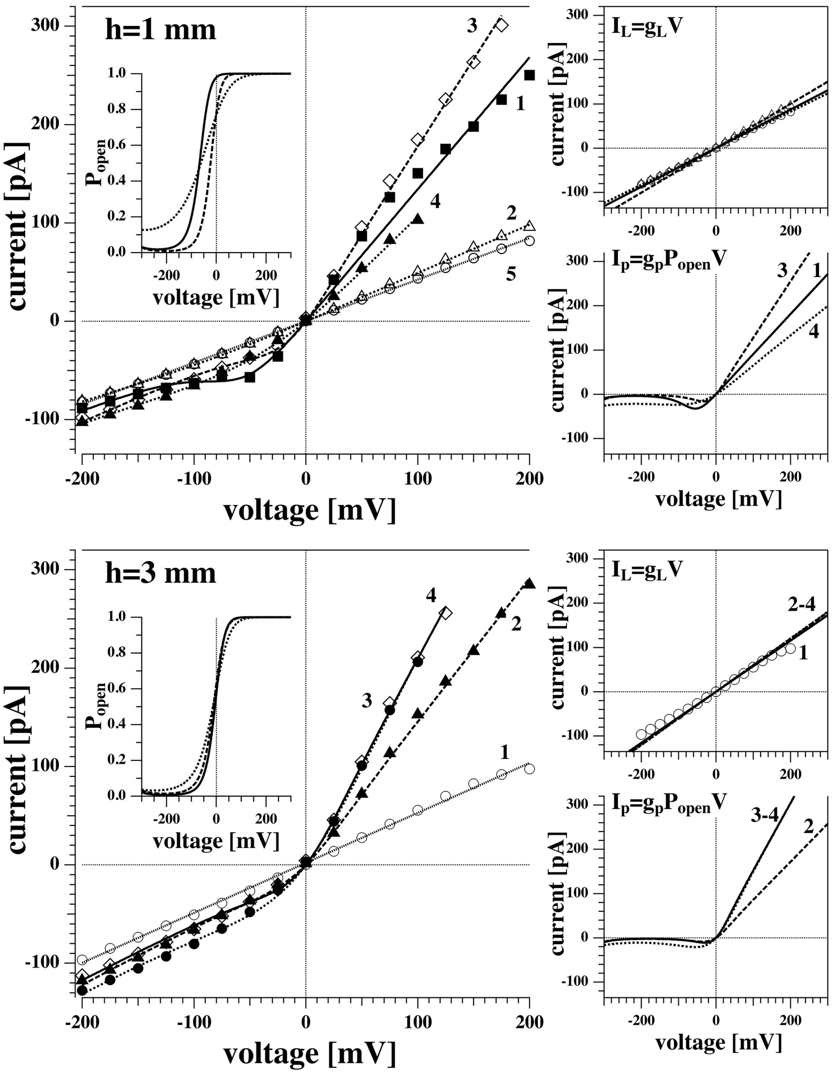

FIGURE 7 | I-V recordings of the same membrane as **Figure 5** (membrane 1) at different depths below the air/water interface. **(Top)** Tip 1 mm below the surface. **(Bottom)** Tip 3 mm below the surface. Both sets of recordings show two different electrical behaviors, with both linear and non-linear I-V relationships. The curves were measured in sequence and are numbered in order of appearance. Only the average values of the current are displayed for clarity. The dotted lines are fit to all current data points.

each voltage-jump sequence, one behavior was consistently maintained while in the next sequence one can observe a different behavior. For instance, in **Figure 7** top left, the first trace was outward rectified, the second was linear, the 3rd and 4th trace were rectified and finally the 5th was linear. The reason for this behavior is not clear. It seems that the linear contribution of the conductance is the same in both, linear and rectified profiles—but that it is not always possible to activate pores. The values of the voltage offset as obtained from the fit vary slightly from one recording to the other, but they are comparable between the two different positions. On average, it is 243 (±34) mV at 1 mm depth and 221 (±20) mV on average at a depth of 3 mm. The leak conductance g_L and the pore conductance g_p were larger at larger depth of the patch pipette. For membrane 1, the conductance g_L increased by 32% and the pore conductance g_p by 37% when going from 1 to 3 mm depth.

It is interesting to note that trace 1 in the top left panel of **Figure 7** displays a voltage regime around −50 mV, in which the dependence of the current on voltage, dI/dV, is negative. This is impossible without a voltage-dependent conductance. It can be explained if one considers that around −200 mV, all pores are closed while at −50 mV some pores are open. For this reason, one can find a larger negative current at −50 mV than at −200 mV.

3.3.4. Channel Activity

Non-linear I-V curves and outward rectification are not the only properties of the lipid membranes studied here that resembled those of biological membranes. We also find that several recordings of membranes showed current fluctuations and quantized steps that are typical of ion channel activity.

Figure 8 shows two current responses of membrane 2 to the same voltage protocol as describe in section 2.3. The membrane had the same lipid composition as the one of **Figures 5–7**. The two recordings shown here were obtained with the membrane at 4 mm (left) and 8 mm (right) below the water surface.

One can recognize that the I-V profiles in both cases are non-linear. They display a larger conductance at positive voltages, which is more pronounced at the depth of 8 mm as compared to the 4 mm recording. Further, one recognizes discontinuous

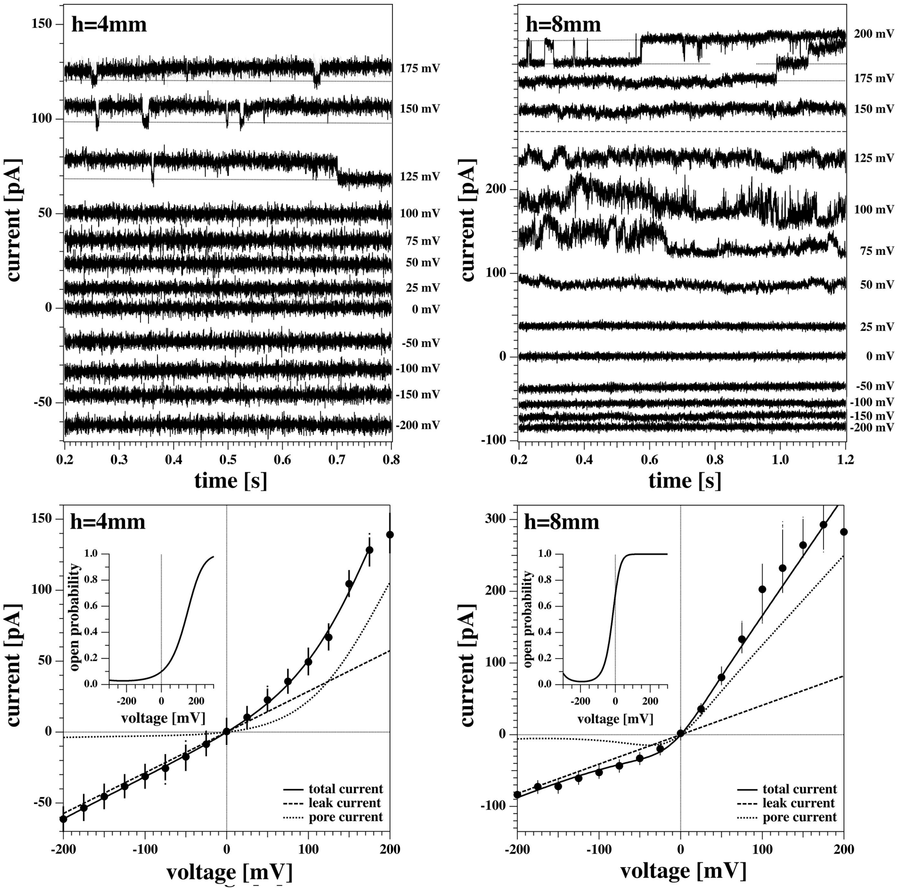

FIGURE 8 | Current response of membrane 2 at 4 mm **(Left)** and 8 mm **(Right)** below the water surface. The current response to negative voltages doesn't show current fluctuations. **(Left)** The membrane current at high positive voltages shows quantized steps to a lower current value before jumping down to it and staying there for the lower voltages. The current response at 200 mV shows a constant drift in the baseline and is not shown here. **(Right)** The current responses to 200, 175, and 150 mV have been shifted to the top panel for clarity as they overlap. The membrane shows current fluctuations for increasing voltages. They end up in well-defined quantized steps at high voltages when pores are open most of the time.

conduction steps in both experiments, which are also more pronounced at 8 mm depth. The fits to the I-V profile are performed as in **Figures 6**, **7**.

A continuous recording of this membrane at 4 mm depth and a fixed holding voltage allowed to observe consistent channel-like activity for a longer period of time. **Figure 9** shows the first 5 s of the raw current trace. The trace shows clear quantized steps from a baseline at 94 pA that was slightly drifting to a set value of about 106 pA. The step-size was about 13 pA, corresponding to a single lipid channel conductance of about ∼68 pS, very similar to the single channel conductance in the same experiment at 150 and 125 mV. Thus, the single channel conductance is probably independent of voltage, as already found in Blicher and Heimburg (2013). The step size at 200 mV for the 8 mm depth recording in **Figure 8** (right, top) yields a single channel conductance of about 137 pS, which is twice as high as in the 4 mm recording in the left panels. The current traces in **Figure 8** indicate that at high positive voltage, pores can be open most of the time.

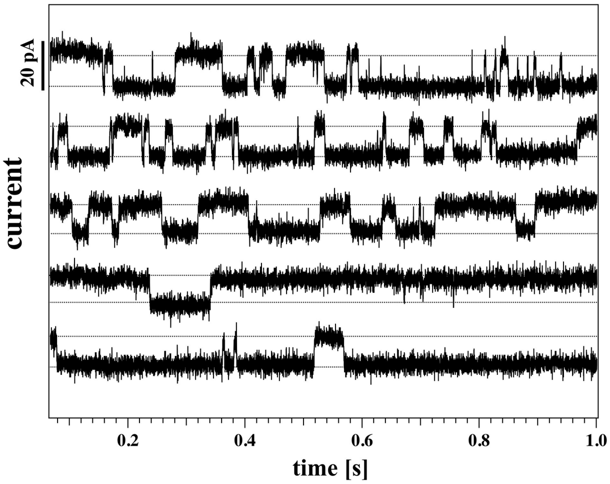

FIGURE 9 | Continuous current recording for the same membrane as **Figure 8** (membrane 2) at a holding voltage of 190 mV, 4 mm below the water surface (T = 297.15 K). The graph shows 5 consecutive seconds of recording, starting from the top row. The time-intervals are presented as a stack for clarity.

The above recordings were observed when the pipette tip was 4 and 8 mm below the water surface, so slightly lower than the recordings shown for membrane 1 in **Figure 7**.

We observed channels at high positive voltages and at different depths. In membrane 2 (**Figures 8**, **9**), channel activity seemed to increase with increasing depth of the tip in the water bath. At the same time, the voltage threshold for activity onset seemed to decrease with increasing depth/pressure. However, we have only three data points in this sense (i.e., three different depths). Note that the depths here are larger than those for the previous membrane. Interestingly, also the first membrane showed current fluctuations when brought 10 mm below the air-water interface. This is shown in **Figure 10**. The current traces correspond to voltage steps in the range 200−0 mV (we did not record traces for negative voltage because at 0 V the membrane ruptured).

The membrane in **Figure 10** ruptured at 0 mV. Indeed, membrane rupture at large depths was one of the main obstacles to investigating this phenomenon further. In fact, membrane instability seemed to increase with increasing depth.

Summarizing, it seems that larger depth of the pipette enhances channel activity, and they occur at lower voltage. In the previous section, we have also found large conductances g_L and g_p at larger depth. This suggests that the lipid membrane channels are mechanosensitive.

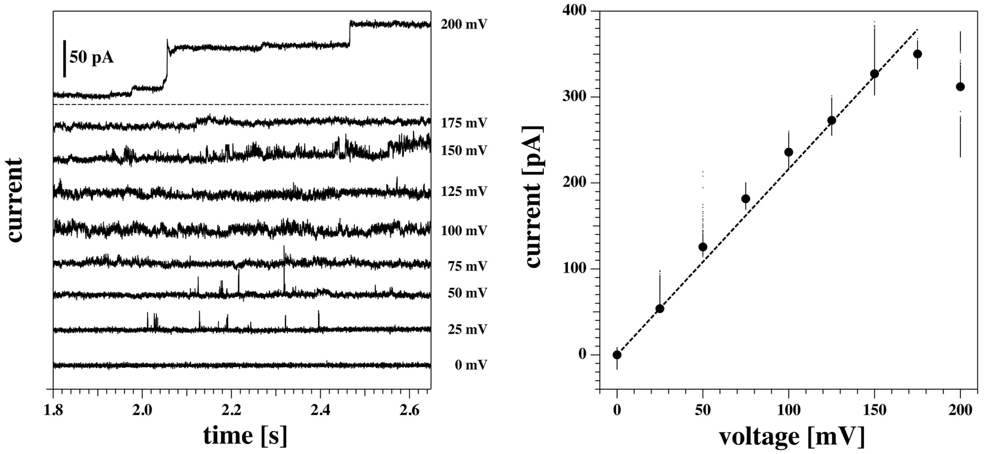

FIGURE 10 | Current response of the same membrane as **Figures 6**, **7** (membrane 1) at a depth of 10 mm below the water surface. The membrane ruptured at 0 mV. Hence only the positive range is shown. **(Left)** Current traces at different voltages. The top trace is the response to the first jump of the protocol (from 0 to 200 mV), and it has been plotted separately for clarity. At this voltage, the membrane shows a step-wise increase in conductance, from an initial value of about 1.2 nS to a final one of roughly 1.8 nS. In the bottom panel, the other traces are shown. Current fluctuations start to appear in the form of spikes already at 50 mV, and increase in number and duration at higher voltages. **(Right)** Current-voltage relationship for the traces shown at the left. A linear fit gives a value of the conductance of 1.8 nS. This is in line with the final value of conductance for the trace at 200 mV. Due to its transient behavior, however, this trace has not been included in the fit.

3.3.5. Symmetric I-V Profiles in Black Lipid Membranes

In a previous publication (Zecchi et al., 2017) we suggested that the offset voltage responsible for the asymmetry and the apparent outward rectification of the I-V profiles is caused by flexoelectricity. Bending of the membrane creates an electrical polarization that is roughly proportional to the curvature (Petrov, 2001; Petrov and Sachs, 2002; Mosgaard et al., 2015b). The tip diameter of a patch pipette is small. The maximum curvature possible is that of a half sphere with a radius that corresponds to the radius of the tip opening. For a pipette with 1 µm diameter, the maximum curvature is $c = 1/500nm$. However, if one uses black lipid membranes spanning a hole with a diameter of about 100 µm, the maximum possible curvature is 100 times smaller (see Zecchi et al., 2017 for details about this argument). If the voltage offset were in fact caused by flexoelectricity, the voltage offset would be practically absent in black lipid membrane measurements. This means that patch pipettes allow for high curvature, while black lipid membranes rather imply membranes without or with low curvature.

Figure 11 shows a black lipid membrane experiment made with the Ionovation Explorer (see section 2). The aperture in this experiment had a diameter of about 120 µm. In the patch experiment it was ∼8 µm, i.e., about 15 times smaller. We used a membrane with 77.3% DMPC, 7.7% DLPC, and 15% cholesterol and a temperature of 32°C at the upper end of the melting transition of this membrane (**Figure 1**). Cholesterol is known for largely broadening the melting transitions of membranes, thus reducing domain formation and fluctuations. This renders membranes more stable. This is an important factor in black lipid membrane measurements because of the notorious instability of the membranes close to transitions.

We found an I-V profiles that is completely symmetric, i.e., it does not display a significant voltage offset (the fit yields ∼−5 mV). We found a leak conductance of $g_L = 270$ pS and a pore conductance of $g_p = 863$ pS when fitting it with Equation (4). The conductance steps at 100 mV correspond to 78 pA, comparable to a single channel conductance of ∼78 pS. This is similar to the single channel conductance of the traces in **Figure 7** where we found ∼68 pS. This indicates that the magnitude of the conductance steps does not depend on the size of the membrane. Most interestingly though, the near absence of a voltage offset allows seeing that the rectification pattern is also symmetric, and that channel activity appears both at positive and negative voltages in the non-linear part of the I-V profile that we attribute to pore formation. This supports our interpretation of having two conduction processes present.

3.3.6. Membrane Relaxation

In section 3.3.2 we described how after a voltage jump one finds transient equilibration processes that consist of capacitive currents and time-dependent changes in conductance (**Figure 4**). We have argued that one expects (at least) two relaxation processes. One is related to charging the capacitor via the electrolyte and a second one is coupled to changes in membrane structure with effects both on conductance and capacitance. In the present set of experiments, we performed voltage jumps from zero to a fixed voltage, and back to zero. The voltage across the membrane must not necessarily be equal to the voltage adjusted by the setup. The resistance of the pipette is a series resistance of glass pipette and membrane. Occasionally, our membrane ruptured during the experiment (e.g., **Figure 8**). Thus, one can observe the resistance of the setup with and without membrane after an instantaneous process. We found that in the absence of a membrane, the resistance is at least 2 orders of magnitude smaller

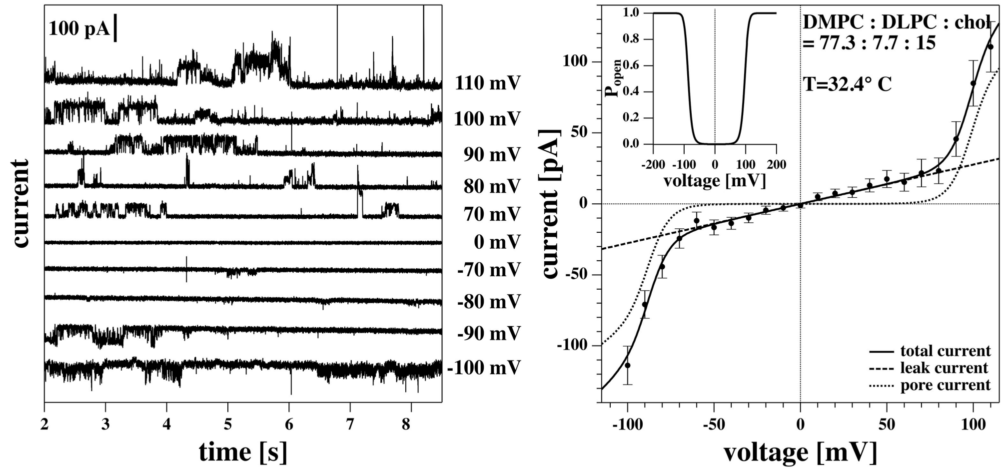

FIGURE 11 | Recordings on a DMPC:DLPC:chol. = 77.3:7.7:15 BLM measured at 32.4°C. **(Left)** Current traces. For better visibility, they are evenly spaced on the vertical axis. Note, the current traces in the linear regime of the I-V profile are not shown. **(Right)** I-V-profile. The solid line is a fit of the I-V profile to Equation (5). The insert represents the pore open probability. Note that for the BLM, the I-V profile is symmetric and the channel activity occurs at both higher positive and higher negative voltages.

than in the presence of the membrane. From this we concluded that the adjusted voltage was practically identical to the voltage across the membrane and that the resistance and capacitance of the pipette (with a tip diameter of about 8 µm) do not contribute much to the observed currents.

We describe the relaxation process by a bi-exponential function (see **Figure 4** and Theory section):

$$I(t) = g_a V_a + A_0 e^{-\frac{t}{\tau_0}} + A_m e^{-\frac{t}{\tau_m}}$$

We fitted the relaxation profiles shown in **Figures 12A,B** with biexponential profiles. We found that one obtains good fits of the relaxation profiles if the same relaxation times were taken for a given membrane for all voltages jumps from zero to a fixed voltage (**Figure 12A**, 0 → V) and back (**Figure 12B**, V → 0). Empirically, we adjusted the two relaxation times to 258 µs (dominated by the digital filter time constant of the experiment) and 1.74 ms for all profiles. What is fitted are the amplitudes A_0 and A_m of the two relaxation processes (**Figures 12C,D**).

We find that the bi-exponential relaxation profiles with fixed time constants describe the experimental data well. The amplitude A_m of the slow process displays a linear dependence on the voltage for both the linear and the rectified I-V-relation shown in the top panels of **Figures 12C,D** (blue symbols). In contrast, the fast process with amplitude A_0 (red symbols) is similar to the voltage dependence of the IV relation. It displays a linear behavior for the linear IV relation in **Figure 12C**, and a rectified behavior for the rectified I-V relation in **Figure 12D**. The analysis of the data in **Figure 8** yields a similar result. Taking into account the similarities between the voltage-dependence of the fast process and the steady state current, it seems plausible to assume that the fast relaxation processes contains elements from the relaxation of the conductance after a voltage jump. Since we attributed the non-linearity of the I-V profile to the opening of pores in the Theory section, we suggest that the fast process is related to the timescale of pore opening.

4. DISCUSSION

In this work, we studied the conductance of DMPC:DLPC = 10:1 and DMPC:DLPC:cholesterol = 77.3:7.7:15 membranes subject to voltage jumps of different magnitude and direction. The experiments had different aspects: (1) Studying I-V profiles at different depths of a patch pipette in the aqueous buffer. (2) Studying discrete channel opening- and closing events. (3) Comparing BLMs with lipid patches. (4) Determination of the kinetics of membrane equilibration after a voltage jump.

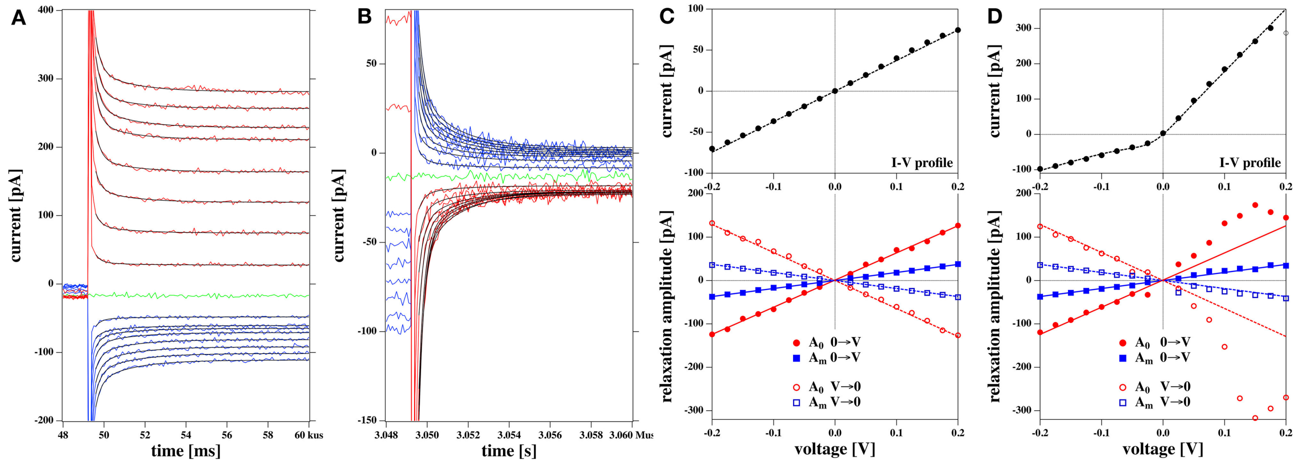

FIGURE 12 | Relaxation processes corresponding to the I-V profiles shown in **Figures 5C,D**: **(A)** Relaxation processes after a jump from 0 volt to a fixed voltage for the rectified I-V profile shown in **Figure 5D**. The thin black lines represent the fits to a biexponential function. V. **(B)** Relaxation processes after jump from a fixed voltage V to zero volts for the rectified I-V profile shown in **Figure 5D**. **(C)** Bottom panel: The fit parameters of the relaxation processes corresponding to **Figure 5C**. The top panel shows the corresponding I-V relation Both the amplitudes of the fast and the slow process, A_0 and A_m are linear as is the IV profile. **(D)** Bottom panel: The fit parameters of the relaxation processes corresponding to **Figure 5D**. Here, A_m is linear in voltage and equal in magnitude in both experiments (blue lines). Amplitude A_0 displays a non-linear voltage dependence for the rectified I-V profile (right). The solid lines at the bottom are the same in **(C,D)**. In **(D)** they serve as a guide to the eye to demonstrate the non-linearity of the voltage dependence for amplitude A_0. The current relaxation profiles in **(A,B)** were not corrected for a slight current offset from zero.

For each of the two membranes that were stable enough for an extended experimental sequence in the patch clamp experiments that we describe here, we found two quantitatively different current-voltage profiles. We either found linear I-V relationships or outward rectified I-V profiles, even under the same conditions and for the same membrane. We could well describe these profiles with a model that allows for two electrical conduction processes: A voltage-independent leakage and a voltage-dependent pore-formation (i.e., the occurrence of lipid ion channels). This is consistent with our observation that membrane channels are usually found in the rectified profiles at positive voltages. The asymmetry of the rectified I-V profile is a consequence of an offset potential V_0, i.e., a polarization of the membrane. The leakage-current of the rectified profiles was within error identical to that of the linear I-V profiles found for the same membrane in the absence of pores. One therefore has to conclude that the pore-formation sometimes lacks the nucleation sites for pore formation [sometimes called a pre-pore in the literature (Böckmann et al., 2008)]. Sometimes pores are present and sometimes they aren't. Details of this somewhat stochastic process remain to be explored. In contrast, the leak current is always present. In our theory, we assumed that the voltage-dependence of the free energy of the pores is quadratic in voltage, which has been proposed earlier (Winterhalter and Helfrich, 1987; Blicher and Heimburg, 2013; Mosgaard et al., 2015a). In Winterhalter and Helfrich (1987), it was also proposed that voltage may stabilize the formation of pores with a given radius, i.e., pores of fixed conductance, which we have also found here. Interestingly, the I-V relations of the BLM measurement was non-linear but symmetric, in agreement with previous findings (Wodzinska et al., 2009).

In the past, we have attributed an offset potential of the membrane to a spontaneous polarization of the membrane. Since our lipids are uncharged, the polarization may arise from membrane curvature due to an effect called flexoelectricity (Petrov, 2006; Mosgaard et al., 2015a). It arises from the asymmetric distribution of lipid dipoles in curved membranes. It may also arise from the asymmetric attachment of membranes to the glass pipette or from a lipid asymmetry (not likely in the present experiments). The offset potential V_0 results in the rectified profiles. The voltage dependence of the pore open probability is also relative to the voltage V_0.

We have changed the depth of the pipettes in the aqueous medium. This changes the pressure difference and might potentially lead to a change in the offset potential. For membrane 1 we found 243 ($\pm$34) mV on average in 1 mm depth, while we found 221 ($\pm$20) mV on average at a depth of 3 mm. The difference of these two values of V_0 is smaller than the standard deviation. Similarly, for membrane 2 we found $V_0 = 221$ mV at 4 mm depth and $V_0 = 193$ mV at 8 mm depth. Thus, while it might be that the offset potential is smaller at larger depth, the error margin does not allow us to make a trustworthy statement about its depth dependence. It seems that the origin of membrane polarization is not primarily the pressure difference across the membrane. However, it was generally true that the leak conductance g_L and the pore conductance g_p were larger at larger depth of the patch pipette. For membrane 1, the conductance g_L increased by 32% and the pore conductance g_p by 37%. For membrane 2, g_L change by 43% upon going from 4 to 8 mm depth, and g_p changed by 86%, respectively.

Interestingly, one does not find a measurable offset potential in black lipid membranes (**Figure 11**). We attribute that to the fact that the maximum possible curvature for a membrane across an aperture of 120 μm in our BLMs is much smaller that of a lipid patch spanning a tip aperture of about 8 μm.

We reported that the rectified I-V relations are often accompanied by the voltage-gated opening of single lipid ion channels (see also Laub et al., 2012; Blicher and Heimburg, 2013; Mosgaard and Heimburg, 2013). This is surprising because it is usually believed that voltage-gated conduction-events are an exclusive feature of protein channels. In our experiments, the minimum pore open probability is found for $V - V_0 = 0$, i.e., at a voltage around -200 mV. One expects opening of pores below about -400 mV (outside of our experimental range) and above about 0 V. This has in fact been observed in **Figure 8**. In the BLM measurements that do not display a voltage offset, the formation of channel events displays symmetric voltage-dependence, i.e., it occurs at both higher positive and negative voltages. In patch experiments, we found a single channel conductance at 8 mm depth that was 2.0 times larger than the single channel conductance at 4 mm depth ($\gamma = 137$ pS vs. $\gamma = 68$ pS, respectively). In the BLM experiment, the single channel conductance was $\gamma = 78$ pS.

In the previous section, we outlined that the conductance g_p of the I-V profile associated with open pores was about 2 times larger at 8 mm depth than at 4 mm depth. These numbers are well in agreement with the difference in single channel conductance. This indicates that interpreting a conduction process related to pore-formation is reasonable. The second conduction process that we called a leak-current is voltage-independent and does not display discrete channel events. Larger depth of the pipette enhances channel activity, and they occur at lower voltage. This suggests that the lipid membrane channels are mechanosensitive.

The conductance of the lipid pores is of a magnitude typical for single channel proteins. Llano et al. (1988) reported single potassium channel conductances of $\gamma = 10$, 20, and 40 pS in the squid axon. Salkoff et al. (2006) found that the so-called SLO-potassium channel family may have larger conductances, e.g., $\gamma = 100$–270 pS (SLO1), $\gamma = 60$–140 pS (SLO2.1), $\gamma = 100$–180 pS (SLO2.2), and $\gamma = 70$–100 pS (SLO3). Sakmann and Trube (1984) described a potassium channel with a single channel conductance of 27 pS. Below we show that also the voltage-gating properties of our membranes are similar to potassium channels. This suggests that the phenomenology of lipid and protein channels is practically indistinguishable.

After a voltage jump one finds a transient time regime of about 10 ms, in which the membrane equilibrates to a new state. In the theory section we outlined that one expects at least two relaxation processes. One of them is the charging of the membrane (and pipette) capacitor with a timescale independent of the membrane state, and the second one is a structural variation of the membrane leading to changes in capacitance, polarization and membrane conductivity. The second timescale reflects relaxation processes in the membrane. We could describe all current traces with bi-exponential fits containing a fast timescale of about 300 μs (dominated by the low pass-filter time constant of the experiment) and a slow timescale of about 2 ms. The amplitude of the slow process was linear with the magnitude of the voltage jump and did not depend on whether the I-V profile was rectified or linear. In contrast, the amplitude of the fast process reflected the voltage-dependence of the steady-state conductance of the membrane after the voltage jump. We conclude that there exists a fast process altering the conductance by changing the membrane state. This could be reflected in a timescale of channel opening or of the overall membrane area. Usually one would assume that the membrane-related process is the slow process, which is opposite to the experimental evidence showing that the fast process reflects that rectification. The reasons for this remain to be explained. It is further not clear why the I-V profiles are sometimes rectified and sometimes not.

4.1. Comparison of Membrane Conductance With the Potassium Channel of Hodgkin and Huxley

We have found that many of the I-V curves are rectified, which we explained by the voltage-gated opening of pores. These pores can be recognized in many of the current traces. Our analysis allows for a determination of the probability of pore opening. We found that close to the offset-voltage V_0, the pores are mostly closed, while the open probability increase as a function of $(V^2 + 2VV_0)$

Rectified behavior has usually been attributed to voltage-gated protein ion channels. These channels were originally introduced by Hodgkin and Huxley in order to explain the properties of the nervous impulse in squid axons (Hodgkin and Huxley, 1952a). In their model they introduced two channels (or more accurately: two gating mechanisms) for the conduction of sodium and potassium. The conductances of the potassium channel, g_K, and of the sodium channels, g_{Na} were described by

$$\begin{aligned} g_K &= g_{K,0} \cdot n^4(V,t) \\ g_{Na} &= g_{Na,0} \cdot m^3(V,t) \cdot h(V,t) \end{aligned} \tag{10}$$

where $n(V,t)$, $m(V,t)$, and $h(V,t)$ are voltage and time-dependent functions describing single-exponential kinetics of gate-opening in the channels. The potassium channel is described by four independent and identical gates. After a voltage jump from V_0 to V, the conductance of the potassium channel is described by

$$n(V,t) = n_\infty(V) - (n_\infty(V) - n_\infty(V_0)) \cdot \exp\left(-\frac{t}{\tau_n(V)}\right) \tag{11}$$

where the relaxation time $\tau_n(V)$ and the steady state values of n, $n_\infty(V)$, and $n_\infty(V_0)$ are given by

$$n_\infty(V) = \frac{\alpha_n(V)}{\alpha_n(V) + \beta_n(V)} \quad \text{and} \quad \tau_n(V) = \frac{1}{\alpha_n(V) + \beta_n(V)} \tag{12}$$

with

$$\begin{aligned} \alpha_n(V) &= \frac{10^4 \cdot (V + 0.055)}{1 - \exp\left(-\frac{V+0.055}{0.010}\right)} \quad ; \\ \beta_n(V) &= 125 \cdot \exp\left(-\frac{V + 0.065}{0.08}\right) \end{aligned} \tag{13}$$

where the voltage V is given in units of [V].[1] The functions $\alpha_n(V)$ and $\beta_n(V)$ were not derived from first principles but rather parameterized from experimental voltage-clamp data (Hodgkin et al., 1952; Hodgkin and Huxley, 1952b). The steady state open probability of the potassium channel is then given by

$$P_{open,K}(V) = n^4_\infty(V) \tag{14}$$

This function is shown in **Figure 13** (solid black line). It is interesting to compare it to the open probability of the pure lipid membranes of the experiments described above (blue traces).

We took the calculated open probabilities of five selected traces from **Figures 7**, **8** and plotted them in comparison to the steady state open probability of the K$^+$-channel determined by Hodgkin and Huxley. While the curves are not identical, they are in fact quite similar. **Figure 8** shows that the open probability in fact goes along with the opening of pores. For comparison, we also added the normalized conductance of the voltage-gated KvAP channel (red symbols, Lee et al., 2005; Schmidt et al., 2006) that displays a voltage-dependent conductance that is very similar to the HH-potassium channel and the lipid channels from this publication. This demonstrates that many properties of the potassium channel can be described by the rectified properties of the lipid membrane in the absence of any macromolecules. The similarity of lipid membrane behavior with that of potassium channels has in fact been noticed before (Blicher and Heimburg, 2013; Mosgaard and Heimburg, 2013).

Interestingly, Seeger et al. (2010) showed that the both mean conductance and open channel life-times of the KcsA potassium channels reconstituted into a synthetic lipid membrane are proportional to the heat capacity of the lipid membrane. They used a POPG:POPG = 3:1 mixture, which is commonly used in conduction studies on reconstituted proteins. For instance,

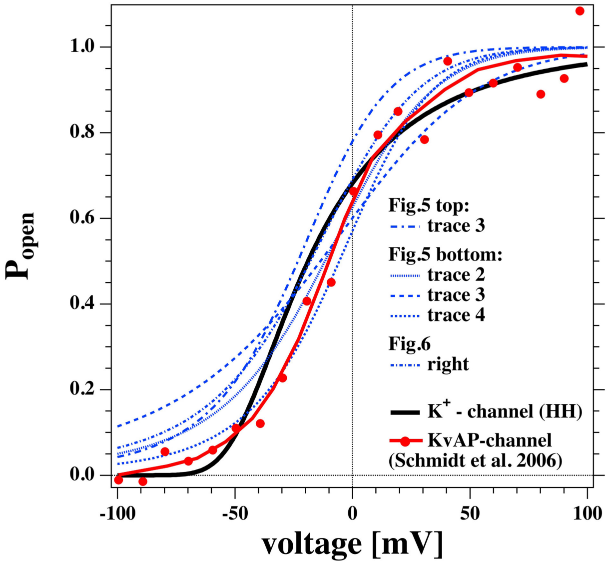

FIGURE 13 | Comparison of the open probability of the K$^+$-channel of Hodgkin and Huxley (1952a) (fat line), the KvAP channel reconstituted into a POPE/POPC = 3:1 membrane (Schmidt et al., 2006) (fat red line and symbols), and selected open probabilities from **Figures 7**, **8** in the voltage regime of physiological relevance.

---

[1] Note that in Hodgkin and Huxley (1952a) the voltage was defined relative to the resting potential.

it was used as a demonstration for how lipids change the function of the KvAP channel (Schmidt et al., 2006). This mixture shows a transition exactly at room temperature (the experimental temperature in Schmidt et al.). This shows that even in membranes containing protein channels, it may be impossible to understand the results without studying the thermodynamics of the host matrix. Since this lipid mixture is so common, it is likely that in some of the respective studies the function of the protein may have been confused with that of the host membrane. This behavior would be a logical consequence of membrane fluctuations if the membrane conductance originated from the lipid membrane alone. Since the conductance of the membrane was still proportional to the concentration of K-channels in the membrane, we have proposed in the past that the conductance in the membrane originates from membrane pores that are catalyzed by the channel protein (Mosgaard and Heimburg, 2013).

4.2. Membrane Conductance and the State of the Lipid Membrane

Membrane conductance depends on the thermodynamic state of the lipid membrane, which is influenced by all intensive variables. These may be temperature, pressure and membrane tension, but also voltage and the chemical potentials of membrane components, e.g., due to lipid composition, membrane proteins and to drugs associated to the membrane. In this manuscript, we focused on voltage and pressure differences across the membrane that are responsible for membrane curvature.

We treated the temperature dependence and chemical potential changes (in terms of an anesthetic drug) in earlier papers. The temperature dependence of the membrane conductance is closely associated with the temperature dependence of membrane melting (Blicher et al., 2009). In the past we have shown that one can seemingly "block" lipid pores by anesthetics (e.g., ethanol and octanol) in a manner which resembles that being reported for some protein receptors, such as the nicotinic acetylcholine receptor, N-methyl-D-aspartate (NMDA), serotonin [5-HT(3)], glycine and GABA receptors (Wodzinska et al., 2009). The reason is that anesthetics affect the melting profiles of membranes (Heimburg and Jackson, 2007; Græsbøll et al., 2014). Therefore, anesthetic drugs actually do not block pores but change the thermodynamics of the membrane. This is a clear case for an action of a drug on conductance that can convincingly be explained by its effect on lipid membranes. Anything that alters the membrane state will alter the likelihood of lipid pore formation. These are not only the anesthetics, but also neurotransmitters, such as serotonin that display a large effect on lipid melting (Cantor, 2003; Seeger et al., 2007) (Robert Cantor called some of the neurotransmitters "endogenous anesthetics"), and proteins (Heimburg and Biltonen, 1996; Heimburg and Marsh, 1996; Mosgaard and Heimburg, 2013). We have also studied the effect of tetrodotoxin (TTX) on lipid membranes but did not find a measurable effect on lipid transitions (unpublished data). This is evidence for that TTX specifically acts on macromolecules and not un-specifically on lipid membranes. Thus, proteins are involved in TTX-dependent processes but probably not in the action of anesthetics. We have proposed in the past that proteins could affect the thermodynamics of membranes and act as catalysts for lipid pores (Mosgaard and Heimburg, 2013). Proteins have chemical potentials and add to the free energy of the membrane. This effect may be influenced by specifically binding drugs, such as TTX because they can alter the chemical potentials of the proteins.

4.3. Thermodynamic Variables and Protein Channels

The lipid melting transition is a function of the chemical potential difference between gel and fluid lipids, which depends on temperature, pressure, lateral tension, voltage, and the chemical potentials of the components (Heimburg, 2007). The open-close probability of pores is related to this chemical potential difference. It would not make sense to distinguish between heat- and cold sensing pores, mechanosensitive pores, voltage-gated pores, or pores created by changes in composition, protein and drug concentration, or pH-dependence. The lipid pores naturally are sensitive to all of these changes. We have demonstrated this here for mechanosensitivity and voltage, and previously for temperature and anesthetics. The effect of drugs, such as anesthetics can be reversed by pressure, temperature, or pH changes (Heimburg and Jackson, 2007; Heimburg, 2019; Mužić et al., 2019). It is therefore interesting to compare this with protein channels and receptors. In the protein field is believed that there exist proteins that "sense" different variables separately and that they are specialized receptors for thermodynamic variables. Receptors for temperature changes that have been proposed include the TRPM8- and TRPA1-channels for cold reception (and simultaneously for menthol), whereas TRPV1, TRPV2, TRPV3, and TRPV4 are believed to be activated by heating (Voets et al., 2005). Other proteins are voltage sensors, e.g., the KcsA potassium and other K^+-channels (Doyle et al., 1998; Bezanilla, 2005) or sodium channels (Hodgkin and Huxley, 1952b). A lot of attention has been given to mechanosensitive channels that are activated by changes in membrane tension (Martinac et al., 1990; Sukharev et al., 1994), e.g., the piezo1 and piezo2 channels (Coste et al., 2010; Syeda et al., 2016) and the TMC1 and TMC2 proteins (Jia et al., 2020). As we have shown here, lipid channels are equally sensitive to membrane tension and are mechanosensitive.

As for the lipid channels, the kinetics for opening and closing of protein channels should depend on the chemical potential differences, which generally are functions of all variables. Some changes of the variables will activate and others deactivate channels. In general, also the channel events observed in the presence of proteins will depend on all thermodynamics variables. It is possible that many of the effects of changes in the variables on proteins may originate from the lipids. Thus, it is not surprising that the cold-sensing protein TRPA1 can be activated by calcium. Calcium increases the melting temperature of charged and uncharged lipid membranes due to its effect on the electrostatics. Uncharged membranes melt at higher temperature than charged membranes (Träuble et al., 1976). Therefore, the change in the state of a membrane upon addition of calcium is similar to that one obtains upon cooling. Likewise, it would be straight-forward to predict that TRPA1 is activated be lowering the pH because this has a similar effect on electrostatics than binding calcium. Interestingly, lowering pH reverses anesthesia. We have pointed out that many aspects of the phenomenology of TRP-channels can be found in artificial membranes (Laub et al., 2012). The cold activation of TRPM8 displays a similar critical temperature (19°C) and width (about 10°) as the melting transitions in biological membranes (Mosgaard and Heimburg, 2013; Mužić et al., 2019). Mechanosensitive channels from *E. coli* can be activated by membrane-soluble amphipathic drugs, such as trinitrophenol and chlorpromazine (a neuroleptic), or by changes in their chemical potential, respectively. This resembles the effect of anesthetics on lipid membranes and its channel activity discussed above. Martinac et al. (1990) in fact suggested that this could be explained by a lipid membrane effect because the effect is related to their membrane solubility. This is also the case for the effect of general anesthetics on lipid channels that obey the famous Meyer-Overton relation (Heimburg and Jackson, 2007; Blicher et al., 2009).

5. CONCLUSION

We describe the voltage-gated opening of channels in pure lipid membrane. When the I-V profiles are outward rectified, in most cases one finds single channel events at high voltage. When I-V profiles are linear, one does not see single channels. I-V profiles in BLMs are symmetric and show lipid channels at higher voltage. We concluded that there are two conduction processes: One leak current not related to membrane channels and with a conductance that is independent of voltage, and single channel events that are voltage-gated. We reported evidence for that channel-opening is mechanosensitive. The properties of the membrane channels resemble those of potassium channels.

DATA AVAILABILITY STATEMENT

The raw data supporting the conclusions of this article will be made available by the authors, without undue reservation.

AUTHOR CONTRIBUTIONS

KZ designed and performed the experiments and wrote parts of the manuscript. TH designed the project, wrote parts of the manuscript, and provided the theory. All authors contributed to the article and approved the submitted version.

FUNDING

This work was supported by the Villum Foundation (VKR 022130).

REFERENCES

Antonov, V. F., Anosov, A. A., Norik, V. P., and Smirnova, E. Y. (2005). Soft perforation of planar bilayer lipid membranes of dipalmitoylphosphatidylcholine at the temperature of the phase transition from the liquid crystalline to gel state. *Eur. Biophys. J.* 34, 155–162. doi: 10.1007/s00249-004-0438-8

Antonov, V. F., Petrov, V. V., Molnar, A. A., Predvoditelev, D. A., and Ivanov, A. S. (1980). The appearance of single-ion channels in unmodified lipid bilayer membranes at the phase transition temperature. *Nature* 283, 585–586. doi: 10.1038/283585a0

Bezanilla, F. (2005). Voltage-gated ion channels. *IEEE Trans. Nanobiosci.* 4, 34–48. doi: 10.1109/TNB.2004.842463

Blicher, A., and Heimburg, T. (2013). Voltage-gated lipid ion channels. *PLoS ONE* 8:e65707. doi: 10.1371/journal.pone.0065707

Blicher, A., Wodzinska, K., Fidorra, M., Winterhalter, M., and Heimburg, T. (2009). The temperature dependence of lipid membrane permeability, its quantized nature, and the influence of anesthetics. *Biophys. J.* 96, 4581–4591. doi: 10.1016/j.bpj.2009.01.062

Böckmann R, de Groot, R., Kakorin, S., Neumann, E., and Grubmüller H. (2008). Kinetics, statistics, and energetics of lipid membrane electroporation studied by molecular dynamics simulations. *Biophys. J.* 95, 1837–1850. doi: 10.1529/biophysj.108.129437

Cantor, R. S. (2003). Receptor desensitization by neurotransmitters in membranes: are neurotransmitters the endogenous anesthetics? *Biochemistry* 42, 11891–11897. doi: 10.1021/bi034534z

Corey, D. P., Garcia-Anoveros, J., Holt, J. R., Kwan, K. Y., Lin, S. Y., Vollrath, M. A., et al. (2004). TRPA1 is a candidate for the mechanosensitive transduction channel of vertebrate hair cells. *Nature* 432, 723–730. doi: 10.1038/nature03066

Coste, B., Mathur, J., Schmidt, M., Earley, T. J., Ranade, S., Petrus, M. J., et al. (2010). Piezo1 and piezo2 are essential components of distinct mechanically activated cation channels. *Science* 330, 55–60. doi: 10.1126/science.1193270

Cruickshank, C. C., Minchin, R. F., Le Dain, A. C., and Martinac, B. (1997). Estimation of the pore size of the large-conductance mechanosensitive ion channel of *Escherichia coli*. *Biophys. J.* 73, 1925–1931. doi: 10.1016/S0006-3495(97)78223-7

Doyle, D. A., Morais, J., Gulbis, J. M., Cohen, A. L., Chait, B. T., and MacKinnon, R. (1998). The structure of the potassium channel: molecular basis of K^+ conduction and selectivity. *Science* 280:69. doi: 10.1126/science.280.5360.69

Gehl, J. (2003). Electroporation: theory and methods, perspectives for drug delivery, gene therapy and research. *Acta Physiol. Scand.* 177, 437–447. doi: 10.1046/j.1365-201X.2003.01093.x

Glaser, R. W., Leikin, S. L., Chernomordik, L. V., Pastushenko, V. F., and Sokirko, A. I. (1988). Reversible breakdown of lipid bilayers: formation and evolution of pores. *Biochim. Biophys. Acta* 940, 275–287. doi: 10.1016/0005-2736(88)90202-7

Græsbøll K, Sasse-Middelhoff, H., and Heimburg, T. (2014). The thermodynamics of general and local anesthesia. *Biophys. J.* 106, 2143–2156. doi: 10.1016/j.bpj.2014.04.014

Grabitz, P., Ivanova, V. P., and Heimburg, T. (2002). Relaxation kinetics of lipid membranes and its relation to the heat capacity. *Biophys. J.* 82, 299–309. doi: 10.1016/S0006-3495(02)75395-2

Gutsmann, T., Heimburg, T., Keyser, U., Mahendran, K. R., and Winterhalter, M. (2015). Protein reconstitution into freestanding planar lipid membranes for electrophysiological characterization. *Nat. Protoc.* 10, 188–198. doi: 10.1038/nprot.2015.003

Hanke, W., Methfessel, C., Wilmsen, U., and Boheim, G. (1984). Ion channel reconstruction into lipid bilayer membranes on glass patch pipettes. *Bioelectrochem. Bioenerg.* 12, 329–339. doi: 10.1016/0302-4598(84)87013-0

Heimburg, T. (2007). *Thermal Biophysics of Membranes*. Berlin: Wiley VCH.

Heimburg, T. (2010). Lipid ion channels. *Biophys. Chem.* 150, 2–22. doi: 10.1016/j.bpc.2010.02.018

Heimburg, T. (2012). The capacitance and electromechanical coupling of lipid membranes close to transitions. The effect of electrostriction. *Biophys. J.* 103, 918–929. doi: 10.1016/j.bpj.2012.07.010

Heimburg, T. (2019). "Phase transitions in biological membranes," in *Thermodynamics and Biophysics of Biomedical Nanosystems. Series in BioEngineering*, eds C. Demetzos and N. Pippa (Singapore: Springer Nature), 39–61. doi: 10.1007/978-981-13-0989-2_3

Heimburg, T., and Biltonen, R. L. (1996). A Monte Carlo simulation study of protein-induced heat capacity changes. *Biophys. J.* 70, 84–96. doi: 10.1016/S0006-3495(96)79551-6

Heimburg, T., and Jackson, A. D. (2007). The thermodynamics of general anesthesia. *Biophys. J.* 92, 3159–3165. doi: 10.1529/biophysj.106.099754

Heimburg, T., and Marsh, D. (1996). "Thermodynamics of the interaction of proteins with lipid membranes," in *Biological Membranes: A Molecular Perspective From Computation and Experiment*, eds K. M. Merz and B. Roux (Boston, MA: Birkhäuser), 405–462. doi: 10.1007/978-1-4684-8580-6_13

Hille, B. (1992). *Ionic Channels of Excitable Membranes*. Cambridge: Cambridge University Press.

Hodgkin, A. L., and Huxley, A. F. (1952a). A quantitative description of membrane current and its application to conduction and excitation in nerve. *J. Physiol.* 117, 500–544. doi: 10.1113/jphysiol.1952.sp004764

Hodgkin, A. L., and Huxley, A. F. (1952b). Currents carried by sodium and potassium ions through the membrane of the giant axon of loligo. *J. Physiol.* 116, 449–472. doi: 10.1113/jphysiol.1952.sp004717

Hodgkin, A. L., Huxley, A. F., and Katz, B. (1952). Measurement of current-voltage relations in the membrane of the giant axon of loligo. *J. Physiol.* 116, 424–448. doi: 10.1113/jphysiol.1952.sp004716

Højholt KL, Mužić T, Jensen, S. D., Bilgin, M., Nylandsted, J., Heimburg, T., et al. (2019). Calcium electroporation and electrochemotherapy for cancer treatment: importance of cell membrane composition investigated by lipidomics, calorimetry and *in vitro* efficacy. *Sci. Rep.* 9, 4758. doi: 10.1038/s41598-019-41188-z

Jia, Y., Zhao, Y., Kusakizako, T., Wang, Y., Pan, C., Zhang, Y., et al. (2020). TMC1 and TMC2 proteins are pore-forming subunits of mechanosensitive ion channels. *Neuron* 105, 310–321. doi: 10.1016/j.neuron.2019.10.017

Kaufmann, K., and Silman, I. (1983). The induction by protons of ion channels through lipid bilayer membranes. *Biophys. Chem.* 18, 89–99. doi: 10.1016/0301-4622(83)85002-9

Laub, K. R., Witschas, K., Blicher, A., Madsen, S. B., and Lückhoff A, Heimburg, T. (2012). Comparing ion conductance recordings of synthetic lipid bilayers with cell membranes containing trp channels. *Biochim. Biophys. Acta* 1818, 1–12. doi: 10.1016/j.bbamem.2012.01.014

Lee, S. Y., Lee, A., Chen, J., and MacKinnon, R. (2005). Structure of the KvAP voltage-dependent K^+ channel and its dependence on the lipid membrane. *Proc. Natl. Acad. Sci. U.S.A.* 102, 15441–15446. doi: 10.1073/pnas.0507651102

Llano, I., Webb, C. K., and Bezanilla, F. (1988). Potassium conductance of the squid giant axon. Single-channel studies. *J. Gen. Physiol.* 92, 179–196. doi: 10.1085/jgp.92.2.179

Martinac, B., Adler, J., and Kung, C. (1990). Mechanosensitive ion channels of *Escherichia coli* activated by amphipaths. *Nature* 348, 261–263. doi: 10.1038/348261a0

Mosgaard, L. D., and Heimburg, T. (2013). Lipid ion channels and the role of proteins. *Acc. Chem. Res.* 46, 2966–2976. doi: 10.1021/ar4000604

Mosgaard, L. D., Zecchi, K. A., and Heimburg, T. (2015a). Mechano-capacitive properties of polarized membranes. *Soft Matter* 11, 7899–7910. doi: 10.1039/C5SM01519G

Mosgaard, L. D., Zecchi, K. A., Heimburg, T., and Budvytyte, R. (2015b). The effect of the nonlinearity of the response of lipid membranes to voltage perturbations on the interpretation of their electrical properties. A new theoretical description. *Membranes* 5, 495–512. doi: 10.3390/membranes5040495

Mužić T, Tounsi, F., Madsen, S. B., Pollakowski, D., Konrad, M., and Heimburg, T. (2019). Melting transitions in biomembranes. *Biochim. Biophys. Acta* 1861:183026. doi: 10.1016/j.bbamem.2019.07.014

Nagle, J. F., and Scott, H. L. (1978). Lateral compressibility of lipid mono- and bilayers. Theory of membrane permeability. *Biochim. Biophys. Acta* 513, 236–243. doi: 10.1016/0005-2736(78)90176-1

Neumann, E., Kakorin, S., and Tænsing K. (1999). Fundamentals of electroporative delivery of drugs and genes. *Bioelectrochem. Bioenerg.* 48, 3–16. doi: 10.1016/S0302-4598(99)00008-2

Papahadjopoulos, D., Jacobson, K., Nir, S., and Isac, T. (1973). Phase transitions in phospholipid vesicles. Fluorescence polarization and permeability measurements concerning the effect of temperature and cholesterol. *Biochim. Biophys. Acta* 311, 330–340. doi: 10.1016/0005-2736(73)90314-3

Petrov, A. G. (2001). Flexoelectricity of model and living membranes. *Biochim. Biophys. Acta* 1561, 1–25. doi: 10.1016/S0304-4157(01)00007-7

Petrov, A. G. (2006). Electricity and mechanics of biomembrane systems: flexoelectricity in living membranes. *Anal. Chim. Acta* 568, 70–83. doi: 10.1016/j.aca.2006.01.108

Petrov, A. G., and Sachs, F. (2002). Flexoelectricity and elasticity of asymmetric biomembranes. *Phys. Rev. E* 65, 021905-1–021905-5. doi: 10.1103/PhysRevE.65.021905

Sabra, M. C., and Jørgensen K, Mouritsen, O. G. (1996). Lindane suppresses the lipid-bilayer permeability in the main transition region. *Biochim. Biophys. Acta* 1282, 85–92. doi: 10.1016/0005-2736(96)00042-9

Sachs, F., and Qin, F. (1993). Gated, ion-selective channels observed with patch pipettes in the absence of membranes: novel properties of a gigaseal. *Biophys. J.*, 65, 1101–1107. doi: 10.1016/S0006-3495(93)81149-4

Sakmann, B., and Trube, G. (1984). Conductance properties of single inwardly rectifying potassium channels in ventricular cells from guinea pig heart. *J. Physiol.* 347, 641–657. doi: 10.1113/jphysiol.1984.sp015088

Salkoff, L., Butler, A., Ferreira, G., Santi, C., and Wei, A. (2006). High-conductance potassium channels of the slo family. *Nat. Rev. Neurosci.* 7, 921–931. doi: 10.1038/nrn1992

Schmidt, D., Jiang, Q. X., and MacKinnon, R. (2006). Phospholipids and the origin of cationic gating charges in voltage sensors. *Nature* 444, 775–779. doi: 10.1038/nature05416

Seeger, H. M., Aldrovandi, L., Alessandrini, A., and P Facci, P. (2010). Changes in single K^+ channel behavior induced by a lipid phase transition. *Biophys. J.* 99, 3675–3683. doi: 10.1016/j.bpj.2010.10.042

Seeger, H. M., Gudmundsson, M. L., and Heimburg, T. (2007). How anesthetics, neurotransmitters, and antibiotics influence the relaxation processes in lipid membranes. *J. Phys. Chem. B* 111, 13858–13866. doi: 10.1021/jp075346b

Stoddart, D., Ayub, M., Hoefler, L., Raychaudhuri, P., Klingelhoefer, J. W., Maglia, G., et al. (2014). Functional truncated membrane pores. *Proc. Natl. Acad. Sci. U.S.A.* 111, 2425–2430. doi: 10.1073/pnas.1312976111

Sukharev, S. I., Blount, P., Martinac, B., Blattner, F. R., and Kung, C. (1994). A large-conductance mechanosensitive channel in *E. coli* encoded by Mscl alone. *Nature* 368, 265–268. doi: 10.1038/368265a0

Syeda, R., Florendo, M. N., Cox, C. D., Kefauver, J. M., Santos, J. S., Martinac, B., et al. (2016). Piezo1 channels are inherently mechanosensitive. *Cell Rep.* 17, 1739–1746. doi: 10.1016/j.celrep.2016.10.033

Träuble H, Teubner, M., Woolley, P., and Eibl, H. (1976). Electrostatic interactions at charged lipid membranes. I. Effects of pH and univalent cations on membrane structure. *Biophys. Chem.* 4, 319–342. doi: 10.1016/0301-4622(76)80013-0

Voets, T., Droogmans, G., Wissenbach, U., Janssens, A., Flockerzi, V., and Nilius, B. (2004). The principle of temperature-dependent gating in cold- and heat-sensitive TRP channels. *Nature* 430, 748–754. doi: 10.1038/nature02732

Voets, T., Talavera, K., Owsianik, G., and Nilius, B. (2005). Sensing with TRP channels. *Nat. Chem. Biol.* 1, 85–92. doi: 10.1038/nchembio0705-85

Winterhalter, M., and Helfrich, W. (1987). Effect of voltage on pores in membranes. *Phys. Rev. A* 36, 5874–5876. doi: 10.1103/PhysRevA.36.5874

Wodzinska, K., Blicher, A., and Heimburg, T. (2009). The thermodynamics of lipid ion channel formation in the absence and presence of anesthetics. BLM experiments and simulations. *Soft Matter* 5, 3319–3330. doi: 10.1039/b909877a

Wunderlich, B., Leirer, C., Idzko, A., Keyser, U. F., Myles, V., Heimburg, T., et al. (2009). Phase state dependent current fluctuations in pure lipid membranes. *Biophys. J.* 96, 4592–4597. doi: 10.1016/j.bpj.2009.02.053

Zecchi, K. A., Mosgaard, L. D., and Heimburg, T. (2017). Mechano-capacitive properties of polarized membranes and the application to conductance measurements of lipid membrane patches. *J. Phys. Conf. Ser.* 780:012001. doi: 10.1088/1742-6596/780/1/012001

Conflict of Interest: The authors declare that the research was conducted in the absence of any commercial or financial relationships that could be construed as a potential conflict of interest.

frontiers
in Cell and Developmental Biology

ORIGINAL RESEARCH
published: 28 January 2021
doi: 10.3389/fcell.2020.629775

An Evidence for a Novel Antiviral Mechanism: Modulating Effects of Arg-Glc Maillard Reaction Products on the Phase Transition of Multilamellar Vesicles

***Lijing Ke*[1]*, *Sihao Luo*[1]*, *Pingfan Rao*[1]**, *Jeremy P. Bradshaw*[2]**, *Farid Sa'adedin*[2]*, *Michael Rappolt*[3] *and Jianwu Zhou*[1]**

[1] Food Nutrition Sciences Centre, Zhejiang Gongshang University, Hangzhou, China, [2] Royal (Dick) School of Veterinary Studies, College of Medicine & Veterinary Medicine (MVM), The University of Edinburgh, Edinburgh, United Kingdom, [3] School of Food Science and Nutrition, University of Leeds, Leeds, United Kingdom

Maillard reaction products (MRPs) of protein, amino acids, and reducing sugars from many foods and aqueous extracts of herbs are found to have various bioactivities, including antiviral effects. A hypothesis was proposed that their antiviral activity is due to the interaction with the cellular membrane. Aiming to estimate the possible actions of MRPs on phospholipid bilayers, the Arg-Glc MRPs were prepared by boiling the pre-mixed solution of arginine and glucose for 60 min at 100°C and then examined at a series of concentrations for their effects on the phase transition of MeDOPE multilamellar vesicles (MLVs), for the first time, by using differential scanning calorimetry (DSC) and temperature-resolved small-angle X-ray scattering (SAXS). Arg-Glc MRPs inhibited the lamellar gel–liquid crystal (L_β-L_α), lamellar liquid crystal–cubic (L_α-Q_{II}), and lamellar liquid crystal–inverted hexagonal (L_α-H_{II}) phase transitions at low concentration (molar ratio of lipid vs. MRPs was 100:1 or 100:2), but promoted all three transitions at medium concentration (100:5). At high concentration (10:1), the MRPs exhibited inhibitory effect again. The fusion peptide from simian immunodeficiency virus (SIV) induces membrane fusion by promoting the formation of a non-lamellar phase, e.g., cubic (Q_{II}) phase, and inhibiting the transition to H_{II}. Arg-Glc MRPs, at low concentration, stabilized the lamellar structure of SIV peptide containing lipid bilayers, but facilitated the formation of non-lamellar phases at medium concentration (100:5). The concentration-dependent activity of MRPs upon lipid phase transition indiciates a potential role in modulating some membrane-related biological events, e.g., viral membrane fusion.

Keywords: Maillard reaction products, phase transition, multilamellar vesicles, MeDOPE, x-ray scattering

Edited by:
Yuru Deng,
University of Chinese Academy of Sciences, China

Reviewed by:
Shutao Liu,
Fuzhou University, China
Yiguang Jin,
Academy of Military Medical Sciences (AMMS), China

****Correspondence:***
Pingfan Rao
pingfanrao@zjgsu.edu.cn;
pingfan.rao@gmail.com
Jeremy P. Bradshaw
J.Bradshaw@ed.ac.uk;
jpb70@bath.ac.uk

Specialty section:
This article was submitted to Cellular Biochemistry, a section of the journal Frontiers in Cell and Developmental Biology

Received: *15 November 2020*
Accepted: *18 December 2020*
Published: *28 January 2021*

Citation:
Ke L, Luo S, Rao P, Bradshaw JP, Sa'adedin F, Rappolt M and Zhou J (2021) An Evidence for a Novel Antiviral Mechanism: Modulating Effects of Arg-Glc Maillard Reaction Products on the Phase Transition of Multilamellar Vesicles. Front. Cell Dev. Biol. 8:629775. doi: 10.3389/fcell.2020.629775

INTRODUCTION

The Maillard reaction is a non-enzymatic browning chemistry reaction between amino acids (or peptides, or proteins) and a reducing sugar, usually requiring heat. As a major chemical change that occurs during food processing, herb decocting, and physiological aging, Maillard reaction products (MRPs) have been associated with a number of functions and bioactivities, such as flavoring, coloring, modification of proteins and lipids with glycation, and formation of antioxidant or mutagenic compounds. Both positive and negative influences of MRPs on cell reproduction have been reported (Einarsson et al., 1983; Harris and Tan, 1999; Kundinger, 2004; Rufián-Henares and Morales, 2006). MRPs from amino acids and glucose showed significant impacts on the growth of the microorganisms (Harris and Tan, 1999). This impact varies according to which amino acid was used. MRPs derived from reaction of arginine, glycine, and histidine with glucose promoted the growth of *Staphylococcus aureus* and *Salmonella enteritidis*, while MRPs of cysteine and glucose inhibited the growth of both germs.

Maillard reaction occurs widely during the preparation of boiling water extracts of herbs including herbal traditional Chinese medicine (TCM). The decoction of botanically distinguished herbs, e.g., *Isatidis Radix, Momordica charantia*, and ginseng, possesses antiviral activities by inhibiting influenza A virus adsorption on epithelial cells (Chen et al., 2006; Ke et al., 2012). Arginine and glucose are the most abundant Maillard reactants found in these herbs, implying that arginine-glucose MRPs (Arg-Glc MRPs) are the representative of MRPs in the decoction. Hemagglutination is mediated by the binding of viral envelope glycoprotein hemagglutinin (HA) to cellular plasma membrane receptors, sialic acid residues of glycolipids (Rogers et al., 1985; Wiley and Skehel, 1987; Kobasa et al., 2004). Arg-Glc MRPs inhibited the attachment of influenza virus to erythrocytes, which indicates that they may tackle the interaction between HA and lipid membrane of cells (Ke, 2010).

In order to infect the host cell, both enveloped and non-enveloped viruses have to penetrate the barrier of a cellular membrane. For enveloped viruses, influenza virus A for example, penetration involves membrane fusion. For non-enveloped viruses, picornaviruses, for instance, penetration involves membrane lysis or pore formation (Marsh and Helenius, 2006). Non-lamellar structures have been discovered either at the sites of membrane fusion or membrane pore formation. Peptides or proteins, which promote membrane fusion or lyse membrane, facilitate the formation of non-lamellar phases, either micelles, cubic phases, or hexagonal phases (Epand, 1998). Membrane fusion is a critical early event for an influenza virus to transfer its genetic information to human epithelial cells and complete its replication. From there, the new virus particles are formed and released to infect other cells. Nevertheless, membrane fusion is also involved in the budding of newly formed virus particles before they are released from the host cells.

In this study, we set off to elucidate whether Arg-Glc MRPs interrupt viral infection by interacting with lipid bilayers of the cells and blocking the formation of non-lamellar phases, hiring the MLVs of an unsaturated phosphatidylethonalamine as model vesicles. The potential inhibitory effects of MRPs on peptide-induced membrane fusion were examined, using simian immunodeficiency virus (SIV) fusion peptide as an example.

METHODS AND MATERIALS

Materials

1,2-Dioleoyl-sn-glycero-3-phosphoethanolamine-N-methyl (MeDOPE) was purchased from Avanti Polar Lipids Inc., USA, and used without further purification. Chloroform, methanol, and buffers are all graded AR and purchased from Sigma-Aldrich (Irvine, UK).

Sample Preparation

For X-ray diffraction measurement, the MLVs were prepared by dispersing 15 wt% of MeDOPE in PIPES buffer [pH 7.4, 20 mM Piperazine-N,N'-bis(2-ethanesulfonic acid), 150 mM NaCl], Sigma-Aldrich (Irvine, UK). Various samples including Arg-Glc MRPs and SIV fusion peptide (GVFVLGFLGFLA, >99%) were dissolved in deionized water or methanol and mixed thoroughly with lipid MLVs by vigorous vortex for 2 min.

Differential Scanning Calorimetry

MeDOPE MLVs were prepared as reported previously (Harroun et al., 2003) with modifications. After the lipids were dissolved in chloroform, the samples were added and mixed thoroughly by vortex and sonication. The lipid/sample suspensions were then dried up with nitrogen stream and left in vacuum overnight. Lipid concentration in the corresponding vesicle suspension was 100 mM for all the samples. MRPs were dissolved in PIPES buffer (pH 7.4, 20 mM, 150 mM NaCl) added as a serial molar ratio of 0, 1, 5, 10, 20, 30, 40, 50–100 lipid molecules. The SIV peptide was dissolved in methanol and added to the lipid solution at 1 and 2 mol%.

The dried lipid film was rehydrated with PIPES buffer at a temperature higher than T_{M} and vortexed to make 100 mM vesicle suspension. The suspension was sonicated for 1–2 min and soaked in liquid nitrogen (-180°C). The suspension was then defrosted at a temperature of at least 20°C above the T_{M}. The freeze–thaw cycle was repeated six times to obtain a unified lipid packing by wiping off the memory of lipids on their thermal history. The vesicles were mixed thoroughly prior to being injected and sealed into the aluminum sample pan. The pans were weighted as both empty and sealed; thereby, the actual amount of lipids sealed in the pan was calculated. A Pyris 1 Differential Scanning Calorimeter (Perkin Elmer, USA) was employed, at a scan rate of 40°C/min. The sample chamber held 30 μl of vesicle suspension. Continuous heating scans were run from -30°C through to 85°C for MeDOPE MLVs (Sykora et al., 2005).

The transition peak was analyzed with the curve-fitting program (Pyris) based on non-linear least-squares minimization. The onset phase transition temperature (T_{M}, T_{Q}, and T_{H} for melting transition, transition to cubic phase, and transition to hexagonal phase, respectively), energy consumption (ΔH_{f}), transition peak height (h), and peak area (A) were calculated automatically by the software. The transition peak height and peak area were then used to calculate the transition temperature range ΔT (Equation 1), presenting the homogeneous degree of phases existing in the phase transition.

$$\Delta T = \frac{2 \times A \times T}{h \times t} \quad (1)$$

T, temperature from the scan rate (°C); t, time from the scan rate (s).

Temperature-Resolved SAXS

The X-ray diffraction experiments were performed on the Austrian SAXS beamline at ELETTRA, Trieste, Italy (Amenitsch et al., 1998; Rappolt et al., 2003). Diffraction patterns of MeDOPE MLVs were recorded by a one-dimensional position-sensitive detector (Petrascu et al., 1998) covering the corresponding s-range of interest from ~1/450 to 1/12 Å^{-1} [$s = 2\pi \,\text{Sin}(\theta)/\lambda$]. As shown in **Figures 4**, **5**, the angular calibration was performed with silver-behenate [$CH_3(CH_2)_{20}$ -COOAg] for the detector: $d001 = 58.378$ Å, $\lambda = 1.54$ Å (Huang et al., 1993). The specimen-to-detector length was ~0.75 m. Equation (2) was obtained for the calculation of s-range by drawing a linear curve of "s" as a function of detector channels. Each sample was sealed in a steel chamber with a pair of thin mica film on both the entrance and exit windows, held in a steel block that was in thermal contact with a water circuit connected to a programmable temperature control unit (Unistat CC, Huber, Offenburg, Germany). The temperature was continuously monitored with a thermocouple fixed to the sample chamber in a linear fashion at a heating rate of 60 K/h, written into the data files automatically. Each frame of data collection lasted for 10–20 s depending on the scattering intensity, and for every 0.5°C (collecting for 10 s) or 1.0°C (collecting for 20 s). The X-ray beams conduct a minimal effect of thermal radiation.

X-Ray Diffraction Data Analysis

The raw data were corrected for detector efficiency. The background scattering of water and the sample chamber was subtracted from the corrected raw data. The location, width, and amplitude of each Bragg peak were then fitted by Lorentzian distributions (SigmaPlot, Systat Software Inc.). After the sample temperature curve was drawn as a function of frames, the transition temperature of each sample was determined by identifying the initiate point of non-lamellar phases. The square root of the peak intensity was used for determination of the form factor F of each individual reflection. The electron density maps of the phospholipid samples in the H_{II} phases were derived from the small-angle x-ray diffractograms by standard procedures (e.g., see Harper et al., 2001; Rappolt et al., 2003).

The following equation was used for calculating the s-range of diffraction.

$$S(\text{Å}^{-1}) = 0.0001 \times \text{channel–}0.008, R^2 = 1.000 \quad (2)$$

RESULTS

Lipids with smaller head groups and bigger tail groups present a cone shape. This type of lipids, e.g., MeDOPE, forms non-lamellar phases and allows us to monitor the influence of MRPs on the lamellar to non-lamellar phase transition. Primarily, the MeDOPE forms three types of structure in its aqueous dispersions: lamellar, cubic, and hexagonal, depending on the temperature, concentration, and thermal history. The non-lamellar structures are believed to relate to the initiation of peptide-induced membrane fusion. The presence of non-lamellar structure in MeDOPE samples indicates a destabilization of the lipid layers; thus, MeDOPE MLVs were used as a model lipid system for evaluating the effects of MRPs on membrane fusion induced by the SIV fusion peptide.

Arg-Glc MRPs Affected Phase Transitions of MeDOPE MLVs

Three phase transitions of MeDOPE MLVs, L_β-L_α, L_α-Q_{II}, and L_α-H_{II}, were observed by DSC. In general, as shown in **Figure 1**, Arg-Glc MRPs exhibited the concentration-dependent effects on the phase transitions. Despite the transition temperatures of all three phases being fluctuated with MRP concentration, MRPs increased the transition temperatures at moderate concentrations (lipid:MRPs = 10:1 by molar ratio), but decreased them at the higher concentrations, particularly at the highest concentration of 10:5 by molar ratio. The influences of Arg-Glc MRPs on ΔH_f varied among the three phase transitions. When the L_β-L_α transition reported the highest heat consumption of 30–50 kJ/mol, the L_α-Q_{II} reported the least, which was generally below 2 kJ/mol. The heat consumption of the L_α-H_{II} transition was higher than that of L_α-Q_{II}, around 5 kJ/mol and below.

As shown in **Figure 1A**, the initial L_β-L_α phase transition temperature (T_M) was ~−7.5°C, consistent with a previous report (Kusube et al., 2006). Arg-Glc MRPs decreased this temperature gradually to ~−8.2°C along the increasing concentration, with an exceptional but significant increase of 1.0°C at the molar ratio 10:1. Although both the decrease and increase were small by numbers, they were statistically highly significant ($n = 4$; $P < 0.01$). The presence of 1 mol% MRPs did not affect the T_M significantly, but remarkably increased the standard errors of measurements. The ΔH_f was decreased to ~30 kJ/mol at 5 mol% of MRPs and then gradually increased along the increasing concentrations of MRPs and stabilized at ~50 kJ/mol.

The MRPs increased the initial temperature of transition (T_Q) significantly from 62 to 68°C at the molar ratio of 10:1 (as shown in **Figure 1B**). At either lower or higher ratios, MRPs decreased the T_Q with greater standard errors ($P < 0.05$). No L_α-Q_{II} phase transition was observed at molar ratios of 100:5 or 10:5. The ΔH_f was decreased from 4 to ~1 kJ/mol in the presence of 1 mol% Arg-Glc MRPs.

In comparison, Arg-Glc MRPs possessed little influence on the L_α-H_{II} phase transition with two exceptions (as shown in **Figure 1C**). The first, Arg-Glc MRPs (5 mol%) decreased the

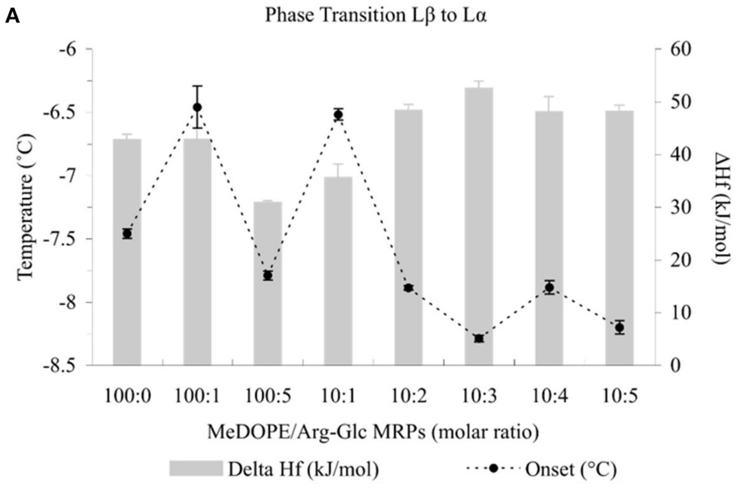

L_β-L_α phase transition

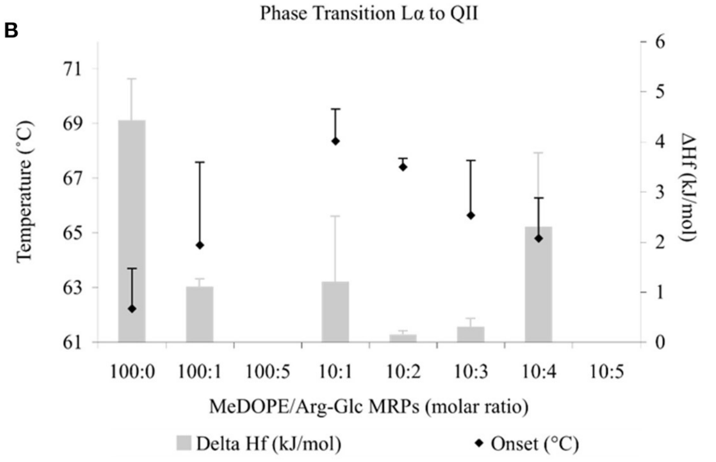

L_α-Q_{II} phase transition

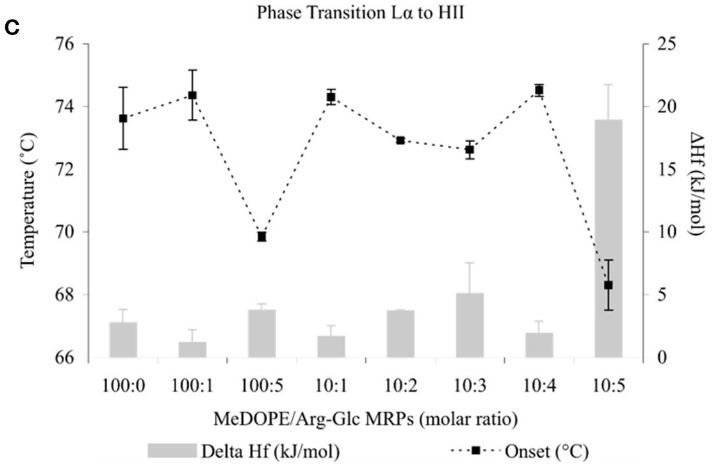

L_α - H_{II} phase transition

FIGURE 1 | Thermodynamic effects of Arg-Glc MRPs on lipid phase transitions of MeDOPE MLVs. Examined by differential scanning calorimeter at the scan rate of 40 K/min. The continuous heating scans were performed from −30 to 85°C and repeated for at least five times for each sample. **(A)** Lamellar–lamellar (L_β-L_α) phase transtition. ●, T_M; ▨, ΔH_f ($n = 4$; $P < 0.01$). **(B)** Lamellar–inverted cubic (L_α-Q_{II}) phase transition. ◆, T_Q; ▨, ΔH_f ($n = 4$; $P < 0.05$). **(C)** Lamellar–inverted hexagonal (L_α-H_{II}) phase transition. ■, T_H; ▨, ΔH_f ($n = 4$; $P < 0.01$).

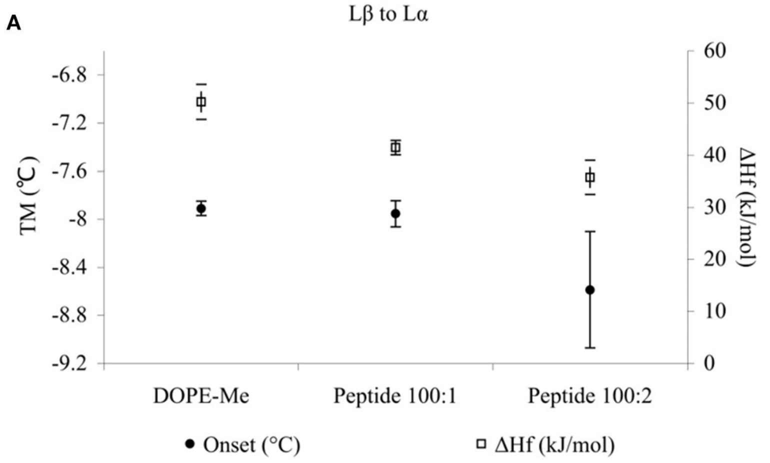

Effects of SIV on T_{M} (●) and ΔH_{f} of L_{β}-L_{α} transition (□).

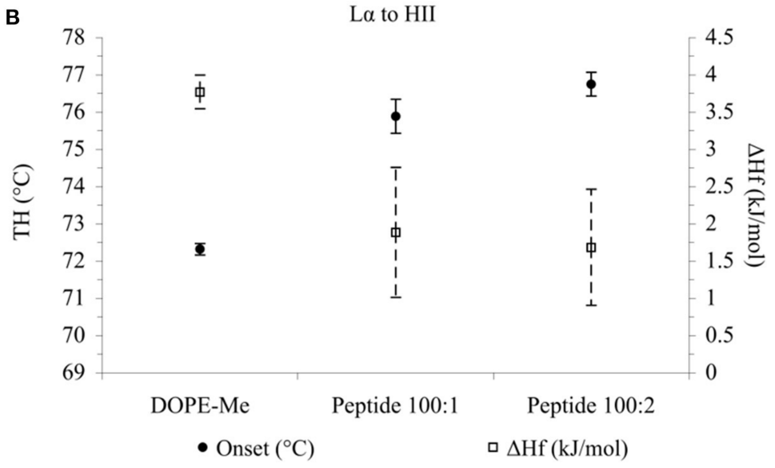

Effects of SIV on T_{H} (●) and ΔH_{f} of L_{α}-H_{II} transition (□).

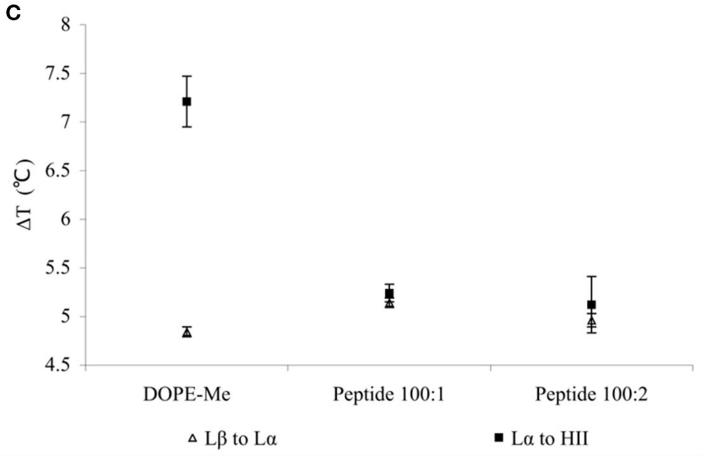

Effects of SIV on ΔT_{M} (▵) and ΔT_{H} (■).

FIGURE 2 | Effects of SIV peptide on phase behavior obtained in MeDOPE MLVs with DSC. Scan rate: 40 K/min. Temperature range of scanning: −30 to 85°C. Lipid concentration: 100 mM ($n = 5$; $P < 0.01$).

L_α-H_{II} phase transition temperature (T_H) from 73.6°C of pure MeDOPE to 69.9°C, and to 68.3°C at the higher molar ratio of lipid:MRPs (10:5). The second, the ΔH_f was dramatically increased to 19 kJ/mol at the molar ratio of 10:5.

SIV peptide slightly decreased the T_M of MeDOPE MLVs ($P < 0.05$ at 100:2) but increased T_H by 4°C ($P < 0.01$). In terms of transition temperatures and heat consumptions, the higher SIV concentration (100:2) was eventually not more effective than 100:1, although it did result in the greater standard errors. The heat consumptions of both transitions were reduced by SIV ($P < 0.01$). The peptide decreased the temperature range of lamellar/non-lamellar phase transition by 2°C, but slightly increased that of gel-liquid crystalline phase transition by about 0.3°C ($P < 0.01$ for 100:1 SIV).

Arg-Glc MRPs Affected MLV Phase Transitions in the Presence of SIV Fusion Peptide

As reported previously, the SIV fusion peptide induces membrane fusion by oblique insertion into the phospholipid bilayers, promoting negative curvature, and thereby encouraging the formation of non-lamellar structures of lipid packing around the insertion site.

The influences of Arg-Glc MRPs on the peptide-induced membrane fusion were observed by determination of the phase transition profiles of MeDOPE MLVs in the presence or absence of SIV fusion peptide. In the L_β-L_α phase transition (as shown in **Figure 2A**), the T_M of MeDOPE vesicles was −7.5 ± 0.05°C, which was decreased by SIV peptide to −8.0°C. The MRPs increased the T_M of containing 100:1 SIV peptide by 0.8°C at 100:2 ($P < 0.01$), decreased the T_M to −8.2°C at 100:5 ($P < 0.05$) and increased T_M back to −7.5°C at 10:1 ($P < 0.01$). SIV peptide decreased the temperature range (ΔT) of this phase transition in MeDOPE vesicles to 5.1°C (as shown in **Figure 2C**) when Arg-Glc MRPs increased it to 5.7°C at 10:1 ($P < 0.01$). However, in the presence of 100:1 SIV, the MRPs increased the temperature range of L_β-L_α phase transition by 0.4°C at 100:5 ($P < 0.05$) and then decreased it by 0.3°C at 10:1 ($P < 0.01$). MRPs promoted the transition at 100:5 (lipid/MRPs molar ratio) but inhibited the transition at the lower (100:2) or higher concentrations (10:1) in the presence or absence of SIV peptide.

In the L_α-H_{II} phase transition (as shown in **Figure 2B**), the effects of Arg-Glc MRPs showed different impacts. The MRPs promoted the transition at 100:5 but inhibited the transition at the lower (100:2) or higher concentrations (10:1) in the absence of SIV. As shown in **Figure 3**, in the presence of 100:1 SIV, the effects of Arg-Glc MRPs became much milder. T_H of the MeDOPE vesicles was 72.6 ± 0.4°C, which was elevated to 75.9 ± 0.5°C in the presence of 100:1 peptide ($P < 0.01$) and brought back to 74.1 ± 0.1°C by adding 100:5 Arg-Glc MRPs ($P < 0.01$), and to 75.1 ± 0.1°C by adding 10:1 Arg-Glc MRPs ($P < 0.01$). Furthermore, the ΔT_H of L_α-H_{II} phase transition was significantly affected by Arg-Glc MRPs, but only at 100:2. The opposite effects were observed in the presence or absence of SIV. The MRPs decreased the ΔT_H by 3°C in the absence of SIV, but increased the ΔT_H by 2.8°C in the presence of SIV ($P < 0.01$). At the higher concentrations of the MRPs, 100:5 and 100:10, the MRPs did not affect ΔT_H as potent as it was at 100:2.

Structural Rearrangements in the Phase Transitions: SAXS Study

To gain more details of the structural rearrangements involved in the phase transition, small angle X-ray scattering (SAXS) was used to investigate the transitions from lamellar phase (L_α) to inverted hexagonal phase (H_{II}) and/or from L_α to inverted cubic phase (Q_{II}) in the presence of Arg-Glc MRPs.

As shown in **Figure 5**, three phases, the lamellar, cubic, and hexagonal phase, were characterized with temperature-resolved SAXS in MeDOPE MLVs by determining the membrane structure-corresponding scattering density profiles at a heating rate of 1 K/min. At least two cubic structures, possibly the diamond and primitive bicontinuous phases, were observed while two orders of diffraction peaks in lamellar and hexagonal phase each were measured. The continuous existence and coexistence of different phases makes it possible to evaluate the influence of MRPs, SIV fusion peptide, and fusion inhibitor (LPC) on MeDOPE MLVs. For example, the L_α-to-H_{II} and L_α-to-Q_{II} phase transitions were promoted in the presence of Arg-Glc MRPs (100:5), indicated by the dropping T_H and T_Q, as shown in **Figure 6**.

As shown in **Figures 4**, **5**, the coexistence of H_{II} and Q_{II} phase was observed in the pure lipid vesicle. The T_H was 69.3°C. The inverted cubic phase started at 72.2°C. The scattering profile indicates that lipid bilayer in the cubic phase has more than one structure, possibly the double-diamond (P_{n3m}) and primitive phase (I_{m3m}). The addition of 100:2 Arg-Glc MRPs raised the T_H to 70.9°C and the T_Q to 74.3°C (**Figure 6**). However, when the concentration of Arg-Glc MRPs was increased to 100:5, the T_Q decreased to 69.4°C, while the T_H decreased to 66.9°C. At this proportion, the MRPs induced a 2°C gap between the L_α and H_{II} phase where no structure was observed. When the proportion of Arg-Glc MRPs reached 10:1, the T_H and T_Q were 1.3°C and 3.7°C lower than the blank vesicle, respectively.

SIV fusion peptide (1 mol%) lowered the T_Q to 64.3°C, but increased the T_H to 85.0°C. SIV weakened and broadened the scattering profile of liquid crystalline phase, and extended the end of this phase to 72.7°C (**Figure 6**, "SIV 1%"). However, since the shape and intensity of the Bragg peak were not identical to those of the normal L_α phase, a further analysis needs to be performed on the lattice spacing and electron density. Different from the pure lipid, SIV induced a coexistence of L_α and Q_{II} phase at the temperature ranging from 64.3 to 72.7°C, and a coexistence of Q_{II} and H_{II} phase at the temperature ranging from 85.0°C to the end of scan (90°C). This indicates the dominant impacts of SIV on the lipid phase behavior.

The low concentration of Arg-Glc MRPs (100:2) raised the T_H to 85.5°C in the lipid bilayer with 1% SIV, which was slightly higher than the T_H of SIV, whereas the T_Q was not affected. The end of the lamellar phase was raised by 6.9°C, which narrowed down the gap from L_α to H_{II}. The rise in the T_H and the extension of lamellar phase both suggest a stabilizing effect of Arg-Glc MRPs (100:2) on SIV containing lipid bilayers. The T_Q remains

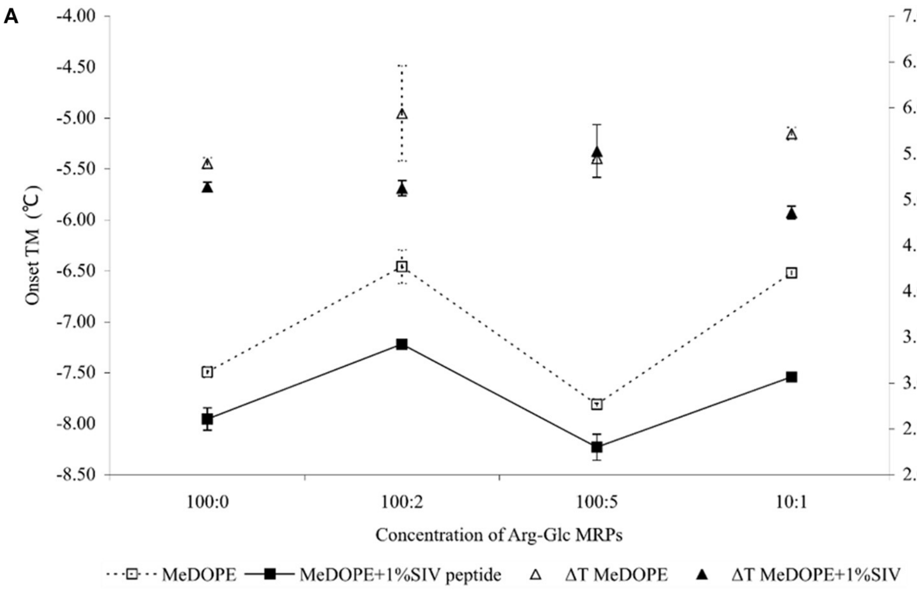

Effects of Arg-Glc MRPs on T_M (□/■) and ΔT_M (△/▲) of MeDOPE MLVs.

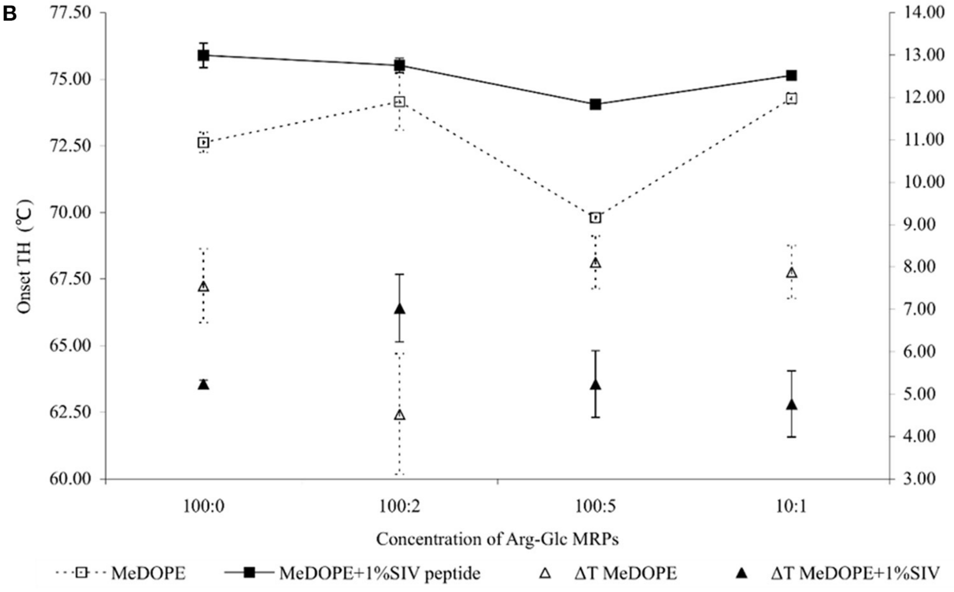

Effects of Arg-Glc MRPs on T_H (□/■) and ΔT_H (△/▲) of MeDOPE MLVs.

FIGURE 3 | Effects of Arg-Glc MRPs on the phase transition behavior of MeDOPE MLVs obtained in the presence of 100:1 SIV peptide by DSC. Scan rate: 40 K/min. Scanning temperature range: −30–85°C. Lipid concentration: 100 mM. Data of 100:1 SIV on MeDOPE vesicles (labeled as "100:0") was included for comparison (n = 4; $P < 0.01$).

the same as that of SIV, which implies that the cubic phase is more preferable than the hexagonal phase in the presence of the MRPs.

At medium concentration, Arg-Glc MRPs lowered all of the T_H, T_Q, and the end of the L_α phase in the presence of SIV while inducing the largest temperature gap between the L_α and H_{II} phase (**Figure 6**). This indicates a destabilizing effect of MRPs on the lamellar structure. The stronger scattering intensity of all the phases observed upon 100:5 MRPs may suggest the more ordered packing of lipids in each phase.

DISCUSSION

The polyphasic structural transformation of MeDOPE has been extensively studied with a variety of techniques (Ellens et al., 1986; Siegel et al., 1994; Colotto et al., 1996; Harroun et al.,

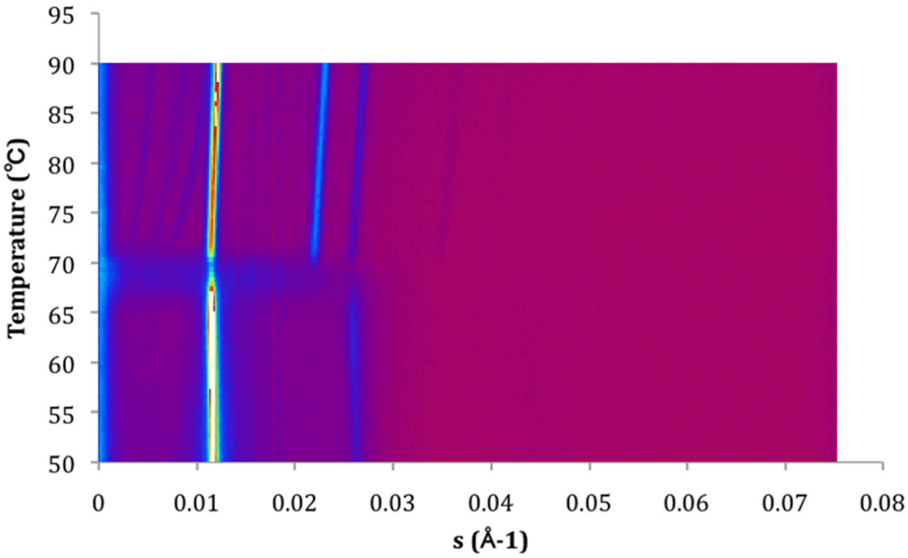

FIGURE 4 | Contour plot of X-ray scattering of MeDOPE MLVs. Temperature scan rate of 1 K/min. The figure shows a L_{α}-to-H_{II} transition around 70°C and a coexisting of H_{II} and Q_{II}.

2003; Kusube et al., 2006). The cubic structure is observed as a metastable phase when the vesicles are transferring from the lamellar phase to the hexagonal phase. This depends on the heating rate (thermal scan rate) across the lamellar-to-hexagonal phase transition (van Gorkom et al., 1992).

A wide range of temperature has been reported for the inverse hexagonal phase transition. As revealed in an X-ray diffraction study reported by Cherezov, the Q_{II} phase appears at 59.1°C while the H_{II} phase appears at 63.5°C, at a scan rate of 1.5 K/h. T_H increased by 2°C when the scan rate was raised to 6 K/h (Cherezov et al., 2003). Harroun et al. (2003) reported the T_H of 64°C and the T_Q of ~75°C at the scan rate of 30 K/h. In this study, there is a main phase transition at 72.6°C recorded by DSC at the much faster scan rate, 40 K/min. The transition is presumably T_H, that is from the lamellar phase (L_{α}) to the inverted hexagonal phase (H_{II}), since the hexagonal phase is the major visible structure of MeDOPE MLVs at high temperature. The T_Q between the lamellar phase (L_{α}) and the inverted cubic phase (Q_{II}) was about 62.0°C. The T_H determined in this study is much higher than the reported value. A remarkable difference among these measurements is the scan rate. It is 40 K/min in the DSC measurement compared to 1.5–30 K/h in the X-ray diffraction measurements. There was another phase transition at the lower temperature (~62°C), presumably the T_Q, which did not appear in every single isothermal scan of DSC measurement. Data are given in **Figure 1B** for reference.

Firstly, either stabilization or destabilization effects of Arg-Glc MRPs were observed on the different phase of the MLVs. At the concentration of 100:5, Arg-Glc MRPs destabilized the MeDOPE bilayers in the lamellar phase, both gel and liquid crystalline phases, and accordingly lowered the T_M and T_H (**Figures 1A,C**). However, when the ratio went up to 10:1, the MRPs stabilized the bilayer in the lamellar phase and elevated the T_M, T_Q, and T_H. At ratios higher than 10:1, the MRPs destabilized the bilayers again. However, T_H was constantly going down, like what occurred to T_M and T_Q. T_H rose back to about the same temperature as that of pure MeDOPE, at a ratio of 10:4, indicating another stabilization in the lipid structure before it transfers to inverted hexagonal phase. At the highest ratio, a bilayer breaking down was implied by the acute drop in T_H and rise in ΔH_f.

Taking together the effects of Arg-Glc MRPs across all three phase transitions, a general pattern of MRPs' effects emerges. The stabilization actions of the MRPs are split into two stages. Firstly, the MRPs fill up the spaces in the head group region of leaflet and keep the hydrophilic heads away from each other. This prevents the development of negative curvature strain in the bilayers and subsequently inhibits the lamellar/non-lamellar transition. The bilayers prefer to remain in gel or liquid crystal phase. MRPs at a molar ratio of 10:1 performed the strongest stabilization effects of this kind. Secondly, when more MRP molecules accumulate in the bilayers, they start to destabilize the lamellar structure of lipids and favor the lamellar-inverted cubic transition. Once the lipids transfer to non-lamellar structure, the lipids prefer to stay in the cubic phase rather than the hexagonal phase. The best example for this kind is bilayers containing Arg-Glc MRPs at a molar ratio of 10:4. MRPs decreased the T_M and T_Q but raised the T_H. At concentrations beyond this point, the bilayer was further destabilized and became easier to transfer to the inverted hexagonal phase.

A drop in transition temperature can correlate with a rise in heat consumption, such as that observed in MeDOPE MLVs in the presence of Arg-Glc MRPs. For example, Arg-Glc MRPs, at the molar ratio of 10:5, decreased the temperature of lamellar-inverted hexagonal transition and increased the heat consumption. Similar outputs were observed in the gel-liquid crystalline phase transition at higher molar ratios than 10:1.

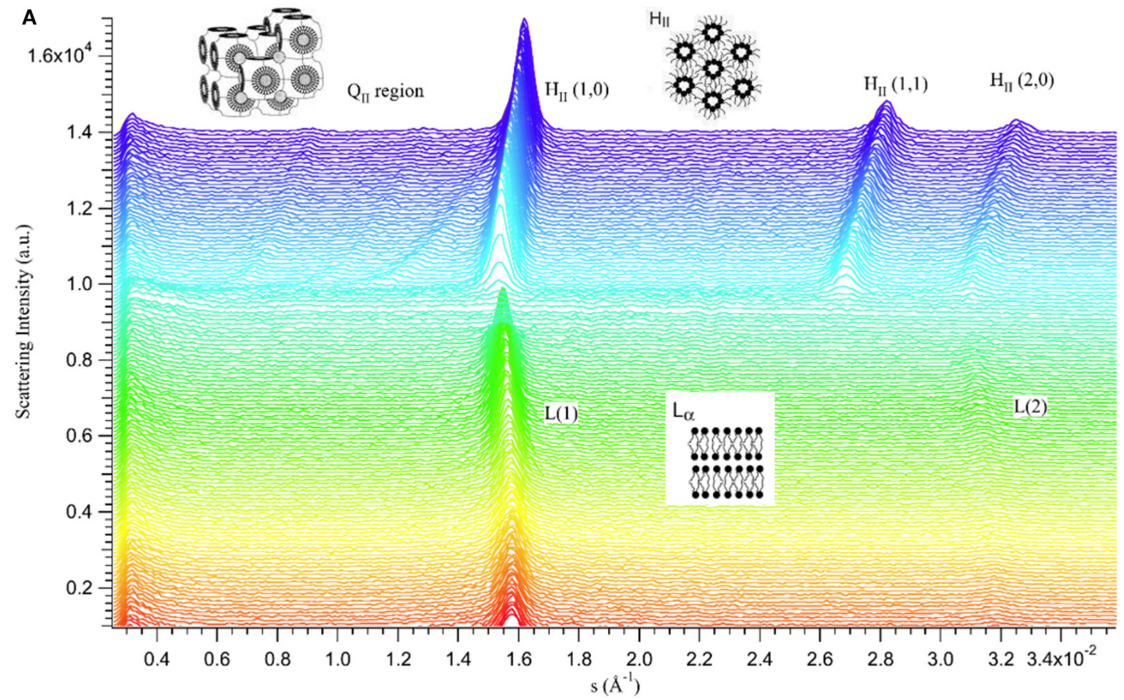

Temperature-resolved 3D scattering density profiles of lipid MLVs with 100:5 Arg-Glc MRPs.

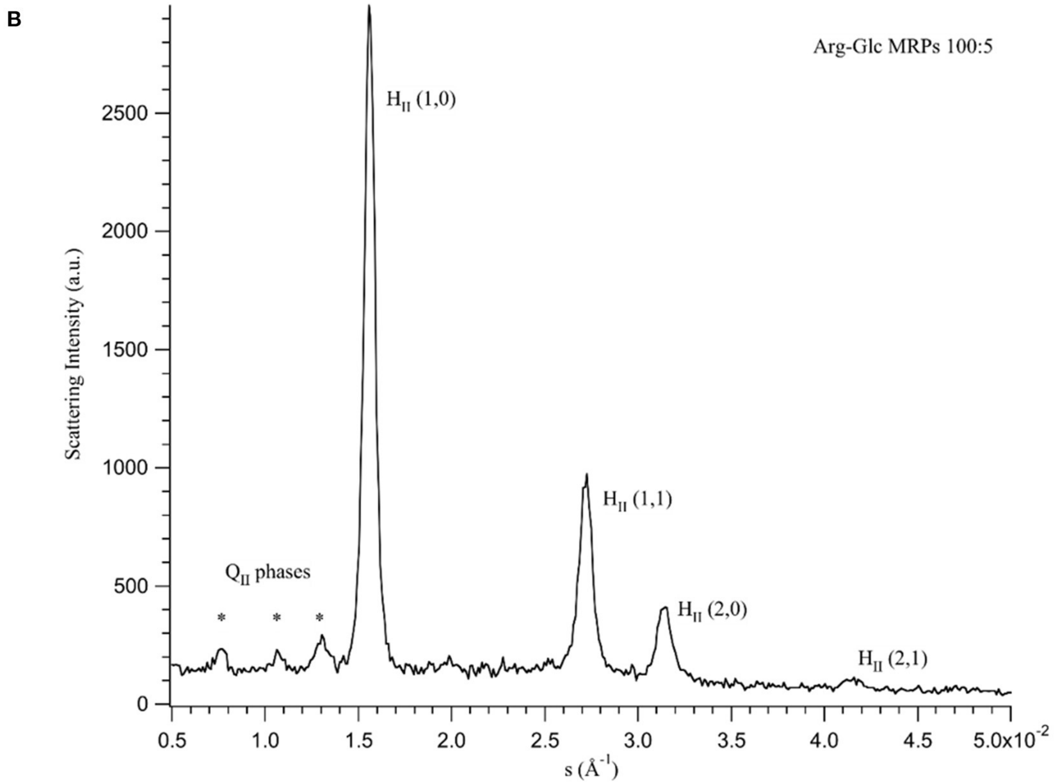

The scattering profiles as function of s-range at 74.4°C.

FIGURE 5 | Scattering profiles of MeDOPE MLVs in the presence of Arg-Glc MRPs (100:5). **(A)** Temperature-resolved 3D scattering density profiles. **(B)** The scattering density profiles as a function of s-range at 74.4°C ($T_H + 7.5$°C). L(1) refers to the first-order scattering peak of L_α phase. L(2) refers to the second-order scattering peak of L_α phase. Q_{II} refers to the inverted cubic phase, in which three diffraction peaks were observed, labeled with *. H_{II} (1,0)/(1,1)/(2,0)/(2,1) refer to the first and second order of the inverted hexagonal phase.

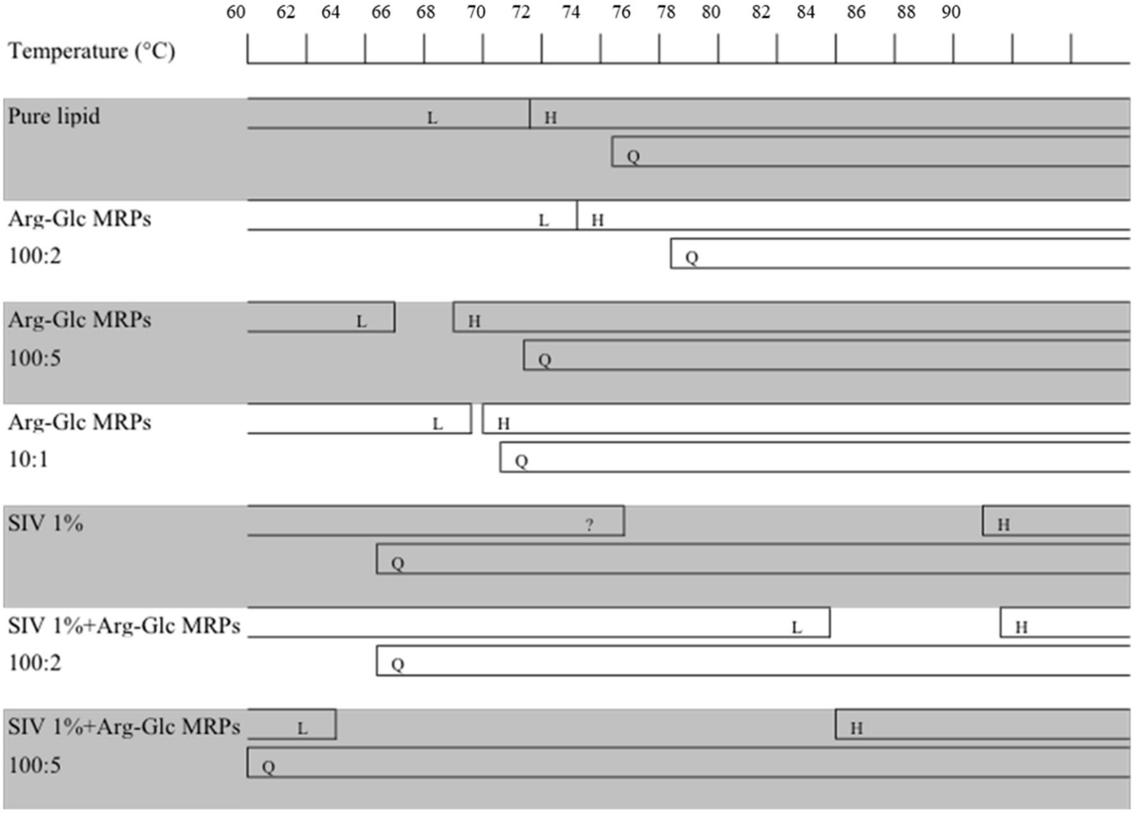

FIGURE 6 | Schematic summary of the phase behavior of MeDOPE MLVs and the MeDOPE in the presence of Arg-Glc MRPs and/or SIV fusion peptide. The transition temperatures were measured by a temperature scanning at 1 K/min from 30 to 90°C with the temperature-resolved X-ray diffraction.

This implies that Arg-Glc MPRs destabilize the lipid bilayers at high concentrations and promote the phase transition from an ordered to a less ordered status. Meanwhile, due to the possible coexistence of several sub-phases induced by interference of MRPs, the amount of energy in terms of heat as a function of time, was increased to overcome the overall energy barrier and encourage the formation of a regular structure.

Secondly, the SIV fusion peptide changed the phase behavior of the lipid vesicles, which was regulated by Arg-Glc MRPs. In the DSC study, SIV fusion peptide raises the T_H of MeDOPE by 4°C but decreases T_M at a high temperature scan rate (40 K/min). This is consistent with X-ray diffraction data (Harroun et al., 2003), in which the SIV peptide (lipid/peptide = 100:1) raises T_H by 10°C (to about 74°C) at the temperature scan rate of 30 K/h, while at 100:2 SIV, the hexagonal phase is eliminated. In contrast, the SIV peptide (lipid/peptide = 100:1) raises T_H to about 76°C at the scan rate of 40 K/min in this study. At 100:2 SIV, the hexagonal phase is still observed as T_H is about 77°C. It has been described for T_H to be scan-rate-dependent (Colotto et al., 1996), which is presumably varied along the different temperature scan rates. This might explain why the T_H of MeDOPE MLVs obtained in my DSC study is higher by 2°C than that of X-ray data at 60°C/h. However, one can also attribute this variation to the differences in the sensitivity of the two methods. By analyzing the Gaussian peaks, a minor change in structure of bilayers can be detected and examined with X-ray scattering. DSC is capable of examining main phase transition events like lamellar-to-hexagonal phase transition but has a limited capacity to track transient structures of intermediates, e.g., cubic phase, at the relatively high scan rate employed in this study.

SIV promotes the breakdown of lamellar structure and the formation of the cubic phase (Harroun et al., 2003). Some effects of SIV on lamellar-to-cubic phase transition, such as lowering the T_Q, are not readily measured by DSC as shown in **Figure 1B**, since the transient phases are in continuous change. However, the fusogenic nature of the peptide is still implied by the drop in ΔT_H and heat consumption of the L_α-H_{II} phase transition. The 2°C decline in the temperature range of this transition, in the presence of 100:1 SIV, possibly suggests that a relatively uniform lipid packing is installed in the transient structure prior to the occurrence of the L_α-H_{II} transition. Furthermore, in terms of its effect on T_M, T_H, ΔH_f, and ΔT_H, the 100:2 SIV peptide is more potent than 100:1 SIV, but not much. It is also consistent with previous X-ray diffraction data reported by Harroun et al.

Arg-Glc MRPs partly offset the effects of SIV peptide on MeDOPE phase transition, in a concentration-dependent manner. In the presence of 100:1 SIV, the MRPs at 100:2 and 10:1 stabilize the gel phase when 100:5 MRPs destabilize the gel phase and liquid crystal phase. The MRPs reversed the destabilizing effects of SIV fusion peptide on the lamellar phase of liposome, to potentially inhibit membrane fusion induced by SIV.

By measuring the phase transition as a function of temperature with SAXS, the influences of Arg-Glc MRPs on the SIV peptide-induced membrane fusion are revealed. The rise in the transition temperature of non-lamellar phases, induced by 100:2 Arg-Glc MRPs, implies a stabilization of lamellar structure conducted by the MRPs. However, the effects of Arg-Glc MRPs on T_{H} and T_{Q} are reversed by increasing their proportion in lipid bilayer to 100:5. The MRPs destabilize the lamellar bilayer and encourage the formation of non-lamellar phase. At a higher MRP concentration (10:1), the promoting effects of Arg-Glc MRPs on the inverted hexagonal phase become weaker, while the T_{Q} was dropping. This implies that the high concentration of Arg-Glc MRPs mildly affected L_{α}-to-H_{II} transition while promoting L_{α}-to-Q_{II} transition. This observation is in good agreement with the phase transition studies conducted with DSC.

The action of fusion peptides on the inverse hexagonal phase is separated from their ability to inducing inverse cubic phase (Darkes et al., 2002). It has been reported that the SIV peptide dramatically delayed the inverse hexagonal phase while inducing “a gap between the phase where no structure was presented” (Harroun et al., 2003). In my study, SIV acts very similarly except the gap between L_{α} and H_{II} phases is covered up by the extension of a lamellar-like phase. SIV tends to promote the formation of an inverse cubic phase when bypassing the intermediate structures leading to the hexagonal phase. Arg-Glc MRPs (100:2) stabilize the bilayer and increase the temperature range of lamellar phase by about 7°C. However, the MRPs at 100:5 destabilize the lamellar phase and promote the formation of the inverse cubic phase and inverse hexagonal phase, while partially offsetting the delay in lamellar-to-hexagonal transition caused by the fusion peptide. Therefore, the overall influences of MRPs at 100:5 on the peptide-induced membrane fusion remains uncertain and warrants further study.

CONCLUSION

In summary, Arg-Glc MRPs stabilize the lamellar phase and inhibit the SIV-induced negative curvature strain of bilayer at a low concentration (100:2). Although this inhibitory effect seemed to fade away at higher concentrations (100:5) of MRPs, the regulating activity of the MRPs upon lipid lamellar-to-non-lamellar phase transition indicates their potential role in modulating the membrane-related biological events, e.g., viral membrane fusion. The real antiviral efficacy of Arg-Glc MRPs, based on this novel mechanism, is worth further evaluation by using living biological models *in vitro* and *in vivo*.

DATA AVAILABILITY STATEMENT

The original contributions presented in the study are included in the article/supplementary materials, further inquiries can be directed to the corresponding authors.

AUTHOR CONTRIBUTIONS

LK planned and conducted the experiments and wrote the manuscript. PR and JB participated in the data analysis and editing the manuscript. FS helped with the sample preparations and SAXS experiments. MR helped with SAXS experiments and the data analysis as the synchrotron station scientist. JZ helped with chemical tests and writing up. All authors contributed to the article and approved the submitted version.

FUNDING

This study was supported by the National Key R&D Program of China (2016YFD0400202).

REFERENCES

Amenitsch, H., Rappolt, M., Kriechbaum, M., Mio, H., Laggner, P., and Bernstorff, S. (1998). First performance assessment of the small-angle X-ray scattering beamline at ELETTRA. *J. Synchrotron. Radiat.* 5, 506–508. doi: 10.1107/S090904959800137X

Chen, Z. W., Wu, L. W., Liu, S. T., Cai, C. P., Rao, P. F., and Ke, L. J. (2006). Mechanism study of anti-influenza effects of radix isatidis water extract by red blood cells capillary electrophoresis. *China J. Chin. Materia Med.* 31, 1715–1719.

Cherezov, V., Siegel, D. P., Shaw, W., Burgess, S. W., and Caffrey, M. (2003). The kinetics of non-lamellar phase formation in DOPE-me: relevance to biomembrane fusion. *J. Membrane Biol.* 195, 165–182. doi: 10.1007/s00232-003-0617-z

Colotto, A., Martin, I., Ruysschaert, J. M., Sen, A., Hui, S. W., and Epand, R. M. (1996). Structural study of the interaction between the SIV fusion peptide and model membranes. *Biochemistry* 35, 980–989.

Darkes, M. J., Harroun, T. A., Davies, S. M., and Bradshaw, J. P. (2002). The effect of fusio inhibitors on the phase behaviour of N-methylated dioleoylphosphatidylethanolamine. *Biochem. Biophys. Acta* 78220, 1–10. doi: 10.1016/S0005-2736(01)00464-3

Einarsson, H., Snygg, B. G., and Eriksson, C. (1983). Inhibition of bacterial growth by maillard reaction products. *J. Agric. Food Chem.* 31, 1043–1047. doi: 10.1021/jf00119a031

Ellens, H., Bentz, J., and Szoka, F. C. (1986). Fusion of phosphatidylethanolamine-containing liposomes and mechanism of the L alpha-HII phase transition. *Biochemistry* 25, 4141–4147. doi: 10.1021/bi00362a023

Epand, R. M. (1998). Lipid polymorphism and protein-lipid interactions. *Biochim. Biophys. Acta* 1376, 353–368. doi: 10.1016/S0304-4157(98)00015-X

Harper, P. E., Mannock, D. A., Lewis, R. N., Mcelhaney, R. N., Gruner, S. M., and Gruner, S. M. (2001). X-ray diffraction structures of some phosphatidylethanolamine lamellar and inverted hexagonal phases. *Biophys. J.* 81, 2693–2706. doi: 10.1016/S0006-3495(01)75912-7

Harris, N. D., and Tan, B. K. (1999). “Effect of maillard reaction products on microbial growth,” in *The IFT Annual Meeting* (Chicago, IL), 37D–31.

Harroun, T. A., Balali-Mood, K., Gourlay, I., and Bradshaw, J. P. (2003). The fusion peptide of simian immunodeficiency virus and the phase behaviour of N-methylated dioleoylphosphatidylethanolamine. *Biochim. Biophys. Acta* 1617, 62–68. doi: 10.1016/j.bbamem.2003.09.003

Huang, T. C., Toraya, H., Blanton, T. N., and Wu, Y. (1993). X-ray powder diffraction analysis of silver behenate, a possible low-angle diffraction standard. *J. Appl. Cryst.* 26, 180–184. doi: 10.1107/S0021889892009762

Ke, L., Wen, T., Bradshaw, J., Zhou, J., and Rao, P. (2012). Antiviral decoction of isatidis radix (Bn Lán Gēn) inhibited influenza virus adsorption on MDCK cells by cytoprotective activity. *J. Tradit. Complement. Med.* 2, 47–51. doi: 10.1016/S2225-4110(16)30070-0

Ke, L. (2010). *Mechanism of Anti-Influenza Virus Activity of Maillard Reaction Products Derived From Isatidis Roots*. Edinburgh: The University of Edinburgh.

Kobasa, D., Takada, A., Shinya, K., Hatta, M., Halfmann, P., Theriault, S., et al. (2004). Enhanced virulence of influenza A viruses with the haemagglutinin of the 1918 pandemic virus. *Nature* 431, 703–707. doi: 10.1038/nature02951

Kundinger, M. M. (2004). *Growth and Virulence Response of Salmonella Typhimurium to Soluble Maillard Reaction Products*. River Falls, WI: University of Wisconsin-River Falls.

Kusube, M., Goto, M., Tamai, N., Matsuki, H., and Kaneshina, S. (2006). Bilayer phase transitions of N-methylated dioleoylphosphatidylethanolamines under high pressure. *Chem. Phys. Lipids* 142, 94–102. doi: 10.1016/j.chemphyslip.2006.03.004

Marsh, M., and Helenius, A. (2006). Virus entry: open sesame. *Cell* 124, 729–740. doi: 10.1016/j.cell.2006.02.007

Petrascu, A.-M., Koch, M. H. J., and Gabriel, A. (1998). A beginners' guide to gas-filled proportional detectors with delay line readout. *Chem. Phys.* 37, 463–483. doi: 10.1080/00222349808220487

Rappolt, M., Hickel, A., Bringezu, F., and Lohner, K. (2003). Mechanism of the lamellar/inverse hexagonal phase transition examined by high resolution X-ray diffraction. *Biophys. J.* 84, 3111–3122. doi: 10.1016/S0006-3495(03)70036-8

Rogers, G. N., Daniels, R. S., Skehel, J. J., Wiley, D. C., Wang, X. F., Higa, H. H., et al. (1985). Host-mediated selection of influenza virus receptor variants. sialic acid-alpha 2,6Gal-specific clones of a/Duck/Ukraine/1/63 revert to sialic acid-alpha 2,3Gal-specific wild type in Ovo. *J. Biol. Chem.* 260, 7362–7367. doi: 10.1016/0168-1702(85)90329-6

Rufián-Henares, J. A., and Morales, F. J. (2006). A new application of a commercial microtiter plate-based assay for assessing the antimicrobial activity of maillard reaction products. *Food Res. Int.* 39, 33–39. doi: 10.1016/j.foodres.2005.06.002

Siegel, D. P., Green, W. J., and Talmont, Y. (1994). The mechanism of lamellar-to-inverted hexagonal phase transitions: a study using temperature-jump cryo-electron microscopy. *Biophys. J.* 66, 402–414. doi: 10.1016/S0006-3495(94)80790-8

Sykora, J., Jurkiewicz, P., Epand, R. M., Kraayenhof, R., Langner, M., and Hof, M. (2005). Influence of the curvature on the water structure in the headgroup region of phospholipid bilayer studied by the solvent relaxation technique. *Chem. Phys.* 135, 213–221. doi: 10.1016/j.chemphyslip.2005.03.003

van Gorkom, L. C., Nie, S. Q., and Epand, R. M. (1992). Hydrophobic lipid additives affect membrane stability and phase behavior of N-monomethyldioleoylphosphatidylethanolamine. *Biochemistry* 31, 671–677. doi: 10.1021/bi00118a006

Wiley, D. C., and Skehel, J. J. (1987). The structure and function of the hemagglutinin membrane glycoprotein of influenza virus. *Annu. Rev. Biochem.* 56, 365–394. doi: 10.1146/annurev.bi.56.070187.002053

Conflict of Interest: The authors declare that the research was conducted in the absence of any commercial or financial relationships that could be construed as a potential conflict of interest.

frontiers
in Cell and Developmental Biology

ORIGINAL RESEARCH
published: 11 February 2021
doi: 10.3389/fcell.2021.617984

Plasmalogen-Based Liquid Crystalline Multiphase Structures Involving Docosapentaenoyl Derivatives Inspired by Biological Cubic Membranes

Angelina Angelova[1]*, Borislav Angelov[2], Markus Drechsler[3], Thomas Bizien[4], Yulia E. Gorshkova[5] and Yuru Deng[6]

[1] Institut Galien Paris-Saclay UMR8612, Université Paris-Saclay, CNRS, Châtenay-Malabry, France, [2] Institute of Physics, ELI Beamlines, Academy of Sciences of the Czech Republic, Prague, Czech, [3] Keylab "Electron and Optical Microscopy", Bavarian Polymer Institute, University of Bayreuth, Bayreuth, Germany, [4] Synchrotron SOLEIL, L'Orme des Merisiers, Saint-Aubin, France, [5] Frank Laboratory of Neutron Physics, Joint Institute for Nuclear Research, Dubna, Russia, [6] Wenzhou Institute, University of Chinese Academy of Sciences, Wenzhou, China

OPEN ACCESS

Edited by:
Yeshayahu Talmon,
Technion Israel Institute
of Technology, Israel

Reviewed by:
Dwijendra K. Gupta,
Jai Prakash Vishwavidyalaya, India
Montserrat Samso,
Virginia Commonwealth University,
United States

***Correspondence:**
Angelina Angelova
angelina.angelova@
universite-paris-saclay.fr

Specialty section:
This article was submitted to
Cellular Biochemistry,
a section of the journal
Frontiers in Cell and Developmental
Biology

Received: 15 October 2020
Accepted: 04 January 2021
Published: 11 February 2021

Citation:
Angelova A, Angelov B,
Drechsler M, Bizien T, Gorshkova YE
and Deng Y (2021)
Plasmalogen-Based Liquid Crystalline
Multiphase Structures Involving
Docosapentaenoyl Derivatives
Inspired by Biological Cubic
Membranes.
Front. Cell Dev. Biol. 9:617984.
doi: 10.3389/fcell.2021.617984

Structural properties of plasmenyl-glycerophospholipids (plasmalogens) have been scarcely studied for plasmalogens with long polyunsaturated fatty acid (PUFA) chains, despite of their significance for the organization and functions of the cellular membranes. Elaboration of supramolecular assemblies involving PUFA-chain plasmalogens in nanostructured mixtures with lyotropic lipids may accelerate the development of nanomedicines for certain severe pathologies (e.g., peroxisomal disorders, cardiometabolic impairments, and neurodegenerative Alzheimer's and Parkinson's diseases). Here, we investigate the spontaneous self-assembly of bioinspired, custom-produced docosapentaenoyl (DPA) plasmenyl (ether) and ester phospholipids in aqueous environment (pH 7) by synchrotron small-angle X-ray scattering (SAXS) and cryogenic transmission electron microscopy (cryo-TEM). A coexistence of a liquid crystalline primitive cubic *Im3m* phase and an inverted hexagonal (H_{II}) phase is observed for the DPA-ethanolamine plasmalogen (C16:1p-22:5n6 PE) derivative. A double-diamond cubic *Pn3m* phase is formed in mixed assemblies of the phosphoethanolamine plasmalogen (C16:1p-22:5n6 PE) and monoolein (MO), whereas a coexistence of cubic and lamellar liquid crystalline phases is established for the DPA-plasmenyl phosphocholine (C16:1p-22:5n6 PC)/MO mixture at ambient temperature. The DPA-diacyl phosphoinositol (22:5n6-22:5n6 PI) ester lipid displays a propensity for a lamellar phase formation. Double membrane vesicles and multilamellar onion topologies with inhomogeneous distribution of interfacial curvature are formed upon incorporation of the phosphoethanolamine plasmalogen (C16:1p-22:5n6 PE) into dioleoylphosphocholine (DOPC) bilayers. Nanoparticulate formulations of plasmalogen-loaded cubosomes, hexosomes, and various multiphase cubosome- and hexosome-derived architectures and mixed type nano-objects (e.g., oil droplet-embedding vesicles or core–shell particles with soft corona) are produced with PUFA-chain phospholipids and lipophilic antioxidant-containing membrane compositions that are characterized by synchrotron SAXS and cryo-TEM imaging. The obtained multiphase nanostructures reflect the changes in the membrane curvature induced by the inclusion of DPA-based PE and PC plasmalogens, as well as DPA-PI ester derivative, and open new opportunities for exploration of these bioinspired nanoassemblies.

Keywords: docosapentaenoyl phospholipids, lipid cubic phase, inverted hexagonal phase, plasmalogen-loaded cubosomes, hexosomes, SAXS, cryo-TEM

INTRODUCTION

Plasmenyl-phospholipids (plasmalogens) are a class of ether-type (1-alkyl-1′-enyl, 2-acyl) glycerophospholipids with essential functions for the living cells in the brain, retina, heart, lung, skeletal muscles, and testis (Gross, 1985; Creuwels et al., 1997; Batenburg and Haagsman, 1998; Snyder, 1999; Goldfine, 2010; Wallner and Schmitz, 2011; Saab et al., 2014; Dean and Lodhi, 2018; Jiménez-Rojo and Riezman, 2019; Paul et al., 2019). They are recognized as crucial for the human health considering that plasmalogens deficiency is associated with the disease progress in various pathologies (Han et al., 2001; Munn et al., 2003; Brites et al., 2004; Braverman and Moser, 2012; Brosche et al., 2013; Sutter et al., 2015; Jang et al., 2017; Messias et al., 2018). Decreased ethanolamine plasmalogen levels have been established with the progression of Alzheimer's (AD) and Parkinson's (PD) diseases, psychiatric disorders, and also in neuromuscular impairments, glaucoma, coronary artery disease, and acute myocardial infarction (Farooqui et al., 1997; Dragonas et al., 2009; Brodde et al., 2012; Sutter et al., 2016; Dorninger et al., 2017a,b, 2019; Paul et al., 2019; Su et al., 2019). The plasmalogen lipids modulate the membrane fluidity and dynamics, influence the membrane protein organization, and provide reservoirs of secondary messengers as well as precursors of inflammatory mediators (Bogdanov et al., 1999; Thai et al., 2001; Mannock et al., 2010; Koivuniemi, 2017; Jenkins et al., 2018; Pohl and Jovanovic, 2019; Fontaine et al., 2020). The vinyl ether moiety at the sn-1 position of glycerol backbone is significant for the antioxidant (scavenger) properties of plasmalogens and the protection of neuronal, cardiac, and muscle cells from oxidative stress (Reiss et al., 1997; Zoeller et al., 1999; Leßig and Fuchs, 2009; Wallner and Schmitz, 2011; Yamashita et al., 2015; Sibomana et al., 2019).

In this work, we aim at deeper understanding of the structural polymorphism of hydrated polyunsaturated fatty acid (PUFA) plasmalogens and esters and their capacity to form self-assembled nanoscale structures as pure lyotropic lipids or in mixtures with other amphiphilies. **Figure 1** presents the major polymorphic states of hydrated lyotropic lipids (Mariani et al., 1988; Seddon and Templer, 1995). The arrangement of lipids and amphiphiles in supramolecular assemblies is governed by intermolecular hydrophobic and electrostatic interactions, temperature, degree of hydration, and the geometry of the molecules (Israelachvili et al., 1976; Cullis and de Kruijff, 1979; Cui et al., 2007; Shaharabani et al., 2016).

The non-lamellar phase-forming tendencies of some ether lipid types have been evaluated in an isolated state based on measurements of their lamellar-gel to lamellar-fluid chain-melting characteristics and also of lamellar-to-non-lamellar inverted hexagonal (H_{II}) phase transition temperatures (Goldfine et al., 1981; Malthaner et al., 1987). Such parameters have been determined for ethanolamine plasmalogen derivatives extracted from egg, beef heart, or *Clostridium butyricum* (Goldfine et al., 1987a) using differential scanning calorimetry (DSC) and nuclear magnetic resonance (^{31P}NMR) spectroscopic

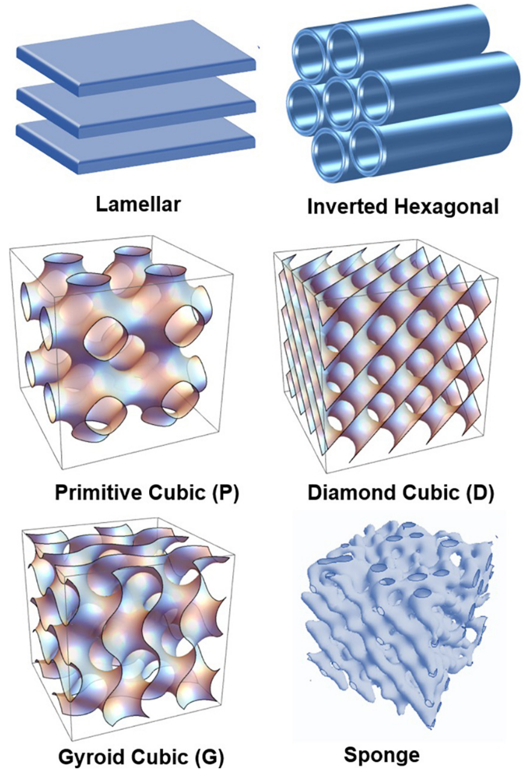

FIGURE 1 | Schematic presentation of lamellar and non-lamellar liquid crystalline phase structures resulting from the structural polymorphism of lyotropic lipid/water mixtures: lamellar bilayer, inverted hexagonal (H_{II}), primitive cubic (P), bicontinuous double-diamond cubic (D), bicontinuous gyroid cubic (G), and sponge phases.

studies of lipid membrane systems (Boggs et al., 1981; Lohner et al., 1984; Malthaner et al., 1987). It has been intriguing to establish whether the non-lamellar phase behavior of plasmalogen lipids is a result of the location of carbon–carbon double bond (Goldfine et al., 1981, 1987a). The presence of $1'$-carbon–carbon double bond at sn-1 position of the glycerol backbone of ethanolamine plasmalogens has been expected to influence lipid polymorphism through the degree of polarity of polar–apolar interfaces of lipid membranes (Goldfine et al., 1987b; Rog and Koivuniemi, 2016).

High-resolution structural data have been required to better understand the formation of non-lamellar liquid crystalline phases by plasmenyl phospholipids and the relationship between molecular structure and phase behavior (**Figure 1**). Such studies have been initiated in the past for plasmalogens with C16:0, C18:0, and C18:1 aliphatic moieties (Lohner et al., 1984, 1991). The performed small-angle X-ray scattering (SAXS) investigations have indicated that the induction of non-lamellar phases, in particular of an inverted hexagonal (H_{II}) phase, is promoted by the increase in the hydrocarbon chain length (e.g., from C16 to C18) as well as by the increase in the degree of chain unsaturation (e.g., from di-C18:1 to di-C18:2; Lohner, 1996). The hydration of the headgroups and their interaction with the solvent has also been an important determinant for the physicochemical differences, which have been observed in the phase behaviors of the studied lipid types (Lohner et al., 1984). To our knowledge, structural SAXS data are not available yet for plasmalogens with PUFA chains.

Ultrastructural studies of subcellular organelles by transmission electron microscopy (TEM) have indicated the role of plasmalogens in the induction of non-lamellar cubic membrane structures under starvation stress conditions (Chong and Deng, 2012; Deng et al., 2017). From a structural viewpoint, docosapentaenoic acid (DPA) has been identified as the critical PUFA determinant for the cubic lipid membrane formation in amoeba *Chaos* mitochondria (Deng et al., 2009; Almsherqi et al., 2010). It has been emphasized that plasmalogens are structural membrane components that act also as antioxidants in the *Chaos* cells. The survival mechanism (from the applied cellular stress) has been explained by the formation of nanoperiodic arrangements of biological cubic membranes during cellular stress response to unfavorable environmental cues (Deng and Almsherqi, 2015). The presence of cubic membranes has been associated with improved cell survival during long-term starvation (Deng et al., 2009). In addition, it has been reported that the inverted hexagonal (H_{II}) phase of plasmenyl-phosphoethanolamines promotes the membrane fusion (Boggs et al., 1981; Han and Gross, 1990; Glaser and Gross, 1994).

The lack of effective treatments of neurodegenerative diseases is an urgent challenge at present. Nanoparticles and nanoassemblies may offer innovative combinations of multiple bioactive molecules to target the various mechanisms of multiple neurodegenerative diseases (Angelova et al., 2011, 2019b; Fonseca-Santos et al., 2015; Angelova and Angelov, 2017; Harilal et al., 2019). In recent works, we have exploited self-assembly-based nanotechnologies for combination delivery of a key neurotrophic protein [brain-derived neurotrophic factor (BDNF)], curcumin, and omega-3 polyunsaturated fatty acids (ω-3 PUFAs) in order to trigger and promote neuro-repair (Guerzoni et al., 2017; Angelova et al., 2018; Rakotoarisoa et al., 2019). Biomedical studies have emphasized that AD patients lose up to 60% of plasmalogens from the brain cell membranes (Farooqui et al., 1997; Su et al., 2019). There is rising evidence that phospholipids of the plasmalogen-phosphatidylethanolamine type may provide a novel therapeutic approach to impact the neuronal functions in AD and PD pathologies (Hossain et al., 2013; Yamashita et al., 2015; Che et al., 2018, 2020; Mawatari et al., 2020). Results from recent clinical trials have shown that PUFA-chain ethanolamine plasmalogens can be 100-fold more powerful in stimulating neuro-repair as compared to the conventional ω-3 PUFA species (Fujino et al., 2017; Fujino et al., 2018). Biological assays also revealed that the suppression of the neuronal cell apoptosis by plasmalogens is more efficient for lipids with longer PUFA chains such as C18:0/p-22:6-PE or C18:0/p-22:6-PC (Yamashita et al., 2015; Che et al., 2020). Hence, further investigations of PUFA-chain phospholipid phase behavior, miscibility in lipid bilayers, effects on membrane curvature, membrane fusion, formation of transient, or permanent nanoperiodic arrangements, compartmentalization (Muallem et al., 2017; Bharadwaj et al., 2018; Casares et al., 2019), and nanostructure formation are needed in order to define prospective nanomedicine-based therapeutic strategies.

In this context, we report here a structural study of novel custom-synthesized plasmenyl (ether) and ester phospholipids with long PUFA (22:5n6) chains. They were designed by bioinspiration from the main constituents of the biological cubic membranes identified in mitochondria of starved amoeba *Chaos* cells (Deng et al., 2009; Almsherqi et al., 2010; Deng and Almsherqi, 2015; Deng et al., 2017). The choice of the docosapentaenoyl (DPA, 22:5n6) PUFA chains was determined by the lipidomic (gas liquid chromatography and mass spectrometry) analysis of membranous compositions extracted from amoeba *Chaos* mitochondria (Deng et al., 2009; Almsherqi et al., 2010).

Figure 2 shows the chemical structures of the custom-synthesized PUFA-chain phospholipid compounds, namely, plasmenyl phosphoethanolamine (C16:1p-22:5n6 PE), plasmenyl phosphocholine (C16:1p-22:5n6 PC), and DPA-diacyl phosphoinositol (22:5n6-22:5n6 PI) ester. The formation of lyotropic liquid crystalline phases by these synthetic phospholipids and their mixtures with a non-lamellar lipid monoolein (MO) or a lamellar phospholipid DOPC, serving as matrix colipids, was studied by synchrotron SAXS at selected compositions. Stable dispersions of nanostructured particles, involving PUFA-chain phospholipids and natural small molecule antioxidants (vitamin E and coenzyme Q10), were produced. The effects of PUFA-chain phospholipids (plasmalogens or esters) on the membrane curvature were exploited in order to create liquid crystalline nanoparticles with different topologies and inner organizations, which were evidenced by SAXS and cryo-TEM imaging. Then, the significance of the particle topologies, crystalline organizations, and compartmentalization for prospective biomedical applications is discussed.

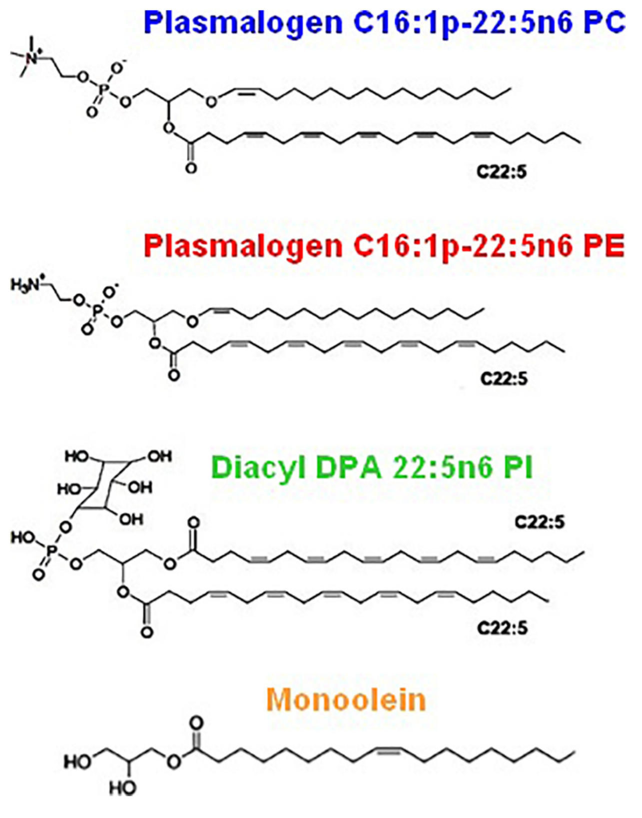

FIGURE 2 | Chemical structures of custom-produced polyunsaturated fatty acid (PUFA)-ether or ester type glycerophospholipids with long tails comprised of docosapentaenoyl (DPA) chains. Plasmalogens (1-alkyl-1′-enyl,2-acyl ether phospholipids) are obtained with phosphocholine and phosphoethanolamine headgroups, namely, 1-O-1′-(Z)-hexadecenyl-2-(4Z,7Z,10Z,13Z,16Z-docosapentaenoyl)-sn-glycero-3-phosphocholine, C16:1p-22:5n6 PC (top), and 1-O-1′-(Z)-hexadecenyl-2-(4Z,7Z,10Z,13Z,16Z-docosapentaenoyl)-sn-glycero-3-phosphoethanolamine, C16:1p-22:5n6 PE (middle). As a diacyl ester lipid, 1,2-bis(4Z,7Z,10Z,13Z,16Z-docosapentaenoyl)-sn-glycero-3-phosphoinositol, 22:5n6 PI, is enriched in docosapentaenoyl (DPA) moieties in order to increase the hydrophobic lipid volume with regard to the bulky phosphoinositol (PI) polar headgroup. Monoolein (bottom) is a single-chain monoglyceride used as a colipid in the studied mixed nanoassemblies.

RESULTS

Self-Assembled Bulk Liquid Crystalline Lipid/Water Phases of Docosapentaenoyl-Plasmalogens and DPA-Phospholipid Constituents Chosen by Bioinspiration From Biological Cubic Membranes

The structural polymorphism of synthetic PUFA-phospholipid/water phases resulting from the rationally chosen lipid chemical structures is characterized here by synchrotron SAXS. The following features are considered: (i) structural role of the hydrocarbon chains through a study of synthetic plasmalogen derivatives with long polyunsaturated DPA (C22:5n6) chains and (ii) structural role of the polar headgroups through a study of DPA-glycerophospholipids with PE, PC, and PI headgroups. The SAXS investigations were performed under neutral pH condition taking into account that the alkenyl (vinyl ether) bond in the plasmalogen molecules is susceptible to hydrolysis at strong acidic pH.

It is of great interest to find out whether the PUFA-chain plasmalogens and esters involving docosapentaenoyl (DPA, C22:5n6) tails (**Figure 2**) may generate non-lamellar liquid crystalline phases (**Figure 1**) upon self-assembly in a pure state in aqueous environment as well as whether they may induce non-lamellar bicontinuous cubic phase formation upon mixing with membrane lipids in synthetic self-assembled systems. These findings should add new knowledge about (i) the membrane curvature-modifying capacity of the designed DPA-phospholipid derivatives and (ii) the usefulness of nanocrystalline arrangements for the development of non-lamellar nanoparticles of bioactive lipids.

Non-lamellar Cubic and Inverted Hexagonal Phases Formed by Hydrated DPA-Plasmalogen Phosphoethanolamine

The SAXS patterns of the DPA-phosphoethanolamine plasmalogen (C16:1p-22:5n6 PE) in a hydrated bulk state are presented in **Figure 3A**. The investigated hydration level is determined by a lipid/water ratio of 50/50 (wt/wt). The positions of Bragg diffraction peaks detected in the SAXS pattern 1 (red plot) are indexed in **Figure 3B**. A coexistence of a liquid crystalline primitive cubic *Im3m* phase with an inverted hexagonal (H_{II}) phase is identified at a temperature of 22°C for the freshly prepared bulk-phase DPA-ethanolamine plasmalogen (C16:1p-22:5n6 PE)/water system (**Figure 3A**, plot 1). The first Bragg peak of the primitive cubic *Im3m* phase is resolved at $q = 0.0453$ Å^{-1}, while the first Bragg peak of H_{II} phase is recorded at $q = 0.0994$ Å^{-1} (**Figure 3B**). The *Im3m* cubic lattice parameter (estimated from the sequence of Braggs peaks spaced in the ratio $\sqrt{2}:\sqrt{4}:\sqrt{6}:\sqrt{8}:\sqrt{10}:\sqrt{12}:\sqrt{14}:\sqrt{16}:\sqrt{18}$) is $a_{Q(Im3m)} = 19.6$ nm. The H_{II}-phase is characterized by a lattice parameter of $a_H = 7.23$ nm. A closer examination of the SAXS plot in **Figure 3B** reveals an overlap of a Bragg diffraction peak of the primitive cubic *Im3m* phase with the first Bragg peak of the inverted hexagonal (H_{II}) phase at $q = 0.0994$ Å^{-1}. This coexistence characterizes the polymorphism of the liquid crystalline DPA-plasmenyl-PE/water system, which was studied at room temperature. The fact that the PE-plasmalogen does not form a unique stable non-lamellar mesophase suggests that the flexible long polyunsaturated DPA chains may impart a propensity for the formation of domain structures of this lipid in biological membranes.

The SAXS plots (2)–(4) in **Figure 3A** demonstrate the radiation-sensitive behavior of the hydrated plasmalogen (C16:1p-22:5n6 PE) assembly. The synthetic lipid membranes undergo a cubic-to-hexagonal phase transition, which reaches a weakly ordered lipid state upon repeated exposure to the X-ray beam. The Bragg peaks of the primitive *Im3m* cubic phase progressively vanish owing to the radiation-induced interconversion. The peaks of the inverted hexagonal (H_{II}) phase

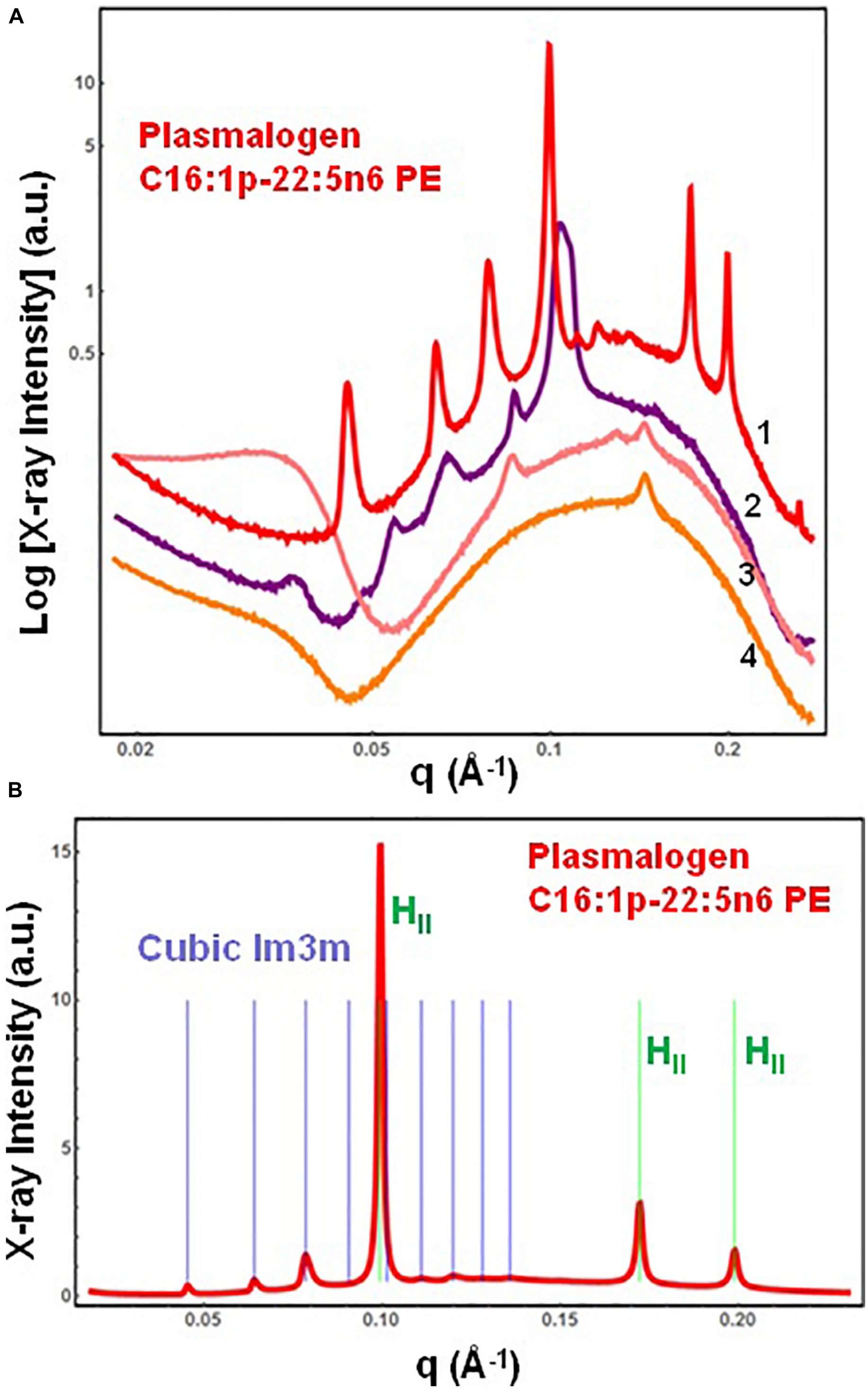

FIGURE 3 | (A) Synchrotron small-angle X-ray scattering (SAXS) patterns of a hydrated bulk-phase plasmenyl-phospholipid [DPA-ethanolamine plasmalogen (C16:1p-22:5n6 PE)] at a lipid/water ratio of 50/50 (wt%/wt%) and aqueous phosphate buffer environment (1.10^{-2} M) of pH 7 with added 2,6-di-tert-butyl-4-methylphenol (BHT). Pattern (1) corresponds to a freshly prepared plasmalogen/water sample examined by synchrotron SAXS. Plots (2)–(4) display the progressive vanishing of the cubic phase peaks upon multiple SAXS recordings with the same sample. **(B)** Indexing of the Bragg diffraction peaks resolved in the SAXS pattern (1) from **(A)**. In a linear scale, the two sets of Bragg peaks index: (i) a primitive cubic phase of the *Im3m* space group of symmetry [purple bars corresponding to the (110), (200), (211), (220), (310), (222), (321), (400), and (411) cubic lattice reflections for peak positions spaced in the ratio $\sqrt{2}:\sqrt{4}:\sqrt{6}:\sqrt{8}:\sqrt{10}:\sqrt{12}:\sqrt{14}:\sqrt{16}:\sqrt{18}$] and (ii) an inverted hexagonal (H_{II}) phase [green bars corresponding to the (10), (11), and (20) reflections at peak positions spaced in the ratio $1:\sqrt{3}:\sqrt{4}$]. Temperature is 22°C.

are detectable in the SAXS plots (2)–(4) in **Figure 3A** and thus represent a longer-lived, more stable non-lamellar structure.

Cubic Phases and Structural Intermediates in Two-Component Bulk Phases of Docosapentaenoyl-Phospholipids and Monoolein

The single-component DPA-plasmalogen did not form a stable unique bicontinuous cubic phase at room temperature (**Figure 3**). Taking into account the instability on storage of the cubic *Im3m* liquid crystalline phase of the hydrated DPA-plasmalogen and the observed radiation-induced interconversion of the single-lipid system (**Figure 3**), mixed lipid phases were subsequently formulated using a colipid. The lyotropic single-chain lipid monoolein (MO; **Figure 2**) was added at a selected molar ratio to the studied double-chain ether or ester phospholipids involving polyunsaturated (22:5n6) tails. The impact of 15 mol.% DPA-phospholipid incorporation on the structural organization of self-assembled bulk two-component lipid/water phases was evidenced by SAXS. Under the investigated conditions, hydrated MO forms a bicontinuous cubic phase of the double-diamond *Pn3m* space group of symmetry (**Figure 4**, orange plot). The recorded first Bragg peak is centered at $q = 0.083$ Å^{-1}. It belongs to a set of Bragg peaks, spaced in the ratio $\sqrt{2}:\sqrt{3}:\sqrt{4}:\sqrt{6}:\sqrt{8}:\sqrt{9}:\sqrt{10}:\sqrt{11}:\sqrt{12}:\sqrt{14}\ \ldots$, which determines a cubic lattice parameter $a_{Q(Pn3m)} = 10.8$ nm.

The red plot in **Figure 4** shows the SAXS pattern of a hydrated MO assembly incorporating 15 mol.% DPA-ethanolamine plasmalogen (C16:1p-22:5n6 PE). The PE-plasmalogen, containing a single polyunsaturated (22:5n6) fatty acid chain (**Figure 2**), preserves the non-lamellar organization of the host lipid/water system. The sequence of Bragg diffraction peaks, spaced in the ratio $\sqrt{2}:\sqrt{3}:\sqrt{4}:\sqrt{6}:\sqrt{8}:\sqrt{9}:\sqrt{10}:\sqrt{11}:\sqrt{12}\ \ldots$ (with a first maximum centered at $q = 0.092$ Å^{-1}), defines a distinct bicontinuous cubic phase structure of the double-diamond *Pn3m* space group of symmetry. The lattice parameter of the DPA-plasmalogen phosphoethanolamine (C16:1p-22:5n6 PE)/MO mixed cubic phase is $a_{Q(Pn3m)} = 9.65$ nm, which suggests that the plasmalogen-ethanolamine modifies the hydration level of the aqueous channel networks in the host MO lipid cubic phase.

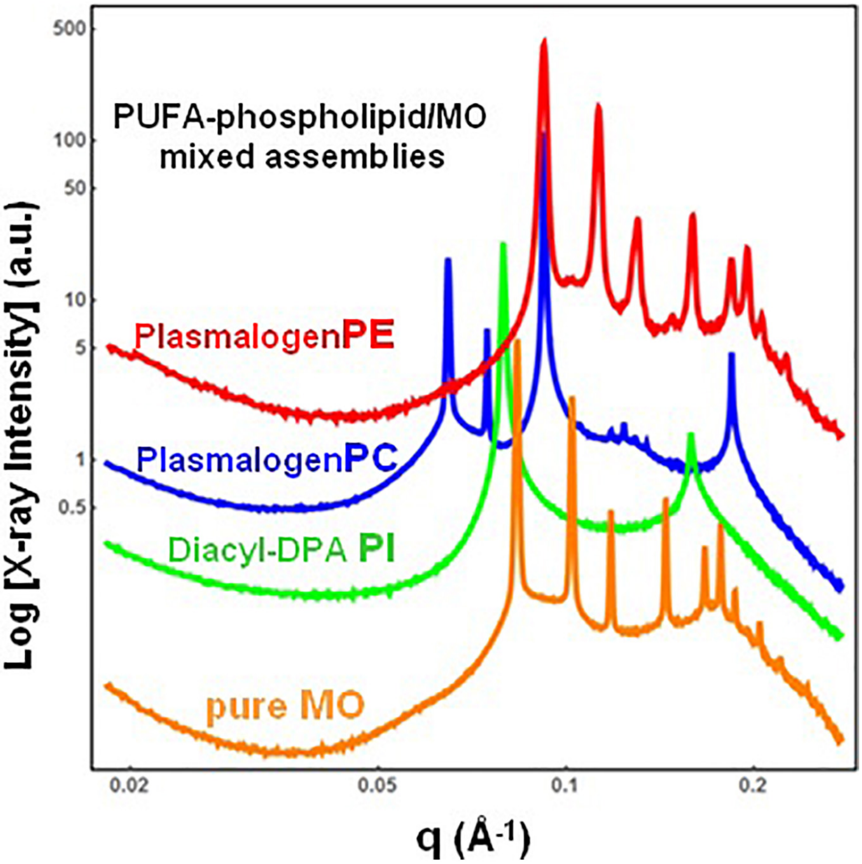

FIGURE 4 | Synchrotron small-angle X-ray scattering (SAXS) patterns of bulk-phase mixtures of monoolein (MO) with incorporated 15 mol.% docosapentaenoyl (DPA, 22:5n6)-modified plasmalogen-phosphoethanolamine C16:1p-22:5n6 PE (red plot), plasmalogen phosphocholine C16:1p-22:5n6 PC (blue plot), or DPA-diacyl phosphoinositol 22:5n6-22:5n6 PI ester lipid (green plot). The red, blue, and green plots correspond to 15/85 (mol/mol) ratio between the polyunsaturated fatty acid (PUFA) phospholipids and monoolein (MO). The orange plot presents the SAXS pattern for the pure MO/buffer system. The lipid/water ratio is 40/60 (wt/wt). Aqueous phase: 1.10^{-2} M phosphate buffer containing 2,6-di-tert-butyl-4-methylphenol (BHT). Temperature is 22°C.

Differences in the phospholipid headgroup type (PE, PC, or PI) and the hydrocarbon chain structure are reflected in the liquid crystalline mixed-phase formation (**Figure 4**). The investigated lipid/water ratio of 40/60 (wt/wt) corresponds to a hydration level, which might not ensure homogeneous hydration of the bulk self-assembled mixture of MO and DPA-phosphocholine plasmalogen (C16:1p-22:5n6 PC). The sequence of Bragg peaks, displaying a first peak centered at $q = 0.0635$ Å^{-1}, evidences a distinct domain of a cubic symmetry in the mixed assembly (**Figure 4**, blue plot). The Bragg peaks spaced in the ratio $\surd 2{:}\surd 3{:}\surd 4{:}\surd 6{:}\surd 8{:}\surd 9{:}\surd 10{:}\surd 11 \ldots$ define a double-diamond *Pn3m* cubic phase structure with a lattice parameter $a_{Q(Pn3m)} = 14.0$ nm. The obtained swollen diamond-type *Pn3m* cubic phase (D_{Large}) appears to coexist with a domain of a less hydrated liquid crystalline structure. The Bragg peaks at $q_1 = 0.092$ Å^{-1} and $q_2 = 0.184$ Å^{-1}, correspond to the first and the second orders of a lamellar phase with a bilayer periodicity $d = 6.83$ nm. This result indicates that the DPA-plasmalogen phosphocholine (C16:1p-22:5n6 PC)/MO assembly forms distinct mixed cubic phase domains (of the double-diamond *Pn3m* space group of symmetry), which coexist with a mixed lamellar phase. It should be noted that the structural parameters of the obtained binary plasmenyl-PC/MO lipid phases significantly differ from those of the pure MO, for which $a_{Q(Pn3m)} = 10.8$ nm (at full hydration) and $d = 4.6$ nm [under limited hydration conditions, e.g., at lipid/water ratios above 60/40 (wt/wt)].

When the long-chain DPA-diacyl phosphoinositol (22:5n6-22:5n6 PI) ester lipid was mixed with the colipid MO, the bulk liquid crystalline sample entirely transformed into a lamellar structure (**Figure 4**, green plot). The well-resolved Braggs peaks for the mixed di-22:5n6-22:5n6 PI/MO lamellar phase ($q_1 = 0.079$ Å^{-1} and $q_2 = 0.158$ Å^{-1}) define a bilayer periodicity $d = 7.95$ nm. This repeat spacing is essentially bigger as compared to that of single-component MO bilayers ($d = 4.6$ nm), which may be obtained at lipid/water ratios above 60/40 (wt/wt).

Nanoparticles Loaded With Docosapentaenoyl-Plasmalogens or Docosapentaenoyl Diacyl Phosphoinositol Ester as Reservoirs for PUFA and Antioxidants

Despite that the biological activities of the novel synthetic ether or ester PUFA-phospholipids (**Figure 2**) are not yet known, we used these compounds to design nanoparticles as potential PUFA delivery carriers with antioxidant properties. The ongoing development of neutracetical formulations combining plasmalogen derivatives with natural antioxidants is motivated by the reports that emphasize the link between decreased ethanolamine plasmalogen concentrations and the risk of AD (Paul et al., 2019; Su et al., 2019). Recently, a marine-based plasmalogen formulation with curcumin supplement called "NeuroPlas Plasmalogen complex" (*Bio-Mer International*) has been offered to patients suffering from memory loss (brain fatigue) and having a risk of neurodegenerative diseases (e.g., AD and other types of dementia).

Here, stable nanoparticulate PUFA-plasmalogen (ether) and PUFA-ester-containing dispersions were fabricated, in excess aqueous medium, with the synthetic phospholipids in mixtures with co-amphiphiles [MO and D-α-tocopherol polyethylene glycol-1000 succinate ($VPGS\text{-}PEG_{1000}$)] as well as lipophilic antioxidants (vitamin E and coenzyme Q_{10}). In this way, the PUFA-phospholipids were protected by incorporation into nanocarriers, which were dispersed in a buffer environment of neutral pH. The cryo-TEM images, presented below (**Figures 5–11**), show the nanoparticle topologies, which were produced with selected mixed amphiphilic compositions. At full hydration, the liquid crystalline phase states were characterized by SAXS for each formulation involving DPA-phospholipids.

Nanoparticles Containing Plasmalogen Phosphocholine (C16:1p-22:5n6 PC)

A cubosome dispersion of the synthetic plasmalogen-phosphocholine (C16:1p-22:5n6 PC)/MO self-assembled system, involving vitamin E (10 mol.%) and coenzyme Q_{10} (1 mol.%), was achieved using the amphiphile $VPGS\text{-}PEG_{1000}$ (6 mol.%) for fragmentation of the lipid cubic phase into nanoparticles (**Figure 5**). The cubosomal organization was evidenced by the SAXS pattern in **Figure 5A** and the cryo-TEM image in **Figure 5B**. The positions of the Bragg peaks spaced in the ratio $\surd 2{:}\surd 3{:}\surd 4{:}\surd 6{:}\surd 8{:}\surd 9{:}\surd 10{:}\surd 11 \ldots$ (with a first peak maximum resolved at $q = 0.053$ Å^{-1}) characterize the inner structure of cubosome particles through the double-diamond *Pn3m* cubic space group. A *Pn3m* lattice parameter $a_{Q(Pn3m)} = 16.76$ nm is determined for the particles with a distinct cubic symmetry (cubosomes). The Bragg peaks in the SAXS pattern in **Figure 5A** are superimposed on a broad maximum ($q \sim 0.092$ Å^{-1}) arising from the presence of double-membrane vesicles or weakly packed 3D bilayer membrane architectures, which are referred to as cubosomal intermediates. The cryo-TEM image in **Figure 5C** shows that nanoparticles with inner liquid crystalline structures are accompanied by vesicular membranes. The inclusion of the PEGylated agent $VPGS\text{-}PEG_{1000}$ (6 mol.%) in the lipid system causes certain disorder of the interfaces of the small cubosomes. The presence of vesicular membranes in the surrounding of cubosomes in fully hydrated non-lamellar lipid systems is often due to the sonication process employed for nanoparticles production (Yaghmur and Glatter, 2009).

To probe the self-assembly properties of the DPA-plasmalogen-phosphocholine (C16:1p-22:5n6 PC), the synthetic lipid was dispersed in a mixture with the lipophilic antioxidant vitamin E and the PEGylated surfactant $VPGS\text{-}PEG_{1000}$ in an excess aqueous buffer medium. A colipid monoolein was not added in this sample. The SAXS pattern in **Figure 6A** and the cryo-TEM images in **Figures 6B–F** reveal a multilamellar bilayer behavior of the dispersed plasmalogen-phosphocholine (C16:1p-22:5n6 PC)/vitamin E/$VPGS\text{-}PEG_{1000}$ system. The broad maximum at $q \sim 0.093$ Å^{-1} in the SAXS pattern is a characteristic for the presence of bilayer membrane fragments in the formulation. The absence of sharp Bragg diffraction peaks in **Figure 6A** suggests that the bilayers are not packed in a periodic inner lamellar structure inside the nanoparticles. The observed slope ($\sim q^{-3}$) in the small q-vector range ($q < 0.029$ Å^{-1}) is

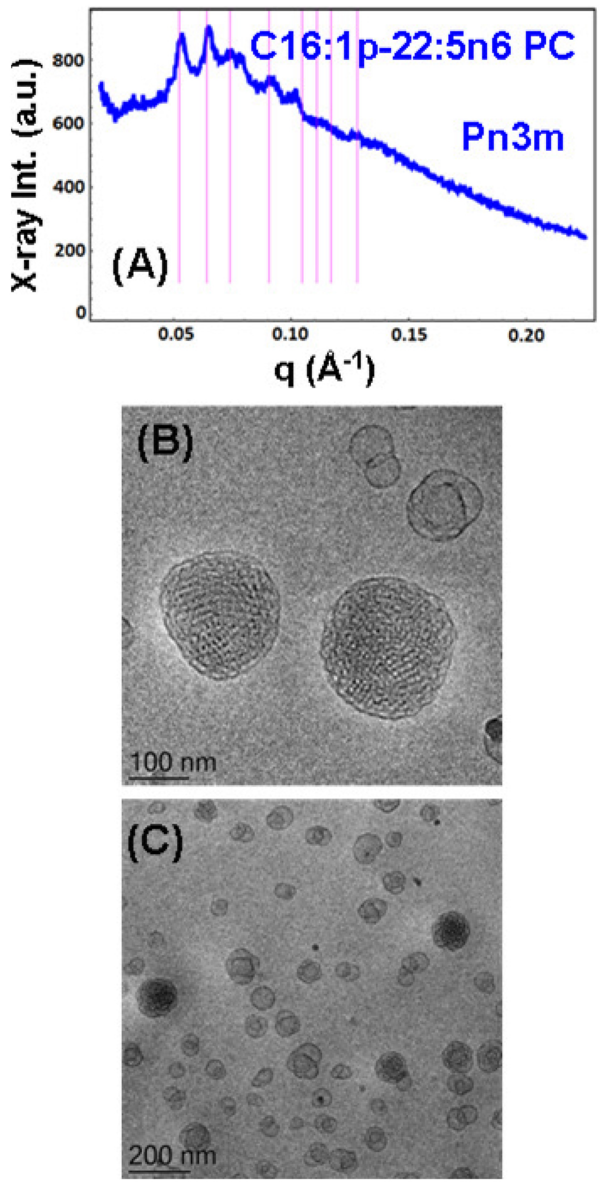

FIGURE 5 | (A) Synchrotron small-angle X-ray scattering (SAXS) pattern and **(B,C)** cryogenic transmission electron microscopy (cryo-TEM) images of a self-assembled nanoparticulate plasmalogen-phosphocholine (C16:1p-22:5n6 PC)/monoolein (MO)/vitamin E/coenzyme Q_{10}/VPGS-PEG_{1000} system with a plasmalogen-PC/MO molar ratio of 15/85 (mol/mol) and added vitamin E (10 mol.%) and coenzyme Q_{10} (1 mol.%). Aqueous phase: 1.10^{-2} M phosphate buffer containing 2,6-di-tert-butyl-4-methylphenol (BHT). Dispersion content: 5 wt% lipid/95 wt% aqueous buffer. The set of Bragg peaks in **(A)** indexes an inner cubic structure of the double-diamond *Pn3m* cubic lattice space group. The bars indicate the (110), (111), (200), (211), (220), (221), (310), and (311) reflections, for which the peak positions are spaced in the ratio $\sqrt{2}:\sqrt{3}:\sqrt{4}:\sqrt{6}:\sqrt{8}:\sqrt{9}:\sqrt{10}:\sqrt{11}\ldots$ The topologies of the cubosome particles, stabilized by VPGS-PEG_{1000} (6 mol.%), and coexisting vesicular membranes are presented in **(B,C)**.

characteristic for particles with rough surfaces. Actually, the cryo-TEM imaging results demonstrate an abundance of onion-type nanoparticulate topologies resulting from the dispersion of the mixed amphiphilic assemblies (**Figures 6B–F**). A number of fragmented multilamellar membranes appear to be of irregular shapes and non-periodic arrangements (**Figures 6B,C,F**). Other object shapes are found to be intermediate between small cylinders (tubules), disks, and spheres (**Figures 6D,E**). These features imply an inhomogeneous distribution of membrane curvature in the studied mixed assembly. The diverse topologies, comprised of double membrane vesicles, multilayer onions, and other multimembrane architectures consisting of more than two bilayers, or large vesicles encapsulating several smaller bilayer-type particles, are formed under full hydration conditions (**Figures 6B–F**).

Incorporation of Plasmalogen-Phosphoethanolamine (C16:1p-22:5n6 PE) in DOPC Membrane Nanostructures

The effect of the non-lamellar lipid DPA-plasmalogen phosphoethanolamine (C16:1p-22:5n6 PE) on the formation of mixed membrane nanostructures with the colipid 1,2-dioleoyl-sn-glycero-3-phosphocholine (DOPC) was examined by SAXS and cryo-TEM techniques at 15 mol.% DPA-plasmalogen content. The SAXS pattern of the dispersed plasmalogen-phosphoethanolamine (C16:1p-22:5n6 PE)/MO/coenzyme Q_{10}/VPGS-PEG_{1000} system is shown in **Figure 7A**. Correlation peaks, indicating the presence of non-periodic membrane arrangements, are observed at q_1 ~0.05 $Å^{-1}$ and q_2 ~0.099 $Å^{-1}$. The latter maximum coincides with the position of the strongest Bragg peak for the bulk DPA-plasmalogen ethanolamine (C16:1p-22:5n6 PE) liquid crystalline phase. Nevertheless, the structural results do not demonstrate a topological transition from a lamellar to a non-lamellar phase in excess aqueous medium. The non-lamellar plasmalogen lipid does not induce a periodic cubic phase arrangement in the mixed self-assembled DPA-phosphoethanolamine (C16:1p-22:5n6 PE)/DOPC/Q_{10}/VPGS-PEG_{1000} system. Thus, the lamellar phase, which is typical for the pure DOPC, represents the dominant structure in the dispersed amphiphilic system.

The cryo-TEM images in **Figures 7B–F** display various nanoscale object topologies with smooth interfaces (**Figures 7B–D,F**). Double-membrane particles and weakly packed multimembrane assemblies are mostly formed upon incorporation of the DPA-plasmalogen ethanolamine, at 15 mol.% content, in host DOPC glycerophospholipid membranes (**Figures 7B–F**). The topology of the lipid particles in **Figure 7E** suggests a locally inhomogeneous distribution of the membrane curvature. The inhomogeneous curvature distribution along the lipid bilayer scaffolds evidently results in the formation of hierarchical-type objects such as large vesicle shells encapsulating smaller particles as well as elongated tubular membranes (**Figures 6E**, **7B**).

Nanoparticles Containing Plasmalogen-Phosphoethanolamine (C16:1p-22:5n6 PE)

An abundance of nanoparticles of liquid crystalline topologies was produced with DPA-plasmalogen phosphoethanolamine (C16:1p-22:5n6 PE)-involving non-lamellar (MO) lipid mixtures stabilized by the D-α-tocopherol polyethylene

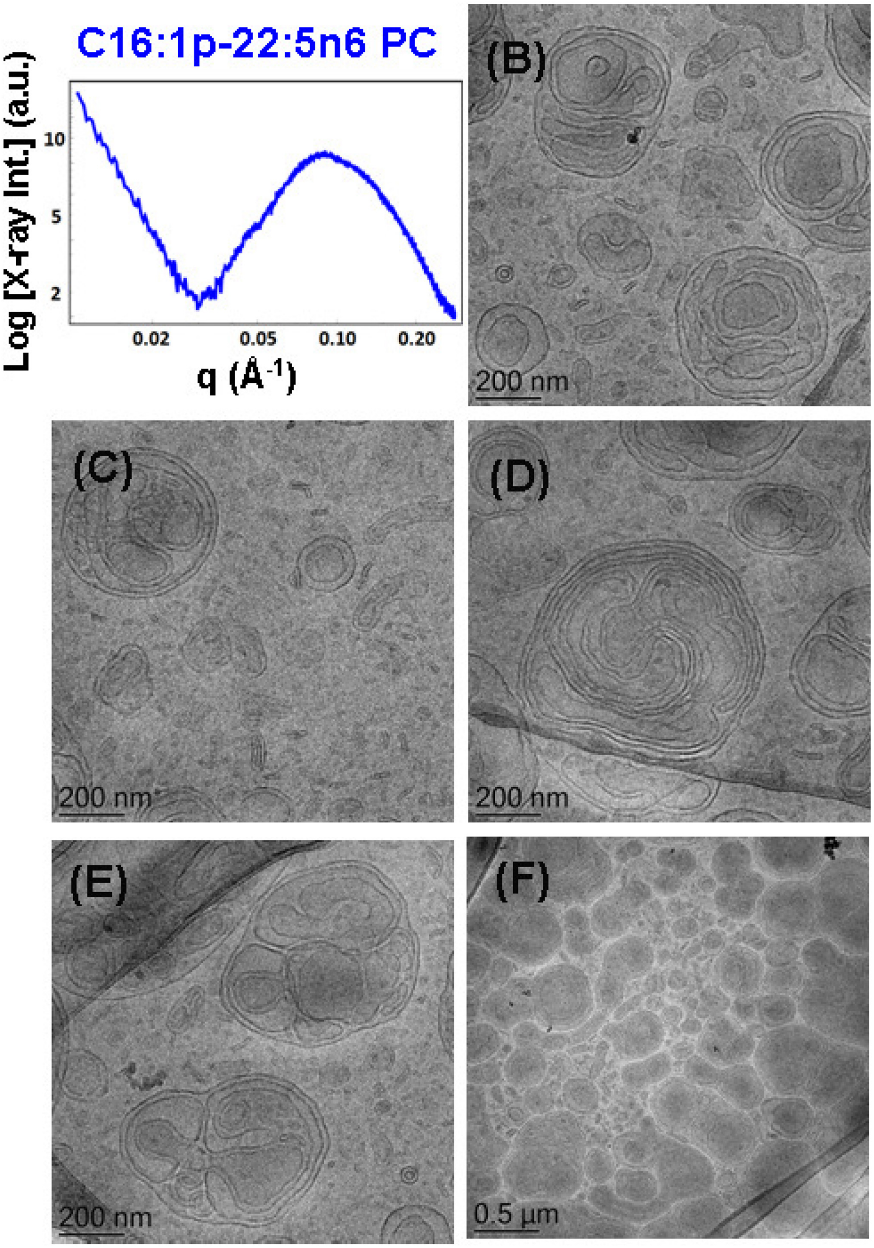

FIGURE 6 | (A) Synchrotron small-angle X-ray scattering (SAXS) pattern and **(B–F)** cryogenic transmission electron microscopy (cryo-TEM) images of a nanoparticulate plasmalogen-phosphocholine (C16:1p-22:5n6 PC)/vitamin E/VPGS-PEG$_{1000}$ system obtained by self-assembly and dispersion in an excess aqueous phosphate buffer (1.10^{-2} M) phase containing 2,6-di-tert-butyl-4-methylphenol (BHT). Dispersion content: 5 wt% lipid phase/95 wt% aqueous phase.

glycol-1000 succinate (VPGS-PEG$_{1000}$) amphiphile (6 mol.%). Two molar ratios between the plasmenyl-PE and MO lipids were investigated, namely, 15/85 (mol/mol), and 20/80 (mol/mol).

The mixture of the synthetic DPA-plasmalogen phosphoethanolamine (C16:1p-22:5n6 PE) with MO [molar ratio, 20/80 (mol/mol)] was dispersed *via* the PEGylated amphiphile VPGS-PEG$_{1000}$ (6 mol.%) in an excess buffer medium. The SAXS pattern in **Figure 8A** shows distinct Bragg peaks, which are superimposed on a broad hump (q ~0.05–0.1 Å^{-1}). The latter arises from the presence of fully hydrated polydispersed vesicular objects (vesicle sizes in the range of 40–200 nm). The positions of the Bragg peaks at q_1 = 0.114 Å^{-1}, q_2 = 0.145 Å^{-1}, and q_3 = 0.228 Å^{-1} (a very weak third peak) determine a space group derived from the sequence 1:$\sqrt{3}$:$\sqrt{4}$ … This result implies that the obtained nanoparticles were produced by the dispersion of an inverted hexagonal (H$_{II}$) phase, for which the inner structure is characterized by a lattice parameter a$_H$ = 6.37 nm.

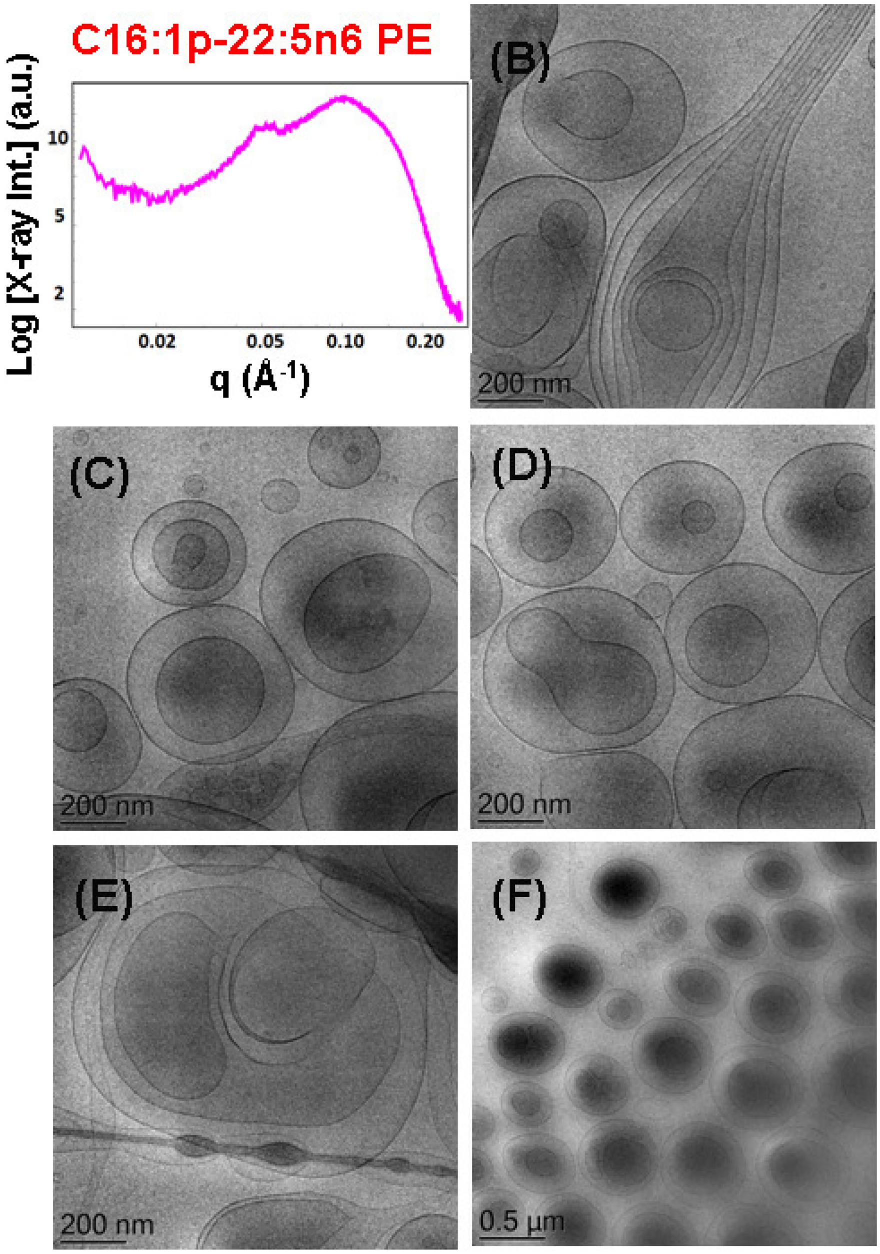

FIGURE 7 | (A) Synchrotron small-angle X-ray scattering (SAXS) pattern and **(B–F)** cryogenic transmission electron microscopy (cryo-TEM) images of a dispersed plasmalogen-phosphoethanolamine (C16:1p-22:5n6 PE)/dioleoylphosphocholine (DOPC)/coenzyme Q_{10}/VPGS-PEG_{1000} system at a docosapentaenoyl (DPA)-plasmalogen PE/monoolein (MO) molar ratio of 15/85 (mol/mol) and containing a coenzyme Q_{10} (1 mol.%) and VPGS-PEG_{1000} (6 mol.%). Aqueous phase: 1.10^{-2} M phosphate buffer with dissolved 2,6-di-tert-butyl-4-methylphenol (BHT). Dispersion content: 5 wt% lipid phase/95 wt% aqueous buffer phase.

The cryo-TEM images in **Figures 8B–F** reveal the formation of dense-core particles, vesicles, and intermediate structures derived from the fragmented liquid crystalline phase of the plasmalogen-phosphoethanolamine (C16:1p-22:5n6 PE)/MO/VPGS-PEG_{1000} assembly. The increased percentage of the DPA-plasmenyl-ethanolamine (20 mol.%.) in the amphiphilic mixture might lead to a phase separation of the PUFA-PE phospholipid, which has a propensity for non-lamellar phase formation. **Figure 8E** shows a large fragment of a H_{II}-phase domain, which coexists with vesicles produced upon the dispersion of the bulk amphiphilic mixture. A coexistence of a small hexosome nanoparticle with single-bilayer and double-membrane vesicles is shown in **Figure 8B**. Dense core (H_{II}-phase) particles coexisting with vesicles are presented also in the cryo-TEM images in **Figures 8C,D**. Several mixed type nanoscale objects, involving dense H_{II}-phase domain joint with a vesicle, are observed in **Figures 8C,D,F**. The coexisting populations of two-compartment nano-objects (dense non-lamellar-domain embedding vesicles)

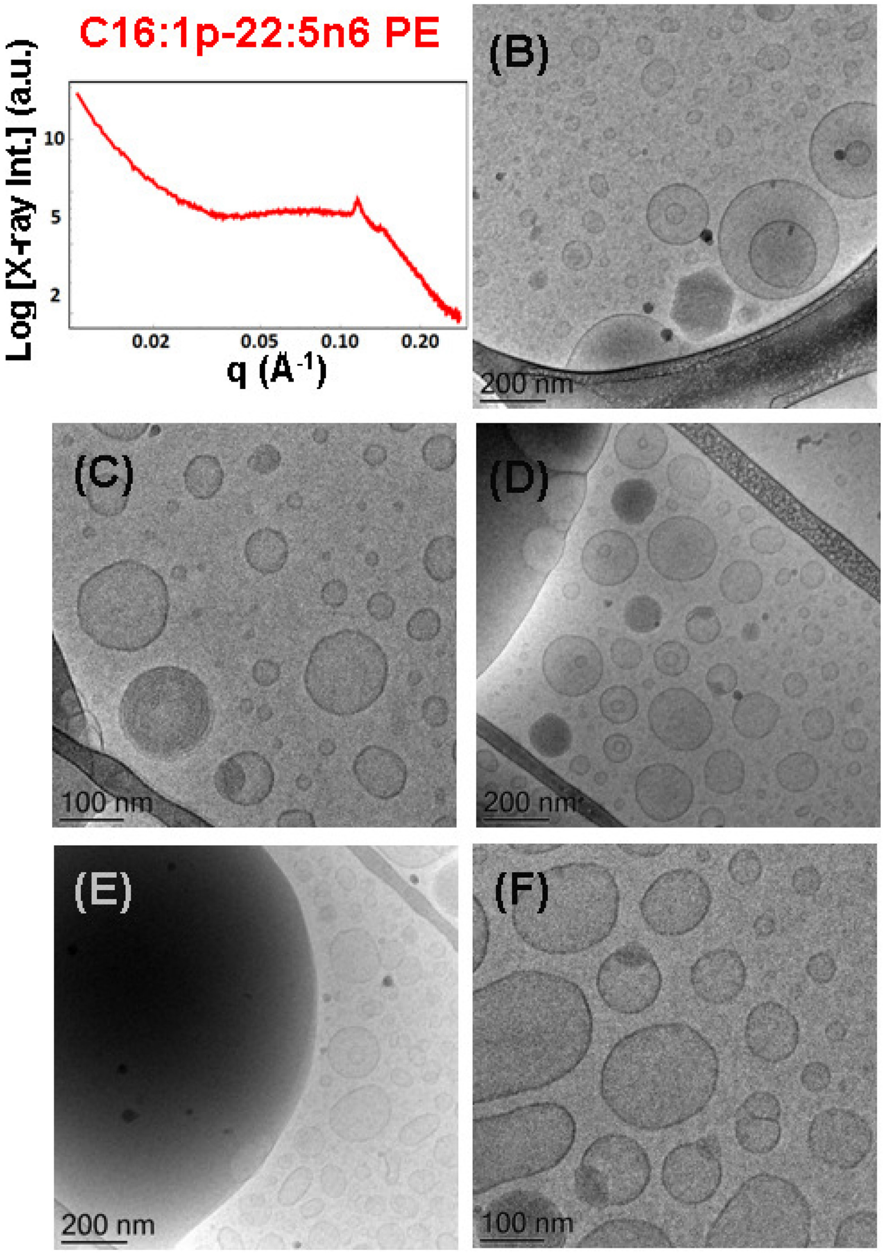

FIGURE 8 | (A) Synchrotron small-angle X-ray scattering (SAXS) pattern and **(B–F)** cryogenic transmission electron microscopy (cryo-TEM) images of a nanoparticulate plasmalogen-phosphoethanolamine (C16:1p-22:5n6 PE)/monoolein (MO)/VPGS-PEG$_{1000}$ system with a docosapentaenoyl (DPA)-plasmalogen PE/MO molar ratio of 20/80 (mol/mol) and dispersed by VPGS-PEG$_{1000}$ (6 mol.%). Aqueous phase: 1.10^{-2} M phosphate buffer with dissolved 2,6-di-tert-butyl-4-methylphenol (BHT). Dispersion content: 5 wt% lipid phase/95 wt% aqueous phase.

and vesicles of non-spherical shapes in the cryo-TEM images (**Figures 8D,F**) evidence that the particles are derived from a DPA-plasmalogen phosphoethanolamine (C16:1p-22:5n6 PE)-based lipid dispersion with a non-lamellar propensity.

The SAXS pattern of the self-assembled plasmalogen-phosphoethanolamine (C16:1p-22:5n6 PE)/MO/vitamin E/coenzyme Q$_{10}$/VPGS-PEG$_{1000}$ system with a DPA-plasmalogen PE/MO molar ratio of 20/80 (mol/mol) with additional loading of small-molecule antioxidants, such as coenzyme Q$_{10}$ (1 mol.%) and vitamin E (5 mol.%), is presented in **Figure 9A**. The inclusion of vitamin E and coenzyme Q$_{10}$ stabilizes the inner inverted hexagonal (H$_{II}$) structural organization of the PUFA-phospholipid/MO assembly. This is evidenced by distinct Bragg peaks at q-vector positions of 0.113, 0.196, and 0.224 Å^{-1}. The Bragg peaks are spaced in the ratio $1{:}\sqrt{3}{:}\sqrt{4}$ and determine a lattice parameter of the inverted hexagonal (H$_{II}$) phase structure a_H = 6.42 nm. The broad hump (q ~0.03–0.09 Å^{-1}) in

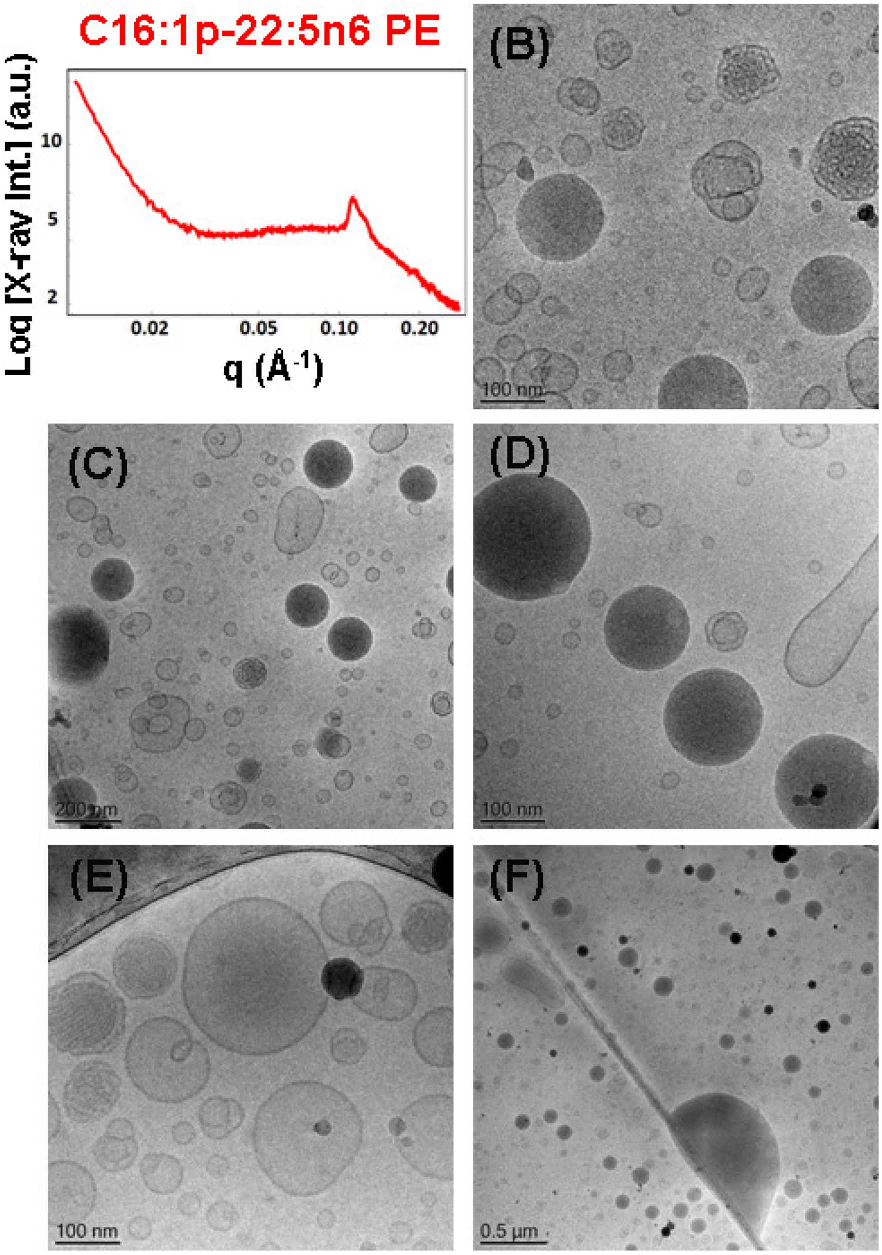

FIGURE 9 | (A) Synchrotron small-angle X-ray scattering (SAXS) pattern and **(B–F)** cryogenic transmission electron microscopy (cryo-TEM) images of a self-assembled nanoparticulate plasmalogen-phosphoethanolamine (C16:1p-22:5n6 PE)/monoolein (MO)/vitamin E/coenzyme Q_{10}/VPGS-PEG_{1000} system with a plasmalogen-PE/MO molar ratio of 20/80 (mol/mol) and added vitamin E (5 mol.%) and coenzyme Q_{10} (1 mol.%). Aqueous phase: 1.10^{-2} M phosphate buffer containing 2,6-di-tert-butyl-4-methylphenol (BHT). Dispersion content: 5 wt% lipid phase/95 wt% aqueous phase.

the SAXS pattern (**Figure 9A**) indicates that the hexosome nanoparticles coexist with vesicular membranes in the lipid dispersion.

The morphological results for the plasmalogen-phosphoethanolamine (C16:1p-22:5n6 PE)/MO/vitamin E/coenzyme Q_{10}/VPGS-PEG_{1000} assemblies in **Figures 9B–F** also evidence the formation of vesicular membranes, dense hexosome nanoparticles, and some non-lamellar structural intermediates. The latter involve the formation of soft corona of nanochannels, which is characteristic for weakly packed 3D membrane architectures.

The SAXS patterns in **Figure 10A** and the cryo-TEM images in **Figures 10B–F** characterize the dispersed plasmalogen-phosphoethanolamine (C16:1p-22:5n6 PE)/MO/vitamin E/coenzyme Q_{10}/VPGS-PEG_{1000} particles containing coenzyme Q_{10} (1 mol.%) and vitamin E (10 mol.%) for plasmalogen-PE/MO molar ratio of 15/85 (mol/mol). The first three Bragg peaks, resolved at q-vectors of 0.112, 0.194, and 0.224 $Å^{-1}$ in the

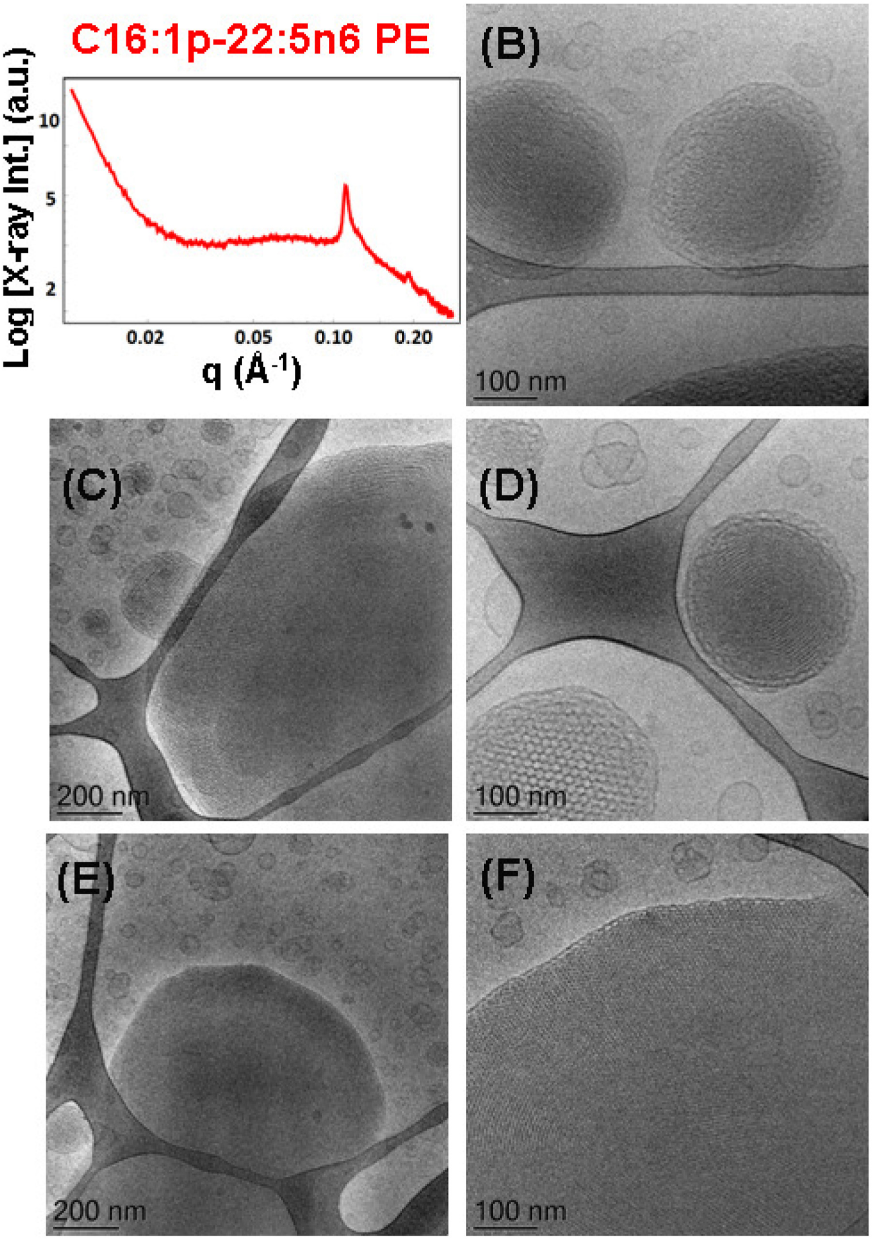

FIGURE 10 | (A) Synchrotron small-angle X-ray scattering (SAXS) pattern and **(B–F)** cryogenic transmission electron microscopy (cryo-TEM) images of a self-assembled nanoparticulate plasmalogen-phosphoethanolamine (C16:1p-22:5n6 PE)/monoolein (MO)/vitamin E/coenzyme Q_{10}/VPGS-PEG_{1000} system with a plasmalogen-PE/MO molar ratio of 15/85 (mol/mol) and added vitamin E (10 mol.%) and coenzyme Q_{10} (1 mol.%). Aqueous phase: 1.10^{-2} M phosphate buffer containing 2,6-di-tert-butyl-4-methylphenol (BHT). The Bragg peak positions spaced in the ratio $1:\sqrt{3}:\sqrt{4}$ correspond to (10), (11), and (20) reflections of an inverted hexagonal (H_{II}) phase inner organization of the lipid nanoparticles (hexosomes). Dispersion content: 5 wt% lipid phase/95 wt% aqueous phase. The topologies of the hexosome nanoparticles surrounded with soft coronas and stabilized by VPGS-PEG_{1000} (6 mol.%) and fragments of a dense inverted hexagonal (H_{II}) phase are presented in **(B–F)**.

SAXS pattern, correspond to the (10), (11), and (20) reflections of an inverted hexagonal (H_{II}) phase structure in the lipid nanoparticles. The inner H_{II}-phase structure of hexosomes is characterized by a lattice parameter $a_H = 6.48$ nm.

Multiphase nanoparticles and hierarchical structures were observed upon dispersion of the mixed amphiphilic composition [plasmenyl-PE/MO lipid molar ratio of 15/85 (mol/mol) stabilized by the PEGylated surfactant]. The cryo-TEM images of the nanoparticulate plasmalogen-phosphoethanolamine (C16:1p-22:5n6 PE)/MO/vitamin E/coenzyme Q_{10}/VPGS-PEG_{1000} system are displayed in **Figures 10B–F**. **Figures 10C,E,F** show large domains with distinct inner inverted hexagonal symmetry. They represent a weakly hydrated self-assembled structure with a densely packed hexagonal lattice ($a_H = 6.48$ nm).

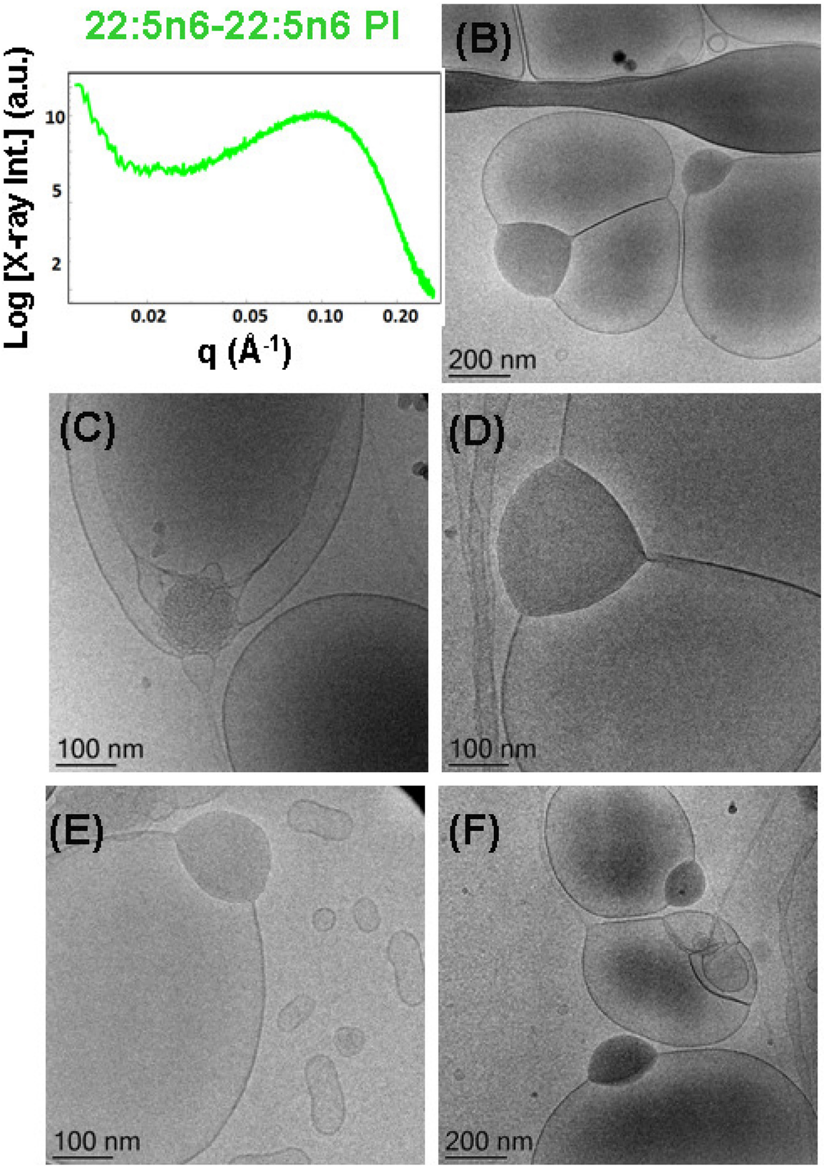

FIGURE 11 | (A) Synchrotron small-angle X-ray scattering (SAXS) pattern and **(B–F)** cryogenic transmission electron microscopy (cryo-TEM) images of a self-assembled nanoparticulate docosapentaenoyl (DPA)-diacyl phosphoinositol (22:5n6-22:5n6 PI)/monoolein (MO)/vitamin E/coenzyme Q_{10}/VPGS-PEG_{1000} system with a DPA-diacyl PI/MO molar ratio of 15/85 (mol/mol) and added vitamin E (10 mol.%) and coenzyme Q_{10} (1 mol.%). The PEGylated amphiphile VPGS-PEG_{1000} is included at 6 mol.%. Aqueous phase: 1.10^{-2} M phosphate buffer containing 2,6-di-tert-butyl-4-methylphenol (BHT). Dispersion content: 5 wt% lipid/95 wt% aqueous buffer.

The periphery of the hexosome nanoparticles, shown in **Figures 10B,D**, is less densely packed and comprises a soft corona of nanochannels. Moreover, a cubosome particle with large channels is visualized as a transitional state in the cryo-TEM image in **Figure 10D**. The swollen cubosomes, coexisting with vesicular particles, contribute to the scattering in the q-vector range ~0.03–0.095 $Å^{-1}$. Therefore, it can be concluded that the produced nanoparticles predominantly involve inverted hexagonal inner liquid crystalline structure surrounded by soft, less densely packed corona of nanochannels at this plasmalogen-phosphoethanolamine (C16:1p-22:5n6 PE) content. The stabilization of the formulation is provided by the included antioxidants and the coexisting vesicular membrane particles.

Nanoparticles Containing DPA-Diacyl Phosphoinositol (22:5n6-22:5n6 PI)

Liquid crystalline nanostructures including the synthetic PUFA-diacyl phosphoinositol ester species were obtained by dispersion of DPA-diacyl phosphoinositol (22:5n6-22:5n6 PI)/MO/vitamin E/coenzyme Q_{10}/VPGS-PEG_{1000} mixed assembly using the PEGylated amphiphile VPGS-PEG_{1000}. The SAXS pattern in

Figure 11A displays a hump, rather than sharp Bragg peak maxima of multilamellar structures that are established with the DPA-diacyl phosphoinositol ester-containing bulk phase (**Figure 4**, green plot). The correlation peak at $q \sim 0.093$ Å^{-1} corresponds to a correlation distance of the bilayers $L = 6.75$ nm and indicates a non-periodic bilayer membrane organization.

The cryo-TEM images in **Figures 11B–F** indicate phase separation of the DPA-diacyl phosphoinositol (22:5n6-22:5n6 PI) component in an amphiphilic mixture, which results in the formation of multicompartment and multiphase particles. Indeed, vesicular nanoparticles with aqueous core are joined with large oil domains and thus comprise oil droplet-embedding vesicles. These mixed objects are built up by a dense compartment (rich in PUFA-phospholipid) and a vesicular membrane, which indicates the little miscibility of the single- and double-chain lipids inside the inner structure of the nanocarriers. This leads to an abundance of nanoparticles with a mixed-type of liquid crystalline inner organizations and the presence of non-periodic membrane scaffolds.

It may be suggested that the formation of intermediate structures (e.g., oil droplet-embedding vesicles) are governed by the unsaturated chains of the PUFA-phospholipid and their miscibility with the MO matrix. Similar multicompartment topologies have been found in self-assembled systems of MO and single-chain PUFA species (Angelova et al., 2018). In the case of the dispersed eicosapentaenoic acid (EPA, C20:5)/MO mixtures, the correlation peak in the SAXS pattern has been positioned at $q \sim 0.15$ Å^{-1}. Correspondingly, the determined correlation distance was smaller ($L = 4.2$ nm) and thus associated with thinner lipid membrane formation in the EPA/MO system with regard to the double-chain PUFA-phospholipid/MO mixtures, which are investigated in the present work.

DISCUSSION

Biological membranes contain significant amounts of non-lamellar-forming lipids, but their exact *in vivo* functions remain not fully understood. Lipids with PUFA chains [e.g., eicosapentaenoic (EPA, C20:5), docosahexaenoic (DHA, C22:6), and docosapentaenoic (DPA, C22:5)] acids exhibit diverse health effects and present strong current interest for structural investigations in view of biomedical applications. DPA exists in two isomeric forms, namely, C22:5n6 (*all-cis*-4,7,10,13,16-docosapentaenoic acid or 4Z,7Z,10Z,13Z,16Z-DPA) and C22:5n3 (*all-cis*-7,10,13,16,19-docosapentaenoic acid or 7Z,10Z,13Z,16Z,19Z-DPA). The use of the first isomer (DPA, C22:5n6) in the present work for the design of PUFA-plasmalogens (ether) or ester species is motivated by the increased percentage of DPA (C22:5n6) derivatives found in biological cubic membrane structures (Deng et al., 2009).

The performed SAXS investigations demonstrated the formation of non-lamellar, primitive cubic (*Im3m*), and inverted hexagonal (H_{II}) phases by the hydrated DPA-ethanolamine plasmalogen (C16:1p-22:5n6 PE). Cubic liquid crystalline phases were formed also in hydrated mixed assemblies of monoolein with DPA-plasmalogen phosphoethanolamine (C16:1p-22:5n6 PE) and DPA-plasmalogen phosphocholine (C16:1p-22:5n6 PC). The colipid MO was found to maintain the stability of the mesophases embedding the polyunsaturated DPA-plasmalogen phosphoethanolamine and phosphocholine lipids and the DPA-diacyl phosphoinositol (22:5n6-22:5n6 PI). The structural effects related to the differences in the phospholipid headgroup type (PE, PC, or PI) were found to be more significant at the hydration level employed for bulk lipid phases preparation [e.g., lipid/water ratio of 40/60 (wt/wt)] as compared to the mixtures dispersed in excess aqueous environment [i.e., lipid/water ratio of 5/95 (wt/wt) allowing full lipid hydration].

The tendency for induction of curved membrane structures and short-lived intermediates appears to be important for the comprehension of the role of the plasmalogen lipids in the cellular membranes (Lohner, 1996; Almsherqi et al., 2010; Koivuniemi, 2017; West et al., 2020). By inducing transient cubic phase intermediates or higher curvature regions in the membranes of subcellular organelles, the plasmenyl lipids may exert effects on the organization and the activity of membrane proteins or of proteins anchored to the plasma membranes. It has been claimed that non-bilayer-type lipids affect peripheral and integral membrane proteins *via* changes in the lateral pressure profile (Lee, 2004). This can induce modifications in the activity of membrane proteins under oxidative stress conditions (Pohl and Jovanovic, 2019). In fact, phosphatidylethanolamine is a crucial target for reactive aldehydes. Modifications of the lipid shape and membrane properties due to lipid peroxidation-derived aldehydes can alter the membrane curvature, lipid bilayer elastic properties, and lateral pressure profile. As a consequence, this may affect the functions of membrane receptors, transporters, channels, and enzymes (Pohl and Jovanovic, 2019). The modulation of the function of transporter and ion channel proteins by non-lamellar-structure forming plasmalogen species deserves more attention in future investigations. Curvature-dependent recognition of ethanolamine phospholipids by peptide fragments represents another promising direction for future research.

The propensity for formation of an inverted hexagonal (H_{II}) phase (Seddon, 1990), as well as of non-lamellar structural intermediates, has been suggested as essential for the promotion of fusion properties of the membranes, into which plasmalogen lipids are embedded (Lohner, 1996). Primarily, the H_{II}-phase formation has been reported in the literature for plasmalogens with a single double bond in the hydrocarbon tails (Lohner et al., 1991).

For the DPA-plasmalogen ethanolamine, involving long PUFA chains (C16:1p-22:5n6 PE), investigated here, a coexistence of a liquid crystalline primitive cubic *Im3m* phase with an inverted hexagonal (H_{II}) phase is established in the performed synchrotron SAXS study. The failure for the DPA-PE plasmalogen to form a unique stable non-lamellar mesophase could be due to the flexible conformation of its PUFA chain. The cubic-to-H_{II} phase coexistence suggests that the number of double bonds in the long polyunsaturated DPA chain (22:5n6) might correspond to the threshold limit for the formation of an inverted hexagonal (H_{II}) phase structure. Indeed, H_{II} phases have been observed for plasmalogens of lower degree of unsaturation of the tails, e.g., C16:1, C18:1, or di-C18:2 (Lohner et al., 1991). The capacity of DPA-PE plasmalogen to form non-lamellar phase coexistences and structural intermediates might be of key importance for its role in the dynamics of biological membranes under stress conditions (Deng et al., 2017).

Depending on the head group type (PE, PC, and PI), the studied membrane lipid compositions were characterized by either non-lamellar or lamellar liquid crystalline phase formation in the mixed PUFA-phospholipid/MO assemblies. The incorporation of plasmalogen phosphocholine (C16:1p-22:5n6 PC) in the host lipid (MO) matrix induced a phase coexistence of a swollen double-diamond *Pn3m* cubic phase [with a D_{Large} lattice parameter $a_{Q(Pn3m)}$ = 14.0 nm] and a lamellar phase with a much thicker repeat bilayer spacing (d = 6.83 nm) with regard to the periodicity of pure MO phases. The topological transition from a cubic to a lamellar phase, observed for the DPA-diacyl phosphoinositol (22:5n6-22:5n6 PI)-containing mixture, can be explained by the bulky character of the PI headgroup, which lowers the critical packing parameter of this lipid and hence determines its propensity for a lamellar phase formation.

Whereas single-chain PUFAs have been found to reduce the membrane bilayer thickness (Feller et al., 2002), the incorporation of DPA-plasmenyl phospholipids resulted in an essentially increased thickness of the lipid bilayers. This was evidenced by the SAXS results for the plasmalogen C16:1p-22:5n6 PC/MO and di-1p-22:5n6:1p-22:5n6 PI/MO mixtures. The lamellar phase of the MO/DPA-diacyl phosphoinositol (22:5n6-22:5n6 PI)/MO mixture was characterized by a very large repeat bilayer spacing (d = 7.95 nm) as compared to the bilayer periodicity of weakly hydrated MO (d = 4.6 nm). Thickening of the bilayers in the liquid crystalline assemblies confirms that PUFA-plasmalogens and PUFA-esters play a role of structural determinant components in the membranes. Studies with other plasmalogen species have established thickening of 1-palmitoyl-2-oleoyl-sn-glycero-3-phosphocholine (POPC) bilayers upon incorporation of increasing amounts of plasmalogen (Rog and Koivuniemi, 2016; West et al., 2020). It should be noted that a bilayer thickness mismatch in mixed lipid membranes controls the domain size and the phase separation, which is of crucial importance for the embedded proteins. Thickening of the lipid bilayers may dramatically influence the organization of membrane proteins (Dean and Lodhi, 2018; Fontaine et al., 2020). It is known that membrane receptor clustering and domain formation may interfere with the protein function and signaling activation (Angelov and Angelova, 2017).

Self-assembly has been intensively exploited in recent years for the fabrication of liquid crystalline nanocarriers for various applications including therapeutic delivery (Yaghmur and Glatter, 2009; Fong et al., 2010, 2014, 2019; Azmi et al., 2015; Angelova et al., 2018, 2019a; Shao et al., 2018; Wang et al., 2018; Li et al., 2019; Talaikis et al., 2019; Zhai et al., 2019). Drug loading and release capacities have been shown to depend on the internal structural organization of the delivery vehicles (Yaghmur and Glatter, 2009; Rakotoarisoa et al., 2019; Zhai et al., 2019). Multiphase structures have been observed in lipid mixtures of multiple amphiphilic components as well as upon loading of

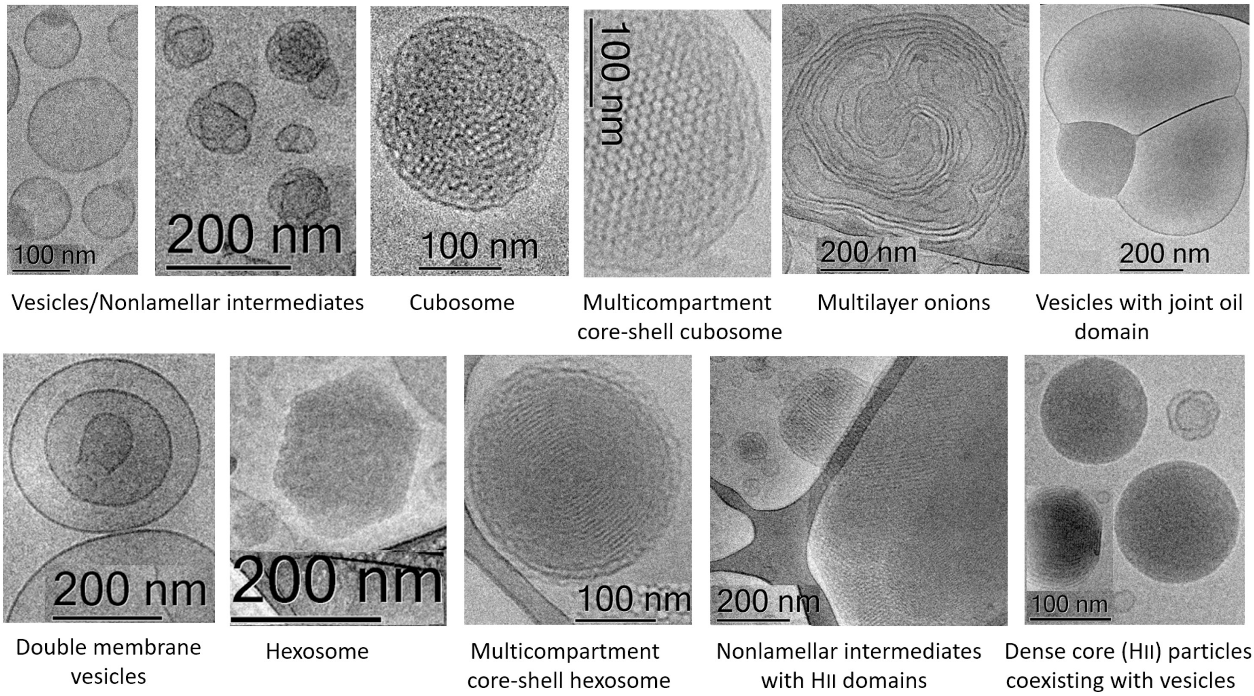

Vesicles/Nonlamellar intermediates

Cubosome

Multicompartment core-shell cubosome

Multilayer onions

Vesicles with joint oil domain

Double membrane vesicles

Hexosome

Multicompartment core-shell hexosome

Nonlamellar intermediates with HII domains

Dense core (HII) particles coexisting with vesicles

FIGURE 12 | Summary of the different nanoscale topology types of docosapentaenoyl (DPA) plasmalogen- and ester-based liquid crystalline multiphase structures generated by spontaneous assembly in excess aqueous medium. Examples of individual cubosome and hexosome particles are given together with multiphase nanoparticles and intermediate structures formed as a result of inhomogeneous curvature distribution in the studied polycomponent lipid mixtures.

TABLE 1 | Summary of the nanoscale liquid crystalline structures identified for the different mixed lipid compositions upon spontaneous assembly in excess aqueous medium.

Multicomponent amphiphilic mixture	Liquid crystalline structures	Figures
Plasmalogen-phosphocholine (C16:1p-22:5n6 PC, 15 mol%)/MO/vitamin E/coenzyme Q10/VPGS-PEG$_{1000}$	Cubosomes coexisting with vesicles; Cubosomal intermediates	**Figure 5B** **Figure 5C**
Plasmalogen-phosphocholine (C16:1p-22:5n6 PC)/vitamin E/VPGS-PEG$_{1000}$	Multilayer onions; Multimembrane fragments; Double membrane vesicles	**Figures 6B–F** **Figure 6C**
Plasmalogen-phosphoethanolamine (C16:1p-22:5n6 PE, 15 mol.%)/DOPC/coenzyme Q$_{10}$/VPGS-PEG$_{1000}$	Multimembrane structures; Double membrane vesicles	**Figure 7B** **Figures 7C,D**
Plasmalogen-phosphoethanolamine (C16:1p-22:5n6 PE, 20 mol.%)/MO/VPGS-PEG$_{1000}$	Hexosome coexisting with vesicles; Dense H$_{II}$-phase domain joint with vesicle; dense core (H$_{II}$) particles coexisting with vesicles	**Figure 8B** **Figures 8C,D,F** **Figures 8C–F**
Plasmalogen-phosphoethanolamine (C16:1p-22:5n6 PE, 20 mol.%)/MO/vitamin E/coenzyme Q$_{10}$/VPGS-PEG$_{1000}$	Non-lamellar intermediates; Dense core (H$_{II}$) particles coexisting with vesicles	**Figures 9B,E** **Figures 9C,D,F**
Plasmalogen-phosphoethanolamine (C16:1p-22:5n6 PE, 15 mol.%)/MO/vitamin E/coenzyme Q$_{10}$/VPGS-PEG$_{1000}$ system	Multicompartment core-shell hexosomes; Non-lamellar intermediates with H$_{II}$ domains; H$_{II}$-phase domain fragments	**Figure 10B** **Figures 10C–F** **Figures 10E,F**
DPA-diacyl phosphoinositol (22:5n6-22:5n6 PI, 15 mol.%)/MO/vitamin E/coenzyme Q$_{10}$/VPGS-PEG$_{1000}$	Multicompartment vesicles with joint oil domains	**Figures 11B–F**

therapeutic proteins and peptides in nanostructured assemblies (Angelov et al., 2014; Angelova et al., 2019b).

Stable synthetic liquid crystalline structures with new topological properties were obtained by self-assembly of the DPA-phospholipids with colipids and amphiphiles. The results indicated that abundant liquid crystalline structures and shapes can be fabricated as a consequence of the lyotropic lipid polymorphism of the DPA-based plasmalogens and ester phospholipids (plasmalogen-phosphoethanolamine C16:1p-22:5n6 PE, plasmalogen phosphocholine C16:1p-22:5n6 PC, and DPA-diacyl phosphoinositol 22:5n6-22:5n6 PI; **Figures 5–11**).

Figure 12 and **Table 1** outline the nanoscale object types obtained as a result of the structural polymorphism of the investigated lyotropic lipid/DPA-phospholipid-containing systems at room temperature. Apart from the antioxidant properties of the encapsulated plasmalogen lipids, the biomedical usefulness of the resulting topologies will depend on the envisioned strategy for plasmalogen administration at target therapeutic sites. Some crystalline arrangements may be more desirable than others in controlled release applications. It has been indicated that cubosomes and hexosomes display different drug release profiles (Fong et al., 2014; Azmi et al., 2015; Wang et al., 2018), the release from hexosome nanocarriers being essentially slower. The inner structural organization of the cubosome carriers is advantageous for enhanced entrapment and protective encapsulation of hydrophilic proteins, peptides, and nucleic acids (Angelova et al., 2011). The shape of the nanoparticles is crucial for the transport and diffusion properties of the drug delivery carriers. Generally, drug transport via particles with elongated tubular shapes is different from that from sphere-shaped objects. Hexosomes with elongated, cylinder-like topologies may be more efficient in controlled release applications because of their increased circulation time as well as increased residence time at biological membrane barriers (Li et al., 2019). For combination therapy applications with bioactive lipids, core–shell multiphase cubosomes and hexosomes as well as multicompartment vesicles with joint oil domains (i.e., oil droplet embedding vesicles) have advantages for dual and multidrug delivery (Angelova and Angelov, 2017; Angelov et al., 2017; Angelova et al., 2018).

The fact that plasmalogens may behave as stimuli-responsive phospholipid biomaterials has been exploited for elaboration of controlled release systems (Anderson and Thompson, 1992; Thompson et al., 1996). In perspective, it would be of interest to investigate the stimuli-responsive properties of the prepared nanoformulations. Multiple features of the designed antioxidant-involving nanoparticles with multiphase organization may be advantageous for the achievement of stimuli-activated drug release and pH-sensitive or temperature-controlled release properties in novel biomedical applications.

CONCLUSION

The performed structural investigations established that DPA plasmenyl phospholipids dramatically modulate the membrane curvature upon spontaneous assembly with colipids. They show a propensity for domain formation in membranes. For same DPA content of the hydrocarbon tails, the lipid miscibility in the two-component membrane assemblies varies depending on the phospholipid type (ether or ester) and the nature of the headgroups (PC, PE, or PI). The revealed multiphase liquid crystalline structure formation may be crucial for certain membrane-governed cell processes in the heart, lung, skeletal muscles, retina, immune cells, and brain (especially in the plasmalogen-rich human white matter frontal cortex and the human gray matter parietal cortex). The induction of non-lamellar or lamellar domains, enriched in PUFA-plasmalogens or ester phospholipids, provides a better understanding about the effects of these phospholipid species on different events occurring at the cellular and subcellular organelle level, e.g., molecular trafficking, signaling, receptor clustering and activation in membranes, lipid metabolism (cholesterol efflux), and biogenesis of cubic membranes.

The presented cryo-TEM data demonstrate the formation of multiphase nanoparticles and nanostructures with distinct symmetries or hierarchical organizations that result from variable curvature in the multicomponent membranes. The variety of inner liquid crystalline multicompartment topologies and nanoparticle shapes (cubosomes, hexosomes, double-membrane vesicles, multilayer onions, mixed objects with jointed vesicular and oil compartments, and core–shell structures) open the door to exploit plasmalogen-based soft nanoparticle architectures for novel bioinspired applications.

MATERIALS AND METHODS

Lipids, Chemicals, and Sample Preparation

Plasmalogen derivatives with DPA chains and two types of headgroups (PE and PC) as well as a double-chain polyunsaturated DPA-phosphoinositol ether analog (**Figure 2**) were obtained by custom synthesis from Avanti Polar Lipids Inc. (Alabama), namely, 1-O-1′-(Z)-hexadecenyl-2-(4Z,7Z,10Z,13Z,16Z-docosapentaenoyl)-sn-glycero-3-phosphocholine, C16:1p-22:5n6 PC (M.W. 791.58), 1-O-1′-(Z)-hexadecenyl-2-(4Z,7Z,10Z,13Z,16Z-docosapentaenoyl)-sn-glycero-3-phosphoethanolamine, C16:1p-22:5n6 PE, (M.W. 749.54), and 1,2-bis(4Z,7Z,10Z,13Z,16Z-docosapentaenoyl)-sn-glycero-3-phosphoinositol (ammonium salt), di-22:5n6 PI, (M.W. 958.56). The synthetic glycerophospholipids were of high purity (>99%) and were characterized by the provider via thin-layer chromatography (TLC), mass spectrometry (MS), and NMR analyses. According to the provider, the achieved purity of the synthetic plasmalogen was the highest possible for performance of structural SAXS investigations. The products were received as lipid solutions in chloroform. Monoolein (1-oleoyl-rac-glycerol, MO, C18:1c9, MW 356.54, powder, ≥99%), DOPC, Vitamin E, coenzyme Q10, and D-α-tocopherol polyethylene glycol-1000 succinate (Vitamin E-TPGS or VPGS-PEG$_{1000}$) were purchased from Sigma-Aldrich. For sample preparation, we took into account that the alkenyl (vinyl ether) bond is susceptible to hydrolysis under strong acidic conditions. A buffer medium of a neutral pH was prepared using the inorganic salts NaH_2PO_4 and Na_2HPO_4 (p.a. grade) and 2,6-di-tert-butyl-4-methylphenol (BHT; Sigma-Aldrich). The MilliQ water (Millipore Co.), serving for the preparation of the aqueous phase, was purged by nitrogen gas in order to eliminate the dissolved oxygen. The obtained aqueous medium, containing the antioxidant BHT, ensured the oxidative stability of the formulations.

Bulk phase samples from the DPA-phospholipid/MO mixtures were prepared by self-assembly at a lipid/water ratio of 50/50 (wt/wt) using aqueous phosphate buffer (NaH_2PO_4/Na_2HPO_4, 1.10^{-2} M, pH 7) with dissolved small amount of BHT. The chloroform solutions of the lipid compounds were handled under stream of nitrogen gas to prevent oxidation of the vinyl ether bond of plasmalogen. Lipid nanoparticles were prepared at a lipid/water ratio of 95/5 (wt/wt). Both the bulk mesophases and the dispersed lipid particles were produced by the method of hydration of a dry lipid film followed by physical agitation (Angelova et al., 2018). The lipids were mixed at chosen proportions [95/5, 90/10, 85/15, and 80/20 (mol/mol)], and the solvent was evaporated under flux of nitrogen gas. The obtained fine and homogeneous lipid films were lyophilized overnight under cooling. Vortexing and agitation in an ice bath were applied in repeating cycles of 1 min each. Ultrasonic cycles with a total duration of <10 min (Branson 2510 ultrasonic bath, “set sonics” mode, power 60 W) were sufficient to produce dispersions of lipid nanoparticles in the presence of PEGylated amphiphile VPGS-PEG$_{1000}$.

Synchrotron Small-Angle X-Ray Scattering

Bulk liquid crystalline phases formed by hydrated lipid assemblies and dispersed nanoparticles were investigated at the SWING beamline of synchrotron SOLEIL (Saint Aubin, France) as recently reported (Rakotoarisoa et al., 2019). The samples were placed in capillaries or in a designed gel holder with (X, Y, and Z) positioning. Temperature was 22°C. The sample-to-detector distance was 3 m, and the X-ray beam spot size on the samples was $25 \times 375\ \mu m^2$. The patterns were recorded with a two-dimensional Eiger X 4M detector (Dectris, Baden-Daettwil Switzerland) at 12 keV allowing measurements in the q-range from 0.00426 to 0.37 $Å^{-1}$. The q-vector was defined as $q = (4\pi/\lambda) \sin \theta$, where 2θ is the scattering angle. The synchrotron radiation wavelength was $\lambda = 1.033$ Å, and the exposure time was 250 or 500 ms. The q-range calibration was done using a standard sample of silver behenate ($d = 58.38$ Å). An average of five spectra per sample was acquired. Data processing of the recorded 2D images was performed by the FOXTROT software (David and Pérez, 2009).

Toward nanostructure determination, the positions of the resolved Bragg diffraction peaks were fitted according to the relationships of the Miller indexes. A sequence of Bragg peak positions spaced in the ratio $\sqrt{2}:\sqrt{3}:\sqrt{4}:\sqrt{6}:\sqrt{8}:\sqrt{9}:\sqrt{10}:\sqrt{11}:\sqrt{12}:\sqrt{14}$ is a characteristic of a bicontinuous *Pn3m* double-diamond cubic lattice. The primitive *Im3m* cubic lattice is characterized by peaks spaced as $\sqrt{2}:\sqrt{4}:\sqrt{6}:\sqrt{8}:\sqrt{10}:\sqrt{12}:\sqrt{14}:\sqrt{16}:\sqrt{18}:\sqrt{20}:\sqrt{22}$, whereas the sequence of Bragg peaks positions spaced in the ratio $\sqrt{6}:\sqrt{8}:\sqrt{14}:\sqrt{16}:\sqrt{20}:\sqrt{22}:\sqrt{24}:\sqrt{26}$ defines a gyroid *Ia3d* cubic lattice structure. The Bragg peak positions of multilamellar bilayer structures are spaced in the ratio 1:2:3:4:... For an inverted hexagonal (H_{II}) phase, the corresponding relationship is $1:\sqrt{3}:\sqrt{4}$....

Cryogenic Transmission Electron Microscopy

The methodology of the cryo-TEM study was analogous to the previously described work (Angelova et al., 2019a). In brief, a sample droplet of 2 μl was put on a lacey carbon-film-covered copper grid (Science Services, Munich, Germany), which was hydrophilized by glow discharge (Solarus, Gatan, Munich, Germany) for 30 s. Most of the liquid was then removed with blotting paper, leaving a thin film stretched over the lace holes. The specimen was instantly shock frozen by rapid immersion into liquid ethane and cooled to approximately 90 K by liquid nitrogen in a temperature- and humidity-controlled freezing unit (Leica EMGP, Wetzlar, Germany). The temperature and humidity were monitored and kept constant in the chamber during all sample preparation steps. The specimen was inserted into a cryo-transfer holder (CT3500, Gatan, Munich, Germany) and transferred to a Zeiss EM922 Omega energy-filtered TEM (EFTEM) instrument (Carl Zeiss Microscopy, Jena, Germany). Examinations were carried out at temperatures around 90 K. The TEM instrument was operated at an acceleration voltage of 200 kV. Zero-loss-filtered images (DE = 0 eV) were taken under reduced dose conditions (100–1,000 e/nm^2). The images were recorded digitally by a bottom-mounted charge-coupled device (CCD) camera system (Ultra Scan 1000, Gatan, Munich, Germany) and combined and processed with a digital imaging processing system (Digital Micrograph GMS 1.9, Gatan, Munich, Germany). The sizes of the investigated nanoparticles were in the range or below the film thickness, and no deformations were observed. The images were taken very close to focus or slightly under the focus (some nanometers) due to the contrast-enhancing capabilities of the in-column filter of the employed Zeiss EM922 Omega. In EFTEMs, the deep underfocused images can be totally avoided.

DATA AVAILABILITY STATEMENT

The raw data supporting the conclusions of this article will be made available by the authors, without undue reservation.

AUTHOR CONTRIBUTIONS

AA: conceptualization of manuscript. YD: lipids conception and management. AA, BA, and MD: experimental investigation. TB and MD: instrument management and software. BA, MD, and AA: analysis and data processing. BA, YG, and YD: funding and materials. AA: writing—original draft. BA, YD, and AA: writing—review and editing. AA: supervision. All authors agreed to be accountable for the content of the work.

FUNDING

YD was supported by the National Natural Science Foundation of China (Grant No. 31670841) and Wenzhou Institute, University of Chinese Academy of Sciences (Grant No. WIUCASQD2019005). BA was supported by the projects "Structural dynamics of biomolecular systems" (ELIBIO; CZ.02.1.01/0.0/0.0/15_003/0000447), "Advanced research using high-intensity laser produced photons and particles" (CZ.02.1.01/0.0/0.0/16_019/0000789; ADONIS) from the European Regional Development Fund, and a cooperation with JINR, Dubna, Russia (3 + 3 program, No. 204, item 27 from 25.03.2020).

ACKNOWLEDGMENTS

AA and BA acknowledged the beamtime allocated to the projects 20170933 and 20181489 at the beamline SWING of Synchrotron SOLEIL (France). MD was supported by the collaborative research center SFB840 of the German Science Foundation DFG. AA acknowledged a membership in GDR 2088 "BIOMIM" (CNRS, France).

REFERENCES

Almsherqi, Z. A., Margadant, F., and Deng, Y. (2010). The cubic "Faces" of biomembranes. *Adv. Plan. Lipid Bilay. Liposom.* 12, 79–99. doi: 10.1016/b978-0-12-381266-7.00004-3

Anderson, V. C., and Thompson, D. H. (1992). Triggered release of hydrophilic agents from plasmalogen liposomes using visible light or acid. *Biochim. Biophys. Acta* 1109, 33–42. doi: 10.1016/0005-2736(92)90183-m

Angelov, B., and Angelova, A. (2017). Nanoscale clustering of the neurotrophin receptor TrkB revealed by super-resolution STED microscopy. *Nanoscale* 9, 9797–9804. doi: 10.1039/c7nr03454g

Angelov, B., Angelova, A., Filippov, S., Drechsler, M., Štěpánek, P., and Lesieur, S. (2014). Multicompartment lipid cubic nanoparticles with high protein upload: millisecond dynamics of formation. *ACS Nano* 8, 5216–5226. doi: 10.1021/nn5012946

Angelov, B., Garamus, V. M., Drechsler, M., and Angelova, A. (2017). Structural analysis of nanoparticulate carriers for encapsulation of macromolecular drugs. *J. Mol. Liq.* 235, 83–89. doi: 10.1016/j.molliq.2016.11.064

Angelova, A., and Angelov, B. (2017). Dual and multi-drug delivery nanoparticles towards neuronal survival and synaptic repair. *Neural Regen. Res.* 12, 886–889. doi: 10.4103/1673-5374.208546

Angelova, A., Angelov, B., Mutafchieva, R., Lesieur, S., and Couvreur, P. (2011). Self-assembled multicompartment liquid crystalline lipid carriers for protein, peptide, and nucleic acid drug delivery. *Acc. Chem. Res.* 44, 147–156. doi: 10.1021/ar100120v

Angelova, A., Drechsler, M., Garamus, V. M., and Angelov, B. (2018). Liquid crystalline nanostructures as PEGylated reservoirs of omega-3 polyunsaturated fatty acids: structural insights toward delivery formulations against neurodegenerative disorders. *ACS Omega* 3, 3235–3247. doi: 10.1021/acsomega.7b01935

Angelova, A., Angelov, B., Garamus, V. M., and Drechsler, M. (2019a). A vesicle-to-sponge transition via the proliferation of membrane-linking pores in omega-3 polyunsaturated fatty acid-containing lipid assemblies. *J. Mol. Liq.* 279, 518–523. doi: 10.1016/j.molliq.2019.01.124

Angelova, A., Drechsler, M., Garamus, V. M., and Angelov, B. (2019b). Pep-lipid cubosomes and vesicles compartmentalized by micelles from self-assembly of multiple neuroprotective building blocks including a large peptide hormone PACAP-DHA. *Chem. Nano Mat.* 5, 1381–1389. doi: 10.1002/cnma.201900468

Azmi, I. D., Moghimi, S. M., and Yaghmur, A. (2015). Cubosomes and hexosomes as versatile platforms for drug delivery. *Ther. Deliv.* 6, 1347–1364. doi: 10.4155/tde.15.81

Batenburg, J. J., and Haagsman, H. P. (1998). The lipids of pulmonary surfactant: dynamics and interactions with proteins. *Prog. Lipid Res.* 37, 235–276. doi: 10.1016/s0163-7827(98)00011-3

Bharadwaj, P., Solomon, T., Malajczuk, C. J., Mancera, R. L., Howard, M., Arrigan, D. W. M., et al. (2018). Role of the cell membrane interface in modulating production and uptake of Alzheimer's beta amyloid protein. *Biochim. Biophys. Acta Biomemb.* 1860, 1639–1651. doi: 10.1016/j.bbamem.2018.03.015

Bogdanov, M., Umeda, M., and Dowhan, W. (1999). Phospholipid-assisted refolding of an integral membrane protein: minimum structural features for phosphatidylethanolamine to act as a molecular chaperone. *J. Biol. Chem.* 274, 12339–12345. doi: 10.1074/jbc.274.18.12339

Boggs, J. M., Stamp, D., Hughes, D. W., and Deber, C. M. (1981). Influence of ether linkage on the lamellar to hexagonal phase transition of ethanolamine phospholipids. *Biochemistry* 20, 5728–5735. doi: 10.1021/bi00523a015

Braverman, N., and Moser, A. (2012). Functions of plasmalogen lipids in health and disease. *Biochim. Biophys. Acta* 1822, 1442–1452. doi: 10.1016/j.bbadis.2012.05.008

Brites, P., Waterham, H. R., and Wanders, R. J. A. (2004). Functions and biosynthesis of plasmalogens in health and disease. *Biochim. Biophys. Acta* 1636, 219–231. doi: 10.1016/j.bbalip.2003.12.010

Brodde, A., Teigler, A., Brugger, B., Lehmann, W. D., Wieland, F., Berger, J., et al. (2012). Impaired neurotransmission in ether lipid-deficient nerve terminals. *Hum. Mol. Genet.* 21, 2713–2724. doi: 10.1093/hmg/dds097

Brosche, T., Bertsch, T., Sieber, C. C., and Hoffmann, U. (2013). Reduced plasmalogen concentration as a surrogate marker of oxidative stress in elderly septic patients. *Archiv. Gerontol. Geriatr.* 57, 66–69. doi: 10.1016/j.archger.2013.02.007

Casares, D., Escribá, P. V., and Rosselló, C. A. (2019). Membrane lipid composition: Effect on membrane and organelle structure, function and compartmentalization and therapeutic avenues. *Int. J. Mol. Sci.* 20:2167. doi: 10.3390/ijms20092167

Che, H., Li, Q., Zhang, L., Ding, L., Zhang, L., Shi, H., et al. (2018). A comparative study of EPA-enriched ethanolamine plasmalogen and EPA-enriched phosphatidylethanolamine on Abeta 42 induced cognitive deficiency in a rat model. *Food Funct.* 9, 3008–3017. doi: 10.1039/c8fo00643a

Che, H., Zhang, L., Ding, L., Xie, W., Jiang, X., Xue, C., et al. (2020). EPA-enriched ethanolamine plasmalogen and EPA-enriched phosphatidylethanolamine enhance BDNF/TrkB/CREB signaling and inhibit neuronal apoptosis in vitro and in vivo. *Food Funct.* 11, 1729–1739. doi: 10.1039/c9fo02323b

Chong, K., and Deng, Y. (2012). The three dimensionality of cell membranes: lamellar to cubic membrane transition as investigated by electron microscopy. *Methods Cell Biol.* 108, 317–343. doi: 10.1016/b978-0-12-386487-1.00015-8

Creuwels, L. A. J. M., Van Golde, L. M. G., and Haagsman, H. P. (1997). The pulmonary surfactant system: biochemical and clinical aspects. *Lung* 175, 1–39. doi: 10.1201/9780367812812-1

Cui, H., Hodgdon, T. K., Kaler, E. W., Abezgauz, L., Danino, D., Lubovsky, M., et al. (2007). Elucidating the assembled structure of amphiphiles in solution via cryogenic transmission electron microscopy. *Soft Matter.* 3, 945–955. doi: 10.1039/b704194b

Cullis, P. R., and de Kruijff, B. (1979). Lipid polymorphism and the functional roles of lipids in biological membranes. *Biochim. Biophys. Acta* 559, 399–420. doi: 10.1016/0304-4157(79)90012-1

David, G., and Pérez, J. (2009). Combined sampler robot and high-performance liquid chromatography: a fully automated system for biological small-angle X-ray scattering experiments at the synchrotron SOLEIL SWING beamline. *J. Appl. Crystallogr.* 42, 892–900. doi: 10.1107/s0021889809029288

Dean, J. M., and Lodhi, I. J. (2018). Structural and functional roles of ether lipids. *Protein Cell* 9, 196–206. doi: 10.1007/s13238-017-0423-5

Deng, Y., and Almsherqi, Z. A. (2015). Evolution of cubic membranes as antioxidant defence system. *Interf. Focus* 5:20150012. doi: 10.1098/rsfs.2015.0012

Deng, Y., Almsherqi, Z. A., Shui, G. H., Wenk, M. R., and Kohlwein, S. D. (2009). Docosapentaenoic acid (DPA). is a critical determinant of cubic membrane formation in amoeba Chaos mitochondria. *FASEB J.* 23, 2866–2871. doi: 10.1096/fj.09-130435

Deng, Y., Lee, L. H. E., Chong, K., and Almsherqi, Z. A. (2017). Evaluation of radical scavenging system in amoeba Chaos carolinense during nutrient deprivation. *Interf. Focus* 7:20160113. doi: 10.1098/rsfs.2016.0113

Dorninger, F., Gundacker, A., Zeitler, G., Pollak, D. D., and Berger, J. (2019). Ether lipid deficiency in mice produces complex behavioral phenotype mimicking aspects of human psychiatric disorders. *Int. J. Mol. Sci.* 20:3929. doi: 10.3390/ijms20163929

Dorninger, F., Forss-Petter, S., and Berger, J. (2017a). From peroxisomal disorders to common neurodegenerative diseases - the role of ether phospholipids in the nervous system. *FEBS Lett.* 591, 2761–2788. doi: 10.1002/1873-3468.12788

Dorninger, F., Herbst, R., Kravic, B., Camurdanoglu, B. Z., Macinkovic, I., Zeitler, G., et al. (2017b). Reduced muscle strength in ether lipid-deficient mice is accompanied by altered development and function of the neuromuscular junction. *J. Neurochem.* 143, 569–583. doi: 10.1111/jnc.14082

Dragonas, C., Bertsch, T., Sieber, C. C., and Brosche, T. (2009). Plasmalogens as a marker of elevated systemic oxidative stress in Parkinson's disease. *Clin. Chem. Lab. Med.* 47, 894–897.

Farooqui, A. A., Rapoport, S. I., and Horrocks, L. A. (1997). Membrane phospholipid alterations in Alzheimer's disease: deficiency of ethanolamine plasmalogens. *Neurochem. Res.* 22, 523–527.

Feller, S. E., Gawrisch, K., and MacKerell, A. D. (2002). Polyunsaturated fatty acids in lipid bilayers: intrinsic and environmental contributions to their unique physical properties. *J. Am. Chem. Soc.* 124, 318–326. doi: 10.1021/ja0118340

Fong, C., Weerawardena, A., Sagnella, S. M., Mulet, X., Waddington, L., Krodkiewska, I., et al. (2010). Monodisperse nonionic phytanyl ethylene oxide surfactants: high throughput lyotropic liquid crystalline phase determination and the formation of liposomes, hexosomes and cubosomes. *Soft Matter.* 6, 4727–4741. doi: 10.1039/c0sm00454e

Fong, W. K., Salentinig, S., Prestidge, C. A., Mezzenga, R., Hawley, A., and Boyd, B. J. (2014). Generation of geometrically ordered lipid-based liquid-crystalline nanoparticles using biologically relevant enzymatic processing. *Langmuir* 30, 5373–5377. doi: 10.1021/la5003447

Fong, W. K., Sánchez-Ferrer, A., Rappolt, M., Boyd, B. J., and Mezzenga, R. (2019). Structural transformation in vesicles upon hydrolysis of phosphatidylethanolamine and phosphatidylcholine with phospholipase C. *Langmuir* 35, 14949–14958. doi: 10.1021/acs.langmuir.9b02288

Fonseca-Santos, B., Gremião, M. P. D., and Chorilli, M. (2015). Nanotechnology-based drug delivery systems for the treatment of Alzheimer's disease. *Int. J. Nanomed.* 10, 4981–5003. doi: 10.2147/ijn.s87148

Fontaine, D., Figiel, S., Felix, R., Kouba, S., Fromont, G., Maheo, K., et al. (2020). Roles of endogenous ether lipids and associated PUFAs in the regulation of ion channels and their relevance for disease. *J. Lipid Res.* 61, 840–858. doi: 10.1194/jlr.ra120000634

Fujino, T., Yamada, T., Asada, T., Ichimaru, M., Tsuboi, Y., Wakana, C., et al. (2018). Effects of plasmalogen on patients with mild cognitive impairment: a randomized, placebo-controlled trial in Japan. *J. Alzheimers Dis. Parkins.* 8:419.

Fujino, T., Yamada, T., Asada, T., Tsuboi, Y., Wakana, C., Mawatari, S., et al. (2017). Efficacy and blood plasmalogen changes by oral administration of plasmalogen in patients with mild Alzheimer's disease and mild cognitive impairment: a multicenter, randomized, double-blind, placebo-controlled trial. *EBiomedicine* 17, 199–205. doi: 10.1016/j.ebiom.2017.02.012

Glaser, P. E., and Gross, R. W. (1994). Plasmenylethanolamine facilitates rapid membrane fusion: a stopped-flow kinetic investigation correlating the propensity of a major plasma membrane constituent to adopt an HII phase with its ability to promote membrane fusion. *Biochemistry* 33, 5805–5812. doi: 10.1021/bi00185a019

Goldfine, H. (2010). The appearance, disappearance and reappearance of plasmalogens in evolution. *Prog. Lipid Res.* 49, 493–498. doi: 10.1016/j.plipres.2010.07.003

Goldfine, H., Johnston, N. C., Mattai, J., and Shipley, G. G. (1987a). Regulation of bilayer stability in *Clostridium hufyricurn*: studies on the polymorphic phase behavior of ether lipids. *Biochemistry* 26, 2814–2822. doi: 10.1021/bi00384a024

Goldfine, H., Rosenthal, J. J. C., and Johnston, N. C. (1987b). Lipid shape as a determinant of lipid composition in *Clostridium hutyricum*: effects of incorporation of various fatty acids on the ratios of the major ether lipids. *Biochim. Biophys. Acta* 904, 283–289. doi: 10.1016/0005-2736(87)90377-4

Goldfine, H., Johnston, N. C., and Phillips, M. C. (1981). Phase behavior of ether lipids from *Clostridium butyricum*. *Biochemistry* 20, 2908–2916. doi: 10.1021/bi00513a030

Gross, R. W. (1985). Identification of plasmalogen as the major phospholipid constituent of cardiac sarcoplasmic reticulum. *Biochemistry* 24, 1662–1668. doi: 10.1021/bi00328a014

Guerzoni, L. P. B., Nicolas, V., and Angelova, A. (2017). *In vitro* modulation of TrkB receptor signaling upon sequential delivery of curcumin-DHA loaded carriers towards promoting neuronal survival. *Pharm. Res.* 34, 492–505. doi: 10.1007/s11095-016-2080-4

Han, X., and Gross, R. W. (1990). Plasmenylcholine and phosphatidylcholine membrane bilayers possess distinct conformational motifs. *Biochemistry* 29, 4992–4996. doi: 10.1021/bi00472a032

Han, X., Holtzman, D. M., and McKeel, D. W. Jr. (2001). Plasmalogen deficiency in early Alzheimer's disease subjects and in animal models. *J. Neurochem.* 77, 1168–1180. doi: 10.1046/j.1471-4159.2001.00332.x

Harilal, S., Jose, J., Parambi, D. G. T., Kumar, R., Mathew, G. E., Uddin, M. S., et al. (2019). Advancements in nanotherapeutics for Alzheimer's disease: current perspectives. *J. Pharm. Pharmacol.* 71, 1370–1383. doi: 10.1111/jphp.13132

Hossain, M. S., Ifuku, M., Take, S., Kawamura, J., Miake, K., and Katafuchi, T. (2013). Plasmalogens rescue neuronal cell death through an activation of AKT and ERK survival signaling. *PLoS One* 8:e83508. doi: 10.1371/journal.pone.0083508

Israelachvili, J. N., Mitchell, D. J., and Ninham, B. W. J. (1976). Theory of self - assembly of hydrocarbon amphiphiles into micelles and bilayers. *Chem. Soc. Faraday Trans. II* 72, 1525–1568. doi: 10.1039/f29767201525

Jang, J. E., Park, H.-S., Yoo, H. J., Koh, E. H., and Lee, K. U. (2017). Protective role of endogenous plasmalogens against hepatic steatosis and steatohepatitis in mice. *Hepatology* 66, 416–431. doi: 10.1002/hep.29039

Jenkins, C. M., Yang, K., Liu, G., Moon, S. H., Dilthey, B. G., and Gross, R. W. (2018). Cytochrome c is an oxidative stress-activated plasmalogenase that cleaves plasmenylcholine and plasmenylethanolamine at the sn-1 vinyl ether linkage. *J. Biol. Chem.* 293, 8693–8709. doi: 10.1074/jbc.ra117.001629

Jiménez-Rojo, N., and Riezman, H. (2019). On the road to unraveling the molecular functions of ether lipids. *FEBS Lett.* 593, 2378–2389. doi: 10.1002/1873-3468.13465

Koivuniemi, A. (2017). The biophysical properties of plasmalogens originating from their unique molecular architecture. *FEBS Lett.* 591, 2700–2713. doi: 10.1002/1873-3468.12754

Lee, A. G. (2004). How lipids affect the activities of integral membrane proteins. *Biochim.Biophys. Acta* 1666, 62–87. doi: 10.1016/j.bbamem.2004.05.012

Leßig, J., and Fuchs, B. (2009). Plasmalogens in biological systems: their role in oxidative processes in biological membranes, their contribution to pathological processes and aging and plasmalogen analysis. *Curr. Med. Chem.* 16, 2021–2041. doi: 10.2174/092986709788682164

Li, Y., Angelova, A., Hu, F., Garamus, V. M., Peng, C., Li, N., et al. (2019). pH-Responsiveness of hexosomes and cubosomes for combined delivery of *Brucea javanica* oil and doxorubicin. *Langmuir* 35, 14532–14542. doi: 10.1021/acs.langmuir.9b02257

Lohner, K. (1996). Is the high propensity of ethanolamine plasmalogens to form non-lamellar lipid structures manifested in the properties of biomembranes? *Chem. Phys. Lipids* 81, 167–184. doi: 10.1016/0009-3084(96)02580-7

Lohner, K., Balgavy, P., Hermetter, A., Paltauf, F., and Laggner, P. (1991). Stabilization of non-bilayer structures by the ether lipid ethanolamine plasmalogen. *Biochim. Biophys. Acta Biomembr.* 1061, 132–140. doi: 10.1016/0005-2736(91)90277-f

Lohner, K., Hermitter, A., and Paltauf, F. (1984). Phase behavior of ethanolamine plasmalogen. *Chem. Phys. Lipids* 34, 163–170. doi: 10.1016/0009-3084(84)90041-0

Malthaner, M., Hermetter, A., Paltauf, F., and Seelig, J. (1987). Structure and dynamics of plasmalogen model membranes containing cholesterol: a deuterium NMR study. *Biochim. Biophys. Acta* 900, 191–197. doi: 10.1016/0005-2736(87)90333-6

Mannock, D. A., Lewis, R. N. A. H., McMullen, T. P. W., and McElhaney, R. N. (2010). The effect of variations in phospholipid and sterol structure on the nature of lipid-sterol interactions in lipid bilayer model membranes. *Chem. Phys. Lipids* 163, 403–448. doi: 10.1016/j.chemphyslip.2010.03.011

Mariani, P., Luzzati, V., and Delacroix, H. (1988). Cubic phases of lipid - containing systems. Structure analysis and biological implications. *J. Mol. Biol.* 204, 165–189. doi: 10.1016/0022-2836(88)90607-9

Mawatari, S., Ohara, S., Taniwaki, Y., Tsuboi, Y., Maruyama, T., and Fujino, T. (2020). Improvement of blood plasmalogens and clinical symptoms in Parkinson's disease by oral administration of ether phospholipids: A preliminary report. *Parkinson's Dis.* 2020:2671070.

Messias, M. C. F., Mecatti, G. C., Priolli, D. G., and De Oliveira Carvalho, P. (2018). Plasmalogen lipids: functional mechanism and their involvement in gastrointestinal cancer. *Lipids Health Dis.* 17:41. doi: 10.1016/0009-3084(90)90147-j

Muallem, S., Chung, W. Y., Jha, A., and Ahuja, M. (2017). Lipids at membrane contact sites: cell signaling and ion transport. *EMBO Rep.* 18, 1893–1904. doi: 10.15252/embr.201744331

Munn, N. J., Arnio, E., Liu, D., Zoeller, R. A., and Liscum, L. (2003). Deficiency in ethanolamine plasmalogen leads to altered cholesterol transport. *J. Lipid Res.* 44, 182–192. doi: 10.1194/jlr.m200363-jlr200

Paul, S., Lancaster, G. I., and Meikle, P. J. (2019). Plasmalogens: a potential therapeutic target for neurodegenerative and cardiometabolic disease. *Prog. Lipid Res.* 74, 186–195. doi: 10.1016/j.plipres.2019.04.003

Pohl, E. E., and Jovanovic, O. (2019). The role of phosphatidylethanolamine adducts in modification of the activity of membrane proteins under oxidative stress. *Molecules* 24:4545. doi: 10.3390/molecules24244545

Rakotoarisoa, M., Angelov, B., Espinoza, S., Khakurel, K., Bizien, T., and Angelova, A. (2019). Cubic liquid crystalline nanostructures involving catalase and curcumin: BioSAXS study and catalase peroxidatic function after cubosomal nanoparticle treatment of differentiated SH-SY5Y cells. *Molecules* 24:E3058.

Reiss, D., Beyer, K., and Engelmann, B. (1997). Delayed oxidative degradation of polyunsaturated diacyl phospholipids in the presence of plasmalogen phospholipids in vitro. *Biochem. J.* 323, 807–814. doi: 10.1042/bj3230807

Rog, T., and Koivuniemi, A. (2016). The biophysical properties of ethanolamine plasmalogens revealed by atomistic molecular dynamics simulations. *Biochim. Biophys. Acta Biomembr.* 1858, 97–103. doi: 10.1016/j.bbamem.2015.10.023

Saab, S., Mazzocco, J., Creuzot-Garcher, C. P., Bron, A. M., Bretillon, L., Acar, N., et al. (2014). Plasmalogens in the retina: from occurrence in retinal cell membranes to potential involvement in pathophysiology of retinal diseases. *Biochimie* 107(Pt A), 58–65. doi: 10.1016/j.biochi.2014.07.023

Seddon, J. M. (1990). Structure of the inverted hexagonal (HII). phase, and non-lamellar phase transitions of lipids. *Biochim. Biophys. Acta Biomembr.* 1031, 1–69. doi: 10.1016/0304-4157(90)90002-t

Seddon, J. M., and Templer, R. H. (1995). "Polymorphism of lipid-water systems," in *Handbook of Biological Physics: Structure and Dynamics of Membranes*, eds R. Lipowsky and E. Sackmann (London: Elsevier Science), 97–153. doi: 10.1016/s1383-8121(06)80020-5

Shaharabani, R., Ram-On, M., Avinery, R., Aharoni, R., Arnon, R., Talmon, Y., et al. (2016). Structural transition in myelin membrane as initiator of multiple sclerosis. *J. Am. Chem. Soc.* 138, 12159–12165. doi: 10.1021/jacs.6b04826

Shao, X., Bor, G., Al-Hosayni, S., Salentinig, S., and Yaghmur, A. (2018). Structural characterization of self-assemblies of new omega-3 lipids: docosahexaenoic acid and docosapentaenoic acid monoglycerides. *Phys. Chem. Chem. Phys.* 20, 23928–23941. doi: 10.1039/c8cp04256j

Sibomana, I., Grobe, N., Delraso, N. J., and Reo, N. V. (2019). Influence of myo-inositol plus ethanolamine on plasmalogens and cell viability during oxidative stress. *Chem. Res. Toxicol.* 32, 265–284. doi: 10.1021/acs.chemrestox.8b00280

Snyder, F. (1999). The ether lipid trail: a historical perspective. *Biochim. Biophys. Acta* 1436, 265–278.

Su, X. Q., Wang, J., and Sinclair, A. J. (2019). Plasmalogens and Alzheimer's disease: a review. *Lipids Health Dis.* 18:100.

Sutter, I., Klingenberg, R., Othman, A., Rohrer, L., Landmesser, U., Heg, D., et al. (2016). Decreased phosphatidylcholine plasmalogens - A putative novel lipid signature in patients with stable coronary artery disease and acute myocardial infarction. *Atherosclerosis* 246, 130–140. doi: 10.1016/j.atherosclerosis.2016.01.003

Sutter, I., Velagapudi, S., Othman, A., Riwanto, M., Manz, J., Rohrer, L., et al. (2015). Plasmalogens of high-density lipoproteins (HDL). are associated with coronary artery disease and anti-apoptotic activity of HDL. *Atherosclerosis* 241, 539–546. doi: 10.1016/j.atherosclerosis.2015.05.037

Talaikis, M., Valldeperas, M., Matulaitiene, I., Borzova, J. L., Barauskas, J., Niaura, G., et al. (2019). On the molecular interactions in lipid bilayer-water assemblies of different curvatures. *J. Phys. Chem. B* 123, 2662–2672. doi: 10.1021/acs.jpcb.8b11387

Thai, T.-P., Rodemer, C., Jauch, A., Hunziker, A., Moser, A., Gorgas, K., et al. (2001). Impaired membrane traffic in defective ether lipid biosynthesis. *Hum. Mol. Genet.* 10, 127–136. doi: 10.1093/hmg/10.2.127

Thompson, D. H., Gerasimov, O. V., Wheeler, J. J., Rui, Y., and Anderson, V. C. (1996). Triggerable plasmalogen liposomes: improvement of system efficiency. *Biochim. Biophys. Acta* 1279, 25–34. doi: 10.1016/0005-2736(95)00210-3

Wallner, S., and Schmitz, G. (2011). Plasmalogens the neglected regulatory and scavenging lipid species. *Chem. Phys. Lipids* 164, 573–589. doi: 10.1016/j.chemphyslip.2011.06.008

Wang, W., Zetterlund, P. B., Boyer, C., Boyd, B. J., Atherton, T. J., and Spicer, P. T. (2018). Large hexosomes from emulsion droplets: Particle shape and mesostructure control. *Langmuir* 34, 13662–13671. doi: 10.1021/acs.langmuir.8b02638

West, A., Zoni, V., Teague, W. E. Jr., Leonard, A. N., Vanni, S., Gawrisch, K., et al. (2020). How do ethanolamine plasmalogens contribute to order and structure of neurological membranes? *J. Phys. Chem. B* 124, 828–839. doi: 10.1021/acs.jpcb.9b08850

Yaghmur, A., and Glatter, O. (2009). Characterization and potential applications of nanostructured aqueous dispersions. *Adv. Colloid Interf. Sci.* 147-148, 333–342. doi: 10.1016/j.cis.2008.07.007

Yamashita, S., Kanno, S., Nakagawa, K., Kinoshita, M., and Miyazawa, T. (2015). Extrinsic plasmalogens suppress neuronal apoptosis in mouse neuroblastoma Neuro-2A cells: importance of plasmalogen molecular species. *RSC Adv.* 5, 61012–61020. doi: 10.1039/c5ra00632e

Zhai, J., Fong, C., Tran, N., and Drummond, C. J. (2019). Non-lamellar lyotropic liquid crystalline lipid nanoparticles for the next generation of nanomedicine. *ACS Nano* 13, 6178–6206. doi: 10.1021/acsnano.8b07961

Zoeller, R., Lake, A., Nagan, N., Gaposchkin, D., Legner, M., and Lieberthal, W. (1999). Plasmalogens as endogenous antioxidants: somatic cell mutants reveal the importance of the vinyl ether. *Biochem. J.* 338, 769–776. doi: 10.1042/0264-6021:3380769

Conflict of Interest: The authors declare that the research was conducted in the absence of any commercial or financial relationships that could be construed as a potential conflict of interest.

The handling editor declared a past co-authorship with several of the authors.

frontiers
in Cell and Developmental Biology

REVIEW
published: 16 February 2021
doi: 10.3389/fcell.2021.618102

The Potential Role of Bioactive Plasmalogens in Lung Surfactant

*Ruijiang Zhuo[1], Pu Rong[2], Jieli Wang[2], Rokshana Parvin[2] and Yuru Deng[1,2]**

[1] Eye Hospital, School of Ophthalmology and Optometry, School of Biomedical Engineering, Wenzhou Medical University, Wenzhou, China, [2] Wenzhou Institute, University of Chinese Academy of Sciences, Wenzhou, China

Neonatal respiratory distress syndrome (NRDS) is a type of newborn disorder caused by the deficiency or late appearance of lung surfactant, a mixture of lipids and proteins. Studies have shown that lung surfactant replacement therapy could effectively reduce the morbidity and mortality of NRDS, and the therapeutic effect of animal-derived surfactant preparation, although with its limitations, performs much better than that of protein-free synthetic ones. Plasmalogens are a type of ether phospholipids present in multiple human tissues, including lung and lung surfactant. Plasmalogens are known to promote and stabilize non-lamellar hexagonal phase structure in addition to their significant antioxidant property. Nevertheless, they are nearly ignored and underappreciated in the lung surfactant-related research. This report will focus on plasmalogens, a minor yet potentially vital component of lung surfactant, and also discuss their biophysical properties and functions as anti-oxidation, structural modification, and surface tension reduction at the alveolar surface. At the end, we boldly propose a novel synthetic protein-free lung surfactant preparation with plasmalogen modification as an alternative strategy for surfactant replacement therapy.

Keywords: lung surfactant, plasmalogen, tubular myelin, lamellar bodies, antioxidant, cubic membrane

Edited by:
Jorge Bernardino De La Serna,
Imperial College London,
United Kingdom

Reviewed by:
Jesus Perez-Gil,
Complutense University of Madrid,
Spain
Elena Lopez-Rodriguez,
Charité—Universitätsmedizin Berlin,
Germany

****Correspondence:***
Yuru Deng
dengyr@wibe.ac.cn

Specialty section:
This article was submitted to
Cellular Biochemistry,
a section of the journal
Frontiers in Cell and Developmental Biology

Received: *16 October 2020*
Accepted: *08 January 2021*
Published: *16 February 2021*

Citation:
Zhuo R, Rong P, Wang J, Parvin R and Deng Y (2021) The Potential Role of Bioactive Plasmalogens in Lung Surfactant.
Front. Cell Dev. Biol. 9:618102.
doi: 10.3389/fcell.2021.618102

INTRODUCTION

In 1959, Avery and Mead reported that the saline extracts of lungs from premature infants succumbing to neonatal respiratory distress syndrome (NRDS) were surfactant deficient as compared with those newborn dying of other causes (Halliday, 2017). This discovery spurred enormous interest in the following lung surfactant research. Decades later, pulmonary surfactant replacement therapy was proved to effectively reduce the morbidity and mortality of NRDS (Kim and Won, 2018). According to clinical studies, animal-derived surfactants are the more desirable choice than currently available protein-free synthetic ones (Ardell et al., 2015; Kim and Won, 2018). Nevertheless, the synthetic surfactant preparations produced in the laboratory have significant advantages in purity, reproducibility, safety, and quality control as compared with the animal-derived products (Notter et al., 2007). Although two major surfactant membrane proteins, SP-B and SP-C, are considered to be critical for the adsorption and spreading of surfactant film at the air–water interface (Johansson and Curstedt, 1997), it is still difficult to prepare artificial surfactant with these two surfactant proteins (Walther et al., 2019). SP-B molecule is too big and structurally complex to be synthesized by organic chemistry methods; also the expression of functionally active recombinant SP-B has not been successful yet (Curstedt et al., 2013; Parra and Pérez-Gil, 2015). SP-C is also difficult to obtain due to its extreme hydrophobicity and structural instability, especially in its pure form (Curstedt et al., 2013; Parra and Pérez-Gil, 2015).

Although the synthetic surfactant preparations can be produced in the presence of synthetic peptides that are simplified surrogates of the surfactant proteins, they are still not available in the market (Hentschel et al., 2020). The increased understanding of mechanisms involved in the formation and preservation of surfactant film at alveolar surface has led to uncover a bioactive phospholipid (PL) component in lung surfactant, plasmalogen, which has been somehow underappreciated in lung surfactant research; and its unique features as structural attribute and antioxidant allow us to boldly propose new protein-free artificial surfactant preparations with plasmalogen modification as an alternative strategy for effective surfactant replacement therapies.

LUNG SURFACTANT: COMPOSITION, STRUCTURE, AND FUNCTION

The respiratory surface of the mammalian lung is stabilized by pulmonary surfactant, a membrane-based system. The primary function of lung surfactant is to minimize the surface tension at alveolar air–liquid interface, optimize the mechanics of breathing, and avoid alveolar collapse, especially at the end of expiration (Parra and Pérez-Gil, 2015). Lung surfactant is synthesized, stored, secreted, and recycled through type II alveolar cells (Notter et al., 2007), which emerge at the 24th gestation week and mature at the 34th–36th gestation week. The preterm babies (<34 weeks) with insufficient lung surfactant have much higher risk of developing NRDS, the main cause of perinatal mortality.

The composition and biosynthesis of lung surfactant are only better understood since 1950s due to the start of recognition of NRDS (Notter, 2000). Lung surfactant is a mixture of lipids (90%) and proteins (10%) (**Figure 1**). In mammals, dipalmitoylphosphatidylcholine (DPPC) contributes the largest fraction of total lung surfactant. DPPC, a di-saturated PL is considered to be indispensable to allow for a reduction of surface tension at alveolar air–water interface (Wüstneck et al., 2005; Olmeda et al., 2017). Phosphatidylglycerol (PG), the second most abundant PL in lung surfactant mixture (Pfleger et al., 1972; Hallman and Gluck, 1975), may improve the property of surfactant in stabilizing the alveoli (Hallman et al., 1977; Orgeig et al., 2003). The rest of the lipid fraction is constituted by other polyunsaturated PLs including bioactive plasmalogen and cholesterol as well.

The content of plasmalogens in alveolar surfactant has been rarely investigated. The concentration of total plasmalogens is around 2% in rat surfactant (Rüstow et al., 1994) and 5–6% in dog surfactant (Rana et al., 1993). There is about 1.2% plasmalogens extracted from total lipids of pig surfactant (Body, 1971). The relative percentage of plasmalogens in the term healthy infants is 1.8 ± 0.9% (Rüdiger et al., 2000). Plasmalogen phosphocholine (PC) was first identified in the mammalian lung surfactant preparations obtained from both adult cow and lamb fetal pulmonary lavage (Rana et al., 1993). Of particular interest, the amount of plasmalogen PC in these preparations is reported to be unexpectedly comparable with that of PG, the second most abundant PL in lung surfactant lipid mixture at the fractional level (Rana et al., 1993). Thus, the presence of plasmalogen PC in pulmonary surfactant might have significant impact on animal and human physiology and suggest new directions of biochemical and biophysical studies of lung surfactant (Rana et al., 1993). Another minor yet important component of lung surfactant lipids is cholesterol, which may optimize the surfactant activity (Orgeig et al., 2003) and is considered crucial as well in surfactant function.

As for the protein part, three out of total four surfactant proteins present in the alveolar hypophase (SP-A, SP-B, and SP-C) are membrane associated, and even with small amounts, they may have profound effect on surfactant membrane structure and function (Casals, 2001; Serrano and Pérez-Gil, 2006; Cabré et al., 2018). SP-A is able to bind to a wide variety of microorganisms (Lawson and Reid, 2000; Ariki et al., 2012), although it is hydrophilic, and together with SP-B (Suzuki et al., 1989; Knudsen and Ochs, 2018), it may participate in the formation of tubular myelin (TM), a liquid crystal membrane structure found within the alveolar space (**Figure 2A**). The structure of TM and its ability of being viscoelastically deformed have been suggested to explain the mechanism behind the reduction of work required for air breathing (Ninham et al., 2017). The addition of Ca^{2+} also promoted lamellar to hexagonal (H_{II}) transitions in the mixtures of phosphatidylethanolamine (PE) and phosphatidylserine (Cullis et al., 1978). SP-B and SP-C, the hydrophobic surfactant proteins, have been demonstrated crucial for surfactant activity inside the alveoli, and their incorporation into the lipid mixtures could facilitate proper interfacial adsorption, film stability, and re-spreading abilities of lung surfactant (Wang et al., 1996; Cruz et al., 2000; Serrano and Pérez-Gil, 2006). Meanwhile, both SP-A and SP-D are part of the innate immune system at alveolar surface and may regulate the functions of other important innate immune cells such as macrophages (Vaandrager and van Golde, 2000; Matalon and Wright, 2004; Pastva et al., 2007; Kharlamova et al., 2020).

THE SIGNIFICANCE OF PLASMALOGENS

Plasmalogens are a class of PLs carrying a vinyl ether bond at sn-1 and an ester bond at sn-2 position of the glycerol backbone (Nagan and Zoeller, 2001; Wallner and Schmitz, 2011; Jiménez-Rojo and Riezman, 2019). They constitute 15–20% of total PLs of cell membranes (Braverman and Moser, 2012). Plasmalogens are abundant in the brain, retina, leukocytes (immune cells), sperm, heart, and skeletal muscle in the mammals (Braverman and Moser, 2012). They are also concentrated in specialized membranes, such as myelin, and secreted membranes such as synaptic vesicles and lung surfactant (Braverman and Moser, 2012). The physiological role of plasmalogens in cells has been proposed to range from free radical scavenging to promoting membrane fusion; it has been still difficult to assess their biophysical roles in cell membrane partly due to their variable concentration in different cell types and the change during development (Koivuniemi, 2017).

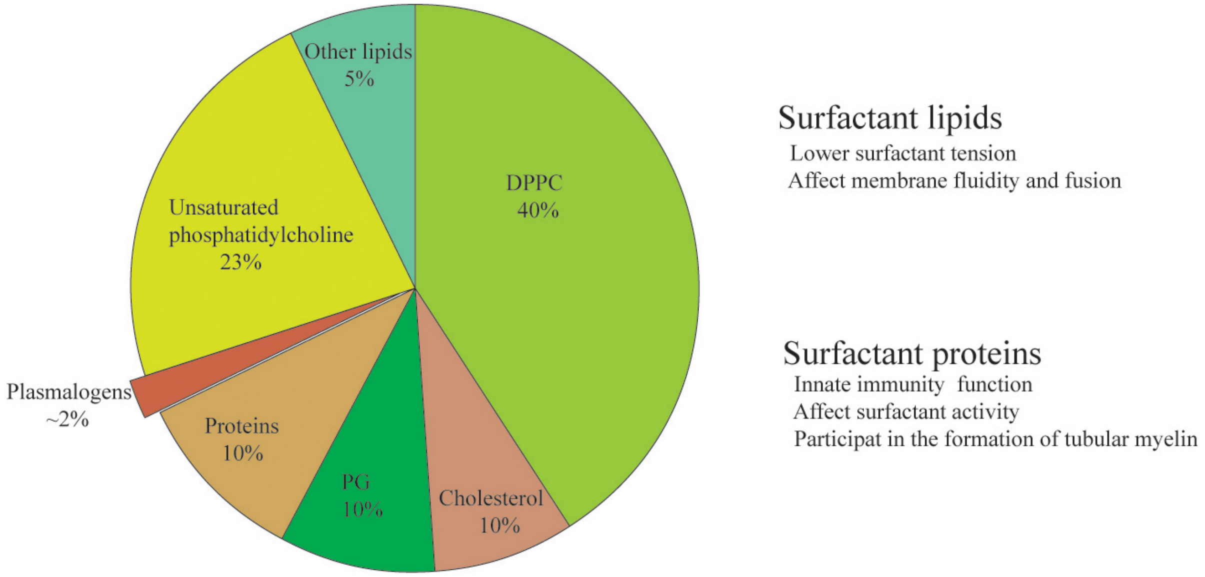

FIGURE 1 | The composition and function of lung surfactant. The constitution of phospholipids% might be slightly different in different publications, and the discrepancy might be due to differences in the source (animal species) and the method of extraction (either from lavage or from whole minced tissue). Plasmalogen, a minor yet bioactive ether phospholipid of lung surfactant, is the ethanolamine and choline phospholipids vs. its ester counterpart.

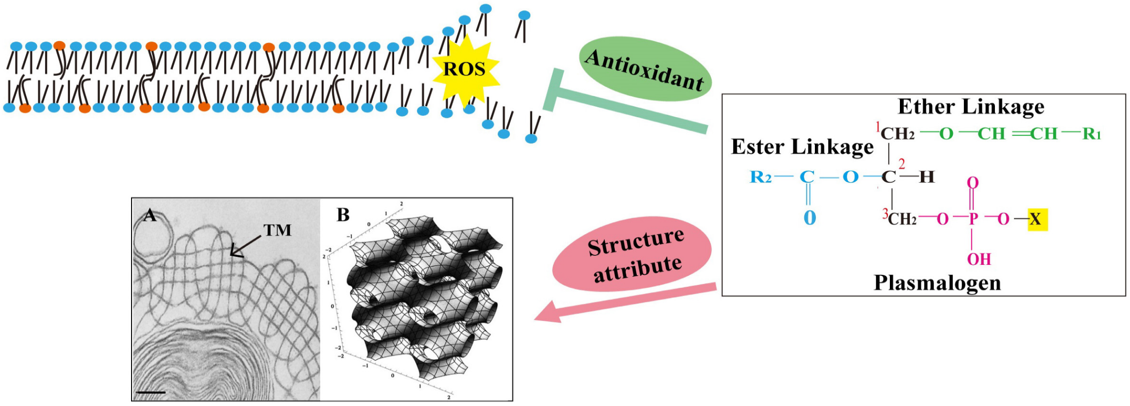

FIGURE 2 | The chemical structure of plasmalogen and its potential role in lung surfactant. Plasmalogens are a class of phospholipids carrying a vinyl ether bond at sn-1 and an ester bond at sn-2 position of the glycerol backbone. The vinyl ether bond at sn-1 position is highly prone to attack by reactive oxygen species (ROS). This was proposed to prevent the oxidative damage of polyunsaturated fatty acids and other vulnerable membrane lipids, suggesting a role for plasmalogens as sacrificial molecules (antioxidant). Plasmalogens also promote the formation of non-lamellar membrane structures, including tubular myelin (TM) (a deformed P-cubic structure). Orange spheres mark plasmalogens, and blue spheres mark other phospholipids. **(A)** Transmission electron microscopy (TEM) image containing TM structure (arrow) was adapted from Williams (1977) with permission; scale bar = 100 nm. **(B)** A tP model of TM bilayer structure with the minimal surface describes the center of the bilayer. Adapted from Larsson and Larsson (2014) with permission.

Plasmalogens as endogenous antioxidants to protect cell membrane PLs and lipoprotein particles against oxidative damage are still controversial (Yavin and Gatt, 1972; Khaselev and Murphy, 1999; Farooqui and Horrocks, 2001; Zemski Berry and Murphy, 2005; Richard et al., 2008). However, the high susceptibility of vinyl ether bond of plasmalogens to reactive oxygen species (ROS) and traces of acids has suggested their sacrificing role as a first-line defense system in a biological system (Yavin and Gatt, 1972; Khaselev and Murphy, 1999; Farooqui and Horrocks, 2001; Zemski Berry and Murphy, 2005; Richard et al., 2008). Plasmalogen-deficient cultured cells and animals have long been known to be more sensitive to oxidative damage than their wild-type counterparts, strongly suggesting that plasmalogens may act as an endogenous antioxidant in cells (Reiss et al., 1997; Morand et al., 1988; Zoeller et al., 1988; Nagan and Zoeller, 2001; Lessig and Fuchs, 2009; Wallner and Schmitz, 2011; Luoma et al., 2015). Cellular plasmalogens are also reported to act as antioxidants against ultraviolet light-induced lipid peroxidation (Zoeller et al., 1988). Moreover, plasmalogens seem to be able to act as antioxidants to protect low-density lipoproteins (LDLs) (Jürgens et al., 1995), whose oxidation is crucial in promoting atherogenesis in humans.

The depletion of plasmalogens, or their reduced amount, is associated with lipid raft microdomain (a cholesterol-rich membrane region) stability and raft involvement in cellular signaling (Pike et al., 2002; Munn et al., 2003; Rodemer et al., 2003). Both cholesterol and plasmalogen are of great significance in cell membrane fluidity and stability (Pike et al., 2002; Orgeig et al., 2003; Rodemer et al., 2003). Both may act as helper lipids to modify lung surfactant membrane structure (Lohner et al., 1991; Andersson et al., 2017). Model membrane system consisting of plasmalogens may go through the transformation from lamellar gel to liquid crystalline at the lower temperature (4–5°C) compared with their diacyl counterparts (Lohner, 1996). More striking is the observation that plasmalogens promote non-lamellar structures (including H_{II}) at or below 30°C, while the diacyl analogs at much higher temperatures (Lohner, 1996; Nagan and Zoeller, 2001). These non-lamellar structures result in increased leakage of membranes and promotion of membrane fusion (Lohner, 1996; Nagan and Zoeller, 2001). This might be significant in certain cell processes such as endocytosis and exocytosis, highly depending on membrane fusion (Nagan and Zoeller, 2001). Plasmalogens are a key player in promoting H_{II} phase structure in biomembranes and might be important in membrane fusion-mediated events. This biophysical property of plasmalogens has been suggested to link to the potential role in facilitating cell membrane and intracellular molecule trafficking (Dean and Lodhi, 2018).

Of particular interest, human leukocytes (neutrophils) are also enriched in plasmalogens (Gottfried, 1967; Getz et al., 1968; Mueller et al., 1982, 1984; Sugiura et al., 1982; Tencé et al., 1985; MacDonald and Sprecher, 1989; Manning et al., 1995). Membrane plasmalogen level may determine the characteristics of plasma membrane, such as the formation of lipid rafts, which are crucial for efficient signal transduction and optimal phagocytosis of macrophages (Rubio et al., 2018). Plasmalogens may thus modulate the phagocytotic activity of macrophages (Rubio et al., 2018). Since both SP-A and SP-D are part of the innate immunity of cell and may thus modulate the phagocytotic activity of macrophages (Vaandrager and van Golde, 2000; Matalon and Wright, 2004; Pastva et al., 2007). In an *in vitro* study, the alveolar lining materials obtained from rats have been shown to enhance the bactericidal capacity of alveolar macrophages against *Staphylococcus aureus* (Juers et al., 1976). It deserves further studies on both lung surfactant proteins (SP-A, SP-D) and how they may work together with plasmalogens to modulate the function of macrophages through their membrane.

ANTIOXIDANT PROPERTY OF LUNG SURFACTANT: FOCUS ON PLASMALOGENS

Lung tissues of preterm newborns are particularly sensitive to the exposure of high oxygen as level compared with staying inside the womb of the mother. Moreover, the main treatment options for NRDS, oxygen supplementation and mechanical ventilation, are both known to promote oxidative stress and regional pro-inflammatory responses (Worthen et al., 1987; Pierce and Bancalari, 1995). Endotracheal surfactant therapy may prevent oxidative damage of the alveoli (Matalon et al., 1990). The bronchoalveolar lavage of preterm neonates treated with surfactant presented lower levels of pro-oxidant markers than untreated neonates (Dani and Poggi, 2014). It was demonstrated in the animal model that the natural calf lung surfactants contain a measurable amount of superoxide dismutase (SOD) and catalase (CAT), and both antioxidant enzymes have been demonstrated to exert consistent scavenging activity when incubated with a definite amount of H_2O_2 (Matalon et al., 1990). The administration of exogenous surfactant has been shown to decrease the oxidative damages in the lungs of mice (Machado et al., 2018). However, the main antioxidant activity of surfactant probably depends on different mechanisms, which can be enzymatic or non-enzymatic scavenger molecules naturally contained in surfactant mixtures (Cantin et al., 1990). Plasmalogens and polyunsaturated PLs are the main molecules putatively responsible for non-enzymatic antioxidant activity of natural lung surfactants (Yavin and Gatt, 1972; Khaselev and Murphy, 1999; Farooqui and Horrocks, 2001; Zemski Berry and Murphy, 2005; Richard et al., 2008).

Analysis of murine lung surfactant revealed several plasmalogen PE lipid species, encompassing ∼38% of total PE species. Upon exposure of ozone to murine surfactant, plasmalogen PE as sacrificing molecules preferentially reacted, as compared with their diacyl counterparts (Wynalda and Murphy, 2010). Interestingly, peroxisome numbers were substantially increased in Clara and alveolar type II cells, implying an increased requirement for peroxisome metabolism that may secure sufficient plasmalogen synthesis (Karnati and Baumgart-Vogt, 2009). Since the lung is a direct target of ROS, plasmalogens might protect against respiratory diseases in general by virtue of their role as an antioxidant. Finally, although not using a plasmalogen-deficient cell line, Zoeller et al. (2002) showed that increasing plasmalogen levels in human pulmonary artery endothelial cells protected them in response to oxidative stress by prolonging survival and reducing ROS accumulation.

Premature infants who received surfactant replacement preparations with higher amount of plasmalogens showed much better respiratory outcomes (Rüdiger et al., 2005). Interestingly, plasmalogens in type II alveolar cells are composed of 93% plasmalogen PE and 7% plasmalogen PC, while plasmalogens isolated from the lung surfactant contain 36.5% plasmalogen PC and 63.5% plasmalogen PE (Rüstow et al., 1994). This discrepancy may partially explain the membrane structure conversion of a lamellar body (LB) (in type II alveolar cell) to TM (at alveolar surface), and it deserves further exploration and studies.

3D MEMBRANE STRUCTURES OF LUNG SURFACTANT

Structure and function are most likely interdependent and interrelated. As for lung surfactant, it undergoes three major structural transformations, namely, in the form of intracellular and extracellular LB, extracellular TM, and a surface monolayer (Sorokin, 1966; Weibel et al., 1966; Weibel and Gil, 1968; Kikkawa, 1970). Each of these forms has a distinct function, based on the structures they possess. First, lung surfactants containing LB are secreted by type II alveolar cells. Upon the release from type II alveolar cells, LB may convert to TM, which then forms a monolayer (Gil and Reiss, 1973; Paul et al., 1977). A lipid monolayer enriched in DPPC covering the air–water interface is considered to be responsible for the low surface tension. LBs are attached to the lipid monolayer, and together they make up the surface film, as visualized by transmission electron microscopy (TEM) (Veldhuizen and Haagsman, 2000). Though LBs have specific activity, which could directly adsorb and form surface-active films without being first converted into TM, the intact alveolar surfactant (a surface film that consists of a monolayer and a bilayer) performed better along with time (Magoon et al., 1983). The lung lavage subfractions rich in TM absorbed rapidly to air–liquid interfaces and reduced surface tension to very low values upon compression of the surface, and the preparations lacking TM were much less surface active, even though they contained identical PL composition (Thet et al., 1979; Young et al., 1992). Appearance of TM may give rise to a PL monolayer at alveolar air–liquid interface, and this PL monolayer together with LB may further elaborate the actual function and activity of lung surfactant (Weibel et al., 1966; Paul et al., 1977).

In order to compare the different membrane structures of lung surfactant from patients dying with/without NRDS, the lungs of 35 infants with NRDS and 19 without NRDS as control were examined by deMello et al. (1987) through light microscopy and electron microscopy. TEM data showed that the TM structure was not observed in the lungs of 35 infants who died with NRDS (**Figure 3A**), without exception. Abundant TM membrane structures, identified as characteristic lattice form (**Figure 3B**), were distinctly observed in 16 out of 19 control samples. TM as an intermediate phase between LB and monolayer appears indispensible in healthy lungs (Weibel et al., 1966; Gil and Reiss, 1973; deMello et al., 1987) and is thus considered as one of the polymorphic membrane structures of lung surfactant to act properly under normal physiological condition.

From the above-mentioned study, it is apparent that the absence of TM at alveolar surface of infants dying with NRDS showed a decrease in surface monolayer, which might finally lead to inactivity of lung surfactant. Therefore, it is important to know the key components that may contribute to the structure attribute of TM. Suzuki et al. (1989) have reconstituted TM *in vitro* with Ca^{2+} in a mixture of synthetic lipids (DPPC and PG) and surfactant proteins (SP-A and SP-B). The significance of Ca^{2+} on TM formation has been further evidenced by Sanders et al. (1980) and Benson et al. (1984).

TM was described by a tetragonally deformed P-based cubic surface (**Figure 2B**) (Schröder-Turk et al., 2006; Larsson and Larsson, 2014; Ninham et al., 2017), which is also used to depict intracellular cubic membranes (CMs) (Landh, 1995; Almsherqi et al., 2006, 2009). CMs represent highly curved, 3D nano-periodic membrane structures that correspond to mathematically well-defined triply periodic minimal and level surfaces (Landh, 1995; Almsherqi et al., 2006, 2009; Deng et al., 2017). Experimental data from ameba Chaos studies showed that CM is enriched with unique ether PLs, plasmalogens carrying very long-chain polyunsaturated fatty acids (PUFAs) (Deng et al., 2009, 2017; Deng and Almsherqi, 2015). Deng and Almsherqi (2015) proposed that these PLs not only facilitated CM formation but also together might act as an antioxidant defense system to provide a protective shelter for RNA (Deng and Almsherqi, 2015). The potential interaction of CM with RNA may reduce the amount of RNA oxidation and promote more efficient protein translation (Deng and Almsherqi, 2015; Deng et al., 2017). Specifically, intracellular membranes may transform into CM organizations in response to multiple pathological, inflammatory, and oxidative stress conditions (Almsherqi et al., 2009; Deng and Almsherqi, 2015). CM has been observed in numerous cell types from all kingdoms and in virtually any membrane-bound subcellular organelles (Almsherqi et al., 2009).

PLASMALOGENS MAY MODIFY PHASE STRUCTURES OF PHOSPHOLIPID MIXTURES

Perkins et al. (1996) demonstrated that a lipid mixture with dioleoylphosphatidylethanolamine (DOPE):DPPC:cholesterol in a molar ratio of 7:3:7 at 37°C appeared to be a co-existence structure of lamellar and H_{II} phases. The H_{II} transition might facilitate lipid transfer to air–water interface through unstable transition intermediates (Possmayer et al., 1984). The spreading rate of this lipid mixture formulation is similar to that observed in Curosurf® natural surfactant preparations (Perkins et al., 1996), suggesting that lipid polymorphic phase behavior might be essential to maintain surfactant activity and function. It is interesting to note that Curosurf® is a porcine surfactant with the highest content of plasmalogen and higher performance and efficiency than other commercially available nature surfactant products (Rüdiger et al., 2005).

It is important to establish the potential role of plasmalogens in 3D membrane structure of lung surfactant. Lohner et al. (1991) first reported the findings on biophysical property of plasmalogens in promotion and stabilization of non-lamellar membrane phase structure. The lipid mixtures of PE and PC of natural and synthetic surfactant preparations tend to assume the LB-like structure. The curved H_{II} phase structure is unlikely to be seen when the content of PC in lipid mixture is high (>25 mol%) (Cullis and de Kruijff, 1978; Cullis et al., 1978), suggesting that the role of PC is to stabilize the planar bilayer structure of biomembrane. Nevertheless, this circumstance can be modified and reversed by plasmalogen, a curvature-modified ether lipid (Lohner et al., 1991). In the presence of 38 mol% PC and 62 mol% plasmalogen, H_{II} phase is formed at 60°C (Lohner et al., 1991). The biophysical property of plasmalogens may determine the optimized packing of H_{II} at interface area, and this could be well-explained by their unique conformation of vinyl ether bond at sn-1 chain (Cullis et al., 1978; Malthaner et al., 1987). Nevertheless,

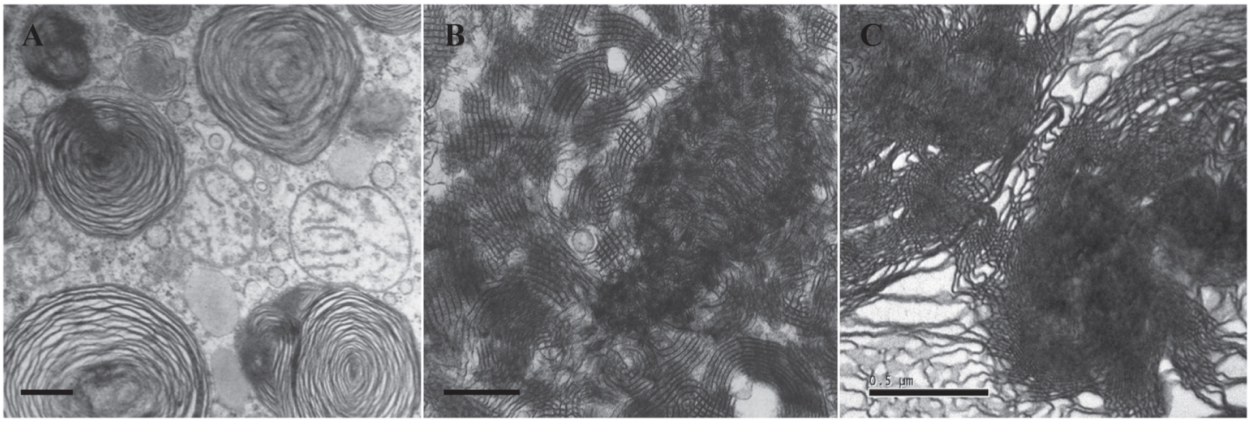

FIGURE 3 | Transmission electron microscopy (TEM) micrographs of lung surfactant membrane structures and liposome construction of ameba-derived lipids. **(A)** Lung surfactant membrane structures display mainly as lamellar body (LB) in a premature infant with neonatal respiratory distress syndrome (NRDS). **(B)** Tubular myelin (TM)-rich surfactant membrane structure from a full-term newborn without NRDS. **(C)** Liposomal construct using cubic membrane-derived plasmalogen-rich ameba lipids. TEM images of **(A,B)** are adapted from deMello et al. (1987) with permission. All scale bars = 500 nm.

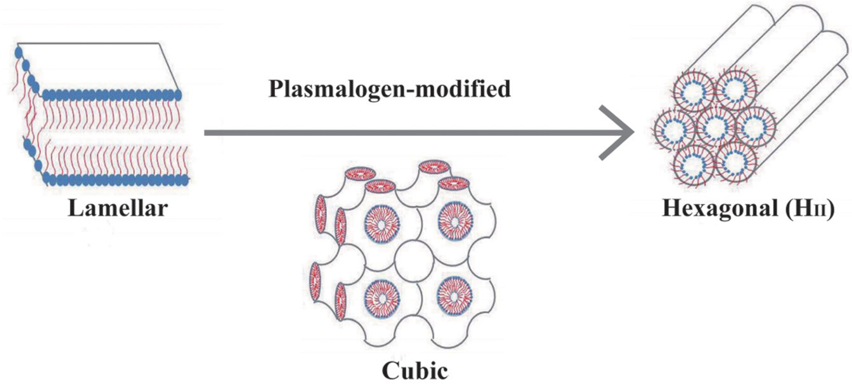

FIGURE 4 | A schematic drawing demonstrates that plasmalogen modification may promote lamellar to non-lamellar (cubic and hexagonal) phase transitions. Lipidic phase structures were adapted from Huang and Gui (2018) with permission.

the role of plasmalogens as structural attributes in lung surfactant requires more studies to be confirmed.

PLASMALOGENS MAY MODIFY SURFACE TENSION AND SURFACE VISCOSITY OF SURFACTANT-LIKE PHOSPHOLIPID MIXTURE

The optimized performance of surfactant-like PL mixture with plasmalogen modification was first reported by Rüdiger et al. (1998). The measurements of surface tension in lipid mixtures with different concentrations of plasmalogens were analyzed and compared. The experimental data revealed that plasmalogens effectively lowered the surface tension of surfactant-like PL mixtures (Rüdiger et al., 1998). Only 2% plasmalogen of total PLs was able to dramatically lower the surface tension of about 10 mN/m (Rüdiger et al., 1998), suggesting that plasmalogen-modified lung surfactant preparations could effectively reduce the surface tension and might further promote the mechanics of breathing.

Highly PUFA-containing PLs (PUFA-PLs) and plasmalogen content in tracheal aspirate of preterm infants may reduce the risk of developing chronic lung diseases (Rüdiger et al., 2000). So far, biophysical properties of lung surfactant are best described and characterized with two parameters, surface tension and surface viscosity (Rüdiger et al., 2005). In order to clarify the relations between lipid mixtures and surface viscosity of lung surfactant, the lipid composition and surface properties of three commercial surfactant preparations (Alveofact®, Curosurf®, and Survanta®) were examined and compared (Rüdiger et al., 2005). The experimental data suggested that either vinyl ether link plasmalogen or ester link PUFA-PLs are both required for lowering the surface viscosity of the surfactant mixtures (Rüdiger et al., 2005); however, plasmalogen is superior and more effective than PUFA-PLs (Tölle et al., 1999). With the deeper understanding and appreciation of this special ether lipid molecule, it becomes clear that plasmalogens might indeed play a vital role in activity and function of pulmonary surfactant.

CONCLUSION

Plasmalogens are not only a structural component of biomembranes and a reservoir for secondary messengers, but they also participate in multiple cell processes, including membrane fusion, cholesterol efflux, and antioxidation (Nagan and Zoeller, 2001; Lessig and Fuchs, 2009; Wallner and Schmitz, 2011; Luoma et al., 2015). The membrane plasmalogen level may determine characteristics of cell membrane such as membrane fluidity and formation of lipid rafts microdomains, which are essential for efficient signal transduction prepared for optimal phagocytosis of macrophages (Rubio et al., 2018).

Two proposed roles of plasmalogens may serve for proper activity and function of lung surfactant. First, plasmalogens are considered as powerful endogenous antioxidants that can be supported by experiment data directly (Wynalda and Murphy, 2010). The main function of lung is engaged in the air breathing, and plasmalogens may protect lungs from the damage of oxygen-free radicals potentially from air breathing. Second, plasmalogens may promote non-lamellar (cubic or hexagonal) phase formation *in vitro* (Lohner, 1996; Koivuniemi, 2017). The presence of non-lamellar phase may speed the spreading rate of lipid mixture formulation, and the spreading rate is similar to that observed in Curosurf® (Perkins et al., 1996). There is still lack of direct evidence to support that plasmalogens may promote non-lamellar membrane structure such as TM in lung surfactant; nevertheless, the *in vitro* lipidic phase studies (Lohner et al., 1991; Lohner, 1996) in addition to the liposomal construction data (**Figure 3C**) by using ameba Chaos CM-derived lipids rich in plasmalogens (Deng et al., 2009) have led to the current hypothesis of having potential contribution of plasmalogens in non-lamellar TM (CM-like) formation of lung surfactant. Of great interest, an extensive literature survey has revealed that intracellular membranes may rearrange into CM organization in response to external and/or internal environmental cues (Almsherqi et al., 2009), especially oxidative stress (Deng and Almsherqi, 2015; Deng et al., 2017), and the evolution of CM has been proposed as an antioxidant defense system in the eukaryotes (Deng and Almsherqi, 2015).

A schematic representation in **Figure 4** demonstrates how plasmalogen modification may be involved in membrane phase transitions in general. In this report, we simply and humbly intend to introduce the potential roles of plasmalogens in lung surfactant, as they may provide vital functions as antioxidation, phase modification, surface tension, and viscosity reduction in addition to immunity modulation even though they might be just a minor component of PLs in lung surfactant. A question emerges that whether a novel surfactant preparation without the requirement of surfactant proteins may provide a protein-free solution for the current synthetic surfactant products to avoid or eliminate the unwanted cellular immune responses potentially caused by surfactant proteins of animal origins. It might offer a novel synthetic surfactant preparations free from cultural and religion concerns, as compared with the preparations from the bovine or porcine origin.

AUTHOR CONTRIBUTIONS

YD and RZ conceived the review and wrote the manuscript. PR, JW, and RP revised the literature and helped to writing the manuscript. YD supervised the overall project and edited the manuscript. All authors had the opportunity to discuss and comment on the manuscript.

FUNDING

This work was supported by grants from the National Natural Science Foundation, China (Grant No. 31670841) and Wenzhou Institute, University of Chinese Academy of Sciences (Grant No. WIUCASQD2019005) to YD.

REFERENCES

Almsherqi, Z. A., Kohlwein, S. D., and Deng, Y. (2006). Cubic membranes: a legend beyond the Flatland* of cell membrane organization. *J. Cell Biol.* 173, 839–844. doi: 10.1083/jcb.200603055

Almsherqi, Z. A., Landh, T., Kohlwein, S. D., and Deng, Y. (2009). Chapter 6: cubic membranes the missing dimension of cell membrane organization. *Int. Rev. Cell. Mol. Biol.* 274, 275–342. doi: 10.1016/S1937-6448(08)02006-6

Andersson, J. M., Grey, C., Larsson, M., Ferreira, T. M., and Sparr, E. (2017). Effect of cholesterol on the molecular structure and transitions in a clinical-grade lung surfactant extract. *Proc. Natl. Acad. Sci. U.S.A.* 114, E3592–E3601. doi: 10.1073/pnas.1701239114

Ardell, S., Pfister, R. H., and Soll, R. (2015). Animal derived surfactant extract versus protein free synthetic surfactant for the prevention and treatment of respiratory distress syndrome. *Cochrane Database Syst. Rev.* 26:CD000144. doi: 10.1002/14651858.CD000144.pub2

Ariki, S., Nishitani, C., and Kuroki, Y. (2012). Diverse functions of pulmonary collectins in host defense of the lung. *J. Biomed. Biotechnol.* 2012:532071. doi: 10.1155/2012/532071

Benson, B. J., Williams, M. C., Sueishi, K., Goerke, J., and Sargeant, T. (1984). Role of calcium ions the structure and function of pulmonary surfactant. *Biochim. Biophys. Acta* 793, 18–27. doi: 10.1016/0005-2760(84)90048-1

Body, D. R. (1971). The phospholipid composition of pig lung surfactant. *Lipids* 6, 625–629. doi: 10.1007/BF02531518

Braverman, N. E., and Moser, A. B. (2012). Functions of plasmalogen lipids in health and disease. *Biochim. Biophys. Acta* 1822, 1442–1452. doi: 10.1016/j.bbadis.2012.05.008

Cabré, E. J., Martínez-Calle, M., Prieto, M., Fedorov, A., Olmeda, B., Loura, L. M. S., et al. (2018). Homo- and hetero-oligomerization of hydrophobic pulmonary surfactant proteins SP-B and SP-C in surfactant phospholipid membranes. *J. Biol. Chem.* 293, 9399–9411. doi: 10.1074/jbc.RA117.000222

Cantin, A. M., Fells, G. A., Hubbard, R. C., and Crystal, R. G. (1990). Antioxidant macromolecules in the epithelial lining fluid of the normal human lower respiratory tract. *J. Clin. Invest.* 86, 962–971. doi: 10.1172/JCI114798

Casals, C. (2001). Role of surfactant protein A (SP-A)/lipid interactions for SP-A functions in the lung. *Pediatr. Pathol. Mol. Med.* 20, 249–268.

Cruz, A., Worthman, L. A., Serrano, A. G., Casals, C., Keough, K. M., and Pérez-Gil, J. (2000). Microstructure and dynamic surface properties of surfactant protein SP-B/dipalmitoylphosphatidylcholine interfacial films spread from lipid-protein bilayers. *Eur. Biophys. J.* 29, 204–213. doi: 10.1007/pl00006647

Cullis, P. R., van Dijck, P. W., de Kruijff, B., and de Gier, J. (1978). Effects of cholesterol on the properties of equimolar mixtures of synthetic phosphatidylethanolamine and phosphatidylcholine. A 31P NMR and differential scanning calorimetry study. *Biochim. Biophys. Acta* 513, 21–30. doi: 10.1016/0005-2736(78)90108-6

Cullis, P. R., and de Kruijff, B. (1978). The polymorphic phase behaviour of phosphatidylethanolamines of natural and synthetic origin. A 31P NMR study. *Biochim. Biophys. Acta* 513, 31–42. doi: 10.1016/0005-2736(78)90109-8

Curstedt, T., Calkovska, A., and Johansson, J. (2013). New generation synthetic surfactants. *Neonatology* 103, 327–330. doi: 10.1159/000349942

Dani, C., and Poggi, C. (2014). "Antioxidant properties of surfactant," in *Perinatal and Prenatal Disorders, Oxidative Stress in Applied Basic Research and Clinical Practice*, eds P. Dennery, G. Buonocore, and O. Saugstad (New York, NY: Springer), 245–254. doi: 10.1007/978-1-4939-1405-0_12

Dean, J. M., and Lodhi, I. J. (2018). Structural and functional roles of ether lipids. *Protein Cell* 9, 196–206. doi: 10.1007/s13238-017-0423-5

deMello, D. E., Chi, E. Y., Doo, E., and Lagunoff, D. (1987). Absence of tubular myelin in lungs of infants dying with hyaline membrane disease. *Am. J. Pathol.* 127, 131–139.

Deng, Y., Almsherqi, Z. A., Shui, G., Wenk, M. R., and Kohlwein, S. D. (2009). Docosapentaenoic acid (DPA) is a critical determinant of cubic membrane formation in amoeba Chaos mitochondria. *FASEB J.* 23, 2866–2871. doi: 10.1096/fj.09-130435

Deng, Y., and Almsherqi, Z. A. (2015). Evolution of cubic membranes as antioxidant defence system. *Interf. Focus* 5:20150012. doi: 10.1098/rsfs.2015.0012

Deng, Y., Lee, E. L., Chong, K., and Almsherqi, Z. A. (2017). Evaluation of radical scavenging system in amoeba Chaos carolinense during nutrient deprivation. *Interf. Focus* 7:20160113. doi: 10.1098/rsfs.2016.0113

Farooqui, A. A., and Horrocks, L. (2001). Plasmalogens: workhorse lipids of membranes in normal and injured neurons and glia. *Neuroscientist* 7, 232–245. doi: 10.1177/107385840100700308

Getz, G. S., Bartley, W., Lurie, D., and Notton, B. M. (1968). The phospholipids of various sheep organs, rat liver and of their subcellular fractions. *Biochim. Biophys. Acta* 152, 325–339. doi: 10.1016/0005-2760(68)90040-4

Gil, J., and Reiss, O. K. (1973). Isolation and characterization of lamellar bodies and tubular myelin from rat lung homogenates. *J. Cell Biol.* 58, 152–171. doi: 10.1083/jcb.58.1.152

Gottfried, E. L. (1967). Lipids of human leukocytes: relation to celltype. *J. Lipid Res.* 8, 321–327.

Hallman, M., and Gluck, L. (1975). Phosphatidylglycerol in lung surfactant. II. Subcellular distribution and mechanism of biosynthesis in vitro. *Biochim. Biophys. Acta* 409, 172–191. doi: 10.1016/0005-2760(75)90152-6

Hallman, M., Feldman, B. H., Kirkpatrick, E., and Gluck, L. (1977). Absence of phosphatidylglycerol (PG) in respiratory distress syndrome in the newborn. Study of the minor surfactant phospholipids in newborns. *Pediatr. Res.* 11, 714–720. doi: 10.1203/00006450-197706000-00003

Halliday, H. L. (2017). The fascinating story of surfactant. *J. Paediatr. Child Health* 53, 327–332. doi: 10.1111/jpc.13500

Hentschel, R., Bohlin, K., van Kaam, A., Fuchs, H., and Danhaive, O. (2020). Surfactant replacement therapy: from biological basis to current clinical practice. *Pediatr. Res.* 88, 176–183. doi: 10.1038/s41390-020-0750-8

Huang, Y., and Gui, S. (2018). Factors affecting the structure of lyotropic liquid crystals and the correlation between structure and drug diffusion. *RSC Adv.* 8, 6978–6987. doi: 10.1039/C7RA12008G

Jiménez-Rojo, N., and Riezman, H. (2019). On the road to unraveling the molecular functions of ether lipids. *FEBS Lett.* 593, 2378–2389. doi: 10.1002/1873-3468.13465

Johansson, J., and Curstedt, T. (1997). Molecular structures and interactions of pulmonary surfactant components. *Eur. J. Biochem.* 244, 675–693. doi: 10.1111/j.1432-1033.1997.00675.x

Juers, J. A., Rogers, R. M., McCurdy, J. B., and Cook, W. W. (1976). Enhancement of bactericidal capacity of alveolar macrophages by human alveolar lining material. *J. Clin. Invest.* 58, 271–275. doi: 10.1172/JCI108468

Jürgens, G., Fell, A., Ledinski, G., Chen, Q., and Paltauf, F. (1995). Delay of copper-catalyzed oxidation of low density lipoprotein by in vitro enrichment with choline or ethanolamine Plasmalogens. *Chem. Phys. Lipids* 77, 25–31. doi: 10.1016/0009-3084(95)02451-n

Karnati, S., and Baumgart-Vogt, E. (2009). Peroxisomes in airway epithelia and future prospects of these organelles for pulmonary cell biology. *Histochem. Cell Biol.* 131, 447–454. doi: 10.1007/s00418-009-0566-4

Kharlamova, O. S., Nikolaev, K. Y., Ragino, Y. I., and Voevoda, M. I. (2020). Surfactant proteins A and D: role in the pathogenesis of community-acquired pneumonia and possible predictive perspectives. *Ter. Arkh.* 92, 109–115. doi: 10.26442/00403660.2020.03.000275

Khaselev, N., and Murphy, R. C. (1999). Susceptibility of plasmenyl glycerophosphoethanolamine lipids containing arachidonate to oxidative degradation. *Free Radic. Biol. Med.* 26, 275–284. doi: 10.1016/s0891-5849(98)00211-1

Kikkawa, Y. (1970). Morphology of alveolar lining layer. *Anat. Rec.* 167, 389–400. doi: 10.1002/ar.1091670403

Kim, H. C., and Won, Y. Y. (2018). Clinical, technological, and economic issues associated with developing new lung surfactant therapeutics. *Biotechnol. Adv.* 36, 1185–1193. doi: 10.1016/j.biotechadv.2018.03.017

Knudsen, L., and Ochs, M. (2018). The micromechanics of lung alveoli: structure and function of surfactant and tissue components. *Histochem. Cell Biol.* 150, 661–676. doi: 10.1007/s00418-018-1747-9

Koivuniemi, A. (2017). The biophysical properties of plasmalogens originating from their unique molecular architecture. *FEBS Lett.* 591, 2700–2713. doi: 10.1002/1873-3468.12754

Landh, T. (1995). From entangled membranes to eclectic morphologies: cubic membranes as subcellular space organizers. *FEBS Lett.* 369, 13–17. doi: 10.1016/0014-5793(95)00660-2

Larsson, M., and Larsson, K. (2014). Periodic minimal surface organizations of the lipid bilayer at the lung surface and in cubic cytomembrane assemblies. *Adv. Colloid Interf. Sci.* 205, 68–73. doi: 10.1016/j.cis.2013.07.003

Lawson, P. R., and Reid, K. B. (2000). The roles of surfactant proteins A and D in innate immunity. *Immunol. Rev.* 173, 66–78. doi: 10.1034/j.1600-065x.2000.917308.x

Lessig, J., and Fuchs, B. (2009). Plasmalogens in biological systems: their role in oxidative processes in biological membranes, their contribution to pathological processes and aging and plasmalogen analysis. *Curr. Med. Chem.* 16, 2021–2041. doi: 10.2174/092986709788682164

Lohner, K., Balgavy, P., Hermetter, A., Paltauf, F., and Laggner, P. (1991). Stabilization of non-bilayer structures by the etherlipid ethanolamine plasmalogen. *Biochim. Biophys. Acta* 1061, 132–140. doi: 10.1016/0005-2736(91)90277-f

Lohner, K. (1996). Is the high propensity of ethanolamine plasmalogens to form non-lamellar lipid structures manifested in the properties of biomembranes? *Chem. Phys. Lipids* 81, 167–184. doi: 10.1016/0009-3084(96)02580-7

Luoma, A. M., Kuo, F., Cakici, O., Crowther, M. N., Denninger, A. R., Avila, R. L., et al. (2015). Plasmalogen phospholipids protect internodal myelin from oxidative damage. *Free Radic. Biol. Med.* 84, 296–310. doi: 10.1016/j.freeradbiomed.2015.03.012

MacDonald, J. I., and Sprecher, H. (1989). Distribution of arachidonic acid in choline- and ethanolamine-containing phosphoglycerides in subfractionated human neutrophils. *J. Biol. Chem.* 264, 17718–17726.

Machado, D. F., Campos, K. K. D., da Silva, N. P., de Oliveira Ramos, C., Cangussú, S. D., de Paula Costa, G., et al. (2018). The administration of surfactant decreased oxidative stress in lungs of mice exposed to cigarette smoke. *Int. Immunopharmacol.* 54, 275–279. doi: 10.1016/j.intimp.2017.11.023

Magoon, M. W., Wright, J. R., Baritussio, A., Williams, M. C., Goerke, J., Benson, B. J., et al. (1983). Subfractionation of lung surfactant. Implications for metabolism and surface activity. *Biochim. Biophys. Acta* 750, 18–31. doi: 10.1016/0005-2760(83)90200-x

Malthaner, M., Hermetter, A., Paltauf, F., and Seelig, J. (1987). Structure and dynamics of plasmalogen model membranes containing cholesterol: a deuterium NMR study. *Biochim. Biophys. Acta* 900, 191–197. doi: 10.1016/0005-2736(87)90333-6

Manning, R., Fallani, A., and Ruggieri, S. (1995). Lipid changes in HL-60 cells on differentiation into macrophages by treatment with a phorbol ester. *Lipids* 30, 811–815. doi: 10.1007/BF02533956

Matalon, S., Holm, B. A., Baker, R. R., Whitfield, M. K., and Freeman, B. A. (1990). Characterization of antioxidant activities of pulmonary surfactant mixtures. *Biochim. Biophys. Acta* 1035, 121–127. doi: 10.1016/0304-4165(90)90105-6

Matalon, S., and Wright, J. R. (2004). Surfactant proteins and inflammation: the Yin and the Yang. *Am. J. Respir. Cell Mol. Biol.* 31, 585–586. doi: 10.1165/rcmb.F286

Morand, O. H., Zoeller, R. A., and Raetz, C. R. (1988). Disappearance of plasmalogens from membranes of animal cells subjected to photosensitized oxidation. *J. Biol. Chem.* 263, 11597–11606.

Mueller, H. W., O'Flaherty, J. T., Greene, D. G., Samuel, M. P., and Wykle, R. L. (1984). 1-O-alkyl-linked glycerophospholipids of human neutrophils: distribution of arachidonate and other acyl residues in the ether-linked and diacyl species. *J. Lipid Res.* 25, 383–388.

Mueller, H. W., O'Flaherty, J. T., and Wykle, R. L. (1982). Ether lipid content and fatty acid distribution ipolymorphonuclear neutrophil phospholipids. *Lipids* 17, 72–77. doi: 10.1007/BF02535178

Munn, N. J., Arnio, E., Liu, D., Zoeller, R. A., and Liscum, L. (2003). Deficiency in ethanolamine plasmalogen leads to altered cholesterol transport. *J. Lipid Res.* 44, 182–192. doi: 10.1194/jlr.m200363-jlr200

Nagan, N., and Zoeller, R. A. (2001). Plasmalogens: biosynthesis and functions. *Prog. Lipid Res.* 40, 199–229. doi: 10.1016/s0163-7827(01)00003-0

Ninham, B. W., Larsson, K., and Lo Nostro, P. (2017). Two sides of the coin. Part 2. Colloid and surface science meets real biointerfaces. *Colloids Surf. B Biointerf.* 159, 394–404. doi: 10.1016/j.colsurfb.2017.07.090

Notter, R. H. (2000). *Lung Surfactants: Basic Science and Clinical Applications*. New York, NY: Marcel Dekker Inc.

Notter, R. H., Schwan, A. L., Wang, Z., and Waring, A. J. (2007). Novel phospholipase-resistant lipid/peptide synthetic lung surfactants. *Mini. Rev. Med. Chem.* 7, 932–944. doi: 10.2174/138955707781662627

Olmeda, B., Martínez-Calle, M., and Pérez-Gil, J. (2017). Pulmonary surfactant metabolism in the alveolar airspace: biogenesis, extracellular conversions, recycling. *Ann. Anat.* 209, 78–92. doi: 10.1016/j.aanat.2016.09.008

Orgeig, S., Daniels, C. B., Johnston, S. D., and Sullivan, L. C. (2003). The pattern of surfactant cholesterol during vertebrate evolution and development: does ontogeny recapitulate phylogeny? *Reprod. Fertil. Dev.* 15, 55–73. doi: 10.1071/rd02087

Parra, E., and Pérez-Gil, J. (2015). Composition, structure and mechanical properties define performance of pulmonary surfactant membranes and films. *Chem. Phys. Lipids* 185, 153–175. doi: 10.1016/j.chemphyslip.2014.09.002

Pastva, A. M., Wright, J. R., and Williams, K. L. (2007). Immunomodulatory roles of surfactant proteins A and D: implications in lung disease. *Proc. Am. Thorac. Soc.* 4, 252–257. doi: 10.1513/pats.200701-018AW

Paul, G. W., Hassett, R. J., and Reiss, O. K. (1977). Formation of lung surfactant films from intact lamellar bodies. *Proc. Natl. Acad. Sci. U.S.A.* 74, 3617–3620. doi: 10.1073/pnas.74.8.3617

Perkins, W. R., Dause, R. B., Parente, R. A., Minchey, S. R., Neuman, K. C., Gruner, S. M., et al. (1996). Role of lipid polymorphism in pulmonary surfactant. *Science* 273, 330–332. doi: 10.1126/science.273.5273.330

Pfleger, R. C., Henderson, R. F., and Waide, J. (1972). Phosphatidyl glycerol–a major component of pulmonary surfactant. *Chem. Phys. Lipids* 9, 51–68. doi: 10.1016/0009-3084(72)90033-3

Pierce, M. R., and Bancalari, E. (1995). The role of inflammation in the pathogenesis of bronchopulmonary dysplasia. *Pediatr. Pulmonol.* 19, 371–378. doi: 10.1002/ppul.1950190611

Pike, L. J., Han, X., Chung, K. N., and Gross, R. W. (2002). Lipid rafts are enriched in arachidonic acid and plasmenylethanolamine and their composition is independent of caveolin-1 expression: A quantitative electrospray ionization/mass spectrometric analysis. *Biochemistry* 41, 2075–2088. doi: 10.1021/bi0156557

Possmayer, F., Yu, S. H., Weber, J. M., and Harding, P. G. (1984). Pulmonary surfactant. *Can. J. Biochem. Cell Biol.* 62, 1121–1133. doi: 10.1139/o84-146

Rana, F. R., Harwood, J. S., Mautone, A. J., and Dluhy, R. A. (1993). Identification of phosphocholine plasmalogen as a lipid component in mammalian pulmonary surfactant using high-resolution 31P NMR spectroscopy. *Biochemistry* 32, 27–31. doi: 10.1021/bi00052a005

Reiss, D., Beyer, K., and Engelmann, B. (1997). Delayed oxidative degradation of polyunsaturated diacyl phospholipids in the presence of plasmalogen phospholipids in vitro. *Biochem. J.* 323(Pt 3), 807–814. doi: 10.1042/bj3230807

Richard, D., Kefi, K., Barbe, U., Bausero, P., and Visioli, F. (2008). Polyunsaturated fatty acids as antioxidants. *Pharmacol. Res.* 57, 451–455. doi: 10.1016/j.phrs.2008.05.002

Rubio, J. M., Astudillo, A. M., Casas, J., Balboa, M. A., and Balsinde, J. (2018). Regulation of phagocytosis in macrophages by membrane ethanolamine plasmalogens. *Front. Immunol.* 9:1723. doi: 10.3389/fimmu.2018.01723

Rüstow, B., Kolleck, I., Guthmann, F., Haupt, R., Kunze, D., and Stevens, P. (1994). Synthesis and secretion of plasmalogens by type-II pneumocytes. *Biochem. J.* 302(Pt 3), 665–668. doi: 10.1042/bj3020665

Rodemer, C., Thai, T. P., Brugger, B., Kaercher, T., Werner, H., Nave, K. A., et al. (2003). Inactivation of ether lipid biosynthesis causes male infertility, defects in eye development and optic nerve hypoplasia in mice. *Hum. Mol. Genet.* 12, 1881–1895. doi: 10.1093/hmg/ddg191

Rüdiger, M., Kolleck, I., Putz, G., Wauer, R. R., Stevens, P., and Rüstow, B. (1998). Plasmalogens effectively reduce the surface tension of surfactant-like phospholipid mixtures. *Am. J. Physiol.* 274, L143–L148. doi: 10.1152/ajplung.1998.274.1.L143

Rüdiger, M., Tölle, A., Meier, W., and Rüstow, B. (2005). Naturally derived commercial surfactants differ in composition of surfactant lipids and in surface viscosity. *Am. J. Physiol. Lung Cell Mol. Physiol.* 288, L379–L383. doi: 10.1152/ajplung.00176.2004

Rüdiger, M., von Baehr, A., Haupt, R., Wauer, R. R., and Rüstow, B. (2000). Preterm infants with high polyunsaturated fatty acid and plasmalogen content in tracheal aspirates develop bronchopulmonary dysplasia less often. *Crit. Care Med.* 28, 1572–1577. doi: 10.1097/00003246-200005000-00052

Sanders, R. L., Hassett, R. J., and Vatter, A. E. (1980). Isolation of lung lamellar bodies and their conversion to tubular myelin figures in vitro. *Anat. Rec.* 198, 485–501. doi: 10.1002/ar.1091980310

Schröder-Turk, G. E., Fogden, A., and Hyde, S. T. (2006). Bicontinuous geometries and molecular self-assembly:comparison of local curvature and global packing variations in genus-three cubic, tetragonal and rhombohedral surfaces. *Eur. Phy. J. B* 54, 509–524. doi: 10.1140/epjb/e2007-00025-7

Serrano, A. G., and Pérez-Gil, J. (2006). Protein-lipid interactions and surface activity in the pulmonary surfactant system. *Chem. Phys. Lipids* 141, 105–118. doi: 10.1016/j.chemphyslip.2006.02.017

Sorokin, S. P. (1966). A morphologic and cytochemical study on the great alveolar cell. *J. Histochem. Cytochem.* 14, 884–897. doi: 10.1177/14.12.884

Sugiura, T., Onuma, Y., Sekiguchi, N., and Waku, K. (1982). Ether phospholipids in guinea pig polymorphonuclear leukocytes and macrophages. Occurrence of high levels of 1-O-alkyl-2-acyl-sn-glycero-3-phosphocholine. *Biochim. Biophys. Acta* 712, 515–522.

Suzuki, Y., Fujita, Y., and Kogishi, K. (1989). Reconstitution of tubular myelin from synthetic lipids and proteins associated with pig pulmonary surfactant. *Am. Rev. Respir. Dis.* 140, 75–81. doi: 10.1164/ajrccm/140.1.75

Tencé, M., Jouvin-Marche, E., Bessou, G., Record, M., and Benveniste, J. (1985). Ether-phospholipid composition in neutrophils and platelets. *Thromb. Res.* 38, 207–214. doi: 10.1016/0049-3848(85)90148-3

Thet, L. A., Clerch, L., Massaro, G. D., and Massaro, D. (1979). Changes in sedimentation of surfactant in ventilated excised rat lungs. Physical alterations in surfactant associated with the development and reversal of atelectasis. *J. Clin. Invest.* 64, 600–608. doi: 10.1172/JCI109499

Tölle, A., Meier, W., Greune, G., Rüdiger, M., Hofmann, K. P., and Rüstow, B. (1999). Plasmalogens reduce the viscosity of a surfactant-like phospholipid monolayer. *Chem. Phys. Lipids* 110, 81–87.

Vaandrager, A. B., and van Golde, L. M. (2000). Lung surfactant protein A and D and innate immune defense. *Biol. Neonate* 77(Suppl. 1), 9–13. doi: 10.1159/000047051

Wang, Z., Gurel, O., Baatz, J. E., and Notter, R. H. (1996). Differential activity and lack of synergy of lung surfactant proteins SP-B and SP-C in interactions with phospholipids. *J. Lipid Res.* 37, 1749–1760.

Wynalda, K. M., and Murphy, R. C. (2010). Low-concentration ozone reacts with plasmalogen glycerophosphoethanolamine lipids in lung surfactant. *Chem. Res. Toxicol.* 23, 108–117. doi: 10.1021/tx900306p

Veldhuizen, E. J., and Haagsman, H. P. (2000). Role of pulmonary surfactant components in surface film formation and dynamics. *Biochim. Biophys. Acta* 1467, 255–270. doi: 10.1016/s0005-2736(00)00256-x

Wallner, S., and Schmitz, G. (2011). Plasmalogens the neglected regulatory and scavenging lipid species. *Chem. Phys. Lipids* 164, 573–589. doi: 10.1016/j.chemphyslip.2011.06.008

Walther, F. J., Gordon, L. M., and Waring, A. J. (2019). Advances in synthetic lung surfactant protein technology. *Expert. Rev. Respir. Med.* 13, 499–501. doi: 10.1080/17476348.2019.1589372

Weibel, E. R., and Gil, J. (1968). Electron microscopic demonstration of an extracellular duplex lining layer of alveoli. *Respir. Physiol.* 4, 42–57. doi: 10.1016/0034-5687(68)90006-6

Weibel, E. R., Kistler, G. S., and Töndury, G. (1966). A stereologic electron microscope study of "Tubular Myelin Figures" in alveolar fluids of rat lungs. *Z. Zellforsch. Mikrosk. Anat.* 69, 418–427. doi: 10.1007/BF00406293

Williams, M. C. (1977). Conversion of lamellar body membranes into tubular myelin in alveoli of fetal rat lungs. *J. Cell Biol.* 72, 260–277. doi: 10.1083/jcb.72.2.260

Worthen, G. S., Haslett, C., Rees, A. J., Gumbay, R. S., Henson, J. E., and Henson, P. M. (1987). Neutrophil-mediated pulmonary vascular injury. synergistic effect of trace amounts of lipopolysaccharide and neutrophil stimuli on vascular permeability and neutrophil sequestration in the lung. *Am. Rev. Respir. Dis.* 136, 19–28. doi: 10.1164/ajrccm/136.1.19

Wüstneck, R., Perez-Gi, J., Wüstneck, N., Cruz, A., Fainerman, V. B., and Pison, U. (2005). Interfacial properties of pulmonary surfactant layers. *Adv. Colloid Interf. Sci.* 117, 33–58. doi: 10.1016/j.cis.2005.05.001

Yavin, R. A., and Gatt, S. (1972). Oxygen-dependent cleavage of the vinylether linkage of plasmalogens. 2. Identification of the lowmolecular-weight active component and the reaction mechanism. *Eur. J. Biochem.* 25, 437–446. doi: 10.1111/j.1432-1033.1972.tb01713.x

Young, S. L., Fram, E. K., and Larson, E. W. (1992). Three-dimensional reconstruction of tubular myelin. *Exp. Lung Res.* 18, 497–504. doi: 10.3109/01902149209064342

Zemski Berry, K. A., and Murphy, R. C. (2005). Free radical oxidation of plasmalogen glycerophosphocholine containing esterified docosahexaenoic acid: structure determination by mass spectrometry. *Antioxid. Redox Signal.* 7, 157–169. doi: 10.1089/ars.2005.7.157

Zoeller, R. A., Grazia, T. J., LaCamera, P., Park, J., Gaposchkin, D. P., and Farber, H. W. (2002). Increasing plasmalogen levels protects human endothelial cells during hypoxia. *Am. J. Physiol. Heart Circ. Physiol.* 283, H671–H679. doi: 10.1152/ajpheart.00524.2001

Zoeller, R. A., Morand, O. H., and Raetz, C. R. (1988). A possible role for plasmalogens in protecting animal cells against photosensitized killing. *J. Biol. Chem.* 263, 11590–11596.

Conflict of Interest: The authors declare that the research was conducted in the absence of any commercial or financial relationships that could be construed as a potential conflict of interest.

frontiers
in Cell and Developmental Biology

REVIEW
published: 18 February 2021
doi: 10.3389/fcell.2021.629503

Brain Ultrastructure: Putting the Pieces Together

Patrick C. Nahirney and Marie-Eve Tremblay*

Division of Medical Sciences, University of Victoria, Victoria, BC, Canada

Unraveling the fine structure of the brain is important to provide a better understanding of its normal and abnormal functioning. Application of high-resolution electron microscopic techniques gives us an unprecedented opportunity to discern details of the brain parenchyma at nanoscale resolution, although identifying different cell types and their unique features in two-dimensional, or three-dimensional images, remains a challenge even to experts in the field. This article provides insights into how to identify the different cell types in the central nervous system, based on nuclear and cytoplasmic features, amongst other unique characteristics. From the basic distinction between neurons and their supporting cells, the glia, to differences in their subcellular compartments, organelles and their interactions, ultrastructural analyses can provide unique insights into the changes in brain function during aging and disease conditions, such as stroke, neurodegeneration, infection and trauma. Brain parenchyma is composed of a dense mixture of neuronal and glial cell bodies, together with their intertwined processes. Intracellular components that vary between cells, and can become altered with aging or disease, relate to the cytoplasmic and nucleoplasmic density, nuclear heterochromatin pattern, mitochondria, endoplasmic reticulum and Golgi complex, lysosomes, neurosecretory vesicles, and cytoskeletal elements (actin, intermediate filaments, and microtubules). Applying immunolabeling techniques to visualize membrane-bound or intracellular proteins in neurons and glial cells gives an even better appreciation of the subtle differences unique to these cells across contexts of health and disease. Together, our observations reveal how simple ultrastructural features can be used to identify specific changes in cell types, their health status, and functional relationships in the brain.

Keywords: electron microscopy, brain, neurons, glial cells, organelles, health, aging, disease

Edited by:
Yuru Deng,
University of Chinese Academy of Sciences, China

Reviewed by:
Melvin Ray Hayden,
University of Missouri, United States
Christel Genoud,
University of Lausanne, Switzerland

****Correspondence:***
Patrick C. Nahirney
nahirney@uvic.ca

Specialty section:
This article was submitted to Cellular Biochemistry, a section of the journal Frontiers in Cell and Developmental Biology

Received: *15 November 2020*
Accepted: *20 January 2021*
Published: *18 February 2021*

Citation:
Nahirney PC and Tremblay M-E (2021) Brain Ultrastructure: Putting the Pieces Together. Front. Cell Dev. Biol. 9:629503. doi: 10.3389/fcell.2021.629503

INTRODUCTION

The first electron microscope was invented in 1931 by Max Knoll and Ernst Ruska (Savage et al., 2018). An electron microscope is a microscope that uses a beam of accelerated electrons as a source of illumination (Egerton, 2016). Because the wavelength of an electron can be up to 100,000 times shorter than visible light photons, electron microscopy (EM) has a higher resolving power than

---

Abbreviations: BBB, blood-brain barrier; CCD, charge-coupled device; EM, electron microscopy; GFAP, glial fibrillary acidic protein; IBA1, ionized calcium binding adaptor molecule 1; PSD, post-synaptic density; SEM, scanning electron microscopy; TEM, transmission electron microscopy; 2D, two-dimensional; 3D, three-dimensional.

light microscopy, and can reveal the structure of much smaller objects. The original form of an electron microscope, the transmission electron microscope (TEM) uses an electron beam to create an image. A heated filament is used as a source of electrons. The beam is accelerated at high voltage, focused by electrostatic and electromagnetic lenses, and transmitted through an ultrathin (∼60–70 nm) specimen. As it goes through the specimen the beam carries information about its structure. The spatial variation in that information is afterward magnified by the objective lens system of the microscope which is then projected on a phosphor screen and captured by film or recorded with a charge-coupled device (CCD) camera (Knott and Genoud, 2013; Winey et al., 2014; Egerton, 2016).

To study the brain, for example in rodents, samples are normally fixed by transcardial perfusion of the animals with buffered aldehydes and then sliced to a 50–100 μm thickness using a vibratome. The vibratome sections are post-fixed with buffered osmium tetroxide (1–2%) which stabilizes membranes and enhances their contrast under the electron microscope. The sections are afterward embedded in a plastic resin, cut at 50–70 nm thickness with a diamond knife on an ultramicrotome, and collected onto grids, as required for imaging by TEM. Immunostaining with peroxidase, which produces an electron dense precipitate visible with EM, or with immunogold, can also be performed prior to embedding (Dykstra and Reuss, 2003; Skepper and Powell, 2008; Ligorio et al., 2009; Burry, 2010; Tremblay et al., 2010b; Savage et al., 2018). These steps need to be performed meticulously from brain sample fixation until plastic resin embedding to prevent ultrastructural degradation which would compromise the integrity of cellular membranes, organelles, and other subcellular elements (Dykstra and Reuss, 2003; Tremblay et al., 2010b; Bisht et al., 2016a; St-Pierre et al., 2019).

Over the last 60 years, ultrastructural examinations have provided important insights into the functional roles of neurons, synapses and glial cells under various conditions (Theodosis et al., 2008; Tremblay et al., 2010a; Paolicelli et al., 2011; Bourne and Harris, 2012; Schafer et al., 2012; Kettenmann et al., 2013; Knott and Genoud, 2013; Chung et al., 2015; Savage et al., 2018; Verkhratsky and Nedergaard, 2018). The neuronal, microglial, astrocytic as well as oligodendrocytic compartments can be identified using EM based on their different shape, size, nuclear heterochromatin pattern, organelles and cytoskeletal elements, as well as relationships with each other among the brain parenchyma. Plasma membranes, basement membranes, clefts in gap junctions, actin filaments, intermediate filaments, microtubules, ribosomes, extracellular spaces, glycogen granules, synaptic vesicles, dense-core vesicles, nuclear pores, and lysosomes, are only or best resolved with EM, at the highest resolution (reaching 1 nm) for a biological technique (Tremblay et al., 2010b; Savage et al., 2018; SynapseWeb, 2021). Although super-resolution microscopy, and more recently, expansion microscopy, were developed to resolve small structures, notably in correlation with EM (Carrier et al., 2020; Hoffman et al., 2020; Parra-Damas and Saura, 2020; Soria et al., 2020), the capacity of EM to reveal the ultrastructure of cells and their constituents without selective staining (although staining can be used to provide better visualization of membranes, cytoskeletal elements, and ribosomes, for instance; Dykstra and Reuss, 2003; Svitkina, 2009) confers an important advantage (Tremblay et al., 2010b; Savage et al., 2018).

Considering that only EM provides the resolution needed to reconstruct neuronal circuits completely with single-synapse information, EM with three-dimensional (3D) reconstruction is the main tool for the connectomics research, which aims to map the brain-wide circuits underlying behavior (Ohno et al., 2015; Swanson and Lichtman, 2016; Kubota et al., 2018). Several tools were developed in recent years to facilitate the acquisition, registration and segmentation which is the tracing of the elements of interest in all the pictures to generate 3D reconstructions (Knott and Genoud, 2013; Miranda et al., 2015; Savage et al., 2018; Carrier et al., 2020), allowing to identify and quantify organelles as well as cell types in the brain using deep machine learning analysis (Perez et al., 2014; García-Cabezas et al., 2016; Abdollahzadeh et al., 2019; Calì et al., 2019; Gómez-de-Mariscal et al., 2019; Santuy et al., 2020). Recent technological advances in scanning electron microscopy (SEM) have facilitated the automated acquisition of large tissue volumes in 3D at nanometer-resolution. Cutting-edge techniques, such as serial-block face and focused-ion beam SEM imaging (Knott and Genoud, 2013; Miranda et al., 2015; Savage et al., 2018, 2020; Carrier et al., 2020), combined with x-ray based modalities which allow to detect and correlate EM findings with disease hallmarks or neuroanatomical features in 3D, based on their electron density (Pacureanu et al., 2019; Töpperwien et al., 2020), will revolutionize the understanding of brain development, function, and plasticity across stages of the lifespan, regions, and contexts of health and disease.

This review article will summarize the series of identification criteria that we have developed in our EM studies to identify brain cells and their constituents, mainly within the cerebral cortex and the hippocampus of rodent models. Ultrastructural observations can provide thorough insights into the cellular and subcellular mechanisms underlying brain function and dysfunction in an unbiased manner, by revealing all cell types and their constituents simultaneously, without the restrictive use of markers that only show the elements of interest. Our goal with this review is to provide well-established and accessible resources that will help neuroscientists to identify biomarkers of aging and disease, including stroke, neurodegeneration, infection and trauma, as well as the outcome of various treatment strategies, with the use of EM. Our descriptions are based on the criteria defined by Peters et al. (Peters et al., 1990) and others (Skoff and Hamburger, 1974; Deitch and Banker, 1993; Fiala et al., 1998; SynapseWeb, 2021) that were refined over the years with the investigation of neuronal, microglial and astrocytic response to stress, aging, neurodegenerative disease pathology, and stroke, notably (Tremblay et al., 2010a, 2012; Nahirney et al., 2016; Henry et al., 2018; El Hajj et al., 2019; Savage et al., 2020). Our observations build on and complement the identification criteria that were historically established based on correlative light and EM (Luse, 1956; Herndon, 1964; Mori and Leblond, 1969; Griffin et al., 1972; Murabe and Sano, 1982; Shapiro et al., 2009). Emerging techniques that prevent aldehyde-fixation based artifacts, notably the reduction in extracellular space volume (Syková and Nicholson, 2008), such as cryo-EM, are beyond the scope of this review and covered elsewhere (Korogod et al., 2015; Subramaniam, 2019). Best practices in sample preparation to avoid hypoxia-induced artifacts are also discussed at length in excellent resources (Kuwajima et al., 2013).

AN OVERVIEW OF THE ULTRASTRUCTURAL IDENTIFICATION CRITERIA WE USE

In the brain parenchyma, neurons can be dispersed or organized into layers depending on the brain region, while glial cells are generally dispersed, occupying satellite positions around neuronal cell bodies or interacting structurally with one another (Peters et al., 1990). Direct contacts between glial cell bodies, often taking place at the vasculature (Bardehle et al., 2013), can also suggest recent division events (Tremblay et al., 2012). While glial cells generally occupy non-overlapping territories (Bushong et al., 2002; Sousa et al., 2017), this organization can be lost upon neurological pathology, for instance epilepsy (Oberheim et al., 2008), and depends on visualization method (Stratoulias et al., 2019). Except where noted differently, the identification criteria summarized in this section are from Peters et al. (1990), SynapseWeb, and Fine Structure of the Aging Brain | Boston University.

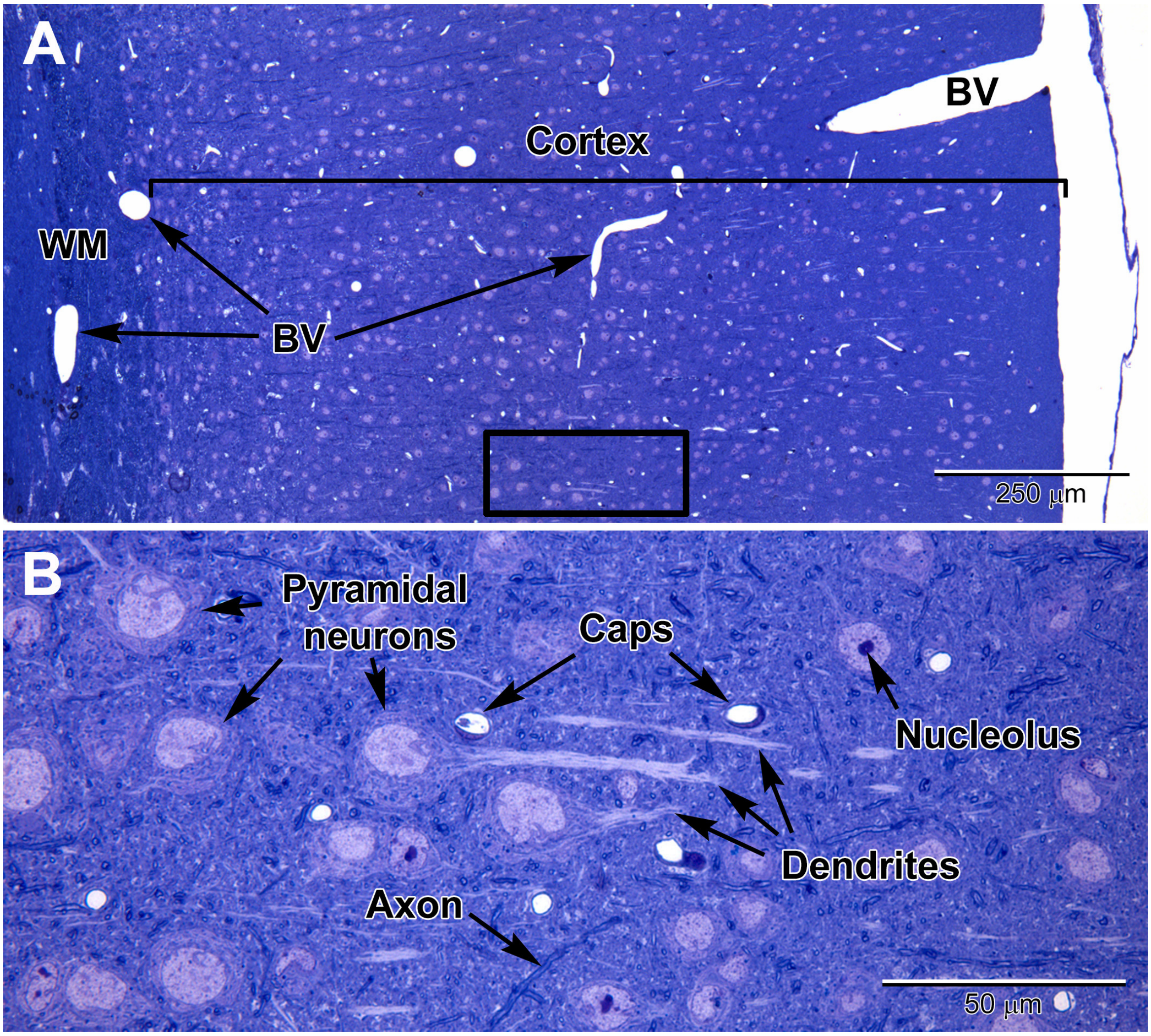

FIGURE 1 | Light micrographs of a toluidine blue-stained plastic section from the adult mouse somatosensory brain region seen at low **(A)** and high **(B)** magnification. The cortex is arranged into layers that contain different types of neurons, with the largest neurons (pyramidal) in layers 4–6 which contain large euchromatic nuclei with nucleoli. Pyramidal neurons have prominent dendrites that project toward the outer cortex. At the surface of the cortex is a thin pia mater layer with underlying blood vessels (BV) that are present throughout the cortex. Deep to the cortex are myelinated axons of the white matter (WM). **(B)** At high magnification, capillaries (Caps) are evenly distributed in the brain parenchyma amongst the neurons, along with glial cells, which are less obvious, and contain smaller nuclei. Dispersed myelinated axons stain deeper blue and appear as wormlike structures in the parenchyma.

Cell Bodies

Neurons can be identified in microscopic sections by their pale cytoplasm, a large and round euchromatic nucleus, as well as the presence of one or more electron dense nucleoli (**Figures 1–3**). Depending on the type of neuron, cell bodies can range dramatically in size. Typical pyramidal neurons in the deeper layers of the cortex range in size from ~15 to 30 μm in diameter in rodents, and contain multiple cell processes including several dendrites traveling mostly toward the cortical surface and a single axon projecting deep toward the white matter. Small patches of heterochromatin are present in the nucleus, typically peripheral in location under the nuclear envelope which contains abundant nuclear pores (**Figure 2B**). Their surrounding cytoplasm, or perikaryon, contains an abundance of organelles that vary in shape and volume with the neuronal activity (Antón-Fernández et al., 2015; Tao-Cheng, 2018). A prominent Golgi complex(es) (**Figure 2B**) is/are present near the nucleus along with long flattened cisternae of rough endoplasmic reticulum (RER) studded with ribosomes (Peters et al., 1990). Free ribosomes, or groups of ribosomes (polyribosomes), occupy the interstitial spaces between organelles. Round to ovoid mitochondria are dispersed throughout the cytoplasm and occasional lysosomes filled with electron dense material (lipofuscin) are also present. Neurons contain an extensive array of neurofilaments and microtubules that extend into large dendrites emanating from the cell body. Multivesicular bodies, filled with small 40–80 nm sized vesicles, are also present near the Golgi complex, likely to be transported into the axon where they become concentrated at axon terminals (Peters et al., 1990).

Astrocytes, the largest and most populous of glial cells in the brain, are classified as either fibrous or protoplasmic. Elaborate and branched cell processes emanate from the stellate-shaped cell bodies into the neuropil. Protoplasmic astrocytes are recognized by their triangular shaped protuberances, pale nuclei with a thin rim of heterochromatin and pale irregular cytoplasm (**Figure 4A** and **Supplementary Figure 1**), often containing intermediate filaments (glial fibrillary acidic protein, GFAP) ranging in diameter from 8 to 12 nm (**Figure 4B**) (Peters et al., 1990). Astrocytes are distinguished by the relative sparseness of electron dense material in the cytoplasm. In addition, in our preparations with reduced osmium postfixation, we could identify astrocytic cell bodies and processes based on the fact that their mitochondrial membranes were less electron dense (lighter) than those found in neighboring neuronal and glial compartments (e.g., in neurons, dendrites, microglia, and oligodendrocytes) or in the endothelium and pericytes (Nahirney et al., 2016) (see **Figure 4A** and **Supplementary Figure 1**). This suggests that the membranes of astrocytic mitochondria contain a less dense concentration of lipids and/or proteins, which does not appear to be affected by the state of health or disease including stroke pathology (Nahirney et al., 2016). At the level of small blood vessels of the brain, astrocytes are an integral component of the blood-brain barrier (BBB) (**Figures 5**, **6**). Expansions of astrocytic processes embrace capillaries and form so-called astrocytic (perivascular) end-feet. The BBB functions to protect neurons and glial cells in the CNS from drugs, toxins, as well as pro-inflammatory mediators and peripheral immune cells that would perturb the homeostasis, and includes in addition to astrocytes the microglia, which contribute to the *glia limitans* (Bisht et al., 2016c; Joost et al., 2019). Astrocytes, microglia, the endothelium and pericytes form together the neurovascular unit that regulates vascular remodeling and blood flow according to the needs of the neurons and glial cells (Andreone et al., 2015; Liu et al., 2020).

Compared with astrocytes, oligodendrocytes have a darker, electron-dense cytoplasm (**Figure 7**). They are mainly distinguished from neurons and other glial cells by their heterogeneous nuclear chromatin pattern, as well as squarish or rectangular-shape cytoplasm. Oligodendrocytes have short and wide endoplasmic reticulum cisternae organized in the vicinity of their nucleus, ribosomes, and wider space between nuclear membranes compared with microglia (Peters et al., 1990). The oligodendrocytic precursor cells look very different and sometimes occupy positions beside neurons (**Figure 3**). In many respects they resemble astrocytes. However, their nucleus is more irregular in shape. Their cytoplasm is pale, electron-lucent but they do not contain intermediate filaments nor extend processes making acute angles in the neuropil. Their stretches of endoplasmic reticulum are short, and their mitochondria are smaller than those of astrocytes. In addition, they do not accumulate lipidic inclusions during aging and in disease, even in old monkeys (Peters and Folger Sethares, 2020), contrary to neurons and other glial cells in the CNS (Tremblay et al., 2012).

Similar to oligodendrocytes, microglia have a dark, electron-dense cytoplasm. Microglial cell bodies are recognized by their small size, frequent triangle shape, and the cheetah-pattern clumps of peripheral chromatin beneath their nuclear envelope and throughout their nucleoplasm (Tremblay et al., 2012; Savage et al., 2018). Examples of perivascular and perineuronal microglial cells are seen in **Figures 8** and **9**. The microglial cytoplasm often contains long stretches of endoplasmic reticulum cisternae and lipidic inclusions (i.e., lipofuscin, lipid bodies or droplets, and lysosomes; to be described in the *Organelles* section below) (Savage et al., 2018), which accumulate with aging. Microglia are frequently associated with pockets of extracellular space, contrary to other cell types in the mature healthy brain, and interact with both the vasculature and synapses (Tremblay et al., 2010a, 2012; Bisht et al., 2016c), as well as myelinated axons (Lampron et al., 2015; Bordeleau et al., 2020).

Neuropil Elements

In the neuropil, which occupies most of the brain parenchyma outside of cell body layers and white matter, the intertwined neuronal and glial profiles can be identified according to criteria well defined previously (Skoff and Hamburger, 1974; Peters et al., 1990; Deitch and Banker, 1993; Harris and Weinberg, 2012), as summarized in Tremblay et al. (2007; 2009; 2010a; 2012).

Dendritic branches are distinguished from unmyelinated axons by their more irregular contours, fewer microtubules, frequent protuberances (spines, filopodia, and small branches), and usual synaptic contacts with axon terminals (Tremblay et al., 2009). Dendritic spines display a characteristic "fluffy" or "cotton candy" type content due to their actin cytoskeleton (Papa et al., 1995). Spines (e.g., mushroom spines) may contain

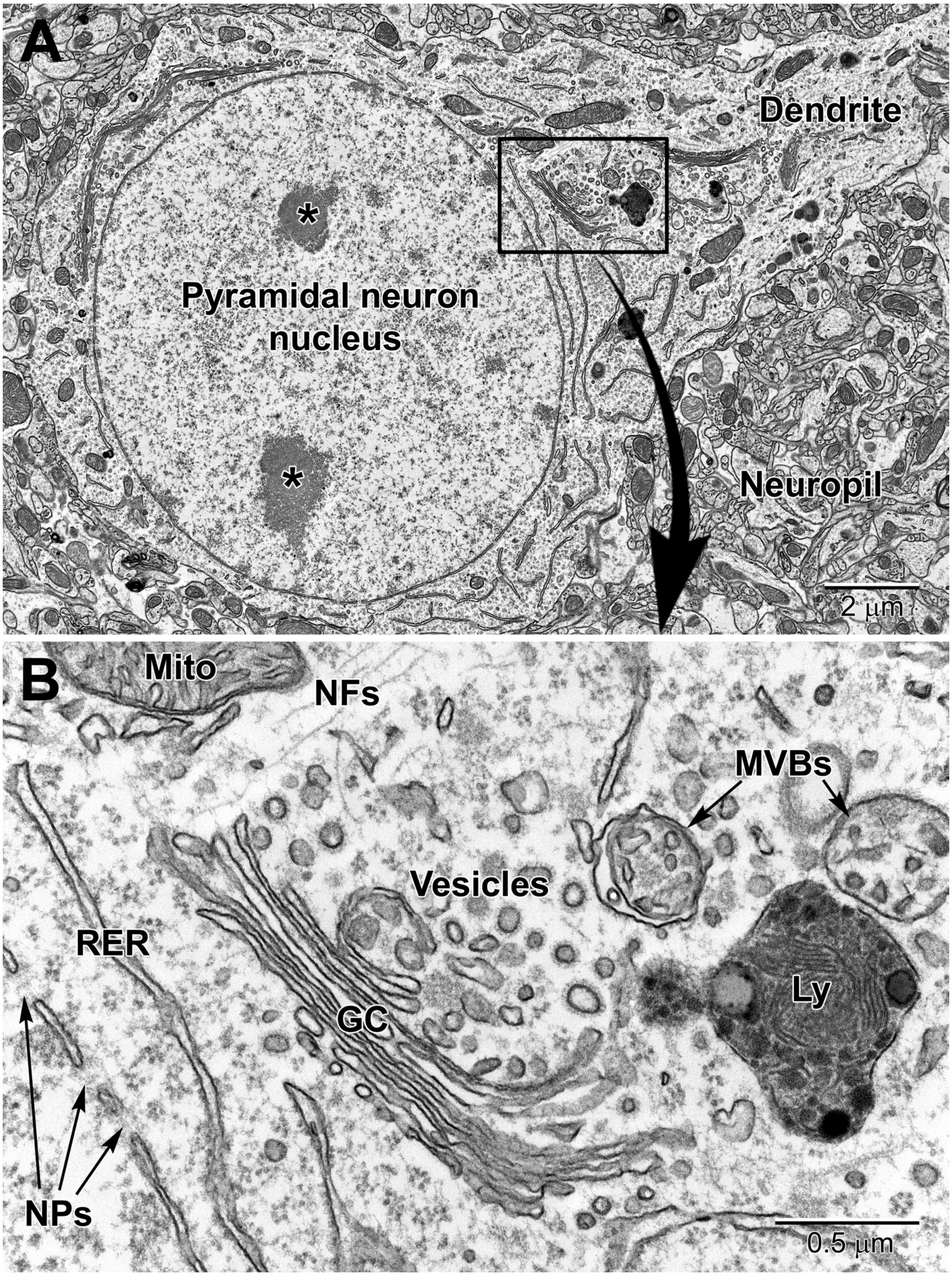

FIGURE 2 | Low **(A)** and high **(B)** magnification EM images of a pyramidal neuron in layer 4/5 of the somatosensory cortex. The neuron contains a large euchromatic nucleus with two nucleoli (*) and a large primary dendrite emanates from the cell body. Surrounding the neuronal cell body is the neuropil consisting of a mixture of glial and neuronal processes, including synapses. The nuclear envelope contains numerous nuclear pores (NPs) and the perinuclear cytoplasm has a rich collection of organelles including mitochondria (Mito), RER, and Golgi complexes (GC) cisternae, vesicles, multivesicular bodies (MVBs), and lysosomes (Ly). Free ribosomes and neurofilaments (NFs) are dispersed in between the organelles.

a spine apparatus, and receive frequent synaptic contacts from axon terminals (**Figure 10**). Their post-synaptic density, where receptors for neurotransmitters are located, is electron dense and visible without any immunostaining. Dendritic filopodia, which are considered to be immature spines (Berry and Nedivi, 2017), identified when seen protruding from dendritic branches, are

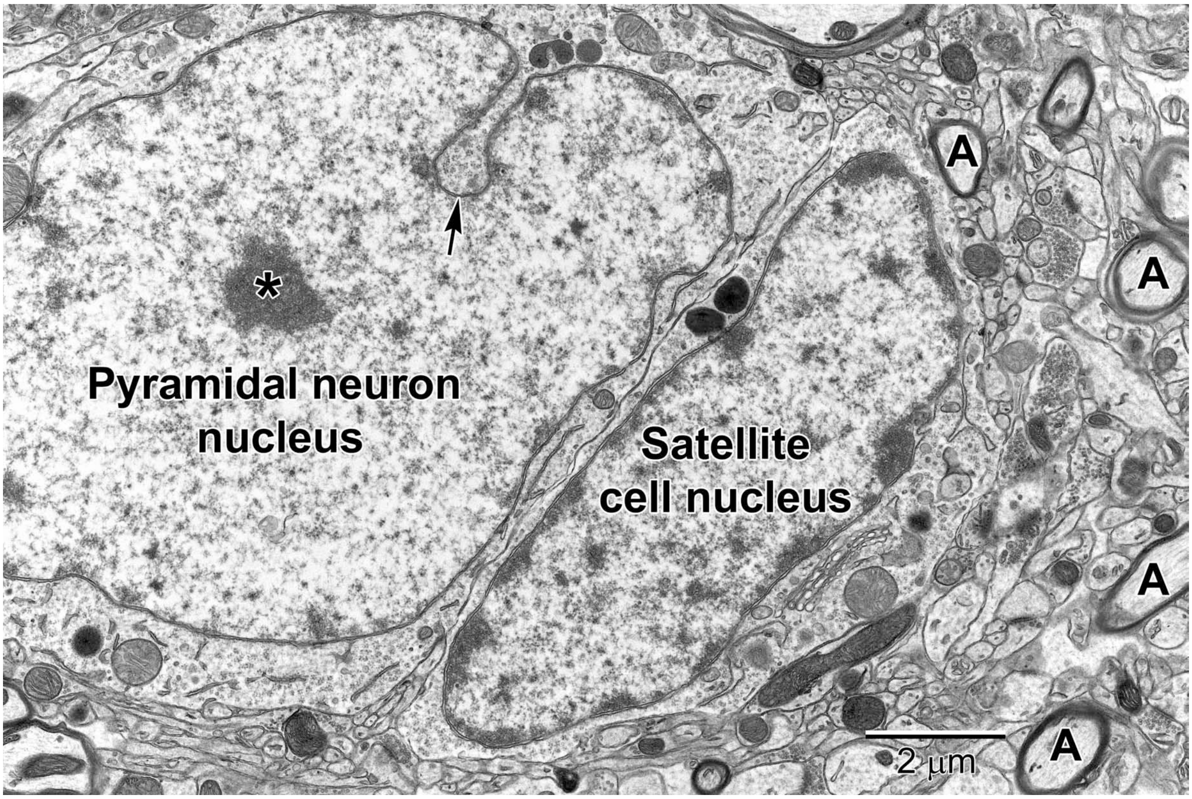

FIGURE 3 | A pyramidal neuron in layer 5 with a satellite cell that displays ultrastructural features of an oligodendrocyte precursor cell closely abutting its cell body. The pyramidal neuron contains a large euchromatic nucleus with a centrally located nucleolus (*). Nuclear envelope invaginations (arrow) are occasionally seen in highly active neurons (Wittmann et al., 2009). Some neurons have intimately associated satellite cells (microglia and oligodendrocyte precursor cells) with a smaller ovoid nucleus. The surrounding neuropil contains synapses, axons (A) and glial cell processes.

distinguished from spines by their absence of a post-synaptic density, thinner neck, greater length, and pointed, rather than bulbous, head (Fiala et al., 1998). Unmyelinated axons are positively identified when they are found within fascicles or bundles of similar profiles. Axons becoming myelinated are also observed, either wrapped by oligodendrocytic processes with moderately dark cytoplasm or ensheathed by just a few turns of compact myelin and loose outer sheets (Tremblay et al., 2009). Axonal varicosities (also named "boutons") correspond to enlarged portions of axons containing aggregated synaptic vesicles with neurotransmitters and frequently show "en passant" synaptic specializations, while axon terminals similarly display aggregated synaptic vesicles and synaptic specializations, but only at axonal extremities (Mechawar et al., 2000; Parent and Descarries, 2008; Tremblay et al., 2009).

In certain areas of the brain, such as the substantia nigra (**Figure 10**), up to three types of axon terminals can be identified by their vesicle diameter and shape (cholinergic, glutamatergic, and GABAergic) (Umbriaco et al., 1995; Mechawar et al., 2000; Ligorio et al., 2009). Synapses are identified by their synaptic cleft, i.e., direct apposition with less than 20 nm extracellular space between pre-synaptic axon terminals and post-synaptic dendritic spines or dendritic shafts, as revealed by tilt tomography (**Supplementary Video 1**) and more recently by focused ion-beam SEM in 3D (Savage et al., 2020). Only synaptic profiles presenting an unequivocal post-synaptic density are considered as asymmetric or excitatory in ultrathin section (Tremblay et al., 2007). Axonal growth cones are identified as considerable enlargements of axons, presenting a dark cytoplasm filled with large amounts of smooth endoplasmic reticulum and pleomorphic vesicles (Skoff and Hamburger, 1974; Peters et al., 1990; Deitch and Banker, 1993). They are distinguished from dendritic growth cones by their more frequent filopodial extensions, which often contact dendritic branches instead of axon terminals. Occasionally, these profiles are seen in direct continuity with axon terminals. Axonal filopodia are identified when extending from axonal growth cones. Nevertheless, distinction between axonal and dendritic growth cones or filopodia is not always obvious (Tremblay et al., 2009).

In health conditions, processes from protoplasmic astrocytes are recognized by their irregular and angular shapes, making acute angles as they go in-between the other elements of neuropil (**Figure 4** and **Supplementary Figure 1**). In samples devoid of aldehyde-fixation artifacts (cryo-EM), astrocytic processes are more voluminous and make less acute angles around the other elements of neuropil, notably synapses (Korogod et al., 2015). By contrast, profiles from neurons and other types of glial cells (i.e.,

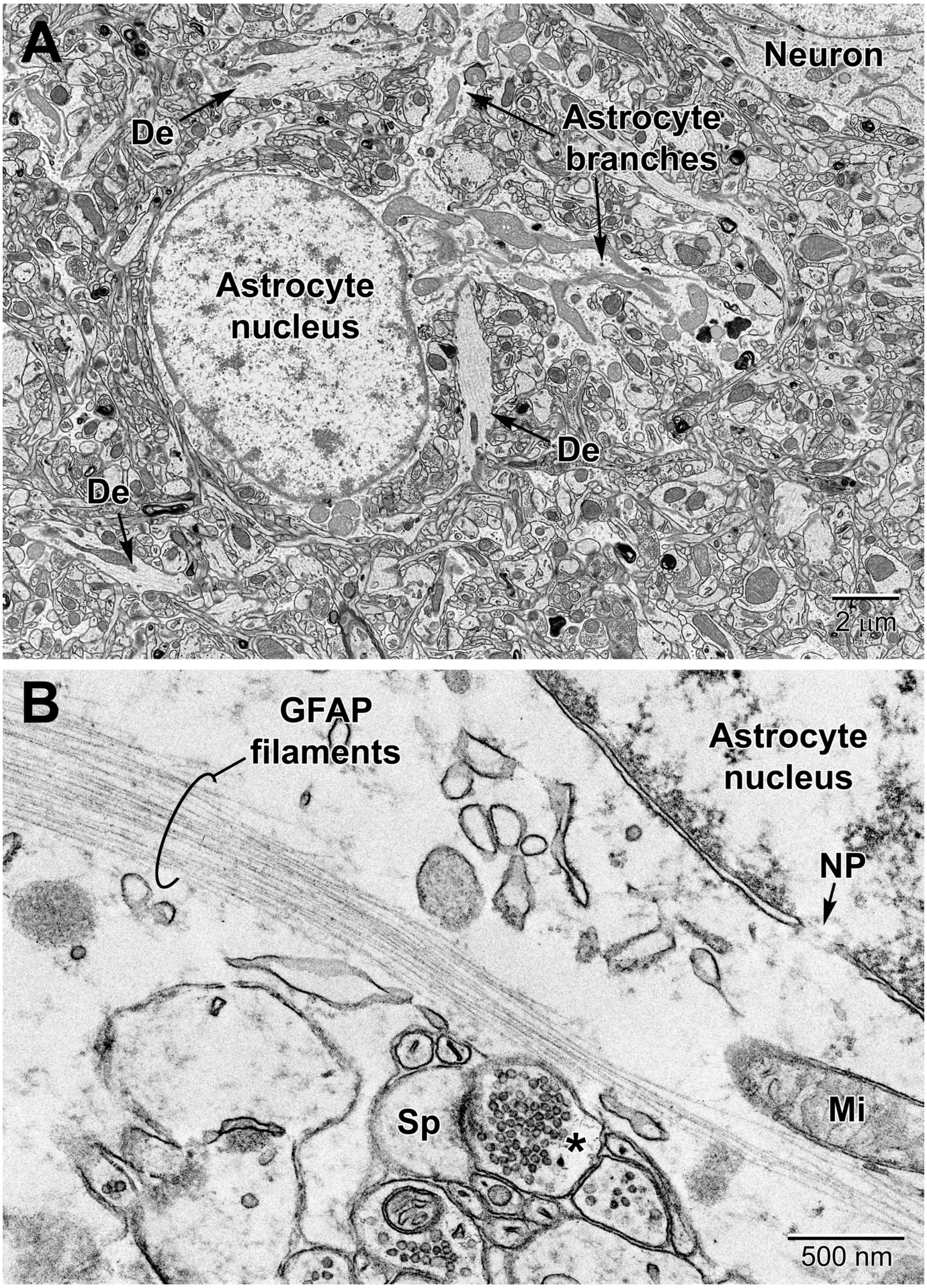

FIGURE 4 | Protoplasmic astrocyte in the mouse cerebral cortex **(A)** and high magnification view of a fibrous astrocyte in the CA1 region of a rat hippocampus **(B)**. **(A)** In the cortex, astrocytes are branched and contain a relatively clear cytoplasm with a variety of organelles including mitochondria, RER, lysosomes, perinuclear Golgi complexes. In rodent astrocytes, mitochondria (Mi) stain relatively lighter after postfixation with reduced osmium. De, dendrite; Sp, dendritic spine; *, presynaptic terminal.

microglia and oligodendrocytic lineage cells) have a characteristic rounded shape. The processes from protoplasmic astrocytes frequently ensheath and can also phagocytose synapses, both pre-synaptic axon terminals and post-synaptic dendritic spines, within cellular inclusions during normal physiological conditions (Witcher et al., 2007; Theodosis et al., 2008; Chung et al.,

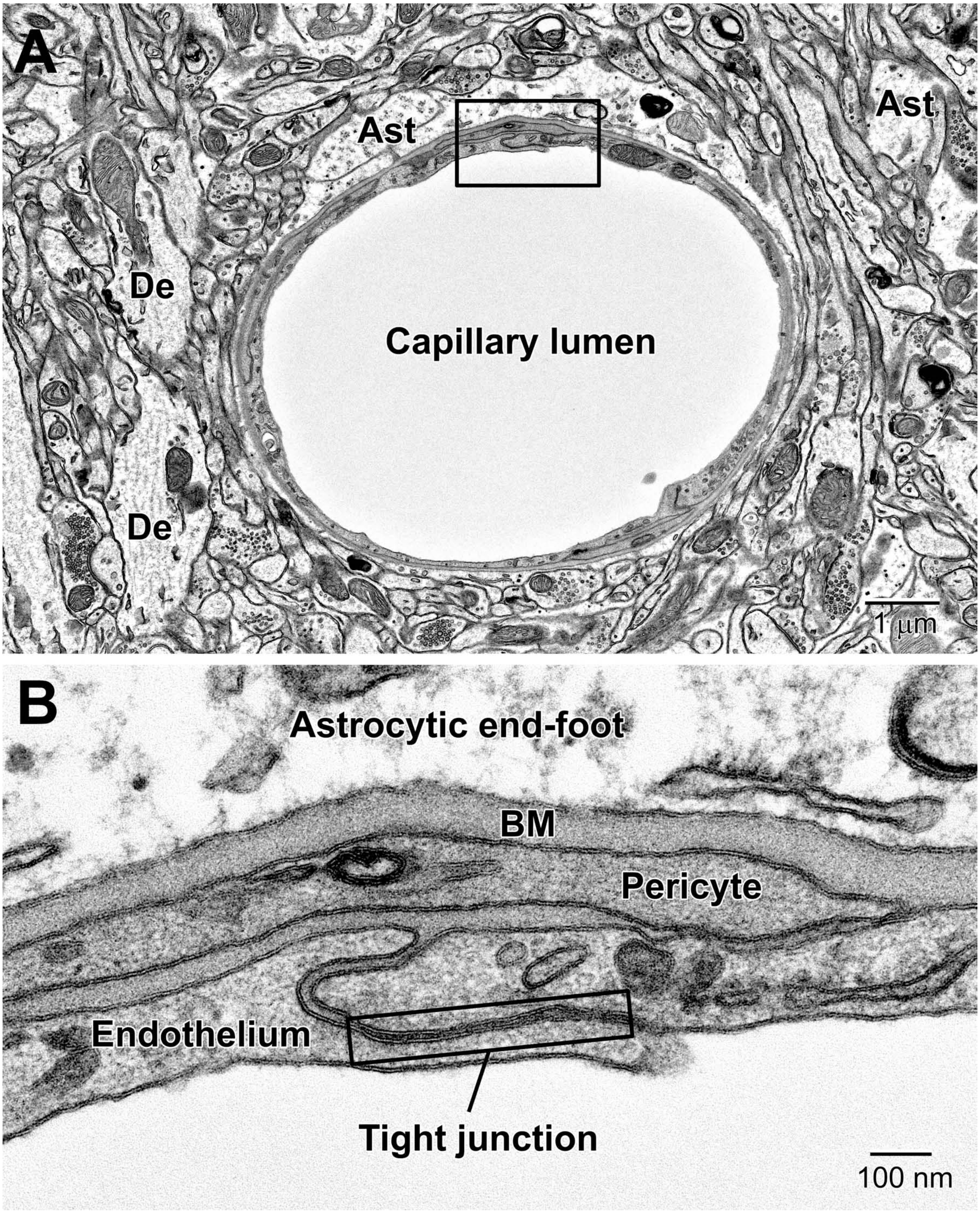

FIGURE 5 | Components of the blood-brain barrier (BBB) and neurovascular unit. **(A)** Transverse section through a mouse cortical capillary showing the highly attenuated endothelium with small branches of pericytes sitting on their abluminal surface. **(B)** The BBB consists of the capillary endothelium with their tight junctions, underlying pericytes, both surrounded by a prominent amorphous basement membrane (BM) and astrocytic end-feet. End-feet connect with neighboring end-feet of other astrocytes via gap junctions. Ast, astrocyte; De, dendrite.

2015; Verkhratsky and Nedergaard, 2018; Lee et al., 2020). Astrocytic processes have a clear, electron lucent cytoplasm, while oligodendrocytic and microglial processes have a moderately dense cytoplasm, and neurons have a cytoplasm showing intermediate gray levels between astrocytes and the other two glial cells (Peters et al., 1990). Oligodendrocytic processes display

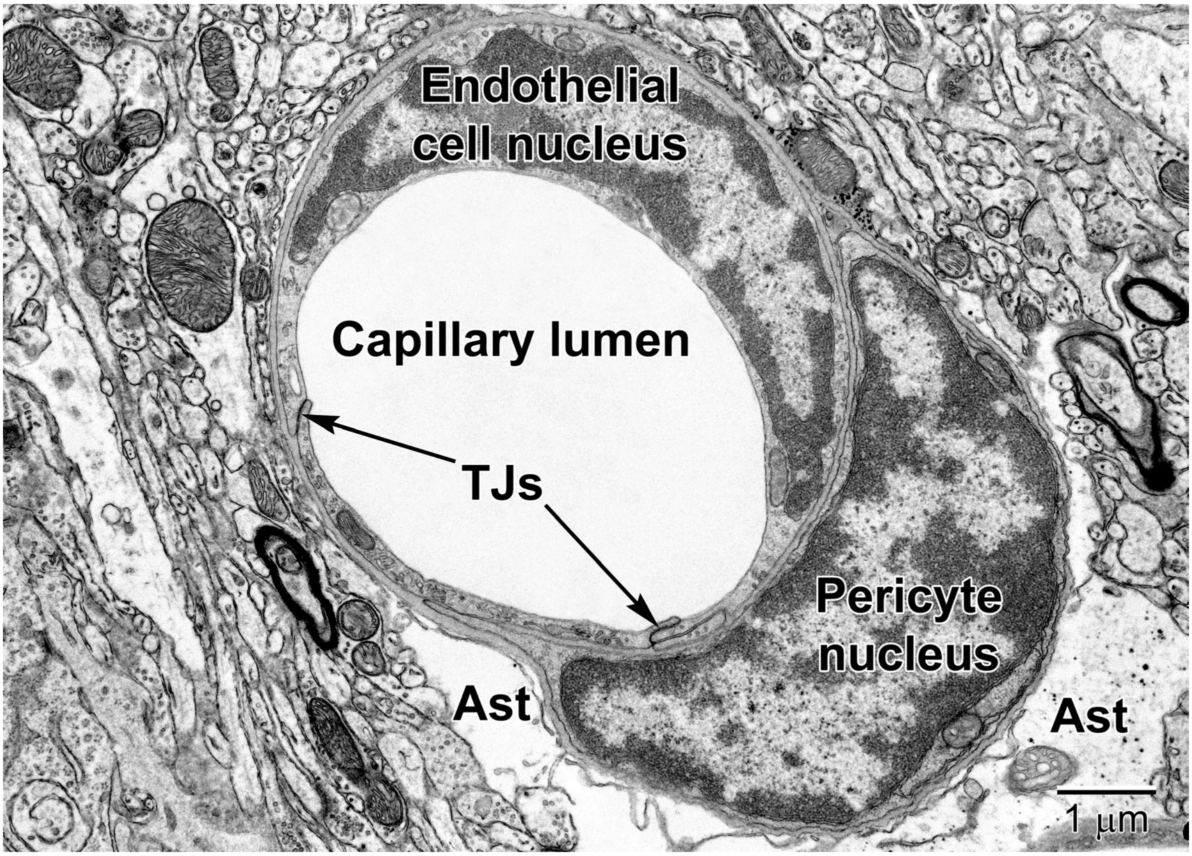

FIGURE 6 | A fortuitous section of a mouse cortical capillary showing an endothelial cell and a pericyte at the level of their nuclei. Notice how the crescent-shaped heterochromatic nuclei take on the shape of the capillary. Tight junctions (TJs) link neighboring endothelial cells. The pericyte embraces the endothelium and resides within the same basement membrane. The position and branching nature of its processes are strategically situated to change the capillary lumen diameter. The relatively clear astrocyte end-feet (Ast) occupy the surrounding region around the capillary in the lower part of the image. Some electron dense glycogen granules are visible within the astrocyte.

obtuse angles among the neuropil, similar to microglial processes, and are positively identified when their membrane is in direct continuity with myelinating or myelinated axons (Tremblay et al., 2009). However, it should be noted that microglial processes also interact with myelinated axons (Bordeleau et al., 2020).

Microglial processes display irregular contours with obtuse angles, a dense cytoplasm, numerous large vesicles, frequent endosomes and cellular inclusions (e.g., large lipidic vesicles, profiles of cellular membranes, and profiles of other structural elements including dendritic spines and axon terminals), as well as distinctive long stretches of endoplasmic reticulum (Tremblay et al., 2010a; El Hajj et al., 2019). They are typically surrounded by pockets of extracellular space that can vary in volume by two orders of magnitude (Tremblay et al., 2010a). These morphological characteristics of microglia were defined using immunocytochemical TEM against the marker ionized calcium binding adaptor molecule 1 (IBA1; Tremblay et al., 2010a) and allowed the identification of microglial processes in non-immunostained brain tissue, as confirmed using serial-section TEM (Tremblay et al., 2010a).

AN OVERVIEW OF THE ULTRASTRUCTURAL CHANGES OBSERVED WITH STRESS, STROKE, AGING AND DISEASE

Changes to Cell Bodies

With stress, aging and disease, darker cells are frequently observed within the brain parenchyma. The condensation state of the cytoplasm and nucleoplasm is associated with cellular shrinkage, considered a marker of cellular stress, and could explain this increased electron density (Bisht et al., 2016b).

Dark neurons display ultrastructural features of neurons, in terms of size, shape and organelles, as well as synaptic contacts (Peters and Folger Sethares, 2020). They are defined by their electron-dense cytoplasm and nucleoplasm, giving them a dark appearance under EM examination. They often display an accumulation of mitochondria and nuclear indentations (Tremblay et al., 2012) associated with structural remodeling and plasticity (Versaevel et al., 2014) or cellular stress, and various

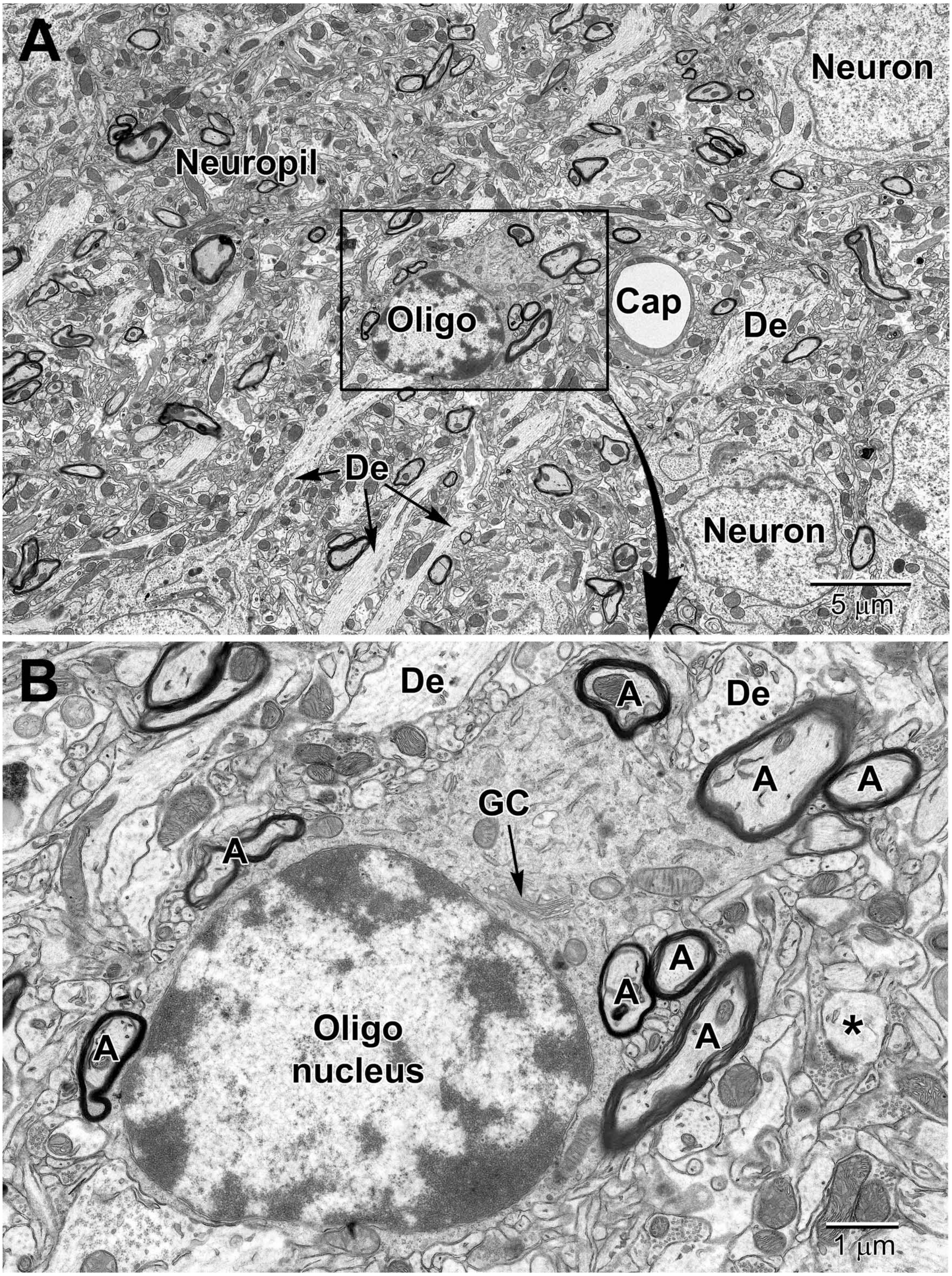

FIGURE 7 | Low **(A)** and medium **(B)** magnification images of a typical oligodendrocyte (Oligo) sectioned at the level of its small heterochromatic nucleus in layer 5 of the mouse cortex. Several neurons are seen in the surrounding region for comparison of nuclear size and chromatin density. A neighboring capillary (Cap) and numerous dendrites (De) are seen in the surrounding neuropil. **(B)** A collection of myelinated axons **(A)** juxtapose and appear partially embedded within the relatively electron-dense cytoplasm of the oligodendrocyte. The dense cytoplasm contains a prominent perinuclear Golgi complex (GC), scattered mitochondria and small segments of rough endoplasmic reticulum. A spine head (*) synapses on a presynaptic terminal in the lower right of the image.

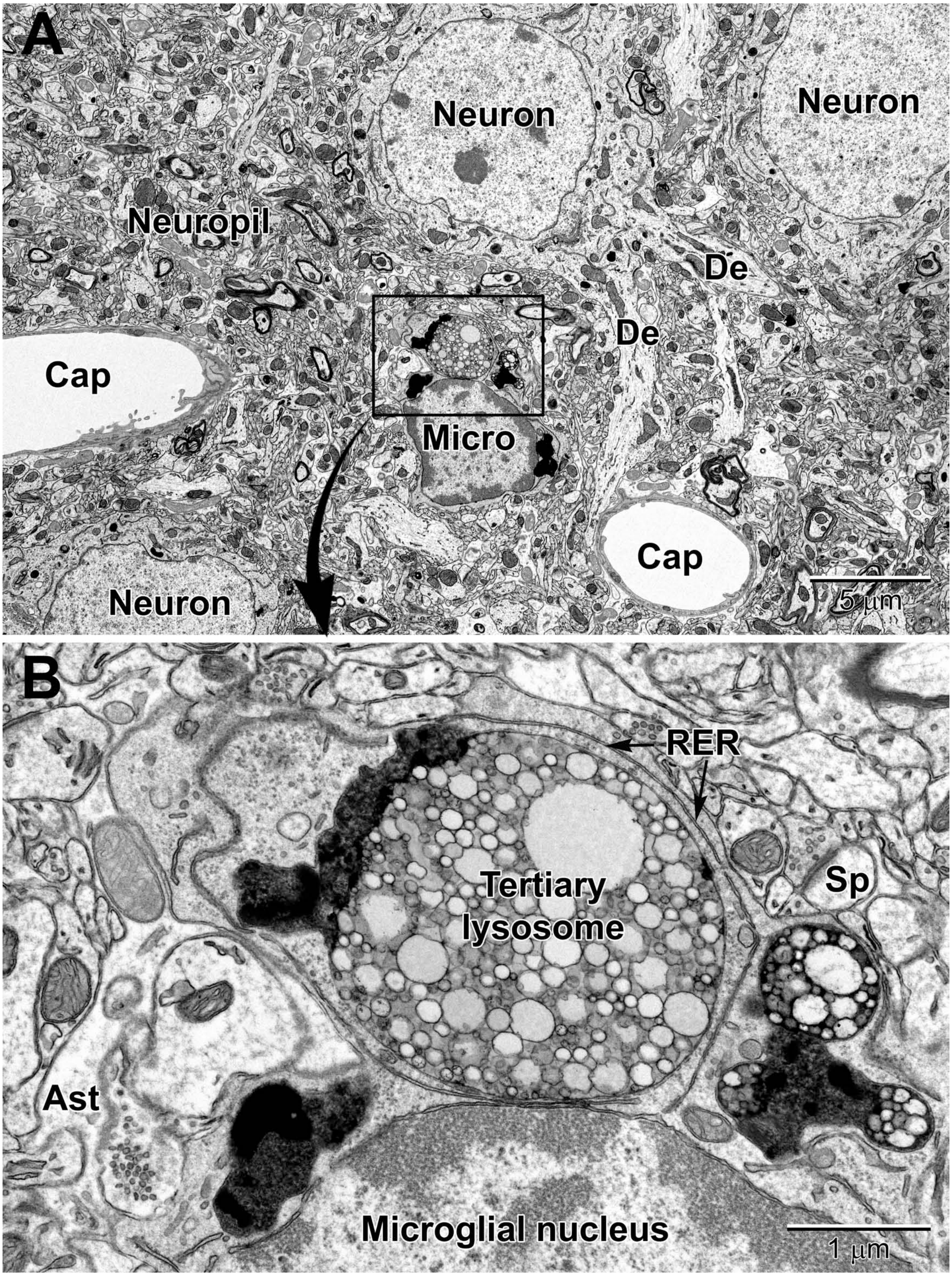

FIGURE 8 | Low **(A)** and high **(B)** magnification views of a perivascular microglial cell in the cerebral cortex of an aged mouse (18 mo old). The nuclei of microglia are small and pleomorphic, and contain relatively more heterochromatin than neurons. Large, tertiary lysosomes with undigestible debris occupy the cytoplasm. Long stretches of rough endoplasmic reticulum (RER) characterize microglia that are active, in terms of producing inflammatory cytokines and other mediators. A dendritic spine (Sp) forms a synapse with a presynaptic terminal near the microglial cell, and an astrocytic branch (Ast) is in close proximity. Microglia are strategically situated between neurons and capillaries (Cap), and function as the resident immune cell and phagocyte required for maintaining brain health throughout life.

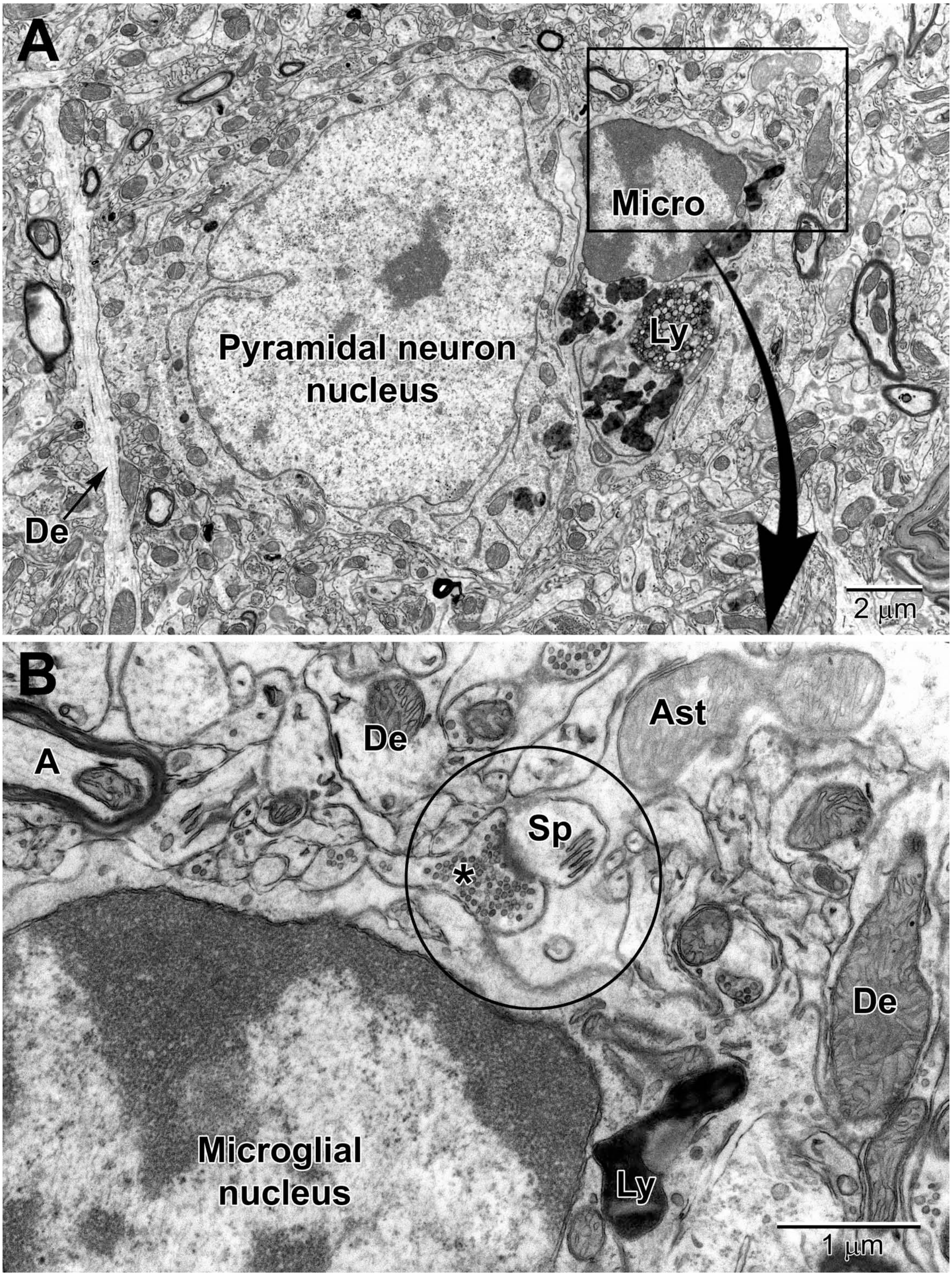

FIGURE 9 | Low **(A)** and high **(B)** magnification views of a perineuronal microglial cell closely abutting a pyramidal neuron in the aged mouse cortex. Microglia are now believed to play an integral part in maintaining the synapse (aka quadpartite synapse, encircled) which includes the presynaptic terminal (*), dendritic spine (Sp), astrocyte process (Ast), and microglia. A, axon; De, dendrite; Ly, lysosome.

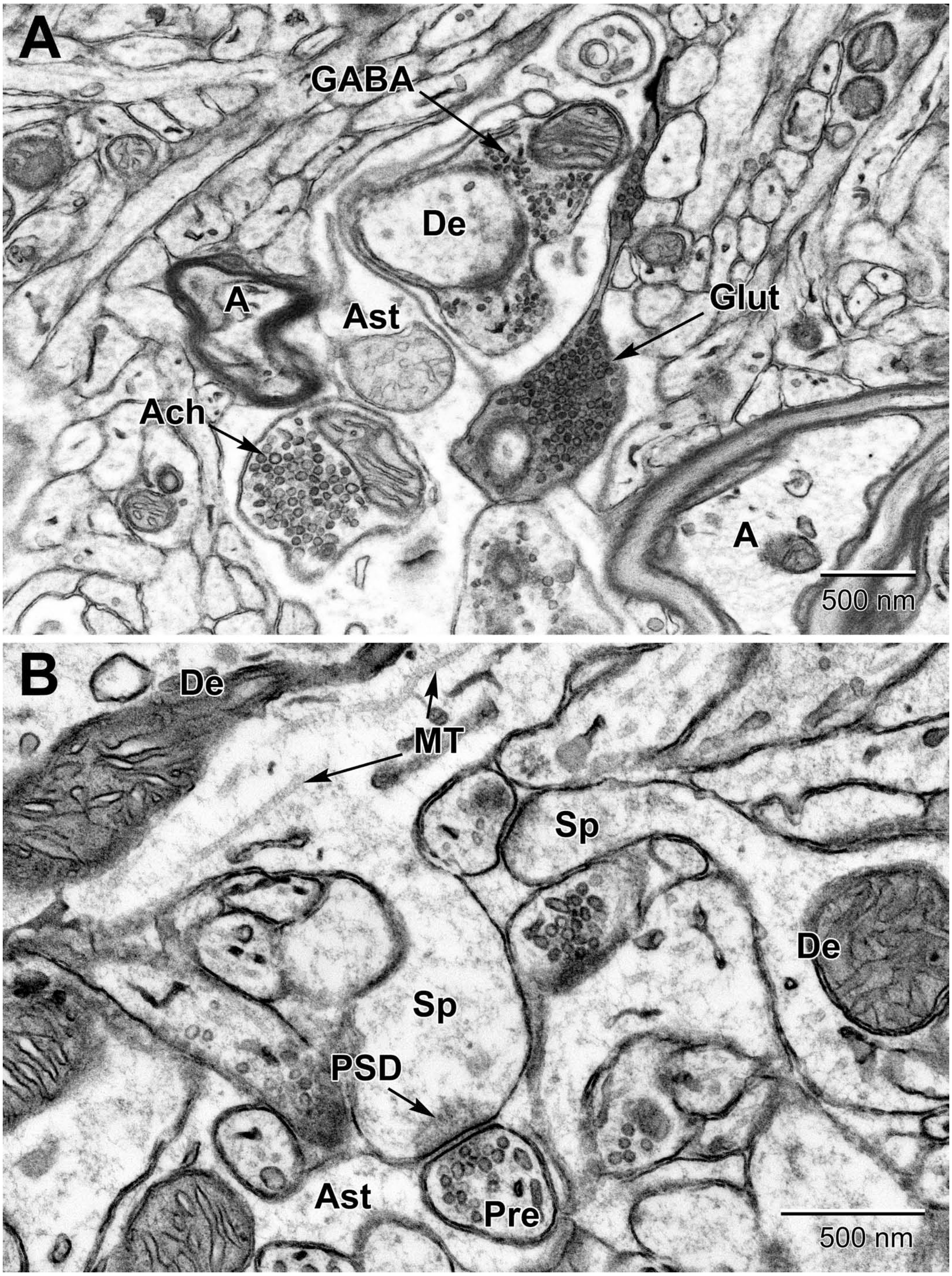

FIGURE 10 | Examples of synapses in the mouse substantia nigra **(A)** and dentate gyrus **(B)**. **(A)** Three types of presynaptic terminals are evident in the substantia nigra: Cholinergic (Ach) with large (50–70 nm) vesicles, glutamatergic (Glut) with medium sized (35–50 nm) vesicles, and GABAergic (inhibitory) with small ovoid (20–35 nm) vesicles. **(B)** High magnification view of dendritic spines (Sp) emanating from dendrites (De) and synapsing with glutamatergic pre-synaptic terminals (Pre). post-synaptic densities (PSD) characterize glutamatergic synapses. Astrocytic processes (Ast) occupy the intervening spaces between these structures. Microtubules (MT) are seen running along the length of the dendrite. A, axon.

other markers of cellular stress (e.g., dilation of the endoplasmic reticulum and Golgi complex) (Henry et al., 2018). Dark cells were identified as putative oligodendrocytes by Dr. Alan Peters, based on their very close proximity to myelin sheaths. These cells contained autophagic vacuoles and small spherical bodies (Peters and Folger Sethares, 2020).

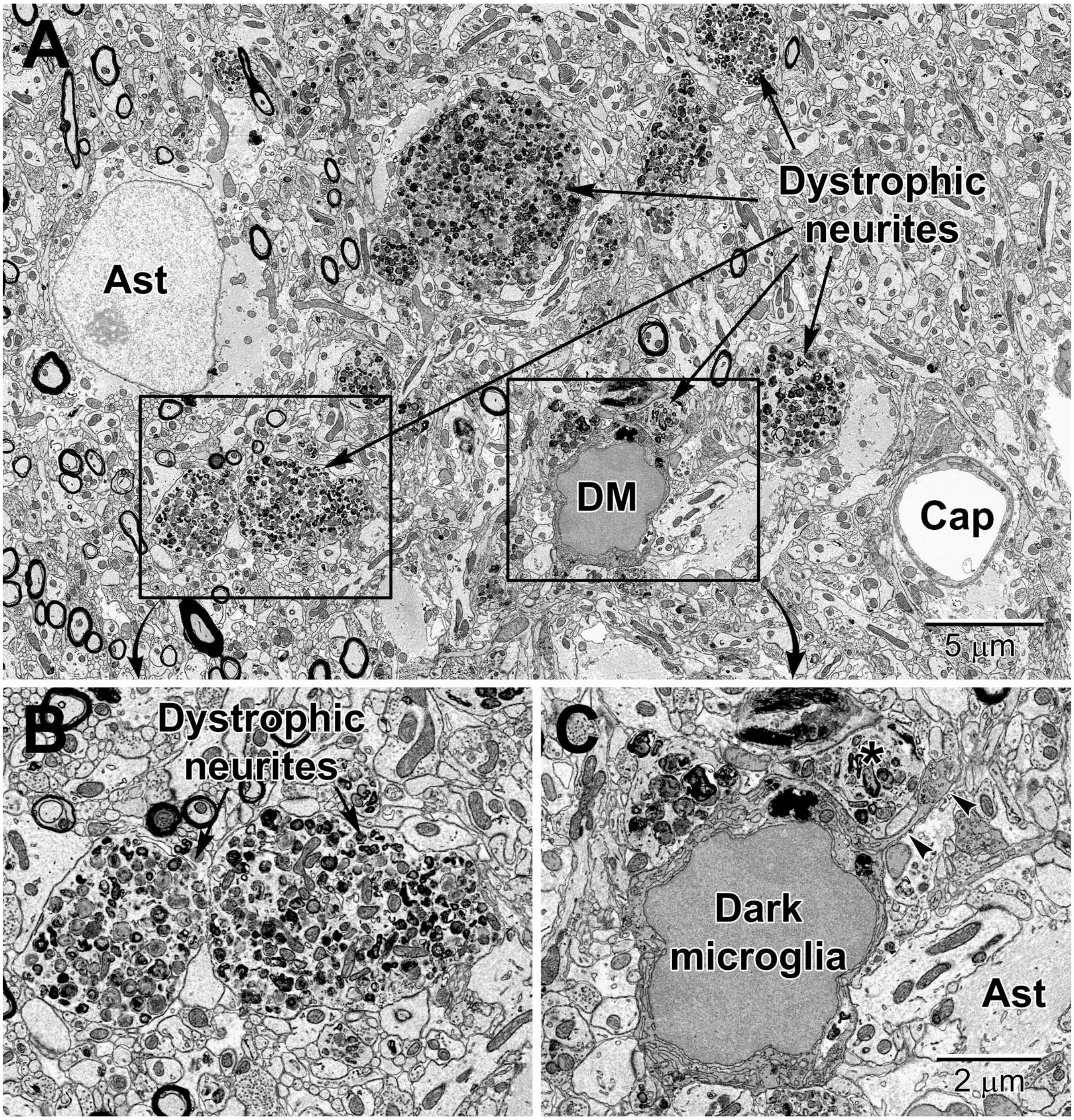

FIGURE 11 | Dystrophic neurites closely surrounded by glial cells in the hippocampal CA1 region of a 20 mo old APP-PS1 mouse, a model of Alzheimer disease pathology **(A)**. Magnified regions are shown in panels **(B)** and **(C)**. An abnormally large astrocyte (Ast) contains distinctive intermediate filaments, while a dark microglia (DM) is recognized by the condensation state of its cytoplasm and nucleoplasm, in addition to its microglial features (e.g., long stretches of endoplasmic reticulum). **(C)** The dark microglia contains lipidic inclusions and extends a process (arrowheads) that contacts a synapse and encircles a dystrophic neurite (*). Cap, capillary.

Dark microglia display ultrastructural features of microglia, in terms of size, shape and organelles (e.g., long stretches of endoplasmic reticulum, associated pockets of extracellular space). They are, however, strikingly different from typical microglia due to their electron-dense cytoplasm and nucleoplasm, giving them a dark appearance in EM and their various markers of cellular stress (e.g., dilation of the endoplasmic reticulum and Golgi complex, alteration to mitochondrial ultrastructure, and loss of the microglial nuclear heterochromatin patterning). These cells frequently associate with the vasculature (see **Supplementary Video 2**), generally ensheathing the basement membrane while contributing to the *glia limitans* of capillaries (Bisht et al., 2016c). Another difference between the dark and typical microglia pertains to their synaptic interactions. Typical microglia rarely display processes directly protruding from their cell body in ultrathin

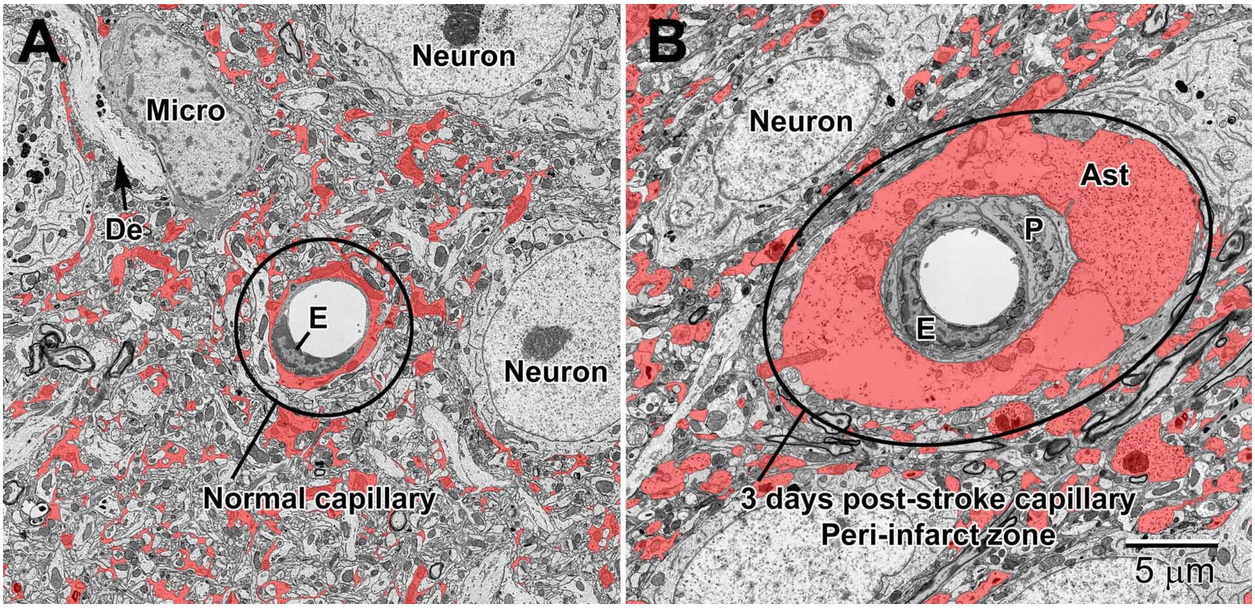

FIGURE 12 | Normal **(A)** and 3 day post-stroke capillaries **(B)** in the peri-infarct zone of the mouse cortex. Astrocytes (shaded red) are pseudocolored to illustrate the drastic increase in volume after ischemia. The endothelium (E) and pericytes (P) are also enlarged after stroke. Note the accumulation of glycogen granules in the perivascular end-feet of the astrocytes. De, dendrite; Micro, microglial cell.

section (Tremblay et al., 2010a), while dark microglia display several hyper-ramified processes, wrapping around instead of making focal contacts with synapses, and making acute angles in the neuropil (Bisht et al., 2016c; Hui et al., 2018a; St-Pierre et al., 2020). The contacted synapses include dystrophic neurites that are defined by their accumulation of autophagic vacuoles (Nixon, 2007) in Alzheimer disease pathology (**Figure 11**) (Bisht et al., 2016c). Dark microglia frequently contain endosomes with cellular elements such as axon terminals and dendritic spines which indicates a high phagocytic capacity and is suggestive of their specific involvement with the pathological remodeling of neuronal circuits (Bisht et al., 2016c).

Perivascular dark cells were also described recently, but it still remains undetermined whether these cells are dark microglia transiting from the parenchyma, or peripheral cells coming from the periphery (Bordeleau et al., 2020). These cells were identified by their markers of cellular stress, similar to dark microglia (Bisht et al., 2016c).

In addition, apoptotic cells, whether they are neuronal or glial, appear dark in EM (Bordeleau et al., 2020). They are recognized by their pyknotic nucleus, fragmentation and blebbing of the nuclear membrane, and accumulation of autophagosomes (see *Organelles* section for description) (Zhang et al., 1999).

Changes to Cell Processes

Stroke is one of the main pathological conditions associated with apoptotic cell death to neurons, but it also involves swelling of glial cell processes in the brain parenchyma. Astrocytes in the peri-infarct zone respond to stroke by swelling and accumulating glycogen granules in their perivascular end-feet (**Figures 12**, **13**). Together with the other cellular elements of the neurovascular unit (i.e., endothelium and pericytes), astrocytes become drastically enlarged after stroke (Nahirney et al., 2016) and this change is thought to be associated with their uptake of water, notably mediated via astrocytic aquaporin 4 channels, which was shown to modulate edema formation, as well as reflect a beneficial mechanism operating to minimize brain damage upon ischemia (Steiner et al., 2012; Stokum et al., 2015; Xiang et al., 2016). In addition, it was proposed that the astrocytic swelling during stroke may represent a beneficial response to BBB dysfunction, contributing to limiting the egress of plasma constituents and blood (hemorrhage) into the brain (Xiang et al., 2016). Our ultrastructural findings further revealed that the mechanisms causing BBB disruption upon stroke involve endothelial transport mediated via caveolae or vacuoles, instead of tight junction loss, and are associated with an increased thickness of the basement membrane (Nahirney et al., 2016). These effects of stroke on the BBB were diminished with normal aging (Nahirney et al., 2016), suggesting a reduced capacity of astrocytes and other cells of the neurovascular unit to cope with homeostatic challenges during aging. Biological aging is associated with reduced immunity and an increased risk of developing various disease conditions including the highly prevalent Alzheimer disease and stroke (Montecino-Rodriguez et al., 2013; Tay et al., 2017b).

In deeper regions of the peri-infarct region of an ischemic stroke (i.e., closer to the necrotic core), more drastic changes can be seen in astrocytic and neuronal processes including mitochondrial disruption and rupturing of membranes

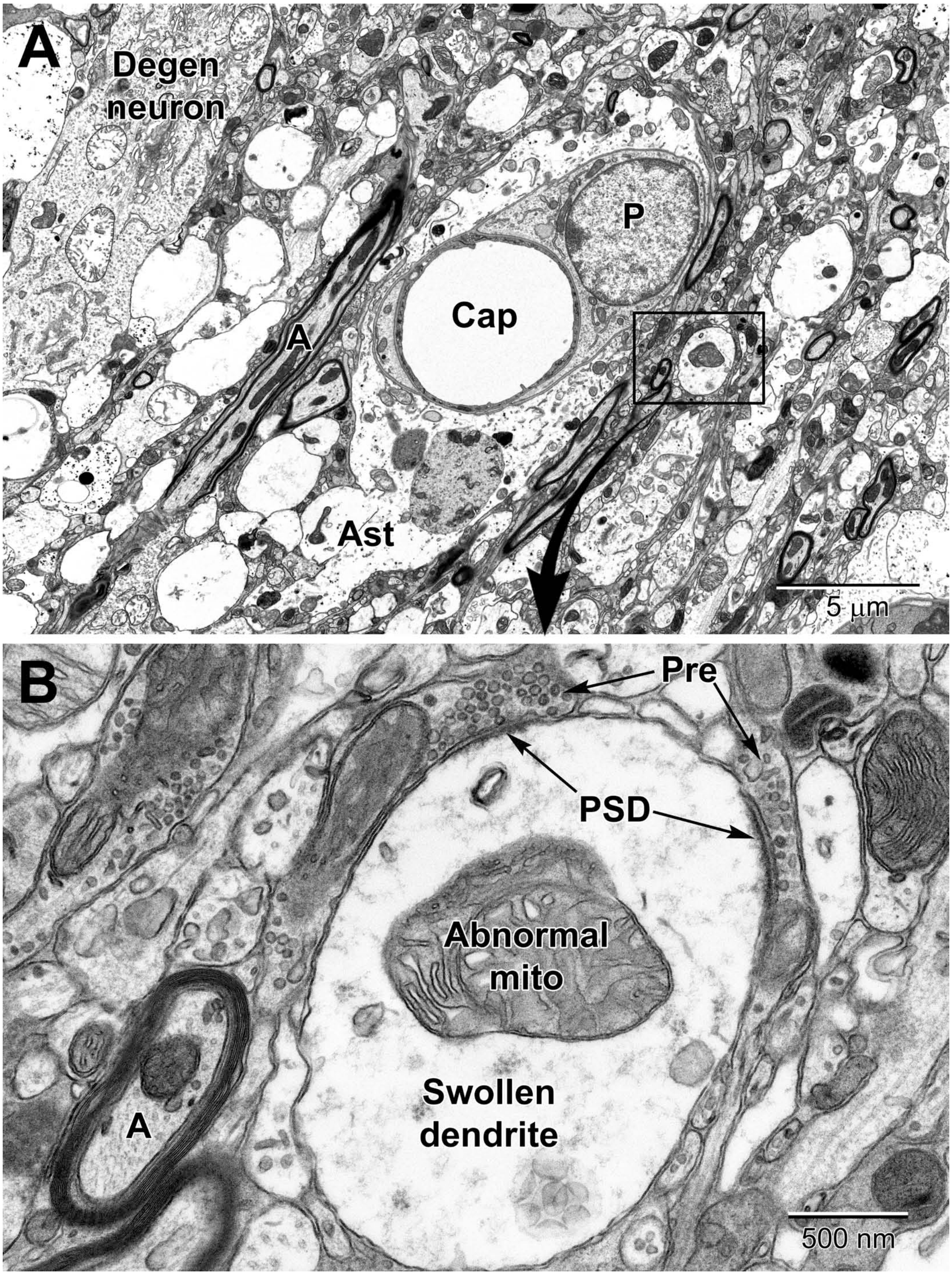

FIGURE 13 | Low **(A)** and high **(B)** magnification views of changes to neurons and dendritic branches following ischemic stroke (3 days post-stroke) deep in the peri-infarct zone of the mouse cortex. A portion of a degenerating neuron (Degen neuron) is seen in the upper left and contains swollen mitochondria. Dendrites in the peri-infart zone swell and appear to absorb the spinous processes with evidence of the synapses apparent at the edges of the dendrite; note the post-synaptic densities (PSD) at the presynaptic terminal (Pre) contacts in **(A)**. Mitochondria in the swollen dendrite undergo dysplastic changes and exhibit dilated, loosely arranged cristae. Note the increase in size of the pericyte surrounding the capillary and the swollen astrocyte (Ast). Compare to a normal capillary in **Figure 6**.

(**Figure 13A**). Axons and dendrites, and especially dendrites, show significant swelling in the peri-necrotic zone where they appear to lose their spinous processes (they get absorbed into the dendrite as it swells) as post-synaptic densities are commonly observed inside dendrites in contact with glutamatergic axon terminals (**Figure 13B**).

Changes to Intracellular Elements

In neurons and glial cells, several markers of cellular stress or aging, as well as dystrophy, degeneration, and disease, can be identified ultrastructurally. The most frequently investigated ones are described below.

The best characterized marker of cellular stress is dilation of the endoplasmic reticulum and/or Golgi complex, which is associated with an accumulation of dysfunctional proteins. This feature is noted when the swelling between endoplasmic reticulum and/or Golgi cisternal membranes extends beyond 50 nm (Welch and Suhan, 1985; Schönthal, 2012; El Hajj et al., 2019). Autophagosomes are involved in autophagy – the removal of dysfunctional cellular components, and accumulate with cellular stress and aging (Leidal et al., 2018). They are observed in neurons and glial cells, and are identified by the presence of digested elements within endosomes enclosed by a double membrane (size ranging from 325 nm to 1.2 μm) (Hui et al., 2018a). Mitochondrial elongation, which is associated with mitochondrial stress, is noted in neurons and glial cells when their length exceeds 1 μm (Henry et al., 2018; Hui et al., 2018b; St-Pierre et al., 2019; Bordeleau et al., 2020). Lipofuscin granules, which are considered a hallmark of cellular aging, are identified in neurons and glial cells (except oligodendrocytic precursor cells; Tremblay et al., 2012) by their oval or round structure and finely granular composition endowed with a unique fingerprint-like pattern associated with their amorphous materials (Sohal and Wolfe, 1986; Henry et al., 2018). Lipid bodies, associated as well with cellular aging in glial cells, are further identified by their circular shape and homogenous core ranging from a size of 160 nm to 2.2 μm (Fujimoto et al., 2013; El Hajj et al., 2019).

In microglia, lysosomes – the organelles which fuse with endosomes to degrade cellular cargo during phagocytosis – are identified by their dense heterogeneous contents within a single membrane (De Duve, 1963; Holtzman et al., 1967; El Hajj et al., 2019). Primary lysosomes possess a homogenous granular content and their diameter ranges from 0.3 to 0.5 μm. Secondary lysosomes are 1 to 2 μm across, and their content is heterogeneous showing fusion with vacuoles. They are differentiated from primary lysosomes by their contacts with fusion endosomes. Tertiary lysosomes range in diameter between 1.5 and 2.5 μm, and they are usually fused to one or two vacuoles associated with lipofuscin granules, as well as lipidic inclusions showing signs of degradation (**Figures 8**, **9**). Lipidic inclusions are identified as the clustering of round organelles with an electron dense, either opaque or limpid, cytoplasm enclosed by a single membrane (El Hajj et al., 2019; Bordeleau et al., 2020). A phagocytic index can be compiled by summing up the endosomes containing cellular materials such as membranes, axon terminals with 40 nm synaptic vesicles and dendritic spines with a postsynaptic density, on a microglial cell body or process basis (Milior et al., 2016; Lecours et al., 2020). The proportion of "gitter" cells, which are microglia filled with lipid bodies and cellular debris, can be determined by counting microglial cell bodies with more than four lipid bodies and at least one lipofuscin granule, or cells with at least one large lipid body and multiple lipofuscin granules (Tremblay et al., 2012).

Changes to Extracellular Elements and Intercellular Relationships

In the vicinity of microglial cell bodies and processes, degradation activities (e.g., degenerating myelin and extracellular digestion) were found to be exacerbated with aging and disease. In particular, extracellular space pockets containing debris, which could result from "exophagy" (the degradation of cellular constituents by lysosomal enzymes released extracellularly), exocytosis (the process of expelling the contents of a membrane-bound vesicle into the extracellular space, often lysosomal and in preparation for phagocytosis (Haka et al., 2016), or pinocytosis (also named bulk-phase endocytosis, by which immune cells can take up extracellular contents in a non-phagocytic manner; Kruth, 2011) become more prevalent with Alzheimer disease pathology. These space pockets containing debris are defined by the appearance of degraded materials (including cellular membranes and organelles) or debris in the extracellular space nearby microglia (El Hajj et al., 2019). In contrast, degenerating myelin is recognized by ballooning, swelling or distancing of myelin sheaths (Peters et al., 1990; Bordeleau et al., 2020) and is more often observed in aging (Peters and Folger Sethares, 2020) and demyelinating diseases such as multiple sclerosis pathology (Lampron et al., 2015). In addition, the prevalence of microglial contacts with synaptic clefts, termed synaptic contacts, which has been shown to be altered in disease states, such as Huntington disease pathology, can be determined by counting direct appositions between microglial plasma membrane and synapses between pre-synaptic axon terminals (identified by their synaptic vesicles) and post-synaptic dendritic spines (post-synaptic density) (Savage et al., 2020). Microglia perform various types of functional interventions at synapses, including synaptic stripping, which is the physical separation of pre- and post-synaptic elements by their intervening processes (Trapp et al., 2007). Microglial active contribution as the fourth element of the quadpartite synapse (**Figure 9**) is associated with important roles in synapse formation, maturation, structural, and functional plasticity, as well as elimination throughout life (Tay et al., 2017a,b). Considering the recent findings on dark microglia, which make extensive interactions with synapses, even more than the typical microglia, an updated version including these cells as the fifth element of synapses is also proposed here.

CONCLUSION AND PERSPECTIVE

Overall, this review provides a survey analysis of distinctive ultrastructural features that can inform on the state of health, stress, dystrophy or degeneration of the neurons and different types of glial cells (astrocytes, oligodendrocytes, and microglia) in the brain parenchyma (see **Table 1** for summary). Comparing nanoscale information about cell bodies, processes, organelles and cytoskeletal elements, without

TABLE 1 | Main ultrastructural identification criteria and pathological features of the parenchymal brain cells discussed in this review.

Type	**Electron density**	**Structures and their features**			**Alterations**
		Cell bodies		***Processes***	
		Nucleus	***Perikaryon***		
Neurons	Intermediate gray levels between astrocytes / oligodendrocyte precursors & mature oligodendrocytes / microglia	– Large and round euchromatic nucleus – Small patches of heterochromatin under the nuclear envelope – One or more electron dense nucleoli – Abundant nuclear pores	– Golgi complex(es) – Long flattened cisternae of rough ER – Free ribosomes and polyribosomes – Round to ovoid mitochondria – Occasional lysosomes with lipofuscin – Neurofilaments and microtubules – Multivesicular bodies	– Dendrites: irregular contours, few microtubules, frequent protrusions (spines, filopodia, small branches) – Spines: Bulbous head, fluffy' or 'cotton candy' content, axonal input, spine apparatus (ER), post-synaptic density – Filopodia: Absence of post-synaptic density, thin neck, long length, pointed head – Unmyelinated axons: Found within fascicles or bundles of similar profiles – Myelinated axons: Ensheathed by compact myelin – Axonal varicosities (or 'boutons'): axonal enlargements with aggregated synaptic vesicles & 'en passant' synaptic specializations – Axon terminals: axonal extremities with aggregated synaptic vesicles and synaptic specializations – Synapses: direct apposition between pre-synaptic axon terminals and post-synaptic dendritic spines or shafts	– Dark neurons: electron-dense cytoplasm and nucleoplasm, accumulation of mitochondria, nuclear indentations, and other markers of cellular stress (e.g., ER and Golgi dilation) Apoptotic neurons: electron-dense, pyknotic nucleus, fragmentation and blebbing of nuclear membrane, accumulation of autophagosomes Swollen dendrites: loss of dendritic spines Swollen axons
Astrocytes	Pale	– Thin rim of heterochromatin	– Stellate-shaped – Irregular contours – Frequent intermediate filaments – Sparseness of electron dense material – Mitochondria with lighter membranes than other cell types	– Irregular and angular shapes contrary to other glial processes (except dark microglia) – Frequently ensheath synapses, making direct contacts with pre-synaptic axon terminals, synaptic clefts, and post-synaptic elements (spines, dendrites), and neuronal cell bodies – Can contain phagocytosed synapses (both pre-synaptic axon terminals and post-synaptic dendritic spines) within endosomes	– Reactive astrocytes: abundant intermediate filaments, swelling and accumulation of glycogen granules in perivascular end-feet, mitochondrial disruption
Mature oligodendrocytes	Dark	– Heterogeneous heterochromatin pattern	– Squarish or rectangular-shaped – Short and wide ER cisternae – Ribosomes – Wider space between nuclear membranes than for microglia	– Obtuse angles in the neuropil – Positively identified when their plasma membrane is in direct continuity with myelinated axons	– Dark oligo-dendrocytes: cellular stress markers (ER and Golgi dilation), autophagosomes, elongated mitochondria, lipofuscin and other lipidic inclusions
Oligodendrocyte precursors	Pale	– Thin rim of heterochromatin	– Pale cytoplasm – Devoid of intermediate filaments – Short ER – Small mitochondria – Satellite positions	– Obtuse angles in the neuropil	– Do not accumulate lipidic inclusions during aging and in disease, contrary to other cell types

(Continued)

TABLE 1 | Continued

Type	Electron density	Structures and their features			Alterations
		Cell bodies		*Processes*	
		Nucleus	*Perikaryon*		
Microglia	Dark	– Small size – Triangle-shaped – Cheetah-pattern clumps of heterochromatin beneath the nuclear envelope and throughout the nucleoplasm	– Often contains long stretches of ER cisternae – Frequent lipidic inclusions (i.e., lipofuscin, lipid bodies or droplets, lysosomes) – Associated pockets of extracellular space, contrary to other cell types in the mature healthy brain – Frequent contacts with synapses (pre-synaptic axon terminals, synaptic clefts, post-synaptic dendrites or spines) – Satellite positions	– Irregular contours with obtuse angles (except for the dark microglia which make acute angles in the neuropil) – Frequent contacts with synapses (pre-synaptic axon terminals, synaptic clefts, post-synaptic dendrites and spines) and neuronal cell bodies – Frequent contacts with other glial cells – Numerous large vesicles and endosomes – Frequent cellular inclusions (e.g., large lipidic vesicles, cellular membranes, myelin, and profiles of other structural elements including pre-synaptic axon terminals and post-synaptic dendritic spines) – Distinctive long stretches of ER cisternae, contrary to the other glial cell types – Associated pockets of extracellular space, contrary to other cell types in the mature healthy brain	– Dark microglia: stress markers (e.g., dilated ER and Golgi, alteration to mitochondrial ultrastructure), loss of microglial nuclear heterochromatin patterning, frequent association with the vasculature, extensive synaptic interactions – Both typical and dark microglia can display changes in phagocytosis, exophagy, and synaptic contacts with pathology

ER, endoplasmic reticulum.

selective staining to visualize the elements of interest, all at once and with the very best spatial resolution afforded by a biological technique (1 nm), reveals differences in their cellular function and dysfunction. The ultrastructural analysis becomes especially enlightening when comparing brain regions, stages of life, and contexts of health or disease, as well as sexes and species. The recent developments in the field of imaging have allowed to significantly increase the speed and automation of EM imaging acquisition, registration and segmentation, for both two-dimensional (2D) and 3D visualization (Miranda et al., 2015; Savage et al., 2018; Carrier et al., 2020), as well as organelle and cell type identification in the brain (Perez et al., 2014; García-Cabezas et al., 2016; Abdollahzadeh et al., 2019; Calì et al., 2019; Gómez-de-Mariscal et al., 2019; Santuy et al., 2020; among others). Recent breakthroughs further allowed researchers to image biological samples at a subatomic resolution and without any aldehyde fixation artifacts (e.g., cryo-EM; Subramaniam, 2019, named method of the year in 2016 by Nature Methods). In addition, various strategies were proposed for the efficient correlation of light and EM data, including with X-ray modalities (Begemann and Galic, 2016; Pacureanu et al., 2019; Töpperwien et al., 2020). Together, these advancements are expected to tremendously enhance the possibilities of identifying biomarkers and validating treatment strategies with EM.

AUTHOR CONTRIBUTIONS

PN and M-ET designed and wrote the review manuscript. PN prepared the figures.

FUNDING

M-ET is a Canada Research Chair – Tier 2 in *Neurobiology of Aging and Cognition*. PN is supported by a grant from CIHR (Grant #159548).

ACKNOWLEDGMENTS

We acknowledge that University of Victoria is located on the territory of the Lekwungen peoples and that the Songhees, Esquimalt and WSÁNEĆ peoples have relationships to this land. We thank Dr. Craig Brown (Division of Medical Sciences, University of Victoria) for providing mouse brain tissue samples, and Marie-Kim St-Pierre and Micaël Carrier for the dark microglia image. We are also grateful to Sammy Weiser Novak for generating the FIB-SEM z stack video.

SUPPLEMENTARY MATERIAL

The Supplementary Material for this article can be found online at: https://www.frontiersin.org/articles/10.3389/fcell.2021.629503/full#supplementary-material

REFERENCES

Abdollahzadeh, A., Belevich, I., Jokitalo, E., Sierra, A., and Tohka, J. (2019). DeepACSON: automated segmentation of white matter in 3D electron microscopy. *bioRxiv*[Preprint]. doi: 10.1101/828541

Andreone, B. J., Lacoste, B., and Gu, C. (2015). Neuronal and vascular interactions. *Annu. Rev. Neurosci.* 38, 25–46. doi: 10.1146/annurev-neuro-071714-033835

Antón-Fernández, A., León-Espinosa, G., DeFelipe, J., and Muñoz, A. (2015). Changes in the golgi apparatus of neocortical and hippocampal neurons in the hibernating hamster. *Front. Neuroanat.* 9:157. doi: 10.3389/fnana.2015.00157

Bardehle, S., Krüger, M., Buggenthin, F., Schwausch, J., Ninkovic, J., Clevers, H., et al. (2013). Live imaging of astrocyte responses to acute injury reveals selective juxtavascular proliferation. *Nat. Neurosci.* 16, 580–586. doi: 10.1038/nn.3371

Begemann, I., and Galic, M. (2016). Correlative light electron microscopy: connecting synaptic structure and function. *Front. Synaptic Neurosci.* 8:28. doi: 10.3389/fnsyn.2016.00028

Berry, K. P., and Nedivi, E. (2017). Spine dynamics: are they all the same? *Neuron* 96, 43–55. doi: 10.1016/j.neuron.2017.08.008

Bisht, K., El Hajj, H., Savage, J. C., Sánchez, M. G., and Tremblay, M. -È (2016a). Correlative light and electron microscopy to study microglial interactions with β-amyloid plaques. *J. Vis. Exp.* 112:54060. doi: 10.3791/54060

Bisht, K., Sharma, K., Lacoste, B., and Tremblay, M. -È (2016b). Dark microglia: why are they dark? *Commun. Integr. Biol.* 9:e1230575. doi: 10.1080/19420889.2016.1230575

Bisht, K., Sharma, K. P., Lecours, C., Sánchez, M. G., El Hajj, H., Milior, G., et al. (2016c). Dark microglia: a new phenotype predominantly associated with pathological states. *Glia* 64, 826–839. doi: 10.1002/glia.22966

Bordeleau, M., Lacabanne, C., Fernández de Cossío, L., Vernoux, N., Savage, J. C., González-Ibáñez, F., et al. (2020). Microglial and peripheral immune priming is partially sexually dimorphic in adolescent mouse offspring exposed to maternal high-fat diet. *J. Neuroinflamm.* 17:264. doi: 10.1186/s12974-020-01914-1

Bourne, J. N., and Harris, K. M. (2012). Nanoscale analysis of structural synaptic plasticity. *Curr. Opin. Neurobiol.* 22, 372–382. doi: 10.1016/j.conb.2011.10.019

Burry, R. W. (2010). "Electron microscopic immunocytochemistry," in *Immunocytochemistry: A Practical Guide for Biomedical Research*, ed. R. W. Burry (New York, NY: Springer), 175–189. doi: 10.1007/978-1-4419-1304-3_15

Bushong, E. A., Martone, M. E., Jones, Y. Z., and Ellisman, M. H. (2002). Protoplasmic astrocytes in CA1 stratum radiatum occupy separate anatomical domains. *J. Neurosci.* 22, 183–192. doi: 10.1523/jneurosci.22-01-00183.2002

Calì, C., Agus, M., Kare, K., Boges, D. J., Lehväslaiho, H., Hadwiger, M., et al. (2019). 3D cellular reconstruction of cortical glia and parenchymal morphometric analysis from serial block-face electron microscopy of juvenile rat. *Prog. Neurobiol.* 183:101696. doi: 10.1016/j.pneurobio.2019.101696

Carrier, M., Robert, M. -È, González Ibáñez, F., Desjardins, M., and Tremblay, M. -È (2020). Imaging the neuroimmune dynamics across space and time. *Front. Neurosci.* 14:903. doi: 10.3389/fnins.2020.00903

Chung, W.-S., Allen, N. J., and Eroglu, C. (2015). Astrocytes control synapse formation, function, and elimination. *Cold Spring Harb. Perspect. Biol.* 7:a020370. doi: 10.1101/cshperspect.a020370

De Duve, C. (1963). The lysosome. *Sci. Am.* 208, 64–72. doi: 10.1038/scientificamerican0563-64

Deitch, J. S., and Banker, G. A. (1993). An electron microscopic analysis of hippocampal neurons developing in culture: early stages in the emergence of polarity. *J. Neurosci.* 13, 4301–4315. doi: 10.1523/JNEUROSCI.13-10-04301.1993

Dykstra, M. J., and Reuss, L. E. (2003). *Biological Electron Microscopy: Theory, Techniques, and Troubleshooting*, 2nd Edn. Boston, MA: Springer US, doi: 10.1007/978-1-4419-9244-4

Egerton, R. F. (2016). *Physical Principles of Electron Microscopy: An Introduction to TEM, SEM, and AEM*, 2nd Edn. New York, NY: Springer International Publishing, doi: 10.1007/978-3-319-39877-8

El Hajj, H., Savage, J. C., Bisht, K., Parent, M., Vallières, L., Rivest, S., et al. (2019). Ultrastructural evidence of microglial heterogeneity in alzheimer's disease amyloid pathology. *J. Neuroinflammation* 16:87. doi: 10.1186/s12974-019-1473-9

Fiala, J. C., Feinberg, M., Popov, V., and Harris, K. M. (1998). Synaptogenesis via dendritic filopodia in developing hippocampal area CA1. *J. Neurosci.* 18, 8900–8911. doi: 10.1523/JNEUROSCI.18-21-08900.1998

Fujimoto, T., Ohsaki, Y., Suzuki, M., and Cheng, J. (2013). Imaging lipid droplets by electron microscopy. *Methods Cell Biol.* 116, 227–251. doi: 10.1016/B978-0-12-408051-5.00012-7

García-Cabezas, M. Á, John, Y. J., Barbas, H., and Zikopoulos, B. (2016). Distinction of neurons, glia and endothelial cells in the cerebral cortex: an algorithm based on cytological features. *Front. Neuroanat.* 10:107. doi: 10.3389/fnana.2016.00107

Gómez-de-Mariscal, E., Maška, M., Kotrbová, A., Pospíchalová, V., Matula, P., and Muñoz-Barrutia, A. (2019). Deep-learning-based segmentation of small extracellular vesicles in transmission electron microscopy images. *Sci. Rep.* 9:13211. doi: 10.1038/s41598-019-49431-3

Griffin, R., Illis, L. S., and Mitchell, J. (1972). Identification of neuroglia by light and electronmicroscopy. *Acta Neuropathol.* 22, 7–12. doi: 10.1007/BF00687546

Haka, A. S., Barbosa-Lorenzi, V. C., Lee, H. J., Falcone, D. J., Hudis, C. A., Dannenberg, A. J., et al. (2016). Exocytosis of macrophage lysosomes leads to digestion of apoptotic adipocytes and foam cell formation. *J. Lipid Res.* 57, 980–992. doi: 10.1194/jlr.M064089

Harris, K. M., and Weinberg, R. J. (2012). Ultrastructure of synapses in the mammalian brain. *Cold Spring Harb. Perspect. Biol.* 4:a005587. doi: 10.1101/cshperspect.a005587

Henry, M. S., Bisht, K., Vernoux, N., Gendron, L., Torres-Berrio, A., Drolet, G., et al. (2018). Delta opioid receptor signaling promotes resilience to stress under the repeated social defeat paradigm in mice. *Front. Mol. Neurosci.* 11:100. doi: 10.3389/fnmol.2018.00100

Herndon, R. M. (1964). The fine structure of the rat cerebellum. II. The stellate neurons, granule cells, and glia. *J. Cell Biol.* 23, 277–293. doi: 10.1083/jcb.23.2.277

Hoffman, D. P., Shtengel, G., Xu, C. S., Campbell, K. R., Freeman, M., Wang, L., et al. (2020). Correlative three-dimensional super-resolution and block-face electron microscopy of whole vitreously frozen cells. *Science* 367:eaaz5357. doi: 10.1126/science.aaz5357

Holtzman, E., Novikoff, A. B., and Villaverde, H. (1967). Lysosomes and gerl in normal and chromatolytic neurons of the rat ganglion nodosum. *J. Cell Biol.* 33, 419–435. doi: 10.1083/jcb.33.2.419

Hui, C. W., St-Pierre, A., El Hajj, H., Remy, Y., Hébert, S. S., Luheshi, G. N., et al. (2018a). Prenatal immune challenge in mice leads to partly sex-dependent behavioral. Microglial, and molecular abnormalities associated with schizophrenia. *Front. Mol. Neurosci.* 11:13. doi: 10.3389/fnmol.2018.00013

Hui, C. W., St-Pierre, M.-K., Detuncq, J., Aumailley, L., Dubois, M.-J., Couture, V., et al. (2018b). Nonfunctional mutant Wrn protein leads to neurological deficits, neuronal stress, microglial alteration, and immune imbalance in a mouse model of Werner syndrome. *Brain Behav. Immun.* 73, 450–469. doi: 10.1016/j.bbi.2018.06.007

Joost, E., Jordão, M. J. C., Mages, B., Prinz, M., Bechmann, I., and Krueger, M. (2019). Microglia contribute to the glia limitans around arteries, capillaries and veins under physiological conditions, in a model of neuroinflammation and in human brain tissue. *Brain Struct. Funct.* 224, 1301–1314. doi: 10.1007/s00429-019-01834-8

Kettenmann, H., Kirchhoff, F., and Verkhratsky, A. (2013). Microglia: new roles for the synaptic stripper. *Neuron* 77, 10–18. doi: 10.1016/j.neuron.2012.12.023

Knott, G., and Genoud, C. (2013). Is EM dead? *J. Cell Sci.* 126, 4545–4552. doi: 10.1242/jcs.124123

Korogod, N., Petersen, C. C., and Knott, G. W. (2015). Ultrastructural analysis of adult mouse neocortex comparing aldehyde perfusion with cryo fixation. *eLife* 4:e05793. doi: 10.7554/eLife.05793

Kruth, H. S. (2011). Receptor-independent fluid-phase pinocytosis mechanisms for induction of foam cell formation with native LDL particles. *Curr. Opin. Lipidol.* 22, 386–393. doi: 10.1097/MOL.0b013e32834adadb

Kubota, Y., Sohn, J., and Kawaguchi, Y. (2018). Large volume electron microscopy and neural microcircuit analysis. *Front. Neural Circuits* 12:98. doi: 10.3389/fncir.2018.00098

Kuwajima, M., Mendenhall, J. M., and Harris, K. M. (2013). Large-volume reconstruction of brain tissue from high-resolution serial section images acquired by SEM-based scanning transmission electron microscopy. *Methods Mol. Biol.* 950, 253–273. doi: 10.1007/978-1-62703-137-0_15

Lampron, A., Larochelle, A., Laflamme, N., Préfontaine, P., Plante, M.-M., Sánchez, M. G., et al. (2015). Inefficient clearance of myelin debris by microglia impairs remyelinating processes. *J. Exp. Med.* 212, 481–495. doi: 10.1084/jem.20141656

Lecours, C., St-Pierre, M.-K., Picard, K., Bordeleau, M., Bourque, M., Awogbindin, I. O., et al. (2020). Levodopa partially rescues microglial numerical, morphological, and phagolysosomal alterations in a monkey model of Parkinson's disease. *Brain Behav. Immun.* 90, 81–96. doi: 10.1016/j.bbi.2020.07.044

Lee, J.-H., Kim, J., Noh, S., Lee, H., Lee, S. Y., Mun, J. Y., et al. (2020). Astrocytes phagocytose adult hippocampal synapses for circuit homeostasis. *Nature* doi: 10.1038/s41586-020-03060-3 [Epub ahead of print].

Leidal, A. M., Levine, B., and Debnath, J. (2018). Autophagy and the cell biology of age-related disease. *Nat. Cell Biol.* 20, 1338–1348. doi: 10.1038/s41556-018-0235-8

Ligorio, M., Descarries, L., and Warren, R. A. (2009). Cholinergic innervation and thalamic input in rat nucleus accumbens. *J. Chem. Neuroanat.* 37, 33–45. doi: 10.1016/j.jchemneu.2008.08.003

Liu, L.-R., Liu, J.-C., Bao, J.-S., Bai, Q.-Q., and Wang, G.-Q. (2020). Interaction of microglia and astrocytes in the neurovascular unit. *Front. Immunol.* 11:1024. doi: 10.3389/fimmu.2020.01024

Luse, S. A. (1956). Electron microscopic observations of the central nervous system. *J. Biophys. Biochem. Cytol.* 2, 531–542. doi: 10.1083/jcb.2.5.531

Mechawar, N., Cozzari, C., and Descarries, L. (2000). Cholinergic innervation in adult rat cerebral cortex: a quantitative immunocytochemical description. *J. Comp. Neurol.* 428, 305–318. doi: 10.1002/1096-9861(20001211)428:2<305::aid-cne9<3.0.co;2-y

Milior, G., Lecours, C., Samson, L., Bisht, K., Poggini, S., Pagani, F., et al. (2016). Fractalkine receptor deficiency impairs microglial and neuronal responsiveness to chronic stress. *Brain Behav. Immun.* 55, 114–125. doi: 10.1016/j.bbi.2015.07.024

Miranda, K., Girard-Dias, W., Attias, M., de Souza, W., and Ramos, I. (2015). Three dimensional reconstruction by electron microscopy in the life sciences: an introduction for cell and tissue biologists. *Mol. Reprod. Dev.* 82, 530–547. doi: 10.1002/mrd.22455

Montecino-Rodriguez, E., Berent-Maoz, B., and Dorshkind, K. (2013). Causes, consequences, and reversal of immune system aging. *J. Clin. Invest.* 123, 958–965. doi: 10.1172/JCI64096

Mori, S., and Leblond, C. P. (1969). Identification of microglia in light and electron microscopy. *J. Comp. Neurol.* 135, 57–79. doi: 10.1002/cne.901350104

Murabe, Y., and Sano, Y. (1982). Morphological studies on neuroglia. V. Microglial cells in the cerebral cortex of the rat, with special reference to their possible involvement in synaptic function. *Cell Tissue Res.* 223, 493–506. doi: 10.1007/BF00218471

Nahirney, P. C., Reeson, P., and Brown, C. E. (2016). Ultrastructural analysis of blood-brain barrier breakdown in the peri-infarct zone in young adult and aged mice. *J. Cereb. Blood Flow Metab.* 36, 413–425. doi: 10.1177/0271678X15608396

Nixon, R. A. (2007). Autophagy, amyloidogenesis and alzheimer disease. *J. Cell Sci.* 120, 4081–4091. doi: 10.1242/jcs.019265

Oberheim, N. A., Tian, G.-F., Han, X., Peng, W., Takano, T., Ransom, B., et al. (2008). Loss of astrocytic domain organization in the epileptic brain. *J. Neurosci.* 28, 3264–3276. doi: 10.1523/JNEUROSCI.4980-07.2008

Ohno, N., Katoh, M., Saitoh, Y., and Saitoh, S. (2015). Recent advancement in the challenges to connectomics. *Microscopy* 65, 97–107. doi: 10.1093/jmicro/dfv371

Pacureanu, A., Maniates-Selvin, J., Kuan, A. T., Thomas, L. A., Chen, C.-L., Cloetens, P., et al. (2019). Dense neuronal reconstruction through X-ray holographic nano-tomography. *bioRxiv*[Preprint]. doi: 10.1101/653188

Paolicelli, R. C., Bolasco, G., Pagani, F., Maggi, L., Scianni, M., Panzanelli, P., et al. (2011). Synaptic pruning by microglia is necessary for normal brain development. *Science* 333, 1456–1458. doi: 10.1126/science.1202529

Papa, M., Bundman, M., Greenberger, V., and Segal, M. (1995). Morphological analysis of dendritic spine development in primary cultures of hippocampal neurons. *J. Neurosci.* 15, 1–11. doi: 10.1523/JNEUROSCI.15-01-00001.1995

Parent, M., and Descarries, L. (2008). Acetylcholine innervation of the adult rat thalamus: distribution and ultrastructural features in dorsolateral geniculate, parafascicular, and reticular thalamic nuclei. *J. Comp. Neurol.* 511, 678–691. doi: 10.1002/cne.21868

Parra-Damas, A., and Saura, C. A. (2020). Tissue clearing and expansion methods for imaging brain pathology in neurodegeneration: from circuits to synapses and beyond. *Front. Neurosci.* 14:914. doi: 10.3389/fnins.2020.00914

Perez, A. J., Seyedhosseini, M., Deerinck, T. J., Bushong, E. A., Panda, S., Tasdizen, T., et al. (2014). A workflow for the automatic segmentation of organelles in electron microscopy image stacks. *Front. Neuroanat.* 8:126. doi: 10.3389/fnana.2014.00126

Peters, A., and Folger Sethares, C. (2020). *Chapter 16 – Dark cCells» Fine Structure of the Aging Brain*. Available online at: https://www.bu.edu/agingbrain/chapter-16-dark-cells/ (accessed November 4, 2020)

Peters, A., Palay, S. L., and Webster, H. F. (1990). *The Fine Structure of the Nervous System: Neurons and Their Supporting Cells*, 3rd Edn. New York, NY: Oxford University Press.

Santuy, A., Tomás-Roca, L., Rodríguez, J.-R., González-Soriano, J., Zhu, F., Qiu, Z., et al. (2020). Estimation of the number of synapses in the hippocampus and brain-wide by volume electron microscopy and genetic labeling. *Sci. Rep.* 10:14014. doi: 10.1038/s41598-020-70859-5

Savage, J. C., Picard, K., González-Ibáñez, F., and Tremblay, M. -È (2018). A brief history of microglial ultrastructure: distinctive features, phenotypes, and functions discovered over the past 60 years by electron microscopy. *Front. Immunol.* 9:803. doi: 10.3389/fimmu.2018.00803

Savage, J. C., St-Pierre, M.-K., Carrier, M., El Hajj, H., Novak, S. W., Sanchez, M. G., et al. (2020). Microglial physiological properties and interactions with synapses are altered at presymptomatic stages in a mouse model of huntington's disease pathology. *J. Neuroinflamm.* 17:98. doi: 10.1186/s12974-020-01782-9

Schafer, D. P., Lehrman, E. K., Kautzman, A. G., Koyama, R., Mardinly, A. R., Yamasaki, R., et al. (2012). Microglia sculpt postnatal neural circuits in an activity and complement-dependent manner. *Neuron* 74, 691–705. doi: 10.1016/j.neuron.2012.03.026

Schönthal, A. H. (2012). Endoplasmic reticulum stress: its role in disease and novel prospects for therapy. *Scientifica (Cairo)* 2012:857516. doi: 10.6064/2012/857516

Shapiro, L. A., Perez, Z. D., Foresti, M. L., Arisi, G. M., and Ribak, C. E. (2009). Morphological and ultrastructural features of Iba1-immunolabeled microglial cells in the hippocampal dentate gyrus. *Brain Res.* 1266, 29–36. doi: 10.1016/j.brainres.2009.02.031

Skepper, J. N., and Powell, J. M. (2008). Immunogold staining of epoxy resin sections for Transmission Electron Microscopy (TEM). *Cold Spring Harb. Protoc.* 2008:db.rot5015. doi: 10.1101/pdb.prot5015

Skoff, R. P., and Hamburger, V. (1974). Fine structure of dendritic and axonal growth cones in embryonic chick spinal cord. *J. Comp. Neurol.* 153, 107–147. doi: 10.1002/cne.901530202

Sohal, R. S., and Wolfe, L. S. (1986). "Chapter 11 lipofuscin: characteristics and significance," in *Progress in Brain Research Aging of the Brain and Alzheimer's Disease*, eds D. F. Swaab, E. Fliers, M. Mirmiran, W. A. Van Gool, and F. Van Haaren (Amsterdam: Elsevier), 171–183. doi: 10.1016/S0079-6123(08)64304-6

Soria, F. N., Miguelez, C., Peñagarikano, O., and Tønnesen, J. (2020). Current techniques for investigating the brain extracellular space. *Front. Neurosci.* 14:570750. doi: 10.3389/fnins.2020.570750

Sousa, C., Biber, K., and Michelucci, A. (2017). Cellular and molecular characterization of microglia: a unique immune cell population. *Front. Immunol.* 8:198. doi: 10.3389/fimmu.2017.00198

Steiner, E., Enzmann, G. U., Lin, S., Ghavampour, S., Hannocks, M.-J., Zuber, B., et al. (2012). Loss of astrocyte polarization upon transient focal brain ischemia as a possible mechanism to counteract early edema formation. *Glia* 60, 1646–1659. doi: 10.1002/glia.22383

Stokum, J. A., Kurland, D. B., Gerzanich, V., and Simard, J. M. (2015). Mechanisms of astrocyte-mediated cerebral edema. *Neurochem. Res.* 40, 317–328. doi: 10.1007/s11064-014-1374-3

St-Pierre, M.-K., Bordeleau, M., and Tremblay, M. (2019). Visualizing dark microglia. *Methods Mol. Biol.* 2034, 97–110. doi: 10.1007/978-1-4939-9658-2_8

St-Pierre, M.-K., Šimončičová, E., Bögi, E., and Tremblay, M. (2020). Shedding light on the dark side of the microglia. *ASN Neuro.* 12:1759091420925335. doi: 10.1177/1759091420925335

Stratoulias, V., Venero, J. L., Tremblay, M., and Joseph, B. (2019). Microglial subtypes: diversity within the microglial community. *EMBO J.* 38:e101997. doi: 10.15252/embj.2019101997

Subramaniam, S. (2019). The cryo-EM revolution: fueling the next phase. *IUCrJ* 6:1–2. doi: 10.1107/S2052252519000277

Svitkina, T. (2009). Imaging cytoskeleton components by electron microscopy. *Methods Mol. Biol.* 586, 187–206. doi: 10.1007/978-1-60761-376-3_10

Swanson, L. W., and Lichtman, J. W. (2016). From cajal to connectome and beyond. *Annu. Rev. Neurosci.* 39, 197–216. doi: 10.1146/annurev-neuro-071714-033954

Syková, E., and Nicholson, C. (2008). Diffusion in brain extracellular space. *Physiol. Rev.* 88, 1277–1340. doi: 10.1152/physrev.00027.2007

SynapseWeb (2021). Available online at: https://synapseweb.clm.utexas.edu/home (accessed January 1, 2021).

Tao-Cheng, J.-H. (2018). Stimulation-induced structural changes at the nucleus, endoplasmic reticulum and mitochondria of hippocampal neurons. *Mol. Brain* 11:44. doi: 10.1186/s13041-018-0387-2

Tay, T. L., Béchade, C., D'Andrea, I., St-Pierre, M.-K., Henry, M. S., Roumier, A., et al. (2017a). Microglia gone rogue: impacts on psychiatric disorders across the lifespan. *Front. Mol. Neurosci.* 10:421. doi: 10.3389/fnmol.2017.00421

Tay, T. L., Savage, J. C., Hui, C. W., Bisht, K., and Tremblay, M. -È (2017b). Microglia across the lifespan: from origin to function in brain development, plasticity and cognition. *J. Physiol.* 595, 1929–1945. doi: 10.1113/JP272134

Theodosis, D. T., Poulain, D. A., and Oliet, S. H. R. (2008). Activity-dependent structural and functional plasticity of astrocyte-neuron interactions. *Physiol. Rev.* 88, 983–1008. doi: 10.1152/physrev.00036.2007

Töpperwien, M., van der Meer, F., Stadelmann, C., and Salditt, T. (2020). Correlative x-ray phase-contrast tomography and histology of human brain tissue affected by alzheimer's disease. *NeuroImage* 210:116523. doi: 10.1016/j.neuroimage.2020.116523

Trapp, B. D., Wujek, J. R., Criste, G. A., Jalabi, W., Yin, X., Kidd, G. J., et al. (2007). Evidence for synaptic stripping by cortical microglia. *Glia* 55, 360–368. doi: 10.1002/glia.20462

Tremblay, M.-E., Riad, M., Bouvier, D., Murai, K. K., Pasquale, E. B., Descarries, L., et al. (2007). Localization of EphA4 in axon terminals and dendritic spines of adult rat hippocampus. *J Comp. Neurol.* 501, 691–702. doi: 10.1002/cne.21263

Tremblay, M.-E., Riad, M., Chierzi, S., Murai, K. K., Pasquale, E. B., and Doucet, G. (2009). Developmental course of EphA4 cellular and subcellular localization in the postnatal rat hippocampus. *J. Comp. Neurol.* 512, 798–813. doi: 10.1002/cne.21922

Tremblay, M.-E., Riad, M., and Majewska, A. (2010b). Preparation of mouse brain tissue for immunoelectron microscopy. *J. Vis. Exp.* 41:2021. doi: 10.3791/2021

Tremblay, M. -È, Lowery, R. L., and Majewska, A. K. (2010a). Microglial interactions with synapses are modulated by visual experience. *PLoS Biol.* 8:e1000527. doi: 10.1371/journal.pbio.1000527

Tremblay, M. -È, Zettel, M. L., Ison, J. R., Allen, P. D., and Majewska, A. K. (2012). Effects of aging and sensory loss on glial cells in mouse visual and auditory cortices. *Glia* 60, 541–558. doi: 10.1002/glia.22287

Umbriaco, D., Garcia, S., Beaulieu, C., and Descarries, L. (1995). Relational features of acetylcholine, noradrenaline, serotonin and GABA axon terminals in the stratum radiatum of adult rat hippocampus (CA1). *Hippocampus* 5, 605–620. doi: 10.1002/hipo.450050611

Verkhratsky, A., and Nedergaard, M. (2018). Physiology of astroglia. *Physiol. Rev.* 98, 239–389. doi: 10.1152/physrev.00042.2016

Versaevel, M., Braquenier, J.-B., Riaz, M., Grevesse, T., Lantoine, J., and Gabriele, S. (2014). Super-resolution microscopy reveals LINC complex recruitment at nuclear indentation sites. *Sci. Rep.* 4:7362. doi: 10.1038/srep07362

Welch, W. J., and Suhan, J. P. (1985). Morphological study of the mammalian stress response: characterization of changes in cytoplasmic organelles, cytoskeleton, and nucleoli, and appearance of intranuclear actin filaments in rat fibroblasts after heat-shock treatment. *J. Cell Biol.* 101, 1198–1211. doi: 10.1083/jcb.101.4.1198

Winey, M., Meehl, J. B., O'Toole, E. T., and Giddings, T. H. (2014). Conventional transmission electron microscopy. *Mol. Biol. Cell* 25, 319–323. doi: 10.1091/mbc.E12-12-0863

Witcher, M. R., Kirov, S. A., and Harris, K. M. (2007). Plasticity of perisynaptic astroglia during synaptogenesis in the mature rat hippocampus. *Glia* 55, 13–23. doi: 10.1002/glia.20415

Wittmann, M., Queisser, G., Eder, A., Wiegert, J. S., Bengtson, C. P., Hellwig, A., et al. (2009). Synaptic activity induces dramatic changes in the geometry of the cell nucleus: interplay between nuclear structure. Histone H3 phosphorylation, and nuclear calcium signaling. *J. Neurosci.* 29, 14687–14700. doi: 10.1523/JNEUROSCI.1160-09.2009

Xiang, J., Tang, Y., Li, C., Su, E. J., Lawrence, D. A., and Keep, R. F. (2016). Mechanisms underlying astrocyte endfeet swelling in stroke. *Acta Neurochir. Suppl.* 121, 19–22. doi: 10.1007/978-3-319-18497-5_4

Zhang, J., Reedy, M. C., Hannun, Y. A., and Obeid, L. M. (1999). Inhibition of caspases inhibits the release of apoptotic bodies: Bcl-2 inhibits the Initiation of formation of apoptotic bodies in chemotherapeutic agent-induced apoptosis. *J. Cell Biol.* 145, 99–108. doi: 10.1083/jcb.145.1.99

Conflict of Interest: The authors declare that the research was conducted in the absence of any commercial or financial relationships that could be construed as a potential conflict of interest.

frontiers
in Cell and Developmental Biology

REVIEW
published: 12 March 2021
doi: 10.3389/fcell.2021.630242

Coronavirus-Induced Host Cubic Membranes and Lipid-Related Antiviral Therapies: A Focus on Bioactive Plasmalogens

Yuru Deng[1]* *and Angelina Angelova*[2]

[1] *Wenzhou Institute, University of Chinese Academy of Sciences, Wenzhou, China,* [2] *Université Paris-Saclay, CNRS, Institut Galien Paris-Saclay UMR 8612, Châtenay-Malabry, France*

Edited by:
Allen Liu,
University of Michigan, United States

Reviewed by:
Undurti Narasimha Das,
UND Life Sciences LLC,
United States
Miguel A. Martín-Acebes,
Instituto Nacional de Investigación y Tecnología Agroalimentaria (INIA),
Spain

***Correspondence:**
Yuru Deng
dengyr@wibe.ac.cn

Specialty section:
This article was submitted to Cellular Biochemistry,
a section of the journal
Frontiers in Cell and Developmental Biology

Received: *17 November 2020*
Accepted: *22 February 2021*
Published: *12 March 2021*

Citation:
Deng Y and Angelova A (2021) Coronavirus-Induced Host Cubic Membranes and Lipid-Related Antiviral Therapies: A Focus on Bioactive Plasmalogens.
Front. Cell Dev. Biol. 9:630242.
doi: 10.3389/fcell.2021.630242

Coronaviruses have lipid envelopes required for their activity. The fact that coronavirus infection provokes the formation of cubic membranes (CM) (denoted also as convoluted membranes) in host cells has not been rationalized in the development of antiviral therapies yet. In this context, the role of bioactive plasmalogens (vinyl ether glycerophospholipids) is not completely understood. These lipid species display a propensity for non-lamellar phase formation, facilitating membrane fusion, and modulate the activity of membrane-bound proteins such as enzymes and receptors. At the organism level, plasmalogen deficiency is associated with cardiometabolic disorders including obesity and type 2 diabetes in humans. A straight link is perceived with the susceptibility of such patients to SARS-CoV-2 (severe acute respiratory syndrome-coronavirus-2) infection, the severity of illness, and the related difficulty in treatment. Based on correlations between the coronavirus-induced modifications of lipid metabolism in host cells, plasmalogen deficiency in the lung surfactant of COVID-19 patients, and the alterations of lipid membrane structural organization and composition including the induction of CM, we emphasize the key role of plasmalogens in the coronavirus (SARS-CoV-2, SARS-CoV, or MERS-CoV) entry and replication in host cells. Considering that plasmalogen-enriched lung surfactant formulations may improve the respiratory process in severe infected individuals, plasmalogens can be suggested as an anti-viral prophylactic, a lipid biomarker in SARS-CoV and SARS-CoV-2 infections, and a potential anti-viral therapeutic component of lung surfactant development for COVID-19 patients.

Keywords: plasmalogen, cubic membrane, coronavirus, virus-host interaction, TEM, COVID-19

INTRODUCTION

All seven coronaviruses capable of infecting humans, including severe acute respiratory syndrome-coronavirus-2 (SARS-CoV-2), severe acute respiratory syndrome coronavirus (SARS-CoV), Middle East respiratory syndrome coronavirus (MERS-CoV), human coronavirus OC43 (HCoV-OC43), human coronavirus 229E (HCoV-229E), human coronavirus HKU1 (HCoV-HKU1), and human coronavirus NL63 (HCoV-NL63), employ lipid-binding domains for viral entry into host cells, intracellular lipid membrane modifications and host lipid reservoirs for viral replication and proliferation (Knoops et al., 2008; Miller and Krijnse-Locker, 2008; Ulasli et al., 2010; Oudshoorn et al., 2017; Abu-Farha et al., 2020). Lipids play an essential role during viral infection involving membrane fusion of virus to host cell, viral internalization through receptor-mediated or lipid-microdomain-mediated endocytosis, viral replication and viral exocytosis (Heaton and Randall, 2011; Belouzard et al., 2012; Li, 2016; Alsaadi and Jones, 2019). **Figure 1** presents an earlier scheme about the viral entry and the replication cycle during coronaviruses infection. An emphasis is given on the locations of the membrane interactions, namely the endoplasmic reticulum (ER) from where double-membrane vesicles (DMV) and endoplasmic reticulum Golgi intermediate compartments (ERGIC) are generated. SARS-CoV-2 virus also enters the targeted host cell via endocytosis and fusion of the viral membrane with the host cell membrane.

Apart from endocytosis, coronaviruses such as SARS-CoV-2 can infect cells through direct fusion with the plasma membrane after activation of the human transmembrane protease serine 2 (TMPRSS2) (Li, 2015; Lukassen et al., 2020; Wan et al., 2020). The TMPRSS2 protein is essential for the viral infectivity by facilitating virus-cell membrane fusion through ACE2. The membrane fusion process between viral and host cells is a crucial step during coronavirus infection (Goldsmith et al., 2004; Wu et al., 2012). After binding of the surface-exposed spike protein trimer of SARS-CoV-2 virus to its high affinity receptor angiotensin-converting enzyme 2 (ACE2) in the host membranes, the viral entry occurs through fusion of glycoprotein and remodeling of host cell membranes (Li et al., 2003, 2005; Li, 2015; Wan et al., 2020). The membrane fusion has been considered to be several fold more efficient than endocytosis during viral infection. The role of lipid membrane properties in this process have not been examined in details. Membrane fusion of SARS-CoV and of SARS-CoV-2 results in RNA release into the cytoplasm of host cell followed by viral replication (Alsaadi and Jones, 2019).

The (+)ssRNA viruses exploit diverse intracellular membranes in host cells in order to assemble RNA replication complexes (Stapleford and Miller, 2010; Heaton and Randall, 2011) through creating compartments for viral genome amplification. Lipids from host cells are used for generation of lipid membrane envelope shape called double-membrane vesicles (DMV) (**Figure 1**). Coronavirus-induced DMVs are formed by protrusion and budding of the endoplasmic reticulum (ER) cisternae followed by the detachment of closed vesicular objects (Oudshoorn et al., 2017; Zhang et al., 2020). The organelle-like membranous replicative structures serve as sites of viral RNA synthesis. Of interest, they are generated through topological transitions and curvature changes of the ER membranes. DMVs have been observed upon remodeling of convoluted membranes or reticulovesicular networks occurring after deformation and compartmentization of the continuous ER membranes (Knoops et al., 2008; Oudshoorn et al., 2017; Snijder et al., 2020; Zhang et al., 2020).

During SARS-CoV-2 virus life, the S-protein adopts closed and open conformations (Yan et al., 2020). High resolution structural studies of the receptor-binding domains (RBD) of coronavirus S proteins have established that they involve pockets of a tube-like shape and a size, which matches that of a free fatty acid molecule when in a closed conformation of S protein (Yan et al., 2020). Several studies have supported the evidence that lipid-binding domains in virus proteins are essential for virus replication (Stapleford and Miller, 2010; Jeon and Lee, 2017; Yan et al., 2020). Moreover, it has been demonstrated that viral proliferation requires the increased fatty acid and cholesterol biosynthesis as well as release of free fatty acids from lipid droplets (Su et al., 2002; Miller and Krijnse-Locker, 2008; Heaton et al., 2010; Heaton and Randall, 2010; Yin et al., 2010; Jeon and Lee, 2017). An exogenous supply of linoleic acid (LA) and arachidonic acid (AA) has been shown to inhibit the viral replication of MERS-CoV and HCoV-229E (Yan et al., 2019). LA and AA are polyunsaturated omega-6 fatty acids, which modulate the activity of enzymes including membrane receptor proteins and ion channels of the host cells (Das, 2018; Das, 2020a,b,c,d, 2021).

A free-fatty-acid-binding pocket in the locked structure of SARS-CoV-2 spike protein has been revealed by cryo-EM analysis (Yan et al., 2020). The cryo-EM image of SARS-CoV-2 spike (S) glycoprotein has indicated that the receptor binding domains entrap linoleic acid (LA) in composite binding pockets present also in the revealed 3D structures of SARS-CoV and MERS-CoV coronaviruses. It has been emphasized that free-fatty-acid binding pocket resembles a bent tube, which well fits the size and shape of linoleic acid (LA) (Yan et al., 2020). LA is a metabolic precursor of AA, which mediates host defensive inflammatory response. The ability of SARS-CoV-2 to sequester LA in the binding pockets has been suggested as a tissue-independent mechanism in coronavirus infection, which leads to host inflammation process. Tight LA binding can stabilize the locked conformation of the S-protein in SARS-CoV-2 coronavirus, which may lead to diminished interaction with host ACE2 receptor.

Coronavirus infection modifies both lipid composition and membrane structure, topology and trafficking of the host cells in order to ensure virus particle replication and proliferation. Thus, host lipid biogenesis is crucial for the viral life cycle and replication. Host cell lipid alterations upon coronavirus infection have been analyzed by ultra-high-performance liquid chromatography (UPLC) and mass spectrometry (MS)-based lipidomics approach (Yan et al., 2019). It has been affirmed that viral infection re-programs host lipid metabolism for the purposes of viral proliferation (Schoggins and Randall, 2013). Glycerophospholipids and fatty acids (FAs) have been found to be significantly upregulated in HCoV-229E-infected host cells. HCoV-229E viral infection has increased the levels of lyso-phospholipids [lysoPCs (16:0/0:0) and lysoPEs (16:0/0:0)] and also unsaturated/saturated FAs arachidonic acid (AA), linoleic acid (LA), palmitic acid (PA), and oleic acid (OA) (Yan et al., 2019). For coronaviruses, the LA-AA metabolic pathway is indispensable for host lipid remodeling (Zaman et al., 2010) and has been highlighted as a niche for therapeutic interventions (Yan et al., 2020).

The possibilities of targeting host lipid metabolism and host membrane trafficking in order to inhibit the viral cycle have

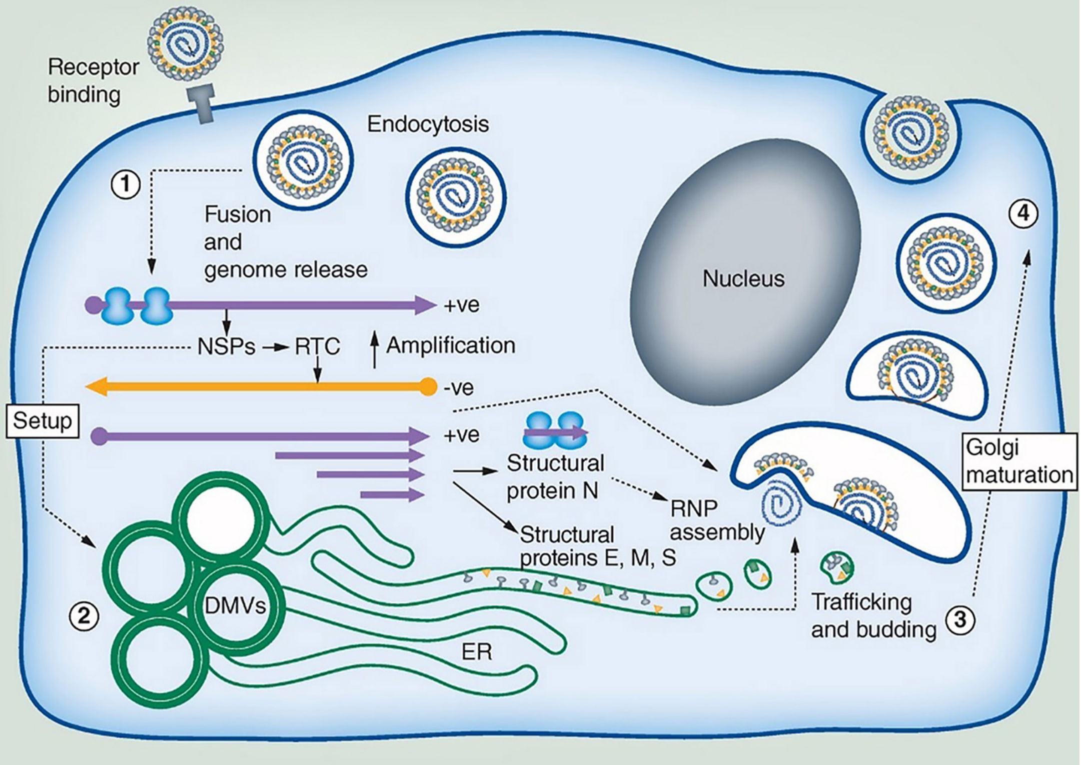

FIGURE 1 | Coronavirus replication cycle highlighting areas where membrane interaction takes place (ER, Endoplasmic reticulum; DMV, Double-membrane vesicles; ERGIC, Endoplasmic reticulum Golgi intermediate compartments). SARS-CoV-2 viral particles consist of four proteins: S ("Spike"), M ("Membrane"), E ("Envelope"), and N ("Nucleocapsid"). The pathway of membrane interactions involves: (1) Viral internalization through binding of the viral spike (S) protein to the membrane protein receptor as human angiotensin-converting enzyme 2 (ACE2). The coronavirus particle enters the host cell by receptor-mediated endocytosis followed by RNA release and translation into virus polyproteins, which encode for non-structural proteins (NSPs). (2) NSPs stimulate the production of DMV compartments and the formation of replication transcription complexes (RTC). Translation of the structural proteins (M, E, and S) occurs in the ER membrane organelles. (3) Coronavirus assembly occurs in the intermediate compartment between the ER and ERGIC. The protein cargos migrate through Golgi stacks resulting in new virus particles that are embedded in vesicles (4). These vesicles can further fuse with the plasma membrane and egress. Reprinted from Alsaadi and Jones (2019) with permission.

been intensely discussed recently (Abu-Farha et al., 2020; Das, 2020a,b,c,d, 2021; Glebov, 2020; Xiu et al., 2020). Such approach is much less susceptible to the development of viral resistance as compared to the strategies focusing on viral mutations. Targeting lipid metabolism thus has been suggested as an alternative antiviral strategy (Das, 2020a,b,c,d, 2021). **Figure 2** presents the advances in antiviral drug development including (i) inhibition of fatty acid and cholesterol synthesis, and (ii) inhibition of viral entry, membrane fusion, or endocytosis.

Of interest, cholesterol is involved in multiple steps of the coronavirus life cycle, and therefore targeting cholesterol has been suggested as an antiviral strategy (Abu-Farha et al., 2020). Cholesterol is well distributed in the microdomains of cell membranes. Considering that microdomains are implicated in coronavirus-host membrane interactions, drugs that alter microdomain formation and composition have been tested in antiviral approaches. An example of a drug with antiviral activity, which targets lipid metabolism, is statin. It is well known that statin impairs the biosynthetic pathway of cholesterol. As an inhibitor of cholesterol synthesis, statin has been considered as a generic drug against SARS-CoV-2 and other related viruses, among other agents that are specific for inhibition of fatty acid biosynthesis (**Figure 2**).

The development of therapeutic compounds that target the cell membrane has stimulated the emergent field of membrane lipid therapy (MLT) (Escribá et al., 2015). The new therapeutic approach aims at regulation of the lipids in pathological biomembranes (Escribá, 2017). Thus, the cellular membranes, rather than specific proteins alone, constitute the therapeutic targets. The rationale of this strategy accounts for the fact that coronaviruses cause extensive host cell membrane perturbations. Therefore, host membrane rearrangements have been considered as a target as a novel remedy for antiviral drug development.

An example of a drug for coronavirus membrane targeting is 2-hydroxyoleic acid (Minerval®). Minerval interacts with the membrane lipids and modifies the composition and structure of host cellular membrane (Prades et al., 2008). The drug influences the phospholipid packing in the polar region of lipid bilayers at the interface with contact proteins and increases the non-lamellar propensity of the lipid membrane assembly. The resulting increased bilayer fluidity may permit (i) deeper hydrophobic

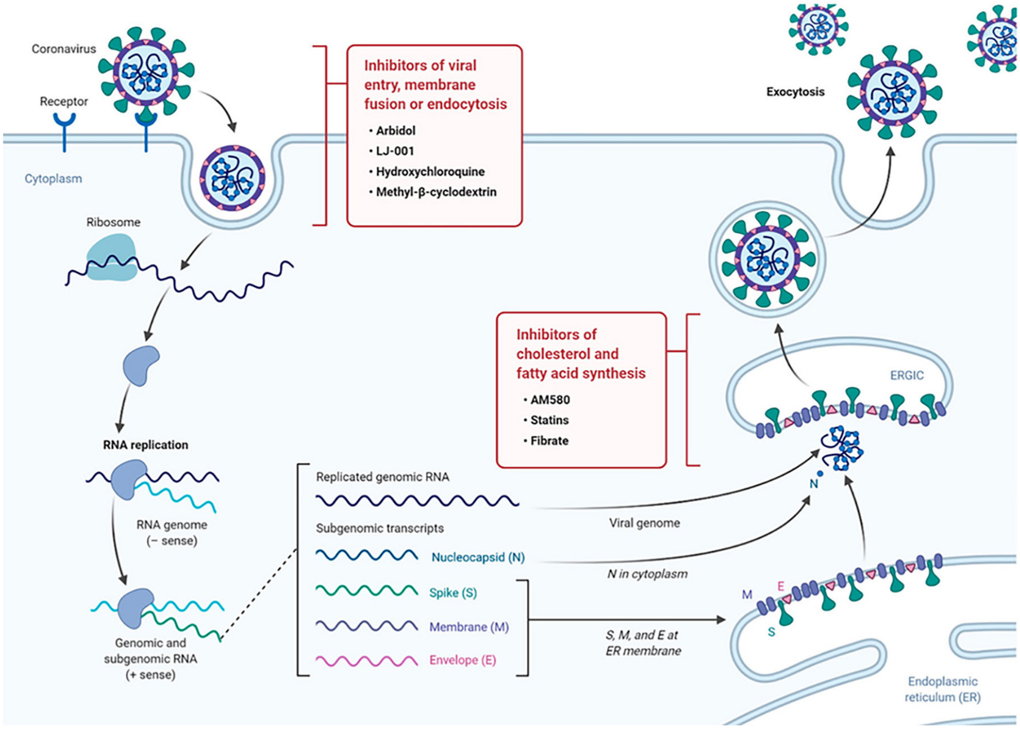

FIGURE 2 | Drug targeting strategies in viral infection exploiting the role of lipid metabolism. The scheme of the life cycle of SARS-COV-2 indicates the locations where lipid-modifying drugs may act as broad-spectrum antiviral compounds to inhibit viral entry, membrane fusion, endocytosis or host cholesterol and fatty acid biosynthesis. Reprinted from Abu-Farha et al. (2020) with permission.

regions of the membrane to interact with hydrophobic domains of peripheral proteins, or (ii) fatty acid moieties of phospholipids to protrude out of the bilayer plane. These structural effects can activate anchored enzymes such as PKC and sphingomyelin synthase involved in the lipid metabolism process.

Although detergents and detergent-based disinfectants may permeabilize the lipid membrane shell of coronavirus by creating pores and thus destroy the virion, they cannot be used as antiviral drugs in humans because they have the risks of causing death of the patients due to the massive destruction of cell membranes. At variance, antiviral lipids may alter the membrane properties and trafficking as well as affect signaling and intracellular transport dynamics, which should be explored as antiviral strategies.

Membrane folding and formation of three-dimensional (3D) lipid membrane topologies can be provoked by changes in the membrane lipid composition, protein clustering, bilayer bending caused by embedded or anchored proteins, or lipid membrane curvature alteration under the influence of environmental factors (Almsherqi et al., 2006). Whereas lipids of a cylinder-like shape (like the typical glycerophospholipids) favor the formation of lamellar structures, lipids of a truncated-cone molecular shape tend to form curved membrane assemblies such as bicontinuous cubic, bicontinuous sponge or inverted hexagonal structures (Angelova et al., 2021). Among them, cubic membranes are characterized by periodic structural arrangement of bicontinuous lipid bilayers organized in cubic lattice networks (**Figure 3**, top panel).

Bilayer lipid membranes may rearrange into 3D cubic membranes under stress conditions, which correspond to either altered lipid metabolism or protein overexpression (Almsherqi et al., 2006) in disease states as well as other types of environmental stress including viral infection (Deng et al., 2010), pH changes, presence of ions or solutes of increased concentrations, temperature changes, light, electric field, *etc*. (Almsherqi et al., 2009). Out-of-plane membrane shape deformations of interconnected bilayers have been termed convoluted membranes (Knoops et al., 2008; Oudshoorn et al., 2017; Snijder et al., 2020; **Figure 3**, bottom panel). Formation of cellular cubic membranes or convoluted membranes can be induced through reprogrammed lipid metabolism, altered lipid-protein interactions or by specific protein-protein interactions. Such non-lamellar structures are considered as transient states associated with the membrane bending, instabilities and rearrangement caused by the non-lamellar phase transition.

OPEN QUESTIONS IN THE CURRENT FOCUS

Accumulating evidence suggests that lipid treatment of virus-infected cells is a strategy for SARS-CoV-2 inhibition (Das, 2020a,b,c,d, 2021). Whereas the role of different phospholipid and fatty acid types has received prior attention in the pathology of cardiometabolic disorders, obesity, and type 2 diabetes, the

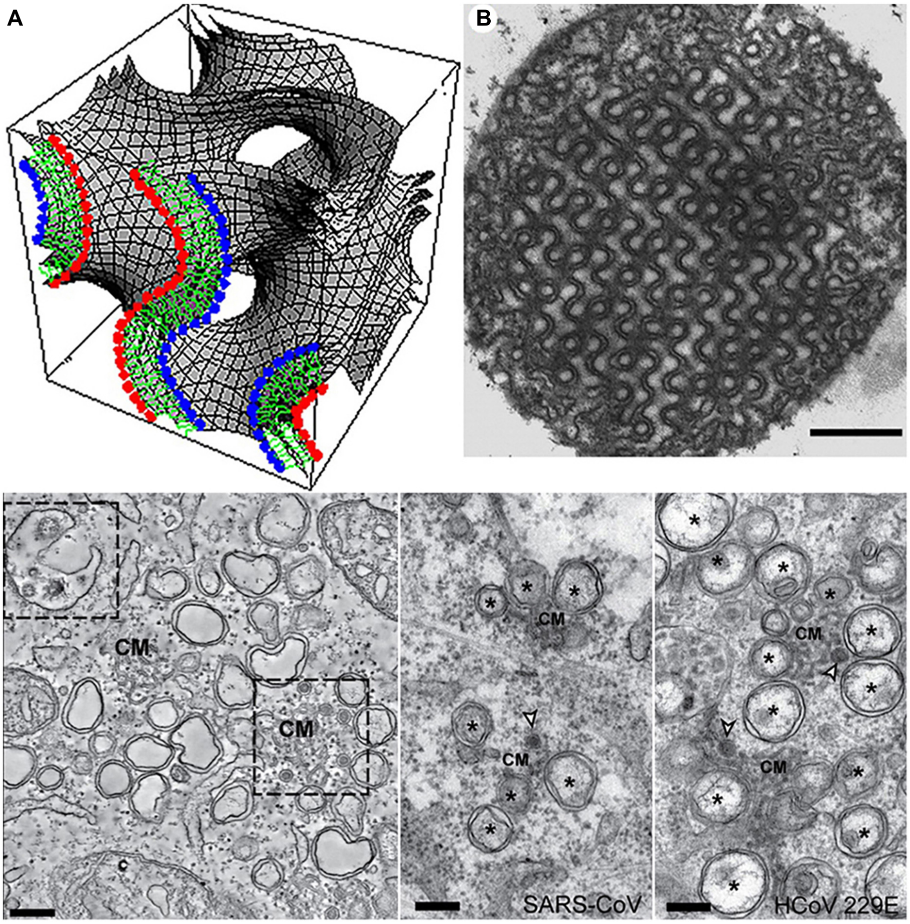

FIGURE 3 | Top panel: Cubic membrane topology represented by a mathematical model of the lipid bilayer organized on a 3D cubic lattice **(A)** and 2D-projected transmission electron microscopy (TEM) image of cubic membranes found in the mitochondria of 10-day starved ameba Chaos cells **(B)**. Scale bar: 500 nm. Reprinted from Deng and Almsherqi (2015) with permission. Bottom panel: TEM images of interconnected convoluted membrane structures (CM) induced by MERS-CoV infection in mammal Huh7 cells (left) and SARS-CoV and HCoV-229E coronavirus induced convoluted membranes (CM), double-membrane vesicles (DMV), and double-membrane spherules (middle and right). Scale bars: 250 nm. Reprinted from Snijder et al. (2020) with permission.

question regarding how to exploit the individual lipid classes against coronavirus SARS-CoV-2 entry and replication is still at an initial stage of comprehension. Arachidonic acid and other polyunsaturated fatty acids, as well as their derived metabolites, have been proposed to serve as antiviral molecules to inactivate the enveloped viruses and inhibit their proliferation (Das, 2020a,b,c,d, 2021). However, are there other antiviral lipid species to offer the options for the treatment?

Here we focus on the special phospholipid class of “plasmalogen,” the bioactive molecules as antiviral prophylactics and potential constituents of combination treatments against COVID-19. Plasmalogens are special ether phospholipids that are critical for cell membrane integrity in terms of structure and function. In addition to their role as key membrane components, they are involved in the regulation of cholesterol homeostasis and macrophage phagocytosis in addition to immunomodulation (**Figure 4**). Moreover, their antioxidant properties may determine the outcome of host illness during viral infections. Biosynthesis of endogenous plasmalogens requires functional peroxisomes, the oxidative cell organelles in almost all the eukaryotes. The deficiency of plasmalogens implicated in cardiometabolic and multiple neurodegenerative diseases may render humans host susceptible to SARS-CoV-2 (COVID-19) and other similar viral infections (SARS-CoV or MERS-CoV).

The plasmalogen lipid type has received less attention in the comprehension of the coronavirus infection and therapy as compared to free fatty acids like linoleic acid (LA) and arachidonic acid (AA) (Das, 2020c; Yan et al., 2020). It is of current interest to explore how plasmalogens may participate in the stages of virus-host interaction process including: (1) viral entry host cells via non-receptor microdomain-mediated endocytosis pathways; (2) lipid-modulated host innate immune response; (3) virus-induced host membrane rearrangements, especially cubic membrane (CM) formation. Plasmalogen deficiency, due to impaired nutrition, stress and contemporary lifestyles, does not support host CM formation during viral infections. It will be emphasized here that induced host CM architectures may serve as an

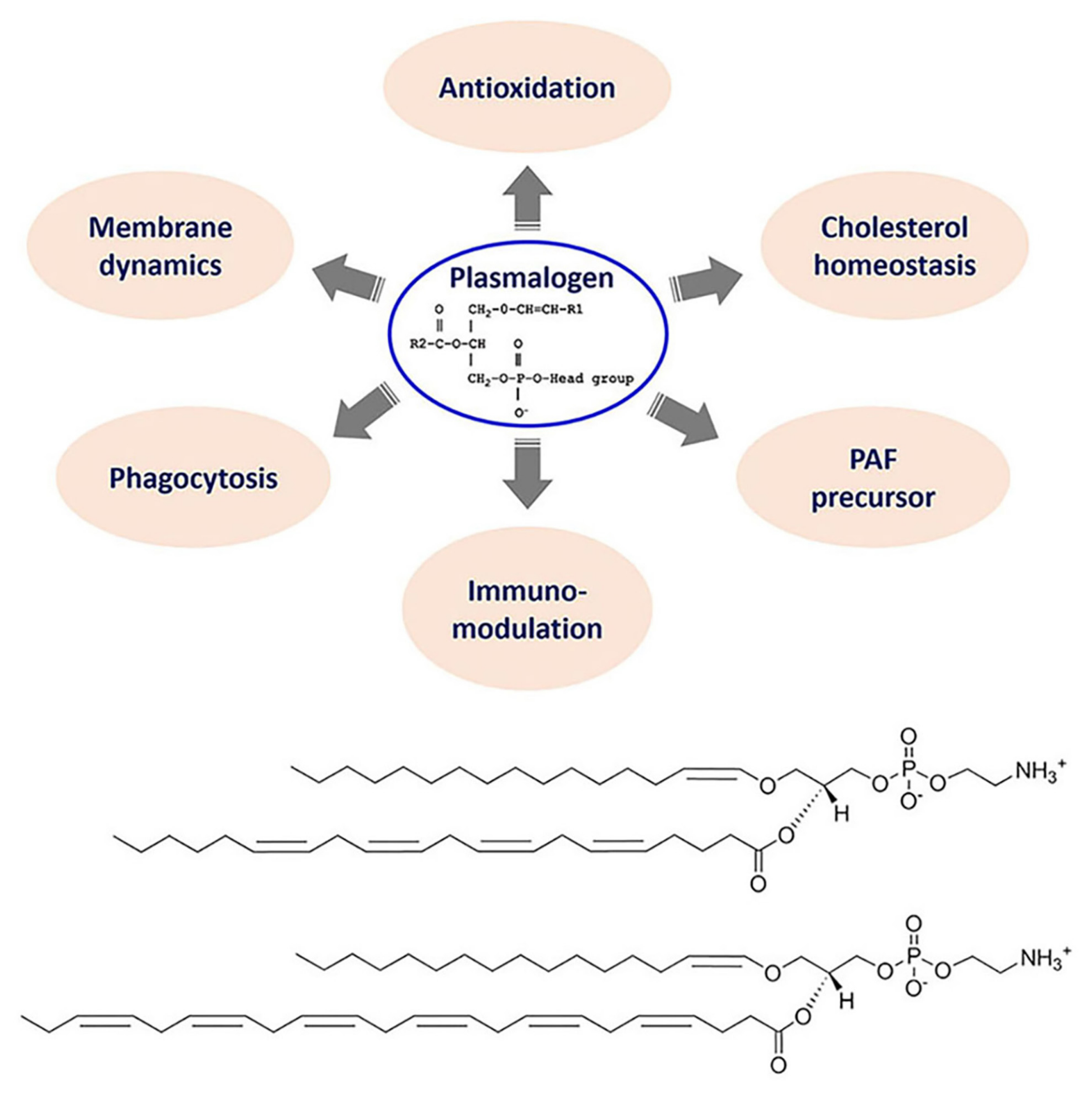

FIGURE 4 | Top panel: General chemical structure and multiple biological functions of bioactive plasmalogens. Bottom panel: Chemical structures of exemplary ether phospholipids (plasmalogens) involving arachidonic acid (AA) and docosahexaenoic acid (DHA) chains, *e.g.,* 1-(1Z-hexadecenyl)-2-arachidonoyl-sn-glycero-3-phosphoethanolamine [C16(Plasm)-20:4 PE] and 1-(1Z-hexadecenyl)-2-docosahexaenoyl-sn-glycero-3-phosphoethanolamine [C16(Plasm)-22:6 PE].

evolutionally conserved antioxidant defense system to favor viral proliferation in a controlled manner and also the fast return of host homeostasis.

Another question is whether a host response treatment approach to viral infections may essentially reduce the severity of COVID-19 illness and improve patient survival. In fact, the balanced immune and inflammatory response is the key for host to live and not to die after SARS-CoV-2 infection. The shift of virus-targeted therapies to host response treatment, especially lipid and membrane factors, might be an alternative solution for the host survival. The presented concept here is based on our previous opinion paper "Do viruses subvert cholesterol homeostasis to induce host cubic membranes?" (Deng et al., 2010). We further ask the questions: (i) What is the role of plasmalogens in the remodeling of host lipid membrane? and (ii) What would be the role of plasmalogens in antiviral therapy? Moreover, the potential applications of plasmalogen-preconditioning treatment and prophylaxis are discussed.

THE SIGNIFICANCE OF PLASMALOGEN LIPID CLASS

Plasmalogens constitute a class of ether phospholipids containing a fatty alcohol with a vinyl-ether bond at sn-1 position and a polyunsaturated fatty acid at sn-2 position of the glycerol backbone (**Figure 4**). Compared to their diacyl counterparts, plasmalogens appear to be highly fusogenic lipids (Glaser and Gross, 1995) enriched in lipid microdomains (Pike et al., 2002) and tend to form more densely packed and thicker bilayer membranes (Rog and Koivuniemi, 2016). Plasmalogens are significant structural components of various subcellular organelle membranes including nucleus, endoplasmic reticulum (ER), post-Golgi network and mitochondria (Honsho et al., 2008). Plasmalogens are determinants in membrane dynamics and trafficking. A recent structural study has revealed that they can strongly influence the membrane thickness and curvature (Angelova et al., 2021). They also serve as endogenous antioxidants, protect against ROS, and prevent lipoprotein oxidation.

Plasmalogens are abundant in human brain, heart, kidney, lung, skeletal muscle and immune cells (Braverman and Moser, 2012). Lipidomic profiling of multiple human cohorts have identified negative associations between plasmalogens and obesity (Weir et al., 2013), type 2 diabetes (Meikle et al., 2013) and cardiovascular diseases (Meikle et al., 2011), supporting the concept of the vital role of plasmalogens in the prevention of cardiometabolic diseases (Paul et al., 2019).

Plasmalogens are prominent for regulation of cholesterol homeostasis (Honsho et al., 2015), which has previously attracted great attentions as a key host factor during multiple viral infections (Deng et al., 2010). Having both enriched in lipid microdomains (Pike et al., 2002), the existence of a metabolic relationship between cholesterol and plasmalogen is therefore directly emergent. Fedson et al. (2020) proposed the prophylaxis use of statins (generic drug to lower cholesterol) for the previous epidemic and current pandemic including influenza (Fedson, 2006), Ebola (Fedson, 2016) and COVID-19 (Fedson et al., 2020). Statin drugs display anti-inflammatory and immunomodulatory effects in the host response treatment approach. Despite that the potential use of plasmalogens in achieving cholesterol homeostasis has been proposed as an alternative to statin therapy (Mankidy et al., 2010), further studies are required toward the translation of plasmalogens into future clinical applications.

Plasmalogens, by virtue of their vinyl ether bond and enrichment in PUFAs moieties (AA and DHA chains), play vital roles in many cellular processes. They provide unique membrane structural attributes to potentially modulate lipid-associated signaling pathways and protecting important macromolecules (nucleic acids and lipids) from oxidative damages (Almsherqi et al., 2008; Deng and Almsherqi (2015). Their metabolic products of DHA and AA derived from physiological breakdown of plasmalogens via phospholipase A2 (PLA2) have been shown to increase the expression of inflammatory cytokines, which also increase the activity of plasmalogen-specific PLA2 (Farooqui, 2010). The neuroinflammatory modulation of plasmalogens has been reported in a couple of studies (Ifuku et al., 2012; Katafuchi et al., 2012).

VIRAL ENTRY DEPENDS ON HOST MEMBRANE LIPID COMPOSITIONS: A FOCUS ON PLASMALOGENS

Viral infection initiates with the virus particles crossing the host plasma membrane, often via receptor-mediated endocytosis pathway (**Figure 1**). However, an alternative non-receptor lipid-microdomain-mediated endocytosis and membrane fusion process may proceed as well. The non-specific lipid-mediated viral entry may possibly explain the puzzling zoonotic viral transmission via jumps of pathogenic viruses between different species (*e.g.,* from bat to human). Even though virions mainly enter host cells through specific proteinaceous receptors, such as ACE2/TMPRSS2 in the case of SARS-CoV-2, the strengthened or weakened attachment and entry of viruses depend on the lipid composition of viral envelopes in addition to host plasma membranes. Although plasmalogens similar to cholesterols have been found to be enriched in membrane microdomains (Pike et al., 2002), the scarce plasmalogen research somehow impedes our understandings of this special lipid class and the potentially significant roles they may act in virus-host interactions.

The increased levels of plasmalogens have been detected in the serum of ZIKA infected subjects (Queiroz et al., 2019) and chronic HBV patients (Schoeman et al., 2016). The strong enrichment of plasmalogens has been noticed in virion lipidome of human cytomegalovirus (Liu et al., 2011) and HIV (Brugger et al., 2006). Moreover, the virus-induced alterations in both plasmalogen levels and peroxisome activity have been examined at host level (Satoh et al., 1990; Farooqui and Horrocks, 2001; Dixit et al., 2010; Odendall and Kagan, 2013; Martin-Acebes et al., 2014).

The endogenous biosynthesis of plasmalogens requires functional peroxisomes in almost all the eukaryotes. Peroxisomes are the important host organelles where certain viral replication may take place (Cook et al., 2019). Peroxisome plasticity in virus-host interaction and its role as double-edged sword in multiple viruses' infections have attracted great attention recently. The increased levels of plasmalogens in the serum of ZIKA (flavivirus) viral infected subjects suggested a strong link between ZIKA virus life cycle and host peroxisomes. The observation that flaviviruses induce peroxisome-mediated lipid alterations in the host cells may further explain the established upregulation of plasmalogens in the serum of ZIKV infected patients (Martín-Acebes et al., 2019; Queiroz et al., 2019). Meanwhile, plasmalogen PC was also reported to play a pivotal role in influenza virus infection (Tanner et al., 2014).

CORONAVIRUS-INDUCED HOST CUBIC MEMBRANE FORMATION FOR BOTH VIRUS AND HOST FITNESS

Severe acute respiratory syndrome-coronavirus infection induces multiple alterations of the lipid membrane architecture in the host cells. Remodeling of endoplasmic reticulum (ER) cisternae upon coronavirus infection starts with detachment of closed vesicular objects called double-membrane vesicles (DMV) (Alsaadi and Jones, 2019; Zhang et al., 2020). In addition to the generation of DMV lipid envelopes (referred to as coronavirus replication organelles), the host membrane may adopt 3D topologies called "convoluted membranes" (Knoops et al., 2008; Zhang et al., 2020). They form through fusion of multiple DMV or other type of structural transitions (Knoops et al., 2008). Examples of such host membrane rearrangements are illustrated by the transmission electron microscopy (TEM) images in **Figure 5**.

In the absence of a clear appreciation of the 3D nature of cytomembraneous inclusions observed in the TEM micrographs of virus-induced host membrane complexes, various terminologies have been used to denote the formation of 3D non-lamellar assemblies of folded membranes (Almsherqi et al., 2005). For instance, "tubule-crystalline inclusions" have been described in HCV-infected liver, "convoluted membraneous mass" in viral St. Louis Encephalitis, and "tubule-reticular structures (TRS)" in AIDS as well as in multiple coronavirus infections including SARS-CoV infected Vero cells (Goldsmith et al., 2004; Almsherqi et al., 2005). TRS has been considered as a specific ultrastructural marker of AIDS in various organs (Maturi and Font, 1996). Most of the time, the 3D membrane rearrangements, observed also in MERS-CoA infected Huh-7 cells (Oudshoorn et al., 2017) and coronavirus MHV infected Hela cells (Ulasli et al., 2010; **Figure 5**) have been termed "Convoluted Membranes" (Knoops et al., 2008; Oudshoorn et al., 2017; Snijder et al., 2020; Zhang et al., 2020). They have been unified by the name "Cubic Membranes" in the last decade (Deng et al., 2010; Deng and Almsherqi, 2015).

Using the direct template matching method in electron microscopy, we have characterized TEM micrographs of host membrane rearrangements, induced by multiple viral infections, as Cubic Membranes (CM) (Almsherqi et al., 2006; Deng et al., 2010). Although the molecular mechanisms behind viral-induced host CM remains unclear, CM was proposed to act as antioxidant defense system in ameba *Chaos* cell model (Deng and Almsherqi, 2015; Deng et al., 2017). This concept fairly supports our current hypothesis that virus-induced CM may not only benefit for viral proliferations in terms of viral assembly and egress (**Figure 5A**), but CM may also help the return of host homeostasis by mitigating the oxidative damages (Deng and Almsherqi, 2015) during viral infection to further promote cell survival (Chong et al., 2018).

In addition to the antioxidant properties of CM nanostructures, plasmalogens pre-conditioning treatment or supplementation may determine the degree of host CM abundance during viral infections. This hypothesis is based on our findings from ameba cell model system (Chong et al., 2018). We have previously asked an intriguing question whether viruses subvert cholesterol homeostasis to induce host CM (Deng et al., 2010). At that time, we were not aware of the emergent links of plasmalogens in multiple viruses' life cycle and the corresponding host CM formation. At present, we highlight the close relationship between plasmalogen and cholesterol metabolism as both species are enriched in membrane rafts microdomains. These microdomains and their associated lipid molecular types might have been overlooked in the process of viral entry and host immune signaling. Plasmalogen pre-conditioning is indispensable in ameba CM formation under cell starvation stress conditions, and it may also apply to host stress response during coronavirus infections. Therefore, the role of CM in the virus-host interaction and balance, host cell response and survival appear of significance.

PEROXISOME-MEDIATED ANTIVIRAL IMMUNE SIGNALING: A FOCUS ON PLASMALOGENS

The host response to infection may turn out to be the key determinant of pathogenesis of emergent infectious diseases including the current COVID-19 pandemics. The first step of virus life cycle is to enter the host cells by crossing the plasma membrane, where the lipid composition might be very crucial. Upon viral infections in humans, peroxisomes act as vital immune signaling organelles, aiding the host by orchestrating antiviral signaling (Cook et al., 2019). Peroxisomes are critical host organelles emerging as a double-edged sword during the progression of viral infections. These cellular organelles, that both host or kill pathogen, can make use of their functions to achieve host antiviral defense or to be hijacked to serve for viral proliferation (Karnati and Baumgart-Vogt, 2008).

The peroxisome was first recognized as a key subcellular signaling center upon the discovery of mitochondrial antiviral signaling (MAVS), an innate host immune response. MAVS, previously thought to be exclusive to the mitochondria, mounts up a rapid antiviral reaction. However, combined with the known detoxification functions of peroxisomes, the recognition of peroxisomal MAVS has resulted in the realization of peroxisomal role in host defense as an antiviral signaling organelle. This was supported by the studies of human cytomegalovirus (HCMV) and herpes simplex type 1 (HSV-1) infections, along with the discovery that these viruses promotes host peroxisome biogenesis during infections (Beltran et al., 2018). Certain cellular lipids, including very-long-chain fatty acids (e.g., DHA) and ether lipids (e.g., plasmalogens), can only be synthesized in peroxisomes.

Plasmalogens, the peroxisome-synthesized lipids are intriguing candidates for various viral infection-induced cell processes, including the construction of viral envelopes, modulation of host cholesterol homeostasis, and maintenance of virus-host balance and fitness. With the knowledge that plasmalogens are enriched in HCMV virions, Liu et al. (2011) have proposed that peroxisomal lipid metabolism might be a general feature of enveloped virus infections. In support of

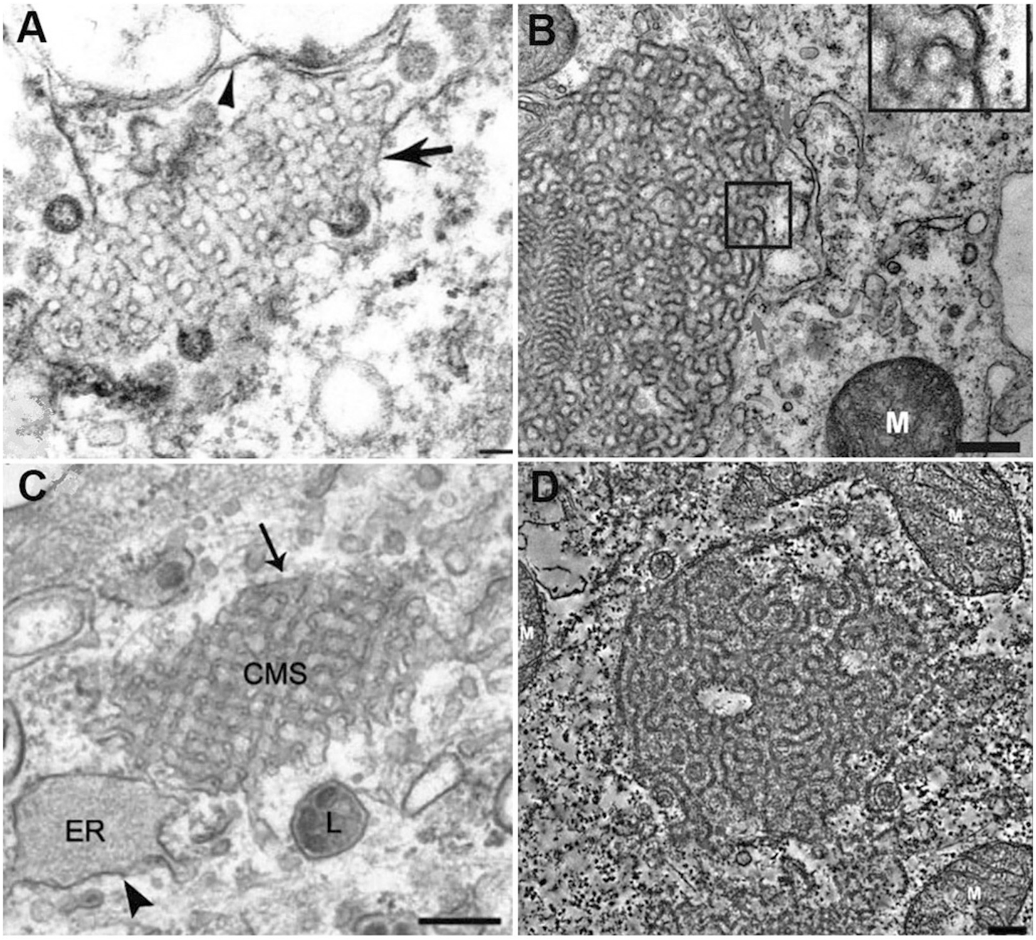

FIGURE 5 | Multiple examples of coronavirus-induced cubic membrane (CM) formation in the host cells. **(A)** SARS-CoV, 3d post-infection (p.i.) Vero-E6 cell with virus particles egress (Goldsmith et al., 2004) **(B)** MERS-CoV nsp3-6, 24h post-transfection, Huh-7 cell (Oudshoorn et al., 2017). **(C)** MHV-59, 8h p.i. HeLa-CEACAM1a cell (Ulasli et al., 2010); **(D)** SARS-CoV (nsp3 + nsp4), 24h post-transfection, 293T cell (Oudshoorn et al., 2017).

this, one study of influenza virus, another RNA virus, showed that host ether lipid metabolism was required and enhanced upon infection, and that peroxisome-derived plasmalogens were enriched in influenza virions (Tanner et al., 2014). Plasmalogen lipids are the key component of several enveloped viruses, including HCMV (Liu et al., 2011), WNV (Martin-Acebes et al., 2014), and influenza. We thus highly suspect that this may also apply to SARS-CoV-2. In this perspective, further lipidomic analysis of COVID-19 samples will be required for a more detailed picture.

THE ROLE OF PLASMALOGENS IN HOST IMMUNE RESPONSE DURING VIRAL INFECTION: A FOCUS ON MACROPHAGES

Macrophages, as the professional phagocytes of host immune system, are capable of detecting and clearing invading pathogens (e.g., viruses) and damaged cells through phagocytosis. Macrophages are essential in host innate immunity and tissue homeostasis in addition to inflammatory modulation and response. Plasmalogen deficiency in macrophages was associated with their reduced phagocytosis, and this reduction was significantly reversed when the cells were exposed to lyso-plasmalogen PE (Rubio et al., 2018). In parallel, restoration of plasmalogen level in macrophages also increased the number and size of lipid microdomains in the membranes of macrophages. The exogenous administration of plasmalogens was thus considered as a potential strategy to optimize the functions of macrophages.

A study on human monocyte to macrophage differentiation, performed by a bioinformatic approach combined with transcriptomic and lipidomic analyses (Wallner et al., 2014), has demonstrated that plasmalogen PE is a potential biomarker of immune system activation. The authors have further pointed out that the dysregulation of monocyte-macrophage differentiation is a hallmark of vascular and metabolic diseases and associated with persistent low grade of inflammation. In parallel, diminished plasmalogen levels have been observed in the obese subjects

(Wallner et al., 2014). All these findings have brought our deep interest to the potential link of host plasmalogen dysregulation and high morbidity and mortality of COVID-19 patients.

Another related ether lipid, such as platelet-activating factor (PAF), may participate in the severe pathology of COVID-19 pneumonia as well. PAF was the first intact phospholipid known to have messenger functions and a mediator of inflammation in the mechanism of human immune response (review see Lordan et al., 2019). PAF is powerful for the activation of human inflammatory cells at extremely low concentrations, which imparts a hormone-like character. PAF is present in many cell types, especially those involved in host defense such as platelets, endothelial cells, neutrophils, monocytes and macrophages. PAF has evolved as a part of protective mechanism in host innate defense system, and with a number of pro-inflammatory properties necessary for host protection from pathogenic insults. When produced in an uncontrolled manner, PAF may have extremely harmful effect, including blood clotting problem which has been reported in severe COVID-19 illness. The relation of PAF precursors to plasmalogen metabolites is indicated in **Figure 4** as a part of the ether lipid role overview.

The increased plasmalogen content may induce the formation of lipid rafts microdomains and further improve the recruitment, oligomerization, and interaction of receptors and signaling proteins involved in the phagocytosis of macrophages. Plasmalogens also reduce the non-lamellar-to-lamellar phase transition temperature, exhibiting a high propensity to form non-lamellar phase structures (Lohner et al., 1991). The non-lamellar structural intermediates are indeed essential for membrane fusion process. The increased abundance of plasmalogens carrying the polyunsaturated fatty acid moieties in the serum of ZIKA patients may explain its important implication in viral particle fusion with host cell membranes. On the other side, polyunsaturated AA and DHA fatty acids carried by plasmalogens are the substrate sources for generation of soluble lipid mediators, which participate in host immune signaling and inflammatory responses.

POTENTIAL ROLE OF PLASMALOGENS IN THE CYTOKINE STORM OBSERVED IN COVID-19 PATIENTS. INTERPLAY WITH A LIPID STORM

Cytokines are a diverse group of small proteins that are secreted by cells for the purposes of intercellular signaling and communication. They include interferons (IFNs), interleukins (ILs), chemokines, and tumor necrosis factors (TNFs). The multiple functions of cytokines span from control of cell proliferation and differentiation to immune and inflammatory responses, which are highly relevant to developing viral infections (Barry et al., 2000; Imashuku, 2002; Yokota, 2003; Jahrling et al., 2004; Huang et al., 2005) such as SARS-CoV-2 (COVID-19) (Castelli et al., 2020; Leisman et al., 2020; Mulchandani et al., 2020).

The devastating "cytokine storms" occurs when the host immune homeostasis is broken due to viral infection and inflammatory responses flaring out of control. They are associated with a wide variety of infectious and non-infectious diseases and may even be an unfortunate consequence of therapeutic intervention attempts. Increased inflammation and a cytokine storm characterize the COVID-19 cases by severe pneumonia that can decompensate to an acute respiratory distress syndrome (Castelli et al., 2020; Leisman et al., 2020; Mulchandani et al., 2020).

In addition to the recognized cytokine storm previously documented (Castelli et al., 2020; Leisman et al., 2020; Mulchandani et al., 2020), analyses of lung fluids of SARS-CoV-2-infected patients have indicated that a "lipid storm" also occurs. Using liquid chromatography combined with tandem mass spectrometry, a recent report has quantified several lung bioactive lipids and has evidenced that the "lipid storm" in severe SARS-CoV-2 infections involves both pro- and anti-inflammatory lipids (Archambault et al., 2020). Bronchoalveolar lavages of severe COVID-19 patients contained large amounts of the bioactive lipids prostaglandins (PGs), leukotrienes (LTs), and thromboxanes (TXs) (Archambault et al., 2020). The established increased oxidative bust in the lungs of severe COVID-19 patients has pointed out the importance of the lipid storm taking place in the lungs of pneumonia patients.

The role of plasmalogens in the cytokine and lipid storms remains to be experimentally elucidated. **Figures 6**, **7** summarize the pathways of plasmalogen turnover, remodeling and degradation, which help identifying the metabolites and the products that may trigger uncontrolled inflammatory responses.

Plasmalogens often carry PUFAs, which can be either of the omega-6 (pro-inflammatory) or of the omega-3 (anti-inflammatory) families (e.g., AA or EPA and DHA). Both types can be catalyzed by cyclooxygenase (PGs, TXs) and lipoxygenase (LTs) in the production of eicosanoids [prostaglandins (PGs), thromboxanes (TXs), and leukotrienes (LTs)] (**Figure 7**). The balance between these two families is important for the host immune homeostasis, which determines the potential development of undesired lipid storm. The controlled formation of eicosanoids is regarded as beneficial because it may help optimize cellular defensive reactions against the invading pathogens including SARS-CoV-2. However, excessive, uncontrolled production of eicosanoids is associated with the "lipid storm" (Archambault et al., 2020). Eicosanoid signaling is a pro-inflammatory component of innate immunity as the cytokine signaling. Unfortunately, lipid storm can be self-destructive in interplay together with the peptide-mediated cytokine storm. Devastating consequence may emerge in the lungs and spread to other tissues in the body of severe COVID-19 patients.

Plasmalogens, enriched in leukocytes, are one of the primary targets of hypochlorous acid (HOCl) due to the sensitivity of the vinyl ether bond to oxidative agents (**Figure 6**; Üllena et al., 2010; Braverman and Moser, 2012). The ether lipids, in contrast to their counterpart ester phospholipids, are the targets of HOCl generated by leukocyte myeloperoxidase as a part of the immune defense reaction (respiratory bust). The direct products, α-chloro fatty aldehyde and lysophospholipids, may produce a family

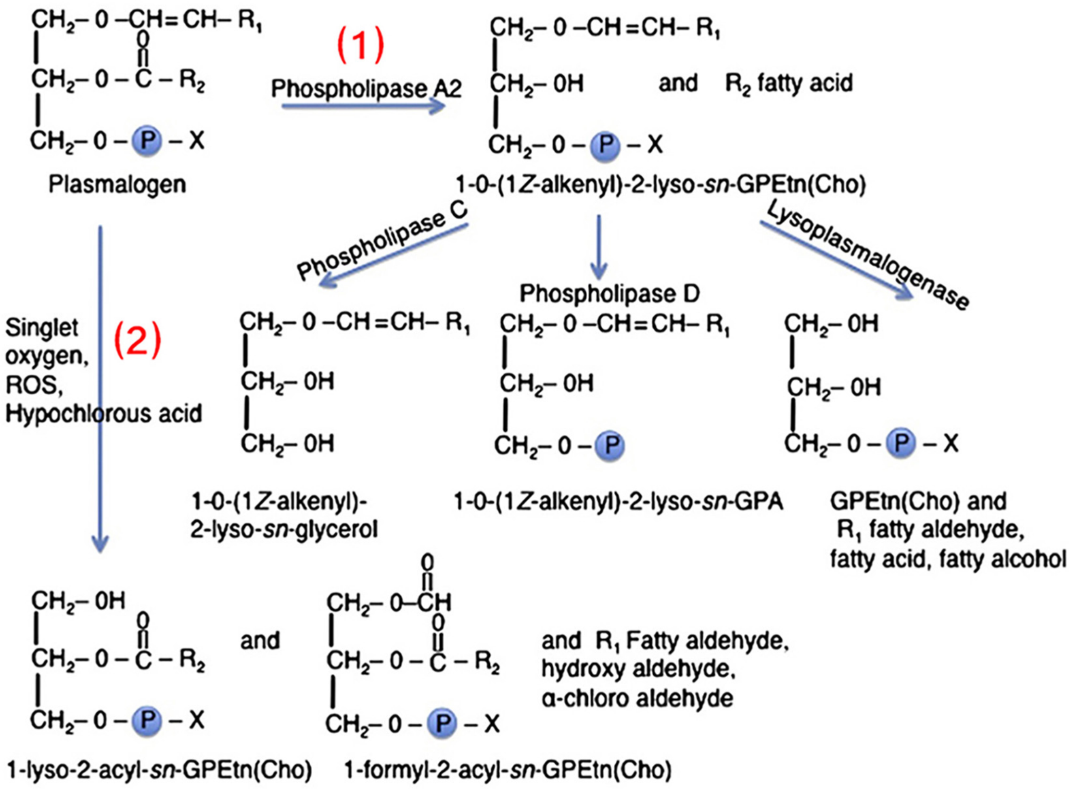

FIGURE 6 | Two pathways of plasmalogen turnover, remodeling and degradation: (1) Through phospholipase A2 (PLA2) and (2) through oxidative stress. Plasmalogens are one of the primary targets of HOCl due to sensitivity of the vinyl-ether bonds to oxidation. X denotes the polar head group, which is typically ethanolamine or choline. R1 denotes the carbon chain at the sn-1 position, and R2 at the sn-2 position. Reprinted from Braverman and Moser (2012) with permission.

of chlorinated lipids that can regulate inflammatory responses. Further inflammatory cascades may deplete the plasmalogen levels (Braverman and Moser, 2012).

In addition to this breakdown due to oxidative stress, plasmalogens can be hydrolyzed by phospholipase A2 (PLA2) into products like lyso-pPE and PUFAs (AA, EPA, or DHA) (Üllena et al., 2010). The lysophosphatidylethanolamine plasmalogen (lyso-pPE) has been identified as a self antigen for natural killer T cells (NKT cells). It is important for the development, the maturation, and the activation of iNKT cells in the thymus, which is vital for innate immunity (Facciotti et al., 2012; Ni et al., 2014). The lyso-pPE is very potent at low nanomolar concentrations and may induce cytokine release from freshly isolated iNKT cells. While this activity is important in immunomodulation, which has been considered as a sensor of inflammation, the proper stimulation of iNKT cells is significant for the protection against autoimmunity (Van Kaer et al., 2013).

To our knowledge, there are no reports on how PUFA metabolism (PGs, LTs, TXs) can be altered by plasmalogens in order to clarify their impact on cytokines. The essential PUFAs metabolism and its role in inflammation have been reviewed by Das (2019) with a special focus on eicosanoids [prostaglandins (PGs), leukotrienes (LTs), and thromboxanes (TXs)]. Eicosanoids and docosanoids are important signaling molecules produced by the oxidation of omega-6 arachidonic acid (AA) or other omega-3 PUFAs, eicosapentaenoic acid (EPA) and docosapentaenoic acid (DHA) from the cell membrane phospholipid pool. Das (2021) has drawn attention to the fact that pro-inflammatory metabolites like prostaglandin E2 (PGE2) and leukotrienes (LTs) (derived from AA) and anti-inflammatory lipoxin A4 (LXA4) as well as resolvins, protectins, and maresins (derived from EPA and DHA) facilitate the generation of M1 (pro-inflammatory) and M2 (anti-inflammatory) macrophages, respectively. Moreover, AA, PGE2, and LXA4 among others inhibit the synthesis of interleukin-6 (IL-6) and tumor necrosis factor-α (TNF-α) (Das, 2019, 2021).

Despite that eicosanoid and cytokine storms are not well characterized in coronavirus infection yet, published works indicate that lipid (eicosanoid and related bioactive lipid mediators) storm might occur before the cytokine storm (**Figure 8**). Coronavirus SARS-CoV-2 infection triggers endoplasmic reticulum (ER) stress response, which may be followed by subsequent eicosanoid and cytokine storms (Hammock et al., 2020). Targeting of the proinflammatory eicosanoids, including PGs, LTs, TXs, would be beneficial for diminishment of the ER stress. With the contribution of lipidomics, a better understanding of the eicosanoid storm,

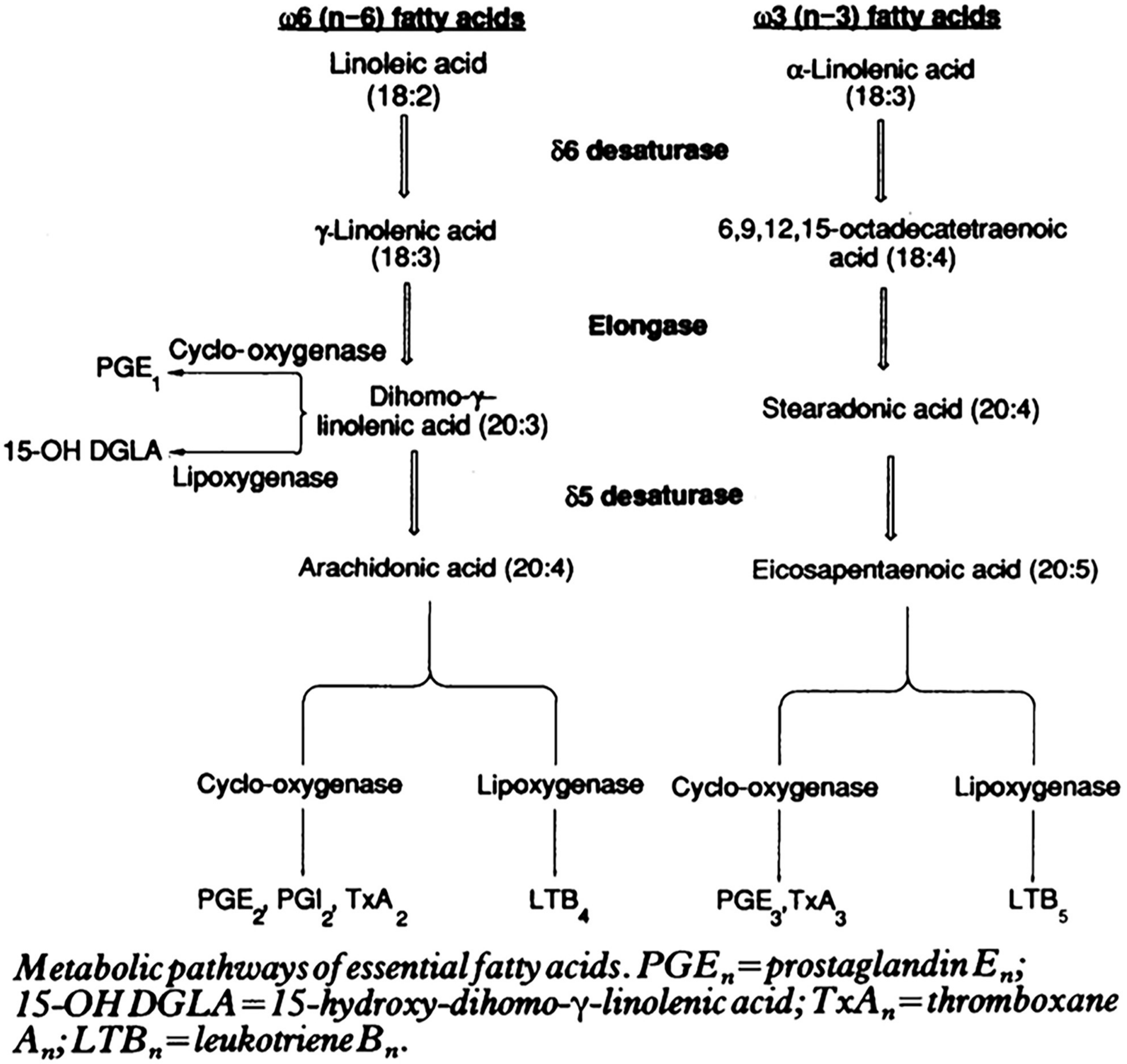

FIGURE 7 | Essential fatty acids in inflammation and potential "lipid storm" in severe COVID-19 patients. Scheme of eicosanoid and related bioactive lipid mediators production due to metabolic pathways of fatty acid alteration (eicosanoid related precursors). Reprinted from Zurrier (1991) with permission.

preceding the cytokine storm in severe inflammation (**Figure 8**), should provide insights toward new strategies for management of coronavirus infection.

Taken together, coronavirus infection is associated with both inflammation and metabolic disorders. Such disorders cause durable damage of subcellular organelles including mitochondrial defects and endoplasmic reticulum (ER) dysfunction (Hotamisligil, 2006). Mitochondrial defects and ER dysfunction are crucial in the activation of various inflammatory pathways and widespread inflammatory responses (**Figure 8**). **Figure 9** represents the impact of the lipid-mediated and cytokine-mediated metabolic and inflammatory cascades at the organelle level. In a further step, this impact should be considered at the lipid membrane level, where the plasmalogen lipid type plays an important role. Plasmalogens yielding docosanoids [bioactive oxygenated polyunsaturated fatty acids (22:6n-3) containing 22 carbons] with anti-inflammatory functions might be the key lipid components helping to inhibit the inflammation.

Regarding the potential role of plasmalogens in cytokine storm seen in COVID-19, we speculate that the host immune homeostasis is broken in response to coronavirus infections. However, with the sufficient level of membrane plasmalogens, it may support the host viral-induced CM formation (Deng et al., 2010). CM formation can lower the oxidative damage (Deng and Almsherqi, 2015; Deng et al., 2017) and promote the quick return of host immune homeostasis, otherwise the host may have

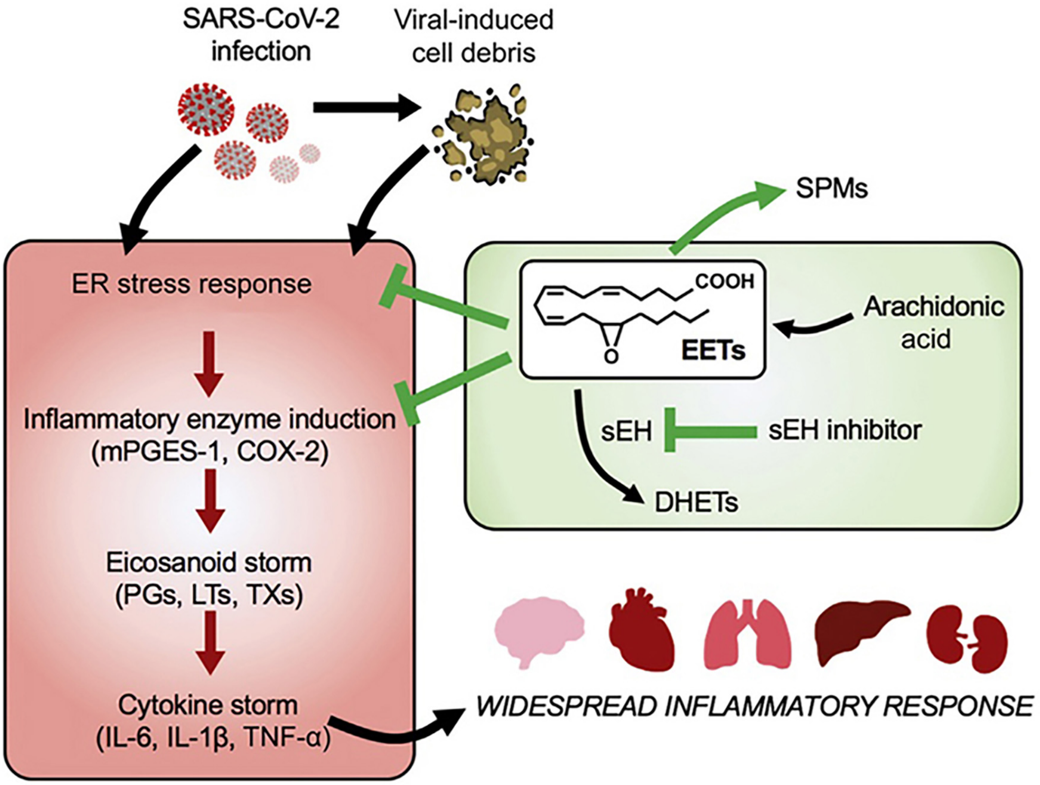

FIGURE 8 | Lipid (eicosanoid) storm may occur before the cytokine storm in SARS-CoV-2 infection. Eicosanoids are bioactive lipid mediators derived from oxygenated polyunsaturated fatty acids (PUFAs). Reprinted from Hammock et al. (2020) with permission.

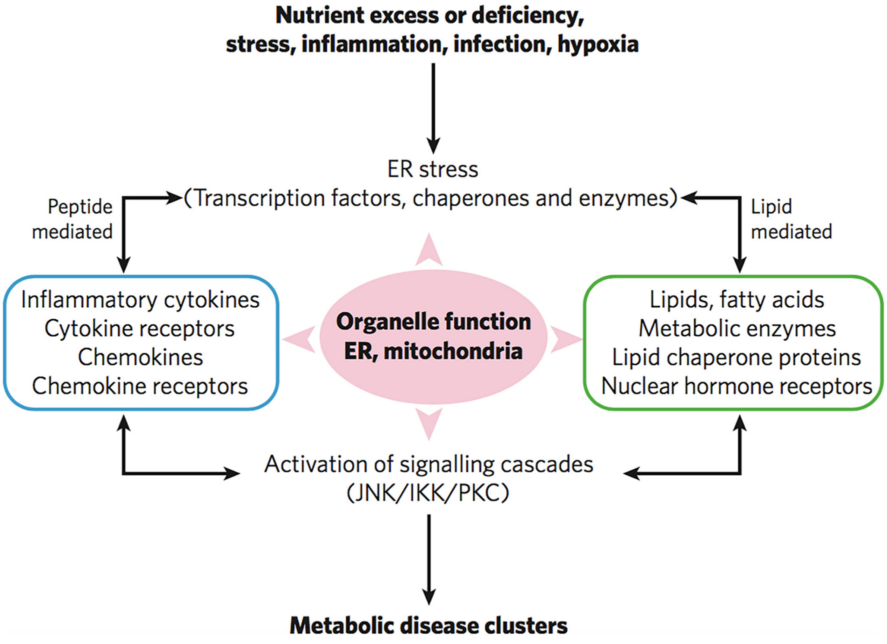

FIGURE 9 | Severe infections trigger inflammatory responses, ER stress and mitochondrial organelle dysfunction through lipid-mediated and cytokine peptide-mediated mechanisms. Reprinted from Hotamisligil (2006) with permission.

higher risk of developing the uncontrolled lipid storm and further entangled with cytokine storms.

PLASMALOGENS IN LUNG SURFACTANT AND ANTIVIRAL PULMONARY SURFACTANT THERAPIES

Coronavirus infection impairs the capacity of the type 2 alveolar epithelium cells to synthesize and secrete pulmonary surfactant required for normal breathing and oxygenation (Schousboe et al., 2020; Zheng et al., 2020). In healthy individuals, lung surfactant covers the alveolar surface, facilitates breathing, and prevents the lungs from collapsing (Hallman et al., 1982; Daniels and Orgeig, 2003). Dysfunctional endogenous lung surfactant in the patients with severe respiratory pathologies provoked by SARS-CoV-2, may be due to the decreased concentrations of surfactant phospholipid and proteins, the altered lung surfactant metabolism and composition, or oxidative inactivation of surfactant proteins (Ahmed et al., 2020; Schousboe et al., 2020). Considering that pulmonary surfactant synthesis is diminished by the severe acute respiratory syndrome-coronavirus-2 pathology, potential therapies of COVID-19 caused pneumonia may include exogenous lung surfactant replacement or delivery to compensate the deficiency of surfactant lipids, which are strongly associated with lung pathogenesis (Mirastschijski et al., 2020).

There is a close interaction and crosstalk between lung surfactant and phagocytosis behavior of alveolar macrophages (Juers et al., 1976; Spragg et al., 2004; Diler et al., 2014; Tschernig et al., 2016). Interestingly, the alveolar macrophages do not kill *in vitro* the pathogens unless the latter have been incubated with alveolar lining material (i.e., lung surfactant) before their phagocytosis. Although plasmalogens in lung surfactant are not the major components of the phospholipid mixture, they have been reported to significantly reduce surface viscosity and surface tension (Rüdiger et al., 1998, 2005; Zhuo et al., 2021). The role of plasmalogens in facilitating membrane fusion has been well recognized (Marrink and Mark, 2004). In this regard, studies with fibroblasts derived from plasmalogen-deficient human patients have shown marked inhibition of exocytosis and endocytosis processes (Perichon et al., 1998; Thai et al., 2001).

Lung surfactant is a multicomponent mixture of lipids (phospholipids, triglycerides, fatty acids, and cholesterols), surfactant proteins, and a small amount of carbohydrates (Bernhard, 2016; Schousboe et al., 2020). The lipid components comprise saturated and unsaturated phospholipids, neutral lipids, and ether lipids (plasmalogens). Phosphatidylcholine (PC) is the predominant lipid class accounting for about 50% of the phospholipids of lung surfactant. Phosphatidylethanolamine (PE) accounts for up to 20% of phospholipids, whereas phosphatidylserine (PS), phosphatidylinositol (PI), and phosphatidylglycerol (PG) constitute 12–15% of the total phospholipid content of lung surfactant. The antiviral activity of the lung surfactant might be due to the pulmonary lipids that may inhibit virus-mediated host inflammation and infection. Of interest, surfactant-associated proteins are required for the formation of tubular myelin (described by a deformed P-based cubic membrane surface) (Larsson and Larsson, 2014) which promotes the adsorption of lipid molecules at the air/water interface and play a role in the monolayer film stability (**Figure 10**).

Plasmalogen is the minor trace but critical component of lung surfactant. This ether phospholipid, together with cholesterol and surfactant-associated proteins, regulate the surfactant monolayer stability and viscosity. Another key feature is that plasmalogens act as antioxidants and protect alveolar cells from oxidative stress that often encountered at alveolar surface (Zhuo et al., 2021). Plasmalogens may contribute to substantial lowering the surface tension (Rüdiger et al., 1998) and viscosity (Rüdiger et al., 2005) of the lipid mixture. It has been emphasized that lower surfactant viscosity may enhance the clinical response to the therapy of respiratory pathology (Bernhard, 2016).

Quantitative lipidomic analysis of mouse lung during postnatal development, using electrospray ionization tandem mass spectrometry, has determined the individual plasmalogen lipid types in the pulmonary surfactant (Karnati et al., 2018). Phosphatidylethanolamine (PE)-based plasmalogens have been found to be much more abundant as compared to ether-phosphatidylcholines (PC) during the postnatal mouse lung development. **Figure 11** shows that PE-based plasmalogens comprise a high content of 20:4, 22:6, 22:5, and 22:4 chains likely to be arachidonic acid (AA), docosahexaenoic acid (DHA), docosapentaenoic acid (DPA), and adrenic acid-rich plasmalogen derivatives. Evidently, this lipid content determines the capacity of the lung surfactant to protect the alveolar epithelium cells from hypoxia and ROS-mediated stress and to reduce the risk of respiratory distress diseases.

Recently, it has been claimed that the lung injury caused by SARS-CoV-2 coronavirus in the pulmonary tissue of COVID-19 pneumonia patients developing acute respiratory distress syndrome (ARDS) strongly resembles the effects of neonatal respiratory distress syndrome (NRDS) (Schousboe et al., 2020). Both disorders are associated with lung surfactant deficiency (Mirastschijski et al., 2020). The clinical consequences from the impact of SARS-CoV-2 on the alveolar type II cells, and the production and turnover of pulmonary surfactant, are associated with alveolar collapse and inflammation, which leads to increased capillary permeability, edema, and microvascular thrombosis (**Figure 12**). The viral infection may cause alterations in the whole lung lipid composition. Moreover, vascular permeability increases as the pulmonary pathology progresses and the pulmonary surfactant gets deactivated, which makes the lungs unstable with time (Walmrath et al., 1996).

It has been proposed that early administration of natural lung surfactant may improve the pulmonary function in COVID-19 patients with severe ARDS (Mirastschijski et al., 2020). The suggested pulmonary surfactant therapy (Walther et al., 2019; Ahmed et al., 2020; Mirastschijski et al., 2020; Pramod et al., 2020) is motivated by the fact that lung surfactant administration is a safe and efficient therapy for neonates with ARDS (Walmrath et al., 1996). Therefore, pulmonary surfactant therapy envisions the development of lung surfactant formulations for pulmonary barrier restoration in patients with COVID-19 pneumonia

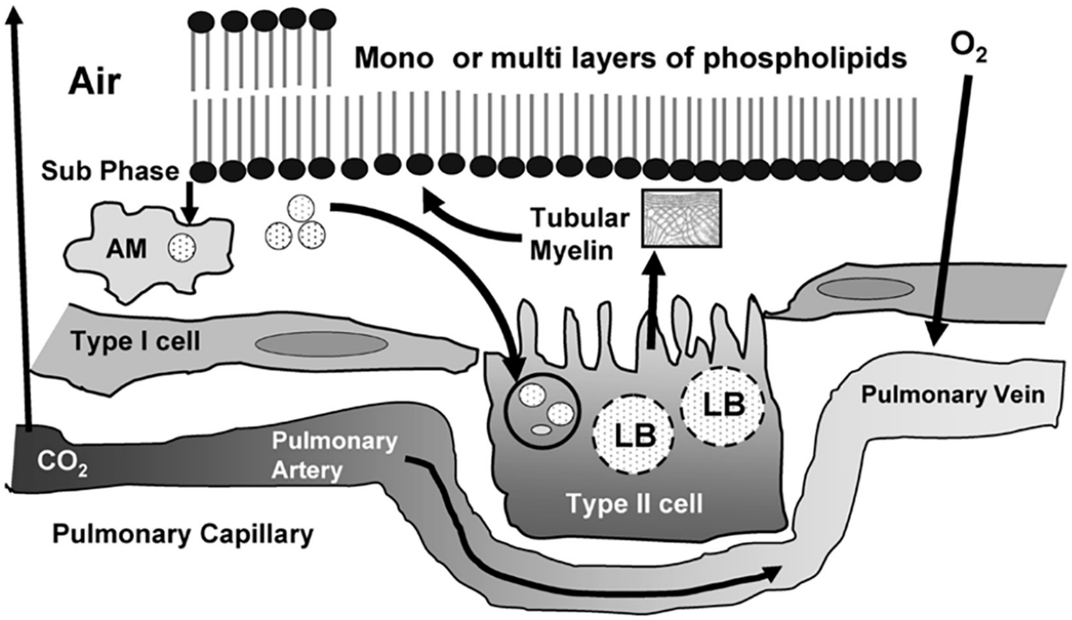

FIGURE 10 | Life cycle of surfactant produced in the lung with an indication of the tubular myelin, lamellar bodies (LB), and alveolar macrophages (AM). Pulmonary surfactant is a surface-active lipo-protein complex produced by type II alveolar cells. Reprinted from Ramanathan (2006) with permission.

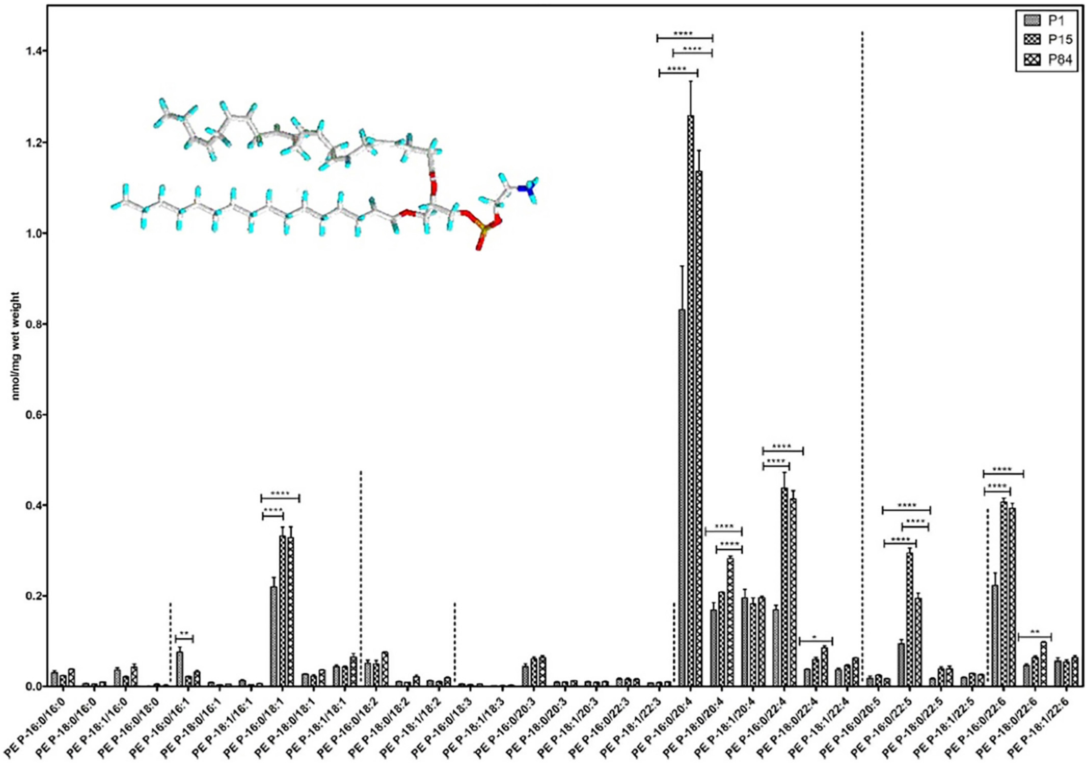

FIGURE 11 | Composition of individual phosphatidylethanolamine PE-based plasmalogen (PE-P) lipid species during postnatal development of mouse lung. High contents of 20:4, 22:6, 22:5, and 22:4 plasmalogen (PE-P) derivatives are detected. PE P-16:0 (sn-1) plasmalogens are present in higher amounts in all 4 groups of ethanolamine plasmalogens, whereas PE P-18:0 and PE P-18:1 account for smaller amounts. Values are represented as nmol/mg wet weight. Reprinted from Karnati et al. (2018) with permission. Statistical significance (*, **, ***): *p*-values <0.05 (significant), < 0.01, < 0.001 (highly significant).

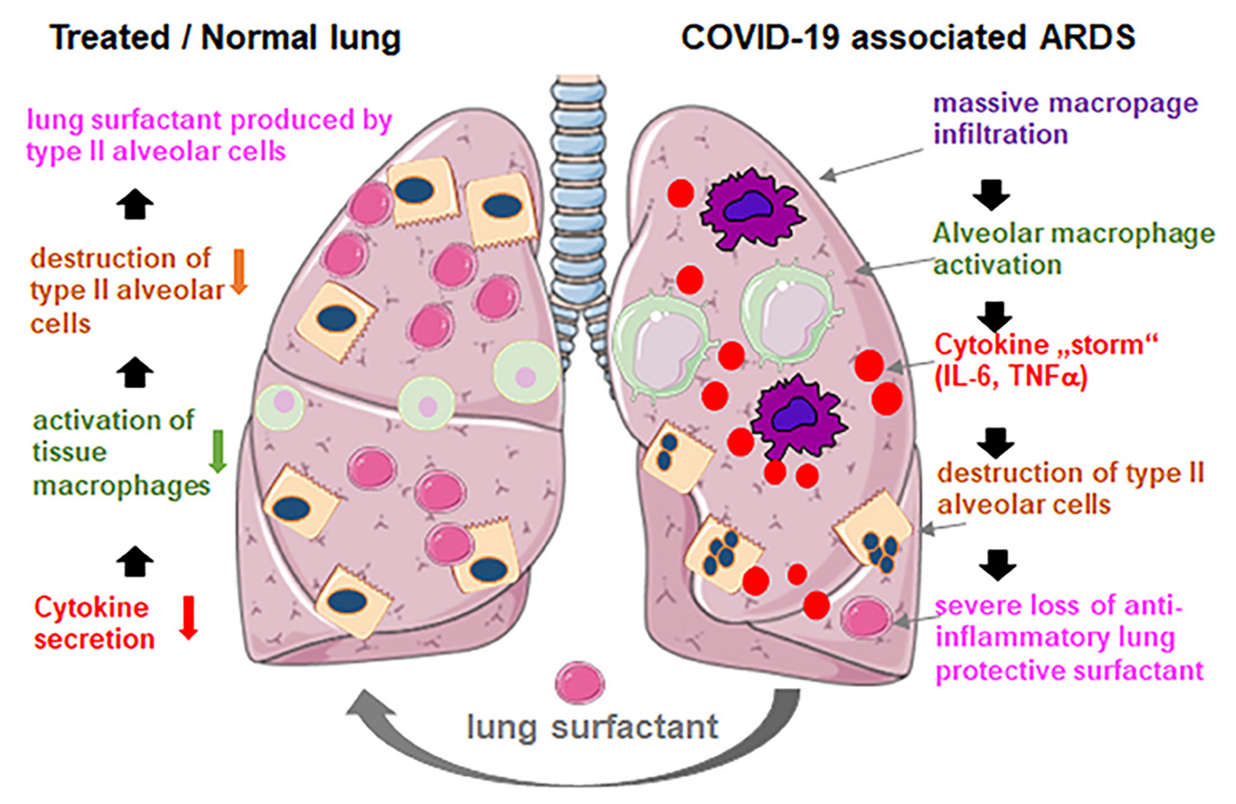

FIGURE 12 | Exogenous lung surfactant delivery suggested as a therapy to reduce inflammation and restore pulmonary barrier in severe COVID-19 associated acute respiratory distress syndrome (ARDS). Reprinted from Mirastschijski et al. (2020) with permission.

(Walther et al., 2019; Mirastschijski et al., 2020; Pramod et al., 2020). It is expected that this approach may improve the treatment outcome of COVID-19 patients.

Whereas the levels of plasmalogens might be insufficient for COVID-19 patient treatment in the clinical studies employing natural lung surfactants, we propose plasmalogen-enriched lung surfactant formulations as the next generation therapeutic opportunity toward more efficient pulmonary surfactant therapy against COVID-19 pneumonia. Taking into account the results of the lipidomics analysis about the major ether lipid components (Karnati et al., 2018), it appears urgent to develop the synthetic surfactants enriched in phosphatidylethanolamine (PE)-based plasmalogens as those presented in **Figure 11**.

INCLUSION OF PLASMALOGENS IN COMBINATION THERAPIES AGAINST CORONAVIRUS INFECTIONS

We hypothesize that the inclusion of plasmalogens in antiviral formulations for combination therapy of severe COVID-19 pneumonia patients may enhance the overall efficacy of anti-SARS-CoV-2 treatment. This antiviral lipid class may render the treatment resistant to eventual viral protein mutations during the viral propagation of the pathology. Both membrane lipid therapy and pulmonary surfactant therapy with plasmalogen-enriched antiviral formulations should be applicable to most of the coronaviruses including SARS-CoV-2, SARS-CoV, and MERS-CoV.

In the absence of clinical data for severe COVID-19 patients, it is early to argue whether plasmalogens have a role simply because they contain PUFAs. Current understanding highlights that the PUFAs content of plasmalogens is important in prevention and management of COVID-19. Das (2021) has emphasized that the PUFA bioactive lipid arachidonic acid (AA, 20:4n-6) has a capacity to inactivate SARS-CoV-2, facilitate macrophage generation, suppress inflammation, and prevent vascular endothelial cell damage, which opens new perspectives for therapeutic uses of AA in anti-coronavirus strategies.

Ongoing early stage inhibitory therapies involve the design of potential entry inhibitors against SARS-CoV-2. Strategies for blocking the viral entry consider that the virus utilizes the angiotensin-converting enzyme 2 (ACE2) as an entry receptor in human cells. Therefore, the S protein is an important target for the development of anti-SARS-CoV-2 therapeutics. Blocking the binding of S protein to ACE2 can be done either by fatty acids or by peptides and antibodies, which will inhibit the SARS-CoV-2 virus proliferation. Peptide therapeutics are promising antagonists in this regard (Struck et al., 2012). However, considering the molecular diversity of the coronavirus entry receptors of host cells (Millet et al., 2020), this targeting mechanism might not be sufficient to stop the pandemics. The analysis of COVID-19 lung samples has revealed a dramatic upregulation of the interferon gamma (IFNγ) protein, which may be accompanied by a large innate immune response (Hu et al., 2020).

Various potential therapeutic approaches (Imai et al., 2005; Struck et al., 2012; Monteil et al., 2020), some of which are highlighted in **Figure 2**, can be combined in multi-therapies toward the aim of SARS-CoV-2 inhibition:

- Development of spike protein-based vaccines;
- Antibody therapy using antibody molecules for targeting and neutralization of the spike proteins, which mediate the viral entry;
- Delivering excessive quantity of soluble form of ACE2;
- Blocking ACE2 receptor;
- Inhibition of transmembrane protease serine 2 (TMPRSS2) activity;
- Using antivirals (RNA polymerase inhibitors) to stop the viral replication;
- Using short interfering RNAs directly or indirectly targeting the viral DNA replication machinery;
- Drugs targeting lipid metabolism;
- Exogenous interferon gamma (IFNγ) delivery to compensate its deficiency in susceptible to virus infection.

In analogy with the human immunodeficiency virus (HIV) treatment regimen using tri-drug combinations, coronavirus research may envision future triple therapies or multi-therapies against SARS-CoV-2 coronavirus infection. Plasmalogens can be included in the category of membrane-lipid targeted therapies in approaches of treating the coronavirus and/or host membranes as antiviral targets. In combination therapies with other antiviral agents, plasmalogens will be significant as antiviral lipids and lung surfactant ingredients to treat severe COVID-19 pneumonia.

CONCLUDING REMARKS

The current COVID-19 pandemics is similar to the previous severe acute respiratory syndrome (SARS-CoV, 2002–2003) and Middle East Respiratory Syndrome (MERS-CoV, 2012-ongoing) outbreaks. All these coronavirus infections are traced through zoonotic transmission. All have similar clinical manifestations mainly as lower respiratory tract diseases with significant mortality especially in the elderly with underlying chronic illnesses (obesity, type 2 diabetes and cardiometabolic diseases).

Plasmalogens are a class of membrane ether glycerophos pholipids with unique properties displaying a propensity for non-lamellar phase formation that may strongly influence the activity of membrane-bound enzymes and receptors. Plasmalogens are crucial in human health and disease and playing roles in immune signaling and as endogenous antioxidants. Increasing evidence supports the correlation between diminished levels of plasmalogens and a number of pathological states including neurodegenerative and cardiometabolic disorders as well as the severe acute respiratory distress syndrome due to the coronavirus infections. Dysregulated levels of plasmalogens are found in infected patients as a result of coronavirus-induced modification of the lipid metabolism. This strongly indicates that plasmalogen is among the key lipids potentially modulating the viral infection.

Based on the features discussed above, we suggest the potential role of plasmalogen pre-conditioning as anti-viral therapeutic and prophylaxis strategy. Along the line, plasmalogen pre-conditioning may promote host cubic membrane (CM) formation in response to multiple stress and diseased conditions including coronavirus infections. CM has been proposed as an evolutionary antioxidant defense system Deng and Almsherqi (2015). The antioxidant plasmalogen molecules participate in the host CM formation and CM in return to act as antioxidant defense system. Host cubic membrane induction in virus infected cells has not been rationalized in the development of antiviral therapies yet. However, the discussed multiple correlations and phenomena here lead to the conclusion that the plasmalogen lipid type is of great interest and significance for the future COVID-19 therapy and might be considered as a biomarker in SARS-CoV-2 infection and treatment. Further work in each of these areas will be necessary to realize the full potential of plasmalogen modulation and CM formation as therapeutic strategies in membrane lipid therapy and antiviral combination remedies for the next pandemics.

AUTHOR CONTRIBUTIONS

YD and AA conceived and wrote the manuscript. Both authors contributed to the article and approved the submitted version.

FUNDING

This work is supported by grants to YD from the National Natural Science Foundation, China (Grant No: 31670841) and Wenzhou Institute, University of Chinese Academy of Sciences (Grant No: WIUCASQD2019005).

ACKNOWLEDGMENTS

AA acknowledges a membership in CNRS GDR2088 BIOMIM research network.

REFERENCES

Abu-Farha, M., Thanaraj, T. A., Qaddoumi, M. G., Hashem, A., Abubaker, J., and Al-Mulla, F. (2020). The role of lipid metabolism in COVID-19 virus infection and as a drug target. *Int. J. Mol. Sci.* 21:3544 doi: 10.3390/ijms21103544

Ahmed, S., Akter, M. S., Roy, K., and Islam, M. S. (2020). Role of surfactant for the treatment of alveolar cells against coronavirus (Covid-19). *Ann. Res. Rev. Biol.* 144:110020 doi: /10.9734/arrb/2020/v35i630233

Almsherqi, Z. A., Hyde, S., Ramachandrana, M., and Deng, Y. (2008). Cubic membranes: a structure-based design for DNA uptake. *J. R. Soc. Interface* 5, 1023–1029. doi: 10.1098/rsif.2007.1351

Almsherqi, Z. A., Kohlwein, S. D., and Deng, Y. (2006). Cubic membranes: a legend beyond the flatland of cell membrane organization. *J. Cell Biol.* 173, 839–844. doi: 10.1083/jcb.200603055

Almsherqi, Z. A., Landh T. Kohlwein S. D., and Deng, Y. (2009). Chapter 6 Cubic membranes: the missing dimension of cell membrane organization. *Int. Rev. Cell Mol. Biol.* 274, 275–342. doi: 10.1016/S1937-6448(08)02006-6

Almsherqi, Z. A., McLachlan, C. S., Mossop, P., Knoops, K., and Deng, Y. (2005). Direct template matching reveals a host subcellular membrane gyroid cubic structure that is associated with SARS virus. *Redox Rep.* 10, 167–171. doi: 10.1179/135100005X57373

Alsaadi, E. A. J., and Jones, I. M. (2019). Membrane binding proteins of coronaviruses. *Future Virol.* 14, 275–2864 doi: 10.2217/fvl-2018-0144

Angelova, A., Angelov, B., Drechsler, M., Bizien, T., Gorshkova, Y. E., and Deng Y. tructures involving docosap(2021). Plasmalogen-based liquid crystalline multiphase sentaenoyl derivatives inspired by biological cubic membranes. *Front. Cell Dev. Biol.* 9:617984 doi: 10.3389/fcell.2021.617984

Archambault, A-S., Zaid, Y., Rakotoarivelo, V., Doré, É., Dubuc, I., Martin, C., et al. (2020). Lipid storm within the lungs of severe COVID-19 patients: extensive levels of cyclooxygenase and lipoxygenase-derived inflammatory metabolites. *MedRxiv [preprint]* doi: 10.1101/2020.12.04.20242115.

Barry, S.M., Johnson, M.A., and Janossy, G. (2000). Cytopathology or immunopathology? the puzzle of cytomegalovirus pneumonitis revisited. *Bone Marrow Transplant.* 26, 591–597. doi: 10.1038/sj.bmt.1702562

Belouzard, S., Millet, J. K., Licitra, B. N., and Whittaker, G. R. (2012). Mechanisms of coronavirus cell entry mediated by the viral spike protein. *Viruses* 4, 1011–1033. doi: 10.3390/v4061011

Beltran P. M. J., Cook, K. C., Hashimoto, Y., Galitzine, C., Murray, L. A., Vitek, O., et al. (2018). Infection-induced peroxisome biogenesis is a metabolic strategy for herpesvirus replication. *Cell Host Microbe.* 24, 526–541.e7 doi: 10.1016/j.chom.2018.09.002

Bernhard, W. (2016). Lung surfactant: function and composition in the context of development and respiratory physiology. *Ann. Anat.* 208, 146–150 doi: 10.1016/j.aanat.2016.08.003

Braverman, N. E., and Moser, A. B. (2012). Functions of plasmalogen lipids in health and disease. *Biochim. Biophys. Acta* 1822, 1442–1452. doi: 10.1016/j.bbadis.2012.05.008

Brugger, B., Glass, B., Haberkant, P., Leibrecht, I., Wieland, F. T., and Krausslich, H. G. (2006). The HIV lipidome: a raft with an unusual composition. *Proc. Natl. Acad. Sci. U.S.A.* 103, 2641–2646 doi: 10.1073/pnas.0511136103

Castelli, V., Cimini, A., and Claudio Ferri, C. (2020). Cytokine storm in COVID-19: "when you come out of the storm, you won't be the same person who walked in". *Front. Immunol.* 11:2132 doi: 10.3389/fimmu.2020.02132

Chong, K., Almsherqi, Z. A., Shen, H. M., and Deng, Y. (2018). Cubic membrane formation supports cell survival of amoeba chaos under starvation-induced stress. *Protoplasma* 255, 517–525. doi: 10.1007/s00709-017-1169-x

Cook, K. C., Moreno, J. A., Jean Beltran, P. M., and Cristea, I. M. (2019). Peroxisome plasticity at the virus–host interface. *Trends Microbiol.* 27, 906–914 doi: 10.1016/j.tim.2019.06.006

Daniels, C. B., and Orgeig, S. (2003). Pulmonary surfactant: the key to the evolution of air breathing. *News Physiol. Sci.* 18, 151–157 doi: 10.1152/nips.01438.2003

Das, U. N. (2018). Arachidonic acid and other unsaturated fatty acids and some of their metabolites function as endogenous antimicrobial molecules: a review. *J. Adv. Res.* 11, 57–66. doi: 10.1016/j.jare.2018.01.001

Das, U. N. (2020a). Bioactive lipids as mediators of the beneficial action(s) of mesenchymal stem cells in COVID-19. *Aging Dis.* 11, 746–755. doi: 10.14336/AD.2020.0521

Das, U. N. (2020b). Can bioactive lipid arachidonic acid prevent and ameliorate COVID-19? *Medicina* 56:418. doi: 10.3390/medicina56090418

Das, U.N. (2019). Can bioactive lipid(s) augment anti-cancer action of immunotherapy and prevent cytokine storm? *Arch. Med. Res.* 50, 342–349. doi: 10.1016/j.arcmed.2019.10.004

Das, U.N. (2020c). Can bioactive lipids inactivate coronavirus (COVID-19)? *Arch. Med. Res.* 51, 282–286. doi: 10.1016/j.arcmed.2020.03.004

Das, U.N. (2020d) Response to: bioactive lipids and coronavirus (COVID-19)-further discussion. *Arch. Med. Res.* 51, 445–449 doi: 10.1016/j.arcmed.2020.04.004

Das, U.N. (2021). Bioactive lipids in COVID-19-further evidence. *Arch. Med. Res.* 52, 107–120. doi: 10.1016/j.arcmed.2020.09.006

Deng, Y., Almsherqi, Z. A., Ng, M. M., and Kohlwein, S. D. (2010). Do viruses subvert cholesterol homeostasis to induce host cubic membranes? *Trends Cell Biol.* 20, 371–379 doi: 10.1016/j.tcb.2010.04.001

Deng, Y., and Almsherqi, Z. A. (2015). Evolution of cubic membranes as antioxidant defence system. *Interface Focus* 5:20150012. doi: 10.1098/rsfs.2015.0012

Deng, Y., Lee, E. L., Chong, K., and Almsherqi, Z. A. (2017). Evaluation of radical scavenging system in amoeba chaos carolinense during nutrient deprivation. *Interface Focus* 7:20160113. doi: 10.1098/rsfs.2016.0113

Diler, E., Schicht, M., Rabung, A., Tschernig, T., Meier, C., Rausch, F., et al. (2014). The novel surfactant protein SP-H enhances the phagocytosis efficiency of macrophage-like cell lines U937 and MH-S. *BMC Res. Notes* 7:851 doi: 10.1186/1756-0500-7-851

Dixit, E., Boulant, S., Zhang, Y., Lee, A. S., Odendall, C., Shum, B., et al. (2010). Peroxisomes are signaling platforms for antiviral innate immunity. *Cell* 141, 668–681 doi: 10.1016/j.cell.2010.04.018

Escribá, P. V. (2017). Membrane-lipid therapy: a historical perspective of membrane-targeted therapies - from lipid bilayer structure to the pathophysiological regulation of cells. *Biochim. Biophys. Acta* 1859, 1493–1506 doi: 10.1016/j.bbamem.2017.05.017

Escribá, P. V., Busquets X., Inokuchi J., Balogh G., Török Z., and Horváth I. . et al. (2015). Membrane lipid therapy: modulation of the cell membrane composition and structure as a molecular base for drug discovery and new disease treatment. *Prog. Lipid Res.* 59, 38–53. doi: 10.1016/j.plipres.2015.04.003

Facciotti, F., Ramanjaneyulu, G. S., Lepore, M., Sansano, S., Cavallari, M., Kistowska, M., et al. (2012). Peroxisome-derived lipids are self antigens that stimulate invariant natural killer T cells in the thymus. *Nat. Immunol.* 13, 474–480. doi: 10.1038/ni.2245

Farooqui, A. A. (2010). Studies on plasmalogen-selective phospholipase A2 in brain. *Mol. Neurobiol.* 41, 267–273. doi: 10.1007/s12035-009-8091-y

Farooqui, A. A., and Horrocks, L. A. (2001). Plasmalogens: workhorse lipids of membranes in normal and injured neurons and glia. *Neuroscientist* 7, 232–245. doi: 10.1177/107385840100700308

Fedson, D. S. (2006). Pandemic influenza: a potential role for statins in treatment and prophylaxis. *Clin. Infect. Dis.* 43, 199–205 doi: 10.1086/505116

Fedson, D. S. (2016). Treating the host response to emerging virus diseases: lessons learned from sepsis, pneumonia, influenza and ebola. *Ann. Transl. Med.* 4:421. doi: 10.21037/atm.2016.11.03

Fedson, D. S., Opal, S. M., and Rordam, O. M. (2020). Hiding in plain sight: an approach to treating patients with severe COVID-19 Infection. *mBio* 11:e00398-20. doi: 10.1128/mBio.00398-20

Glaser, P. E., and Gross, R. W. (1995). Rapid plasmenylethanolamine-selective fusion of membrane bilayers catalyzed by an isoform of glyceraldehyde-3-phosphate dehydrogenase: discrimination between glycolytic and fusogenic roles of individual isoforms. *Biochemistry* 34, 12193–12203. doi: 10.1021/bi00038a013

Glebov, O. O. (2020). Understanding SARS-CoV-2 endocytosis for COVID-19 drug repurposing. *FEBS J.* 287, 3664–3671 doi: 10.1111/febs.15369

Goldsmith, C. S, Tatti, K. M., Ksiazek, T. G., Rollin, P. E., Comer, J. A., Lee, W. W., Rota, P. A., et al. (2004). Ultrastructural characterization of SARS coronavirus. *Emerg. Infect. Dis.* 10, 320–326. doi: 10.3201/eid1002.030913

Hallman, M., Spragg, R., Harrell, J. H., Moser, K. M., and Gluck, L. (1982). Evidence of lung surfactant abnormality in respiratory failure. Study of bronchoalveolar lavage phospholipids, surface activity, phospholipase activity, and plasma myoinositol. *J. Clin. Investig.* 70, 673–683 doi: 10.1172/JCI110662

Hammock, B. D., Wang, W., Gilligan, M. M., and Panigrahy, D. (2020). Eicosanoids: the overlooked storm in COVID-19? *Am. J. Pathol.* 190, 1782–1788 doi: 10.1016/j.ajpath.2020.06.010

Heaton, N. S., and Randall, G. (2010). Dengue virus-induced autophagy regulates lipid metabolism. *Cell Host Microbe* 8, 422–432. doi: 10.1016/j.chom.2010.10.006

Heaton, N. S., and Randall, G. (2011). Multifaceted roles for lipids in viral infection. *Trends Microbiol.* 19, 368–375 doi: 10.1016/j.tim.2011.03.007

Heaton, N. S., Perera, R., Berger, K. L., Khadka, S., Lacount, D. J., Kuhn, R. J., et al. (2010). Dengue virus nonstructural protein 3 redistributes fatty acid synthase to sites of viral replication and increases cellular fatty acid synthesis. *Proc. Natl. Acad. Sci. USA* 107, 17345–17350. doi: 10.1073/pnas.1010811107

Honsho, M., Abe, Y., and Fujiki, Y. (2015). Dysregulation of plasmalogen homeostasis impairs cholesterol biosynthesis. *J. Biol. Chem.* 290, 28822–28833 doi: 10.1074/jbc.M115.656983

Honsho, M., Yagita, Y., Kinoshita, N., and Fujiki, Y. (2008). Isolation and characterization of mutant animal cell line defective in alkyl-dihydroxyacetonephosphate synthase: localization and transport of plasmalogens to post-Golgi compartments. *Biochim. Biophys. Acta* 1783, 1857–1865 doi: 10.1016/j.bbamcr.2008.05.018

Hotamisligil, G. S. (2006). Inflammation and metabolic disorders. *Nature* 444, 860–867. doi: 10.1038/nature05485

Hu, Z. J., Xu, J., Yin, J. M., Li, L., Hou, W., Zhang, L. L., et al. (2020). Lower circulating interferon-gamma is a risk factor for lung fibrosis in COVID-19 patients. *Front. Immunol.* 11:585647 doi: 10.3389/fimmu.2020.585647

Huang, K. J., Su, I. J., Theron, M., Wu, Y. C., Lai, S. K., Liu, C. C., et al. (2005). An interferon-gamma-related cytokine storm in SARS patients. *J. Med. Virol.* 75:185–194 doi: 10.1002/jmv.20255

Ifuku, M., Katafuchi, T., Mawatari, S., Noda, M., Miake, K., Sugiyama, M., et al. (2012). Anti-inflammatory/anti-amyloidogenic effects of plasmalogens in lipopolysaccharide-induced neuroinflammation in adult mice. *J. Neuroinflammation* 9:197 doi: 10.1186/1742-2094-9-197

Imai, Y., Kuba, K., Rao, S., Huan, Y., Guo, F., Guan, B., et al. (2005). Angiotensin-converting enzyme 2 protects from severe acute lung failure. *Nature* 436, 112–116 doi: 10.1038/nature03712

Imashuku, S. (2002). Clinical features and treatment strategies of Epstein-Barr virus-associated hemophagocytic lymphohistiocytosis. *Crit. Rev. Oncol. Hematol.* 44, 259–272. doi: 10.1016/S1040-8428(02)00117-8

Jahrling, P. B., Hensley, L. E., Martinez, M. J., Leduc, J. W., Rubins, K. H., Relman, D. A., et al. (2004). Exploring the potential of variola virus infection of cynomolgus macaques as a model for human smallpox. *Proc. Natl. Acad. Sci. USA* 101, 15196–15200. doi: 10.1073/pnas.0405954101

Jeon, J. H., and Lee, C. (2017). Cellular cholesterol is required for porcine nidovirus infection. *Arch. Virol.* 162, 3753–3767 doi: 10.1007/s00705-017-3545-4

Juers, J. A., Rogers, R. M., McCurdy, J. B., and Cook, W. W. (1976). Enhancement of bactericidal capacity of alveolar macrophages by human alveolar lining material. *J. Clin. Invest.* 58:271e275 doi: 10.1172/JCI108468

Karnati, S., and Baumgart-Vogt, E. (2008). Peroxisomes in mouse and human lung: their involvement in pulmonary lipid metabolism. *Histochem. Cell Biol.* 130, 719–740. doi: 10.1007/s00418-008-0462-3

Karnati, S., Garikapati, V., Liebisch, G., Van Veldhoven, P. P., Spengler, B., Schmitz, G., et al. (2018). Quantitative lipidomic analysis of mouse lung during postnatal development by electrospray ionization tandem mass spectrometry. *PLoS One* 13:e0203464. doi: 10.1371/journal.pone.0203464

Katafuchi, T., Ifuku, M., Mawatari, S., Noda, M., Miake, K., Sugiyama, M., et al. (2012). Effects of plasmalogens on systemic lipopolysaccharide-induced glial activation and β-amyloid accumulation in adult mice. *Ann. N. Y. Acad. Sci.* 1262, 85–92 doi: 10.1111/j.1749-6632.2012.06641.x

Knoops, K., Kikkert, M., van den Worm, S. H. E., Zevenhoven-Dobbe, J. C., van der Meer, Y., Koster, A. J., et al. (2008). SARS-coronavirus replication is supported by a reticulovesicular network of modified endoplasmic reticulum. *PLoS Biol.* 6:e226. doi: 10.1371/journal.pbio.0060226

Larsson, M., and Larsson, K. (2014). Periodic minimal surface organizations of the lipid bilayer at the lung surface and in cubic cytomembrane assemblies. *Adv. Colloid Interface Sci.* 205, 68–73. doi: 10.1016/j.cis.2013.07.003

Leisman, D. E., Ronner, L., Pinotti, R., Taylor, M. D., Sinha, P., Calfee, C. S., et al. (2020). Cytokine elevation in severe and critical COVID-19: a rapid systematic review, meta-analysis, and comparison with other inflammatory syndromes. *Lancet Respir. Med.* 8, 1233–1244. doi: 10.1016/S2213-2600(20)30404-5

Li, F. (2015). Receptor recognition mechanisms of coronaviruses: a decade of structural studies. *J. Virol.* 89, 1954–1964 doi: 10.1128/JVI.02615-14

Li, F. (2016). Structure, function, and evolution of coronavirus spike proteins. *Annu. Rev. Virol.* 3, 237–261 doi: 10.1146/annurev-virology-110615-042301

Li, F., Li, W. H., Farzan, M., and Harrison, S. C. (2005). Structure of SARS coronavirus spike receptor-binding domain complexed with receptor. *Science* 309, 1864–1868. doi: 10.1126/science.1116480

Li, W. H., Moore, M. J., Vasilieva, N., Sui, J. H., Wong, S. K., Berne, M. A., et al. (2003). Angiotensin-converting enzyme 2 is a functional receptor for the SARS coronavirus. *Nature* 426, 450–454 doi: 10.1038/nature02145

Liu, S. T., Sharon-Friling, R., Ivanova, P., Milne, S. B., Myers, D. S., Rabinowitz, J. D., et al. (2011). Synaptic vesicle-like lipidome of human cytomegalovirus virions reveals a role for SNARE machinery in virion egress. *Proc. Natl. Acad. Sci. USA* 108, 12869–12874. doi: 10.1073/pnas.1109796108

Lohner, K., Balgavy, P., Hermetter, A., Paltauf, F., and Laggner, P. (1991). Stabilization of non-bilayer structures by the etherlipid ethanolamine plasmalogen. *Biochim. Biophys. Acta* 1061, 132–140 doi: 10.1016/0005-2736(91)90277-F

Lordan, R., Tsoupras, A., Zabetakis, I., and Demopoulos, C. A. (2019). Forty years since the structural elucidation of platelet-activating factor (PAF): historical, current, and future research perspectives. *Molecules* 24:4414 doi: 10.3390/molecules24234414

Lukassen, S., Chua, R. L., Trefzer, T., Kahn, N. C., Schneider, M. A., and Muley, T. et al. (2020). SARS-CoV-2 receptor ACE2 and TMPRSS2 are primarily expressed in bronchial transient secretory cells. *EMBO J.* 39:e105114. doi: 10.15252/embj.20105114

Mankidy, R., Ahiahonu, P. W., Ma, H., Jayasinghe, D., Ritchie, S. A., Khan, M. A., et al. (2010). Membrane plasmalogen composition and cellular cholesterol regulation: a structure activity study. *Lipids Health Dis.* 9:62 doi: 10.1186/1476-511X-9-62

Marrink, S. J., and Mark, A. E. (2004). Molecular view of hexagonal phase formation in phospholipid membranes. *Biophys. J.* 87, 3894–3900. doi: 10.1529/biophysj.104.048710

Martín-Acebes, M. A., Jiménez de Oya, N., and Saiz, J. C. (2019). Lipid metabolism as a source of druggable targets for antiviral discovery against Zika and other flaviviruses. *Pharmaceuticals* 12:97. doi: 10.3390/ph12020097

Martin-Acebes, M. A., Merino-Ramos, T., Blazquez, A. B., Casas, J., Escribano-Romero, E., Sobrino, F., et al. (2014). The composition of West Nile virus lipid envelope unveils a role of sphingolipid metabolism in flavivirus biogenesis. *J. Virol.* 88, 12041–12054 doi: 10.1128/JVI.02061-14

Maturi, R. K., and Font, R. L. (1996). Ultrastructural features and prevalence of tubuloreticular structures in the ocular vasculature of patients with AIDS: a study of 23 cases. *Br. J. Ophthalmol.* 80, 252–255 doi: 10.1136/bjo.80.3.252

Meikle, P. J., Wong, G., Barlow, C. K., Weir, J. M., Greeve, M. A., MacIntosh, G. L., et al. (2013). Plasma lipid profiling shows similar associations with prediabetes and type 2 diabetes. *PLoS One* 8:e74341 doi: 10.1371/journal.pone.0074341

Meikle, P. J., Wong, G., Tsorotes, D., Barlow, C. K., Weir, J. M., Christopher, M. J., et al. (2011). Plasma lipidomic analysis of stable and unstable coronary artery disease, Arterioscler. *Thromb. Vasc. Biol.* 31, 2723–32 doi: 10.1161/ATVBAHA.111.234096

Miller, S., and Krijnse-Locker, J. (2008). Modification of intracellular membrane structures for virus replication. *Nat. Rev. Microbiol.* 6, 363–374. doi: 10.1038/nrmicro1890

Millet, J. K., Jaimes, J. A., and Whittaker, G. R. (2020). Molecular diversity of coronavirus host cell entry receptors. *FEMS Microbiol. Rev.* doi: 10.1093/femsre/fuaa057 Online ahead of print.

Mirastschijski, U., Dembinski, R., and Maedler, K. (2020). Lung surfactant for pulmonary barrier restoration in patients with COVID-19 Pneumonia. *Front. Med.* 7:254. doi: 10.3389/fmed.2020.00254

Monteil, V., Kwon, H., Prado, P., Hagelkrüys, A., Wimmer, R. A., Stahl, M., et al. (2020). Inhibition of SARS-CoV-2 infections in engineered human tissues using clinical-grade soluble human ACE2. *Cell* 181, 905–913.e7. doi: 10.1016/j.cell.2020.04.004

Mulchandani, R., Lyngdoh, T., and Kakkar, A. K. (2020). Deciphering the COVID-19 cytokine storm: systematic review and meta-analysis. *Eur. J. Clin. Invest.* 51:e13429. doi: 10.1111/eci.13429

Ni, G., Li Z, Liang, K., Wu, T., De Libero, G., and Xia, C. (2014). Synthesis and evaluation of immunostimulant plasmalogen lysophosphatidylethanolamine and analogues for natural killer T cells. *Bioorg. Med. Chem.* 22, 2966–2973. doi: 10.1016/j.bmc.2014.04.012

Odendall, C., and Kagan, J. C. (2013). Peroxisomes and the antiviral responses of mammalian cells. *Subcell. Biochem.* 69, 67–75 doi: 10.1007/978-94-007-6889-5_4

Oudshoorn, D., Rijs, K., Limpens, R. W. A. L., Groen, K., Koster, A. J., Snijder, E. J., et al. (2017). Expression and cleavage of middle east respiratory syndrome coronavirus nsp3-4 polyprotein induce the formation of double-membrane vesicles that mimic those associated with coronaviral RNA replication. *mBio* 8:e01658-17 doi: 10.1128/mBio.01658-17

Paul, S., Lancaster, G. I., and Meikle, P. J. (2019). Plasmalogens: a potential therapeutic target for neurodegenerative and cardiometabolic disease. *Prog. Lipid Res.* 74, 186–195 doi: 10.1016/j.plipres.2019.04.003

Perichon, R., Moser, A. B., Wallace, W. C., Cunningham, S. C., Roth, G. S., and Moser, H. W. (1998). Peroxisomal disease cell lines with cellular plasmalogen deficiency have impaired muscarinic cholinergic signal transduction activity and amyloid precursor protein secretion. *Biochem. Biophys. Res. Commun.* 248, 57–61. doi: 10.1006/bbrc.1998.8909

Pike, L. J., Han, X., Chung, K. N., and Gross, R. W. (2002). Lipid rafts are enriched in arachidonic acid and plasmenylethanolamine and their composition is independent of caveolin-1 expression: a quantitative electrospray ionization/mass spectro- metric analysis. *Biochemistry* 41, 2075–2088. doi: 10.1021/bi0156557

Prades, J., Alemany, R., Perona, J. S., Funari, S. S., Vögler, O., Ruiz-Gutiérrez, V., et al. (2008). Effects of 2-hydroxyoleic acid on the structural properties of biological and model plasma membranes. *Mol. Membr. Biol.* 25, 46–57 doi: 10.1080/09687680701510042

Pramod, K., Kotta, S., Jijith, U. S., Aravind, A., Abu Tahir, M., Manju, C. S., et al. (2020). Surfactant-based prophylaxis and therapy against COVID-19: a possibility. *Med. Hypotheses* 143:110081 doi: 10.1016/j.mehy.2020.110081

Queiroz, A., Pinto, I. F. D., Lima, M., Giovanetti, M., de Jesus, J. G., Xavier, J., et al. (2019). Lipidomic analysis reveals serum alteration of plasmalogens in patients infected with ZIKA virus. *Front. Microbiol.* 10:753. doi: 10.3389/fmicb.2019.00753

Ramanathan, R. J. (2006). Surfactants in the management of respiratory distress syndrome in extremely premature infants. *J. Pediatr Pharmacol. Ther.* 11, 132–144 doi: 10.5863/1551-6776-11.3.132

Rog, T., and Koivuniemi, A. (2016). The biophysical properties of ethanolamine plasmalogens revealed by atomistic molecular dynamics simulations. *Biochim. Biophys. Acta* 1858, 97–103. doi: 10.1016/j.bbamem.2015.10.023

Rubio, J. M., Astudillo, A. M., Casas, J., Balboa, M. A., and Balsinde, J. (2018). Regulation of phagocytosis in macrophages by membrane ethanolamine plasmalogens. *Front. Immunol.* 9:1723. doi: 10.3389/fimmu.2018.01723

Rüdiger, M., Kolleck, I., Putz, G., Wauer, R. R., Stevens, P., and Rüstow, B. (1998). Plasmalogens effectively reduce the surface tension of surfactant-like phospholipid mixtures. *Am J Physiol.* 274, L143–L148. doi: 10.1152/ajplung.1998.274.1.L143

Rüdiger, M., Tölle, A., Meier, W., and Rüstow, B. (2005). Naturally derived commercial surfactants differ in composition of surfactant lipids and in surface viscosity. *Am. J. Physiol. Lung Cell. Mol. Physiol.* 288, L379–L383 doi: 10.1152/ajplung.00176.2004

Satoh, O., Umeda, M., Imai, H., Tunoo, H., and Inoue, K. (1990). Lipid composition of hepatitis B virus surface antigen particles and the particle-producing human hepatoma cell lines. *J. Lipid Res.* 31, 1293–1300. doi: 10.1016/S0022-2275(20)42638-0

Schoeman, J. C., Hou, J., Harms, A. C., Vreeken, R. J., Berger, R., Hankemeier, T., et al. (2016). Metabolic characterization of the natural progression of chronic hepatitis B. *Genome Med.* 8:64. doi: 10.1186/s13073-016-0318-8

Schoggins, J. W., and Randall, G. (2013). Lipids in innate antiviral defense. *Cell Host Microbe* 14, 379–385 doi: 10.1016/j.chom.2013.09.010

Schousboe, P., Wiese, L., Heiring, C., Verder, H., Poorisrisak, P., Verder, P., et al. (2020). Assessment of pulmonary surfactant in COVID-19 patients. *Crit. Care* 24:552 doi: 10.1186/s13054-020-03268-9

Snijder, E. J., Limpens, R.W.A. L., de Wilde, A. H., de Jong, A. W. M., and Zevenhoven-Dobbe JC, Maier HJ. et al. (2020). A unifying structural and functional model of the coronavirus replication organelle: tracking down RNA synthesis. *PLoS Biol.* 18:e3000715. doi: 10.1371/journal.pbio.3000715

Spragg, R. G., Lewis, J. F., Walmrath, H. D., Johannigman, J., Bellingan, G., Laterre, P. F., et al. (2004). Effect of recombinant surfactant protein C-based surfactant on the acute respiratory distress syndrome. *N. Engl. J. Med.* 351, 884–892 doi: 10.1056/NEJMoa033181

Stapleford, K. A., and Miller, D. J. (2010). Role of cellular lipids in positive-sense RNA virus replication complex assembly and function. *Viruses* 2, 1055–1068 doi: 10.3390/v2051055

Struck, A. -W.,Axmann, M., Pfeerle, S., Drosten, C., and Meyer, B. (2012). A hexapeptide of the receptor-binding domain of SARS corona virus spike protein blocks viral entry into host cells via the human receptor ACE2. *Antivir. Res.* 94, 288–296 doi: 10.1016/j.antiviral.2011.12.012

Su, A. I., Pezacki, J. P., Wodicka, L., Brideau, A. D., Supekova, L., Thimme, R., et al. (2002). Genomic analysis of the host response to hepatitis C virus infection. *Proc. Natl. Acad. Sci. U.S.A.* 99, 15669–15674. doi: 10.1073/pnas.202608199

Tanner, L. B., Chng, C., Guan, X. L., Lei, Z., Rozen, S. G., and Wenk, M. R. (2014). Lipidomics identifies a requirement for peroxisomal function during influenza virus replication. *J. Lipid Res.* 55, 1357–1365 doi: 10.1194/jlr.M049148

Thai, T. P., Rodemer, C., Jauch, A., Hunziker, A., Moser, A., Gorgas, K., et al. (2001). Impaired membrane traffic in defective ether lipid biosynthesis. *Hum. Mol. Genet.* 10, 127–136. doi: 10.1093/hmg/10.2.127

Tschernig, T., Veith, N. T., Diler, E., Bischoff, M., Meier, C., and Schicht, M. (2016). The importance of surfactant proteins-new aspects on macrophage phagocytosis. *Ann. Anat.* 208, 142–145. doi: 10.1016/j.aanat.2016.07.005

Ulasli, M., Verheije, M. H., de Haan, C. A., and Reggiori, F. (2010). Qualitative and quantitative ultrastructural analysis of the membrane rearrangements induced by coronavirus. *Cell Microbiol.* 12, 844–861 doi: 10.1111/j.1462-5822.2010.01437.x

Üllena, A., Faulerb, G., Köfelerc, H., Waltla, S., Nussholda, C., Bernharta, E., et al. (2010). Mouse brain plasmalogens are targets for hypochlorous acid-mediated modification in vitro and in vivo. *Free Radic. Biol. Med.* 49, 1655–65. doi: 10.1016/j.freeradbiomed.2010.08.025

Van Kaer, L., Parekh, V. V., and Wu, L. (2013). Invariant natural killer T cells as sensors and managers of inflammation. *Trends Immunol.* 34, 50–58. doi: 10.1016/j.it.2012.08.009

Wallner, S., Grandl, M., Konovalova, T., Sigrüner, A., Kopf, T., Peer, M., et al. (2014). Monocyte to macrophage differentiation goes along with modulation of the plasmalogen pattern through transcriptional regulation. *PLoS One* 9:e94102 doi: 10.1371/journal.pone.0094102

Walmrath, D., Günther, A., Ghofrani, H. A., Schermuly, R., Schneider, T., Grimminger, F., et al. (1996). Bronchoscopic surfactant administration in patients with severe adult respiratory distress syndrome and sepsis. *Am. J. Crit. Care Med.* 154, 57–62 doi: 10.1164/ajrccm.154.1.8680699

Walther, F.J., Gordon, L. M., and Waring, A. J. (2019). Advances in synthetic lung surfactant protein technology. *Expert Rev. Respir. Med.* 13, 499–501 doi: 10.1080/17476348.2019.1589372

Wan, Y., Shang, J., Graham, R., Baric, R. S., and Li, F. (2020). Receptor recognition by the novel coronavirus from Wuhan: an analysis based on decade-long structural studies of SARS coronavirus. *J. Virol.* 94:e00127-20 doi: 10.1128/JVI.00127-20

Weir, J. M., Wong, G., Barlow, C. K., Greeve, M. A., Kowalczyk, A., Almasy, L., et al. (2013). Plasma lipid profiling in a large population-based cohort. *J. Lipid Res.* 54, 2898–2908. doi: 10.1194/jlr.P035808

Wu, K. L., Peng, G. Q., Wilken, M., Geraghty, R. J., and Li, F. (2012). Mechanisms of host receptor adaptation by severe acute respiratory syndrome coronavirus. *J. Biol. Chem.* 287, 8904–8911 doi: 10.1074/jbc.M111.325803

Xiu, S., Dick, A., Ju, H., Mirzaie, S., Abdi, F., Cocklin, S., et al. (2020). Inhibitors of SARS-CoV-2 entry: current and future opportunities. *J. Med. Chem.* 63, 12256–12274. doi: 10.1021/acs.jmedchem.0c00502

Yan, B., Chu, H., Yang, D., Sze, K. H., Lai, P. M., Yuan, S., et al. (2019). Characterization of the lipidomic profile of human coronavirus-infected cells: implications for lipid metabolism remodeling upon coronavirus replication. *Viruses* 11:73 doi: 10.3390/v11010073

Yan, R., Zhang, Y., Li, Y., Xia, L., Guo, Y., and Zhou, Q. (2020). Structural basis for the recognition of SARS-CoV-2 by full-length human ACE2. *Science* 367, 1444–1448 doi: 10.1126/science.abb2762

Yin, J., Glende, J., Schwegmann-Wessels, C., Enjuanes, L., Herrler, G., and Ren, X. (2010). Cholesterol is important for a post-adsorption step in the entry process of transmissible gastroenteritis virus. *Antiviral. Res.* 88, 311–316 doi: 10.1016/j.antiviral.2010.10.002

Yokota, S. (2003). Influenza-associated encephalopathy—patho-physiology and disease mechanisms. *Nippon Rinsho* 61, 1953–1958.

Zaman, M. M., Martin, C. R., Andersson, C., Bhutta, A. Q., Cluette-Brown, J. E., Laposata, M., et al. (2010). Freedman, Linoleic acid supplementation results in increased arachidonic acid and eicosanoid production in CF airway cells and in cftr-/- transgenic mice. *Am. J. Physiol. Lung Cell. Mol. Physiol.* 299, L599–L606 doi: 10.1152/ajplung.00346.2009

Zhang, J., Lan, Y., and Sanyal, S. (2020). Membrane heist: coronavirus host membrane remodeling during replication. *Biochimie* 179, 229–236 doi: 10.1016/j.biochi.2020.10.010

Zheng, Q., Lu, Y., Lure, F., Jaeger, S., and Lu P. (2020). Clinical and radiological features of novel coronavirus pneumonia. *J. Xray Sci. Technol.* 28, 391–404. doi: 10.3233/XST-200687

Zhuo, R., Rong, P., Wang, J., Parvin, R., and Deng, Y. (2021). The potential role of bioactive plasmalogens in lung surfactant. *Front. Cell Dev. Biol.* 9:618102 doi: 10.3389/fcell.2021.618102

Zurrier, B. (1991). Essential fatty acids and inflammation. *Ann. Rheum. Dis.* 50, 745–746. doi: 10.1136/ard.50.11.745

Conflict of Interest: The authors declare that the research was conducted in the absence of any commercial or financial relationships that could be construed as a potential conflict of interest.

frontiers
in Cell and Developmental Biology

MINI REVIEW
published: 18 March 2021
doi: 10.3389/fcell.2021.629820

Bacterial Behavior in Confined Spaces

Hang Du[1,2], Weili Xu[1], Zhizhou Zhang[2] and Xiaojun Han[1]**

[1] State Key Laboratory of Urban Water Resource and Environment, School of Chemistry and Chemical Engineering, Harbin Institute of Technology, Harbin, China, [2] Center for Marine Antifouling Engineering Technology of Shandong Province, School of Marine Science and Technology, Harbin Institute of Technology, Weihai, China

In confined spaces, bacteria exhibit unexpected cellular behaviors that are related to the biogeochemical cycle and human health. Types of confined spaces include lipid vesicles, polymer vesicles, emulsion droplets, microfluidic chips, and various laboratory-made chambers. This mini-review summarizes the behaviors of living bacteria in these confined spaces, including (a) growth and proliferation, (b) cell communication, and (c) motion. Future trends and challenges are also discussed in this paper.

Keywords: bacterial behavior, confined space, growth and proliferation, communication, motion

OPEN ACCESS

Edited by:
Yuru Deng,
University of Chinese Academy of Sciences, China

Reviewed by:
Ott Scheler,
Tallinn University of Technology, Estonia
Lixue Zhang,
Qingdao University, China

****Correspondence:***
Zhizhou Zhang
zhangzzbiox@hitwh.edu.cn
Xiaojun Han
hanxiaojun@hit.edu.cn

Specialty section:
This article was submitted to Cellular Biochemistry, a section of the journal Frontiers in Cell and Developmental Biology

Received: *16 November 2020*
Accepted: *19 February 2021*
Published: *18 March 2021*

Citation:
Du H, Xu W, Zhang Z and Han X (2021) Bacterial Behavior in Confined Spaces. Front. Cell Dev. Biol. 9:629820. doi: 10.3389/fcell.2021.629820

INTRODUCTION

The human body is a representative host of microorganisms. A wide range of bacteria exist in the human intestine and oral cavity and are closely related to human health. The functional behaviors of these bacteria, including oil extraction, nitrogen fixation, and bioremediation, all take place in narrow spaces. Therefore, the study of bacteria in confined spaces is of great significance with respect to the biogeochemical cycle and the healthy balance of the human microbial community. Currently, there is very limited knowledge regarding living matter in confined spaces. Observations and multi-disciplinary investigations of bacterial behaviors in confined spaces have attracted intense interest in recent years.

In the natural environment, the same bacteria may show completely different behaviors in different habitats. The relevant types of behaviors are (a) growth and proliferation, (b) communication, and (c) motion. The habitats are often confined spaces, such as injury sites or intestines. Investigation of bacterial behaviors in restricted spaces will help us to more accurately analyze the factors influencing these behaviors. A confined space usually has good packaging and physical isolation, preventing external interference in bacterial behaviors. Such confined spaces include phospholipid vesicles (Elani et al., 2018; Trantidou et al., 2018), polymer vesicles (Meyer et al., 2015; Luo et al., 2020), emulsion droplets (Zhang et al., 2013; Mahler et al., 2018), and microfluidic chips (Inoue et al., 2001; Keymer et al., 2006).

Herein, we summarize recent research progress on three types of bacteria behaviors in confined spaces: growth and proliferation, communication, and motion. Future prospects are discussed at the end of the paper.

CONFINED SPACES

Bacteria are approximately several microns in size. To study the behavior of bacteria more precisely, confined spaces can be designed to range from several microns to tens of microns. These confined spaces can be roughly divided into four categories: phospholipid vesicles, polymer vesicles, droplets, and microfluidic chips. Phospholipid vesicles can be fabricated by hydration and phase transfer methods, and they serve as a culture environment for bacterial cells.

Methods to prepare polymer vesicles largely depend on the vesicles' compositions. The main polymers used to encapsulate bacteria are gels and porous materials. Droplets can be obtained by mixing the bacterial solution with oils or using microfluidic techniques. Microfluidic chips are fabricated by typical photolithography methods. **Table 1** summarizes studies of bacterial behavior in the abovementioned confined spaces.

BACTERIAL GROWTH AND PROLIFERATION IN CONFINED SPACES

Growth and proliferation are basic behaviors of bacteria. These behaviors in a confined space are different from those observed conventionally.

Juskova et al. (2019) provided a novel method to monitor the real-time activity of bacterial growth inside giant unilamellar vesicles (GUVs) (**Figure 1A**). They reported the encapsulation of single bacteria in small-volume GUVs (1–33 pL), followed by immobilization of the GUVs on a planar lipid bilayer membrane on a glass surface, under which photoelectronic detection could be applied at a single-cell level (Morita et al., 2018). Polyelectrolyte capsules with different numbers of layers have also been used to encapsulate bacteria. The delayed growth of bacteria was significantly correlated with the number of layers of the reticular vesicles. Polyethylene capsules with more than six layers were very solid. Interestingly, cell size and green fluorescent protein (GFP) expression were increased in thicker polyethylene capsules. This was the first demonstration that confined spaces may affect biochemical reactions in bacteria (Rybkin et al., 2019). In microfluidic channels, owing to continuous cell propagation, *Escherichia coli* is greatly compressed in submicron narrow channels that are smaller than its diameter. Although *E. coli* can still grow and divide, this deformation is irreversible, even if the bacteria are later removed from the confined space (Jakiela et al., 2013).

TABLE 1 | Types of bacterial behaviors inside confined spaces.

Confined space	Bacterium	Types of bacterial behavior	Applications	Unexpected behavior (in contrast with traditional methods)	Example references
Lipid vesicles	*E. coli*	(a) Growth and proliferation	To observe bacterial growth and proliferation	The bacteria proliferated more slowly.	Morita et al., 2018
	E. coli	(a) Growth and proliferation	To monitor microbial growth and proliferation	*E. coli* proliferated more slowly, whereas other bacteria elongated without division owing to the accumulation of matter.	Juskova et al., 2019
Polymer vesicles	*E. coli*	(a) Growth and proliferation; (b) communication	To investigate effects of physical barriers against mass gain and cell division	Both the GFP fluorescent signal of bacteria and the cell size increased by factors of more than five and two in the confined space, respectively.	Rybkin et al., 2019
Droplets	*Staphylococcus aureus*	(b) Communication	To study confinement-induced QS	Individual or small groups of *S. aureus* bacteria initiated virulence factor expression.	Carnes et al., 2010
	E. coli and *B. subtilis*	(c) Motion	To observe the swimming behavior of bacteria	Dense suspensions of *E. coli* produced notable periodic vortex reversal.	Hamby et al., 2018
	E. coli	(c) Motion	To observe the motion of bacteria to transfer mechanical energy to the confining environment	The motion of dense *E. coli* inside the droplet propelled droplet movement.	Ramos et al., 2020
	Magnetospirillum gryphiswaldense	(c) Motion	To observe the bacteria self-assembling into a rotating body in a confined space	Living bacteria self-assembled into a rotary motor.	Vincenti et al., 2019
	Two *B. subtilis* strains: the WT 168 and the mutant strain	(c) Motion	To measure the swimming and motion directions of bacterial cells	The microorganisms swam upstream against the spiral vortex.	Lushi et al., 2014
	Pseudomonas aeruginosa	(b) Communication	To study the QS pathways of bacteria	One to three bacteria initiated QS and achieved QS-dependent growth.	Boedicker et al., 2009
Microfluidic chips	*Salmonella typhimurium*	(b) Communication	To observe bacterial cancer-targeting to normal (THLE-2) or cancer hepatocytes (HepG2)	*S. typhimurium* showed a significant preference for HepG2 cells compared with normal hepatocytes.	Hong et al., 2013
	E. coli	(b) Communication	To study the adaptive dynamics of the bacterial metapopulation in heterogeneous habitats	Local bacterial populations coexisted and were weakly coupled with neighbor populations.	Keymer et al., 2006
Porous media	*E. coli*	(c) Motion	To track bacterial motion	Bacteria showed intermittent movement in porous media.	Bhattacharjee and Datta, 2019
	E. coli and *Staphylococcus sciuri*	(c) Motion	To observe the effects of bacteria with different motility on vesicle trapping	The bacteria with higher activity more easily passed through pores.	Luo et al., 2020

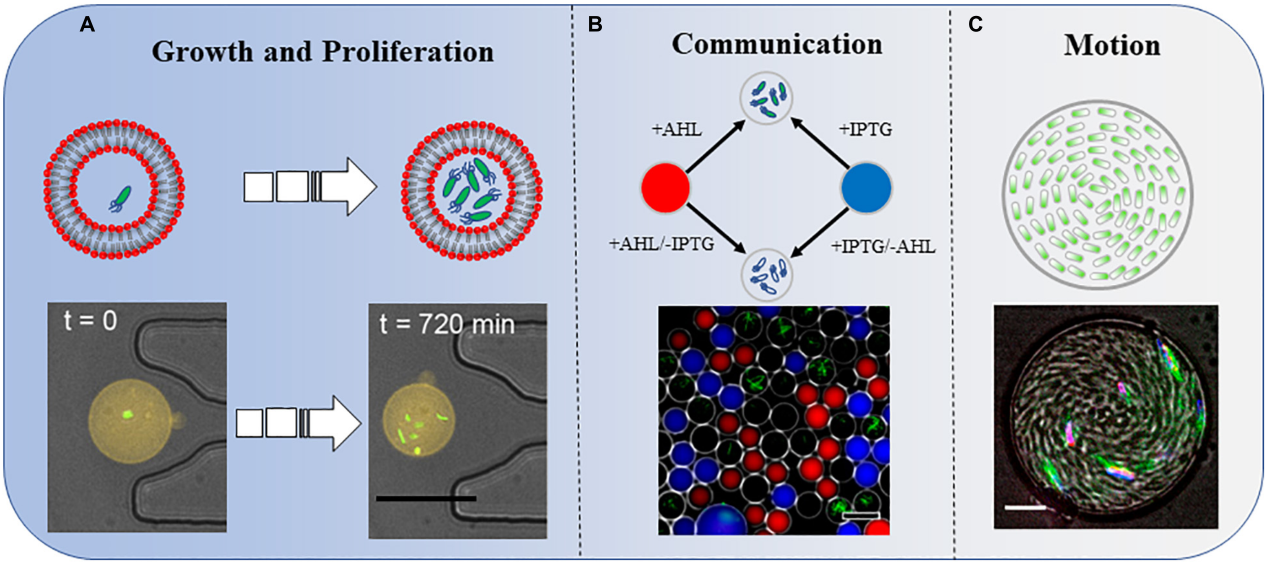

FIGURE 1 | Three types of bacterial behaviors in a confined space. **(A)** Growth and proliferation. Bacterial growth and proliferation in phospholipid vesicles. The shrinkage of the space reduces the growth and proliferation speed of bacteria compared with those in the same culture medium in a non-enclosed space. Scale bar, 25 μm. Adapted with permission from Juskova et al. (2019). Copyright 2019, American Chemical Society. **(B)** Communication. Bacteria sense IPTG and QS molecule AHL diffused into the droplets. The combined effects of these two molecules induce the bacteria to produce GFP. Scale bar, 50 μm. Adapted with permission from Weitz et al. (2014). Copyright 2014, American Chemical Society. **(C)** Motion. A concentrated suspension of bacteria forms a vortex motion in the droplet. Scale bar, 10 μm. Adapted with permission from Lushi et al. (2014). Copyright 2014, National Academy of Sciences.

Some other interesting bacterial behaviors may be observed in confined spaces. For example, when riboflavin-producing bacteria are encapsulated, riboflavin accumulates in vesicles, causing the bacteria to elongate without division (Juskova et al., 2019). Fungi in microfluidic chips have different growth behaviors owing to the limited space. Three conditions were used to explore the mechanism of hyphal extension in a confined space. When fungal hyphae met sharp-angle obstacles, they tended to change direction to avoid the obstacles. When they collided with an obstacle nearly orthogonally, they continued to extend forward after splitting into two hyphae. Finally, the hyphae did not grow after touching the wall (Held et al., 2019).

Studies of bacterial growth and proliferation in confined spaces are at a preliminary stage, as only a few bacterial species have been tested (**Table 1**). Reports on human cancer cells in confined spaces are still rare (Hong et al., 2013). It is difficult for traditional (low-resolution) methods to simultaneously monitor the biological processes of many cells at single-cell resolution. X-ray crystallography and electron microscopy have for many years been used to capture information on the nanometer scale; however, they are only suitable for static observation. In 2020, a resolution of 1.25 Å was achieved with cryo-electron microscopy (Nakane et al., 2020), which is good enough to pinpoint the position of a single atom in a protein. However, X-ray crystallography and electron microscopy do not work in a high-throughput manner and cannot be used to directly observe living cells. Instead, high-throughput cell studies can be carried out in the confined spaces of a microfluidic chip; this may play an indispensable part by generating a huge amount of new data and numerous novel findings.

BACTERIAL COMMUNICATION IN CONFINED SPACES

In nature, bacteria communicate through the perception and secretion of metabolic signals. Some special bacteria have the ability to communicate through magnetic fields (Shcheglov et al., 2002; Vinhas et al., 2020). There are many ways for bacteria to interact, including chemotactic swimming through signaling molecules and quorum-sensing (QS) molecules, and co-cultivation of two defective bacteria that benefit from their respective metabolites. In the past few years, these methods have been used to observe molecular communications among bacteria in different confined chambers.

Quorum-sensing is a phenomenon that occurs among microorganisms with a high population density. The signaling molecules released by bacteria themselves reach a threshold, which in turn affects the expression of specific bacterial genes and regulates the behavior of microorganisms, such as the formation of biofilms, a coordinated response to toxins, and emission of fluorescence. One such signaling molecule is self-inducer AI (auto-inducer, AI). AI can be roughly divided into three categories: (i) high acylserine lactone (AHL) from Gram-negative bacteria; (ii) oligopeptide molecules from Gram-positive bacteria; and (iii) AI-2 from both types of bacteria. Encapsulation of a single or a small number of bacteria in a confined space has been proven to initiate the QS pathway. Bacteria do not need to grow to achieve the high density required to initiate the density-dependent QS reaction (Boedicker et al., 2009).

A single *Staphylococcus aureus* bacterium can detect its restriction after being captured in a confined space and employ QS to activate virulence and metabolic pathways that maintain survival (Carnes et al., 2010). In one study, by analyzing the strength of the fluorescent signal in the droplets, the authors not only investigated the influence of distances on the strength of signal transmission but also added another factor, IPTG, to explore the results of group sensing in space and time (**Figure 1B**; Weitz et al., 2014).

An L-lysine-deficient variant relies on L-lysine-producing *Corynebacterium glutamicum* to produce glutamate to be cultured on a microfluidic chip (Burmeister et al., 2018). The yeast community and methanogenic community cooperate through metabolite exchanges. This "strong partner mix" can be extended to multiple microorganisms (Momeni et al., 2013). Three microorganisms can also survive in the same microhabitat through mutual support under conditions of limited nutrition. There is no evidence for interaction among nitrogenase, *Bacillus licheniformis*, and Bacteroides communities in nature. However, they can coexist by providing nutrients to each other in separated chambers of microfluidic chips, even if the nutrients in the environment are limited. It is necessary to study how bacterial communities interact and perform community functions in natural ecosystems, and how to maintain species diversity of microbial communities in a confined space (Kim et al., 2008).

Bacterial communication is one of the biological communication types that has been studied in confined spaces. The next step would be tissue communication, which involves many different cells in the same tissue. Partial tissue samples could be assembled with single cells in a confined space, and it would even be possible to synthesize human organs by assembling cells in confined spaces for drug screening. To this end, cellular communication and regulation must be elucidated in much more detail. Molecular communications among metabolic modules and signaling transduction pathways also require further investigation in more delicate microfluidic devices. Confined-space-based studies are suitable for simultaneously observing and analyzing communications among many cancerous and normal cells at the single-cell level.

MOTION OF BACTERIA IN CONFINED SPACES

The motion of a single bacterium or cell in a tiny tunnel-like confined space is a physiologically significant behavior. For example, a single-celled organism (amoeba) can travel through the olfactory nerve into the frontal lobe of the brain, which represents a typical case of cell motion in a confined space.

The first direct visualization of bacterial motion at single-cell resolution in three-dimensional (3D) porous media was provided by Bhattacharjee and Datta (2019). They found that bacteria did not simply exhibit run-and-tumble motility as commonly assumed but followed a hop-and-trap model. Although interesting, this study did not consider different bacteria types and pore sizes. The microfluidic environment can enhance the diffusion of swimming bacteria. Bacteria in a geometric maze chip showed typical running and rolling motion. However, the bacteria moving in the maze chip showed stronger motility than free bacteria. It is of great medical significance to study the motion of bacteria in a narrow passage in microfluidic chips, for instance, to better understand the spread of bacteria in the process of infection (Weber et al., 2019).

Bacteria explore their natural environment through frequent motion. Frangipane et al. (2019) built a 3D micro-chamber to study the properties of bacterial random-walk paths and reported some novel results. The mean residence time of swimming bacteria inside the artificial complex microstructures was constrained by the sole free surface to perimeter ratio. As a counterintuitive result, bacteria escape faster from chamber structures with a higher density of obstacles, owing to a reduced accessible surface (Frangipane et al., 2019). In another report, *Bacillus subtilis* within a disk-shaped droplet formed a stable vortex that counterrotated at the periphery. However, under similar confinement, *E. coli* displayed a single periodically reversed-direction vortex on a time scale of seconds (Hamby et al., 2018). More interestingly, once the radius of the confinement chamber was below a critical value, *B. subtilis* formed a steady single vortex within a thin cylindrical chamber. The cells within the spiral vortex swam upstream against the counter-rotating flows (**Figure 1C**; Lushi et al., 2014). Vincenti et al. (2019) reported that motile magnetotactic bacteria confined in water-in-oil droplets self-assembled into a rotary motor under a constant magnetic field.

Chemotaxis is a sensing mechanism by which individual bacterial cells disperse for exogenous sources of nutrients. Researchers found that in the presence of appropriate environmental topologies in a confined space, stressed bacteria formed solitary "moving waves" and that these waves nucleated population collapse of the bacteria into small confining structures, representing a previously unappreciated role of the bacterial chemotaxis system (Park et al., 2003).

Bacteria in some confined spaces not only have their own motion behavior but also promote the motion of the confined space. A dense bacterial suspension of moving bacteria enclosed in droplets drives the droplets with a continuous Brownian motion (Ramos et al., 2020).

Studies of confined-space-based bacterial motion have many applications in biomedical research and significant potential implications. For instance, they provide micron-scale information on processes including the translocation pathogenic microbes in human tissues, life-cycle trafficking of a virus particle in different cells, metastasis of cancerous cells into healthy tissues. There is strong evidence that amyloid plaques in the human brain wrap microbes (Kumar et al., 2016). However, how these microbes (virus, bacterium, or fungus) move through tissues and translocate into the brain remains obscure.

OTHER OBSERVED BACTERIAL BEHAVIORS IN CONFINED SPACE

Multi-cell interaction is a sub-field of systems biology that has not seen any major breakthrough until now. It is still difficult to describe in detail multi-cell or multi-species interactions in any known natural microbial community. Confined spaces offer a good opportunity to investigate multi-cell interactions. The observed phenomena are not limited to bacterial growth, proliferation, communication, and motion. Preliminary studies have shown that the mutant type of *E. coli* is more dominant than the wild type in a confined space, in contrast to observations in plate colonies (Hol et al., 2015). When nutrients are scarce, they do not compete in the entire microfluidic chip but coexist in the same habitat and occupy different niches (Lambert et al., 2011). Park et al. (2011) demonstrated that droplets could be effectively utilized to co-cultivate two to three different microbes and detect symbiotic relationships. In another example, a lysine-producing *C. glutamicum* strain and a lysine auxotrophic variant of the same species produced a symbiotic interaction, relying on each other's metabolites (Burmeister et al., 2018). The authors also investigated bacterial conjugation between *E. coli* S17-1 and *Pseudomonas putida* KT2440 cells and showed that direct cell contact was essential for successful gene transfer *via* conjugation. The spatiotemporal dynamics of synthetic microbial consortia in microfluidic devices (Alnahhas et al., 2019) were obtained by co-culturing two different strains of *E. coli* in microfluidic devices. The size of the cell-trapping region was found to be a critical determinant of the spatiotemporal dynamics.

DISCUSSION

Studies of bacterial behavior within confined spaces provide novel knowledge in the fields of microbiology and medical science. Feasible types of confined macro-scale apparatus include phospholipid vesicles, droplets, polymer vesicles, microfluidic chips, and other chambers. Microfluidic-based devices will probably be the main platform used to provide confined spaces with unlimited structural complexity in the future. In these confined spaces, growth, proliferation, communication, colonization, dispersion, motion, and other bacterial behaviors can be observed, quantified, and modeled in convenient ways. Owing to their delicate inner structure and physical or chemical properties, such confined spaces have a very important role in quantitative studies of the behavior of potentially all types of bacteria. Studies of the behavior of bacteria in confined spaces will undoubtedly be a future trend, with striking results.

AUTHOR CONTRIBUTIONS

HD read all the references of this article and wrote the article. WX provided some suggestions for the article. XH and ZZ helped to establish the logical framework and language polishing of the entire article. All authors contributed to the article and approved the submitted version.

FUNDING

This work was supported by the National Natural Science Foundation of China (Grant Nos. 21773050 and 21929401), the National Natural Science Foundation of Heilongjiang Province for Distinguished Young Scholars (JC2018003), the National Natural Science Foundation of Shandong Province (ZR2018MC002), and Weihai Municipal Sci/Tech Funds (WH2018019 and WH2020008).

REFERENCES

Alnahhas, R. N., Winkle, J. J., Hirning, A. J., Karamched, B., Ott, W., Josic, K., et al. (2019). Spatiotemporal dynamics of synthetic microbial consortia in microfluidic devices. *ACS Synth. Biol.* 8, 2051–2058. doi: 10.1021/acssynbio.9b00146

Bhattacharjee, T., and Datta, S. S. (2019). Bacterial hopping and trapping in porous media. *Nat. Commun.* 10:2075. doi: 10.1038/s41467-019-10115-1

Boedicker, J. Q., Vincent, M. E., and Ismagilov, R. F. (2009). Microfluidic confinement of single cells of bacteria in small volumes initiates high-density behavior of quorum sensing and growth and reveals its variability. *Angew. Chem. Int. Ed. Engl.* 48, 5908–5911. doi: 10.1002/anie.200901550

Burmeister, A., Hilgers, F., Langner, A., Westerwalbesloh, C., Kerkhoff, Y., Tenhaef, N., et al. (2018). A microfluidic co-cultivation platform to investigate microbial interactions at defined microenvironments. *Lab Chip* 19, 98–110. doi: 10.1039/c8lc00977e

Carnes, E. C., Lopez, D. M., Donegan, N. P., Cheung, A., Gresham, H., Timmins, G. S., et al. (2010). Confinement-induced quorum sensing of individual *Staphylococcus aureus* bacteria. *Nat. Chem. Biol.* 6, 41–45. doi: 10.1038/nchembio.264

Elani, Y., Trantidou, T., Wylie, D., Dekker, L., Polizzi, K., Law, R. V., et al. (2018). Constructing vesicle-based artificial cells with embedded living cells as organelle-like modules. *Sci. Rep.* 8:4564. doi: 10.1038/s41598-018-22263-3

Frangipane, G., Vizsnyiczai, G., Maggi, C., Savo, R., Sciortino, A., Gigan, S., et al. (2019). Invariance properties of bacterial random walks in complex structures. *Nat. Commun.* 10:2442. doi: 10.1038/s41467-019-10455-y

Hamby, A. E., Vig, D. K., Safonova, S., and Wolgemuth, C. W. (2018). Swimming bacteria power microspin cycles. *Sci. Adv.* 4:eaau0125. doi: 10.1126/sciadv.aau0125

Held, M., Kaspar, O., Edwards, C., and Nicolau, D. V. (2019). Intracellular mechanisms of fungal space searching in microenvironments. *Proc. Natl. Acad. Sci. U.S.A.* 116, 13543–13552. doi: 10.1073/pnas.1816423116

Hol, F. J., Galajda, P., Woolthuis, R. G., Dekker, C., and Keymer, J. E. (2015). The idiosyncrasy of spatial structure in bacterial competition. *BMC Res Notes* 8:245. doi: 10.1186/s13104-015-1169-x

Hong, J. W., Song, S., and Shin, J. H. (2013). A novel microfluidic co-culture system for investigation of bacterial cancer targeting. *Lab Chip* 13, 3033–3040. doi: 10.1039/c3lc50163a

Inoue, I., Wakamoto, Y., Moriguchi, H., Okano, K., and Yasuda, K. (2001). On-chip culture system for observation of isolated individual cells. *Lab Chip* 1, 50–55. doi: 10.1039/b103931h

Jakiela, S., Kaminski, T. S., Cybulski, O., Weibel, D. B., and Garstecki, P. (2013). Bacterial growth and adaptation in microdroplet chemostats. *Angew. Chem. Int. Ed. Engl.* 52, 8908–8911. doi: 10.1002/anie.201301524

Juskova, P., Schmid, Y. R. F., Stucki, A., Schmitt, S., Held, M., and Dittrich, P. S. (2019). "Basicles": microbial growth and production monitoring in giant lipid vesicles. *ACS Appl. Mater. Interfaces* 11, 34698–34706. doi: 10.1021/acsami.9b12169

Keymer, J. E., Galajda, P., Muldoon, C., Park, S., and Austin, R. H. (2006). Bacterial metapopulations in nanofabricated landscapes. *Proc. Natl. Acad. Sci. U.S.A.* 103, 17290–17295. doi: 10.1073/pnas.0607971103

Kim, H. J., Boedicker, J. Q., Choi, J. W., and Ismagilov, R. F. (2008). Defined spatial structure stabilizes a synthetic multispecies bacterial community. *Proc. Natl. Acad. Sci. U.S.A.* 105, 18188–18193. doi: 10.1073/pnas.0807935105

Kumar, D. K., Choi, S. H., Washicosky, K. J., Eimer, W. A., Tucker, S., Ghofrani, J., et al. (2016). Amyloid-beta peptide protects against microbial infection in mouse and worm models of Alzheimer's disease. *Sci. Transl. Med.* 8:340ra72. doi: 10.1126/scitranslmed.aaf1059

Lambert, G., Liao, D., Vyawahare, S., and Austin, R. H. (2011). Anomalous spatial redistribution of competing bacteria under starvation conditions. *J. Bacteriol.* 193, 1878–1883. doi: 10.1128/JB.01430-10

Luo, R., Pashapour, S., Staufer, O., Platzman, I., and Spatz, J. P. (2020). Polymer−based porous microcapsules as bacterial traps. *Adv. Funct. Mater.* 30:1908855. doi: 10.1002/adfm.201908855

Lushi, E., Wioland, H., and Goldstein, R. E. (2014). Fluid flows created by swimming bacteria drive self-organization in confined suspensions. *Proc. Natl. Acad. Sci. U.S.A.* 111, 9733–9738. doi: 10.1073/pnas.1405698111

Mahler, L., Wink, K., Beulig, R. J., Scherlach, K., Tovar, M., Zang, E., et al. (2018). Detection of antibiotics synthetized in microfluidic picolitre-droplets by various actinobacteria. *Sci. Rep.* 8:13087. doi: 10.1038/s41598-018-31263-2

Meyer, A., Pellaux, R., Potot, S., Becker, K., Hohmann, H. P., Panke, S., et al. (2015). Optimization of a whole-cell biocatalyst by employing genetically encoded product sensors inside nanolitre reactors. *Nat. Chem.* 7, 673–678. doi: 10.1038/nchem.2301

Momeni, B., Brileya, K. A., Fields, M. W., and Shou, W. (2013). Strong inter-population cooperation leads to partner intermixing in microbial communities. *Elife* 2:e00230. doi: 10.7554/eLife.00230

Morita, M., Katoh, K., and Noda, N. (2018). Direct observation of bacterial growth in giant unilamellar vesicles: a novel tool for bacterial cultures. *ChemistryOpen* 7, 845–849. doi: 10.1002/open.201800126

Nakane, T., Kotecha, A., Sente, A., McMullan, G., Masiulis, S., Brown, P., et al. (2020). Single-particle cryo-EM at atomic resolution. *Nature* 587, 152–156. doi: 10.1038/s41586-020-2829-0

Park, J., Kerner, A., Burns, M. A., and Lin, X. N. (2011). Microdroplet-enabled highly parallel co-cultivation of microbial communities. *PLoS One* 6:e17019. doi: 10.1371/journal.pone.0017019

Park, S., Wolanin, P. M., Yuzbashyan, E. A., Lin, H., Darnton, N. C., Stock, J. B., et al. (2003). Influence of topology on bacterial social interaction. *Proc. Natl. Acad. Sci. U.S.A.* 100, 13910–13915. doi: 10.1073/pnas.1935975100

Ramos, G., Cordero, M. L., and Soto, R. (2020). Bacteria driving droplets. *Soft Matter* 16, 1359–1365. doi: 10.1039/c9sm01839e

Rybkin, I., Gorin, D., Sukhorukov, G., and Lapanje, A. (2019). Thickness of polyelectrolyte layers of separately confined bacteria alters key physiological parameters on a single cell level. *Front. Bioeng. Biotechnol.* 7:378. doi: 10.3389/fbioe.2019.00378

Shcheglov, V. S., Alipov, E. D., and Belyaev, I. Y. (2002). Cell-to-cell communication in response of *E. coli* cells at different phases of growth to low-intensity microwaves. *Biochim. Biophys. Acta* 1572, 101–106. doi: 10.1016/s0304-4165(02)00283-0

Trantidou, T., Dekker, L., Polizzi, K., Ces, O., and Elani, Y. (2018). Functionalizing cell-mimetic giant vesicles with encapsulated bacterial biosensors. *Interface Focus* 8:20180024. doi: 10.1098/rsfs.2018.0024

Vincenti, B., Ramos, G., Cordero, M. L., Douarche, C., Soto, R., and Clement, E. (2019). Magnetotactic bacteria in a droplet self-assemble into a rotary motor. *Nat. Commun.* 10:5082. doi: 10.1038/s41467-019-13031-6

Vinhas, A., Almeida, A. F., Goncalves, A. I., Rodrigues, M. T., and Gomes, M. E. (2020). Magnetic stimulation drives macrophage polarization in cell to-cell communication with IL-1beta primed tendon cells. *Int. J. Mol. Sci.* 21:5441. doi: 10.3390/ijms21155441

Weber, A., Bahrs, M., Alirezaeizanjani, Z., Zhang, X., Beta, C., and Zaburdaev, V. (2019). Rectification of bacterial diffusion in microfluidic labyrinths. *Front. Phys.* 7:148. doi: 10.3389/fphy.2019.00148

Weitz, M., Muckl, A., Kapsner, K., Berg, R., Meyer, A., and Simmel, F. C. (2014). Communication and computation by bacteria compartmentalized within microemulsion droplets. *J. Am. Chem. Soc.* 136, 72–75. doi: 10.1021/ja411132w

Zhang, Y., Ho, Y. P., Chiu, Y. L., Chan, H. F., Chlebina, B., Schuhmann, T., et al. (2013). A programmable microenvironment for cellular studies via microfluidics-generated double emulsions. *Biomaterials* 34, 4564–4572. doi: 10.1016/j.biomaterials.2013.03.002

Conflict of Interest: The authors declare that the research was conducted in the absence of any commercial or financial relationships that could be construed as a potential conflict of interest.

frontiers
in Cell and Developmental Biology

ORIGINAL RESEARCH
published: 12 May 2021
doi: 10.3389/fcell.2021.655606

A Putative Lipid-Associating Motif in the West Nile Virus NS4A Protein Is Required for Efficient Virus Replication

Andrea Mikulasova[1], Leah K. Gillespie[2†], Rebecca L. Ambrose[2†], Turgut E. Aktepe[2], Alice M. Trenerry[2], Susann Liebscher[2] and Jason M. Mackenzie[2]*

[1] Department of Physiology Anatomy and Microbiology, La Trobe University, Melbourne, VIC, Australia, [2] Department of Microbiology and Immunology, University of Melbourne, Melbourne, VIC, Australia

OPEN ACCESS

Edited by:
Angelina Angelova,
UMR 8612 Institut Galien Paris Sud
(IGPS), France

Reviewed by:
Margo A. Brinton,
Georgia State University,
United States
Jiri Cerny,
Institute of Biotechnology (ASCR),
Czechia

***Correspondence:**
Jason M. Mackenzie
jason.mackenzie@unimelb.edu.au

†Present address:
Leah K. Gillespie,
WHO Collaborating Centre
for Reference and Research on
Influenza, Peter Doherty Institute
for Infection and Immunity,
Melbourne, VIC, Australia
Rebecca L. Ambrose,
Hudson Institute of Medical Research,
Monash University, Clayton,
Melbourne, VIC, Australia

Specialty section:
This article was submitted to
Cellular Biochemistry,
a section of the journal
Frontiers in Cell and Developmental
Biology

Received: *19 January 2021*
Accepted: *07 April 2021*
Published: *12 May 2021*

Citation:
Mikulasova A, Gillespie LK,
Ambrose RL, Aktepe TE, Trenerry AM,
Liebscher S and Mackenzie JM
(2021) A Putative Lipid-Associating
Motif in the West Nile Virus NS4A
Protein Is Required for Efficient Virus
Replication.
Front. Cell Dev. Biol. 9:655606.
doi: 10.3389/fcell.2021.655606

Flavivirus replication is intimately associated with re-organized cellular membranes. These virus-induced changes in membrane architecture form three distinct membranous "organelles" that have specific functions during the flavivirus life cycle. One of these structures is the replication complex in which the flaviviral RNA is replicated to produce progeny genomes. We have previously observed that this process is strictly dependent on cellular cholesterol. In this study we have identified a putative cholesterol recognition/interaction amino acid consensus (CRAC) motif within the West Nile virus strain Kunjin virus (WNV_{KUN}) NS4A protein. Site-directed mutagenesis of this motif within a WNV_{KUN} infectious clone severely attenuated virus replication and the capacity of the mutant viruses to form the replication complex. Replication of the mutant viruses also displayed reduced co-localization with cellular markers recruited to replication sites during wild-type virus replication. In addition, we observed that the mutant viruses were significantly impaired in their ability to remodel cytoplasmic membranes. However, after extensive analysis we are unable to conclusively reveal a role for the CRAC motif in direct cholesterol binding to NS4A, suggesting additional complex lipid-protein and protein-protein interactions. We believe this study highlights the crucial role for this region within NS4A protein in recruitment of cellular and viral proteins to specialized subdomains on membrane platforms to promote efficient virus replication.

Keywords: West Nile virus, RNA replication, membrane remodeling, NS4A protein, virus-host interactions

INTRODUCTION

Replication of flaviviruses, like all positive-stranded RNA viruses, is associated with specialized cytoplasmic membrane structures that wrap around the active replication complexes (RC), providing a favorable microenvironment that facilitates efficient RNA synthesis. The membrane structures induced in flavivirus-infected cells appear especially intriguing in that they consist of at least two or three well defined compartments with distinct functions during replication (Westaway et al., 1997b; Mackenzie et al., 1999; Mackenzie, 2005). Membranes derived from the endoplasmic reticulum (ER) undergo proliferation and remodeling in the process of their formation. In particular they can be observed as a complex network of convoluted membranes (CM) or paracrystalline arrays (PC), or vesicular/spherular invaginations packed within membrane sacs, termed vesicle packets (VP) (Mackenzie et al., 1996a,b; Westaway et al., 1997b; Mackenzie, 2005). Immunogold-labeling, subcellular fractionation and electron tomography studies have revealed that the VP house the flavivirus RC, whereas the role the CM/PC has been postulated to function during translation and proteolytic maturation of the flavivirus polyprotein (Mackenzie et al., 1996a, 1998, 2007a; Westaway et al., 1997b, 1999).

Our detailed ultrastructural analysis, using an Australian WNV strain Kunjin virus ($\mathrm{WNV_{KUN}}$) as a model system, allowed us to derive the consensus viral protein composition of the $\mathrm{WNV_{KUN}}$ RC. Based on the analysis of purified active membrane fractions and immunoelectron microscopy (cryo-IEM), we identified five of the seven non-structural (NS) proteins (NS1, NS2A, NS3, NS4A, and NS5) involved in replication of the viral RNA (Westaway et al., 1997b, 2002; Mackenzie et al., 1998). NS5 protein contains motifs for methyl transferase and RNA-dependent RNA polymerase (RdRp) motifs (Rice et al., 1985; Koonin, 1993). The remaining NS proteins most likely function as regulatory/accessory molecules and play a role in RC formation, a prerequisite step for productive viral RNA replication. In addition to the role of viral proteins in the formation and integrity of the $\mathrm{WNV_{KUN}}$ RC we have also identified an essential requirement for intracellular cholesterol (Mackenzie et al., 2007b). We observed that drug-induced perturbations that reduced the synthesis of intracellular cholesterol drastically impaired $\mathrm{WNV_{KUN}}$ replication. This appears to be solely due to the intracellular concentration (or distribution) of cholesterol as treatment of infected cells with methyl-β-cyclodextran did not significantly affect replication *per se*. Subsequently it has been observed that dengue virus replication alters lipid homeostasis (Perera et al., 2012), but is equally dependent on cholesterol, sphingolipid and continual fatty acid synthesis (Rothwell et al., 2009; Heaton et al., 2010; Martin-Acebes et al., 2014). These complementary studies have emphasized the strict requirement of cellular lipids in providing a membrane platform for efficient flavivirus replication.

Since the RC of all positive-sense RNA viruses are dependent on membrane interactions, lipids are expected to play a major role in facilitating viral replication and proliferation. Indeed, these RNA viruses actively modulate cellular lipid metabolism to provide a lipid-rich environment suitable for structural and functional integrity of their RC. Cellular lipid requirements vary between different virus families and individual members, as do the intracellular sites and cellular membranes/organelles utilized during virus replication (Miller and Krijnse-Locker, 2008). In the last years, the role of cholesterol in infection has gained much attention. Studies based on transcriptome and proteomic analyses have demonstrated that the expression of genes related to the synthesis and transport of cholesterol and fatty acids is dysregulated in Hepatitis C virus (HCV) infected cells (Fujino et al., 2010). Moreover, results investigating HCV replication using statins (inhibitors of cholesterol synthesis) and other compounds specific for inhibition of fatty acid biosynthesis, have clearly shown that a decrease in cellular fatty acid and cholesterol biosynthesis reduces HCV replication (Su et al., 2002; Ye et al., 2003). Recent investigations of flavivirus-infected cells have revealed that dengue virus (DENV)-infected cells have altered lipid homeostasis (Perera et al., 2012), increased fatty acid synthesis (Heaton et al., 2010) and appear to degrade lipid droplets to release free fatty acids (Heaton and Randall, 2010). In addition, it was recently shown that WNV also alters lipid biosynthesis and requires sphingolipid metabolism for efficient production of WNV virions (Martin-Acebes et al., 2014). These recent studies provide increasingly evidence for the role of lipids in the replication of the *Flaviviridae*.

In this study we have extended our previous finings to define a potential role for cholesterol-rich micro-domains within the ER in facilitating $\mathrm{WNV_{KUN}}$ RC formation and function. We have also identified a region within the N-terminus of the $\mathrm{WNV_{KUN}}$ protein NS4A that contributes to this. To this end we have performed site-directed mutagenesis within a $\mathrm{WNV_{KUN}}$ infectious clone to inactivate a potential membrane proximal cholesterol recognition/interaction amino acid consensus (CRAC) motif identified within NS4A. We investigated the importance of the CRAC motif on virus replication by generating recombinant viruses containing alternations in this motif.

MATERIALS AND METHODS

Viruses and Cells

Cells were infected with $\mathrm{WNV_{KUN}}$ strain MRM61C at an approximate multiplicity of infection (m.o.i.) of 3 as has been described previously (Westaway et al., 1997a). Vero and BHK cells were maintained in DMEM supplemented with 5% FCS (Lonza, Basel, Switzerland) and penicillin/streptomycin (100 U/mL and 100 μg/mL, respectively, GIBCO-BRL) at 37°C with 5% CO_2.

Antibodies

$\mathrm{WNV_{KUN}}$ specific anti-NS1 (clone 4G4; Macdonald et al., 2005) and anti-NS5 (clone 5H1.1) monoclonal antibodies were generously provided by Dr. Roy Hall (University of Queensland, Brisbane, Australia). $\mathrm{WNV_{KUN}}$-specific rabbit anti-NS4A polyclonal antisera has been described previously (Mackenzie et al., 1998). Rabbit anti-β-1,4-galactosyltransferase (GalT) polyclonal antibodies (Berger et al., 1993) were generously provided by Dr. Eric Berger (University of Zurich, Zurich, Switzerland). Rabbit anti-Erlin-2 antibodies were purchased from Cell Signaling Technologies and mouse anti-dsRNA (clone J2) antibodies were purchased from English & Scientific Consulting Bt. (Hungry). Alexa Fluor 488- and 594-conjugated anti-rabbit and anti-mouse specific IgG were purchased from Molecular Probes (Invitrogen, Leiden, Netherlands).

Plasmids and Transfection

Recombinant cDNA plasmids expressing eGFP-tagged erlin-1, erin-2, prohibitin, stomatin, and flotillin were kindly provided by

Dr. Stephen Robbins (University of Calgary, Canada). Plasmids were introduced into cells via Lipofectamine delivery following the manufacturer's instructions.

Immunofluorescence (IF) Analysis

Vero cell monolayers on coverslips were infected with WNV_{KUN} and incubated at 37°C for 24 h. The cells were subsequently washed with PBS and fixed with 4% paraformaldehyde (Sigma Aldrich, St. Louis, MO) and permeabilized with 0.1% Triton X-100 as previously described (Malet et al., 2007). Primary and secondary antibodies were incubated within blocking buffer (PBS containing 1% BSA) and washed with PBS containing 0.1% BSA between incubation steps. After a final wash with PBS the coverslips were drained and mounted onto glass slides with a quick dry mounting medium (United Biosciences, Brisbane, Australia) before visualization on a Leica TCS SP2 confocal microscope. Images were collected using a Leica digital camera and Leica 3D software before processing for publication using Adobe Photoshop^{TM} software. Colocalization was quantified based on the fluorescence microscopy images and was performed using ImageJ software via the colocalization analysis plug-in JACoP. Images were collected from replicate experiments with at least 20 cells counted from each.

Site-Directed Mutagenesis of WNV_{KUN} (FLSDX) Infectious Clones

Tyrosine to serine (Y/S), at position 28 within NS4A, or lysine to leucine (K/L), at position 35, or double mutations (Y/S + K/L) were generated in the WNV_{KUN} cDNA infectious clone, FLSDX (Khromykh et al., 1998), using site-directed mutagenesis (Stratagene). All clones were sequenced prior to maxiprep amplification (Invitrogen) and transfection.

In vitro Transcription and Electroporation

All replicon templates were linearized with *Xho*I (New England BioLabs) and purified using Phenol/Chloroform extraction and ethanol precipitation. *In vitro* RNAs were transcribed using 1 μg linearized DNA template using established methods previously described (Khromykh and Westaway, 1997; Khromykh et al., 1998), except introduction of the *in vitro* transcribed RNAs into mammalian cells was performed via Lipofectamine-mediated delivery or electroporation via the Neon^{TM} transfection system (Invitrogen) following the manufacturers instructions. Briefly, Vero or BHK cells (1.0×10^7) were electroportated using a 100 μL tip, at 1,300 volts, width 20, and 2 pulses. Cells were resuspended in cell culture media, seeded, and incubated for various periods for examination of virus replication.

Plaque Assay

Vero C1008 cells were seeded in DMEM complete media in 6-well plates and incubated at 37°C overnight. Virus stock was diluted 10-fold in 0.2% BSA/DMEM and cells were infected with 300 μL of stock dilutions (in duplicate) and incubated at 37°C for 60 min. Two milliliter of a semi-solid overlay containing 0.3% w/v low-melting point agarose, 2.5% w/v FCS, 1% Penicillin/Streptomycin, 1% Glutamax, 1% HEPES and 0.1% $NaCO_3$ was added to cells and solidified at 4°C for 30 min. Cells were incubated at 37°C for 3 days, fixed in 4% v/v formaldehyde (in PBS) for 1 hour and stained in 0.4% crystal violet (with 20% v/v methanol and PBS) at RT for 1 hour. Plaques were manually counted and plaque-forming units per mL (pfu/mL) calculated.

Western Blotting

Transfected cells were aspirated in PBS then lysed in SDS lysis buffer (0.5% SDS, 1 mM EDTA, 50 mM Tris-HCl) containing protease inhibitors leupeptin (1 μg/mL) and PMSF (0.5 mM) and phosphatase inhibitors sodium orthovanadate (25 mM), sodium fluoride (25 mM) and β-glycerophosphate (25 mM) (Sigma). Lysates were diluted in LDS loading buffer (Invitrogen), heated at 70°C for 5 min and separated on a 10% Tris-Glycine polyacrylamide gel. Proteins were transferred to Hi-Bond ECL nitrocellulose membrane (Amersham Biosciences) and the membrane was blocked with 5% w/v skim milk (Diploma) in TBS with 0.05% Tween (PBS-T). Primary antibodies were incubated at 4°C with membrane overnight in blocking solution as above. Following primary incubation, the membrane was washed in TBS-T then incubated with secondary antibodies conjugated to Cy5 (Amersham Biosciences), Alexa Fluor 647 or Alexa Flour 488 (Invitrogen) in TBS-T at RT for 2 h. The membrane was washed twice in TBS-T then TBS, and proteins visualized on the Storm Fluorescent scanner (Amersham Biosciences) on either 635 nM or 430 nM emission channel.

Resin Thin Sections for Electron Microscopy

Cells were fixed with 3% glutaraldehyde in 0.1 M cacodylate buffer for 2 h at room temperature. Cells were washed several times in 0.1 M cacodylate buffer followed by fixation with 1% OsO4 in 0.1 M cacodylate buffer for 1 h. After washing of the cells in 0.1 M cacodylate buffer, specimens were dehydrated in graded acetones for 10–20 min each. Subsequently, samples were infiltrated with EPON resin and polymerized in molds for 2 days at 60°C. 50–60 nm thin sections were cut on a Leica UC7 ultramicrotome using a Diatome diamond knife and collected on formvar-coated copper mesh grids. Before viewing in a JEOL 2010 transmission electron microscope cells were post-stained with 2% aqueous uranyl acetate (UA) and Reynold's lead citrate.

Transient Expression of Mutant NS4A Proteins, Immune-Precipitation and Assessment of Cholesterol Content

Tyrosine to serine (Y/S), at position 28 within NS4A, or lysine to leucine (K/L), at position 35, or double mutations (Y/S + K/L) were transferred from the mutant FLSDX to a pcDNA3.1 NS4A(-2K)-6xHis expression construct. Briefly, the NS4A-2K amplicon was amplified from FLSDX using forward (ATGGGCCCACCATGTCTCAAATAGGT) and reverse (TAT

TTCTAGACTAATGGTGATGGTGATGGTGGCGTTGCTTCT CTGGCTCAGG) primers and ligated into pcDNA3.1 using *Eco*RV and *Xba*I (Promega). Following propagation and midiprep purification (QIAGEN), 5 μg of DNA was transfected into 293T cells using Lipofectamine 2000 (Life Technologies) as indicated by manufacturers. At 24 h.p.t, cells were lysed on ice in a cholesterol extraction buffer (50 mM Tris pH 8.0, 150 mM NaCl, 0.1% w/v Digitonin, 0.1% NP-40, 0.5% Triton-X 100 and 0.25% sodium deoxycholate) containing a protease inhibitor cocktail (Astral Scientific), and centrifuged at 10,000 rcf to pellet cellular debris. Immunoprecipitation was performed on the lysates using an anti-His6 antibody (Abcam) coupled with Protein A Sepharose (Life Technologies) to pull-down the expressed NS4A-2K proteins. Lysates and IP samples were then assayed for cholesterol content using the Amplex Red cholesterol assay kit as indicated by the manufacturers. Total cholesterol (in μg) was calculated using internal standard curves and error bars indicate ± 1 standard deviation ($n = 4$).

Statistical Analyses

Data is representative of 3 independent experiments and was analyzed by unpaired Student's *t*-test using GraphPad Prism v8.0.

RESULTS

$\mathrm{WNV_{KUN}}$ RC Is Localized Within Cholesterol-Rich Micro-Domains Within the Membranes of the ER

Previously we have shown that $\mathrm{WNV_{KUN}}$ redistributes intracellular cholesterol to the sites of viral RNA replication, the VP (Mackenzie et al., 2007b). In addition, we have observed that the biogenesis of the VP appears to occur on a membrane platform derived from the ER, and recruitment of both host and viral proteins occurs at a pre-Golgi step (Gillespie et al., 2010). To further characterize the interactions that occur during development of the VP we utilized two GFP-tagged protein markers, erlin-1 and erlin-2, originally used to define cholesterol-rich micro-domains within the ER (Browman et al., 2006). Both proteins fall within the growing family of prohibitin domain-containing (PHB) proteins and are selectively targeted into ER micro-domains in a cholesterol dependent manner (Browman et al., 2006). We examined subcellular distribution of ectopically expressed eGFP-tagged erlin-1/2 proteins within the ER membranes in $\mathrm{WNV_{KUN}}$-infected Vero cells. Immunofluorescence (IF) analysis indicated that a significant pool of erlin-1/2 was confined to the cytoplasmic foci recognized by anti-dsRNA antibody (**Figures 1a–h**). The specific accumulation of erlin proteins within $\mathrm{WNV_{KUN}}$ replication sites was further confirmed by observation that other PHB family members, with different intracellular targets, did not co-localize with anti-dsRNA antibody stained foci (**Figures 1i–t**). In agreement with published findings, eGFP-tagged versions of prohibitin-1, flotillin-1 and stomatin-1a, were found to inhabit lipid micro-domains in the mitochondria (**Figure 1i**) and in endosomes and the plasma membrane (**Figures 1m,q**), respectively, quite distinct from $\mathrm{WNV_{KUN}}$ dsRNA.

These results suggest that $\mathrm{WNV_{KUN}}$ replication is associated with cholesterol enriched membrane domains within the ER, and co-located with the host proteins erlin-1 and 2.

Attenuated Replication Rates of $\mathrm{WNV_{KUN}}$ Recombinant Viruses Carrying Mutation in NS4A CRAC Motif

As we had observed previously and above; cholesterol appears to play a significant role in the biogenesis and establishment of the $\mathrm{WNV_{KUN}}$ RC (**Figure 1**; Mackenzie et al., 2007b) we aimed to identify whether a specific viral gene product is actively involved in lipid recognition/and redistribution. Our initial studies focused on the $\mathrm{WNV_{KUN}}$ NS4A protein as we, and others, had previously observed that flavivirus NS4A has the capacity to remodel intracellular membranes (Roosendaal et al., 2006; Miller et al., 2007). To this end, we utilized gene mining and revealed that NS4A contains a potential cholesterol recognition/interaction amino acid consensus (CRAC) motif $[\mathrm{L/V^{24}\text{-}X_{(1-5)}\text{-}Y^{28}\text{-}X_{(1-5)}\text{-}R/K^{35}}]$ motif near its' N terminus (**Figure 2A**). Sequence alignments revealed that this motif is highly conserved within members of the Japanese Encephalitis subgroup, with limited homology within the other members of the *flavivirus* genus (**Figure 2A**). A CRAC motif has been identified in the peripheral-type benzodiazepine receptor (Li and Papadopoulos, 1998) and other proteins known to bind cholesterol, including caveolin-1 (Parton et al., 2006), human immunodeficiency virus (HIV) gp41 (Vishwanathan et al., 2008) and the influenza M2 protein (Schroeder et al., 2005). Although it should be noted that presence of a CRAC motif does not solely confer the ability of a protein to associate with cholesterol (e.g., caveolin and cholesterol binding; Epand et al., 2005). To interrogate the importance of the CRAC domain on virus replication we generated recombinant viruses containing inhibitory mutations within this motif in the NS4A protein. Mutations were made within the $\mathrm{WNV_{KUN}}$ infectious clone (FLSDX) to alter residues within NS4A at position 28 from tyrosine to serine (Y/S), or to change residue at position 35 from lysine to leucine (K/L). Mutation of these amino acids was previously observed to disrupt cholesterol binding and trafficking of the major myelin protein P0 (Saher et al., 2009) and influenza virus M2 protein (Thaa et al., 2011).

Recombinant viruses harboring corresponding single or combined double mutations (Y/S + K/L) exhibited attenuated phenotypes varying in degrees (**Figure 2B**), of which the double mutation was shown to be extremely attenuated and was difficult to analyze even after subsequent re-infection. Viral replication efficiency was assessed by IF, Western blotting and plaque assay in Vero cells transfected with RNAs transcribed *in vitro* from FLSDX cDNAs (**Figures 2B,D**). It was observed that recombinant viruses harboring the K/L mutation displayed a slight delay in growth kinetics and was moderately attenuated, as assessed by plaque assay (**Figure 2D**). Whereas recombinant viruses harboring the Y/S mutation were more attenuated than the K/L

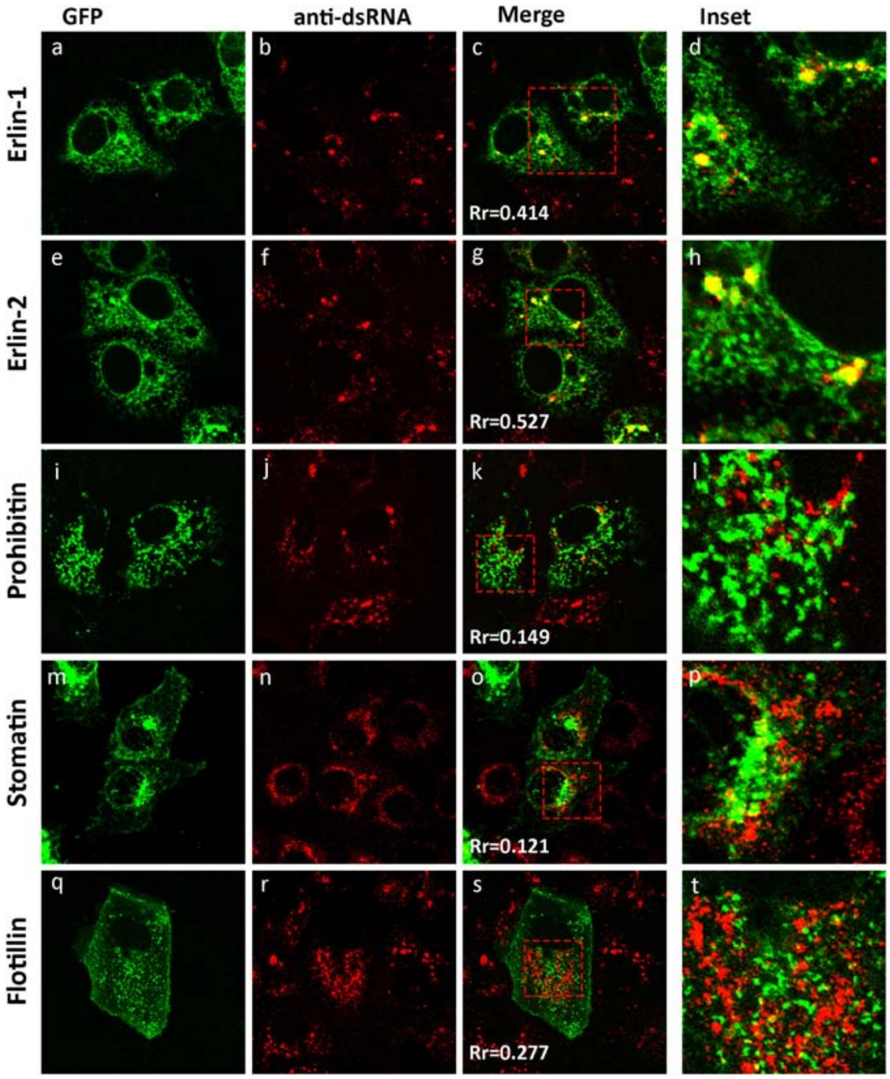

FIGURE 1 | The WNV_{KUN} RC resides within cholesterol-rich domains in the ER. IF analysis of Vero cells transfected with recombinant eGFP-expression plasmids for 24 h **(a,e,i,m,q)** and subsequently infected with WNV_{KUN} for an additional 24 h. Cells were immuno-stained with antibodies to dsRNA, and co-stained with Alexa Fluor 594 **(b,f,j,n,r)**. Prominent co-localization between dsRNA and erlin proteins is observed as a yellow hue in **(c,h)** only. Rr is the Pearson' co-efficient **(c,g,k,o,s)** as assessed in Image J and serves as a quantitative measure of co-localization. Values above 0.4 indicate a significant degree of co-localization **(d,h,l,p,t)**. Represents the inset for the red box in **(c,g,k,o,s)**, respectively.

and WT viruses. We failed to recover any of the double mutant in Vero cells. However, we could detect basal virus protein production and infectious virus release in BHK cells that were electroporated with the viral Y/S + K/L RNA (data not shown). Sequencing analysis of the recovered viruses revealed that no compensatory mutations had occurred, even after prolonged incubation of the transfected cells (data not shown).

These results indicated that the potential CRAC motif within the WNV_{KUN} NS4A protein appeared to play a major role during the replication cycle. The results also indicated that conservation of Tyr at position 28 is critical for efficient replication of the WNV_{KUN} genome and double mutation of Tyr-28 and Lys-35 is lethal to WNV_{KUN} replication in Vero cells.

WNV_{KUN} Replication Complex Formation Is Significantly Impaired Upon Transfection With CRAC Mutant Viruses

To determine the stage in the replication cycle affected by the Y/S and K/L mutants, we assessed the ability of these constructs to form the WNV_{KUN} RC by IF analysis. Vero cells were electroporated with the individual CRAC mutants and at 48 h.p.e., localization and distribution of the RC was determined by immuno-staining for dsRNA and NS4A or NS1 and NS4A (**Figure 3**). For both wild-type (FLSDX) and the K/L mutant, dsRNA and NS1 were detected in individual and often sizable foci scattered throughout the perinuclear/reticular area of the cytoplasm (**Figures 3Aa–c,g–i**), that largely coincided with NS4A

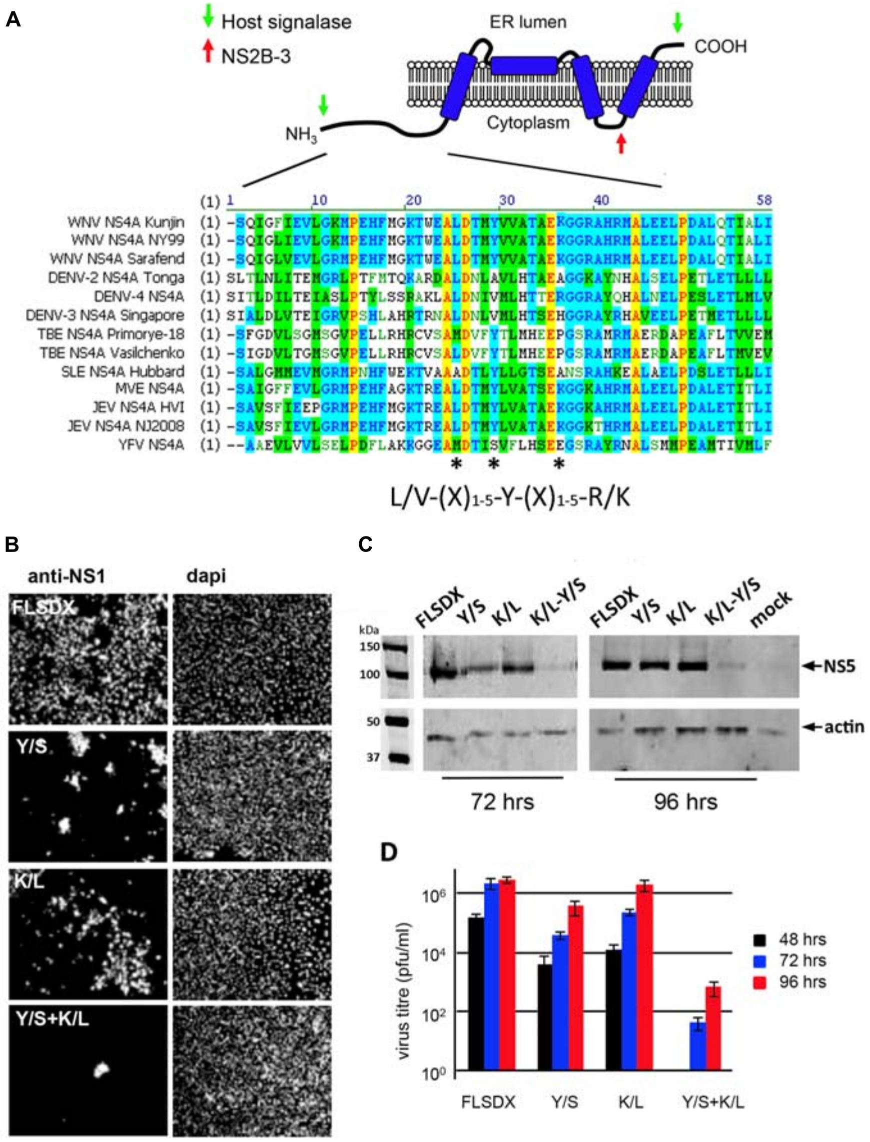

FIGURE 2 | (A) WNV_{KUN} NS4A protein encodes for a potential CRAC motif. NS4A ^{25}L-(X)-^{29}Y-(X)-^{36}K region is highly conserved within the Japanese encephalitis subgroup of the *flavivirus* genus. Various NS4A sequences from the *flavivirus* genus were aligned using ClustalW software (Vector NTI; Invitrogen). Light gray residues are conservative and the amino acids comprising the CRAC motif are highlighted with asterisks (*). The predicted topology of NS4A in the endoplasmic reticulum membrane is modified based on the study by Miller et al. (2007). **(B)** Mutation of the NS4A CRAC motif restricts WNV_{KUN} replication. Single (Y/S or K/L) and double residue (Y/S + K/L) mutations were generated in the CRAC motif in FLSDX using site-directed mutagenesis. RNA was transcribed and transfected into Vero cells and replication was assessed by IF analysis at 72 h.p.e. with antibodies raised against the WNV NS1 protein and counterstained with the nuclear dye dapi. **(C)** In addition, protein lysates were collected at 72 and 96 h.p.e. and analyzed by Western blotting using the antibodies raised against WNV NS5 protein and compared to the internal control actin. **(D)** Tissue culture fluid was collected at 48, 72, and 96 hpe and each time point was analyzed by plaque assay, and visible plaques were used to calculate titers for FLSDX and the Y/S, K/L and Y/S + K/L mutants. Error bars indicate standard deviation derived from replicate experiments (n = 3).

(**Figures 3Ad–f,Bj–l**). Comparatively in the case of the Y/S mutant, dsRNA and NS1 were further dispersed in smaller foci (**Figures 3Cm–o,D**) and there was a reduction in observable co-localization between the dsRNA and NS4A (**Figures 3Cp–r**). These results suggested that RC formation was significantly impaired in the Y/S mutant viruses.

As previously shown, WNV_{KUN} replication is associated with cholesterol enriched membrane domains in the ER (**Figure 1**), and recently YFV replication was observed to localize to detergent resistant membranes high in cholesterol content (Yi et al., 2012). Thus, we aimed to further characterize the defect in RC formation by assessing whether the Y/S and K/L mutants had retained the ability to localize to cholesterol-rich domains within the ER, as marked by the host protein erlin-2. Vero cells were electroporated with mutant genome RNAs and the eGFP-tagged erlin-2 plasmid DNA to define cholesterol-rich

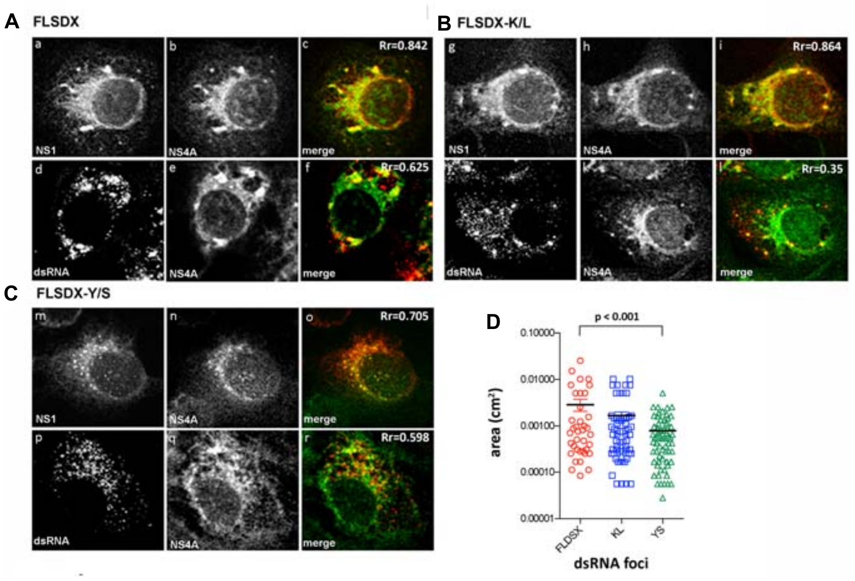

FIGURE 3 | Mutation within the CRAC motif prevents WNV_{KUN} RC formation. Vero cells were transfected with FLSDX WT **(A)**, FLSDX K/L **(B)**, or FLSDX Y/S **(C)** RNAs and at 48 h.p.e. fixed for IF analysis. Transfected cells were then immune-stained with antibodies specific for WNV NS1 (in red) and NS4A (in green) or dsRNA (in red) and NS4A (in green). Images were collected on a confocal microscope; and yellow in the merge images indicates co-localization. **(D)** the size (area) of the dsRNA foci were analyzed by Image J software and statistical significance was determine by Student's *t*-test.

domains in the ER (**Figure 4A**). At 48 h.p.e., localization and distribution of the RC was determined by immuno-staining for dsRNA. In transfected and mock-infected cells, eGFP-erlin-2 was observed to localize in a typical reticular ER-like pattern without any noticeable cytoplasmic foci (**Figures 4Aa–d**). For both FLSDX and the K/L mutant, dsRNA was confined to large reticular/perinuclear cytoplasmic foci where eGFP-erlin-2 was significantly co-located (**Figures 4Ae–h,m–p**). However, we observed that eGFP-erlin-2 and dsRNA were dispersed in visibly smaller foci throughout entire cytoplasm of the cell and revealed reduced co-localization in cells replicating the Y/S mutant (**Figures 4Ai–l**). These results suggested that there was an impairment of the WNV_{KUN} Y/S mutant to localize to lipid microdomains in the ER to establish biogenesis of the RC, an impairment that correlates with attenuation of replication efficiency (**Figure 2**).

To further investigate the defect in RC formation we assessed whether it coincided with a defect in recruitment of cellular proteins known to localize to the RC (Mackenzie et al., 1999). Vero cells were electroporated with mutant genome RNAs and at 48 h.p.e., localization of the RC and *trans*-Golgi network glycoproteins was determined by immunostaining for dsRNA and GalT (**Figure 4B**). For both FLSDX and the K/L mutant, dsRNA and GalT colocalized in foci in the perinuclear/reticular region of the cytoplasm (**Figures 4Ba–d,i–l**). Comparatively in the case of the Y/S mutant, dsRNA and GalT were dispersed in significantly smaller foci throughout the cytoplasm and there was a reduction in the co-localization between the two (**Figures 4Be–h**). These results highlighted that there was dissociation between cellular and viral components that are normally found within the RC in the Y/S mutant viruses.

Overall, our results suggest that the CRAC motif within the WNV_{KUN} NS4A protein appears to play a major role facilitating efficient virus replication. In particular that the Y/S mutation significantly impaired the capacity of the mutant viruses to effectively form the WNV_{KUN} RC complex, which may be related to the inability of mutant viruses to unite the required viral and cellular replicative components to specific subdomains on the ER membrane.

WNV_{KUN}-Induced Membrane Proliferation Is Significantly Impaired Upon Transfection With CRAC Mutant Viruses

During WNV_{KUN} infection ER membranes undergo extensive proliferation and rearrangements such that they can be observed as an intricate network of CM/PC and VP via ultrastructural analysis (Mackenzie et al., 1996a; Westaway et al., 1997b; Mackenzie, 2005). The CM/PC is thought to function during translation and proteolytic maturation of the polyprotein, whereas the VP is known to house the RC (Mackenzie et al., 1996a, 1998, 2007a; Westaway et al., 1997b, 1999). In view of the defect in RC formation in the Y/S mutant observable via IF analysis, we were interested to investigate whether the similar characteristic membrane structures, particularly the VP, were induced in these mutant viruses. Thus, Vero cells were electroporated with the individual CRAC mutants, fixed at 48 h.p.e. and analyzed by electron microscopy (**Figure 5**). Interestingly, VP formation was decreased but observable in the Y/S mutants in comparison to the FLSDX and K/L mutants. More strikingly, however, was that recombinant

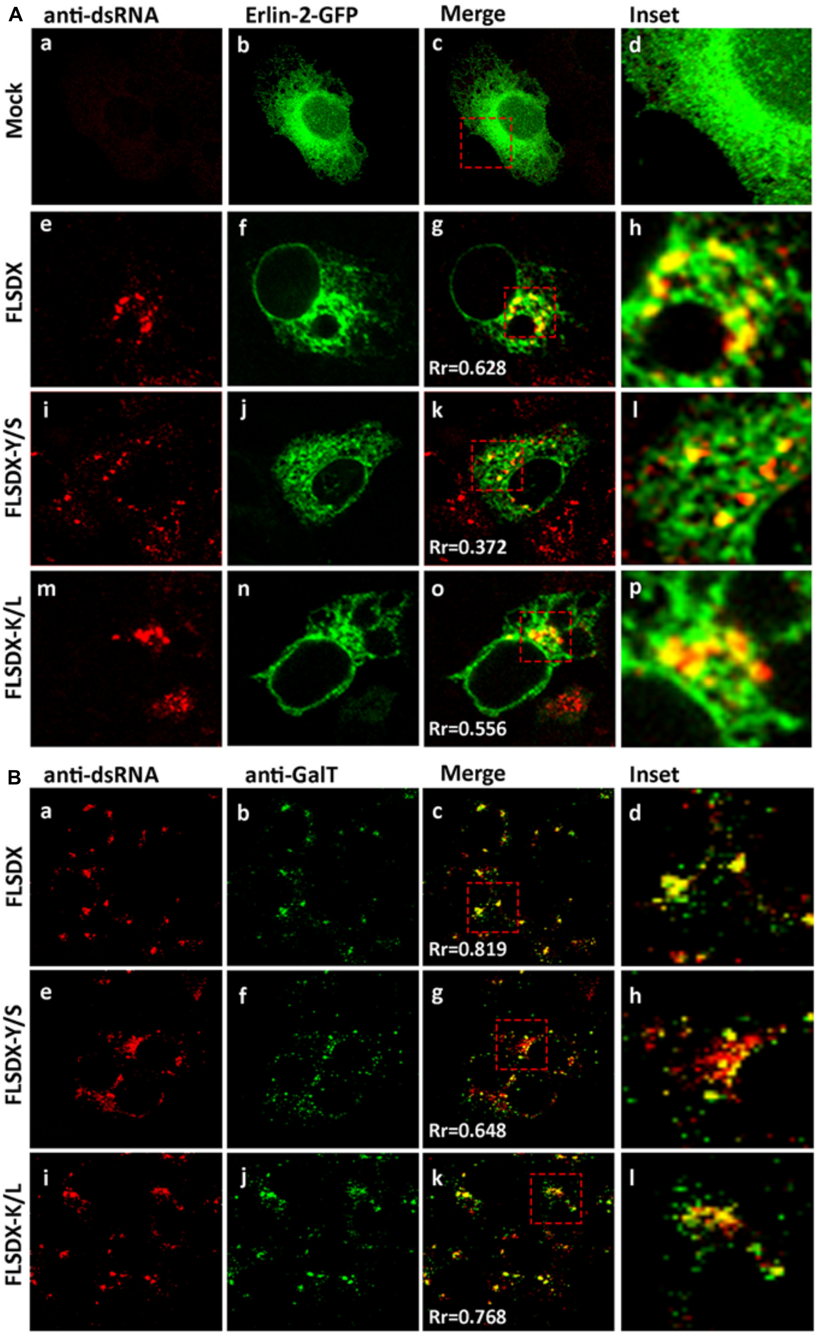

FIGURE 4 | CRAC mutant FLSDX viruses are impaired in their ability to recruit host proteins to the WNV$_{KUN}$ RC. **(A)** Vero cells transfected with recombinant eGFP-erlin-2 plasmids for 24 h and subsequently electroporated with CRAC mutant FLSDX viruses for an additional 48 h. Cells were immuno-stained with antibodies to dsRNA, and co-stained with Alexa Fluor 594 (panels **a, e, i**, and **m**). Prominent co-localization between dsRNA and eGFP-erlin-2 proteins (panels **b,f,j**, and **n**) is observed as a yellow hue in the merge and insert panels **c–d**, **g–h**, **k–l** and **o–p**. **(B)** Cells were immune-stained with antibodies specific to dsRNA and counterstained with species specific Alexa Fluor 594 (panels **a, e**, and **i**), and with antibodies specific to GalT and counterstained with Alexa Fluor 488 (panels **b,f**, and **j**). Co-incidental labeling is depicted as a yellow hue in the merged and insert panels on the right hand side (panels **c–d**, **g–h**, and **k–l**).

viruses harboring the Y/S mutation were observed to be significantly impaired for CM/PC induction; the induced CM/PC structures were abundant and could clearly be defined in the FLSDX and K/L mutants but were almost absent in the Y/S mutants (compare panels in **Figure 5**). All mutant viruses appeared to produce virus particles, albeit greatly reduced in the Y/S mutant. No evidence of infection was observed for the double mutant.

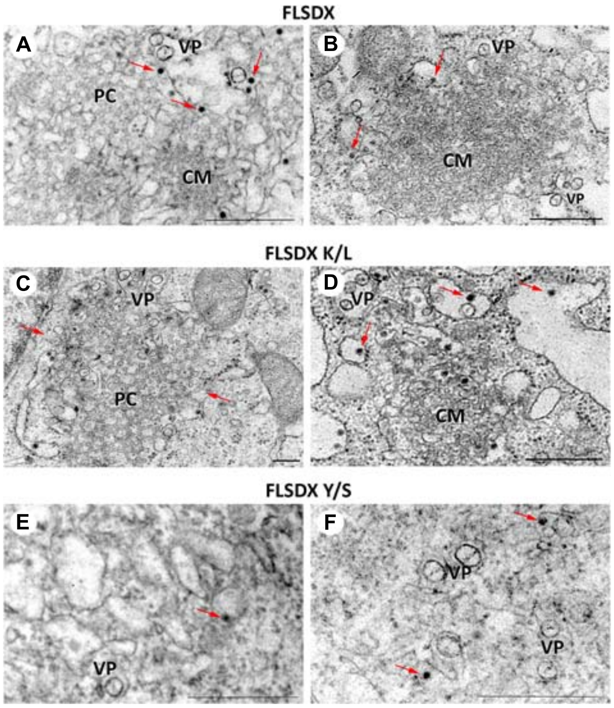

FIGURE 5 | Mutation of the CRAC domain within the $\mathrm{WNV_{KUN}}$ NS4A proteins results in reduced membrane remodeling. Ultrastructural analysis of Vero cells electroporated with CRAC mutant FLSDX *in vitro* transcribed RNAs (FLSDX, **A,B**; K/L mutant, **C,D**; Y/S mutant, **E,F**) at 48 h.p.i. Characteristic flavivirus-induced membrane structures convoluted membranes (CM) and paracrystalline arrays (PC) are only observed in FLSDX- and K/L mutant-electroporated cells. However, vesicle packets (VP) and virus particles (arrows) are observed in all cells. Magnification bars represent 200 nm.

These results indicated that the CRAC motif within the $\mathrm{WNV_{KUN}}$ NS4A protein appeared to play a major role in facilitating membrane proliferation and remodeling.

The CRAC Motif Promotes Colocation of NS4A With Erlin-2 and a Potential Association With Cellular Cholesterol

During our studies we could not directly observe co-location of NS4A with endogenous erlin-2 due to conflict with the same species of antibodies. As an alternative to understand this we transfected Vero cells with cDNA expression plasmids expressing the individual NS4A fused to a 6xHIS tag and co-stained those cells with anti-erlin-2 antibodies (**Figure 6A**). As can be observed expression of WT and all single NS4A mutants induced the formation of cytoplasmic foci that co-located strongly with erlin-2 for WT and NS4A K/L and to a lesser degree for NS4A Y/S (quantitation provided in **Figure 6B** as Manders' co-efficient). In contrast, the NS4A K/L + Y/S mutant displayed a more diffuse cytoplasmic staining with little co-location with erlin-2 (**Figure 6A**).

To address whether the CRAC motif within NS4A conferred a biochemical interaction with cellular cholesterol we expressed the WT and mutant NS4A proteins transiently in 293T cells (due to increased transfection efficiency). Our initial analysis to co-localize intracellular cholesterol (using filipin or perfringolysin-O) with NS4A was unsuccessful (data not shown). Therefore, we aimed to isolate NS4A and determine if we could co-purify cholesterol (or not) after immune-precipitation. As observed in **Figure 6D** we could immune-purify all forms of the NS4A protein and could interact with a similar percent of cholesterol, as determined by the Amplex Red cholesterol assay kit, with the WT and K/L mutant NS4A (**Figure 6C**). In contrast we observed less cholesterol isolated with the Y/S and K/L + Y/S mutant NS4A proteins, however, these results were not significant even after repeated experiments (**Figure 6C**; $n = 4$). At this stage we cannot conclusively determine whether the potential CRAC motif is promoting an association with cholesterol or whether other domains within NS4A or additional protein-protein or protein-lipid interactions are occurring.

Overall, we can conclude that the CRAC motif is important for $\mathrm{WNV_{KUN}}$ replication and appears crucial for the ability of NS4A to co-locate with erlin-2 within microdomains within the ER to remodel intracellular membranes and promote $\mathrm{WNV_{KUN}}$ RC assembly and function. Whether cholesterol is indeed a contributing factor is still unresolved.

DISCUSSION

$\mathrm{WNV_{KUN}}$ replication, like all flaviviruses is intimately linked with membrane induction and remodeling. The $\mathrm{WNV_{KUN}}$ RC itself is formed on a membrane platform derived from the ER and is the site where RNA is replicated to produce progeny viral genomes (Gillespie et al., 2010). Our previous studies have revealed that this process is reliant on cellular cholesterol (Mackenzie et al., 2007b). In this study we extended these findings to define a potential role for cholesterol-rich micro-domains within the ER in facilitating the biogenesis and function of the $\mathrm{WNV_{KUN}}$ RC. Previously, our mutational analyses have revealed that conserved amino acids within the N-terminus confer stability of the NS4A important in membrane remodeling enabling virus replication (Ambrose and Mackenzie, 2015). Here we have extended those studies to show that a putative CRAC domain also within the N-terminus of the $\mathrm{WNV_{KUN}}$ NS4A protein appears to facilitate efficient virus replication within these modified membranes. Mutation of this domain within NS4A significantly impaired coalescence of both viral and cellular factors on the ER membrane to promote efficient virus replication.

Within this report we have extended our list of host proteins co-localizing within the $\mathrm{WNV_{KUN}}$ RC and show that two host proteins known to associate with "lipid raft-like," cholesterol-rich domains within the ER, erlin-1 and erlin-2, co-locate with dsRNA during infection (**Figure 1**). The association of erlin-1 and erlin-2 with the RC strengthens a role for cholesterol in the biogenesis and maintenance of the $\mathrm{WNV_{KUN}}$ RC. Additionally it should be noted that a recent proteomic analysis revealed an association of erlin-2 with DENV NS5 protein (Carpp et al., 2014). Previously we had shown that the $\mathrm{WNV_{KUN}}$ RC could be stained with filipin and chemical modulation of cholesterol homeostasis duly affected virus RNA replication (Mackenzie et al., 2007b).

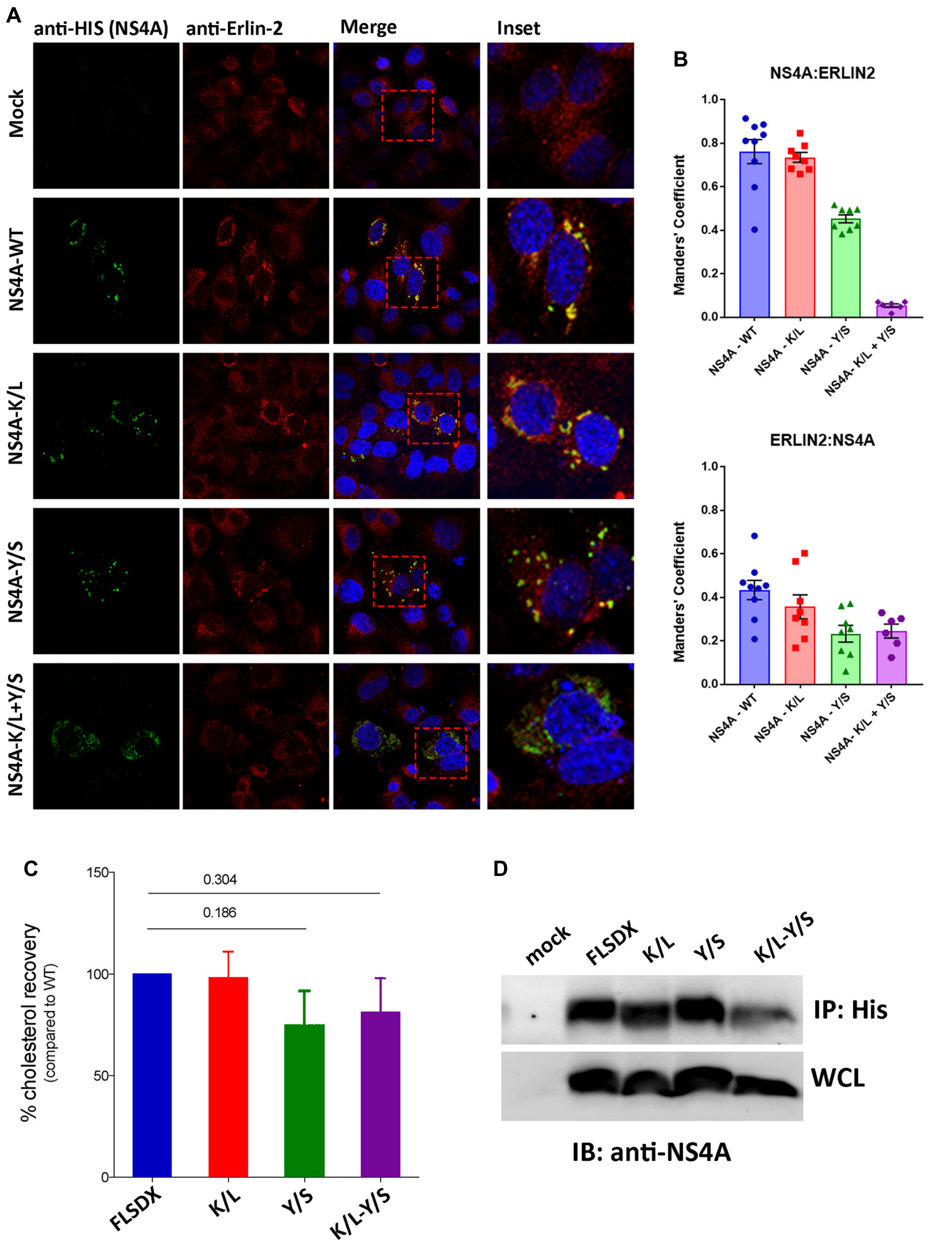

FIGURE 6 | The CRAC motif promotes colocation of NS4A with erlin-2 and a potential association with cellular cholesterol. **(A)** Vero cells transfected with recombinant NS4A-His plasmids for 24 h and subsequently immuno-stained with antibodies to 6xHis co-stained with Alexa Fluor 488 with antibodies to erlin-2 and co-stained with Alexa Fluor 594. Prominent co-localization between dsRNA and eGFP-erlin-2 proteins is observed as a yellow hue in the merge and insert panels on the right-hand side. **(B)** The extent of co-localization was assessed in Image J by evaluating the Manders' coefficient of NS4A-erlin-2 and erlin-2-NS4A. **(C)** Percentage amount of cholesterol recovered from transfected cells after immune-precipitation with anti-His antibodies. Cholesterol recovery was measured via the Amplex Red cholesterol assay kit. Statistical significance was determined by Student's *t*-test. **(D)** A representative western blot showing the expression level of the NS4A mutants in the input whole cell lysate (WCL) and their recovery after IP. Western blot was probed with anti-NS4A antibodies.

In addition, it was recently observed that the host protein DNAJC14, a protein known to reside within detergent-resistant (lipid-raft-like) membranes, was recruited to the Yellow fever virus RC (Yi et al., 2012). Therefore, we suggest that early after translation the flavivirus proteins accumulate within cholesterol-rich patches within the ER, defined by erlin proteins and/or DNAJC14, to promote the biogenesis of the RC. Upon changes in cholesterol concentration, the mobility of proteins within and to these domains, maybe altered impacting on RC formation and thus replication efficiency. It is also pertinent to note that our previous studies revealed a very close association of the CM/PC structures with the cholesterol-synthesizing enzyme

3-hydroxy-methyglutaryl-CoA reductase, HMGCR (Mackenzie et al., 2007b). These individual observations strongly implicate a role for cholesterol and cholesterol synthesis during the flavivirus replication cycle.

We extended these observations further to identify factors responsible for co-ordinating localization within these cholesterol-rich domains within the ER and gene mining identified a potential lipid-binding (CRAC) motif within the N-terminus of NS4A, which is highly conserved within members of the Japanese Encephalitis subgroup of *flaviviruses* (**Figure 2A**). To interrogate the role of this motif during replication we undertook a mutagenesis analysis of this CRAC motif within NS4A. Our investigations revealed that recombinant viruses harboring a double mutation (Y/S + K/L) were significantly impaired in their ability to replicate effectively, so much so that replication was extremely difficult to analyze even following subsequent re-infection (**Figures 2B–D**). The individual K/L mutant was slightly attenuated at earlier time points as demonstrated by IF analysis, viral titer and protein levels, whilst the Y/S mutant was severely attenuated (**Figures 2B–D**). Our analyses also revealed that the Y/S mutant was particularly impaired in its ability to form the RC, unite viral and cellular proteins that house within the RC, target to cholesterol-rich domains within the ER and the capacity to remodel cytoplasmic membranes (**Figures 3–6**). We observed that the Y/S virus replication sites, identified by anti-dsRNA antibodies, were smaller in size compared with the parental FLSDX virus and much more diffuse within the cytoplasm. Additionally, we observed reduced co-localization between dsRNA and NS4A and between the replication proteins NS1 and NS4A in cells transfected with the Y/S mutants (**Figure 3**). This was comparatively reflected in the ability of the Y/S mutant to recruit the host proteins GalT and erlin-2 within the RC (**Figure 4**). In cells transfected with the Y/S mutant GalT maintained a more perinuclear staining pattern consistent with localization within the Golgi apparatus, whereas erlin-2 was more diffusely localized within the cytoplasm. However, it should be noted that we were unable to conclusively demonstrate that the CRAC motif facilitates a direct interaction between NS4A and cholesterol (**Figure 6**), and thus requires further studies to delineate how the RC is formed on these lipid sub-domains. For example, formation of the RC maybe driven via an interaction between NS4A and DNAJC14 or between NS4A and erlin proteins on the ER membrane. It should also be noted that we recently reported that this region of the NS4A protein mediates an interaction with the membrane-bending host protein Reticulon 3A.1 (Aktepe et al., 2017). We also cannot rule out or discount other cellular responses, such as the unfolded protein response, that could also influence membrane proliferation and alteration. These are all areas we are currently investigating.

In addition, to biogenesis of the RC our EM analysis revealed that the CRAC motif within NS4A contributed significantly to the capacity of NS4A to remodel cytoplasmic membranes characteristic of flavivirus infection (**Figure 4**). We observed that cells transfected with the Y/S mutant still produced virus particles and VP, albeit at greatly reduced numbers compared to the K/L and FLSDX viruses. The most notable observation was the complete absence of CM/PC membranous structures in the Y/S transfected cells. We, and others, have shown that NS4A has the capacity to remodel cytoplasmic membranes and induce the formation of CM/PC when expressed alone (Roosendaal et al., 2006; Miller et al., 2007). The results presented here would suggest that the putative CRAC motif is potentially the region within NS4A responsible for this remodeling, a proposal we are currently investigating. The question still remains how the absence of the CM/PC contributes to impaired RNA replication and facilitates the recruitment of host proteins to the VP? We have previously prosed that the CM/PC are the intracellular site of efficient viral protein translation and processing, and our current observations may indicate that they are equally involved with sorting proteins and membrane within the infected cell. It is possible that during established replication viral proteins (and RNA) destined for the VP must in fact transit the CM/PC before delivery, thereby ensuring that only the correct proteins (and lipid) reside within the RC. In the situation observed with the Y/S mutant this obviously does not occur and as such viral proteins remain associated with unmodified ER and thus cannot unite to generate the CM/PC and VP. Although we did observe some VP in our EM analyses of the Y/S mutant, we suggest that this may simply be a situation where the required elements (viral and cellular proteins and lipid) are in the correct vicinity during translation and thus can invoke some limited membrane remodeling.

Overall, we have shown that a conserved motif within the N-terminus of the WNV_{KUN} NS4A protein enables it to remodel cytoplasmic membranes and recruit both viral and host cell proteins to cholesterol-rich microdomains within the ER that facilitate the process of RC biogenesis. Whether this motif is directly responsible for cholesterol recruitment though still remains to be elucidated. Newly developed approaches such as photo-activable cholesterol and mass-spectrometry could enhance to sensitivity and specificity of detection. In the end, this study highlights that a functionally competent NS4A is critical to the formation and remodeling of membrane structures associated with the WNV RC and to recruit both viral and host cell proteins to these structures. The study supports and extends previous reports from ourselves and other, of the importance of the N-terminus of the flavivirus NS4A in facilitating virus replication.

DATA AVAILABILITY STATEMENT

The raw data supporting the conclusions of this article will be made available by the authors, without undue reservation.

AUTHOR CONTRIBUTIONS

AM, LG, RA, TA, and AT performed the experiments. AM, LG, RA, TA, SL, AT, and JM collated and assembled the data. RA, SL, TA, and JM wrote the manuscript. All authors contributed to the article and approved the submitted version.

FUNDING

This research was supported by a Project Grant (No. 1004619) to JM from the National Health and Medical Research Council of Australia.

ACKNOWLEDGMENTS

We thank Drs. Roy Hall, Alexander Khromykh, and Eric Berger for generously supplying antibodies for this study. We thank Dr. Alexander Khromykh for generously providing the WNV_{KUN} infectious cDNA clone, FLSDX. We are also grateful to Dr. Stephen Robbins for providing the recombinant cDNA plasmids expressing eGFP-tagged erlin-1, erlin-2, prohibitin, stomatin, and flotillin.

REFERENCES

Aktepe, T. E., Liebscher, S., Prier, J. E., Simmons, C. P., and Mackenzie, J. M. (2017). The host protein reticulon 3.1A is utilized by flaviviruses to facilitate membrane remodelling. *Cell Rep.* 21, 1639–1654. doi: 10.1016/j.celrep.2017.10.055

Ambrose, R. L., and Mackenzie, J. M. (2015). Conserved amino acids within the N-terminus of the West Nile virus NS4A protein contribute to virus replication, protein stability and membrane proliferation. *Virology* 481, 95–106. doi: 10.1016/j.virol.2015.02.045

Berger, E. G., Grimm, K., Bachi, T., Bosshart, H., Kleene, R., and Watzele, M. (1993). Double immunofluorescent staining of alpha 2,6 sialyltransferase and beta 1,4 galactosyltransferase in monensin-treated cells: evidence for different Golgi compartments? *J. Cell Biochem.* 52, 275–288. doi: 10.1002/jcb.240520304

Browman, D. T., Resek, M. E., Zajchowski, L. D., and Robbins, S. M. (2006). Erlin-1 and erlin-2 are novel members of the prohibitin family of proteins that define lipid-raft-like domains of the ER. *J. Cell Sci.* 119, 3149–3160. doi: 10.1242/jcs.03060

Carpp, L. N., Rogers, R. S., Moritz, R. L., and Aitchison, J. D. (2014). Quantitative proteomic analysis of host-virus interactions reveals a role for GBF1 in dengue infection. *Mol. Cell Proteom.* 13, 2836–2854. doi: 10.1074/mcp.M114.038984

Epand, R. M., Sayer, B. G., and Epand, R. F. (2005). Caveolin scaffolding region and cholesterol-rich domains in membranes. *J. Mol. Biol.* 345, 339–350. doi: 10.1016/j.jmb.2004.10.064

Fujino, T., Nakamuta, M., Yada, R., Aoyagi, Y., Yasutake, K., Kohjima, M., et al. (2010). Expression profile of lipid metabolism-associated genes in hepatitis C virus-infected human liver. *Hepatol. Res.* 40, 923–929. doi: 10.1111/j.1872-034x.2010.00700.x

Gillespie, L. K., Hoenen, A., Morgan, G., and Mackenzie, J. M. (2010). The endoplasmic reticulum provides the membrane platform for biogenesis of the flavivirus replication complex. *J. Virol.* 84, 10438–10447. doi: 10.1128/jvi.00986-10

Heaton, N. S., Perera, R., Berger, K. L., Khadka, S., Lacount, D. J., Kuhn, R. J., et al. (2010). Dengue virus nonstructural protein 3 redistributes fatty acid synthase to sites of viral replication and increases cellular fatty acid synthesis. *Proc. Natl. Acad. Sci. U.S.A.* 107, 17345–17350. doi: 10.1073/pnas.1010811107

Heaton, N. S., and Randall, G. (2010). Dengue virus-induced autophagy regulates lipid metabolism. *Cell Host Microb.* 8, 422–432. doi: 10.1016/j.chom.2010.10.006

Khromykh, A. A., Kenney, M. T., and Westaway, E. G. (1998). trans-Complementation of flavivirus RNA polymerase gene NS5 by using Kunjin virus replicon-expressing BHK cells. *J. Virol.* 72, 7270–7279. doi: 10.1128/jvi.72.9.7270-7279.1998

Khromykh, A. A., and Westaway, E. G. (1997). Subgenomic replicons of the flavivirus Kunjin: construction and applications. *J. Virol.* 71, 1497–1505. doi: 10.1128/jvi.71.2.1497-1505.1997

Koonin, E. V. (1993). Computer-assisted identification of a putative methyltransferase domain in NS5 protein of flaviviruses and lambda 2 protein of reovirus. *J. Gen. Virol.* 74, 733–740. doi: 10.1099/0022-1317-74-4-733

Li, H., and Papadopoulos, V. (1998). Peripheral-type benzodiazepine receptor function in cholesterol transport. Identification of a putative cholesterol recognition/interaction amino acid sequence and consensus patterns. *Endocrinology* 139, 4991–4997. doi: 10.1210/endo.139.12.6390

Macdonald, J., Tonry, J., Hall, R. A., Williams, B., Palacios, G., Ashok, M. S., et al. (2005). NS1 protein secretion during the acute phase of west nile virus infection. *J. Virol.* 79, 13924–13933. doi: 10.1128/jvi.79.22.13924-13933.2005

Mackenzie, J. (2005). Wrapping things up about virus RNA replication. *Traffic* 6, 967–977. doi: 10.1111/j.1600-0854.2005.00339.x

Mackenzie, J. M., Jones, M. K., and Westaway, E. G. (1999). Markers for trans-Golgi membranes and the intermediate compartment localize to induced membranes with distinct replication functions in flavivirus-infected cells. *J. Virol.* 73, 9555–9567. doi: 10.1128/jvi.73.11.9555-9567.1999

Mackenzie, J. M., Jones, M. K., and Young, P. R. (1996a). Immunolocalization of the dengue virus nonstructural glycoprotein NS1 suggests a role in viral RNA replication. *Virology* 220, 232–240. doi: 10.1006/viro.1996.0307

Mackenzie, J. M., Jones, M. K., and Young, P. R. (1996b). Improved membrane preservation of flavivirus-infected cells with cryosectioning. *J. Virol. Methods* 56, 67–75. doi: 10.1016/0166-0934(95)01916-2

Mackenzie, J. M., Kenney, M. T., and Westaway, E. G. (2007a). West Nile virus strain Kunjin NS5 polymerase is a phosphoprotein localized at the cytoplasmic site of viral RNA synthesis. *J. Gen. Virol.* 88, 1163–1168. doi: 10.1099/vir.0.82552-0

Mackenzie, J. M., Khromykh, A. A., and Parton, R. G. (2007b). Cholesterol manipulation by West Nile virus perturbs the cellular immune response. *Cell Host Microb.* 2, 229–239. doi: 10.1016/j.chom.2007.09.003

Mackenzie, J. M., Khromykh, A. A., Jones, M. K., and Westaway, E. G. (1998). Subcellular localization and some biochemical properties of the flavivirus Kunjin nonstructural proteins NS2A and NS4A. *Virology* 245, 203–215. doi: 10.1006/viro.1998.9156

Malet, H., Egloff, M. P., Selisko, B., Butcher, R. E., Wright, P. J., Roberts, M., et al. (2007). Crystal structure of the RNA polymerase domain of the West Nile virus non-structural protein 5. *J. Biol. Chem.* 282, 10678–10689.

Martin-Acebes, M. A., Merino-Ramos, T., Blazquez, A. B., Casas, J., Escribano-Romero, E., Sobrino, F., et al. (2014). The composition of west nile virus lipid envelope unveils a role of sphingolipid metabolism on flavivirus biogenesis. *J. Virol.* 88, 12041–12054. doi: 10.1128/JVI.02061-14

Miller, S., Kastner, S., Krijnse-Locker, J., Buhler, S., and Bartenschlager, R. (2007). The non-structural protein 4A of dengue virus is an integral membrane protein inducing membrane alterations in a 2K-regulated manner. *J. Biol. Chem.* 282, 8873–8882. doi: 10.1074/jbc.m609919200

Miller, S., and Krijnse-Locker, J. (2008). Modification of intracellular membrane structures for virus replication. *Nat. Rev. Microbiol.* 6, 363–374. doi: 10.1038/nrmicro1890

Parton, R. G., Hanzal-Bayer, M., and Hancock, J. F. (2006). Biogenesis of caveolae: a structural model for caveolin-induced domain formation. *J. Cell Sci.* 119, 787–796. doi: 10.1242/jcs.02853

Perera, R., Riley, C., Isaac, G., Hopf-Jannasch, A. S., Moore, R. J., Weitz, K. W., et al. (2012). Dengue virus infection perturbs lipid homeostasis in infected mosquito cells. *PLoS Pathog.* 8:e1002584. doi: 10.1371/journal.ppat.1002584

Rice, C. M., Lenches, E. M., Eddy, S. R., Shin, S. J., Sheets, R. L., and Strauss, J. H. (1985). Nucleotide sequence of yellow fever virus: implications for flavivirus gene expression and evolution. *Science* 229, 726–733. doi: 10.1126/science.4023707

Roosendaal, J., Westaway, E. G., Khromykh, A., and Mackenzie, J. M. (2006). Regulated cleavages at the West Nile virus NS4A-2K-NS4B junctions play a major role in rearranging cytoplasmic membranes and Golgi trafficking of the NS4A protein. *J. Virol.* 80, 4623–4632. doi: 10.1128/jvi.80.9.4623-4632.2006

Rothwell, C., Lebreton, A., Young, N. C., Lim, J. Y., Liu, W., Vasudevan, S., et al. (2009). Cholesterol biosynthesis modulation regulates dengue viral replication. *Virology* 389, 8–19. doi: 10.1016/j.virol.2009.03.025

Saher, G., Quintes, S., Möbius, W., Wehr, M. C., Krämer-Albers, E.-M., Brügger, B., et al. (2009). Cholesterol regulates the endoplasmic reticulum exit of the major membrane protein P0 required for peripheral myelin compaction. *J. Neurosci.* 29, 6094–6104. doi: 10.1523/jneurosci.0686-09.2009

Schroeder, C., Heider, H., Möncke-Buchner, E., and Lin, T.-I. (2005). The influenza virus ion channel and maturation cofactor M2 is a cholesterol-binding protein. *Eur. Biophys. J.* 34, 52–66. doi: 10.1007/s00249-004-0424-1

Su, A. I., Pezacki, J. P., Wodicka, L., Brideau, A. D., Supekova, L., Thimme, R., et al. (2002). Genomic analysis of the host response to hepatitis C virus infection. *Proc. Natl. Acad. Sci. U.S.A.* 99, 15669–15674.

Thaa, B., Levental, I., Herrmann, A., and Veit, M. (2011). Intrinsic membrane association of the cytoplasmic tail of influenza virus M2 protein and lateral membrane sorting regulated by cholesterol binding and palmitoylation. *Biochem. J.* 437, 389–397. doi: 10.1042/bj20110706

Vishwanathan, S. A., Thomas, A., Brasseur, R., Epand, R. F., Hunter, E., and Epand, R. M. (2008). Hydrophobic substitutions in the first residue of the CRAC segment of the gp41 protein of HIV. *Biochemistry* 47, 124–130. doi: 10.1021/bi7018892

Westaway, E. G., Khromykh, A. A., Kenney, M. T., Mackenzie, J. M., and Jones, M. K. (1997a). Proteins C and NS4B of the flavivirus Kunjin translocate independently into the nucleus. *Virology* 234, 31–41. doi: 10.1006/viro.1997.8629

Westaway, E. G., Mackenzie, J. M., Kenney, M. T., Jones, M. K., and Khromykh, A. A. (1997b). Ultrastructure of Kunjin virus-infected cells: colocalization of NS1 and NS3 with double-stranded RNA, and of NS2B with NS3, in virus-induced membrane structures. *J. Virol.* 71, 6650–6661. doi: 10.1128/jvi.71.9.6650-6661.1997

Westaway, E. G., Khromykh, A. A., and Mackenzie, J. M. (1999). Nascent flavivirus RNA colocalized in situ with double-stranded RNA in stable replication complexes. *Virology* 258, 108–117. doi: 10.1006/viro.1999.9683

Westaway, E. G., Mackenzie, J. M., and Khromykh, A. A. (2002). Replication and gene function in Kunjin virus. *Curr. Top. Microbiol. Immunol.* 267, 323–351. doi: 10.1007/978-3-642-59403-8_16

Ye, J., Wang, C., Sumpter, R. Jr., Brown, M. S., Goldstein, J. L., and Gale, M. Jr. (2003). Disruption of hepatitis C virus RNA replication through inhibition of host protein geranylgeranylation. *Proc. Natl. Acad. Sci. U.S.A.* 100, 15865–15870. doi: 10.1073/pnas.2237238100

Yi, Z., Yuan, Z., Rice, C. M., and MacDonald, M. R. (2012). Flavivirus replication complex assembly revealed by DNAJC14 functional mapping. *J. Virol.* 86, 11815–11832. doi: 10.1128/jvi.01022-12

Conflict of Interest: The authors declare that the research was conducted in the absence of any commercial or financial relationships that could be construed as a potential conflict of interest.

frontiers
in Cell and Developmental Biology

REVIEW
published: 11 June 2021
doi: 10.3389/fcell.2021.657886

Formation of Self-Assembled Mesophases During Lipid Digestion

Anna C. Pham[1], *Andrew J. Clulow*[1] *and Ben J. Boyd*[1,2]*

[1] *Drug Delivery, Disposition and Dynamics, Monash Institute of Pharmaceutical Sciences, Parkville, VIC, Australia,* [2] *ARC Centre of Excellence in Convergent Bio-Nano Science and Technology, Monash Institute of Pharmaceutical Sciences, Parkville, VIC, Australia*

Lipids play an important role in regulating bodily functions and providing a source of energy. Lipids enter the body primarily in the form of triglycerides in our diet. The gastrointestinal digestion of certain types of lipids has been shown to promote the self-assembly of lipid digestion products into highly ordered colloidal structures. The formation of these ordered colloidal structures, which often possess well-recognized liquid crystalline morphologies (or "mesophases"), is currently understood to impact the way nutrients are transported in the gut and absorbed. The formation of these liquid crystalline structures has also been of interest within the field of drug delivery, as it enables the encapsulation or solubilization of poorly water-soluble drugs in the aqueous environment of the gut enabling a means of absorption. This review summarizes the evidence for structure formation during the digestion of different lipid systems associated with foods, the techniques used to characterize them and provides areas of focus for advancing our understanding of this emerging field.

Keywords: lipid, liquid crystalline, self-assembly, digestion, lipolysis, mesophase

Edited by:
Angelina Angelova,
UMR 8612 Institut Galien Paris-Sud (IGPS), France

Reviewed by:
Soudamani Singh,
Marshall University, United States
Leonel Malacrida,
Universidad de la República, Uruguay

***Correspondence:**
Ben J. Boyd
ben.boyd@monash.edu

Specialty section:
This article was submitted to Cellular Biochemistry, a section of the journal Frontiers in Cell and Developmental Biology

Received: *24 January 2021*
Accepted: *05 May 2021*
Published: *11 June 2021*

Citation:
Pham AC, Clulow AJ and Boyd BJ (2021) Formation of Self-Assembled Mesophases During Lipid Digestion. Front. Cell Dev. Biol. 9:657886. doi: 10.3389/fcell.2021.657886

INTRODUCTION

Dietary lipids are essential for cellular function and for providing and storing energy in the body. Lipids including triglycerides, phospholipids, and cholesterol are present in a wide variety of foods including fish, vegetables, eggs, meat, nuts, and dairy products. Over 98% of lipids are absorbed by the body following digestion and serve various biological roles (Carey et al., 1983). In infants, the consumption of lipids from human breast milk or infant formula provides approximately 45–55% of dietary energy intake (Castillo and Uauy, 2003). The absorption of long-chain polyunsaturated fatty acids (LCPUFA) such as arachidonic acid and docosahexaenoic acid from infant formula has been shown to be beneficial for cognitive development in infants (Heird, 2001). Furthermore, the metabolism of arachidonic acid produces eicosanoids, which are signaling molecules involved in various anti-inflammatory responses (Lone and Taskén, 2013). Other types of lipids found in human breast milk or infant formula are also essential for growth, improved visual function, and the development of the immune system (Friel and Qasem, 2016). Following infancy, the consumption of dietary lipids continues to provide a rich source of energy for humans (Sikorski et al., 2010). Absorption of fat during digestion not only regulates satiety and energy stores but also assists with the uptake of lipid-soluble vitamins (Goncalves et al., 2015). Other roles that lipids serve in the body include the maintenance of the structural integrity of cells, prevention of water loss in cells, and providing precursors for the synthesis of essential metabolites (Sikorski et al., 2010).

Lipids are not only an essential dietary component but are also often used to facilitate the oral delivery of poorly water-soluble drugs. Nearly 40% of new drug entities are poorly water-soluble, which means that whilst they may exhibit high membrane permeability they suffer from poor dissolution in the aqueous gastrointestinal environment, which hinders their bioavailability (Lipinski, 2002). Co-administering poorly water-soluble drugs with lipids is a useful strategy for improving bioavailability by avoiding the need for dissolution in the gastrointestinal tract and taking advantage of the lipid digestion pathway (Humberstone and Charman, 1997). Lipid absorption, and the use of lipids to dissolve and absorb poorly water-soluble nutrients and drugs critically relies on digestion of the lipids and the subsequent interaction of the co-administered drugs/nutrients with the lipid digestion products (Boyd et al., 2018).

THE PROCESS OF DIGESTION OF DIETARY LIPIDS

The enzymatic digestion of lipids begins in the mouth with lingual lipase partially digesting triglycerides to form diglycerides and fatty acids (Teresa et al., 1984). The digestion continues in the gastric compartment where gastric lipase is secreted from chief cells lining the gastric mucosa. Approximately 10–30% of lipids are hydrolyzed in the stomach by gastric lipases to form a crude emulsion containing diglycerides, monoglycerides, and fatty acids (Carey et al., 1983; Armand et al., 1996). The mechanical churning of the stomach and rhythmic contractions several times per minute act to reduce the particle size of the food chyme to less than 0.5 mm in diameter so that it is able to pass through into the duodenum (Meyer et al., 1976). Triglycerides and diglycerides are then further digested by pancreatic lipase to form two moles of fatty acid and one mole of monoglyceride for each mole of triglyceride originally consumed (Armand et al., 1996; **Figure 1**). The acidic content entering the duodenum from the stomach triggers bicarbonate secretion to increase the pH to approximately 6.2 to 8.1 to allow for optimal lipase activity (Embleton and Pouton, 1997; Kalantzi et al., 2006). Monoglycerides and free fatty acids entering the duodenum also signal for the secretion of bile salts, phospholipids, and cholesterol from the gall bladder to act as an endogenous surfactant, which coats and stabilizes emulsion droplets (Borgström and Patton, 1991). This enables water-soluble colipase/lipase complexes to act at the oil-water interface of the emulsion droplets to hydrolyze fatty acids from the triglycerides, diglycerides, and possibly monoglycerides (Persson et al., 2007). Triglycerides are typically stereospecifically hydrolyzed initially at the sn-3 position, followed by the sn-1 position to form 2-monoglycerides and fatty acids (Borgström and Patton, 1991). These products of digestion then self-assemble into mixed colloidal structures such as vesicles, mixed micelles, and liquid crystalline mesophase systems (Salentinig et al., 2013; Phan et al., 2014).

The pathway by which the fatty acids are transported after absorption is dependent on the chain-length (Hamilton and Kamp, 1999). Digestion to form short to medium fatty acids and monoglycerides results in the passive diffusion of the digestion products across the intestinal epithelium into the enterocytes for direct transport to the portal vein (Porter et al., 2007). Long-chain fatty acids and monoglycerides that have been absorbed into the enterocytes are transported into the endoplasmic reticulum to be re-esterified into triglycerides. The triglycerides are incorporated with cholesterol, proteins, and phospholipids to form lipoproteins called chylomicrons (Stremmel et al., 2001). Lipoproteins are taken up by the lymphatic system and directly enter the systemic circulation, bypassing first pass metabolism in the liver (Stremmel et al., 2001). While these processes post-absorption do not relate directly to the formation of ordered lipids mesophases in the gastrointestinal tract, the rate of availability of the lipids and other components as a consequence of structure formation is likely important for these processes but the links have not yet been made.

TYPES OF LIPID MESOPHASES

Lipid Self-Assembly and the Critical Packing Parameter Concept

The amphiphilic lipids formed upon digestion of triglycerides can self-assemble into ordered structures in the intestinal fluids. The lipids generated from dietary triglycerides are primarily unsaturated and saturated medium chain or long-chain amphiphilic molecules (Pham et al., 2020). Upon liberation by lipase and exposure to excess water, the hydrophilic head groups are specifically hydrated, whilst the lipophilic chains associate with each other to avoid interaction with water. The packing geometry of the lipids results in their self-assembly into different mesophases, with common mesophases observed being of the "inverse" or type 2 topology where the curvature of the interface is toward the aqueous domains. These mesophases include the disordered inverse micellar (L_2), inverse bicontinuous cubic (V_2), inverse hexagonal (H_2) phase, and inverse micellar cubic (I_2, Fd3m space group) phase as well as the fluid lamellar (L_α) phase. The V_2 phase can be further divided into space groups: diamond (Pn3m), gyroid

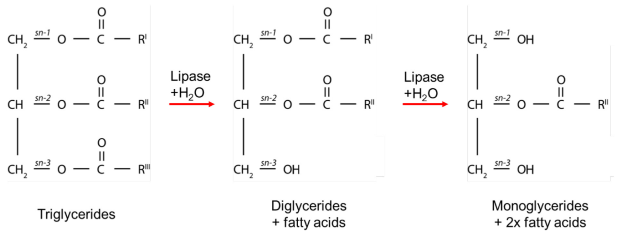

FIGURE 1 | A schematic diagram of the digestion process of triglycerides. R^{I}, R^{II}, and R^{III} represent the alkyl chains that make up the triglycerides, which can comprise the same or different fatty acids. The combinations of alkyl chains are dependent on the source of fat.

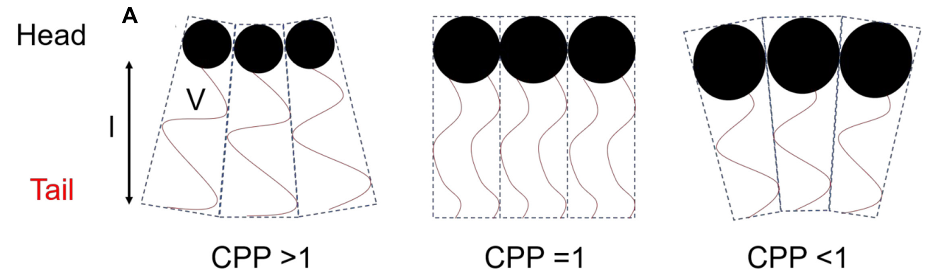

FIGURE 2 | Schematic diagram of the geometry of packing of amphiphilic molecules and corresponding CPP values. This image was based on and redrawn from Du et al. (2014).

(Ia3d), and primitive (Im3m) V_2 phases. Particles with the L_α, V_2, and H_2 mesophases constituting the internal structure are termed liposomes (or vesicles), cubosomes, and hexosomes, respectively. The propensity for different structures to be formed is dependent on the dynamic lipid composition and conditions such as pH and ionic strength. Without preempting too much of discussion to come, it is then conceivable that as droplets of lipids from food form these structures during digestion that the droplets would possess such structures and therefore transform from essentially unstructured triglyceride droplets into cubosomes or other structures depending on the local lipid packing inside the droplet.

The concept that relates the self-assembly of lipids into ordered mesophase structures to the geometry of lipid packing is known as the critical packing parameter (CPP). The value of the CPP is calculated by the ratio of the hydrophobic tail volume of the amphiphilic molecule to the product of the effective head group area and the length of the surfactant tail (Eq. 1) (Israelachvili et al., 1976).

$$Equation\ 1:\ CPP = \frac{V}{al} \tag{1}$$

where V is the volume of the hydrophilic tail, a is the effective area of the head group, and l is the length of the surfactant tail (**Figure 2**). Molecules with larger head groups and smaller hydrophobic chains tend to pack to form type 1 structures which favors curvature toward the lipophilic region of the mesophase (positive curvature). As mentioned above the type 2 structures or inverse structures are formed when curvature is toward the hydrophilic region of the mesophase (negative curvature) and are more commonly found in biological settings and pharmaceutical research (Seddon et al., 2000; Shearman et al., 2006).

The CPP is affected by the temperature of the surrounding environment, ionic strength, additives, and pH of the molecule if it is ionizable (Czeslik et al., 1995; Liu et al., 2013; Tangso et al., 2013; Salentinig et al., 2014). For example, an increase in temperature would effectively increase chain movement which increases V, leading to an increased CPP and curvature toward the aqueous compartment (Israelachvili, 2011).

TECHNIQUES FOR STUDYING LIPID-BASED MESOPHASE SYSTEMS DURING DIGESTION

In vitro Digestion Models

In vitro digestion models enable lipid digestion to be conducted under controlled simulated human gastrointestinal conditions. *In vitro* digestion studies are used to obtain information on the digestion kinetics of a lipid system, the extent of digestion over a given time, and in pharmaceutical applications, the drug distribution within the lipid and aqueous phases (Porter et al., 2004). The most commonly used *in vitro* lipolysis model is the pH-stat model (**Figure 3**; Dahan and Hoffman, 2006, 2008; Fatouros et al., 2007). Using the pH-stat model, the pH is maintained at a specific pH value representative of *in vivo* conditions during digestion, typically at a value between pH 6.5 and 7.5 representative of the small intestine. As the triglycerides are digested by lipase, the fatty acids that are liberated act to reduce the pH of the medium, and the pH-stat system will titrate against those fatty acids through addition of NaOH to maintain the pH at its set point. The amount of NaOH consumed during the digestion is measured over time, enabling a kinetic digestion profile to be established. Samples can be taken during the digestion process and analytical techniques such as gas chromatography or high performance liquid chromatography (HPLC) with mass spectrometric detection can be used to determine the lipid species present (Pham et al., 2020), the degree of drug solubilization or drug precipitation upon digestion of particular lipid systems (Anby et al., 2014; Khan et al., 2015a,b). Other *in vitro* digestion models also include gastric compartments to encompass more of the lipolysis processes occurring *in vivo* (Lee et al., 2013; Ye et al., 2016; Berthelsen et al., 2019).

Lipase inhibitors such as 4-bromophenylboronic acid (4-BPBA) or orlistat can be used to halt the digestion to enable offline analysis of the liquid crystalline (LC) mesophases that form during the lipolysis process. However, the addition of the inhibitor introduces an element of uncertainty as to the effect of the inhibitor on mesophase formation and 4-BPBA was shown to disrupt the packing of some mesophase which would otherwise be present during "online" *in vitro* digestion (Phan et al., 2013). There is also the treatment

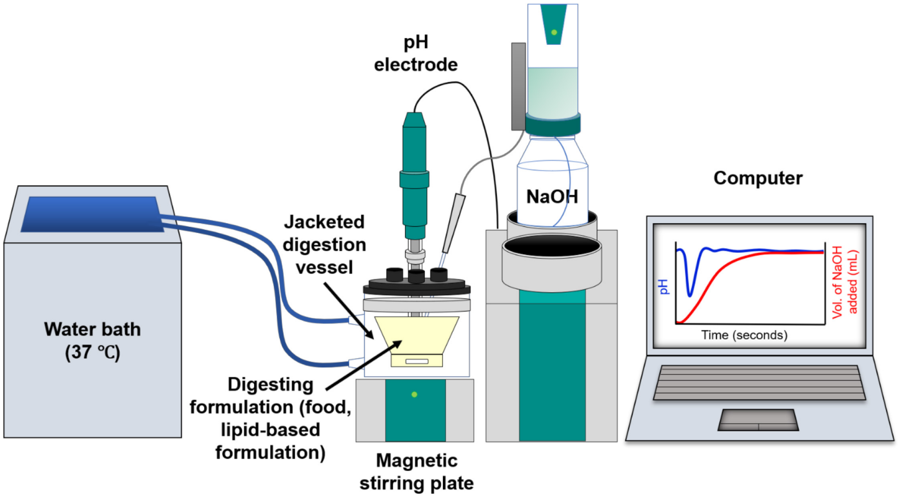

FIGURE 3 | Schematic diagram of the *in vitro* digestion pH-stat apparatus. Digestion of lipids from the formulation generates fatty acids resulting in a drop in pH. This is compensated by automated addition of NaOH to maintain a fixed pH value, enabling the tracking of digestion kinetics on the computer.

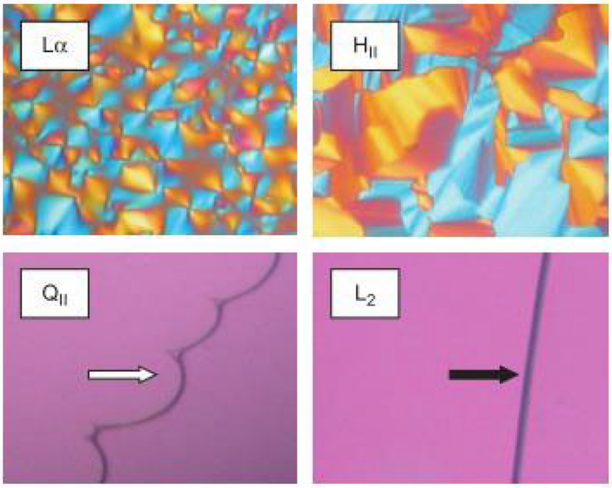

FIGURE 4 | Images of various LC mesophases captured using CPLM. The upper panels are examples of CPLM images of anisotropic mesophases like L_α and H_2 phases show birefringence. The dark appearances on the bottom panels are due to the isotropic nature of the V_2 (called Q_{II} in the original work this image is reproduced from) and L_2 phases. The V_2 and L_2 phases can be distinguished by their appearance at the lipid/water interface. Images were reproduced with permission from Boyd et al. (2009).

and storage of samples taken from a digestion for inhibition prior to study by an appropriate analytical technique that also make "offline" structural determination unattractive. Ideally *in situ* determination of mesophase formation during digestion would be utilized to circumvent these issues, a development described later.

A disadvantage of using the aforementioned *in vitro* lipolysis methods is that there is no absorptive sink present to remove lipid digestion products that would otherwise occur through absorption *in vivo*. The rate of digestion is likely to be faster than absorption (and must precede it in any case) so at least some accumulation of lipid digestion products is to be expected *in vivo* during digestion. Nevertheless, to attempt to address the limitation of the pH-stat model, an absorptive compartment can be included where two digestion vessel compartments are separated by a monolayer of Caco-2 cells (Keemink and Bergström, 2018). Caco-2 cells are similar to the human epithelial cells of the intestine (Sambuy et al., 2005). However, this system requires optimization to prolong the integrity of the Caco-2 cells that are often damaged by the presence of pancreatic lipase or the digestion media (Bu et al., 2016; Sadhukha et al., 2018). Recently, the Caco-2 cells in combination with HT-29-MTX cells (human colon cell line) have been proposed as an alternative absorptive sink for *in vitro* digestions (Hempt et al., 2020). The addition of the HT-29-MTX cells provides a protective layer to the cell monolayer attributed to the mucus secretion from the HT-29-MTX cells. Though cell viability was improved, the evolution of LC structures during the digestion of bovine milk with and without the added Caco-2/HT-29- MTX cells was similar to that with no cell sink, which suggested that more optimization is required to incorporate a fully functional absorptive sink.

In vitro digestion models only provide information on digestion kinetics and other techniques must be employed either on samples retrieved over time or *in situ* to qualitatively and quantitatively analyze the presence of lipid mesophases within a system. Earlier studies have used microscopy to visualize the process of digestion, in which the discovery of the L_α and "viscous isotropic" phases were observed during the digestion of olive oil under simulated physiological conditions (Patton and Carey, 1979). More recently, coupling *in vitro* digestion models to advanced techniques such as small angle X-ray scattering (SAXS) and small angle neutron scattering (SANS) can now provide in-depth information on the structural characterization on a nanoscale (Hyde, 2001; Kirby et al., 2013) as described further below.

Microscopy Techniques

Light Microscopy

Crossed polarized light microscopy (CPLM) is a simple technique that can be used to rapidly characterize the internal structure of a bulk material during digestion (Patton and Carey, 1979; Dong et al., 2006). The bulk material, that is the lipid that has been equilibrated in excess water, is assumed to behave in the same manner as its nano-sized dispersed forms which are more commonly used in oral delivery studies. The samples are generally placed between glass slides that are then viewed under crossed-polarized filters. Samples that are isotropic such as inverse micellar (L_2) or cubic (V_2) phases will have no light passing through the second filter which gives the images a dark appearance (Rosevear, 1954, 1968). Samples containing isotropic materials such as the L_2 and V_2 phase can be distinguished by the appearance at the lipid-water interface (**Figure 4**). The high viscosity of the cubic phase will appear structured at the lipid-water interface, while the micellar (L_2) phase will appear flat (Rosevear, 1968). Samples that are anisotropic such as L_α or H_2 phases will appear bright as they rotate plane polarized light, allowing some light to bypass both polarizer films. Lamellar phases will give a mosaic-like or more disordered brightness while hexagonal phase will give a more fan-like appearance (Rosevear, 1968). This technique is generally used as a preliminary step for characterizing mesophases during digestion as the pH, temperature, and addition of enzymes can be controlled to simulate the digestion of lipids in the gastrointestinal tract.

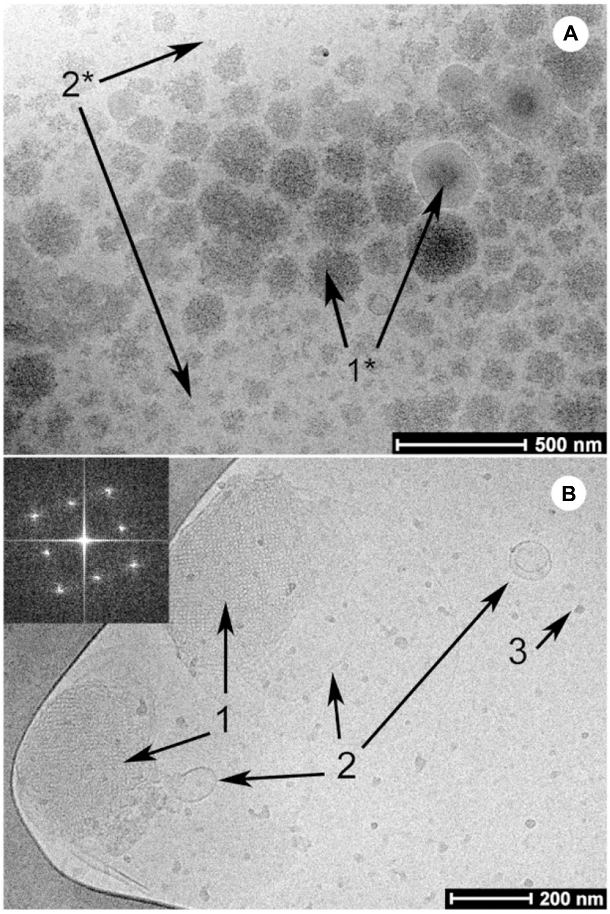

FIGURE 5 | Examples of cryo-TEM images of milk before **(A)** and after digestion **(B)** by Salentinig et al., reproduced with permission from Salentinig et al. (2013). Copyright (2013) American Chemical Society. Panel **A** shows the presence of unstructured emulsion droplets characteristic of bovine milk. The presence of bicontinuous cubic phase (annotated with “1”), lamellar vesicles (annotated with “2”) and protein (annotated with “3”) can be observed in the digested milk in panel **B**.

Confocal laser scanning microscopy is commonly used to study the localized components within cells or other types of specimens (Matsumoto and Hale, 1993). This is done by fluorescently labeling regions of interest to enable contrast from the background using fluorescent lipophilic probes such as Nile Red. Using CLSM, high resolution images can be achieved by focusing a laser onto a fixed spot within a sample, at a defined scanning depth within the sample (Matsumoto and Hale, 1993; Wu and Bruchez, 2004). Fluorescence is emitted from this defined spot and is refined by pinholes before reaching a light detector. Signals that are out of focus are removed by the pinholes to allow only the illuminated in-focus spot to be detected (Zhou and Li, 2015). To visualize mesophases, the scan differential interference contrast (DIC) mode is used obtain contrast within unstained samples (Gallier et al., 2013a,b). The sample requires no preparation and the technique is non-invasive. Information regarding the size of the lipid droplets and the structural changes on the surface of the droplets during digestion can be obtained. Confocal laser scanning microscopy is particularly useful for examining the intracellular interaction of mesophase nanoparticles and has been used to visually observe lipid droplets enveloped by lamellar phases from digested bovine milk (Zeng et al., 2012; Gallier et al., 2013a,b).

Electron Microscopy

Cryogenic-transmission electron microscopy (cryo-TEM) is another microscopy technique that can be used to study the structural morphology of lipid mesophases. The general size of the particles and their internal structure can be observed on a local scale with resolutions down to 1.8 Å (Tan et al., 2008; Fong et al., 2012; Merk et al., 2016). This technique involves pipetting the dispersed material onto a copper grid perforated with carbon films that have been prepared under glow discharge in nitrogen. The copper grid is then immediately submerged into liquid nitrogen or liquid ethane to immediately freeze the sample onto the grid. The samples are then kept under liquid nitrogen until microscopy analysis (Almgren et al., 2000; Spicer et al., 2001; Martiel et al., 2014). This enables the structural integrity of the LC mesophases to remain unaltered at the time of analysis and makes it possible to analyze mesophases in solution. The mesophases observed under cryo-TEM can be quantitatively analyzed using fast Fourier transform analysis (Sagalowicz et al., 2006). Contrary to CPLM or CLSM, the

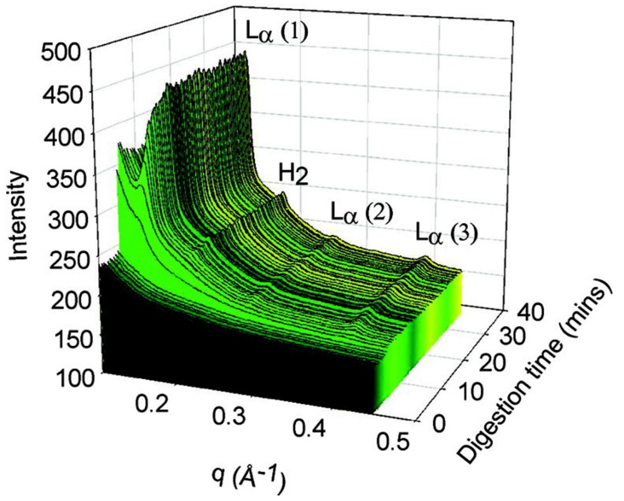

FIGURE 6 | The formation of liquid crystalline structures during the digestion of a self-nanoemulsifying drug delivery system (SNEDDS) by Warren et al. (2011). Scattering profiles of the digest are shown as a function of time (min), and the peaks that arise during digestion were attributed at the time to L_α and H_2 phases although it is likely from more recent studies that the lamellar phase is due to calcium soap formation (Clulow et al., 2018). Adapted with permission from Warren et al. (2011). Copyright (2011) American Chemical Society.

preparation procedure of cryo-TEM is labor intensive and time costly. Furthermore, samples containing high concentrations of sugars such as milk can reduce the contrast in cryo-TEM images, hence, reducing the resolution of self-assembled structures from the background (Duzgunes, 2003). Nonetheless, cryo-TEM is an effective technique for providing 3D visualization of the various mesophases that can occur during digestion (**Figure 5**; Phan et al., 2013; Salentinig et al., 2013).

Scattering Techniques

Small angle X-ray scattering has emerged as one of the most powerful tools for determining mesophase structure formation in lipid systems during digestion. SAXS is a non-invasive technique that involves scattering of X-rays based on the spatial variations in electron density between the aqueous and lipid regions of mesophases (Cullity, 1956; Gregory, 1957; Hyde, 2001). Ordered (crystalline or liquid crystalline) structures produce unique scattering profiles which enable identification. Some of the advantages of using SAXS are that the sample preparation is relatively simple, the acquisition time is rapid (enabling dynamic flow through measurements when using synchrotron sources), the temperature can be controlled, and highly detailed information regarding structure can be determined (Kirby et al., 2013). The real time formation of highly ordered, mesophase structures during digestion was demonstrated when the pH stat digestion model was used in conjunction with SAXS (Fatouros et al., 2007; Warren et al., 2011). An example of LC transformation during *in vitro* digestion coupled with SAXS is shown below in **Figure 6**.

Small angle neutron scattering is analogous to SAXS but involves scattering neutrons through interactions with atomic nuclei. The use of isotopic substitution, particularly substitution of deuterium for hydrogen in either the self-assembling molecules or the solvent can enable determination of localization of specific components in the mixture (Lopez-Rubio and Gilbert, 2009). Where samples (mesophases) have similar electron densities as their surrounding environment (solvent), SANS with deuterium labeling is used in place of SAXS to improve scattering contrast between the two (Chu and Liu, 2000). Deuterium is a heavier isotope of hydrogen, which produces small changes to the sample but significant effect on neutron scattering profiles (Ramsay et al., 2007). Deuterium substantially boosts the coherent neutron scattering power (scattering length density) of a molecule, where hydrogen reduces it. If the scattering length densities of the sample and matrix are similar or the same, there is little scattering contrast and weak or no scattering profiles are observed. By deuterating part of the sample or the matrix, the scattering length densities of the components in the system become substantially different, enhancing scattering contrast and highlighting the components of the sample that have substantially different scattering power to the matrix. The localization of components in mixed bile salt micelles from *in vitro* lipolysis as well as their shape and size can be determined using SANS (Phan et al., 2015; Rezhdo et al., 2017). In the context of studying mesophase formation during digestion, the disadvantage of using SANS is the generally lower flux and lower detector sensitivity of neutron sources than synchrotron X-ray sources, which results in long acquisition times. This precludes true "real time" *in situ* studies of changes in self-assembled structures with time resolution of shorter than several minutes per timepoint using neutrons, compared to seconds with synchrotron-based X-ray approaches.

FORMATION OF MESOPHASES DURING THE DIGESTION OF LIPID SYSTEMS

The process of digestion is essential for the conversion of many lipid systems into mesophases. Depending on the ratio of undigested lipids to digestion products, the lipid mesophases will change as digestion progresses. As mentioned above, the changes in the microstructure of the lipids during the digestion of olive oil was visualized by Patton and Carey (1979) using light microscopy, where the formation of LC phases (L_α or "viscous isotrope") was indicated (**Figure 7**). The digestion of triglycerides was further explored later, again using light microscopy, in which intermediate lipid mesophases were observed during the digestion of either olive oil or emulsified triolein (Patton et al., 1985). This study examined the interplay between lipase and the digesting lipid in the aqueous environment similar to that of intestinal fluids. The concept of light microscopy was explored to visually inspect the enzymatic activity of lipase on lipids that cannot be determined by simply conducting chemical reactions. The relevant digestion components were also isolated as opposed to using human intestinal aspirates to enable key interactions during digestion to be established

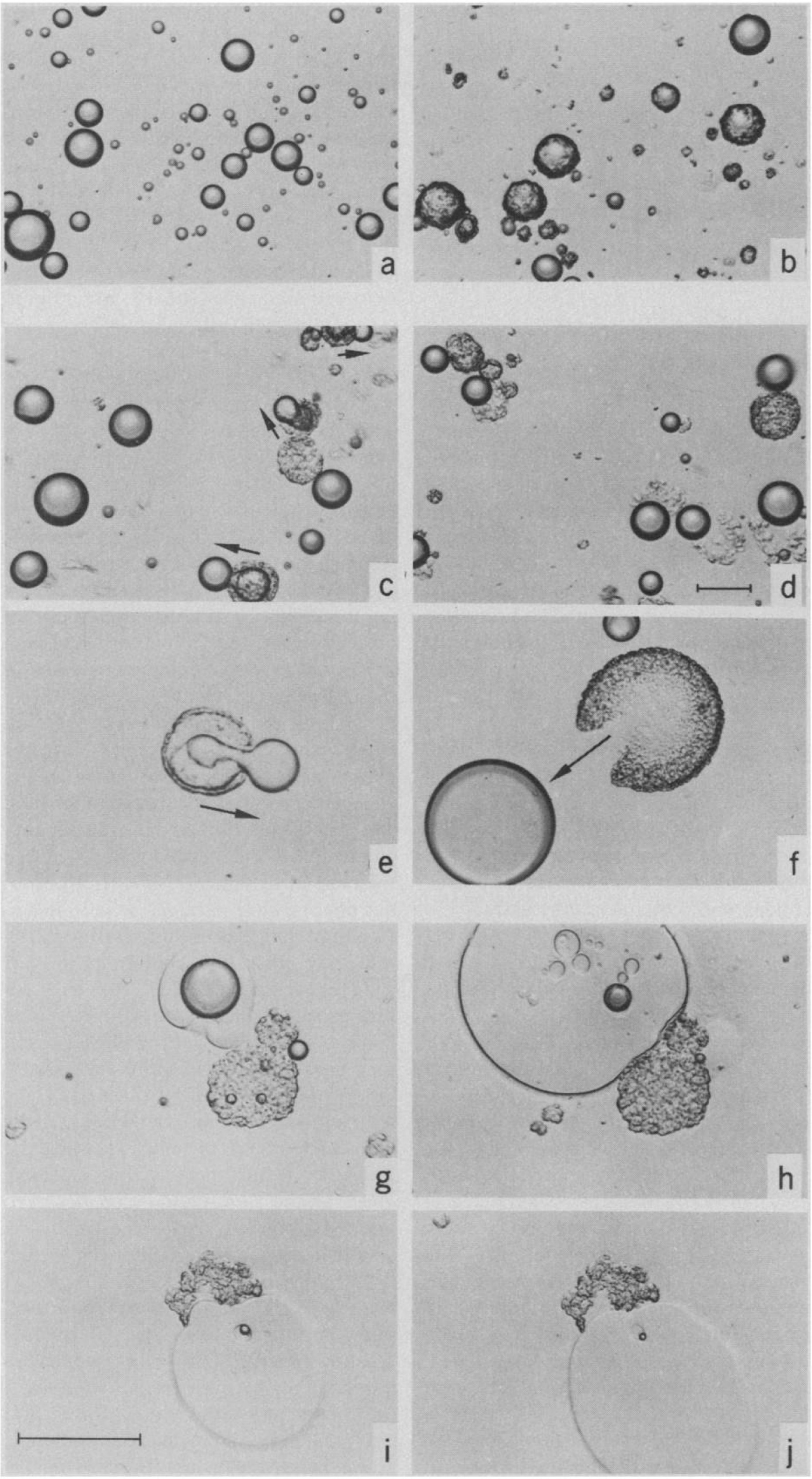

FIGURE 7 | Light microscopy images capturing the digestion process of a droplet of olive oil (Patton and Carey, 1979). Reprinted with permission from AAAS. A lamellar shell was formed following initiation of digestion **(a,b)**, where the shell was later broken leading to extrusion of the undigested lipids **(c–f)**. The presence of "viscous isotrope" phases was later observed **(g–j)**.

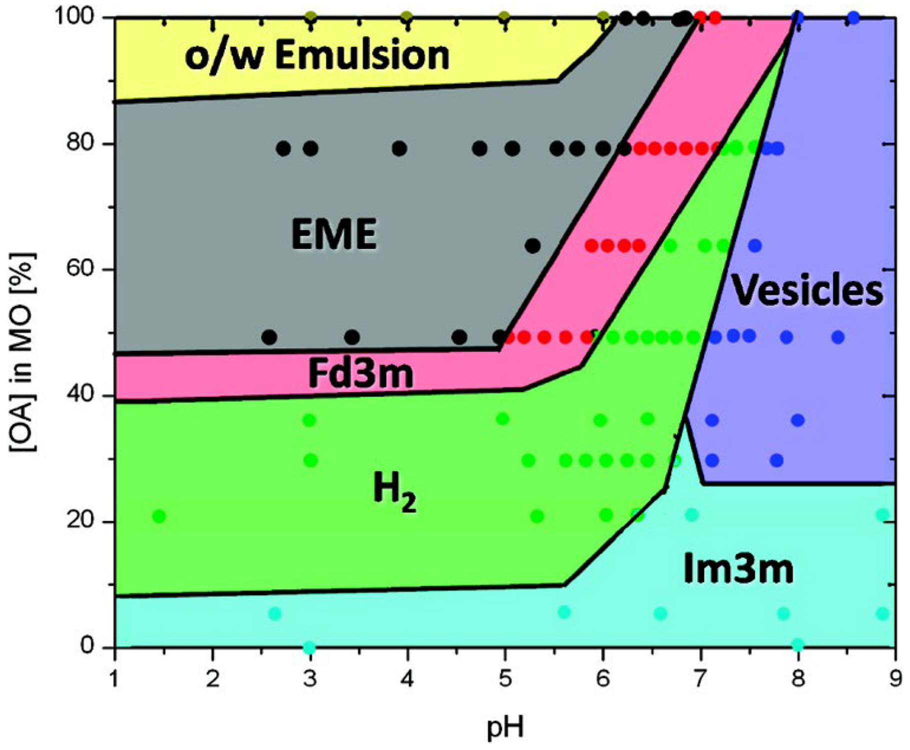

FIGURE 8 | A phase behavior diagram of monoolein and oleic acid mixtures in PBS buffer with pH of 1–9 at 25°C, constructed by Salentinig et al. (2010a). Phases were determined *via* SAXS analysis of pre-made dispersions of the lipids. Adapted with permission from Salentinig et al. (2010a). Copyright (2010) American Chemical Society.

more easily. This was because human intestinal aspirates may not be homogeneously mixed and digested, combined with the presence of other endogenous secretions that can make it more difficult to visualize the changes in the microstructure of lipids under light microscopy. A correlation between the LC structures and the composition of digestion products of olive oil was also established, where the mesophases mainly consisted of monoglycerides and protonated fatty acids.

In the early 2000s Borné et al. (2002) demonstrated the formation of specific mesophases during the digestion of oleic acid-based acylglycerol systems using a combination of CPLM, SAXS, and HPLC. Ternary phase diagrams were established to enable prediction of the mesophases formed at specific concentrations of monoolein and oleic acid/sodium oleate in water that can occur during lipolysis. It was established that decreasing the ratio of glyceryl monooleate to oleic acid will result in the phase transitions from V_2(Im3m), to H_2 phase, the I_2(Fd3m) phase, and then the L_2 phase (Borné et al., 2002). Meanwhile, increasing the ratio of glyceryl monooleate to sodium oleate will result in a phase transition of L_α to H_2 phase.

The prediction of the phases that can occur during the digestion of oleic-based acylglycerol systems was later expandedto encompass the changes in pH during *in vitro* digestion (Salentinig et al., 2010a). A myriad of structures was established from the combination of oleic acid and monoolein under different pH values, ranging from 1 to 9 (**Figure 8**). It was also discovered that the phase changes were reversible with pH. Additional cryo-TEM techniques were incorporated to observe the changes in structural morphology of the digesting lipids in conjunction with SAXS (Salentinig et al., 2010a).

Real-time structural evolution of digested triolein was then examined by using an *in vitro* digestion coupled to SAXS apparatus similar to that established by Fatouros et al. (2007) and Salentinig et al. (2010b). The complex LC structures that arise during the digestion of triolein were demonstrated to be in agreement with previous studies. The changes in mesophase observed during digestion were due to the CPP of the amphiphilic digestion products changing throughout the process.

MESOPHASE STRUCTURE FORMATION DURING DIGESTION IN PHARMACEUTICAL APPLICATIONS

Mesophases possess both lipophilic domains and hydrophilic water channels which are capable of solubilizing both lipophilic and hydrophilic drugs, making them an ideal system for drug delivery (Nguyen et al., 2010, 2011a,b; Phan et al., 2011). Lipids have been utilized as a carrier for many poorly water-soluble drugs to improve their oral bioavailability (Pouton, 2000; Porter et al., 2007; Feeney et al., 2016). Lipid-based mesophases are also already in use in pharmaceutical applications, including

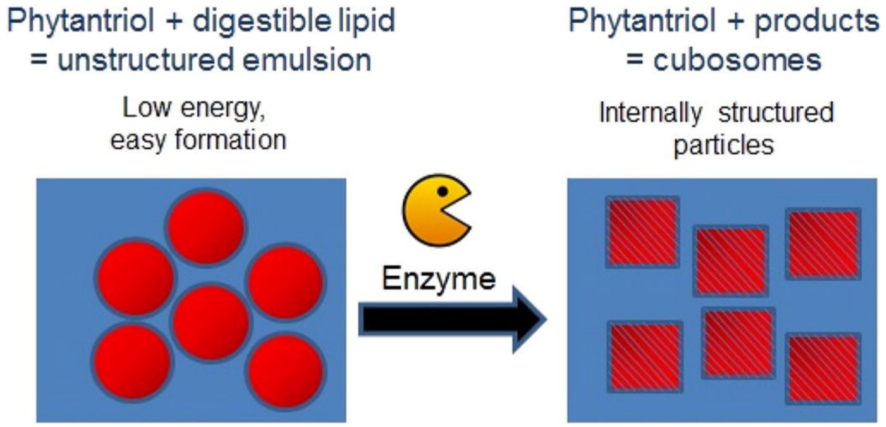

FIGURE 9 | Schematic diagram demonstrating the enzymatic approach to form mesophases particles using a precursor formulation comprising phytantriol and a digestible lipid. Only low energy is required to generate the precursor formulation, in which the digestible lipids partition out of the formulation under digestion to enable the formation of the internally structured particles. Adapted with permission from Fong et al. (2014). Copyright (2014) American Chemical Society.

liposomes (nano-sized lamellar phase) already on the market for the delivery of a range of drugs (Kaminskas et al., 2012; Negrini et al., 2015; Rabinovich et al., 2015), and for slow release injections (Haasen et al., 2017). The dispersed mesophases (comprising nano-sized mesophase particles) are often preferred over the bulk phase as the bulk phases are generally highly viscous (especially in the case of bicontinuous cubic V_2 phase) and difficult to handle (Larsson, 1999). Traditional methods for generating dispersed phases require high levels of energy to break up the bulk aggregates to form stable sub-micron particles. A limitation to this approach is that heat is invariably generated which can degrade heat sensitive materials incorporated into the nanoparticles. Furthermore, this process is energy intensive and is therefore costly for manufacturing. The alternative "bottom up" approach is designed to allow the lipids to self-assemble into LC structures by dissolving lipids into hydrotropes, then diluting the mixture with an aqueous medium (Spicer et al., 2001). Precipitation that occurs within the cubic phase-water miscibility gap allows the formation of cubosomal dispersions (likewise for hexosomal dispersions). However, this process does not allow control of the particle size, which is often an essential requirement for pharmaceutical preparations used for intravenous (IV) administration or medical imaging applications.

An alternative low energy approach to making mesophase dispersions using lipid digestion was recently studied. Precursor unstructured emulsion systems are prepared comprising a non-digestible and a digestible lipid (e.g., triglyceride) which after digestion by pancreatic lipase forms a dispersed mesophase system (**Figure 9**; Fong et al., 2014; Hong et al., 2015). For example, by using a precursor emulsion system composed of non-digestible phytantriol and the digestible short chain triglyceride, tributyrin, exposure to lipase resulted in digestion of the tributyrin, allowing the phytantriol to self-assemble into the bicontinuous cubic V_2 phase (Lee et al., 2009; Nguyen et al., 2011b; Fong et al., 2014; Hong et al., 2015). As a proof of concept demonstration of the *in vivo* behavior of these enzymatically triggered delivery systems, oral administration of the easily formed phytantriol/tributyrin emulsion system containing a model hydrophobic drug cinnarizine, resulted in the same behavior as a formulation prepared using phytantriol alone (Hong et al., 2015; Pham et al., 2016). More recently, the enzymatic digestion of phospholipids to induce phase transformations has also been explored (Fong et al., 2019). The generation of diacylglycerol (DAG) from the action of phospholipase C was studied by NMR and time resolved SAXS was used to study the structural changes occurring during the digestion process. The type of phospholipid present had consequences for the disposition of the DAG digestion products with respect to the lipid bilayers with consequent impacts on self-assembled structures formed.

The type of mesophase formed during the digestion of lipid-based drug delivery systems is also an important factor to consider as different mesophases have not only been demonstrated to exhibit different rates of release but also vary in drug solubilizing capacity to affect the fate of drug absorption during digestion (Kossena et al., 2005; Phan et al., 2011; Yaghmur et al., 2012; Du et al., 2014). In cases where drug solubilization capacity is reduced upon dilution of the lipids in the GI tract, precipitation of the drug may occur and consequently cause a reduction in drug absorption (Khan et al., 2015a). The effect of phase behavior on drug absorption was demonstrated by Kossena et al. (2005) where drug absorption from the lamellar phase was reduced upon exposure to intestinal fluids compared to the V_2 phase.

SELF-ASSEMBLY BEHAVIOR OF LIPID-BASED FOOD DIGESTION PRODUCTS

In recent years, the self-assembly of lipids during the digestion of various food sources has gained interest. It has been hypothesized

TABLE 1 | Summary of food type, the approximate lipid composition (SCT = short chain triglyceride, MCT = medium chain triglyceride, LCT = long chain triglyceride, FA = fatty acid, MG = monoglyceride), and the corresponding mesophase transitions that occur during digestion.

Food product	Percentage of fat (%) used in the starting emulsion	Approximate/average fatty acid composition (mol %)	Mesophase transitions during digestion*	References
Bovine milk (pasteurized and homogenized)	3.8	SCT: 0.4–12 MCT: 10–26 LCT: 74–90	Emulsion $\rightarrow L_\alpha$ $\rightarrow L_\alpha + I_2$(Fd3m) $\rightarrow L_\alpha + H_2$ $\rightarrow L_\alpha + H_2 + V_2$(Im3m)	(Feng et al., 2004; Lindmark-Månsson, 2008; Salentinig et al., 2013; Clulow et al., 2018; Pham et al., 2020)
Human breast milk	2.20 ± 0.13 w/v	SCT: 0 MCT: 5–13 LCT: 87–95	Emulsion $\rightarrow L_\alpha$ I_2(Fd3m)	(Salentinig et al., 2015; Pham et al., 2020)
Goat milk (pasteurized and homogenized)	3.6	SCT: 2–5.7 MCT: 16–27 LCT: 63–78	Emulsion $\rightarrow L_\alpha$ $\rightarrow L_\alpha + I_2$(Fd3m) $\rightarrow L_\alpha + H_2$ $\rightarrow L_\alpha + V_2$(Im3m) $\rightarrow L_\alpha$	(Prosser et al., 2010; Pham et al., 2020)
Soy juice	3.0	SCT: 0 MCT: 0–1 LCT: 99–100	Emulsion I_2(Fd3m)	(Li et al., 2017; Pham et al., 2020)
Infant formula (three different brands)	(1) 3.8	(1) MCT: 3.45 ± 0.24 FA/4.03 ± 0.08 MG LCT: 95.57 ± 0.24 FA/95.97 ± 0.08 MG	(1) Emulsion $\rightarrow L_\alpha$ $\rightarrow I_2$(Fd3m)	(Pham et al., 2020)
	(2) 3.8	(2) MCT: 13.51 ± 0.042 FA/8.15 ± 0.71 MG LCT: 95.57 ± 0.24 FA/95.97 ± 0.08 MG	(2) Emulsion $\rightarrow L_\alpha$ $\rightarrow L_\alpha + H_2$	
	(3) 3.6	(3) MCT: 4.90 ± 0 35 FA/3.89 ± 0.22 MG LCT: 93.81 ± 0.38 FA/96.11 ± 0.22	(3) Emulsion $\rightarrow L_\alpha$	
Mayonnaise	7.15	SCT: 0 MCT: 0 LCT: 100 (Eastwood et al., 1963)	Emulsion $\rightarrow I_2$(Fd3m) $+ L_2$ $\rightarrow H_2$ $\rightarrow V_2$(Pn3m) $\rightarrow L_\alpha$	(Salentinig et al., 2017)
Krill oil	5	SCT: 0 MCT: 0 LCT: 100	Emulsion $\rightarrow L_\alpha \rightarrow H_2$	(Codex Alimentarius Commission, 2017; Yaghmur et al., 2019)

**It is now likely that in many cases where the lamellar phase observed in digesting lipid systems that it is due to calcium soap formation rather than a putative L_a phase (Clulow et al., 2018).*

that the formation of the lipid mesophases is linked to the enhanced uptake of nutrients or to transport poorly water-soluble molecules through the aqueous intestinal fluids (Salentinig et al., 2013; Assenza and Mezzenga, 2019). **Table 1** provides a summary of the different phase transitions that occur during the digestion of various food types. The mesophases described in **Table 1** have been determined by conducting *in vitro* lipolysis coupled to SAXS.

Mesophase Formation During the Digestion of Mammalian Milk

By coupling SAXS with *in vitro* digestion models, it has been shown that the digestion of mammalian milks generates mesophase structures. Mammalian milks contain a myriad mixture of triglycerides and many other components that play a role in mesophase formation during digestion. Bovine milk contains approximately 3.5% fat, of which 98% are

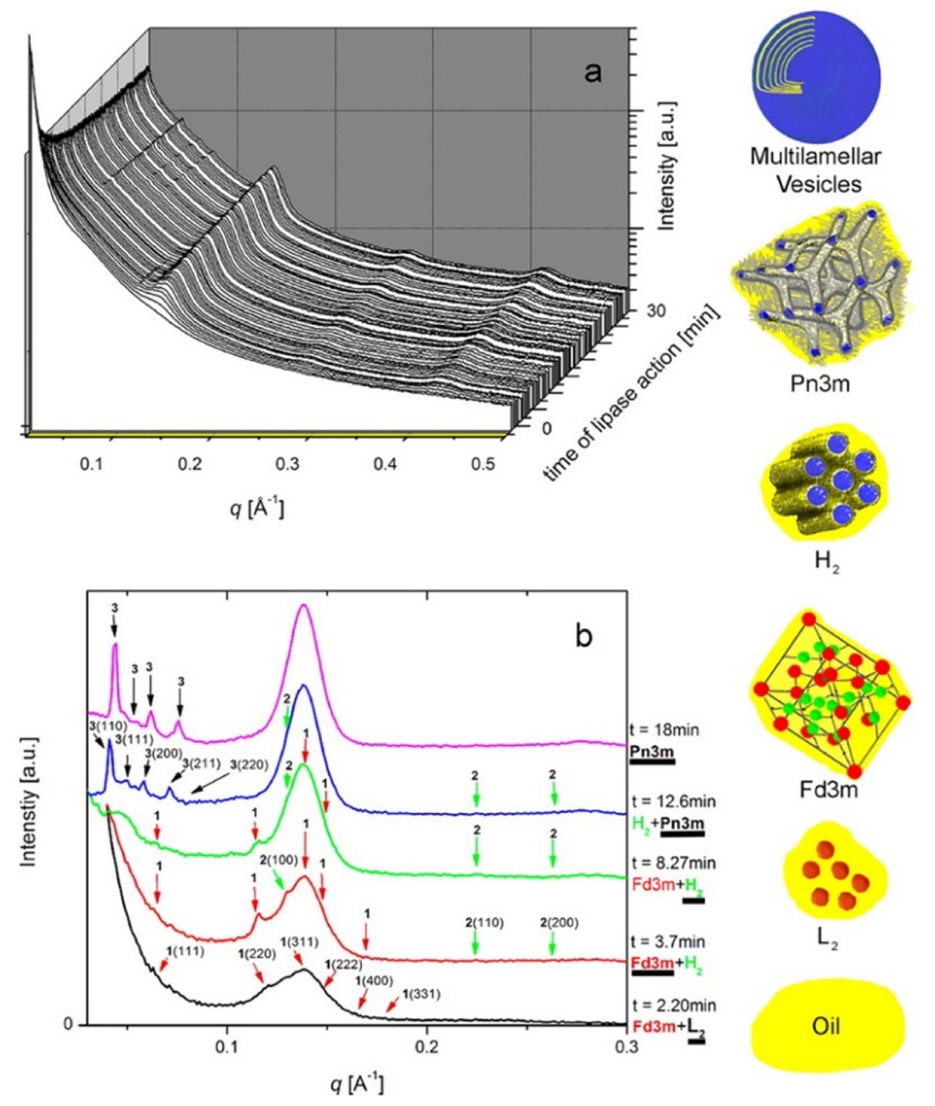

FIGURE 10 | (A) A 3D waterfall plot of the scattering profiles obtained during the digestion of milk coupled to SAXS is presented. **(B)** Offset SAXS profiles of milk during digestion in the absence of bile salt is presented. The peaks corresponding to the various mesophases are indicated with colored arrows, with the corresponding schematic diagrams of the mesophases presented in order of appearance from bottom to top (excluding multilamellar vesicles). This figure was reproduced with permission from Salentinig et al. (2013). Copyright (2013) American Chemical Society.

triglycerides, which undergoes digestion by lipases in the stomach and the upper section of the small intestine, the duodenum. There are over 400 individual different acyl chains that can make up the triglyceride molecules, leading to potentially thousands of different triglycerides (Lindmark-Månsson, 2008). Approximately 75–90% of the fatty acids found in the triglyceride core are long-chain, of which 30% are unsaturated (Lindmark-Månsson et al., 2003; Pham et al., 2020). Salentinig et al. (2013, 2015) reported the formation of mesophases during the digestion of milk using the pH-stat *in vitro* digestion model coupled to SAXS (**Figure 10**).

The composition of lipids changes during digestion of milk due to their digestion, enabling various mesophases to form from the digestion products as a function of time (Pham et al., 2020). Typical phase transitions during the digestion of bovine milks that were subjected to various treatments are shown below in **Figure 11** as illustrated by Clulow et al. (2018).

Similarly, other mammalian milks such as the human breast milk or goat milk have also been demonstrated to form non-lamellar mesophases during digestion (Salentinig et al., 2015; Pham et al., 2020). In particular, the scattering profiles of the digestion of goat milk resembled that of bovine milk. However, the persistent V_2(Im3m) phase seen in bovine milk had disappeared toward the end of the digestion of goat milk. This was attributed to the greater abundance of short- to medium-chain triglycerides in goat milk in comparison to bovine milk (Li et al., 2017; Pham et al., 2020). The scattering profiles of bovine milk, goat milk, and human milk during *in vitro* digestion are

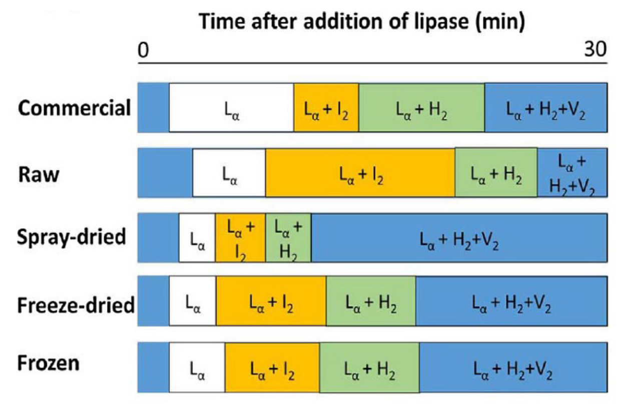

FIGURE 11 | The typical phase transition during the digestion of bovine milk subjected to homogenization and pasteurization (commercial), raw, spray-dried, freeze-dried, and frozen milk reported and reproduced with permission from Clulow et al. (2018). L_α denotes lamellar phases formed by calcium soaps, I_2 denotes the micellar cubic (Fd3m) phase, H_2 denotes hexagonal phase, and V_2 is the bicontinuous cubic (Im3m) phase.

shown below in **Figure 12** (Pham et al., 2020). The differences in mesophase progression observed during the digestion of various types of mammalian milk is of interest as it may influence the absorption of lipophilic nutrients.

Self-Assembly Behavior of Soy Lipids During Digestion

Emulsions prepared using vegetable oils such as canola oil, soybean oil or almond oil are popular as milk substitutes for those who prefer non-dairy beverages. Soy and other vegetable oils are rich in long-chain and unsaturated triglycerides, containing palmitic (C16:0), oleic (C18:1), linoleic (C18:2), and linolenic (omega 3, C18:3), and docosahexaenoic (omega 3, C22:6) fatty acids (Li et al., 2017; Pham et al., 2020). Foods enriched with omega 3 fatty acids have been shown to improve cardiometabolic profiles of people with underlying cardiovascular risks (Barbosa et al., 2017). Like mammalian milk, the triglycerides in soy milk are composed of different combinations of fatty acids on the glycerol backbone, although there are fewer combinations (Brockerhoff and Yurkowski, 1966; Innis, 2011). The digestion of certain brands of commercially available soy emulsions containing soy lipids has recently been demonstrated to form the I_2(Fd3m) phase, similar to that of human breast milk although without the calcium soaps observed to form in digesting human breast milk. The authors suggested that the formation of the I_2(Fd3m) phase was due to the abundance of linoleic acid, which was also the case for human breast milk (Pham et al., 2020). However, the significance of the individual mesophases on the absorption of lipophilic nutrients is yet to be determined.

Self-Assembly Behavior of Infant Formula Lipids During Digestion

Infant formula has been developed over the last century to try to mimic composition provided by the human breast milk and is certainly marketed as such. Infant formulae can contain fat sources from bovine milk, goat milk and vegetable oils depending on the brand and age of the child being provided the formula. Due to the differences in lipid composition, studies have shown that the self-assembly behavior of the lipids in various types of infant formulae exhibit different mesophases during digestion, shown in **Figure 13** (Salim et al., 2019; Pham et al., 2020). The triglyceride content of emulsions attempting to mimic milk has recently been shown to be a key driver for the formation of mesophases commensurate with the milk of a particular species. The lipid self-assembly behavior of human breast milk during digestion was found to be replicated by relatively simple emulsions containing four–seven homotriglycerides mixed together, with a balance of long-chain saturated and unsaturated lipids (Clulow et al., 2020a). Similarly, the structural progression observed by digesting cow milk fat richer in medium and long-chain saturated lipids could be changed to that of digesting human breast milk by mixing it with canola oil, which comprises almost exclusively long-chain unsaturated lipids (Clulow et al., 2020b). These studies indicate the fine balance in lipid composition required to replicate the self-assembly behavior of human breast milk in infant formula products.

Milk is also increasingly recognized as a potential lipid-based drug delivery system due to its ability to dissolve poorly water-soluble drugs (Macheras and Reppas, 1986; Charkoftaki et al., 2010; Boyd et al., 2018; Binte Abu Bakar et al., 2019), which can be enhanced by the process of digestion (Boyd et al., 2018), however, its translation into pharmaceutical products is hindered by the variability in milk composition (Lindmark-Månsson et al., 2003; Lindmark-Månsson, 2008; Taylor and MacGibbon, 2011; Logan et al., 2014). Infant formula has therefore been suggested to play a role in drug delivery to circumvent issues with variability in milk powder. Infant formula is manufactured from a blend of fat sources and is available as a powdered form. The formula composition is tightly controlled to specifications in a manner similar to pharmaceutical excipients and the fat content can be controlled. Recent studies by Salim et al. (2019) showed improved solubilization of the drug clofazimine when digested with infant formula. In order to progress infant formula toward approval as a formal pharmaceutical excipient, more research is needed to understand its behavior during digestion including further studies on how the composition (lipids and other components) and overall fat content impact on structure and interaction with drug cargo.

Examples of Liquid Crystalline Structure Formation in Other Food Products

Recently other food sources have been shown to generate non-lamellar mesophases during digestion. Mayonnaise which is a popular condiment that contains approximately 80% of triglycerides that are derived from vegetable oil. Unlike bovine milk, the triglycerides within mayonnaise are mainly composed of long-chain lipids, of which approximately 90% are unsaturated fatty acids (Eastwood et al., 1963). Interestingly, the mesophase progression of mayonnaise during digestion was found to be similar to that of bovine milk (except for the absence of the

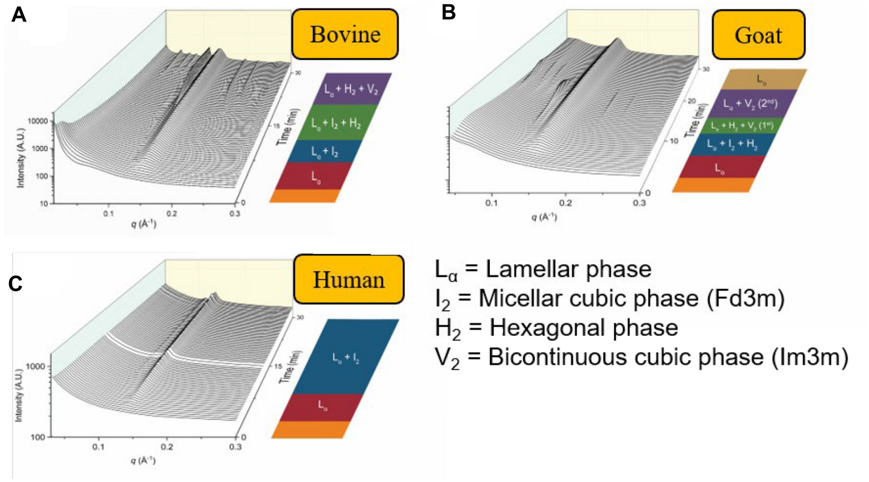

FIGURE 12 | The formation of mesophases during the digestion of mammalian milk. Scattering profiles of **(A)** bovine milk, **(B)** goat milk, and **(C)** human milk during *in vitro* digestion coupled to SAXS are shown. Adapted and reproduced from Pham et al. (2020).

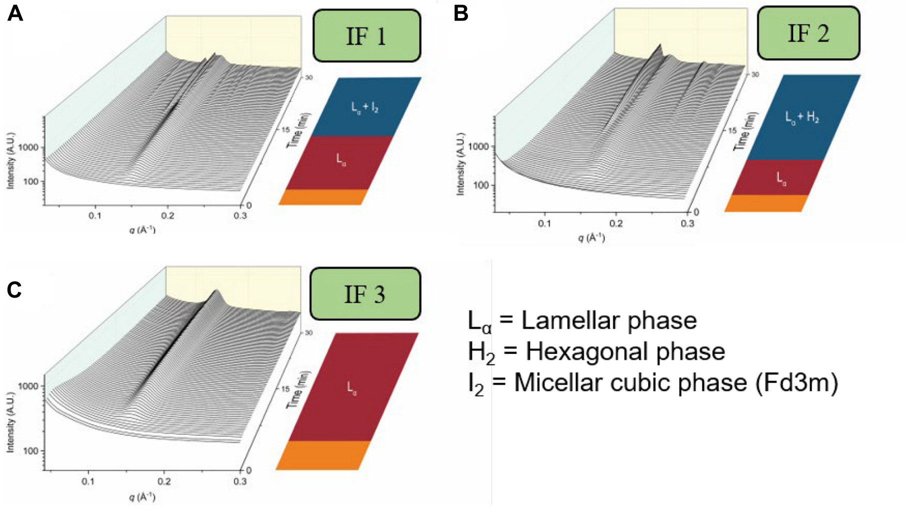

FIGURE 13 | The formation of mesophases during the digestion of various brands of infant formula. Scattering profiles during the digestion of three brands of infant formula are adapted and reproduced from Pham et al. (2020). **(A)** represents the scattering profiles during the digestion of infant formula 1 (IF 1), **(B)** represents the scattering profiles during the digestion of infant formula 2 (IF 2), and **(C)** represents the scattering profiles during the digestion of infant formula 3 (IF 3).

L_α phase), where the lipids of mayonnaise self-assemble into the I_2(Fd3m)/L_2 phase, followed the H_2 phase, and finally the bicontinuous V_2(Pn3m) phase (Salentinig et al., 2017). The absence of the L_α phase during the digestion of mayonnaise in comparison to bovine milk may be due to the lower proportion of palmitic acid in mayonnaise (~20% palmitic acid in mayonnaise, ~37% in bovine milk) which may otherwise contribute to lamellar diffraction peaks from calcium soaps formed during digestion (Ono et al., 1970; Pham et al., 2020). In addition to mayonnaise, krill oil was also found to form structured mesophases during *in vitro* digestion (Yaghmur et al., 2019). Krill oil is a supplement rich in omega-3 polyunsaturated fatty acids, mainly located in phospholipids (Bottino, 1975; Clarke, 1980). The digestion of krill oil resulted in the formation of L_α to H_2 phase when studied using *in vitro* lipolysis coupled to SAXS (Yaghmur et al., 2019). The persistent H_2 phase at the end of the digestion of krill oil may be linked to the abundance of long-chain lipid species in comparison to other systems like that of bovine milk. Therefore, the mesophase structure is more negatively curved relative to the bicontinuous V_2 phase. Nonetheless, several examples of food products have been demonstrated to form complex mesophase systems during digestion which raises the question as to why this unique phenomenon occurs. These recent developments in understanding the dynamic structures formed during digestion may have implications on the transport and delivery of nutrients.

The recognition of the formation of mesophase structures in foods during digestion is becoming more widespread as new techniques are developed that can provide information on these phenomena. The broader question of "what is food?" is becoming an interesting one in this context – for example, mammalian milks have been shown to exhibit rich mesomorphism not seen in vegetable-sourced substitutes. This leads to a tentative sub-question of "what is milk?" – the broader question then of "what is food?" when comparing food from natural sources to formulated foods, may in future be in part answered through a classification based on the structural attributes of each during digestion. Differences in lipid composition at the level of fatty acid distributions are clearly important both for structure (Pham et al., 2020) and nutritional outcome (Li et al., 2010; Palmquist et al., 1986), so it remains an open question as to whether such a distinction eventuates with a link to broader health outcomes.

CONCLUSION

The understanding of the formation of lipid-based mesophases during digestion has accelerated with the advent of time-resolved X-ray scattering capabilities. While the role of the formation of such structures in the digestion process is not yet completely understood, it is becoming clearer that it is a key feature of lipid digestion across a range of lipid-based materials from synthetic lipid systems through formulated food and pharmaceuticals to endogenous lipid materials such as breast milk. Establishing the link between formation of mesophases in lipid systems during digestion and nutritional outcomes is the next major step forward necessary to harness and utilize the phenomenon. It is also important from a food and pharmaceutical design standpoint as formulated systems have potential to either disrupt or enhance the formation of mesophases during digestion with consequences for nutrient and drug delivery.

AUTHOR CONTRIBUTIONS

AP: concept, researching literature, writing original draft, and reviewing and editing. AC: reviewing and editing. BB: concept, reviewing and editing, funding, and project administration. All authors contributed to the article and approved the submitted version.

FUNDING

BB was the recipient of an Australian Research Council Discovery Program (DP160102906). AC was the recipient of an Australian Research Council Discovery Early Career Research Award (DE190100531). AP was supported by an Australian Government Research Training Program Scholarship.

REFERENCES

Almgren, M., Edwards, K., and Karlsson, G. (2000). Cryo transmission electron microscopy of liposomes and related structures. *Colloids Surf. A Physicochem. Eng. Asp.* 174, 3–21. doi: 10.1016/s0927-7757(00)00516-1

Anby, M. U., Nguyen, T.-H., Yeap, Y. Y., Feeney, O. M., Williams, H. D., Benameur, H., et al. (2014). An in vitro digestion test that reflects rat intestinal conditions to probe the importance of formulation digestion vs first pass metabolism in danazol bioavailability from lipid based formulations. *Mol. Pharm.* 11, 4069–4083. doi: 10.1021/mp500197b

Armand, M., Borel, P., Pasquier, B., Dubois, C., Senft, M., Andre, M., et al. (1996). Physicochemical characteristics of emulsions during fat digestion in human stomach and duodenum. *Am. J. Physiol. Gastrointest. Liver Physiol.* 271(1 Pt. 1), G172–G183.

Assenza, S., and Mezzenga, R. (2019). Soft condensed matter physics of foods and macronutrients. *Nat. Rev. Phys.* 1, 551–566. doi: 10.1038/s42254-019-0077-8

Barbosa, M. M. d. A. L., Melo, A. L. T. R. d., and Damasceno, N. R. T. (2017). The benefits of ω-3 supplementation depend on adiponectin basal level and adiponectin increase after the supplementation: a randomized clinical trial. *Nutrition* 34, 7–13. doi: 10.1016/j.nut.2016.08.010

Berthelsen, R., Klitgaard, M., Rades, T., and Mullertz, A. (2019). In Vitro digestion models to evaluate lipid based drug delivery systems; present status and current trends. *Adv. Drug Deliv. Rev.* 142:35. doi: 10.1016/j.addr.2019.06.010

Binte Abu Bakar, S. Y., Salim, M., Clulow, A. J., Hawley, A., and Boyd, B. J. (2019). Revisiting dispersible milk-drug tablets as a solid lipid formulation in the context of digestion. *Int. J. Pharm.* 554, 179–189. doi: 10.1016/j.ijpharm.2018.10.069

Borgström, B., and Patton, J. S. (1991). "Luminal events in gastrointestinal lipid digestion," in *Comprehensive Physiology*, eds S. G. Schultz, M. Field, R. A. Frizzell, and B. B. Rauner (Oxford: Oxford Universitiy Press).

Borné, J., Nylander, T., and Khan, A. (2002). Effect of lipase on different lipid liquid crystalline phases formed by oleic acid based acylglycerols in aqueous systems. *Langmuir* 18, 8972–8981. doi: 10.1021/la020377d

Bottino, N. R. (1975). Lipid composition of two species of antarctic krill: *Euphausia superba* and *E. crystallorophias*. *Comp. Biochem. Physiol. B Comp. Biochem.* 50, 479–484. doi: 10.1016/0305-0491(75)90261-8

Boyd, B. J., Dong, Y. D., and Rades, T. (2009). Nonlamellar liquid crystalline nanostructured particles: advances in materials and structure determination. *J. Liposome Res.* 19, 12–28. doi: 10.1080/08982100802691983

Boyd, B. J., Salim, M., Clulow, A. J., Ramirez, G., Pham, A. C., and Hawley, A. (2018). The impact of digestion is essential to the understanding of milk as a drug delivery system for poorly water soluble drugs. *J. Control. Release* 292, 13–17. doi: 10.1016/j.jconrel.2018.10.027

Brockerhoff, H., and Yurkowski, M. (1966). Stereospecific analyses of several vegetable fats. *J. Lipid Res.* 7, 62–64. doi: 10.1016/s0022-2275(20)39585-7

Bu, P., Narayanan, S., Dalrymple, D., Cheng, X., and Serajuddin, A. T. (2016). Cytotoxicity assessment of lipid-based self-emulsifying drug delivery system with Caco-2 cell model: Cremophor EL as the surfactant. *Eur. J. Pharm. Sci.* 91, 162–171. doi: 10.1016/j.ejps.2016.06.011

Carey, M. C., Small, D. M., and Bliss, C. M. (1983). Lipid digestion and absorption. *Annu. Rev. Physiol.* 45, 651–677.

Castillo, C., and Uauy, R. (2003). Lipid requirements of infants: implications for nutrient composition of fortified complementary foods. *J. Nutr.* 133, 2962S–2972S.

Charkoftaki, G., Kytariolos, J., and Macheras, P. (2010). Novel milk-based oral formulations: proof of concept. *Int. J. Pharm.* 390, 150–159. doi: 10.1016/j.ijpharm.2010.01.038

Chu, B., and Liu, T. (2000). Characterization of nanoparticles by scattering techniques. *J. Nanopart. Res.* 2, 29–41.

Clarke, A. (1980). The biochemical composition of krill, *Euphausia superba* Dana, from South Georgia. *J. Exp. Mar. Biol. Ecol.* 43, 221–236. doi: 10.1016/0022-0981(80)90049-0

Clulow, A. J., Binte Abu Bakar, S. Y., Salim, M., Nowell, C. J., Hawley, A., and Boyd, B. J. (2020b). Emulsions containing optimum cow milk fat and canola oil mixtures replicate the lipid self-assembly of human breast milk during digestion. *J. Colloid Interface Sci.* 588, 680–691. doi: 10.1016/j.jcis.2020.11.067

Clulow, A. J., Salim, M., Hawley, A., and Boyd, B. J. (2018). A closer look at the behaviour of milk lipids during digestion. *Chem. Phys. Lipids* 211, 107–116. doi: 10.1016/j.chemphyslip.2017.10.009

Clulow, A. J., Salim, M., Hawley, A., and Boyd, B. J. (2020a). Milk mimicry–triglyceride mixtures that mimic lipid structuring during the digestion of bovine and human milk. *Food Hydrocoll.* 110:106126. doi: 10.1016/j.foodhyd.2020.106126

Codex Alimentarius Commission (2017). *Codex*Codex Alimentarius Commission, 2017; Zhou and Li, 2015. *Standard for Fish Oils, in: C.S.C. 329-2017.*Rome: Codex Alimentarius Commission.

Cullity, B. D. (1956). *Elements of X-ray Diffraction*. Boston, MA: Addison-Wesley Publishing Company Inc.

Czeslik, C., Winter, R., Rapp, G., and Bartels, K. (1995). Temperature- and pressure-dependent phase behavior of monoacylglycerides monoolein and monoelaidin. *Biophys. J.* 68, 1423–1429. doi: 10.1016/s0006-3495(95)80315-2

Dahan, A., and Hoffman, A. (2006). Use of a dynamic In vitro lipolysis model to rationalize oral formulation development for poor water soluble drugs: correlation with In Vivo data and the relationship to intra-enterocyte processes in rats. *Pharm. Res.* 23, 2165–2174. doi: 10.1007/s11095-006-9054-x

Dahan, A., and Hoffman, A. (2008). Rationalizing the selection of oral lipid based drug delivery systems by an in vitro dynamic lipolysis model for improved oral bioavailability of poorly water soluble drugs. *J. Control. Release* 129, 1–10. doi: 10.1016/j.jconrel.2008.03.021

Dong, Y.-D., Larson, I., Hanley, T., and Boyd, B. J. (2006). Bulk and dispersed aqueous phase behavior of phytantriol: effect of vitamin E Acetate and F127 polymer on liquid crystal nanostructure. *Langmuir* 22, 9512–9518. doi: 10.1021/la061706v

Du, J. D., Liu, Q., Salentinig, S., Nguyen, T.-H., and Boyd, B. J. (2014). A novel approach to enhance the mucoadhesion of lipid drug nanocarriers for improved drug delivery to the Buccal Mucosa. *Int. J. Pharm.* 471, 358–365. doi: 10.1016/j.ijpharm.2014.05.044

Duzgunes, N. (2003). *Methods in Enzymology Liposomes, Part C*. Burlington, VT: Elsevier Science.

Eastwood, G., Watson, P., Bierenbaum, M. L., and Fleischman, A. I. (1963). Fatty acids and other lipids in mayonnaise. *J. Am. Diet. Assoc.* 42, 518–520.

Embleton, J. K., and Pouton, C. W. (1997). Structure and function of gastro-intestinal lipases. *Adv. Drug Deliv. Rev.* 25, 15–32. doi: 10.1016/s0169-409x(96)00488-7

Fatouros, D. G., Deen, G. R., Arleth, L., Bergenstahl, B., Nielsen, F. S., Pedersen, J. S., et al. (2007). Structural development of self nano emulsifying drug delivery systems (SNEDDS) during in vitro lipid digestion monitored by small-angle X-ray scattering. *Pharm. Res.* 24, 1844–1853. doi: 10.1007/s11095-007-9304-6

Feeney, O. M., Crum, M. F., McEvoy, C. L., Trevaskis, N. L., Williams, H. D., Pouton, C. W., et al. (2016). 50 years of oral lipid-based formulations: provenance, progress and future perspectives. *Adv. Drug Deliv. Rev.* 101, 167–194. doi: 10.1016/j.addr.2016.04.007

Feng, S., Lock, A. L., and Garnsworthy, P. C. (2004). Technical note: a rapid lipid separation method for determining fatty acid composition of milk. *J. Dairy Sci.* 87, 3785–3788. doi: 10.3168/jds.s0022-0302(04)73517-1

Fong, W.-K., ánchez-Ferrer, A. S., Rappolt, M., Boyd, B. J., and Mezzenga, R. (2019). Structural transformation in vesicles upon hydrolysis of phosphatidylethanolamine and phosphatidylcholine with phospholipase C. *Langmuir* 35, 14949–14958. doi: 10.1021/acs.langmuir.9b02288

Fong, W.-K., Hanley, T. L., Thierry, B., Kirby, N., Waddington, L. J., and Boyd, B. J. (2012). Controlling the nanostructure of gold nanorod-lyotropic liquid-crystalline hybrid materials using near-infrared laser irradiation. *Langmuir* 28, 14450–14460. doi: 10.1021/la302901q

Fong, W. K., Salentinig, S., Prestidge, C. A., Mezzenga, R., Hawley, A., and Boyd, B. J. (2014). Generation of geometrically ordered lipid-based liquid-crystalline nanoparticles using biologically relevant enzymatic processing. *Langmuir* 30, 5373–5377. doi: 10.1021/la5003447

Friel, J. K., and Qasem, W. A. (2016). "Human milk and infant formula: nutritional content and health benefits," in *Beverage Impacts on Health and Nutrition*, 2nd Edn, eds T. Wilson and N. J. Temple (Cham: Springer International Publishing), 163–177. doi: 10.1007/978-3-319-23672-8_11

Gallier, S., Cui, J., Olson, T. D., Rutherfurd, S. M., Ye, A., Moughan, P. J., et al. (2013a). In Vivo digestion of bovine milk fat globules: effect of processing and interfacial structural changes. I. gastric digestion. *Food Chem.* 141, 3273–3281. doi: 10.1016/j.foodchem.2013.06.020

Gallier, S., Zhu, X. Q., Rutherfurd, S. M., Ye, A., Moughan, P. J., and Singh, H. (2013b). In Vivo digestion of bovine milk fat globules: effect of processing and interfacial structural changes. II. upper digestive tract digestion. *Food Chem.* 141, 3215–3223. doi: 10.1016/j.foodchem.2013.06.019

Goncalves, A., Roi, S., Nowicki, M., Dhaussy, A., Huertas, A., Amiot, M. J., et al. (2015). Fat-soluble vitamin intestinal absorption: absorption sites in the intestine and interactions for absorption. *Food Chem.* 172, 155–160. doi: 10.1016/j.foodchem.2014.09.021

Gregory, N. W. (1957). Elements of X-ray diffraction. *J. Am. Chem. Soc.* 79, 1773–1774.

Haasen, C., Linden, M., and Tiberg, F. (2017). Pharmacokinetics and pharmacodynamics of a buprenorphine subcutaneous depot formulation (CAM2038) for once-weekly dosing in patients with opioid use disorder. *J. Subst. Abuse Treat.* 78, 22–29. doi: 10.1016/j.jsat.2017.04.008

Hamilton, J. A., and Kamp, F. (1999). How are free fatty acids transported in membranes? Is it by proteins or by free diffusion through the lipids? *Diabetes* 48:2255. doi: 10.2337/diabetes.48.12.2255

Heird, W. C. (2001). The role of polyunsaturated fatty acids in term and preterm infants and breastfeeding mothers. *Pediatr. Clin. North Am.* 48, 173–188. doi: 10.1016/s0031-3955(05)70292-3

Hempt, C., Gontsarik, M., Buerki-Thurnherr, T., Hirsch, C., and Salentinig, S. (2020). Nanostructure generation during milk digestion in presence of a cell culture model simulating the small intestine. *J. Colloid Interface Sci.* 574, 430–440. doi: 10.1016/j.jcis.2020.04.059

Hong, L., Salentinig, S., Hawley, A., and Boyd, B. J. (2015). Understanding the mechanism of enzyme-induced formation of lyotropic liquid crystalline nanoparticles. *Langmuir* 31, 6933–6941. doi: 10.1021/acs.langmuir.5b01615

Humberstone, A. J., and Charman, W. N. (1997). Lipid-based vehicles for the oral delivery of poorly water soluble drugs. *Adv. Drug Deliv. Rev.* 25, 103–128. doi: 10.1016/s0169-409x(96)00494-2

Hyde, S. T. (2001). *Identification of Lyotropic Liquid Crystalline Mesophases*. West Sussex: John Wiley & Sons, Ltd.

Innis, S. M. (2011). Dietary triacylglycerol structure and its role in infant nutrition. *Adv. Nutr.* 2, 275–283. doi: 10.3945/an.111.000448

Israelachvili, J. N. (2011). "Soft and biological structures," in *Intermolecular and Surface Forces*, 3rd Edn, ed. J. N. Israelachvili (San Diego, CA: Academic Press), 535–576. doi: 10.1016/b978-0-12-375182-9.10020-x

Israelachvili, J. N., Mitchell, D. J., and Ninham, B. W. (1976). Theory of self-assembly of hydrocarbon Amphiphiles into Micelles and Bilayers. *J. Chem. Soc. Faraday Trans. 2* 72, 1525–1568. doi: 10.1039/f29767201525

Kalantzi, L., Goumas, K., Kalioras, V., Abrahamsson, B., Dressman, J. B., and Reppas, C. (2006). Characterization of the human upper gastrointestinal contents under conditions simulating bioavailability/bioequivalence studies. *Pharm. Res.* 23, 165–176. doi: 10.1007/s11095-005-8476-1

Kaminskas, L. M., McLeod, V. M., Kelly, B. D., Sberna, G., Boyd, B. J., Williamson, M., et al. (2012). A comparison of changes to doxorubicin pharmacokinetics, antitumor activity, and toxicity mediated by PEGylated dendrimer and PEGylated liposome drug delivery systems. *Nanomed. Nanotech. Biol. Med.* 8, 103–111. doi: 10.1016/j.nano.2011.05.013

Keemink, J., and Bergström, C. A. S. (2018). Caco-2 cell conditions enabling studies of drug absorption from digestible lipid-based formulations. *Pharm. Res.* 35:74.

Khan, J., Hawley, A., Rades, T., and Boyd, B. J. (2015a). In Situ lipolysis and synchrotron small-angle X-ray scattering for the direct determination of the precipitation and solid-state form of a poorly water-soluble drug during digestion of a lipid-based formulation. *J. Pharm. Sci.* 105, 2631–2639. doi: 10.1002/jps.24634

Khan, J., Rades, T., and Boyd, B. (2015b). The precipitation behavior of poorly water-soluble drugs with an emphasis on the digestion of lipid based formulations. *Pharm. Res.* 33, 548–562. doi: 10.1007/s11095-015-1829-5

Kirby, N. M., Mudie, S. T., Hawley, A. M., Cookson, D. J., Mertens, H. D. T., Cowieson, N., et al. (2013). A low-background-intensity focusing small-angle X-ray scattering undulator beamline. *J. Appl. Crystallogr.* 46, 1670–1680. doi: 10.1107/s002188981302774x

Kossena, G. A., Charman, W. N., Boyd, B. J., and Porter, C. I. H. (2005). Influence of the intermediate digestion phases of common formulation lipids on the absorption of a poorly water-soluble drug. *J. Pharm. Sci.* 94, 481–492. doi: 10.1002/jps.20260

Larsson, K. (1999). Colloidal dispersions of ordered lipid-water phases. *J. Dispers Sci. Technol.* 20, 27–34. doi: 10.1080/01932699908943777

Lee, K. W. Y., Nguyen, T. H., Hanley, T., and Boyd, B. J. (2009). Nanostructure of liquid crystalline matrix determines in vitro sustained release and in vivo oral absorption kinetics for hydrophilic model drugs. *Int. J.. Pharm.* 365, 190–199. doi: 10.1016/j.ijpharm.2008.08.022

Lee, K. W. Y., Porter, C. J. H., and Boyd, B. J. (2013). Gastric pre-processing is an important determinant of the ability of medium-chain lipid solution formulations to enhance oral bioavailability in rats. *J. Pharm. Sci.* 102, 3957–3965. doi: 10.1002/jps.23690

Li, Q., Zhao, Y., Zhu, D., Pang, X., Liu, Y., Frew, R., et al. (2017). Lipidomics profiling of goat milk, soymilk and bovine milk by UPLC-Q-exactive orbitrap mass spectrometry. *Food Chem.* 224, 302–309. doi: 10.1016/j.foodchem.2016.12.083

Li, Y., Mu, H. L., Andersen, J., Xu, X., Meyer, O., and Orngreen, A. (2010). New human milk fat substitutes from butterfat to improve fat absorption. *Food Res. Int.* 43, 739–744. doi: 10.1016/j.foodres.2009.11.006

Lindmark-Månsson, H. L. (2008). Fatty acids in bovine milk fat. *Food Nutr. Res.* 52, 1–3. doi: 10.3402/fnr.v52i0.1821

Lindmark-Månsson, H., Fonden, R., and Pettersson, H. (2003). Composition of Swedish dairy milk. *Int. Dairy J.* 13, 409–425. doi: 10.1016/s0958-6946(03)00032-3

Lipinski, C. (2002). Poor aqueous solubility–an industry wide problem in drug discovery. *Am. Pharm. Rev.* 5, 82–85.

Liu, Q., Dong, Y.-D., Hanley, T. L., and Boyd, B. J. (2013). Sensitivity of nanostructure in charged cubosomes to phase changes triggered by ionic species in solution. *Langmuir* 29, 14265–14273. doi: 10.1021/la402426y

Logan, A., Auldist, M., Greenwood, J., and Day, L. (2014). Natural variation of bovine milk fat globule size within a herd. *J. Dairy Sci.* 97, 4072–4082. doi: 10.3168/jds.2014-8010

Lone, A., and Taskén, K. (2013). Proinflammatory and immunoregulatory roles of eicosanoids in T cells. *Front. Immunol.* 4:130. doi: 10.3389/fimmu.2013.00130

Lopez-Rubio, A., and Gilbert, E. P. (2009). Neutron scattering: a natural tool for food science and technology research. *Trends Food Sci. Technol.* 20, 576–586. doi: 10.1016/j.tifs.2009.07.008

Macheras, P. E., and Reppas, C. I. (1986). Studies on drug—milk freeze—dried formulations I: bioavailability of sulfamethizole and dicumarol formulations. *J. Pharm. Sci.* 75, 692–696. doi: 10.1002/jps.2600750716

Martiel, I., Sagalowicz, L., Handschin, S., and Mezzenga, R. (2014). Facile dispersion and control of internal structure in lyotropic liquid crystalline particles by auxiliary solvent evaporation. *Langmuir* 30, 14452–14459. doi: 10.1021/la5038662

Matsumoto, B., and Hale, I. L. (1993). "Preparation of retinas for studying photoreceptors with confocal microscopy," in *Methods in Neurosciences*, ed. P. A. Hargrave (San Diego, CA: Academic Press), 54–71. doi: 10.1016/b978-0-12-185279-5.50009-1

Merk, A., Bartesaghi, A., Banerjee, S., Falconieri, V., Rao, P., Davis, M. I., et al. (2016). Breaking Cryo-EM resolution barriers to facilitate drug discovery. *Cell* 165, 1698–1707. doi: 10.1016/j.cell.2016.05.040

Meyer, J. H., MacGregor, I. L., Gueller, R., Martin, P., and Cavalieri, R. (1976). 99mTc-tagged chicken liver as a marker of solid food in the human stomach. *Am. J. Dig. Dis* 21, 296–304. doi: 10.1007/bf01071842

Negrini, R., Fong, W.-K., Boyd, B. J., and Mezzenga, R. (2015). pH-responsive lyotropic liquid crystals and their potential therapeutic role in cancer treatment. *Chem. Commun.* 51, 6671–6674. doi: 10.1039/c4cc10274f

Nguyen, T.-H., Hanley, T., Porter, C. H., and Boyd, B. (2011a). Nanostructured reverse hexagonal liquid crystals sustain plasma concentrations for a poorly water-soluble drug after oral administration. *Drug Deliv. Transl. Res.* 1, 429–438. doi: 10.1007/s13346-011-0045-z

Nguyen, T.-H., Hanley, T., Porter, C. J. H., and Boyd, B. J. (2011b). Nanostructured liquid crystalline particles provide long duration sustained-release effect for a poorly water soluble drug after oral aministration. *J. Control. Release* 153, 180–186. doi: 10.1016/j.jconrel.2011.03.033

Nguyen, T.-H., Hanley, T., Porter, C. J. H., Larson, I., and Boyd, B. J. (2010). Phytantriol and glyceryl monoleate cubic liquid crystalline phases as sustained-release oral drug delivery systems for poorly water soluble drugs II. *In-Vivo* evaluation. *J. Pharm. Pharmacol.* 62, 856–865. doi: 10.1211/jpp.62.07.0006

Ono, F., Sugiyama, N., Sato, F., Fukushima, H., and Machii, Y. (1970). Lipid composition of mayonnaise. *Jpn. J. Nutr. Diet.* 28, 190–193. doi: 10.5264/eiyogakuzashi.28.190

Palmquist, D. L., Jenkins, T. C., and Joyner, A. E. Jr. (1986). Effect of dietary fat and calcium source on insoluble soap formation in the Rumen. *J. Dairy Sci.* 69, 1020–1025. doi: 10.3168/jds.s0022-0302(86)80497-0

Patton, J. S., and Carey, M. C. (1979). Watching fat digestion. *Science* 204, 145–148. doi: 10.1126/science.432636

Patton, J. S., Vetter, R. D., Hamosh, M., Borgström, B., Lindstrom, M., and Carey, M. C. (1985). The light microscopy of triglyceride digestion. *Food Microstruct.* 4, 29–41.

Persson, E., Löfgren, L., Hansson, G., Abrahamsson, B., Lennernäs, H., and Nilsson, R. (2007). Simultaneous assessment of lipid classes and bile acids in human intestinal fluid by solid-phase extraction and HPLC methods. *J. Lipid Res.* 48, 242–251. doi: 10.1194/jlr.d600035-jlr200

Pham, A. C., Hong, L., Montagnat, O., Nowell, C. J., Nguyen, T. H., and Boyd, B. J. (2016). In Vivo formation of cubic phase in situ after oral administration of cubic phase precursor formulation provides long duration gastric retention and absorption for poorly water-soluble drugs. *Mol. Pharm.* 13, 280–286. doi: 10.1021/acs.molpharmaceut.5b00784

Pham, A. C., Peng, K.-Y., Salim, M., Ramirez, G., Hawley, A., Clulow, A. J., et al. (2020). Correlating digestion-driven self-assembly in milk and infant formulas with changes in lipid composition. *ACS Appl. Bio Mater.* 3, 3087–3098. doi: 10.1021/acsabm.0c00131

Phan, S., Fong, W.-K., Kirby, N., Hanley, T., and Boyd, B. J. (2011). Evaluating the link between self-assembled mesophase structure and drug release. *Int. J. Pharm.* 421, 176–182. doi: 10.1016/j.ijpharm.2011.09.022

Phan, S., Hawley, A., Mulet, X., Waddington, L., Prestidge, C. A., and Boyd, B. J. (2013). Structural aspects of digestion of medium chain triglycerides studied in real time using sSAXS and Cryo-TEM. *Pharm. Res.* 30, 3088–3100. doi: 10.1007/s11095-013-1108-2

Phan, S., Salentinig, S., Gilbert, E., Darwish, T. A., Hawley, A., Nixon-Luke, R., et al. (2015). Disposition and crystallization of saturated fatty acid in mixed micelles of relevance to lipid digestion. *J. Colloid Interface Sci.* 449, 160–166. doi: 10.1016/j.jcis.2014.11.026

Phan, S., Salentinig, S., Prestidge, C. A., and Boyd, B. J. (2014). Self-assembled structures formed during lipid digestion, and implications for oral lipid-based drug delivery systems. *Drug Deliv. Transl. Res.* 4, 275–294. doi: 10.1007/s13346-013-0168-5

Porter, C. J. H., Kaukonen, A. M., Taillardat-Bertschinger, A., Boyd, B. J., O'Connor, J. M., Edwards, G. A., et al. (2004). Use of in vitro lipid digestion data to explain the in vivo performance of triglyceride-based oral lipid formulations of poorly water-soluble drugs: studies with halofantrine. *J. Pharm. Sci.* 93, 1110–1121. doi: 10.1002/jps.20039

Porter, C. J. H., Trevaskis, N. L., and Charman, W. N. (2007). Lipids and lipid-based formulations: optimizing the oral delivery of lipophilic drugs. *Nat. Rev. Drug Discov.* 6, 231–248. doi: 10.1038/nrd2197

Pouton, C. W. (2000). Lipid formulations for oral administration of drugs: non-emulsifying, self-emulsifying and 'self-microemulsifying' drug delivery systems. *Eur. J. Pharm. Sci.* 11, S93–S98.

Prosser, C. G., Svetashev, V. I., Vyssotski, M. V., and Lowry, D. J. (2010). Composition and distribution of fatty acids in triglycerides from goat infant formulas with milk fat. *J. Dairy Sci.* 93, 2857–2862. doi: 10.3168/jds.2009-2946

Rabinovich, A., Ramanakumar, A. V., Lau, S., and Gotlieb, W. H. (2015). Prolonged pegylated liposomal doxorubicin treatment for recurrent pelvic cancers: a feasibility study. *Acta Obstet. Gynecol. Scand.* 94, 776–780. doi: 10.1111/aogs.12642

Ramsay, J. D. F., Kainourgiakis, M., Steriotis, T., and Stubos, A. K. (2007). Digital reconstruction of silica gels based on small angle neutron scattering data. *Stud. Surf. Sci. Catal.* 160, 137–144. doi: 10.1016/s0167-2991(07)80019-x

Rezhdo, O., Di Maio, S., Le, P., Littrell, K. C., Carrier, R. L., and Chen, S.-H. (2017). Characterization of colloidal structures during intestinal lipolysis using small-angle neutron scattering. *J. Colloid Interface Sci.* 499, 189–201. doi: 10.1016/j.jcis.2017.03.109

Rosevear, F. B. (1954). The microscopy of the liquid crystalline neat and middle phases of soaps and synthetic detergents. *J. Am. Oil Chem. Soc* 31, 628–639. doi: 10.1007/bf02545595

Rosevear, F. B. (1968). Liquid crystals: the mesomorphic phases of surfactant compositions. *J. Soc. Cosmet. Chem.* 19, 581–594.

Sadhukha, T., Layek, B., and Prabha, S. (2018). Incorporation of lipolysis in monolayer permeability studies of lipid-based oral drug delivery systems. *Drug Deliv. Transl. Res.* 8, 375–386. doi: 10.1007/s13346-017-0383-6

Sagalowicz, L., Michel, M., Adrian, M., Frossard, P., Rouvet, M., Watzke, H., et al. (2006). Crystallography of dispersed liquid crystalline phases studied by cryo-transmission electron microscopy. *J. Microsc.* 221, 110–121. doi: 10.1111/j.1365-2818.2006.01544.x

Salentinig, S., Amenitsch, H., and Yaghmur, A. (2017). *In Situ* monitoring of nanostructure formation during the digestion of mayonnaise. *ACS Omega* 2, 1441–1446. doi: 10.1021/acsomega.7b00153

Salentinig, S., Phan, S., Hawley, A., and Boyd, B. J. (2015). Self-assembly structure formation during the digestion of human breast milk. *Angew. Chem. Int. Ed.* 54, 1600–1603. doi: 10.1002/anie.201408320

Salentinig, S., Phan, S., Khan, J., Hawley, A., and Boyd, B. J. (2013). Formation of highly organized nanostructures during the digestion of milk. *ACS Nano* 7, 10904–10911. doi: 10.1021/nn405123j

Salentinig, S., Sagalowicz, L., and Glatter, O. (2010a). Self-assembled structures and pKa value of oleic acid in systems of biological relevance. *Langmuir* 26, 11670–11679. doi: 10.1021/la101012a

Salentinig, S., Sagalowicz, L., Leser, M. E., Tedeschi, C., and Glatter, O. (2010b). Transitions in the internal structure of lipid droplets during fat digestion. *Soft Matter*. 7, 650–661. doi: 10.1039/c0sm00491j

Salentinig, S., Tangso, K. J., Hawley, A., and Boyd, B. J. (2014). pH-Driven colloidal transformations based on the vasoactive drug nicergoline. *Langmuir* 30, 14776–14781. doi: 10.1021/la503824z

Salim, M., Ramirez, G., Clulow, A. J., Zhang, Y., Ristroph, K. D., Feng, J., et al. (2019). Solid-state behavior and solubilization of flash nanoprecipitated clofazimine particles during the dispersion and digestion of milk-based formulations. *Mol. Pharm.* 16, 2755–2765. doi: 10.1021/acs.molpharmaceut.9b00276

Sambuy, Y., De Angelis, I., Ranaldi, G., Scarino, M. L., Stammati, A., and Zucco, F. (2005). The Caco-2 cell line as a model of the intestinal barrier: influence of cell and culture-related factors on Caco-2 cell functional characteristics. *Cell Biol. Toxicol.* 21, 1–26. doi: 10.1007/s10565-005-0085-6

Seddon, J. M., Robins, J., Gulik-Krzywicki, T., and Delacroix, H. (2000). Inverse micellar phases of phospholipids and glycolipids. Invited Lecture. *Phys. Chem. Chem. Phys.* 2, 4485–4493. doi: 10.1039/b004916f

Shearman, G. C., Ces, O., Templer, R. H., and Seddon, J. M. (2006). Inverse lyotropic phases of lipids and membrane curvature. *J. Condens.* 18, S1105–S1124.

Sikorski, Z. Z. E., Kolakowska, A., and Sikorski, Z. Z. E. (2010). *Chemical, Biological, and Functional Aspects of Food Lipids*. Baton Rouge, LA: Taylor & Francis Group.

Spicer, P. T., Hayden, K. L., Lynch, M. L., Ofori-Boateng, A., and Burns, J. L. (2001). Novel process for producing cubic liquid crystalline nanoparticles (Cubosomes). *Langmuir* 17, 5748–5756. doi: 10.1021/la010161w

Stremmel, W., Pohl, L., Ring, A., and Herrmann, T. (2001). A new concept of cellular uptake and intracellular trafficking of long-chain fatty acids. *Lipids* 36, 981–989. doi: 10.1007/s11745-001-0809-2

Tan, G., Xu, P., John, V. T., He, J., McPherson, G. L., Agarwal, V., et al. (2008). Cryo-field emission scanning electron microscopy imaging of a rigid surfactant mesophase. *Langmuir* 24, 10621–10624. doi: 10.1021/la801645x

Tangso, K. J., Fong, W.-K., Darwish, T., Kirby, N., Boyd, B. J., and Hanley, T. L. (2013). Novel Spiropyran Amphiphiles and their application as light-responsive liquid crystalline components. *J. Phys. Chem. B* 117, 10203–10210. doi: 10.1021/jp403840m

Taylor, M. W., and MacGibbon, A. K. H. (2011). "Milk lipids fatty acids," in *Encyclopedia of Dairy Sciences*, ed. H. Roginski (Amsterdam: Elsevier), 655–659. doi: 10.1016/b978-0-12-374407-4.00332-0

Teresa, H. L., Paul, H., and Margit, H. (1984). Fat digestion by lingual lipase: mechanism of lipolysis in the stomach and upper small intestine. *Pediatr. Res.* 18:402. doi: 10.1203/00006450-198405000-00002

Warren, D. B., Anby, M. U., Hawley, A., and Boyd, B. J. (2011). Real time evolution of liquid crystalline nanostructure during the digestion of formulation lipids using synchrotron small-angle X-ray scattering. *Langmuir* 27, 9528–9534. doi: 10.1021/la2011937

Wu, X., and Bruchez, M. P. (2004). Labeling cellular targets with semiconductor quantum dot conjugates. *Methods Cell Biol.* 75, 171–183. doi: 10.1016/s0091-679x(04)75007-4

Yaghmur, A., Lotfi, S., Ariabod, S. A., Bor, G., Gontsarik, M., and Salentinig, S. (2019). Internal lamellar and inverse hexagonal liquid crystalline phases during the digestion of krill and Astaxanthin oil-in-water emulsions. *Front. Bioeng. Biotech* 7:384. doi: 10.3389/fbioe.2019.00384

Yaghmur, A., Rappolt, M., Østergaard, J., Larsen, C., and Larsen, S. W. (2012). Characterization of bupivacaine-loaded formulations based on liquid crystalline phases and microemulsions: the effect of lipid composition. *Langmuir* 28, 2881–2889. doi: 10.1021/la203577v

Ye, A., Cui, J., Dalgleish, D., and Singh, H. (2016). Formation of a structured clot during the gastric digestion of milk: impact on the rate of protein hydrolysis. *Food Hydrocoll.* 52, 478–486. doi: 10.1016/j.foodhyd.2015.07.023

Zeng, N., Gao, X., Hu, Q., Song, Q., Xia, H., Liu, Z., et al. (2012). Lipid-based liquid crystalline nanoparticles as oral drug delivery vehicles for poorly water-soluble drugs: cellular interaction and In Vivo absorption. *Int. J. Nanomed.* 7, 3703–3718. doi: 10.2147/ijn.s32599

Zhou, X., and Li, Y. Eds (2015). "Chapter 2–techniques for oral microbiology," in *Atlas of Oral Microbiology*, eds X. Zhou and Y. Li (Oxford: Academic Press), 15–40. doi: 10.1016/b978-0-12-802234-4.00002-1

Conflict of Interest: The authors declare that the research was conducted in the absence of any commercial or financial relationships that could be construed as a potential conflict of interest.

frontiers
in Cell and Developmental Biology

ORIGINAL RESEARCH
published: 14 June 2021
doi: 10.3389/fcell.2021.675140

Morphologies and Structure of Brain Lipid Membrane Dispersions

Viveka Alfredsson[1], Pierandrea Lo Nostro[2], Barry Ninham[3] and Tommy Nylander[4,5,6]*

[1] Centre for Analysis and Synthesis, Department of Chemistry, Lund University, Lund, Sweden, [2] Department of Chemistry "Ugo Schiff" and CSGI, University of Florence, Sesto Fiorentino, Italy, [3] Department of Applied Mathematics, Research School of Physical Sciences and Engineering, Australian National University, Canberra, ACT, Australia, [4] Physical Chemistry, Department of Chemistry, Lund University, Lund, Sweden, [5] NanoLund, Lund University, Lund, Sweden, [6] Lund Institute of Advanced Neutron and X-ray Science, Lund, Sweden

This study aims to explore the variety of previously unknown morphologies that brain lipids form in aqueous solutions. We study how these structures are dependent on cholesterol content, salt solution composition, and temperature. For this purpose, dispersions of porcine sphingomyelin with varying amounts of cholesterol as well as dispersions of porcine brain lipid extracts were investigated. We used cryo-TEM to investigate the dispersions at high-salt solution content together with small-angle (SAXD) and wide-angle X-ray diffraction (WAXD) and differential scanning calorimetry (DSC) for dispersions in the corresponding salt solution at high lipid content. Sphingomyelin forms multilamellar vesicles in large excess of aqueous salt solution. These vesicles appear as double rippled bilayers in the images and as split Bragg peaks in SAXD together with a very distinct lamellar phase pattern. These features disappear with increasing temperature, and addition of cholesterol as the WAXD data shows that the peak corresponding to the chain crystallinity disappears. The dispersions of sphingomyelin at high cholesterol content form large vesicular type of structures with smooth bilayers. The repeat distance of the lamellar phase depends on temperature, salt solution composition, and slightly with cholesterol content. The brain lipid extracts form large multilamellar vesicles often attached to assemblies of higher electron density. We think that this is probably an example of supra self-assembly with a multiple-layered vesicle surrounding an interior cubic microphase. This is challenging to resolve. DSC shows the presence of different kinds of water bound to the lipid aggregates as a function of the lipid content. Comparison with the effect of lithium, sodium, and calcium salts on the structural parameters of the sphingomyelin and the morphologies of brain lipid extract morphologies demonstrate that lithium has remarkable effects also at low content.

Keywords: brain lipid, sphingomyelin, cholesterol, structure and morphology, specific ion effects, X-ray diffraction, cryo-TEM

Edited by:
Yuru Deng,
University of Chinese Academy of Sciences, China

Reviewed by:
Michael Rappolt,
University of Leeds, United Kingdom
Borislav Angelov,
Institute of Physics (ASCR), Czechia

****Correspondence:***
Tommy Nylander
Tommy.Nylander@fkem1.lu.se

Specialty section:
This article was submitted to Cellular Biochemistry, a section of the journal Frontiers in Cell and Developmental Biology

Received: *02 March 2021*
Accepted: *30 April 2021*
Published: *14 June 2021*

Citation:
Alfredsson V, Lo Nostro P, Ninham B and Nylander T (2021) Morphologies and Structure of Brain Lipid Membrane Dispersions. Front. Cell Dev. Biol. 9:675140. doi: 10.3389/fcell.2021.675140

INTRODUCTION

The structure—function relationship of brain tissue is poorly understood. The brain structure is a complex design based on a rich variety of lipids, assembled into intriguing structures, crucial to their function in, e.g., signal transduction that sometimes involved coupled proteins (Agranoff et al., 1999). Theories of self-assembly involving lipids (Israelachvili et al., 1976; Larsson, 1989;

Hyde et al., 1997; Ninham et al., 2017a,b) depend mainly on two parameters. One is local curvature at the lipid—aqueous interface set by the balance of head group vs. hydrocarbon tail forces. This is pivotal in many biological systems (Israelachvili et al., 1976; Hyde et al., 1997). It can be characterized by the packing parameter introduced by the Ninham group in the 1970s (Israelachvili et al., 1976; Mitchell and Ninham, 1981). The packing parameter (v/al) considers the ratio between the volume of the hydrophobic chain (v) and the product of the cross-section head group area (a) and the chain length in its fully stretched conformation (l). This concept, originally mostly used to describe "simpler" surfactant and lipid self-assembly system structures (Ninham et al., 2017a), has recently also been found to be useful to describe more complex biological systems (Lauwers et al., 2016; Ninham et al., 2017b). The other crucial determinant of structure is that of global packing constraints. These include geometric and molecular forces between aggregates (Israelachvili et al., 1976; Hyde et al., 1997).

The brain lipid system is quite diverse, both in the headgroup and acyl chain distribution. These are partly polyunsaturated fatty acid (PUFA) chains (Lauwers et al., 2016). The role of lipids with polyunsaturated chains in providing curvature that can facilitate presynaptic function has been pointed out (Antonny et al., 2015). This effect can also be assigned to their higher conformational flexibility. Here, it is interesting to point out that a particular type of phospholipids, plasmenyl-phospholipids (plasmalogens), which are ether-type glycerophospholipids with polyunsaturated chains are present in brain lipids. They have been reported to induce intriguing supramolecular structures (Angelova et al., 2021). Brain lipid extracts usually contains a large fraction of cholesterol, reported to be nearly 23% in the gray matter (Pasquini and Soto, 1972; Dreissig et al., 2009). In this context, it is important to emphasize that cholesterol is known to affect membrane fluidity and packing. Earlier studies show that the main effect of adding cholesterol is on the acyl chain region close to the polar headgroup, leading to higher rigidity and a thicker bilayer for dilaurylphosphatidylcholine (DLPC) and dipalmitoylphosphatidylcholine (DMPC) (McIntosh, 1978). It should here be noted that for polyunsaturated phosphatidylcholine, cholesterol was found to lie flat in the middle of the bilayer (Harroun et al., 2008). The consequence of increasing the stiffness of a curved lipid bilayer is to decrease the packing parameter and, hence, the negative curvature of the lipid bilayer. This has been shown to lead to swelling of a bicontinuous cubic phase in excess water (Tyler et al., 2015). Similar results were obtained in the study of the adsorption of a strong hydrophobe in the lamellar phase of dioleoylphosphatidylcholine (DOPC) (Borsacchi et al., 2016). Cholesterol has been shown to lower the phase transition temperature from gel to liquid crystalline lamellar phase (L_α) of dimyristoylphosphatidylcholine (DMPC) from about 22°C to about 5°C (Mortensen et al., 1988). Interestingly, it was found that at lower content of cholesterol, typically below 14%, rippled bilayer gel phase structure, P_β, is stabilized at temperatures below 22°C. Hjort Ipsen et al. (1987) have investigated in detail the DPPC-cholesterol aqueous phase behavior using theoretical modeling to provide deeper insight. One of the characteristics

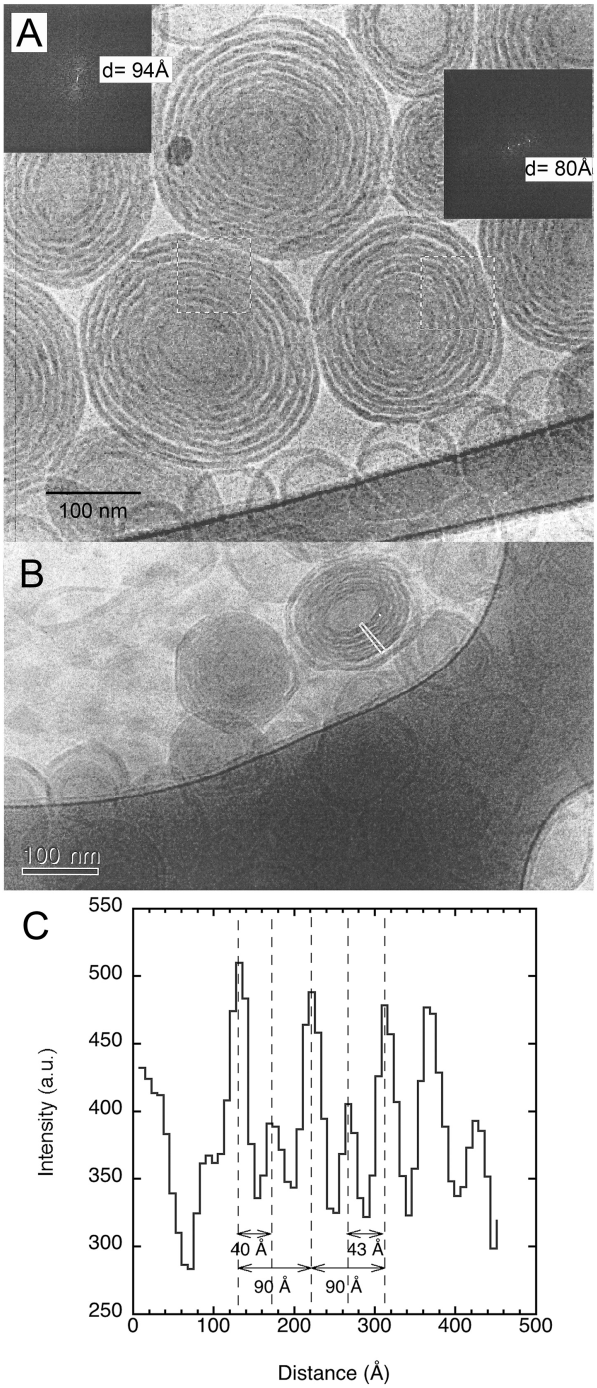

FIGURE 1 | Shows typical cryogenic transmission electron microscopy (cryo-TEM) images of porcine brain sphingomyelin dispersions. The studied dispersion contains 10 wt% lipids in 0.9 wt% (154 mM) NaCl and 1 mM $CaCl_2$. **(A)** An image with inserted Fourier transforms of two marked areas that gave repeat distances of 94 and 80 Å, respectively. **(B)** An image of another sample with the same lipid and salt solution composition. The indicated thin rectangle in the image was analyzed in terms of pixel intensity. **(C)** The results of the analysis of the image in the indicated rectangle. The results are shown as a histogram of intensity vs. distance, where high intensity indicates light areas of the image. The image analysis was performed using ImageJ (Schneider et al., 2012).

of this system is the fact that it features a two-phase regime below between about 10 and 20 mol% cholesterol. Below 40°C, this is a solid ordered and liquid ordered phase, while above this temperature, this is a coexisting liquid disordered and a liquid ordered phase. At lower cholesterol content, this is a single-phase regime, with a solid (gel) phase below 40°C and a liquid disordered phase at higher temperatures. For more than 20 mol%, the liquid ordered phase prevails. It is clear that cholesterol disturbs the order of the gel phase. The existence of phase separation in biomimetic lipid mixtures has triggered debates since the 1970s on whether 2D phase separated domains of so-called "lipid rafts" exist and whether they have some significance in biological systems (Shimshick and McConnell, 1973). A recent review discusses the formation and implications of lipid domain formation in biomimetic as well as biological systems (Kinnun et al., 2020). Of particular relevance for the present study is that sphingomyelin and cholesterol emerge as of particular importance when it comes to domain formation. This motivated our choice to study sphingomyelin, although it has been considered to be only about 5–6% of the brain lipid extract from the gray matter (Dreissig et al., 2009). Domain formation has been demonstrated by using neutron scattering and different isotopic contrasts in the membranes of living *Bacillus subtilis* cells as lateral features of less than 40 nm, considered consistent with the notion of lipid rafts (Nickels et al., 2017).

Neurotransmission has been considered to be facilitated by cholesterol according to several different mechanisms, involving also membrane cluster formation (Milovanovic et al., 2015). These clusters could be imaged thanks to the advancement of super-resolution-stimulated emission depletion (STED) microscopy. Cholesterol levels have also been thought to affect neural diseases like Alzheimer (Fernández-Pérez et al., 2018; Phan et al., 2018; Sparr and Linse, 2019). Increasing cholesterol levels in human embryonic kidney cells and rat hippocampal neurons were found to increase membrane rigidity and promote Aβ-peptide association and aggregation, but reduce membrane disruption (Fernández-Pérez et al., 2018).

Hofmeister or specific ion effects have always been central in biology and affect molecular forces. This has been reviewed

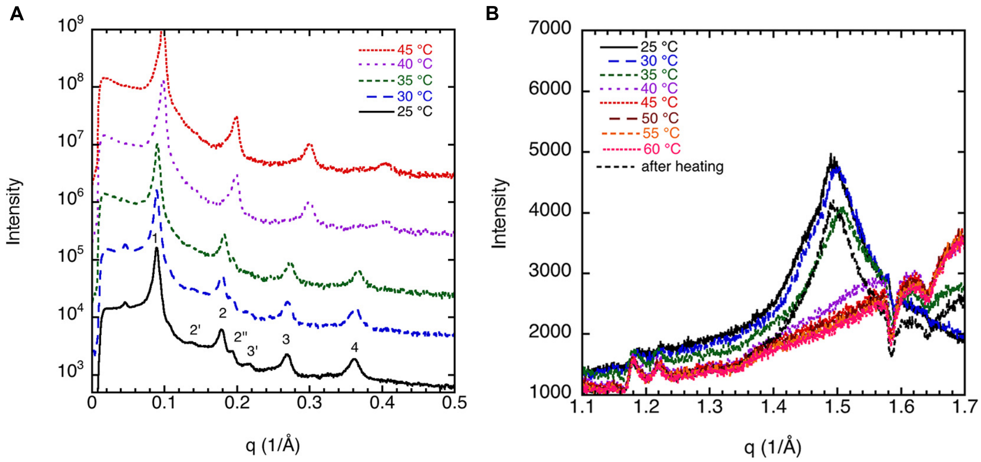

FIGURE 2 | (A) Small-angle X-ray diffraction (SAXD) data for 70 wt% porcine brain sphingomyelin in water containing 0.9 wt% (154 mM) NaCl and 1 mM $CaCl_2$ recorded at different temperatures. Note that the diffractograms are displaced to facilitate comparison. The indexing of the different peaks (1, 2′, 2, 2′′, 3′, 3, and 4) together with their relative intensity are shown in **Table 1**. **(B)** Wide-angle X-ray diffraction (WAXD) data for 70 wt% porcine brain sphingomyelin in 0.9 wt% (154 mM) NaCl and 1 mM $CaCl_2$ recorded at different temperatures upon heating as indicated in the figure. The measurement at 25°C is also repeated after the sample had been heated to 60°C. The peak observed at 25°C and 30°C corresponds to a spacing of 4.20Å, while it decreases slightly to 4.17Å at 35°C. The peak disappears at higher temperature. For the sample remeasured at 25°C after the heating cycle, the value is again 4.20Å.

TABLE 1 | Effect of temperature on the lamellar structures for 70 wt% porcine brain sphingomyelin in water containing 0.9 wt% (154 mM) NaCl and 1 mM $CaCl_2$.

Peak	1		2′		2		2′′		3′		3		4		
T (°C)	d (Å)	I%	d (Å)	I%	d (Å)	I%	d (Å)	I%	d (Å)	I%	d (Å)	I%	d (Å)	I%	a (Å)
25	70.5	100	*44.8*	*0.2*	35.1	2.5	*32.4*	*2.1*	*28.7*	*0.1*	23.3	0.8	17.4	0.6	70.0 ± 0.5
30	70.5	100	*45.3*	*0.2*	35.1	2.3	*32.6*	*2.8*	*28.7*	*0.1*	23.2	0.6	17.4	0.5	70.0 ± 0.5
35	69.9	100			34.4	2.0	*32.4*	*1.7*			22.9	0.5	17.0	0.3	68.9 ± 0.7
40	64.3	100			31.5	1.8					20.8	0.4	15.4	0.1	62.9 ± 1.1
45	60.8	100			30.1	1.3					20.0	0.7	14.8	0.2	60.1 ± 0.6

The table shows a summary of the assignments of the reflection peaks from the diffractograms as shown in ***Figure 2A****. Here d = 2π/q is the interlayer spacing for the different reflections 1, 2, 3, 4 corresponding to the lamellar structure. From these values a lamellar repeat distance, a, is calculated and is given ± standard deviation. The peak height I is calculated as percentage of the main reflection peak after subtracting the estimated baseline. Additional peaks are indicated as 2′, 2′′, and 3′.*

in overview by Lo Nostro and Ninham (2012). It is clear that specific ion effects are at play in numerous systems, where they affect the biological function by changes in self-assembled structures. Here, we have also considered the effect of specific ion effects by studying the effect of adding calcium to a physiological sodium chloride solution as well as replacing part of the sodium chloride with lithium chloride. Lithium chloride is administrated as psychopharmacological treatment to reduce the risk of suicide in people with mood disorders (Cipriani et al., 2013). Specific ion effects with lithium salts are enormous, as is illustrated by the behavior of double-chained sulfosuccinates (Karaman et al., 1994). The sodium salts are hydrophobic and form lamellar phase. Lithium salts swell and form spontaneous vesicles. In viscoelastic surfactant-based worm-like micelles, they significantly affect the phase behavior (Tatini et al., 2021).

This study aims to explore the variety of morphologies that brain lipid extracts do form in aqueous dispersions. We have used both extract as well as samples with two important brain lipid constituents, namely, sphingomyelin and cholesterol. We have varied the cholesterol content, salt solution composition, and temperature. The efficiency as salting-out agent for the ions studied follows the order $Na^+ > Li^+ > Ca^{2+}$ (Lo Nostro and Ninham, 2012). The objective is to reveal the effect of cholesterol as well as the influence of the ion composition. This study has a bearing on the understanding of the mechanisms of action of bioactive molecules, e.g., pheromones and anesthetics.

MATERIALS AND METHODS

The effect of cholesterol on the morphology of aqueous dispersions of brain lipids was investigated. Dispersions of porcine sphingomyelin (56–70 wt%) with varying amounts of cholesterol (0–14 wt%) were prepared in a physiological salt solution (0.9 wt%) (154 mM NaCl and 1 mM $CaCl_2$). Also, the

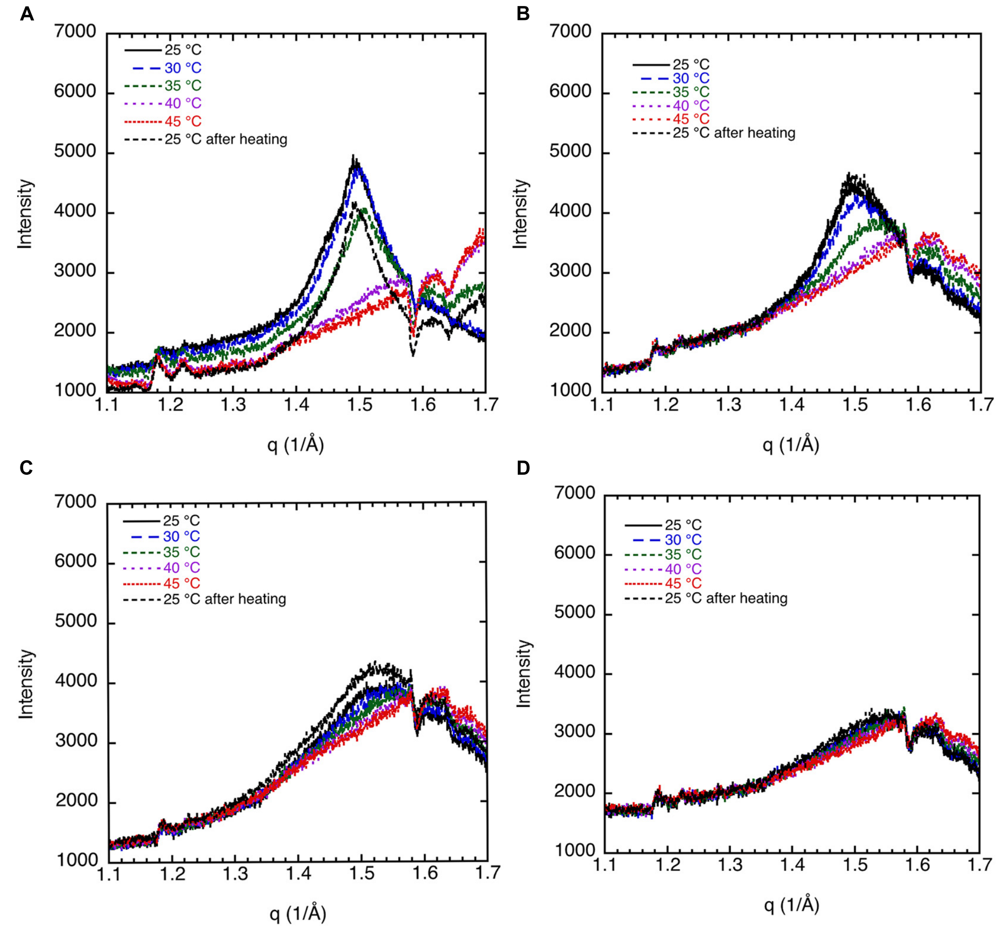

FIGURE 3 | The effect of cholesterol on the crystalline order of porcine brain sphingomyelin in 0.9 wt% (154 mM) NaCl and 1 mM $CaCl_2$ recorded at different temperatures by WAXD. **(A)** Sphingomyelin (70%) and no cholesterol (0% of lipid). Peak position corresponds to spacing of 4.20 Å at 25°C and 30°C, 4.17 Å at 35°C, while no peak at higher temperatures. **(B)** Sphingomyelin (65.1%) and 4.9% cholesterol (7% of lipid). Peak position corresponds to spacing of 4.20 Å at 25°C, 4.17 Å at 30°C, rounded peak at 35°C, while no peak was observed at higher temperatures. **(C)** Sphingomyelin (59.5%) and 10.5% cholesterol (15% of lipid). A rounded peak appears at 25°C, while no peak was observed at higher temperatures. **(D)** Sphingomyelin (56%) and 14% cholesterol (20% of lipid). No defined peak appears at any temperature.

effect on salt solution composition was investigated, comparing 0.9 wt% NaCl with a solution at a total ionic strength of 161 mM, comprising 0.8 wt% NaCl (137 mM) and 0.1 wt% LiCl (24 mM). Dispersions of porcine brain lipid extracts were prepared with 70% lipid in 0.9 wt% NaCl and 1 mM $CaCl_2$ for SAXD and DSC. In addition, the effect of replacing 11% of the sodium by lithium ions on the aggregate morphology in excess of aqueous solvent was investigated by cryo-TEM. No added buffer ions were used, and the same anion was used, focusing on the effect of the cation. Previous reports have shown an adsorption difference between different anions affecting, e.g., pH measurements (Salis et al., 2006).

The porcine brain lipid sample was extracted from a pig brain obtained from a Tuscany slaughterhouse (Italpork, Ponte Buggianese, Pistoia) and immediately frozen at −24°C. We scratched the cortical, external surface (gray matter). Extraction with 1-butanol/water was conducted using the method described by Pasquini and Soto (1972). The organic solvent was dried over sodium sulfate. The solvent was then evaporated, the samples were first freeze dried, and then kept at -24°C in a freezer. Pasquini and Soto (1972) reported that such an extract contained 38.0% phospholipids, 2.8% galactolipids, 22.6% cholesterol, 5.9% proteolipid proteins, and the remainder not determined. It should be noted that in their study, the phospholipid fraction likely included sphingomyelin and plasmalogen.

The samples were investigated by wide-angle (WAXD) and small-angle X-ray diffraction (SAXD) at different temperatures. Small-angle X-ray diffraction (SAXD) was then used to identify the particular LC structure of the samples. SAXD and WAXD measurements were performed on a Kratky compact system with slit collimation equipped with a position-sensitive detector (OED 50 M, Mbraun, Graz, Austria), containing 1,024 channels, each with a width of 53.6 μm. Cu-Kα radiation of wavelength 1.54 Å was provided by a Seifert ID-300 X-ray generator, operating at 50 kV, and 40 mA. A 10-μm-thick nickel filter was used to remove the Kβ radiation, and a 1.5-mm Wolfram filter was used to protect the detector from the primary beam. The beam width (defined as the beam width where the intensity is half of that at the maximum) was 0.59 mm. The sample-to-detector distance was 277 mm, while the wide-angle detector was placed at an angle of 20.2° and with a sample-to-detector distance of 297 mm. In order to minimize scattering from air and increase signal-to-noise ratio, the volume between the sample and the detector was under vacuum. During the measurements, the samples were

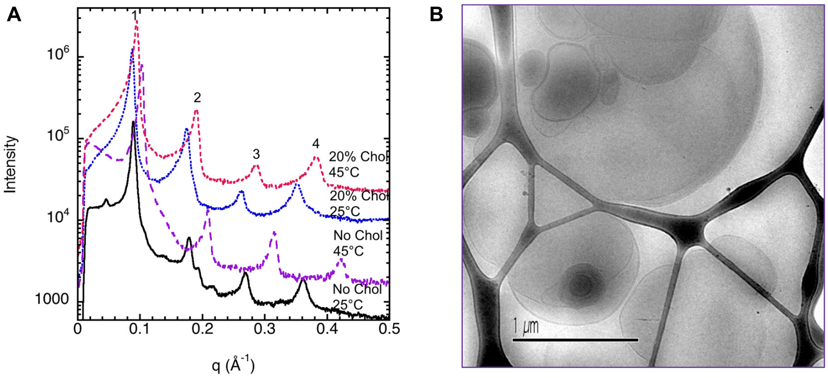

FIGURE 4 | Shows the effect of cholesterol on the ordering of porcine brain sphingomyelin in 0.9 wt% (154 mM) NaCl and 1 mM $CaCl_2$ recorded at 25°C and 45°C. **(A)** SAXD data for 70% sphingomyelin and no cholesterol (0% of lipid) as well as 56% sphingomyelin and 14% cholesterol (20% of lipid) are shown. The interlayer spacing for the different reflections and the relative intensities of the Bragg peaks are summarized in **Table 2**. Note that the intensities of the diffractograms are scaled for better clarity. **(B)** A typical cryo-TEM image of porcine brain sphingomyelin dispersions in the presence of cholesterol. As opposed to in the absence of cholesterol (**Figure 1**), the image features unilamellar vesicles of different sizes. The studied dispersion contains 10 wt% lipid in 0.9 wt% (154 mM) NaCl and 1 mM $CaCl_2$, where 7 wt% of lipids are cholesterol.

TABLE 2 | Effect of adding cholesterol (20 wt% of lipid) on the lamellar structures of 70 wt% porcine brain sphingomyelin in water containing 0.9 wt% (154 mM) NaCl and 1 mM $CaCl_2$.

Peak	**1**		**2**		**3**		**4**		
Conditions	**d (Å)**	**I%**	**d (Å)**	**I%**	**d (Å)**	**I%**	**d (Å)**	**I%**	**a (Å)**
25°C	70.5	100	35.1	2.5	23.3	0.8	17.4	0.6	70.0 ± 0.5
25°C, 20% Cholesterol	71.8	100	35.9	9.4	23.9	0.8	17.9	1.3	71.7 ± 0.1
45	60.8	100	30.1	1.3	20.0	0.7	14.8	0.2	60.1 ± 0.6
45°C, 20% Cholesterol	66.4	100	33.0	7.0	21.9	0.8	16.4	1.3	65.9 ± 0.4

*The table shows a summary of the assignments of the reflection peaks from the diffractograms shown in **Figure 4A**. Here $d = 2\pi/q$ is the interlayer spacing for the different reflections 1, 2, 3, and 4 corresponding to the lamellar structure. From these values, a lamellar repeat distance, a, is calculated and is given as ± standard deviation. The peak height I is calculated as percentage of the main reflection peak after subtracting the estimated baseline. Values for the additional peaks 2′, 2″, and 3′ in the sample without cholesterol at 25°C (absent in other samples) are shown only in **Table 1**.*

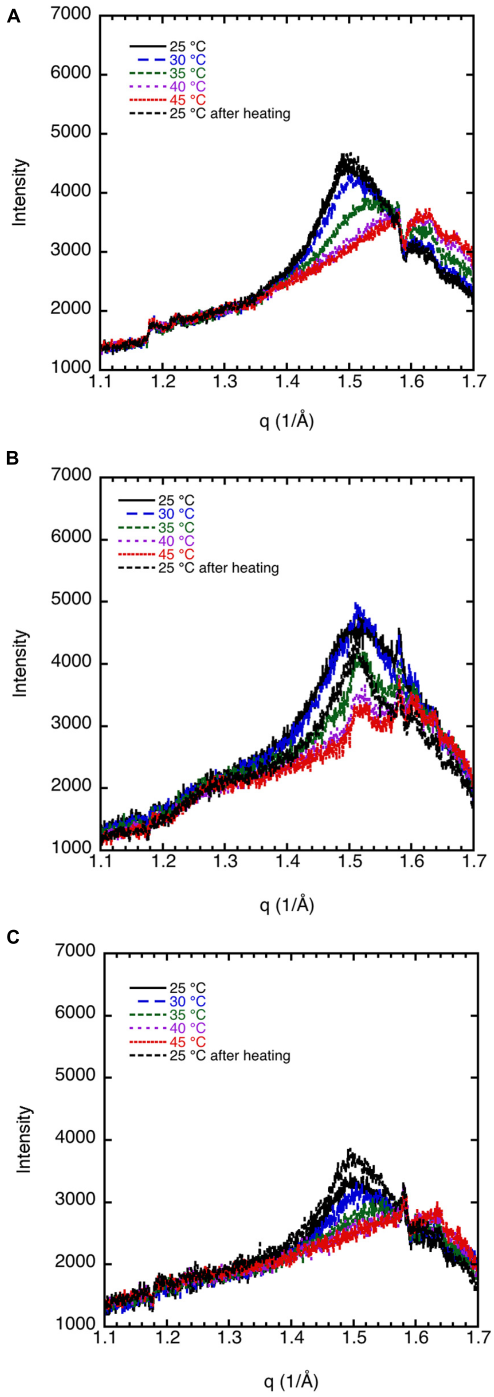

FIGURE 5 | WAXD data show the effect of salt composition on the ordering of porcine brain sphingomyelin, 65.1% sphingomyelin, and 4.9% cholesterol (7% of lipid) recorded at different temperatures. **(A)** In 0.9 wt% (154 mM) NaCl and 1 mM $CaCl_2$, the peak position corresponds to spacing of 4.20 Å at 25°C, 4.17 Å at 30°C, rounded peak at 35°C, while no peak at higher temperatures. **(B)** In 0.9 wt% (154 mM) NaCl, the peak position corresponds to a spacing of 4.15 Å at 25–35°C, and no clear peaks at higher temperature. **(C)** In 0.8 wt% (137 mM) NaCl and in 0.1 wt% (24 mM) LiCl, the peak position corresponds to a spacing of 4.20 Å at 25°C, a less defined peak at 4.15 Å at 30°C, and no peaks at higher temperatures. Note that the intensity is scaled so to obtain the same background for all diffractograms.

placed in a capillary, and the temperature (25°C) was controlled to within 0.1°C by using a Peltier element.

Differential scanning calorimetry (DSC) was performed by means of a DSC-Q2,000 from TA Instruments (Philadelphia, PA, United States). The samples were first cooled from 20 to 60°C at 10°C/min, then heated up to 80°C at 5°C/min, and eventually cooled at the same rate down to -60°C. Measurements were conducted in N_2 atmosphere, with a flow rate of 50 ml/min.

Dilute dispersions (5–10 wt%) were investigated by cryogenic transmission electron microscopy (cryo-TEM). The temperature (25–28°C) and high relative humidity (close to saturation) in the sample vitrification system was adjusted to avoid evaporation and ensured that proper vitreous film was formed. The dispersions were prepared at 30°C and stored at 40°C until application to the grid. Of the lipid dispersion, 5 μl was placed on the carbon film supported by a cupper grid and blotted with filter paper to reduce film thickness. In the sample vitrification system, the temperature was set to 25–28°C, and a high relative humidity (close to saturation) was maintained. This ensures that evaporation is avoided and that a proper vitreous film is formed. The grid was quenched in liquid ethane at -196°C, stored under liquid nitrogen (-196°C), and transferred to a cryo-TEM (Philips CM120 BioTWIN Cryo) equipped with a post-column energy filter (Gatan GIF 100), using an Oxford CT3, 500 cryo-holder and its workstation. The acceleration voltage was 120 kV, and the working temperature was below −180°C. The images were digitally recorded with a CCD camera (Gatan MSC 791) under low-dose conditions. The under focus was approximately 1 μm.

RESULTS AND DISCUSSION

Sphingomyelin

Dispersions of Sphingomyelin in Physiological Salt Solution With $CaCl_2$

In the dilute regime, sphingomyelin forms large multilamellar vesicles (**Figure 1**). Interestingly, these vesicles feature what appear to be double bilayers. Such structures have been reported for biological systems (Eskelinen and Kovács, 2011). They occur too when 15 mol% of the plasmalogen ethanolamine (C16:1p–22:5n6 PE) is incorporated into host dioleoylphosphocholine (DOPC) bilayers (Angelova et al., 2021). Furthermore, the bilayers appear to be rippled, which suggests that this can be a rippled phase rather than a double bilayer. In fact, this has previously been reported for brain sphingomyelin based on freeze-fracture electron microscopy (Meyer et al., 1999). A detailed analysis of the image in **Figure 1A**, using Fourier transformation of two marked areas, gave a repeat distance of 94 and 80 Å, respectively. Here, we note that this analysis is based on a few bilayers, and as indicated by the results, there is a considerable spread in the data. We here note that this is a projection of a 3D object into a 2D plane, which imposes a degree of uncertainty. The image in **Figure 1B** is of another sample with the same lipid and salt solution composition where the "double bilayer" feature appears more clearly. The indicated that the thin rectangle in the image was analyzed in terms of pixel intensity, and the resulting histograms are shown in **Figure 1C**.

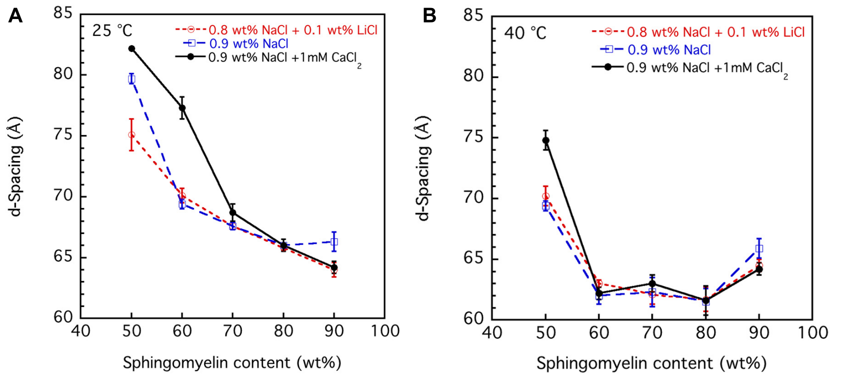

FIGURE 6 | The effect of salt solution composition, i.e., 0.9 wt% (154 mM) NaCl and 1 mM $CaCl_2$, 0.8 wt% (137 mM) NaCl and 0.1 wt% (24 mM) LiCl, and 0.9 wt% (154 mM) NaCl, on the interlamellar spacing (d-spacing) obtained from SAXD data as a function of porcine brain sphingomyelin content recorded at two different temperatures, **(A)** 25°C and **(B)** 40°C. The obtained values are the mean values calculated from all observed first to fourth order of reflections. For the samples with the largest hydration (50 wt% lipid), the third and fourth order peaks are very broad, and therefore, the q value of the peak is uncertain. In those cases, we used only the first and second order reflections. The error bars in the graph are the standard deviation of the calculated mean values.

It should be noted that the high intensity here indicates light areas of the image. For this image, it was possible to resolve areas that were distinctly light, gray, and dark, which can be assigned to different lipid concentrations with the dark area being a high concentration of lipids. The peak-to-peak difference for the light areas is 90 Å, which is close to the value obtained by Fourier transform analysis. The distance from the brightness to the middle of the gray area is about 40–45 Å, depending on the area selected. It is tempting to assume that this might be the extent of the ripples in the ripple phase, but this definitely requires deeper analysis. We note that when these dispersions were prepared at a temperature of about 28°C and equilibrated for 1–2 h at room temperature, the vesicles appear to have a facetted morphology, usually observed for frozen chains.

The corresponding sample at high lipid content (70 w%) gives a diffraction pattern typical for a liquid crystalline lamellar, L_α, phase or the corresponding gel phase with four well-defined peaks (**Figure 2A**). The indexing of the different peaks (1, 2′, 2, 2′′, 3′, 3, and 4) together with their relative intensity compared with that of peak 1 is shown in **Table 1**. The additional weak reflections are suggested to indicate the presence of double bilayer or more likely a ripple phase as discussed in conjunction with the cryo-TEM images in **Figure 1** above. First, it should be noted that d-spacing decreases with increasing temperature above 35°C, from 70.0 ± 0.5 Å at 25°C to 60.1 ± 0.6 Å at 45°C. The sample heated to 45°C was cooled down again to 25°C, and a new diffractogram was recorded. The lamellar peak appears at the same position, but the intensity of the peaks has decreased (data not shown). This suggests that the swelling behavior with temperature is reversible, but the intensity of the Bragg peaks is not. The decrease in intensity can be attributed to the change in domain size induced by annealing at high temperature. The main reflections 1, 2, 3, and 4 at 25°C give a repeat distance of 70.0 ± 0.5 Å that is significantly smaller than the values extracted from the cryo-TEM data. Again, it should be emphasized that the SAXD was performed on a gel (lamellar) phase sample at low water content (70% lipids), while the cryo-TEM data were recorded at excess salt solution with 10% of lipids. Thus, we expect that the cryo-TEM data would reflect a fully swollen sample and, hence, a larger repeat distance of about 90 Å. When it comes to indexing the satellite peaks 2′, 2′′, and 3′, this is more challenging as, in particular, 2′ and 3′ are significantly weaker with a height that is only about 0.1–0.2% of the main peak. If this is the second and third order reflection of a lamellar repeat, this

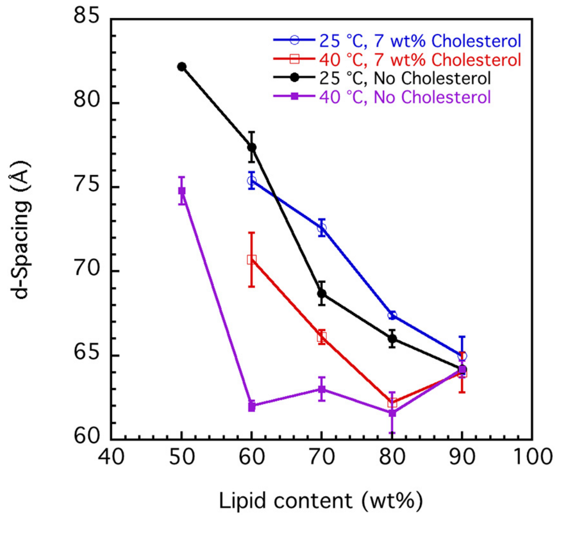

FIGURE 7 | Effect of cholesterol on the interlamellar spacing (d-spacing) obtained from SAXD data as function of porcine brain sphingomyelin content recorded at two different temperatures, 25°C and 40°C. The swelling curves for sphingomyelin in 0.9 wt% (154 mM) NaCl and 1 mM $CaCl_2$ without cholesterol and where 7 wt% of lipid fraction was cholesterol are shown. The obtained values are the mean values calculated from all observed first to fourth order of reflections. For the samples with the largest hydration (50 wt% lipid), the third and fourth order peaks are very broad, and the q value of the peak is, therefore, uncertain. In those cases, we used only the first and second order reflections. The error bars in the graph are the standard deviations of the calculated mean values.

would correspond to a repeat distance of about 90 Å, which is similar to the value observed from image analysis of cryo-TEM data in **Figure 1**. The additional peak, 2′′, corresponds to a repeat distance of about 32 Å. This is about 10 times as intense as the other satellite peaks. In the analysis of the cryo-TEM data, we also observed a repeat distance of 40–45 Å, which corresponds to the position of the 2′, but this might be coincidental. We did not attempt to index the SAXD according to a ripple phase as for the additional reflection peak as discussed by Rappolt and Rapp (1996). It should be noted that the satellite peaks disappear at temperatures above 35°C.

The peak in the WAXD data (**Figure 2B**) observed at 25°C and 30°C corresponds to a spacing of 4.20 Å, while it decreases slightly to 4.17 Å at 35°C. The peak disappears at higher temperature. The sharp peak at $q \approx 1.5$ Å^{-1} or spacing around ≈4.20 Å in the wide-angle regime is typical for crystalline chains. As the temperature is raised to 40°C, these peaks disappear due to the melting of the chains. It should be noted that the peak reappears if the sample heated to 45°C was cooled down again to 25°C, and a new diffractogram was recorded. The crystallinity of the chains is dependent on cholesterol content but also to some extent on the salt solution composition as will be discussed further below. It is remarkable to notice that the melting temperature (without cholesterol) is around 35–40°C, that is, in the same regime as the physiological temperature (McIntosh et al., 1992).

Effect of Cholesterol on Sphingomyelin Dispersions

The effect of cholesterol on the crystalline order of porcine brain sphingomyelin in 0.9 wt% (154 mM) NaCl and 1 mM $CaCl_2$ is recorded at different temperatures by WAXD, and the results are presented in **Figure 3**. Both without cholesterol and when 7% of the lipids consist of cholesterol, the chain melting appears at around 35–40°C as is apparent from the diffractogram. Cholesterol is expected to introduce disorder in the sphingomyelin gel phase, which is manifested in the less sharp WAX peak at $q \approx 1.5$ Å^{-1} at higher cholesterol contents. When 15% of the lipid is cholesterol, a rounded peak appears at 25°C, while no peak occurs at higher temperatures (**Figure 3C**). At a cholesterol content of 20%, there is essentially no clear identifiable peak in the WAXD scattering region, indicating that the chain-melting transition occurs below 25°C (**Figure 3D**). It is clear then that the WAXD diffractogram recorded at different temperatures and cholesterol content reflect the effect of cholesterol on the chain-melting transition.

The SAXD data for the sphingomyelin/cholesterol system that illustrates the effect of cholesterol is shown in **Figure 4A**. **Table 2** shows a summary of the assignments of the reflection peaks from the diffractograms together with the relative peak intensity. Here, we have chosen to show data for samples with 30% of salt solution (154 mM NaCl and 1 mM $CaCl_2$) without cholesterol and when 20% of the lipids consist of cholesterol as we obtain the most resolved diffractogram and largest effect of cholesterol under these conditions. At 25°, we observe a repeat distance of 70.1 ± 0.5 Å without cholesterol. Above the chain-melting temperature, about 40°C as observed in the WAX diffractograms (**Figure 3**), the satellite peaks disappear as is apparent from the data recorded at 45°C (**Figure 4A**) and discussed above. It is also noteworthy that the d-spacing decrease, from 70.0 ± 0.5 Å, with increasing temperature to 60.1 ± 0.6 Å. This amounts to a decrease of nearly 10 Å, which might be assigned to the larger mobility of the chains due to partial melting and thinner bilayer or dehydration of the lamellar phase. The addition of 20% cholesterol removes the double peaks observed in the diffractogram for sphingomyelin without cholesterol already at low temperature. **Figure 4A** and **Table 2** show that the d-spacing is slightly larger for the system with 20% of cholesterol, i.e., 71.7 ± 0.1 Å compared with 70.0 ± 0.5 Å without cholesterol. We also note that the effect of temperature on d-spacing is less pronounced with a decrease in the value of about 6 Å to 65.9 ± 0.4 Å. Another interesting observation is that the height, i.e., intensity of the peak corresponding to the second order reflection increases about five times. This is consistent with an increased order of the phase induced by cholesterol as frequently reported for phospholipid systems (Hjort Ipsen et al., 1987; Mortensen et al., 1988).

We also note that, already with 7% of the lipids exchanged for cholesterol, the morphology of the dispersed aggregates changes profoundly as is observed by comparing **Figure 1**, **4B**. The electron micrographs show that with cholesterol, the apparent double bilayer multilamellar vesicles are replaced with

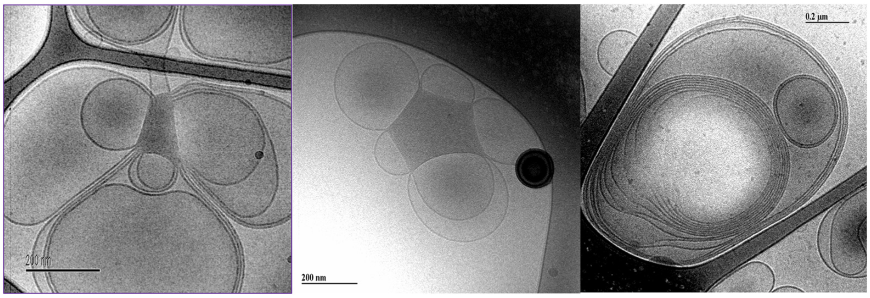

FIGURE 8 | Typical cryo-TEM images of a 10 wt% brain lipid extract dispersion in 0.9 wt% (154 mM) NaCl and 1 mM $CaCl_2$. The images show large multilamellar vesicles often attached to a body of higher electron density.

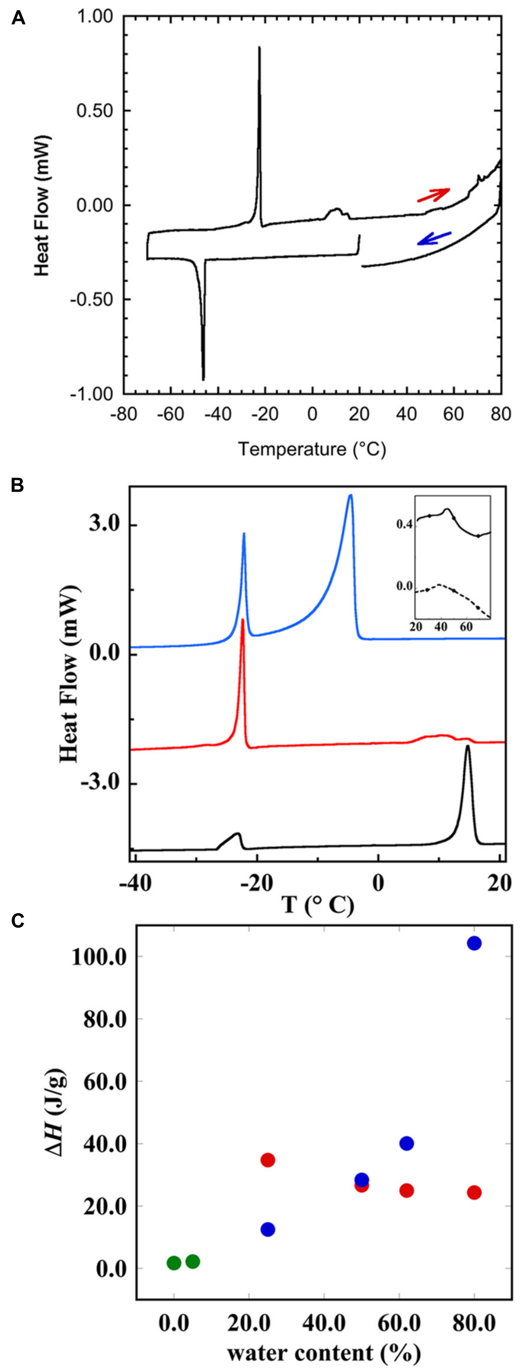

FIGURE 9 | Differential scanning calorimetry (DSC) showing the thermal response of brain lipid extract in 0.9 wt% NaCl and 1 mM CaCl$_2$. **(A)** The thermogram of 50 wt% brain lipid extract in 0.9 wt% NaCl and 1 mM CaCl$_2$, where the heating and cooling cycles are indicated. The vertical line indicates the start of the cooling—heating—cooling cycle. The samples were first cooled from 20°C to -60°C at 10°C/min, and then heated up to 80°C at 5°C/min and eventually cooled at the same rate down to 20°C. **(B)** The thermograms upon heating, where the different curves correspond to different aqueous content [salt solution with 0.9 wt% (154 mM) NaCl and 1 mM CaCl$_2$] of 25 wt% (black), 50 wt% (red), and 80 wt% (blue)]. The inset shows the thermograms obtained from the pure brain lipid extract (full line) and from its *(Continued)*

FIGURE 9 | *(Continued)* hydrated phase (5 wt% of salt solution). **(C)** The enthalpy of the different transition peaks from **(B)** as a function of salt solution content, where green circles refer to the data for pure lipid, and 5 wt% showing only one peak. The other samples show two peaks, one at very low temperature (≈-22°C), and the corresponding enthalpy change is shown as red circles, and the high temperature transition peak is shown as blue circles. The results with onset and peak temperatures and the corresponding enthalpies are summarized in **Table 4**.

large vesicular type of structures with smooth bilayers and of different sizes.

Effect of Salt Solutions on Sphingomyelin

We discuss the effect of the type of salt on the chain melting transition as observed by WAXD. Key data are shown in **Figure 5**. The 70% sphingomyelin sample with 1 mM CaCl$_2$ in the 0.9 wt% (154 mM) NaCl salt solution gives a sharper 4.20 Å peak than for the other conditions. This might be due to the fact that divalent cations are known to bind strongly with, e.g., phospholipids (McLoughlin et al., 2005). We note also that the chain-melting transitions seem to occur at a slightly higher temperature with CaCl$_2$ (≈40°C) than with only monovalent salt. The WAXD peak becomes less defined when part of the NaCl is replaced with LiCl with a peak intensity decrease of about 75%. The chain-melting transition also seems to occur at a lower temperature of 30–35°C in the presence of LiCl, compared with 35–40°C in neat NaCl of the same ionic strength. Here, we again note that Na$^+$ is more efficient as a salting-out ion than Li$^+$ (Lo Nostro and Ninham, 2012), which might explain the slightly higher chain-melting temperature with only NaCl. This is presumably due to the different hydration-free energy of the two cations: for Li$^+$ and Na$^+$ $\Delta_{hydr}G$ is -475 and -365 kJ/mol, respectively (Marcus, 1991).

The SAXD data obtained by studying the swelling in the presence of different salt solution conditions are summarized in **Figure 6**. The values obtained are the mean values calculated from all observed first to fourth order of reflections, and the error bar is the standard deviation. It should be noted for the samples with the largest hydration (50 wt% lipid) that the third and fourth order peaks are very broad. This suggests that under these conditions, the system is close to the swelling limit. The swelling appears to be non-ideal, i.e., it does not follow the one-dimensional swelling law for a lamellar phase (Luzzati et al., 1960). This is particularly apparent at 40°C, which will be discussed further in the next section. We note that the d-spacing values tend to be lower in the presence of the NaCl + LiCl solution. The largest effect is observed at the lower sphingomyelin content. This is consistent with the lowering of the chain-melting temperature in the presence of Li$^+$ ions (**Figure 5**), which implies slightly more disordered acyl chains of the lipids. We also note that in the presence of the Ca^{2+}, which raises the chain-melting temperature slightly, the largest d-spacing is observed. This is consistent with more stretched out lipid chains. When the chains are in the fluid state less (**Figure 6B**), almost no differences between the salts are observed. Also, the value for the d-spacings is different for the different salt solutions.

Swelling Behavior of Sphingomyelin

The swelling curves in **Figure 6** suggest non-ideal swelling behavior within the concentration range investigated. This is particularly evident at 40°C (**Figure 6B**), where the d-spacing does not change with lipid content above 60 wt%. It is possible to make a good linear fit of d-spacing vs. the inverse volume fraction of lipid for the data recorded at 25°C, but the slopes give unreasonable bilayer thickness of 15–20 Å (Luzzati et al., 1960). In **Figure 7**, we present data that illustrate the effect of cholesterol on the swelling behavior in 0.9 wt% (154 mM) NaCl and 1 mM $CaCl_2$. Remarkably, cholesterol has very little effect on the swelling behavior at 25°C. At 40°C, the d-spacing seems to increase with the addition of cholesterol. This is presumably because of the slightly different locations of the cholesterol at the two temperatures. At the higher temperature, the more fluid chains allow penetration of the linear cholesterol molecule deeper into the lipid hydrocarbon chains, so changing effective hydrocarbon volume and increasing head group hydration.

McIntosh et al. studied the thermal, structural, and cohesive properties of bovine brain sphingomyelin (BSM) and N-tetracosanoylsphingomyelin (C24-SM) with and without cholesterol (McIntosh et al., 1992). Their results are rather consistent with our findings, although they only studied the neat, hydrated sphingomyelin and with a 0.5-mol fraction of cholesterol. The acyl chains of C24-SM were found to be tilted and partially interdigitated, which means that the long C24 chain in one bilayer leaflet faces the shorter (unsaturated) sphingosine chain in the other reversed leaflet. This conclusion was made based on the distance between the head groups of about 51 Å in the diffraction pattern, while the distance should be about 57 Å based on the molecular structure. The possible formation of a ripple phase as found for phosphatidylcholine was also discussed but could not be verified with the data presented. Our cryo-TEM images with rippled structure associated with what appears as a double bilayer structure seems to indicate such a rippled structure. This is also consistent with a previous report for brain sphingomyelin based on freeze fracture electron microscopy (Meyer et al., 1999). McIntosh et al. also noted that introducing 50% cholesterol seems to remove the tilt and make the acyl chains disordered. Similar to our findings, they found that the wide-angle X-ray diffraction reflection at 4.15 Å disappears at high cholesterol content, also observed in our present study.

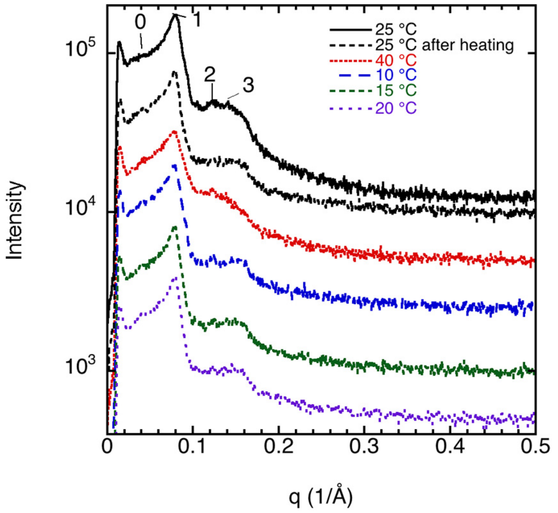

FIGURE 10 | SAXD data for 70 wt% brain lipid extract in 0.9 wt% NaCl and 1 mM $CaCl_2$ as function of temperature. The interlayer spacing of the different peaks (0, 1, 2, and 3), together with their relative intensity, is shown in **Table 3**. Here peak 1 is the only well resolved peak with the highest intensity, while the 0 peak appears as a shoulder. Note the different diffractograms are displaced to facilitate comparison.

TABLE 3 | SAXD data for 70 wt% brain lipid extract in 0.9 wt% (154 mM) NaCl and 1 mM $CaCl_2$ as a function of temperature.

Peak	***0***		***1***		***2***		***3***	
Conditions	**d (Å)**	**I%**	**d (Å)**	**I%**	**d (Å)**	**I%**	**d (Å)**	**I%**
25°C	145	28	79.7	100	50.1	17	44.5	16
25°C, after heating to 40°C	144	37	79.7	100	50.5	28	43.1	13
40°C	145	37	78.9	100	55.4	28	48.5	35
10°C	145	38	79.7	100	52.1	13	41.1	12
15°C	142	34	80.5	100	49.5	13	40.6	12
20°C	140	38	79.7	100	51.4	14	43.1	13

The table shows a summary of the assignments of the reflection peaks from the diffractograms shown in ***Figure 10****. Here d = 2π/q is the interlayer spacing for the different reflections. Four peaks were identified, and the peak with highest intensity is labeled as 1 and is the only peak that can be assigned a d value with high accuracy. The peak height I is calculated as percentage of the main reflection peak after subtracting the estimated baseline.*

Brain Extract

Dispersion of Brain Extract at High Dilutions

The images of dilute dispersions of brain lipid extract do not feature double bilayer-type vesicles. It rather form large multilamellar vesicles often attached to a body of higher electron density (**Figure 8**). Similar patterns are not uncommon for dispersed lipid systems containing mixtures of lamellar forming and inverse phase forming lipids (Wadsäter et al., 2018). Recently, a study shows that self-assembled nanoparticles mainly composed of docosapentaenoyl (DPA)-diacyl phosphoinositol (22:5n6–22:5n6 PI)/monoolein (MO)/vitamin E formed multicompartment and multiphase structures similar to the ones shown in **Figure 8** (Angelova et al., 2021). They suggested that these are built up by dense regions, most likely with lipid mixtures rich in PUFA-phospholipid and vesicular structures. This was suggested to be a consequence of the de-mixing of the different types of lipids. Here we note that apart from lamellar-forming phosphatidylcholine (about 13%), this type of extract also contains about 24% of reverse phase-forming phosphatidylethanolamine (Dreissig et al., 2009). Furthermore, about 20% of the brain phospholipids are plasmalogens, a unique class of phospholipids that contain a fatty alcohol with a vinylether bond at the sn-1 position and enriched in polyunsaturated fatty acids (Braverman and Moser, 2012). In addition, the extracted brain lipids have a high content of cholesterol, so that they are expected to be in the liquid crystalline state. This is verified by the smooth bilayer structures in the Cryo-TEM images (**Figure 8**).

Liquid Crystalline Phases of Brain Lipid Extracts

The liquid crystalline state is doubly confirmed by the DSC measurements, where a typical thermogram is presented in **Figure 9A**. The vertical line indicates the start of the cooling—heating—cooling cycle. The samples were first cooled from 20 to −60°C at 10°C/min, and then heated up to 80°C at 5°C/min and eventually cooled at the same rate down to 20°C. We note here that there is a chain-melting peak at about -20°C. There are some smaller peaks around 10°C in the thermogram suggesting some

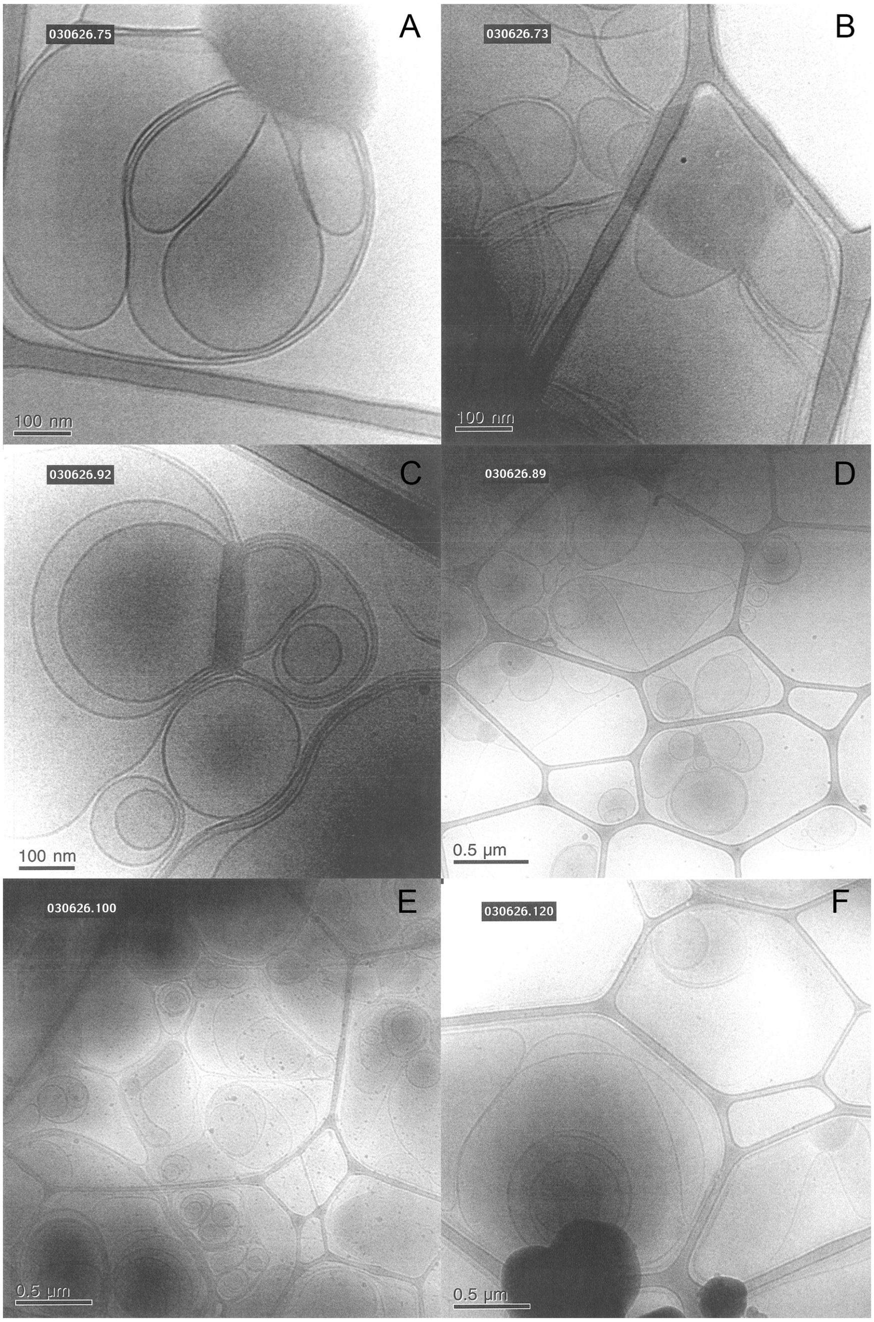

FIGURE 11 | Shows typical cryo-TEM images of 5 wt% brain lipid extract dispersion in aqueous solution with different types of ions, but roughly the same ionic strength. **(A,B)** The images from two different grids of a sample dispersed in 0.9 wt% (154 mM) NaCl and 1 mM $CaCl_2$ salt solution, featuring lamellar structures connected to more dense regions not fully resolved. **(C,D)** The images from two different grids from a sample dispersed in 0.9 wt% NaCl (154 mM) salt solution, featuring lamellar structures connected to more dense regions not fully resolved. **(E,F)** The images from two different grids from a sample dispersed in a salt solution containing 0.8 wt% (137 mM) NaCl and 0.1 wt% (24 mM) LiCl, featuring only lamellar structures.

sort of phase transition. To clarify the nature of this transition, SAXD was used to investigate the brain lipid samples further. The results for 70 wt% brain lipid extract in 0.9 wt% (154 mM) NaCl and 1 mM $CaCl_2$ as a function of temperature are shown in **Figure 10**. **Table 3** shows a summary of the assignments of the reflection peaks from the diffractograms. Four peaks were identified, and the peak with the highest intensity is labeled as 1 and is the only peak that can be assigned a d value with high accuracy. We note that the diffraction pattern is rather complex verifying the multiphase structure that is apparent from the cryo-TEM images in **Figure 8**. The SAXD pattern features several peaks, which are preserved during the temperature cycles. Some can probably be assigned to lamellar-like structures. The pattern features a main peak (1) around 80 Å as well as one peak (0) at about 145 Å and another (3) at 44.5 Å not perfectly matching the first three peaks of a lamellar phase. If we compare with the cryo-TEM image, we note that the repeat distance is slightly more than 100 Å compared with 80 Å extracted from the main peak (1) at 70 wt% lipid. The discrepancy compared with the main peak is likely due to the fact that cryo-TEM images were captured on 10-wt% lipid sample, but SAXD data was recorded using a lipid concentration of 70 wt%. Hence, the lamellar phase is expected to be more swollen in the cryo-TEM sample. We also note that the peaks at 50.1 and 44.5 Å shifted to lower spacing when the sample is heated to 40°C. Cooling down to 10°C gives only small changes to the peak positions. It should be noted that a sample that has been heated to 45°C shows the same diffraction pattern when re-run at 25°C as when the sample was first investigated at 25°C. It is clear that further structural analysis is needed to reveal the details of this very intriguing structure.

Effect of Salt Solution on Brain Lipid Dispersions

We also investigate the effect of different salt solutions on the morphology of the structure formed in dispersions of porcine brain lipids. In this case, the 5 wt% lipid dispersions were prepared using 0.9 wt% NaCl and 1 mM $CaCl_2$, 0.9 wt% NaCl, 0.8 wt% NaCl with 0.1 wt% LiCl similar to the sphingomyelin fraction. Typical images are shown in **Figure 11**, and we note that there are significant effects of salt composition on the morphologies of the aggregates formed. Similarly, as for the sphingomyelin sample, the largest effect was seen by replacing some of the NaCl in the solution by LiCl. Here, we observed only a vesicular type of structure, contrary to the samples with NaCl and NaCl with added $CaCl_2$, where denser aggregates connected to the vesicular structures were formed. The number of these denser aggregates was somewhat higher in the presence of $CaCl_2$. This is quite remarkable as it implies that the dense region observed under other ion compositions are not formed in the presence of LiCl under the conditions employed. It is tempting to suggest that the LiCl has a particularly strong effect on the PUFA type of lipids as they are the ones thought to be responsible for the dense regime of the sample as reported by Angelova et al. (2021).

TABLE 4 | The differential scanning calorimetry (DSC) data for brain lipid extract in 0.9 wt% (154 mM) NaCl and 1 mM $CaCl_2$ as function of aqueous content.

Transition	**T_{peak} (°C)**		**T_{onset} (°C)**		**Δ H (J/g)**	
Water content (wt%)	**Low T**	**High T**	**Low T**	**High T**	**Low T**	**High T**
0	–	41.2	–	23.8	–	1.74
5	–	46.5	–	26.5	–	2.22
25	-22.0	10.6	-39.5	3.3	34.8	12.5
50	-22.3	10.6	-23.3	5.0	26.7	9.7
62	-21.6	-9.4	-22.8	-15.0	24.9	40.1
80	-22.1	-4.5	-23.0	-8.6	24.4	104.3

*The results with peak (T_{peak}) and onset (T_{onset}) temperatures as well as the corresponding enthalpies, ΔH of the transition are shown and determined from the thermogram in **Figure 9**. The baseline was corrected to calculate the onset and peak temperature of the transition as well as the enthalpy.*

Effect of Hydration on Brain Lipid Dispersions

The brain extract samples were dispersed in water at four different concentrations, and their thermal behavior was investigated through DSC and the results are shown in **Figures 9B,C** and summarized in **Table 4**. **Figure 9B** shows the thermogram of three aqueous dispersions of the brain extract, while the inset shows the DSC runs for the pure lipid sample and its hydrated sample (5 wt% of water). In the whole range of temperature investigated, the pure brain lipid (see the black solid line in the inset in **Figure 9B**) shows an endothermic phase transition at about 44.7°C, probably due to the melting of the sample. The hydrated sample (dotted line in the inset) shows a similar behavior with a significant broadening of the signal, centered at 38°C. When the amount of water increases from 25 to 80 wt%, the higher temperature peak progressively shifts to lower temperature and disappears: it is centered at 14.6°C in the 25 wt% sample and is almost vanished at 50 wt% (with some small contributions around 10°C). Interestingly, in the 25 wt% sample (black curve), there seems to be no free water in the sample, but only interstitial freezable bound water that melts at about -23°C. By increasing the water content up to 50 wt% (red curve), the amount of freezable bound water increases significantly, and a melting temperature remains at –22°C. At 80 wt%, we recorded also the presence of freezable water that melts at −4.7°C.

Figure 9C shows the enthalpy as a function of brain lipid content. In the pure lipid and in the samples with 5 wt% salt solution, the peak temperature (**Table 4**) and the corresponding enthalpy change are practically the same (green circles). Starting from the sample with 25 wt% salt solution, interestingly, we see two different peaks in each thermogram. One occurs at very low temperature, around -22°C, and another at higher temperature. For the former, the temperature at which the transition occurs does not change with the lipid concentration, while the enthalpy change slightly decreases as the amount of water increases from 25 to 80% (red circles). The other transition instead is accompanied by a much higher enthalpy change that remarkably increases when the water amount is higher than 50% (blue circles).

These results seem to indicate that hydration significantly modifies the thermal behavior of the brain lipids, in accordance with the structural and morphological investigations. Apparently, at least up to a water content of 50 wt%, water molecules are part of the nanostructures built up by bilayers and strongly bound (as non-freezable bound and interstitial water) to the polar head groups. Here, we would like to note that Gershfeld and coworkers, in a number of studies, have shown that the thermal response of the brain lipid, which in turn depends on the composition, can have physiological implications (Ginsberg et al., 1993). Their studies indicate that when the disease affects membrane lipid composition, the membrane can be destabilized at physiological temperatures.

CONCLUDING REMARKS

At first sight, the observations we have made are most peculiar. However, they are predicted by the modern theory of lipid self-assembly (Ninham et al., 2017a). It is a matter of simple geometry that any closed lipid membrane bilayer, spherical, or cylindrical faces a packing problem. The curved bilayer is necessarily unsymmetric. The outer monolayer has positive curvature; the inner layer necessarily has negative curvature. The bilayer is asymmetric. Correspondingly, the exterior and interior physicochemical conditions are also asymmetric. For a multilayered structure, there comes a point when the inner bilayer can no longer pack. This occurs at a radius of about 200 nm for typical biological lipids. The interior lipid bilayers can adjust to this tension by forming a cubic phase (Larsson, 1989; Ninham et al., 2017b).

States of supra-self-assembly become the rule rather than the exception in biological systems. With mixed lipids, phase separation within a bilayer takes place for the same reasons, with mesh phases—2D cubic phases with catenoidal holes and rafts automatically a consequence of packing constraints (Hyde et al., 1997). Transitions between one state of self-assembly to another, as for transmission of the nervous impulse, occur with ease by the Bonnet transformation (Larsson, 1989; Hyde et al., 1997; Ninham et al., 2017b).

The self-assembled structures demonstrated in this study exhibit such states of supra-self-assembly explicitly. It is clear that further analysis is needed to reveal the details of these very intriguing structures. This can most easily be achieved by changing head group hydration interactions using Hofmeister effects and with different salt solutions. The different morphologies seen under different external solution conditions begin to provide insights into phase changes of brain lipids that are coupled to, and are the source and sink of channel formation for ion exchange of sodium, potassium, and other ions that accompany and drive transmission of the nervous impulse. The effect of salt composition in the solution reflected in changes in lipid assembly morphology is due to specific competitive ion adsorption only, physical not biochemistry. This points at the possible connection to the physiological mechanism behind the successful use of lithium salts for the treatment of bipolar disorder.

DATA AVAILABILITY STATEMENT

The raw data supporting the conclusions of this article will be made available by the authors, without undue reservation.

AUTHOR CONTRIBUTIONS

TN drafted the manuscript, participated in the sample preparation, and X-ray diffraction analysis. VA participated in writing the manuscript, performed sample preparation and X-ray diffraction analysis as well as performed all cryo-TEM imaging. PL initiated the study, prepared the brain lipid, performed the DSC measurements and analysis, and participated in writing the manuscript. BN inspired the study, participated in the analysis of the data, and writing of the manuscript. All authors contributed to the article and approved the submitted version.

FUNDING

TN acknowledges funding from the Swedish research council through several grants, 2020-05421, 2017-06716, and 2016-05390.

ACKNOWLEDGMENTS

We would like to acknowledge the work of Laura Fratoni for the DSC study and data analysis.

DEDICATION

This article is dedicated to the Memory of Prof. Kåre Larsson, 1937–2018, who inspired this study.

REFERENCES

Agranoff, B. W., Benjamins, J. A., and Hajra, A. K. P. (1999). "Properties of brain lipids," in *Basic Neurochemistry: Molecular, Cellular and Medical Aspects*, 6 Edn, eds G. J. Siegel, B. W. Agranoff, R. W. Albers, S. K. Fisher, and M. D. Uhler (Philadelphia, PA: Lippincott-Raven).

Angelova, A., Angelov, B., Drechsler, M., Bizien, T., Gorshkova, Y. E., and Deng, Y. (2021). Plasmalogen-based liquid crystalline multiphase structures involving docosapentaenoyl derivatives inspired by biological cubic membranes. *Front. Cell. Dev. Biol.* 9:617984. doi: 10.3389/fcell.2021.617984

Antonny, B., Vanni, S., Shindou, H., and Ferreira, T. (2015). From zero to six double bonds: phospholipid unsaturation and organelle function. *Trends Cell Biol.* 25, 427–436. doi: 10.1016/j.tcb.2015.03.004

Borsacchi, S., Geppi, M., Macchi, S., Ninham, B. W., Fratini, E., Ambrosi, M., et al. (2016). Phase transitions in hydrophobe/phospholipid mixtures: hints at connections between pheromones and anaesthetic activity. *Phys. Chem. Chem. Phys.* 18, 15375–15383. doi: 10.1039/c6cp00659k

Braverman, N. E., and Moser, A. B. (2012). Functions of plasmalogen lipids in health and disease. *Biochimi. Biophys. Acta* 1822, 1442–1452. doi: 10.1016/j.bbadis.2012.05.008

Cipriani, A., Hawton, K., Stockton, S., and Geddes, J. R. (2013). Lithium in the prevention of suicide in mood disorders: updated systematic review and meta-analysis. *BMJ* 346:f3646. doi: 10.1136/bmj.f3646

Dreissig, I., Machill, S., Salzer, R., and Krafft, C. (2009). Quantification of brain lipids by FTIR spectroscopy and partial least squares regression. *Spectrochim. Acta A* 71, 2069–2075. doi: 10.1016/j.saa.2008.08.008

Eskelinen, E.-L., and Kovács, A. L. (2011). Double membranes vs. lipid bilayers, and their significance for correct identification of macroautophagic structures. *Autophagy* 7, 931–932. doi: 10.4161/auto.7.9.16679

Fernández-Pérez, E. J., Sepúlveda, F. J., Peters, C., Bascuñán, D., Riffo-Lepe, N. O., González-Sanmiguel, J., et al. (2018). Effect of cholesterol on membrane fluidity and association of Aβ oligomers and subsequent neuronal damage: a double-edged sword. *Front. Aging Neurosci.* 10:226. doi: 10.3389/fnagi.2018.00226

Ginsberg, L., Atack, J. R., Rapoport, S. I., and Gershfeld, N. L. (1993). Evidence for a membrane lipid defect in Alzheimer disease. *Mol. Chem. Neuropathol.* 19, 37–46. doi: 10.1007/bf03160167

Harroun, T. A., Katsaras, J., and Wassall, S. R. (2008). Cholesterol is found to reside in the center of a polyunsaturated lipid membrane. *Biochemistry* 47, 7090–7096. doi: 10.1021/bi800123b

Hjort Ipsen, J., Karlstrom, G., Mouritsen, O. G., Wennerstrom, H., and Zuckermann, M. J. (1987). Phase equilibria in the phosphatidylcholine-cholesterol system. *Biochim. Biophys. Acta* 905, 162–172. doi: 10.1016/0005-2736(87)90020-4

Hyde, S. T., Andersson, S., Larsson, K., Blum, Z., Landh, T., Lidin, S., et al. (1997). *The Language of Shape. The Role of Curvature in Condensed Matter: Physics, Chemistry and Biology*. Amsterdam: Elsevier.

Israelachvili, J. N., Mitchell, D. J., and Ninham, B. W. (1976). Theory of self-assembly of hydrocarbon amphiphiles into micelles and bilayers. *J. Chem. Soc. Faraday Trans. II* 72, 1525–1568. doi: 10.1039/f29767201525

Karaman, M. E., Ninham, B. W., and Pashley, R. M. (1994). Some aqueous solution and surface properties of dialkyl sulfosuccinate surfactants. *J. Phys. Chem.* 98, 11512–11518. doi: 10.1021/j100095a036

Kinnun, J. J., Bolmatov, D., Lavrentovich, M. O., and Katsaras, J. (2020). Lateral heterogeneity and domain formation in cellular membranes. *Chem. Phys. Lipids* 232:104976. doi: 10.1016/j.chemphyslip.2020.104976

Larsson, K. (1989). Cubic lipid-water phases: structure and biomembrane aspects. *J. Phys. Chem.* 93, 7304–7314. doi: 10.1021/j100358a010

Lauwers, E., Goodchild, R., and Verstreken, P. (2016). Membrane lipids in presynaptic function and disease. *Neuron* 90, 11–25. doi: 10.1016/j.neuron.2016.02.033

Lo Nostro, P., and Ninham, B. W. (2012). Hofmeister phenomena: an update on ion specificity in biology. *Chem. Rev.* 112, 2286–2322. doi: 10.1021/cr200271j

Luzzati, V., Mustacohi, H., Skoulios, A., and Husson, F. (1960). La structure des colloides d'association. I. Les phases liquide-cristallines des systmes amphiphile-eau. *Acta Cryst.* 13, 660–667. doi: 10.1107/s0365110x60001564

Marcus, Y. (1991). Thermodynamics of solvation of ions. Part 5. -Gbbs free energy of hydration at 298.15 K. *J. Chem. Soc. Faraday Trans.* 87, 2995–2999. doi: 10.1039/ft9918702995

McIntosh, T. J. (1978). The effect of cholesterol on the structure of phosphatidylcholine bilayers *Biochim. Biophys. Acta* 513, 43–58. doi: 10.1016/0005-2736(78)90110-4

McIntosh, T. J., Simon, S. A., Needham, D., and Huang, C.-H. (1992). Structure and cohesive properties of sphingomyelin/cholesterol bilayers. *Biochemistry* 31, 2012–2020. doi: 10.1021/bi00122a017

McLoughlin, D., Dias, R., Lindman, B., Cardenas, M., Nylander, T., Dawson, K., et al. (2005). Surface complexation of DNA with insoluble monolayers. Influence of divalent counterions. *Langmuir* 21, 1900–1907. doi: 10.1021/la047700s

Meyer, H. W., Bunjes, H., and Ulrich, A. S. (1999). Morphological transitions of brain sphingomyelin are determined by the hydration protocol: ripples re-arrange in plane, and sponge-like networks disintegrate into small vesicles. *Chem. Phys. Lipids* 99, 111–123. doi: 10.1016/s0009-3084(99)00029-8

Milovanovic, D., Honigmann, A., Koike, S., Göttfert, F., Pähler, G., Junius, M., et al. (2015). Hydrophobic mismatch sorts SNARE proteins into distinct membrane domains. *Nat. Commun.* 6:5984.

Mitchell, D. J., and Ninham, B. W. (1981). Micelles, vesicles and microemulsions. *J. Chem. Soc. Faraday Trans. 2* 77, 601–629.

Mortensen, K., Pfeiffer, W., Sackmann, E., and Knoll, W. (1988). Structural properties of a phosphatidyleholine-cholesterol system as studied by small.angle neutron scattering: ripple structure and phase diagram. *Biochim. Biophys. Acta* 945, 221–245. doi: 10.1016/0005-2736(88)90485-3

Nickels, J. D., Chatterjee, S., Stanley, C. B., Qian, S., Cheng, X., and Myles, D. A. A. (2017). The in vivo structure of biological membranes and evidence for lipid domains. *PLoS Biol.* 15:e2002214. doi: 10.1371/journal.pbio.2002214

Ninham, B. W., Larsson, K., and Lo Nostro, P. (2017a). Two sides of the coin. Part 1. Lipid and surfactant self-assembly revisited. *Coll. Surf. B* 152, 326–338. doi: 10.1016/j.colsurfb.2017.01.022

Ninham, B. W., Larsson, K., and Lo Nostro, P. (2017b). Two sides of the coin. Part 2. Colloid and surface science meets real biointerfaces. *Coll. Surf. B* 159, 394–404. doi: 10.1016/j.colsurfb.2017.07.090

Pasquini, J. M., and Soto, E. F. (1972). Extraction of proteolipids from nervous tissue with n-butanol-water. *Life Sci.* 11, 433–443. doi: 10.1016/0024-3205(72)90251-2

Phan, H. T. T., Shimokawa, N., Sharma, N., Takagi, M., and Vestergaard, M. C. (2018). Strikingly different effects of cholesterol and 7-ketocholesterol on lipid bilayer-mediated aggregation of amyloid beta (1-42). *Biochem. Biophys. Rep.* 14, 98–103. doi: 10.1016/j.bbrep.2018.04.007

Rappolt, M., and Rapp, G. (1996). Structure of the stable and metastable ripple phase of dipalmitoylphosphatidylcholine. *Eur. Biophys. J.* 24, 381–386. doi: 10.1007/bf00576710

Salis, A., Pinna, M. C., Bilanicova, D., Monduzzi, M., Lo Nostro, P., and Ninham, B. W. (2006). Specific anion effects on glass electrode pH measurements of buffer solutions: bulk and surface phenomena. *J. Phys. Chem. B* 110, 2949–2956. doi: 10.1021/jp0546296

Schneider, C. A., Rasband, W. S., and Eliceiri, K. W. (2012). NIH Image to ImageJ: 25 years of image analysis. *Nat. Methods* 9, 671–675. doi: 10.1038/nmeth.2089

Shimshick, E. J., and McConnell, H. M. (1973). Lateral phase separation in phospholipid membranes. *Biochemistry* 12, 2351–2360. doi: 10.1021/bi00736a026

Sparr, E., and Linse, S. (2019). Lipid-protein interactions in amyloid formation. *Biochim. Biophys. Acta Proteins Proteom.* 1867, 455–457. doi: 10.1016/j.bbapap.2019.03.006

Tatini, D., Raudino, M., Ambrosi, M., Carretti, E., Davidovich, I., Talmon, Y., et al. (2021). Physicochemical characterization of green sodium oleate-based formulations. Part 1. Structure and rheology. *J. Coll. Interface Sci.* 590, 238–248. doi: 10.1016/j.jcis.2021.01.040

Tyler, A. I. I., Barriga, H. M. G., Parsons, E. S., Mccarthy, N. L. C., Ces, O., Law, R. V., et al. (2015). Electrostatic swelling of bicontinuous cubic lipid phases. *Soft Matter* 11, 3279–3286. doi: 10.1039/c5sm00311c

Wadsäter, M., Barauskas, J., Tiberg, F., and Nylander, T. (2018). The lipolytic degradation of highly structured cubic micellar nanoparticles of soy phosphatidylcholine and glycerol dioleate by phospholipase A2 and triacylglycerol lipase. *Chem. Phys. Lipids* 211, 86–92. doi: 10.1016/j.chemphyslip.2017.11.011

Conflict of Interest: The authors declare that the research was conducted in the absence of any commercial or financial relationships that could be construed as a potential conflict of interest.

frontiers
in Cell and Developmental Biology

REVIEW
published: 21 July 2021
doi: 10.3389/fcell.2021.673917

Potential Role of Plasmalogens in the Modulation of Biomembrane Morphology

*Zakaria A. Almsherqi**

Department of Physiology, Yong Loo Lin School of Medicine, National University of Singapore, Singapore, Singapore

Plasmalogens are a subclass of cell membrane glycerophospholipids that typically include vinyl- ether bond at the sn-1 position and polyunsaturated fatty acid at the sn-2 position. They are highly abundant in the neuronal, immune, and cardiovascular cell membranes. Despite the abundance of plasmalogens in a plethora of cells, tissues, and organs, the role of plasmalogens remains unclear. Plasmalogens are required for the proper function of integral membrane proteins, lipid rafts, cell signaling, and differentiation. More importantly, plasmalogens play a crucial role in the cell as an endogenous antioxidant that protects the cell membrane components such as phospholipids, unsaturated fatty acids, and lipoproteins from oxidative stress. The incorporation of vinyl-ether linked with alkyl chains in phospholipids alter the physicochemical properties (e.g., the hydrophilicity of the headgroup), packing density, and conformational order of the phospholipids within the biomembranes. Thus, plasmalogens play a significant role in determining the physical and chemical properties of the biomembrane such as its fluidity, thickness, and lateral pressure of the biomembrane. Insights on the important structural and functional properties of plasmalogens may help us to understand the molecular mechanism of membrane transformation, vesicle formation, and vesicular fusion, especially at the synaptic vesicles where plasmalogens are rich and essential for neuronal function. Although many aspects of plasmalogen phospholipid involvement in membrane transformation identified through *in vitro* experiments and membrane mimic systems, remain to be confirmed *in vivo*, the compiled data show many intriguing properties of vinyl-ether bonded lipids that may play a significant role in the structural and morphological changes of the biomembranes. In this review, we present the current limited knowledge of the emerging potential role of plasmalogens as a modulator of the biomembrane morphology.

Keywords: plasmalogen, biomembranes, dynamic system, cubic membranes, membrane morphological changes

Edited by:
Angelina Angelova,
UMR8612 Institut Galien Paris Sud (IGPS), France

Reviewed by:
Katrin Watschinger,
Biocenter, Medical University of Innsbruck, Austria
Bartosz Rozycki,
Institute of Physics, Polish Academy of Sciences, Poland

***Correspondence:**
Zakaria A. Almsherqi
phszama@nus.edu.sg

Specialty section:
This article was submitted to Cellular Biochemistry, a section of the journal Frontiers in Cell and Developmental Biology

Received: *28 February 2021*
Accepted: *31 May 2021*
Published: *21 July 2021*

Citation:
Almsherqi ZA (2021) Potential Role of Plasmalogens in the Modulation of Biomembrane Morphology. Front. Cell Dev. Biol. 9:673917. doi: 10.3389/fcell.2021.673917

INTRODUCTION

Biomembranes are of fundamental importance in providing cellular compartmentalization and regulation of intracellular activities. An extensive review of the literature reveals that biomembranes are dynamic as they can transform into various morphological architectures and shapes. Biomembrane transformation could be a selective process to fulfill a specific purpose under the continuous and ever-changing intracellular and extracellular environment.

The physical and chemical characteristics of the biomimetic materials determine the structure and morphology of the artificial membranes (Jurak et al., 2018). Similarly, the physicochemical properties of the biological membranes are determined by the membrane's proteins and phospholipids composition. Their unique combination influence the geometry, morphology, and function of the biomembrane. Morphological changes of the biomembrane are often related to the overexpression of certain membrane-resident proteins and, to a lesser extent, to the changes in the membrane lipid profile (Almsherqi et al., 2009). The role of membrane lipids in this regard was speculated based on published reports of biomembrane transformation in mammalian cells upon overexpression or inhibition of key regulatory enzymes of the lipid and cholesterol synthesis such as HMG-CoA reductase (Almsherqi et al., 2009).

In principle, any amphiphilic molecule is capable of inducing membrane transformation. Based on the chemical structure of the lipid bilayer and its interactions with the membrane proteins, several membrane patterns could be generated. Evidence from *in vitro* studies clearly shows that the propensity of membrane-forming lipids to initiate non-lamellar structures is pivoted mainly on their molecular shape concept (Epand, 1997, 2007). For example, biomembranes may adopt different morphologies such as plain lamellar, stacked lamellar, whorls, or hexagonal depending on the phospholipid headgroup size and charge (Epand, 1997; Madrid and Horswell, 2013). Further, the changes in shape and structure of biomembranes are also influenced by the alkyl chain length (e.g., very long chain fatty acids, VLCFA) and the number of double bonds of the unsaturated phospholipid (polyunsaturated fatty acids, PUFA; Deng et al., 2009). More specifically, the alkyl chain length and the degree of unsaturation of the phospholipid are foundational to the structural impact on the complex lipid derivatives in biomembranes. Phospholipids with highly unsaturated docosahexaenoic acid (DHA) or docosapentaenoic acid (DPA) alkyl chains are usually found in cholesterol depleted, non-raft membrane domains (Wassall and Stillwell, 2008), while lipid rafts domain are enriched in arachidonic acid (Pike et al., 2002). The introduction of DHA-rich domains is speculated to induce changes in the conformation of signaling proteins (Wassall and Stillwell, 2008) and to induce non-lamellar, highly curved membrane structures such as hexosomes in DHA-monoglyceride mixture (Yaghmur et al., 2019) or hexagonal and cubic membrane organizations (Deng et al., 2009). Interestingly, the structural impact of omega-3 and omega-6 PUFAs, for example, are profoundly different, in terms of their influence on biomembrane morphology, although the only difference between the two molecules is their respective positions of the double bonds on the acyl chain (Deng et al., 2009).

Besides studying the roles of VLCFA, PUFA, and cholesterol in inducing lipid membrane structural changes, recently, there is a heightened interest in investigating the role of ether phospholipids in biomembrane morphology. Ether phospholipids are ubiquitous and occasionally they are the major components of the cell membranes of anaerobic bacteria, primitive protozoa, fungi, and in the mammals' cell membranes largely in the nervous, cardiovascular and immune systems (Braverman and Moser, 2012; Jiménez-Rojo and Riezman, 2019). There are two types of ether phospholipids, namely, plasmanyl phospholipid, and plasmenyl phospholipid (also known as plasmalogen). Typically, the sn-1 positions in plasmanyl and plasmenyl lipids are occupied by either 16 or 18 carbon attached via ether or vinyl-ether moieties, respectively, (**Figure 1**). In plasmalogens, the sn-2 position often carries PUFAs (Braverman and Moser, 2012; Dorninger et al., 2015). Indeed, ester, ether, and vinyl-ether lipids have their unique structures and physicochemical characteristics that affect biomrmbranes morphology, related to the cross-sectional area of the lipids, the differences in packing, and the interaction with other membrane components such as proteins and cholesterol (Casares et al., 2019). There is an increasing body of evidence demonstrating that vinyl-ether phospholipids have a direct effect on the membrane physicochemical properties including the rigidity/fluidity, fission/fusion, and morphological transition, (Koivuniemi, 2017) while ether lipids have been linked to complex cellular dysfunctions manifested as neurodegenerative and neurodevelopmental disorders (Dorninger et al., 2017). In this review, we mainly focus on plasmalogens, since they represent the major constituents of ether lipids in mammalian membranes, and because the biomembrane structural and morphological changes associated with impaired ether lipids are usually linked to the alteration of plasmalogen levels.

Plasmalogens have a multistage evolutionary history and a unique distribution across living organisms (Goldfine, 2010). Approximately 1 in 5 phospholipids are plasmalogens in human tissue where they are especially enriched in the neuronal, cardiac, and immune cells (Braverman and Moser, 2012). For example, choline plasmalogens account for around 30–40% of choline glycerophospholipids in human heart tissues, whereas ethanolamine plasmalogens account for around 70% of ethanolamine glycerophospholipids in myelin sheaths (Farooqui and Horrocks, 2001). Considering the relatively higher amount of plasmalogens in the cell membranes, it is thus assumed that plasmalogens may potentially have significant effects on the physicochemical properties, and the integrity of the cell membranes.

ROLE OF PLASMALOGENS AS AN INTERNAL ANTIOXIDATIVE DEFENSE AGENT IN BIOMEMBRANES

Since their discovery, it was evident that, in contrast to ester-bonded phospholipids, vinyl-ether bond present in plasmalogens contribute to oxidation/antioxidant activity (Zoeller et al., 1999) as vinyl-ether bond preferentially decomposes during oxidation (Khaselev and Murphy, 1999). More specifically, it was proposed that plasmalogens could play a protective role against lipid peroxidation as a sacrificing/scavenger agent (Sindelar et al., 1999; Zoeller et al., 1999). In a study carried out by Sindelar et al. (1999), oxidative stress was applied to brain phospholipids with and without the presence of plasmalogens in separate liposomal systems. The results revealed that biomarkers for lipid peroxidation were significantly decreased in brain phospholipids

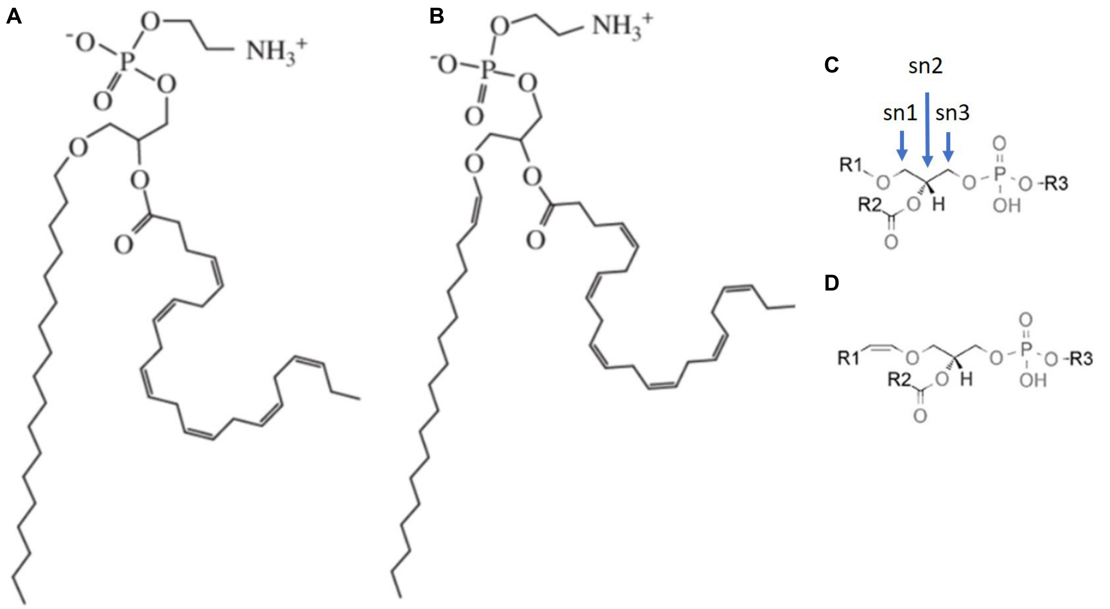

FIGURE 1 | Structure of ether-linked membrane lipids differing in the sn1 linkage. **(A)** Alkyl chain linked to sn1 position via an ether-linkage (plasmanyl ethanolamine) and **(B)** Alkyl group linked to sn1 position via a vinyl ether linkage (plasmenyl ethanolamine). The general structure of **(C)** plasmanyl and **(D)** plasmenyl phospholipid species.

with plasmalogens. Further, upon exposure to high oxidative conditions in normal cells, the plasmalogen levels were shown to decrease, suggesting a possible function as scavengers (Brosche and Platt, 1998; Brites et al., 2004).

Plasmalogens may protect biomembranes from environmental hazards as well. Hoefler et al. (1991), showed that plasmalogen deficient cells from patients with peroxisomal biogenesis disorders were significantly more sensitive to UV radiation exposure as compared to control cells. This observation supported by an *in vitro* study showed that plasmalogens-rich monolayer protects unsaturated lipids against UV-induced oxidation in the biomimetic system (Morandat et al., 2003). These observations imply that plasmalogens might protect polyunsaturated fatty acids of biomembranes from oxidative damage. Additionally, it has been reported that biomembranes relatively rich in plasmalogens exhibit low lipid peroxidation markers (Deng et al., 2017) and may provide protective shelter for biomolecules under oxidative stress conditions (Deng and Almsherqi, 2015).

The presence of vinyl-ether bonds in plasmalogens is probably responsible for providing protection against oxidative stress conditions. Indeed, vinyl ether bonds, the target of several oxidants including singlet oxygen, metal ions, and peroxyl radicals, are more susceptible to oxidation than ester bonds in phospholipids (Brites et al., 2004). However, peroxidation of vinyl-ether bonds by the free radicals might either be less efficient or more stable to abstract the hydrogen ion than alkyl radicals produced during the peroxidation of polyunsaturated fatty acids (Sindelar et al., 1999). It is also possible that during the process, the oxygenated vinyl ether radicals could be dissociated into water-soluble radical compounds leading to the inhibition of the chain reaction and stopping further propagation of lipid peroxidation (Sindelar et al., 1999). Therefore, plasmalogens that are present in sufficient concentrations in the cell membranes and able to cease lipid peroxidation could be classified as efficient internal antioxidants.

EFFECTS OF PLASMALOGENS ON THE PHYSICOCHEMICAL PROPERTIES OF THE BIOMEMBRANES

In addition to protecting phospholipids or lipoprotein and other components of the biomembranes against the damaging effects of reactive oxygen species, a substantial amount of research work supporting the proposition that alteration of the physicochemical and structural properties of the biomembranes could be influenced by the quantity and subtype of their plasmalogens content. *In vitro* studies carried out by Angelova et al. (2021) revealed that ethanolamine plasmalogen (C16:1p-22:5n6 pPE) promotes double-diamond cubic phase whereas primitive cubic phase and inverted hexagonal (H_{II}) are observed in the DPA-ethanolamine plasmalogen (C16:1p-22:5n6 pPE) derivative. Complex morphological architectures such as cubic-lamellar liquid crystalline phases are established in DPA-plasmenyl phosphocholine (C16:1p-22:5n6 pPC)/MO (Monoolein) mixture, while ethanolamine plasmalogen (C16:1p-22:5n6 pPE)/DOPC (Dioleoylphosphocholine) bilayers promote a mix of multilamellar vesicular or whorls architectures (Angelova et al., 2021). The effect of cations on plasmalogen-rich membranes was studied by Cullis et al. (1986). Their experimental data showed that adding Ca^{2+} to a lipid bilayer consisting of negatively charged phospholipids and plasmalogens could alter and convert the flat membrane to a non-lamellar structure. Additionally, the authors have also observed that the addition of Ca^{2+} could promote membrane fusion in plasmalogen-rich membranes. Glaser and Gross (1994) reported that *in vitro*, vesicles with varying ratios of different plasmalogens could induce different non-lamellar structures. They have also demonstrated that different lipid compositions may affect the rate of membrane fusion, suggesting that plasmalogens are able to promote the formation of non-lamellar structures, which can further facilitate the membrane fusion process (Han and Gross, 1990, 1991; Glaser and Gross, 1994).

Lohner (1996) suggested that the tendency of plasmalogens to form highly curved structures such as inverted hexagonal may be attributed to their physicochemical properties. The lack of the carbonyl oxygen in position sn-1 of ether lipids affects the hydrophilicity of the headgroup and allows stronger intermolecular hydrogen bonding between the headgroups of the lipids which promotes the formation of non-lamellar structures. This suggestion is supported by studies that show that model membranes composed of plasmanyl and plasmenyl ethanolamines exhibit lower gel to liquid phase transition compared with diacyl glycerophosphoethanolamine analog (Paltauf, 1994). Detailed studies demonstrate that the optimum transition temperature required for the transformation from lamellar to hexagonal phase is lowered in the presence of plasmalogen (Lohner et al., 1991). Further experimental work showed that plasmalogens are an essential component in regulating several membranous activities (Hermetter et al., 1989; Glaser and Gross, 1995; Braverman and Moser, 2012) such as membrane fusion processes (Brites et al., 2004). Furthermore, physiological studies have shown that the highly heterogeneous bilayers enriched in plasmalogens present in synaptic vesicles (Breckenridge et al., 1973; Braverman and Moser, 2012; Dorninger et al., 2019) support neurotransmitter release and vesicular fusion is very sensitive to the amount and type of ethanolamine plasmalogens (pPE) content. Any minor reduction in either the vinyl-ether and/or the polyunsaturated fatty acid content of vesicles would result in a significant reduction in the number of successful membrane fusion events (Rog and Koivuniemi, 2016). Thus, this mechanism alone might be adequate to rationalize the correlation between the decreased membrane pPE and the neuronal function decline associated with neurodegenerative diseases and aging.

PLASMALOGEN DISTRIBUTION IN BIOLOGICAL MEMBRANES

Effects of plasmalogens on artificial membrane architectures have motivated further studies on their molecular distribution and packing in simulations of lipid membranes comprising plasmalogens and palmitoyl-oleoyl-phosphatidylcholine. Ether lipids in general, and plasmalogens in particular, form more tightly packed membranes than their diacyl analog. Specifically, for pPE, this effect could be attributed to the highly ordered state of sn1 chain and closer packing of the sn1 and sn2 chains where the orientation of the alkyl chain and vinyl-ether linkage of plasmalogens dictate the increased packing of membranes (Han and Gross, 1990; Rog and Koivuniemi, 2016). As such, it is expected that the bilayer thickness, lateral phase segregation, rigidity, and other physicochemical properties of the biomembranes are likely to be influenced by the amount and distribution of plasmalogens (Rog and Koivuniemi, 2016).

Experimental work using human red blood cells showed that the labeled pPE spontaneously spread from the outer to the inner leaflet with a transition half-time comparable to the corresponding diacyl analog. At equilibrium, about 80% of both subclasses of PE were in the inner leaflet whereas only 20% of choline plasmalogen (pPC) was translocated to the inner leaflet (Fellmann et al., 1993). It was further reported that in the sarcolemmal membrane, ethanolamine and pPC were asymmetrically distributed, with the plasmalogens predominating in the inner leaflet (for example, with pPE accounting for 44% and 24% of ethanolamine glycerophospholipids in the inner leaflet and the outer leaflet, respectively; Kirschner and Ganser, 1982; Post et al., 1988). Plasmalogens and diacyl glycerophospholipids segregation can occur laterally as well but this has not been reported in artificial membrane models. If it happens in biological membranes, then it is most likely to be caused by the specific interaction with membrane proteins. It has been speculated that asymmetrical distribution of pPE at the sarcolemmal membrane might be essential for Ca transport (Bick et al., 1991) and *trans*-sarcolemmal sodium-calcium exchange (Ford and Hale, 1996). Interestingly, plasmalogens localized in the inner layer of the plasma membrane are critical for sensing the cellular level of plasmalogens and they play an important role in the regulation of plasmalogen biosynthesis (Honsho et al., 2017). Plasmalogen levels in the cell membranes could affect the intracellular cholesterol distribution (Rodemer et al., 2003) and transportation within biomembranes (Munn et al., 2003).

EFFECTS OF PLASMALOGENS ON ALTERATION OF BIOMEMBRANE MORPHOLOGY

Notwithstanding the significant advances achieved in understanding the role of plasmalogens in the artificial membrane organization (Feller, 2008; Gawrisch and Soubias, 2008; Wassall and Stillwell, 2008), similar studies on the effects of plasmalogens on biomembrane curvature and architecture *in vivo* are limited mainly because of the deficiency of suitable experimental techniques to match the membrane geomorphologies in the cell with specific local membrane lipid composition.

One of the earliest investigations relating plasmalogen to membrane morphology alteration was reported by Teichman et al. (1972) who discovered that mammalian spermatozoa retained highly osmiophilic material when fixed with glutaraldehyde containing malachite green or pyronine. Further analysis of malachite-green-affinity (MGA) material found that MGA consists largely of pPC (Teichman et al., 1974).

Although the highly condensed, plasmalogen-rich MGA material has various morphologies, its homogenous and apparently membranous whorls resembling myelin sheet was the most common architecture observed.

Deng et al. (2009) have demonstrated that during cell starvation, the significant increase in pPC in amoeba *Chaos* was associated with the highly organized and curved cubic membrane formation (**Figure 2**). An unusually high concentration of PUFA has been found in lipid analysis of amoeba *Chaos* (C22:5; DPA; Deng et al., 2009). Three main lipid species, namely pPE (C16:0p/C22:5), pPC (C16:0p/C22:5), and diacyl-PI (C22:5/C22:5), were detected in amoeba *Chaos* lipid extracts. Interestingly, the liposomal constructs obtained from the amoeba *Chaos* lipid extracts, typically display cubic and hexagonal phase organization (**Figure 2**).

Upon cubic membrane formation, under starvation stressed conditions, the relative amounts of PUFA especially DPA increased up to 1.6-fold (Almsherqi et al., 2010), at the expense of linoleic acid (all-*cis*-9,12-octadecadienoic acid; C18:2 omega-6). This suggests a metabolic link via the omega-6 DPA pathway giving rise to omega-6 DPA, rather than omega-3 DPA, which requires Δ15 desaturation of the acyl chain that is absent in animals (Deng et al., 2009). Furthermore, it has been suggested that cubic membranes which harbor a significant amount of plasmalogens (Deng et al., 2009), might act as a "defensive" shield to mitigate the oxidation of biologically vital macromolecules (e.g., lipids, oligonucleotides, and mRNAs; Almsherqi et al., 2008; Deng and Almsherqi, 2015; Deng et al., 2017). In this light, further studies carried out on amoeba *Chaos* showed that when oxidation was imminent in the mitochondria (Wang et al., 2011; Rambold et al., 2015) during cell starvation, the percentage of cell survival in amoeba *Chaos* with cubic membrane (rich in plasmalogens) was significantly higher than those amoeba without mitochondrial cubic membrane transformation (Chong et al., 2018). This suggested that plasmalogens play a role not only in membrane transformation but also as a cytoprotectant to promote cell survival. Similar results were reported in *C. elegans* where the lifespan was reduced by 30% in three different point-mutant strains that resulted in a near-complete loss of plasmalogens. Furthermore, the ability to survive and grow in cold ambient temperature was significantly reduced from 60% in the wild type *C. elegans* to 5–20% in the mutant strains.

CHANGES IN CELLULAR MEMBRANE MORPHOLOGY ARISING FROM EXOGENOUS METABOLIC PRECURSORS AND PLASMALOGENS SUPPLEMENTS

Based on clinical, experimental, and biomimetic simulation observations, alterations of plasmalogen levels and membrane transformation are associated. Thus, the availability of plasmalogens (as a result of supply/deficiency) could influence biomembrane transformation, during cellular/organelle stress conditions.

Experimental data demonstrated that alkylglycerols supplementation to rodents was utilized for ether lipids synthesis including plasmalogens (Hayashi and Oohashi, 1995). Furthermore, adding alkylglycerols to the culture media of plasmalogen-deficient CHRS, RCDP, or CHO cells reinstated the normal plasmalogen levels (Liu et al., 2005). Therefore, it can be deduced that dietary precursors such as alkylglycerols can be utilized for plasmalogen synthesis and restoration of normal levels of ether lipids in various tissues.

Plasmalogen dietary supplementation may aid membrane morphology alteration, particularly in amoeba *Chaos*. Lipid profile data of amoeba *Chaos* food organisms revealed significant differences in the plasmalogen levels of the two food organisms, namely Paramecium multimicronucelatum (hereinafter referred to as Paramecium) and Tetrahymena

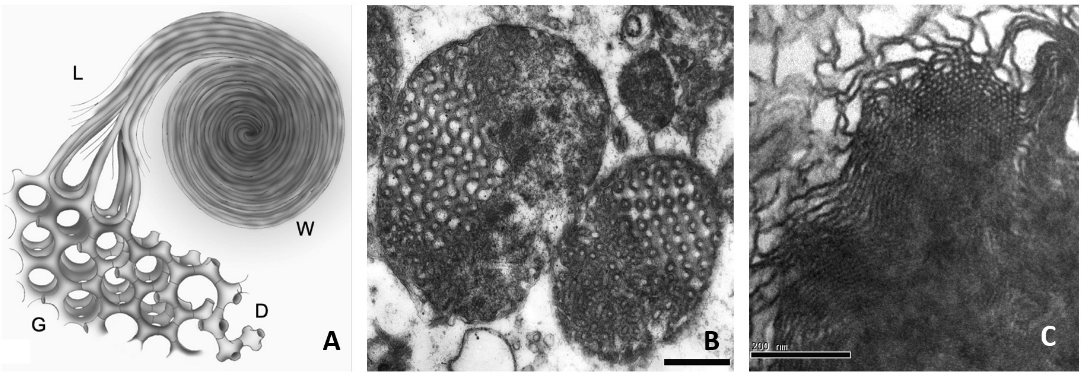

FIGURE 2 | (A) Schematic diagram depicting a model of continuous membrane folding represents the formation of double diamond (D) and gyroid (G) cubic type, hexagonal and lamellar structures (L), and whorls (W) membrane organizations. Cubic membrane organizations have been reported to be rich in plasmalogens. **(B)** Transmission electron microscopy images of cubic membranes transformation of the mitochondria in amoeba *Chaos* cells under starvation stress condition and **(C)** Liposomes generated from the lipids extracted from amoeba *Chaos*, typically display cubic and hexagonal phase organization. **(A,C)** reprinted from Almsherqi et al. (2009) with permission.

pyriformis (hereinafter referred to as Tetra). In particular, pPC was in relatively high abundance in Paramecium compared to Tetrahymena. The higher level of pPC in amoeba *Chaos* cells was observed in Paramecium-fed but not Tetra-fed cells (Deng et al., 2009). Interestingly, feeding amoeba *Chaos* with the extracted lipids from Paramecium (pPC-rich) or polyunsaturated fatty acids, specifically omega-6 DPA, (Deng et al., 2009) were able to induce mitochondrial inner membrane rearrangements into cubic morphology (**Figure 3**). Furthermore, liposome construct using the extracted lipids from amoeba *Chao*s exclusively fed with Paramecium do induce cubic or hexagonal organization *in vitro* (Deng et al., 2009; **Figure 3**).

In a parallel study adopting a similar technique, MO/DOPC nanostructured lipid phases with alteration of plasmalogens carrying DPA (C22:5n-6) were used in order to validate the potency of plasmalogens on the membrane curvature and/or membrane re-arrangements (Angelova et al., 2021). The results showed that plasmalogens-carrying C22:5n-6 fatty acids at sn-2 position effectively curved the lamellar phase structures and induced multiple nanostructures such as inverted hexagonal (H_{II}), double diamond cubic phase, double-membrane vesicles, and multilamellar whorl topologies indicating the importance of DPA-based PE and PC plasmalogens in inducing membrane curvature (Angelova et al., 2021). These observations suggest that plasmalogens and PUFAs (C22:5n-6) each play a role in lipidic phase transition *in vitro* and cubic membrane transformation *in vivo*. Plasmalogens might work synergistically in transitioning the lipid phase to higher-order morphologies. With relevance to biological membrane transformation, it is highly possible that *in vivo*, lipids, proteins, and other ionic milieu or pH factors partake in a morphological transformation of biomembranes.

Translational studies of plasmalogens supplementation in Alzheimer's disease revealed that there were improvements in the learning ability and cognitive function of the rodents when fed with plasmalogen-rich lipids (Yamashita et al., 2017) and significant improvement was observed in mild/early-stage Alzheimer's patients when treated with oral supplements of scallop-derived plasmalogens (Fujino et al., 2017, 2018). However, the bioavailability of oral supplements of plasmalogens or plasmalogen precursors to the neuronal cells is still under investigation. Plasmalogens are carried in the plasma via chaperone proteins like LDL (Wiesner et al., 2009) and delivered to the tissues through LDL receptor-mediated pathway (Dehouck et al., 1997; Candela et al., 2008). Although some studies suggest that plasmalogen precursors (Wood et al., 2011), and DHA in the form of phospholipids can pass through the blood-brain barrier (BBB; Lagarde et al., 2015), plasmalogens may not be able to cross the BBB efficiently. These studies indicate that the brain tissue relies on the *de novo* synthesis of ether lipid rather than on the transportation of peripherally synthesized plasmalogens across the BBB. However, depleted levels of brain DHA, and

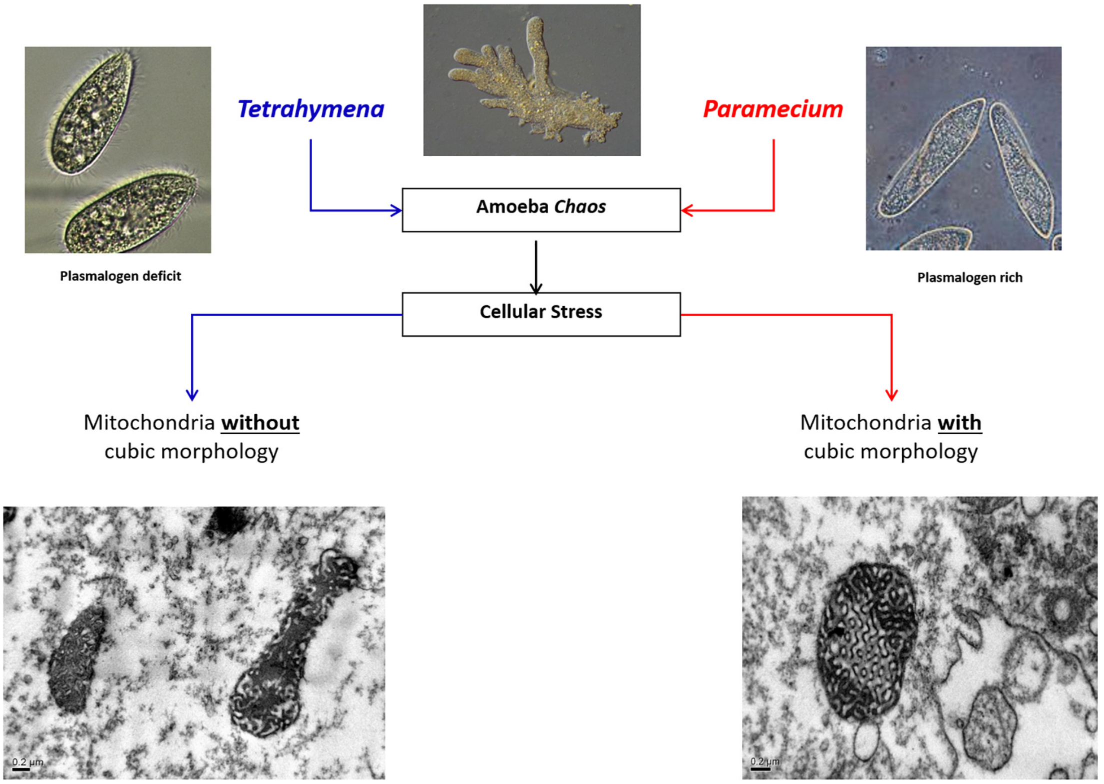

FIGURE 3 | Schematic diagram depicting the effect of food supplements on the mitochondria membrane morphological transformation in amoeba *Chaos*.

presumably DHA-containing plasmalogens, could be replaced by sustained DHA supplementation (Salem et al., 2001). Enriching neuronal cell membranes with plasmalogens could improve neuronal function through modulation of non-lamellar membrane transformations and synaptic plasticity (Paul et al., 2019).

EXPERIMENTAL MODELS TO INVESTIGATE PLASMALOGENS EFFECT ON BIOMEMBRANES

Understanding the role of plasmalogens in biological membranes is key to understanding how plasmalogen depletion may contribute to the onset and progression of pathological conditions. Several knockout (KO) mice models were generated for *in vivo* studies, namely, Pex7 KO mouse (Brites et al., 2011), Pex7 hypomorphic mouse (Braverman et al., 2010), Gnpat KO (Dorninger et al., 2019), Agps hypomorphic mouse (Liegel et al., 2014), and recently, PEDS1 KO mice which lack both plasmanylethanolamine desaturase activity (the key enzyme involved in the initial step of plasmalogen synthesis) and plasmalogens (Werner et al., 2020). A sole mutation of an enzyme leading to a specific plasmalogen deficiency offered by the experimental models could be advantageous for a clear-cut understanding of the biochemistry-pathology relationship.

In addition to KO mice models and human neuronal cell culture, a nematode, *C. elegans*, has lately been established as a model for plasmalogen deficiency (Drechsler et al., 2016; Shi et al., 2016). Unlike murine KO mutants, which are often infertile, the ether lipid mutants *C elegans* are viable and fertile, which offers a valuable model to study severe forms of plasmalogen deficiencies. *C. elegans* is also a suitable model to incorporate dietary tracers which could be detected in the cell membranes and allow detailed measurements of ether lipids distribution in the cell membranes (Dancy et al., 2015).

Free-living giant amoeba *Chaos* could also be proposed as an experimental cell model system to assess the effect of plasmalogen deficiencies on cellular membrane structure and function. In addition to the high cellular dynamic (exocytosis, endocytosis, and pinocytosis), the advantage of studying membranes transformations in amoeba *Chaos* is the ability to trace membrane morphological changes in relation to changes in the diet. Modifying the quantity/quality of the food supply is feasible and controllable (Tan et al., 2005). Further studies could establish a relationship between the exogenous plasmalogens supplementation and cellular membrane activity.

SIGNIFICANCE OF STUDYING THE EFFECT OF PLASMALOGEN ON MEMBRANE MORPHOLOGY

Identification of a mechanistic association between the reduction in plasmalogens within cellular membranes and deterioration of vital cellular functions is important in two aspects: early detection of cellular dysfunction before it progresses to the disease state and secondly, proper planning for prevention and/or therapeutic intervention.

First, plasma plasmalogen levels could be used as a biomarker to indicate the onset of cellular dysfunction and monitor the rate and extent of the deterioration or improvement (Fernandes et al., 2020). Detecting plasmalogens in the blood, for example, would be an advantage over other methods of detection (Fernandes et al., 2020). Second, restoring plasmalogen levels (by oral supplements for example) at the appropriate intervention time could potentially delay or prevent the onset of cellular dysfunction that is associated with neurodegenerative and/or age-related diseases. Restoration of plasmalogens for specific tissues requires an improvement in the bioavailability of plasmalogens or plasmalogen precursors, enhanced BBB penetration ability (e.g., using liposome-based strategies; Vieira and Gamarra, 2016), and the selection of a proper stage (preclinical, early/late clinical) to start the treatment.

CONCLUDING REMARKS

In conclusion, with the potential role of plasmalogens in biomembranes as a modulator of cell membrane physicochemical properties and morphology, plasmalogens cannot be regarded to function only as an internal antioxidant that maintains membrane lipids and proteins integrity. Plasmalogens affect both across the lipid bilayer (lipid asymmetry) and lateral dimension (lipid domains) and facilitate the formation of non-lamellar structures in the cell. Inducing membrane curvature initiates and promotes membrane fusion/fission, vesicular formation, and molecular transportation which are crucial for normal cell function (especially neuronal cells) and adaptation to stress conditions. This new aspect of plasmalogens in the bilayer membrane architecture has been tested in artificial membrane lipid systems and yet to be explored *in vivo*. Furthermore, in-depth study of the underlying molecular mechanism of inducing and selecting a specific spatial arrangement of bilayer-based membranes is indeed critical to the understanding of the association between cell membrane alteration and adjustment of cellular function and adaptation to stress and pathological conditions.

AUTHOR CONTRIBUTIONS

Part of the experimental work cited in the manuscript has been done in the author's laboratory. ZA contributed to the manuscript writing and preparation of figures.

ACKNOWLEDGMENTS

The author would like to thank Craig Mclachlan and Deng Yuru for their critical comments and the reviewers for their insightful suggestions and careful reading of the manuscript.

REFERENCES

Almsherqi, Z., Hyde, S., Ramachandran, M., and Deng, Y. (2008). Cubic membranes: a structure-based design for DNA uptake. *J. R. Soc. Interface* 5, 1023–1029. doi: 10.1098/rsif.2007.1351

Almsherqi, Z. A., Landh, T., Kohlwein, S. D., and Deng, Y. (2009). Cubic membranes: the missing dimension of cell membrane organization. *Int. Rev. Cell. Mol. Biol.* 274, 275–342. doi: 10.1016/S1937-6448(08)02006-6

Almsherqi, Z. A., Margadant, F., and Deng, Y. (2010). The Cubic "Faces" of Biomembranes. *Adv. Planar Lipid Bilayers Liposomes* 12, 79–99. doi: 10.1016/B978-0-12-381266-7.00004-3

Angelova, A., Angelov, B., Drechsler, M., Bizien, T., Gorshkova, Y. E., and Deng, Y. (2021). Plasmalogen-Based Liquid Crystalline Multiphase Structures Involving Docosapentaenoyl Derivatives Inspired by Biological Cubic Membranes. *Front. Cell. Dev. Biol.* 9:617984. doi: 10.3389/fcell.2021.617984

Bick, R. J., Youker, K. A., Pownall, H. J., Van Winkle, W. B., and Entman, M. L. (1991). Unsaturated aminophospholipids are preferentially retained by the fast skeletal muscle CaATPase during detergent solubilization. Evidence for a specific association between aminophospholipids and the calcium pump protein. *Arch. Biochem. Biophys.* 286, 346–352. doi: 10.1016/0003-9861(91)90050-s

Braverman, N. E., and Moser, A. B. (2012). Functions of plasmalogen lipids in health and disease. *Biochim. Biophys. Acta* 22, 1442–1452. doi: 10.1016/j.bbadis.2012.05.008

Braverman, N. E., Zhang, R., Chen, L., Nimmo, G., Scheper, S., Tran, T., et al. (2010). A Pex7 hypomorphic mouse model for plasmalogen deficiency affecting the lens and skeleton. *Mol. Genet. Metab.* 99, 408–416. doi: 10.1016/j.ymgme.2009.12.005

Breckenridge, W. C., Morgan, I. G., Zanetta, I. P., and Vincendon, G. (1973). Adult rat brain synaptic vesicles. II. Lipid composition. *Biochim. Biophys. Acta* 320, 681–686. doi: 10.1016/0304-4165(73)90148-7

Brites, P., Ferreira, A. S., da Silva, T. F., Sousa, V. F., Malheiro, A. R., Duran, M., et al. (2011). Alkyl-glycerol rescues plasmalogen levels and pathology of ether-phospholipid deficient mice. *PLoS One* 6:e28539. doi: 10.1371/journal.pone.0028539

Brites, P., Waterham, H. R., and Wanders, R. J. (2004). Functions and biosynthesis of plasmalogens in health and disease. *Biochim. Biophys. Acta* 1636, 219–231. doi: 10.1016/j.bbalip.2003.12.010

Brosche, T., and Platt, D. (1998). The biological significance of plasmalogens in defense against oxidative damage. *Exp. Gerontol.* 33, 363–369. doi: 10.1016/s0531-5565(98)00014-x

Candela, P., Gosselet, F., Miller, F., Buee-Scherrer, V., Torpier, G., Cecchelli, R., et al. (2008). Physiological pathway for low-density lipoproteins across the blood-brain barrier: transcytosis through brain capillary endothelial cells in vitro. *Endothelium* 15, 254–264. doi: 10.1080/10623320802487759

Casares, D., Escribá, P. V., and Rosselló, C. A. (2019). Membrane Lipid Composition: effect on Membrane and Organelle Structure, Function and Compartmentalization and Therapeutic Avenues. *Int. J. Mol. Sci.* 20:2167. doi: 10.3390/ijms20092167

Chong, K., Almsherqi, Z. A., Shen, H. M., and Deng, Y. (2018). Cubic membrane formation supports cell survival of amoeba Chaos under starvation-induced stress. *Protoplasma* 255, 517–525. doi: 10.1007/s00709-017-1169-x

Cullis, P. R., Hope, M. J., and Tilcock, C. P. S. (1986). Lipid polymorphism and the roles of lipids in membranes. *Chem. Phys. Lipids* 40, 127–144. doi: 10.1016/0009-3084(86)90067- 8

Dancy, B. C., Chen, S. W., Drechsler, R., Gafken, P. R., and Olsen, C. P. (2015). 13C- and 15N-Labeling Strategies Combined with Mass Spectrometry Comprehensively Quantify Phospholipid Dynamics in C. elegans. *PLoS One* 10:e0141850. doi: 10.1371/journal.pone.0141850

Dehouck, B., Fenart, L., Dehouck, M. P., Pierce, A., Torpier, G., and Cecchelli, R. (1997). A new function for the LDL receptor: transcytosis of LDL across the blood-brain barrier. *J. Cell Biol.* 138, 877–889. doi: 10.1083/jcb.138.4.877

Deng, Y., and Almsherqi, Z. A. (2015). Evolution of cubic membranes as antioxidant defence system. *Interface Focus* 5:20150012. doi: 10.1098/rsfs.2015.0012

Deng, Y., Almsherqi, Z. A., Shui, G., Wenk, M. R., and Kohlwein, S. D. (2009). Docosapentaenoic acid (DPA) is a critical determinant of cubic membrane formation in amoeba Chaos mitochondria. *FASEB J.* 23, 2866–2871. doi: 10.1096/fj.09-130435

Deng, Y., Lee, E. L., Chong, K., and Almsherqi, Z. A. (2017). Evaluation of radical scavenging system in amoeba Chaos carolinense during nutrient deprivation. *Interface Focus* 7:20160113. doi: 10.1098/rsfs.2016.0113

Dorninger, F., Brodde, A., Braverman, N. E., Moser, A. B., Just, W. W., Forss-Petter, S., et al. (2015). Homeostasis of phospholipids - The level of phosphatidylethanolamine tightly adapts to changes in ethanolamine plasmalogens. *Biochim. Biophys. Acta* 1851, 117–128. doi: 10.1016/j.bbalip.2014.11.005

Dorninger, F., Forss-Petter, S., and Berger, J. (2017). From peroxisomal disorders to common neurodegenerative diseases - the role of ether phospholipids in the nervous system. *FEBS Lett.* 591, 2761–2788. doi: 10.1002/1873-3468.12788

Dorninger, F., König, T., Scholze, P., Berger, M. L., Zeitler, G., Wiesinger, C., et al. (2019). Disturbed neurotransmitter homeostasis in ether lipid deficiency. *Hum. Mol. Genet.* 28, 2046–2061. doi: 10.1093/hmg/ddz040

Drechsler, R., Chen, S. W., Dancy, B. C., Mehrabkhani, L., and Olsen, C. P. (2016). HPLC-Based Mass Spectrometry Characterizes the Phospholipid Alterations in Ether-Linked Lipid Deficiency Models Following Oxidative Stress. *PLoS One* 11:e0167229. doi: 10.1371/journal.pone.0167229

Epand, R. M. (1997). Studies of membrane physical properties and their role in biological function. *Biochem. Soc. Trans.* 25, 1073–1079. doi: 10.1042/bst0251073a

Epand, R. M. (2007). Membrane lipid polymorphism: relationship to bilayer properties and protein function. *Methods Mol. Biol.* 400, 15–26. doi: 10.1007/978-1-59745-519-0_2

Farooqui, A. A., and Horrocks, L. A. (2001). Plasmalogens: workhorse lipids of membranes in normal and injured neurons and gila. *Neuroscientist* 7, 232–245. doi: 10.1177/107385840100700308

Feller, S. E. (2008). Acyl chain conformations in phospholipid bilayers: a comparative study of docosahexaenoic acid and saturated fatty acids. *Chem. Phys. Lipids* 153, 76–80. doi: 10.1016/j.chemphyslip.2008.02.013

Fellmann, P., Hervé, P., and Devaux, P. F. (1993). Transmembrane distribution and translocation of spin-labeled plasmalogens in human red blood cells. *Chem. Phys. Lipids* 66, 225–230. doi: 10.1016/0009-3084(93)90010-z

Fernandes, A. M., Messias, M. C., Duarte, G. H., de Santis, G. K., Mecatti, G. C., Porcari, A. M., et al. (2020). Plasma Lipid Profile Reveals Plasmalogens as Potential Biomarkers for Colon Cancer Screening. *Metabolites* 10:262. doi: 10.3390/metabo10060262

Ford, D. A., and Hale, C. C. (1996). Plasmalogen and anionic phospholipid dependence of the cardiac sarcolemmal sodium-calcium exchanger. *FEBS Lett.* 394, 99–102. doi: 10.1016/0014-5793(96)00930-1

Fujino, T., Yamada, T., Asada, T., Ichimaru, M., Tsuboi, Y., Wakana, C., et al. (2018). Effects of plasmalogen on patients with mild cognitive impairment: a Randomized, Placebo-Controlled Trial in Japan. *J. Alzheimers Dis. Park.* 8:419. doi: 10.4172/2161-0460.1000419

Fujino, T., Yamada, T., Asada, T., Tsuboi, Y., Wakana, C., Mawatari, S., et al. (2017). Efficacy and blood plasmalogen changes by oral administration of plasmalogen in patients with mild Alzheimer's disease and mild cognitive impairment: a multicenter, randomized, double-blind, placebo-controlled trial. *EbioMedicine* 17, 199–205. doi: 10.1016/j.ebiom

Gawrisch, K., and Soubias, O. (2008). Structure and dynamics of polyunsaturated hydrocarbon chains in lipid bilayers-significance for GPCR function. *Chem. Phys. Lipids* 153, 64–75. doi: 10.1016/j.chemphyslip.2008.02.016

Glaser, P. E., and Gross, R. W. (1994). Plasmenylethanolamine facilitates rapid membrane fusion: a stopped-flow kinetic investigation correlating the propensity of a major plasma membrane constituent to adopt an HII phase with its ability to promote membrane fusion. *Biochemistry* 33, 5805–5812. doi: 10.1021/bi00185a019

Glaser, P. E., and Gross, R. W. (1995). Rapid plasmenylethanolamine-selective fusion of membrane bilayers catalyzed by an isoform of glyceraldehyde-3-phosphate dehydrogenase: discrimination between glycolytic and fusogenic roles of individual isoforms. *Biochemistry* 34, 12193–12203. doi: 10.1021/bi00038a013

Goldfine, H. (2010). The appearance, disappearance and reappearance of plasmalogens in evolution. *Prog. Lipid Res.* 49, 493–498. doi: 10.1016/j.plipres.2010.07.003

Han, X. L., and Gross, R. W. (1990). Plasmenylcholine and phosphatidylcholine membrane bilayers possess distinct conformational motifs. *Biochemistry* 29, 4992–4996. doi: 10.1021/bi00472a032

Han, X. L., and Gross, R. W. (1991). Proton nuclear magnetic resonance studies on the molecular dynamics of plasmenylcholine/cholesterol and phosphatidylcholine/ cholesterol bilayers. *Biochim. Biophys. Acta* 1063, 129–136. doi: 10.1016/0005-2736(91)90362-c

Hayashi, H., and Oohashi, M. (1995). Incorporation of acetyl-CoA generated from peroxisomal beta-oxidation into ethanolamine plasmalogen of rat liver. *Biochim. Biophys. Acta* 1254, 319–325. doi: 10.1016/0005-2760(94)00194-4

Hermetter, A., Stutz, H., Franzmair, R., and Paltauf, F. (1989). l-O-Trityl-sn-glycero-3- phospho-choline: a new intermediate for the facile preparation of mixed-acid 1,2-diacyl- glycero-phosphocholines. *Chem. Phys. Lipids* 50, 57–62. doi: 10.1016/0009-3084(89)90026-1

Hoefler, G., Paschke, E., Hoefler, S., Moser, A. B., and Moser, H. W. (1991). Photosensitized killing of cultured fibroblasts from patients with peroxisomal disorders due to pyrene fatty acid-mediated ultraviolet damage. *J. Clin. Invest.* 88, 1873–1879. doi: 10.1172/JCI115509

Honsho, M., Abe, Y., and Fujiki, Y. (2017). Plasmalogen biosynthesis is spatiotemporally regulated by sensing plasmalogens in the inner leaflet of plasma membranes. *Sci. Rep.* 7:43936. doi: 10.1038/srep43936

Jiménez-Rojo, N., and Riezman, H. (2019). On the road to unraveling the molecular functions of ether lipids. *FEBS Lett.* 593, 2378–2389. doi: 10.1002/1873-3468.13465

Jurak, M., Mroczka, R., and Łopucki, R. (2018). Properties of Artificial Phospholipid Membranes Containing Lauryl Gallate or Cholesterol. *J. Membr. Biol.* 251, 277–294. doi: 10.1007/s00232-018-0025-z

Khaselev, N., and Murphy, R. C. (1999). Susceptibility of plasmenyl glycerophosphoethanolamine lipids containing arachidonate to oxidative degradation. *Free Radic. Biol. Med.* 26, 275–284. doi: 10.1016/s0891-5849(98)00211-1

Kirschner, D. A., and Ganser, A. L. (1982). Myelin labeled with mercuric chloride. Asymmetric localization of phosphatidylethanolamine plasmalogen. *J. Mol. Biol.* 157, 635–658. doi: 10.1016/0022-2836(82)90503-4

Koivuniemi, A. (2017). The biophysical properties of plasmalogens originating from their unique molecular architecture. *FEBS Lett.* 591, 2700–2713. doi: 10.1002/1873-3468.12754

Lagarde, M., Hachem, M., Bernoud-Hubac, N., Picq, M., Véricel, E., and Guichardant, M. (2015). Biological properties of a DHA-containing structured phospholipid (AceDoPC) to target the brain. *Prostaglandins Leukot. Essent. Fatty Acids* 92, 63–65. doi: 10.1016/j.plefa.2014.01.005

Liegel, R. P., Ronchetti, A., and Sidjanin, D. J. (2014). Alkylglycerone phosphate synthase (AGPS) deficient mice: models for rhizomelic chondrodysplasia punctate type 3 (RCDP3) malformation syndrome. *Mol. Genet. Metab. Rep.* 1, 299–311. doi: 10.1016/j.ymgmr.2014.06.003

Liu, D., Nagan, N., Just, W. W., Rodemer, C., Thai, T. P., and Zoeller, R. A. (2005). Role of dihydroxyacetonephosphate acyltransferase in the biosynthesis of plasmalogens and nonether glycerolipids. *J. Lipid Res.* 46, 727–735. doi: 10.1194/jlr.M400364-JLR200

Lohner, K. (1996). Is the high propensity of ethanolamine plasmalogens to form non-lamellar lipid structures manifested in the properties of biomembranes? *Chem. Phys. Lipids* 81, 167–184. doi: 10.1016/0009-3084(96)02580-7

Lohner, K., Balgavy, P., Hermetter, A., Paltauf, F., and Laggner, P. (1991). Stabilization of non-bilayer structures by the etherlipid ethanolamine plasmalogen. *Biochim. Biophys. Acta* 1061, 132–140. doi: 10.1016/0005-2736(91)90277-f

Madrid, E., and Horswell, S. L. (2013). Effect of headgroup on the physicochemical properties of phospholipid bilayers in electric fields: size matters. *Langmuir* 29, 1695–1708. doi: 10.1021/la304455d

Morandat, S., Bortolato, M., Anker, G., Doutheau, A., Lagarde, M., Chauvet, J. P., et al. (2003). Plasmalogens protect unsaturated lipids against UV-induced oxidation in monolayer. *Biochim. Biophys. Acta* 1616, 137–146. doi: 10.1016/j.bbamem.2003.08.001

Munn, N. J., Arnio, E., Liu, D., Zoeller, R. A., and Liscum, L. (2003). Deficiency in ethanolamine plasmalogen leads to altered cholesterol transport. *J. Lipid Res.* 44, 182–192. doi: 10.1194/jlr.m200363-jlr200

Paltauf, F. (1994). Ether lipids in biomembranes. *Chem. Phys. Lipids* 74, 101–139. doi: 10.1016/0009-3084(94)90054-x

Paul, S., Lancaster, G. I., and Meikle, P. J. (2019). Plasmalogens: a potential therapeutic target for neurodegenerative and cardiometabolic disease. *Prog. Lipid Res*. 74, 186–195. doi: 10.1016/j.plipres.2019.04.003

Pike, L. J., Han, X., Chung, K. N., and Gross, R. W. (2002). Lipid rafts are enriched in arachidonic acid and plasmenylethanolamine and their composition is independent of caveolin-1 expression: a quantitative electrospray ionization/mass spectrometric analysis. *Biochemistry* 41, 2075–2088. doi: 10.1021/bi0156557

Post, J. A., Verkleij, A. J., Roelofsen, B., and Op de Kamp, J. A. (1988). Plasmalogen content and distribution in the sarcolemma of cultured neonatal rat myocytes. *FEBS Lett.* 240, 78–82. doi: 10.1016/0014-5793(88)80343-0

Rambold, A. S., Cohen, S., and Lippincott-Schwartz, J. (2015). Fatty acid trafficking in starved cells: regulation by lipid droplet lipolysis, autophagy, and mitochondrial fusion dynamics. *Dev. Cell* 32, 678–692. doi: 10.1016/j.devcel.2015.01.029

Rodemer, C., Thai, T. P., Brugger, B., Kaercher, T., Werner, H., Nave, K. A., et al. (2003). Inactivation of ether lipid biosynthesis causes male infertility, defects in eye development and optic nerve hypoplasia in mice. *Hum. Mol. Genet.* 12, 1881–1895. doi: 10.1093/hmg/ddg191

Rog, T., and Koivuniemi, A. (2016). The physicochemical properties of ethanolamine plasmalogens revealed by atomistic molecular dynamics simulations. *Biochim. Biophys. Acta* 58, 97–103. doi: 10.1016/j.bbamem.2015.10.023

Salem, N. Jr., Litman, B., Kim, H. Y., and Gawrisch, K. (2001). Mechanisms of action of docosahexaenoic acid in the nervous system. *Lipids* 36, 945–959. doi: 10.1007/s11745-001-0805-6

Shi, X., Tarazona, P., Brock, T. J., Browse, J., Feussner, I., and Watts, J. L. (2016). A Caenorhabditis elegans model for ether lipid biosynthesis and function. *J. Lipid Res.* 57, 265–275. doi: 10.1194/jlr.M064808

Sindelar, P. J., Guan, Z., Dallner, G., and Ernster, L. (1999). The protective role of plasmalogens in iron-induced lipid peroxidation. *Free Radic. Biol. Med.* 26, 318–324. doi: 10.1016/S0891-5849(98)00221-4

Tan, O. L., Almsherqi, Z. A., and Deng, Y. (2005). A simple mass culture of the amoeba Chaos carolinense. *Protistology* 4, 185–190.

Teichman, R. J., Cummins, J. M., and Takei, G. H. (1974). The characterization of a malachite green stainable, glutaraldehyde extractable phospholipid in rabbit spermatozoa. *Biol. Reprod.* 10, 565–577. doi: 10.1095/biolreprod10.5.565

Teichman, R. J., Fujimoto, M., and Yanagimachi, R. (1972). A previously unrecognized material in mammalian spermatozoa as revealed by malachite green and pyronine. *Biol. Reprod.* 7, 73–81. doi: 10.1093/biolreprod/7.1.73

Vieira, D. B., and Gamarra, L. F. (2016). Getting into the brain: liposome-based strategies for effective drug delivery across the blood-brain barrier. *Int. J. Nanomedicine* 11, 5381–5414. doi: 10.2147/ijn.s117210

Wang, C. M., Almsherqi, Z. A., McLachlan, C. S., Matthews, S., Ramachandran, M., Tay, S. K. T., et al. (2011). Acute starvation in C57BL/6J mice increases myocardial UCP2 and UCP3 protein expression levels and decreases mitochondrial bio-energetic function. *Stress* 14, 66–72. doi: 10.3109/10253890.2010.506931

Wassall, S. R., and Stillwell, W. (2008). Docosahexaenoic acid domains: the ultimate non-raft membrane domain. *Chem. Phys. Lipids* 153, 57–63. doi: 10.1016/j.chemphyslip.2008.02.010

Werner, E. R., Keller, M. A., Sailer, S., Lackner, K., Koch, J., Hermann, M., et al. (2020). The TMEM189 gene encodes plasmanylethanolamine desaturase which introduces the characteristic vinyl ether double bond into plasmalogens. *Proc. Natl. Acad. Sci. U. S. A.* 117, 7792–7798. doi: 10.1073/pnas.1917461117

Wiesner, P., Leidl, K., Boettcher, A., Schmitz, G., and Liebisch, G. (2009). Lipid profiling of FPLC-separated lipoprotein fractions by electrospray ionization tandem mass spectrometry. *J. Lipid Res.* 50, 574–585. doi: 10.1194/jlr.D800028-JLR200

Wood, P. L., Smith, T., Lane, N., Khan, M. A., Ehrmantraut, G., and Goodenowe, D. B. (2011). Oral bioavailability of the ether lipid plasmalogen precursor, PPI-1011, in the rabbit: a new therapeutic strategy for Alzheimer's disease. *Lipids Health Dis.* 10:227. doi: 10.1186/1476-511x-10-227

Yaghmur, A., Ghazal, A., Ghazal, R., Dimaki, M., and Svendsen, W. E. (2019). A hydrodynamic flow focusing microfluidic device for the continuous production of hexosomes based on docosahexaenoic acid monoglyceride. *Phys. Chem. Chem. Phys.* 21, 13005–13013. doi: 10.1039/c9cp02393c

Yamashita, S., Hashimoto, M., Haque, A. M., Nakagawa, K., Kinoshita, M., Shido, O., et al. (2017). Oral Administration of Ethanolamine Glycerophospholipid Containing a High Level of Plasmalogen Improves Memory Impairment in Amyloid β-Infused Rats. *Lipids* 52, 575–585. doi: 10.1007/s11745-017-4260-3

Zoeller, R. A., Lake, A. C., Nagan, N., Gaposchkin, D. P., Legner, M. A., and Lieberthal, W. (1999). Plasmalogens as endogenous antioxidants: somatic cell mutants reveal the importance of the vinyl ether. *Biochem. J.* 338, 769–776. doi: 10.1042/0264-6021:3380769

Conflict of Interest: The author declares that the research was conducted in the absence of any commercial or financial relationships that could be construed as a potential conflict of interest.

The handling editor declared a shared membership in a society with the author at time of review.

Advantages of publishing in Frontiers

OPEN ACCESS
Articles are free to read
for greatest visibility
and readership

FAST PUBLICATION
Around 90 days
from submission
to decision

HIGH QUALITY PEER-REVIEW
Rigorous, collaborative,
and constructive
peer-review

TRANSPARENT PEER-REVIEW
Editors and reviewers
acknowledged by name
on published articles

Frontiers
Avenue du Tribunal-Fédéral 34
1005 Lausanne | Switzerland

Visit us: www.frontiersin.org
Contact us: frontiersin.org/about/contact

REPRODUCIBILITY OF RESEARCH
Support open data
and methods to enhance
research reproducibility

DIGITAL PUBLISHING
Articles designed
for optimal readership
across devices

FOLLOW US
@frontiersin

IMPACT METRICS
Advanced article metrics
track visibility across
digital media

EXTENSIVE PROMOTION
Marketing
and promotion
of impactful research

LOOP RESEARCH NETWORK
Our network
increases your
article's readership